BULLETIN OF THE MINERAL RESEARCH AND EXPLORATION

Foreign Edition | 2019 | 158 | ISSN : 0026-4563 E-ISSN : 2651-3048

CONTENTS

CONTACT
Redaksiyon Kurulu Başkanlığı
Maden Tetkik ve Arama Genel Müdürlüğü
Genel Müdürlük Binası (A Block)
Üniversiteler Mah. Dumlupınar Bulvarı No: 139
06800 Çankaya/ANKARA/TURKEY
e-mail: redaksiyon@mta.gov.tr

Bull. Min. Res. Exp. is indexed and abstracted in TR Dizin, Emerging Source Citation Index (ESCI), Clarative Analytics Master List, Georef, Geological Abstracts, Mineralogic Abstracts, DOAJ and Scopus database. The Bulletin of the Mineral Research and Exploration is published in two issues in a year. Each bulletin is printed in Turkish and English languages as two separate issues. The English and Turkish issues of the "Bulletin of the Mineral Research and Exploration" can be obtained from "BDT Department" with charge, either directly or ordered by adding postage fee from the correspondence address. E-Mail: bdt@mta.gov.tr The section of "notes to the authors", format, copyright and other information can be obtained from www.mta.gov.tr as PDF files.

Printed Date: 15.04.2019
Printing House: Kuban Matbaacılık - İvedik Organize Sanayi Matbaacılar Sitesi 1514. Sokak No: 20 Phone: 0312 395 2070 Fax: 0312 395 3723 www.kubanmatbaa.com

PERIODICAL

ISSN: 0026-4563

E-ISSN: 2651-3048

Bull. Min. Res. Exp. (2019) 158: 1-29

Bulletin of the Mineral Research and Exploration

http://bulletin.mta.gov.tr

Tectonostratigraphic characteristics of the area between Çayeli (Rize) and İspir (Erzurum)

İsmet ALAN[a*], Veli BALCI[b], Halil KESKİN[c], İbrahim ALTUN[d], Nevzat BÖKE[e], Hünkar DEMİRBAĞ[f], Sedat ARMAN[g], Hasan ELİBOL[h], Mustafa SOYAKİL[i], Alican KOP[j] and Nurullah HANİLÇİ[k]

[a]*General Directorate of Mineral Research and Exploration, Department of Geol. Res., Ankara, TURKEY orcid.org/0000-0002-0072-0580*
[b] *General Directorate of Mineral Research and Exploration, Department of Geol. Res., Ankara, TURKEY orcid.org/0000-0003-0892-0007*
[c] *General Directorate of Mineral Research and Exploration, Department of Geol. Res., Ankara, TURKEY orcid.org/0000-0002-4566-8106*
[d] *General Directorate of Mineral Research and Exploration, Department of Geol. Res., Ankara, TURKEY orcid.org/0000-0002-8239-1281*
[e] *General Directorate of Mineral Research and Exploration Adana District Office, Adana, TURKEY orcid.org/0000-0003-4286-6841*
[f] *General Directorate of Mineral Research and Exploration, Department of Geol. Res., Ankara, TURKEY orcid.org/0000-0001-5666-7988*
[g] *General Directorate of Mineral Research and Exploration (MTA), Konya District Office, Konya, TURKEY orcid.org/0000-0002-6002-2979*
[h] *General Directorate of Mineral Research and Exploration, Department of Geol. Res., Ankara, TURKEY orcid.org/0000-0002-7645-2340*
[i] *General Directorate of Mineral Research and Exploration Adana District Office, Adana, TURKEY orcid.org/0000-0002-2938-0110*
[j] *Kahramanmaraş Sütçü İmam Univ., Fac. of Eng. and Arch., Dept. of Geol. Eng., Kahramanmaraş, TURKEY orcid.org/0000-0002--1420-4042*
[k] *İstanbul Univversity-Cerrahpaaş, Department of Geological Engineering, Avcılar Campus, İst., TURKEY orcid.org/0000-0002-7720-1551*

Research Article

Keywords:
Eastern pontides, Maçka tectonic slice, Taşköprü tectonic slice, tectono-stratigraphy, magmatism.

ABSTRACT

The study area is located in the Eastern Pontides between Rize, Çayeli, Arhavi, İspir and İkizdere. In this area, Maçka Tectonic Slice (MTS) and Taşköprü Tectonic Slice (TTS) are exposed. MTS is composed from old to young; Late Jurassic-Early Cretaceous limestone (Berdiga fm.); Turonian-Santonian conglomerate, sandstone, micritic limestone, siltstone, marl, basaltic, basaltic-andesitic lava, pyroclastites (Çatak fm.); Santonian rhyolitic, dacitic lava, pyroclastites, sandstone, clayey limestone (Kızılkaya fm.); late Santonian-Campanian basaltic, andesitic lava, pyroclastites, sandstone, clayey limestone (Cağlayan fm.); Campanian-Mastrihtian rhyolitic, dacitic lava, pyroclastites, sandstone, clayey limestone (Çayırbağ fm.);late Maastrichtian-Danian sandstone, claystone, tuff, marl, clayey limestone (Cankurtaran fm.). Sedimentary, volcanosedimentary units in the Late Paleocene-Quaternary range (Erenler, Kaplıca, Melyat, Pazar, Hamidiye formations, and Handüzü, Çağırankaya volcanites) unconformably overlies the MTS. In the study area, Turonian-Maastrichtian basaltic andesitic lavaş, pyroclastites and sandstone, micritic limestone, claystone units (Yağmurdere fm.) belonging to TTS are observed, and Early-Middle Eocene sedimentary and volcanosedimentary units (Yedigöze, Çoruh formations) unconformably overlies the TTS. According to Ar/Ar dating, Çayırbağ formation was determined as 83.2 ± 1.0 Ma, Melyat formation as 47.8 ± 1.6 Ma, and Handüzü volcanics as 4.25 ± 0.55 Ma for andesite level and as 3.93 ± 0.46 Ma for dacite level. The MTS was intruded by Cretaceous-Paleocene Kaçkar granitoid I, Eocene Kaçkar granitoid II, Late Eocene Ardeşen gabbro, while the TTS was intruded by Cretaceous-Paleocene Kaçkar granitoid-I, Late Eocene Güllübağ monzonite.

Received Date: 26.02.2016
Accepted Date: 04.05.2018

1. Introduction

The study area is located in the Eastern Pontides and covers an area of approximately 4200 km^2 between the east and south of Rize, Çayeli, Arhavi, İspir and İkizdere (Figure 1). Geologically, the Black Sea mountain range were first described by the Hamilton (1842) as Pontides. The Eastern Pontides were divided by different researchers as; north zone, middle zone and south zone (Gattinger, 1956); north zone and south zone (Bektaş et al., 1995), Hopa-Borçka, Artvin-Yusufeli (Arni, 1939; Bektaş et al.,

* *Corresponding author: İsmet ALAN, ismet.alan@mta.gov.tr*
http://dx.doi.org/10.19111/bulletinofmre.465317.

1987; Güven, 1993; Kurt et al., 2006) and Olur-Tortum zone (Konak et al., 2001). According to these definitions the study area is located in north zon, in Pontide autochthonous of Akeniz (1988), and in Hopa-Borçka zone of Konak et al. (1991, 2001). Yılmaz et al. (1997) stated that Eastern Pontides are part of the southern part of the Trans-Caucasus, and represented by the Adjara-Trialeti unit in the north and the Artvin-Bollisi unit in the south. They also expressed that the Late Cretaceous arc and back-arc deposits of Pontide and Trans-Caucasus are stratigraphically similar. For the first time, data from different studies have been compiled by Güven (1998), and 1/100.000 scaled geological map of a part of the Easrtern Pontides have been derived. This map has been the basis for many of the subsequent studies. The Eastern Pontides have been attracted by many earth scientists (Çağatay and Boyle, 1977; Çağatay, 1993; Gökçe and Spiro, 2000; Arni, 1939; Şengör et al., 1981; Gedik et al., 1992; Okay and Şahintürk, 1997*a*, *b*; Yılmaz et al., 1997; Boztuğ et al., 2001; Eyüboğlu et al., 2014) due to both geodynamic evolution of the region and contained Kuroko-type VMS (volcanogenic massive sulpide) deposits (e.g., Lahanos, Çayeli and Murgul Cu-Zn deposits). Today, both the Kuroko-type deposits occurred associated with the Late Cretaceous dacitic-ryolitic volcanism, and the porphyry, skarn and epithermal type deposits associated with the magmatic intrusions of different age range between the Late Cretaceous and Eocene, attracts by many scientists and the mining industry.

There are different opinions about the geodynamic evolution of the Pontide belt. Subduction polarity of Eastern Pontides suggested as; to northward from the Paleozoic to the Eocene (e.g. Dewey et al., 1973; Eyüboğlu et al., 2007), to northward from the Paleozoic to end of the Eocene (e.g. Adamia et al., 1977; Ustaömer and Robertson, 1996), and to soutward from the Paleozoic to the Middle Jurassic, and then to northward from the Late Cretaceous to end of the Eocene (Şengör and Yılmaz 1981; Okay and Şahintürk, 1997*b*). It is stated that the first transgression on the Paleozoic basement in the Eastern Pontides started in Liassic (e.g. Okay and Şahintürk, 1997*a*; Ustaömer and Robertson, 2010), and the collision between the Pontides and the Anatolid-Taurides occurred during the Paleocene-Early Eocene period (e.g. Ustaömer and Robertson, 1996; Okay and Şahintürk, 1997*a*, *b*). While some researchers separated the Eastern Pontides into nappe structures (Akdeniz et al., 1994; Akdeniz, 1988; Konak et al., 1991-2001), others separated into tectonic slices (Duygu et al., 2013; Uğuz et al., 2011). Uğuz et al. (2011) suggested that these tectonic slices have moved from north to south. Some of these tectonic slices are defined by Duygu et. al. (2013) as Maçka and Taşköprü tectonic slices.

Magmatic activities of different composition have occurred in different age ranges in Eastern Pontides. From these magmatites; the medium potassium calc-alkaline Early Cretaceous granitoids (Çamlıkaya) represent the early arc, the medium to high potassium calc-alkaline Late Cretaceous-Early Paleocene granitoids (Sırtyayla and Morselavat) represent the mature arc, the Paleocene leucogranite (Asniyar) represent the collision period, the high potassium calc-alkaline microgranites (Ayder and Samistal) represent the post collision, the low alkaline monzonite (Güllübağ), quartz monzodiorite (Halkalıtaş) ranging from medium potassium to low tholeiite, the low potassium tholeiitic gabbro (Ardeşen) and the diabase (İsina) represent the Late Eocene extensional period (Boztuğ et al., 2001). In addition, Kovenko (1943), İğdır (1971) and Gedik et al. (1992) stated that the Late Cretaceous volcanism in the Eastern Pontides is acidic and basic in character.

Important Kuroko-type Cu-Zn deposits in Turkey (e.g. Murgul, Çayeli, Kutlular, Lahanos, Kanköy) is located in Eastern Pontides in the Santonian aged Kızılkaya formation, and the Çayeli Cu-Zn deposit is located in study area. The study area has an important potential for such mineralizations, but the Campanian-Maastrichtian aged Çayırbağ formation containing similar lithologies to the Kızılkaya formation in which the mineralization is found is confused along the Eastern Pontides. For the exploration and development of the mineralization potential of the region, it is necessary to well construct the stratigraphic sequence correctly, to make detailed geological maps and to construct the geodynamic evolution of the region in the direction of the data. In this study; (i) for the first time, 1 / 25.000 scaled detail basic geological maps of the region were made in accordance with the stratigraphic relations and standards; (ii) the paleontological and radiometric ages obtained and then the lithostratigraphic and chronostratigraphic units were re-assessed and comments on the stratigraphy of the region were made; (iii) and lithological and volcanic features of the Taçköprü tectonic slices and their relationship with each other have been examined in a regional sense and the tectonostratigraphic location of the region has been tried to be explained.

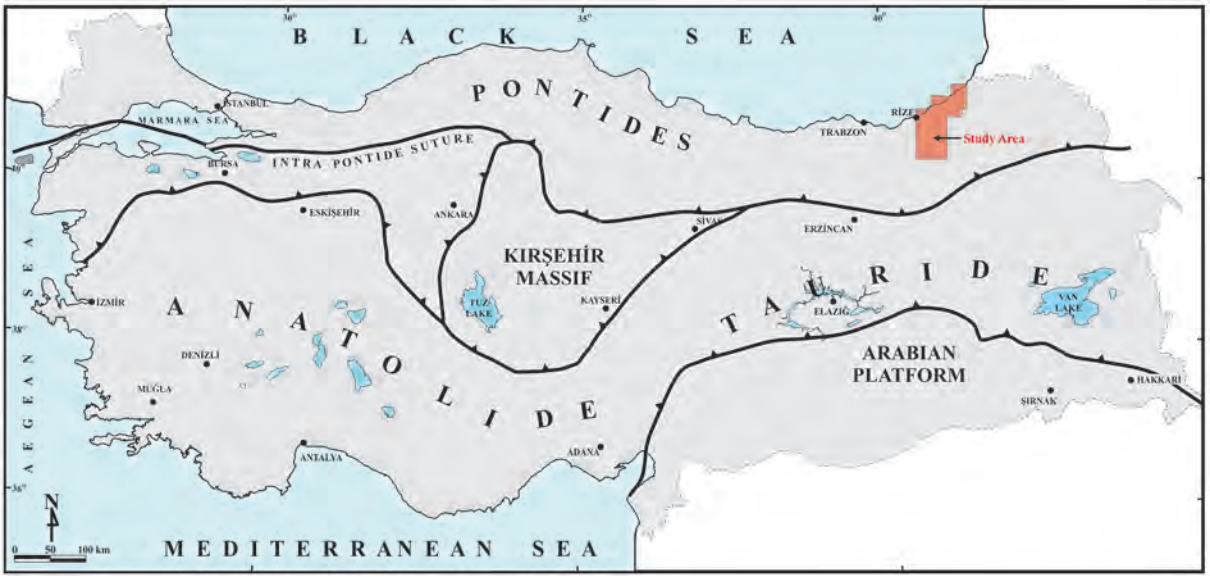

Figure 1- Location map of the study area (Tectonic map simplified from Okay and Tüysüz, 1999; Robertson and Ustaömer, 2009).

2. Methods

Samples were taken in order to make paleontological determinations, petrographic study, and geochronological age determination by taking into consideration relations between upper and lower lithological contact, during mapping.

Thin sections were prepared in the General Directorate of Mineral Research and Exploration (MTA) laboratories from the samples taken for the purpose of petrographic studies and paleontological identification, and rock and texture were defined in polarizing microscope, and age determination was made by the expert paleontologists of the MTA. During these petrographic studies, less altered samples were determined which could be suitable for geochronological age determination. Geochemical analyzes were carried out, and then samples with low loss of ignition (LOI) content were selected for radiometric dating. Thus, for the radiometric age determination, dacite and andesite samples belonging to Handüzü volcanites, one dacite sample belonging to Çayırbağ formation and one basalt sample belonging to Melyat formation were selected. Age determinations of these samples have done geochronology laboratory of Actlabs (Canada) using the method ^{40}Ar / ^{39}Ar (Table 1). The samples wrapped in Al foil was loaded in evacuated and sealed quartz vial with K and Ca salts and packets of LP-6 biotite interspersed with the samples to be used as a flux monitor. The sample was irradiated in the nuclear reactor for 48 hours. The flux monitors were placed between every two samples, thereby allowing precise determination of the flux gradients within the tube. After the flux monitors were run, J values were then calculated for each sample, using the measured flux gradient. LP-6 biotite has an assumed age of 128.1 Ma. The neutron gradient deed not exceeded 0.5% on sample size. The Ar isotope composition was measured in a Micromass 5400 static mass spectrometer. 1200ºC blank of 40Ar did not exceed n*10-10 cc STP.

3. Stratigraphy and Tectonic

Within the study area; the sedimentary, plutonic and volcanic rocks in ages ranging from Late Jurassic-Early Cretaceous to Quaternary are observed. The units within specified age range were mapped by defining them in different tectonic slices (Figure 2a, b). In this study, considering the stratigraphy formed by Güven (1993, 1998) and the tectonic slices defined by Duygu and others (2013) in the vicinity of Maçka district in west of the study area, the units located in the study area were assessed in an order and tried to be explained by correlation. These slices of which their contact relationships are not observed in the study area but well observed in the near west of the study area, separate from each other with a thrust plane extending towards the area. This thrust line follows the Varda village north (Güneyce-Rize), and Polut mountain (Trabzon), and extends from from the north of the Zigana passageway to the study area (Duygu et al.,

Table 1- Within the scope of this study, radiometric age determinations of volcanic rocks with $^{40}Ar/^{39}Ar$ method (See Figure 2b for sample locations).

Sample ID / Separated Mineral	Rock Type	Formation Name	IIA (My) ±1s	TFA ±1 s	WMPA (My)±1s	Ca/K	Comments
HD1 groundmass	Dacite	Çayırbağ Formation	—	80.2±0.9	**83.2±1.0**	0.37-1.15	Three steps plateau
HD2 Amph+Px	Basalt	Melyat Formation	40.0±4.0	50.0±1.4	**47.8±1.6**	3.73-24.79	Three steps plateau
VB1 whole rock	Dacite	Handüzü Formation	10.29±1.76	5.48±0.39	**3.93±0.46**	15.10-52.99	Two steps low temperature intermediate plateau
VB2 whole rock	Andesite	Handüzü Formation	4.08±0.51	4.28±0.39	**4.25±0.55**	1.54-4.91	Four steps plateau

Explanation:
±1 s = Estimated uncertainty (1 sigma); **IIA** = Inverse Isochrone age **TFA** = Total fusion age;
WMPA = Weighted mean plateau age; **Ca/K =** Apparent Ca / K ratios;

2013). The thrust line between these slices, which are described under the name of Maçka and Taşköprü tectonic slices (Figure 2a), is not clearly seen on the field due to the uplift and erosional processes of the Kaçkar granitoid I. The type locality of the Taşköprü tectonic slice, which is observed under the Maçka tectonic slice, is the Taşköprü valley outside the study area in the Yağmurdere district, Gümüşhane province (Duygu et al., 2013). While the volcanic activity is less intense in Taşköprü tectonic slice than Maçka tectonic slice, the sedimentary rocks are more intense.

The Kızılkaya formation, which hosts Kuroko-type Cu-Zn deposits in the Eastern Pontides is in the Maçka tectonic slice. The absence of this formation in the Taşköprü tectonic slice has provide an important guide in distinguishing and to correlation of these tectonic slices. The units of the Maçka tectonic slice, which are well observed along the road route from the Akarsu village (Maçka) to the shore in west of the study area, give wide outcrops in the northern and central parts of the study area. Also in this study, the Kaçkar granitoid I, the Kaçkar granitoid II, the Güllübağ monzonite and the Ardeşen gabbro were explained under separate titles.

3.1. Maçka Tectonic Slice

In the study area, the slice in Late Jurassic-Early Cretaceous to late Maastrichtian-Danian time interval, is unconformably overlain by the Thanetian-Middle Eocene and Early-Middle Eocene units (Figure 3). The Maçka tectonic slice can be correlated with the Karabulduk tectonic slice of Uğuz et al. (2011).

3.1.1. Berdiga Formation (JKb)

The unit consisting mainly of neritic carbonates was named by Pelin (1977) around the Berdiga Mountains of Alucra village, Giresun. The unit give outcrops in limited areas in the study area. It is possible to see the outcrops of the limestones belonging to the Berdiga formation between Çatak formation and Kaçkar granitoid I in the west of Ortayayla (G45 b3), north of Ortayay and near Gölyayla (G45 d1, d2) (Figure 2b).

The formation is represented by gray, beigeish gray, middle-layered, locally cherty, abundant macro fossiliferous limestones deposited in shallow and shelf environments in the study area (Figure 4). The unit, which unconformably overlies the Liassic-Dogger Hamurkesen formation outside of the study area, is intruded by the Kaçkar granitoid I. The upper contact of the unit is unconformable with the Çatak formation (Figure 3). The apparent thickness of the unit, which is observed in limited outcrops in the study area, is between 50 and100 m. However, it is known from previous studies that the thickness of the unit in outside of the study area is varying between 100 and 300 meters.

There was not obtained fossil assemblage that give detailed age from the samples collected from the unit which has limited outcrops in the study area. But, the Early Cretaceous age was obtained from the fossil determination (Table 2) of a sample collected in the formation. According to the research carried out by Uğuz et al. (2011) in the near west of the study area the foraminiferous fossil assemblage of the Late Jurassic-Early Cretaceous age was obtained. The Late Jurassic-Early Cretaceous age was obtained from the

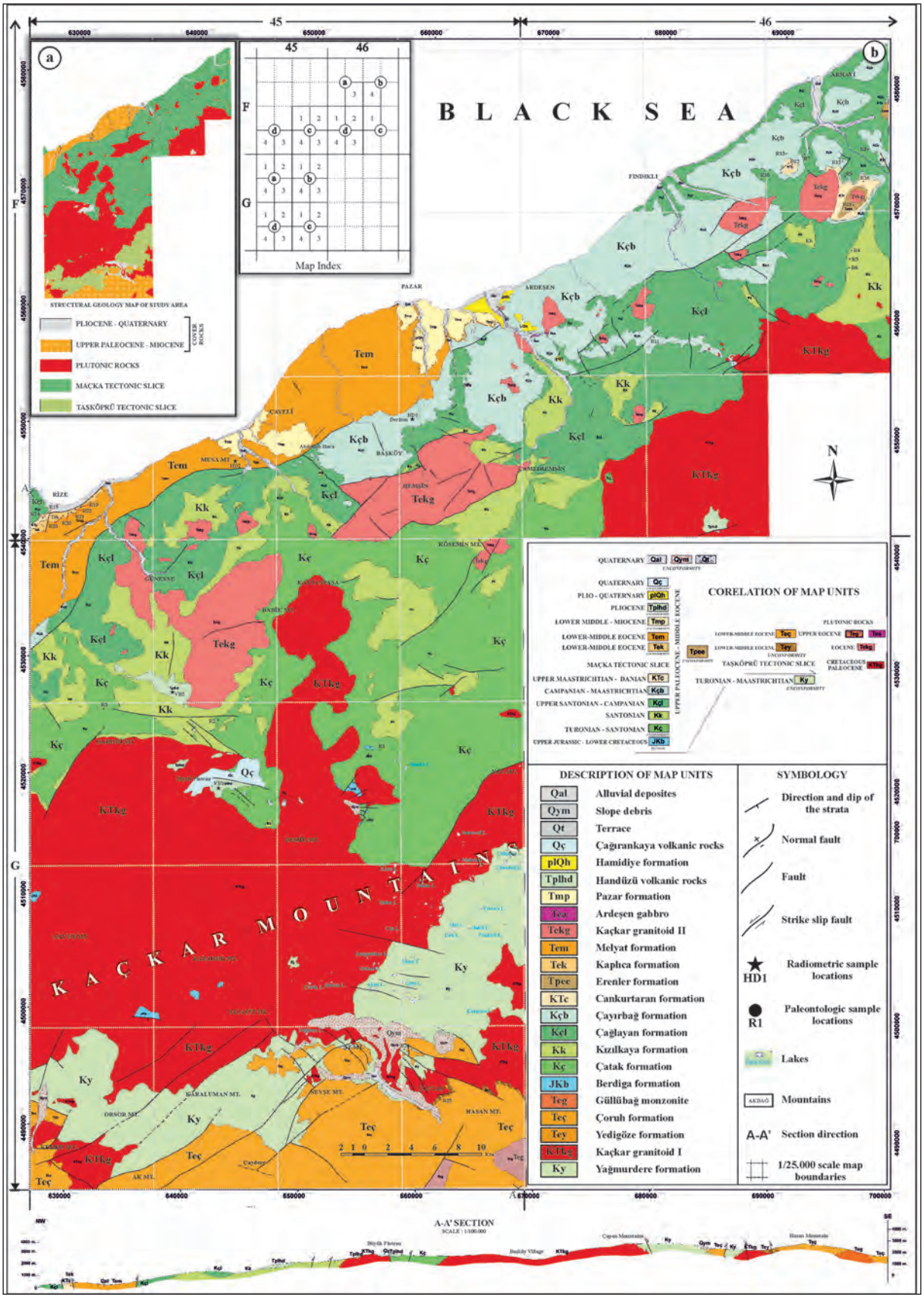

Figure 2- (a) Structural geology and (b) detail geological map and the cross section of the study area (vertical scale in the cross section exaggerated).

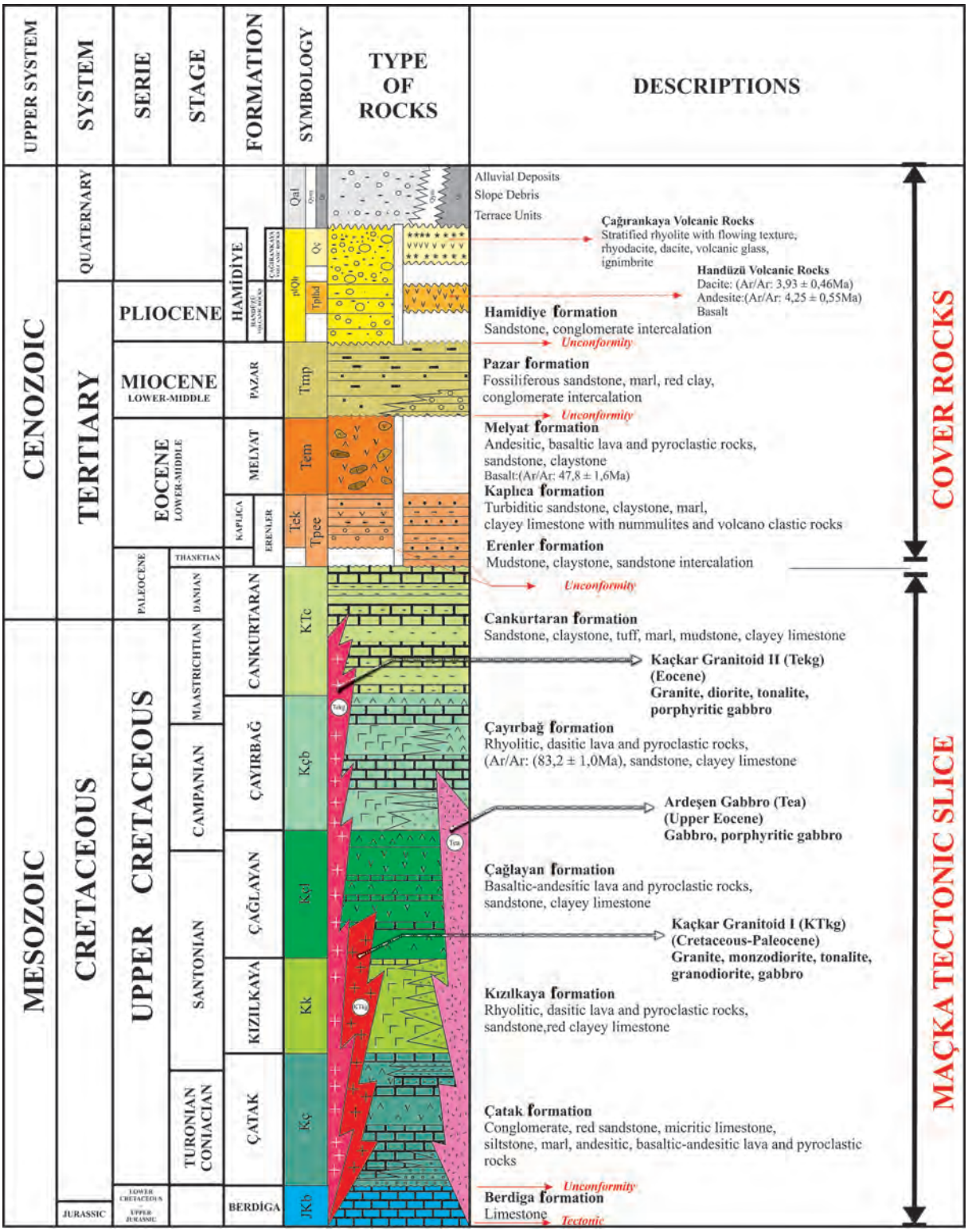

Figure 3- The generalized stratigraphic columnar section of the Maçka tectonic slice and its cover units.

Table 2- Fossil findings obtained from the units belonging to Maçka tectonic slice (Coordinates are UTM ED 1950).

Formation Name	Sample ID on Map (Figure 2b)	Sample Location	Age	Fossils
Berdiga	R1	Y: 655150 X: 4522750	Early Cretaceous	*Vercorsella* sp.
Çatak	R2	Y: 643100 X:4524900	Turonian	*Helvetoglobotruncana* cf. *helvetica* (Bolli), *Marginotruncana pseudolinneiana* Pessagno, *Whiteinella* sp., *Praeglobotruncana gibba* Klaus
	R3	Y: 633224 X: 4525850	Turonian – Santonian	*Macroglobigerinelloides* sp, *Heterohelix* sp., *Marginotruncana coronata (*Bolli), *Marginotruncana pseudolinneiana* Pessagno, *Globigerinelloides* sp.,
Kızılkaya	R6	Y: 696960 X: 4567330	Turonian – Santonian	*Marginotruncana coronata* (Bolli), *Marginotruncana pseudolinneiana* Pessagno, *Heterohelix* sp.
	R5	Y: 696905 X: 4567330	Coniasian– Santonian	*Dicarinella* cf. *concavata* (Brotzen), *Dicarinella asymetrica* (Sigal), *Marginotruncana asymetrica* Pessagno, *Macroglobigerinelloides* sp., *Heterohelix* sp.
	R4	Y: 696985 X: 4567362	Santonian	*Dicarinella asymetrica* (Sigal), *Marginotruncana* sp., *Macroglobigerinelloides* sp., *Heterohelix* sp.,
Çağlayan	R7	Y: 692100 X: 4573425	Santonian	*Dicarinella asymetrica* (Sigal), *Marginotruncana pseudolinneiana* Pessagno, *Marginotruncana coronata* (Bolli), *Heterohelix* sp., *Macroglobigerinelloides* sp., Globigerinellodidae
	R9	Y: 695420 X: 4572870	Late Santonian	*Spirillina* sp., *Dicarinella concavata* (Brotzen), *Dicarinella asymetrica* (Sigal), *Marginotruncana pseudolinneiana* Pessagno, *Marginotruncana coronata* (Bolli), *Inoceranus* sp.
	R10	Y: 688000 X: 4572500	Campanian	*Globotruncana linneiana* (d'Orbigny), *Globotruncanita* cf. *stuartiformis* (Dalbiez), *Globotruncanita* cf. *elevata* (Brotzen), *Rosita fornicata* Plummer, Heterohelixidae
	R8	Y: 698253 X: 4573842	Campanian– Maastrichtian	*Globotruncanita stuartiformis* (Dalbiez), *Globotruncana linneiana* (d'Orbigny), *Globotruncanita* sp., *Globigerinelloides* sp., *Heterohelix* sp. and radyolarya fosilleri
Çayırbağ	R11	Y: 680150 X: 4557775	Campanian– Maastrichtian	**Nannoplankton***: Arkhangelskiella cymbiformis* Vekshina, *Quadrum gothicum* (Deflandre), *Prediscosphaera cretacea* (Arkhangelsky), *Cretarhabdus crenulatus* Bramlette ve Martini, *Ceratolithoides aculeus* (Stradner), *Calculites obscurus* (Deflandre), *Micula decussata* Vekshina, *Lucianorhabus cayeuxii* Deflandre, *Watznaueria barnesae* (Black), *Reinhardtites levis* Prins and Sissingh, *Arkhangelskiella* sp.
	R12	Y: 696512 X: 4571728	Campanian– Maastrichtian	*Globotruncana arca* (Cushman), *Globotruncana linneiana* (d'Orbigny), *Globotruncana* cf. *bulloides* Vogler, *Globotruncana hilli* Pessagno, *Globotruncana* cf. *aegyptiaca* Nakkady, *Globotruncana ventricosa* White, *Globotruncanita angulata* (Tilev), *Globotruncanita stuartiformis* (Dalbiez), *Globotruncanita* cf. *conica* (White), *Contusotruncana* cf. *walfishensis* (Todd) and *Globotruncana* sp.
	R13	Y: 690066 X: 4573000	Campanian– Maastrichtian	*Globotruncana linneiana* (d'Orbigny), *Globotruncana cf. ventricosa* White, Globigerinidae
Cankurtaran	R14	Y: 626300 X: 4541150	Campanian– Maastrichtian	*Globotruncana arca* (Cushman), *Globotruncana linneiana* (d'Orbigny), *Globotruncana* cf. *linneiana* (d'Orbigny), *Globotruncana lapparenti* (Brotzen), *Globotruncana orientalis* El-Naggar, *Globotruncana mariei* Banner and Blow, *Globotruncana falsostuarti Sigal*, *Globotruncana* sp., *Contusotruncana fornicata* (Plummer), *Contusotruncana* cf. *walfishensis* (Todd), *Contusotruncana* cf. *potelliformis* (Gandolfi), *Pseudotextularia nutalli* (Voorwijk), *Heterohelix* sp., *Rugoglobigerina pennyi* Brönnimann, *Kuglerina rotundata* (Brönnimann)
	R16	Y: 696512 X: 4571728	Campanian– Maastrichtian	*Globotruncana bulloides* Vogler, *Globotruncanita stuartiformis* (Dalbiez), *Macroglobigerinelloides* sp., *Heterohelix* sp., Globigerinidae
	R15	Y: 626300 X: 4541150	Campanian– Maastrichtian	**Nannoplankton***: Arkhangelskiella cymbiformis* Vekshina, *Reinhardtites levis* Prins ve Sissingh, *Ceratolithoides aculeus* (Stradner), *Aspidolithus parcus parcus* (Stradner), *Lucianorhabus cayeuxii* Deflandre, *Calculites obscurus* (Deflandre), *Eiffellithus turriseiffelii* (Deflandre), *Micula decussata* Vekshina, *Micula concava* (Stradner), *Quadrum gothicum* (Deflandre), *Quadrum gartneri* Prins and Perch-Nielsen, *Microrhabdulus decoratus* Deflandre, *Glaukolithus compactus* (Bukry), *Prediscosphaera cretacea* (Arkhangelsky), *Stradneria crenulata* Bromlette and Martini, *Cribrosphaerella ehrenbergii* (Arkhangelsky), *Lithraphidites carniolensis carniolensis* Deflandre, *Watznaueria barnesae* (Black)
	R17	Y: 690145 X: 4573529	Maastrichtian	*Gansserina gansseri* (Bolli), *Globotruncanita* cf. *stuartiformis* (Dalbiez), *Globotruncana linneiana* (d'Orbigny), *Globotruncana* sp., *Heterohelix* sp., *Macroglobigerinelloides* sp., Globigerinidae, *Globotruncana arca* (Cushman)

Figure 4- View of gastropods and lamellibranch fossils in limestones of the Berdiga formation, reflecting the shallow marine deposition environments (East of Semköhot yayla, G45 b4).

similar units in Bayburt, Gümüşhane and Trabzon vicinities (Keskin et al.,1991; Korkmaz, 1993; Gürsoy et al., 1993; Güven, 1993-1998; Akdeniz et al., 1994; Okay and Şahintürk, 1997; Kurt et al., 2006)

Considering the lithologies and fossil content of the formation in the study area, it is understood that the formation is deposited in shallow marine environment and show shelf character. The Berdiga formation can be correlated with Sarıçiçek formation (Akdeniz et al., 1994) defined in Bayburt nappe in southern zone, and Hozbirikyayla formation (Ağar, 1977; Keskin et al., 1991) defined in around Bayburt.

3.1.2. Çatak Formation (Kç)

The type locality of the unit consisting of sandstone, siltstone, marl, shale and limestone and basalt, andesitic lava and pyroclastics is the Çatak village, located in south of the Maçka district, and was first named by Güven (1993). It is possible to see the rocks of the formation on the northern slopes of the Kaçkar Mountains, parallel to the ridges (Figure 2b).

Outside the study area, in the vicinity of Maçka, the unit begins to deposit with claret-red sandstones and conglomerates then continues upward with the alternation of grayish siltstone, marl, claystone, clayey limestone intercalating with greenish basaltic, andesitic lavas (Figure 5). In the study area, there are observed greenish, purple colored, spilitic, pillow type basaltic lavas (Figure 5) and medium layered greenish gray and purple colored, silicified, partly cherty micritic limestones alternating with pyroclastics. The andesitic intercalations are also observed in this section which is widely composed of volcanic rocks. There are peperitizations in lava layers occasionally. In the upper levels of the formation there are red to purple colored, fine to medium layered micritic limestones.

The Çatak formation unconformably overlies the Berdiga formation in south of the Kuyuculu Valley (G45 b4). At the same time, there is observed a crosscutting relationship with the Kaçkar granitoid I which its upper boundary is conformably overlain by the Kızılkaya formation (Figure 3). Outside the study area, the apparent thickness of the formation is defined as 1100 m in its type section (Maçka district) (Güven, 1998). However, the apparent thickness of the formation varies from 600 to 700 m in the study area.

The age of the formation was given as Turonian - Santonian from the fossil determinations of the samples collected from the micritic limestones in the formation (Table 2). Together with its faunal characteristics, the existence of turbiditic-pelagic sediments intercalating with volcanites indicates that the formation might have been deposited in slope-basin conditions in which the basic volcanism have accompanied to the sedimentary deposit. The Çatak formation can be correlated with the basic I series of Çekiç et al. (1984).

3.1.3. Kızılkaya Formation (Kk)

The unit, which is generally composed of rhyolite, dacites and pyroclastic rocks and clayey limestones, was first named by Güven (1993) as the Kızılkaya formation. It is possible to see the formation in the

Figure 5- View of pillow basaltic lavas within the Çatak formation (north of Kaptanpaşa, eastward view, G45b1).

form of outcrops, which are difficult to follow laterally, especially due to facial changes in the study area. The outcrops are observed in Yeşildere (G45 a1), Çamlıca (G45 a2), Kantarlı (G45 b1), Meydanköy (G45 b3), Madenköy (F45 c4, d3), Çamlıhemşin and the Fırtına River (F45 d4; figure 2b).

The formation mainly consists of rhyolitic and dacitic lavas and clayey limestones, and also the interlayers of purple sandstone (Figure 6). Dacitic lavas have yellowish beige, grayish green, pinkish colored (columnar) cooling surfaces. The unit, which has very coarse quartz grains, has evident feldspars and porphyritic texture. The alteration is very common in dacites. In these mostly yellowish brown altered areas, beige to white colored unaltered dacites are passed. The dacites are rich in pyrites and there are also observed argillization, chloritization and hematization in them. The rhyolites are mostly grayish white in color. Quartz grains in macroscopic scale are less distinct than dacite and are mainly observed in the form of silica, and they have less propagation than dacites. Ignimbrites are distinctive with their light green color and massive appearance. Pumice grains are dominant in ignimbrites in the form of accretion up to 20 m. Greenish gray, purple micritic limestone and pinkish quartz sandstone layers are also observed in ignimbrites. Since the Kuroko-type Cu-Zn deposits in the Eastern Pontides (Çayeli, Murgul, Lahanos and Kutlular) are located within this formation, the Kızılkaya formation is especially important for such deposits. Particularly the massive section of the Kuroko-type Cu-Zn deposits located in this formation are observed above ignimbrite levels and below micritic limestones and sandstones.

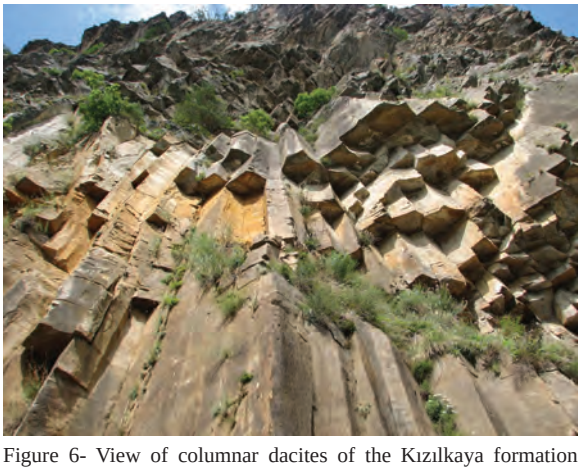

Figure 6- View of columnar dacites of the Kızılkaya formation (outside the study area, in north of the Maçka district, westward view, G43 a4).

The Kızılkaya formation conformably overlies the Turonian-Santonian Çatak formation and underlies the Late Santonian-Campanian Çağlayan formation (Figure 3). The thickness of the formation in the study area is variable, and appeartent thickness ranges between 300 and 400 meters.

In the fossil determination of the samples collected from purple micritic limestones in the formation, the Santonian age, the Coniacian - Santonian age and the Turonian - Santonian ages were obtained. The Santonian age was given to the Kızılkaya formation by taking into consideration the fossil assemblages (Table 2) of the unit, and the relationship of the upper and lower contact units.

Faunal and lithological characteristics of the Kızılkaya formation showed that the formation is deposited in pelagic and turbiditic environments in slope conditions, and acidic volcanism accompanied. The formation can be correlated with the lower level where asidic volcanism is effective in Esiroğlu formation of Uğuz (2011), with the first dacitic series of Schultze-Westrum (1960), with the Kaleciktepe dacitic member of the Tepeköy formation of Pelin (1977) and with the Makenet formation of Özsayar et al. (1982).

3.1.4. Çağlayan Formation (Kçl)

The unit, which overlies the acidic volcanism and is generally formed by the alternation of basalt-andesitic lava, pyroclastics, sandstone, marl and clayey limestone, was named as the Çağlayan formation by Güven (1993). It extends in the study area in east-west and northeast-southwest directions on slopes of the the Kaçkar Mountains by the sea. It is possible to see the outcrops of the formation in Güneysu, Dumankaya, Muradiye (G45 a1), Bulutlu, İslahiye (G45 a2), Yenihisar, Gürgenli and Büyükköy vicinity (F45 d3), Pazar-Hemşin road, (F45 c2, c3) Çamlıhemşin, Topluca district (F46 d4), the vicinity of the Tunca village (F46 d1, d2), south of Arhavi valley interior and the Arılı village (F46 b4; Figure 2b).

The unit consists of sandstone, marl, greenish gray and claret red limestone layers in alternating with basaltic, andesitic lava and pyroclastics. The lavas belonging to the unit bearing peperitic layers are green to dark gray, very hard and fractured. While pillow structures are seen in basaltic lavas, the prismatic (columnar) cooling surfaces are very rarely observed. Tuff and breccia are well bedded and

consist of limestone and lava fragments. Among these basic volcanic rocks, greenish, grayish, burgundy marl, sandstone and micritic limestone layers are seen. Agglomerates, volcano cemented spilites are basaltic and andesitic in composition and fine to medium bedded. There are occasionally observed slip-settlement structures within the unit.

The formation conformably overlies the Santonian Kızılkaya formation at the bottom and underlies the Campanian-Maastrichtian Çayırbağ formation at the top (Figure 3). Between Rize provincial center and the Çayeli district, it is seen tectonically in contact with Eocene units.

The Santonian, Kampanian- Maastrichtian, late Santonian and Campanian ages were obtained in the fossil determinations (Table 2) of the samples taken from the formation. Considering the fossil assemblages, age ranges and the upper and lower contact relationships, the age of the Çağlayan formation was given as the late Santonian-Campanian in this study.

The faunal and lithological features observed in the Çağlayan formation and the slip-settlement structures indicate that the unit may have been deposited under slope conditions where the basic volcanism is effective. The apparent thickness varies between 600 and 700 m in the study area. The Çağlayan formation can be correlated with the section in which the basic volcanism of the Esiroğlu formation is effective of Uğuz et al. (2011), the upper basic series of Schultze-Westrum (1960) and the basic II series of Çekiç et al. (1984).

3.1.5. Çayırbağ Formation (Kçb)

The unit, which is the last phase of the acidic volcano character of the Late Cretaceous period and is named by Güven (1993). It outcrops along the road cut of Pazar-Hemşin where the stone quarries are located (F45 b3), in the Aşıklar and Erenler villages (F45 b4), in the vicinity of Babadağ (F45 b3) and between Ardeşen and Arhavi nearly in NE-SW direction, along the low topography near the sea in the study area (Figure 2b).

The formation mainly consists of rhyolite, dacite, pyroclastics, sandstones and limestones, which constitutes the phases of acidic volcanism products (Figure 7). The rhyolites and dacites are mostly grayish-green and pink-colored and have

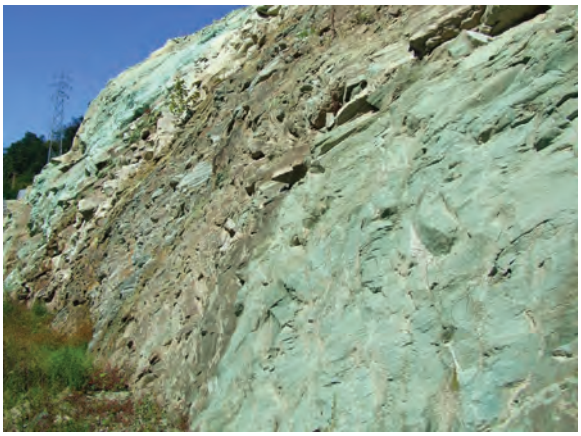

Figure 7- View from ignimbrites (green) and micritic limestones (brown) in the Çayırbağ formation (Rize city, west of Hurmalık village, İyidere-İkizdere road, northeast view, G44 b2).

prismatic (columnar) cooling surfaces in occasion. The alteration is widespread and white, beige and pinkish colored argillized products are encountered. In dacites and rhyolites, quartz grains and feldspars are visible and have porphyritic texture. Unlike the Kızılkaya formation, which has the similar features, there are not observed much pyrites in dacites and rhyolites belonging to the Çayırbağ formation. In the Çayırbağ formation, the light green ignimbrites are dominant and distinctive in pyroclastics and they exhibit a thickness of 15-20 m Greenish gray and burgundy, fine-to-medium bedded micritic limestones can be seen in ignimbrites. These lithologies can be seen especially on ridges of the Derinsu village and in the north of Ardeşen-Tunca village.

The formation conformably overlies the Çağlayan formation and underlies the Cankurtaran formation (Figure 3). In the study, the Early-Middle Eocene Kaplıca formation (without the Cankurtaran formation) unconformably overlies the Çayırbağ formation along the Hemşin road in south of the Pazar district.

The Campanian - Maastrichtian age was obtained in the fossil determinations of the samples collected from the formation (Table 2). Furthermore, radiometric age determinations (^{40}Ar / ^{39}Ar) of dacites (HD1, F45c3, 659500; 4552000) taken from the Çayırbağ formation in the study area were obtained as 83.2 ± 1.0 Ma (Figure 8a). Taking into account the ages and upper and lower contact relations of the unit, the Campanian - Maastrichtian age was given to the Çayırbağ formation.

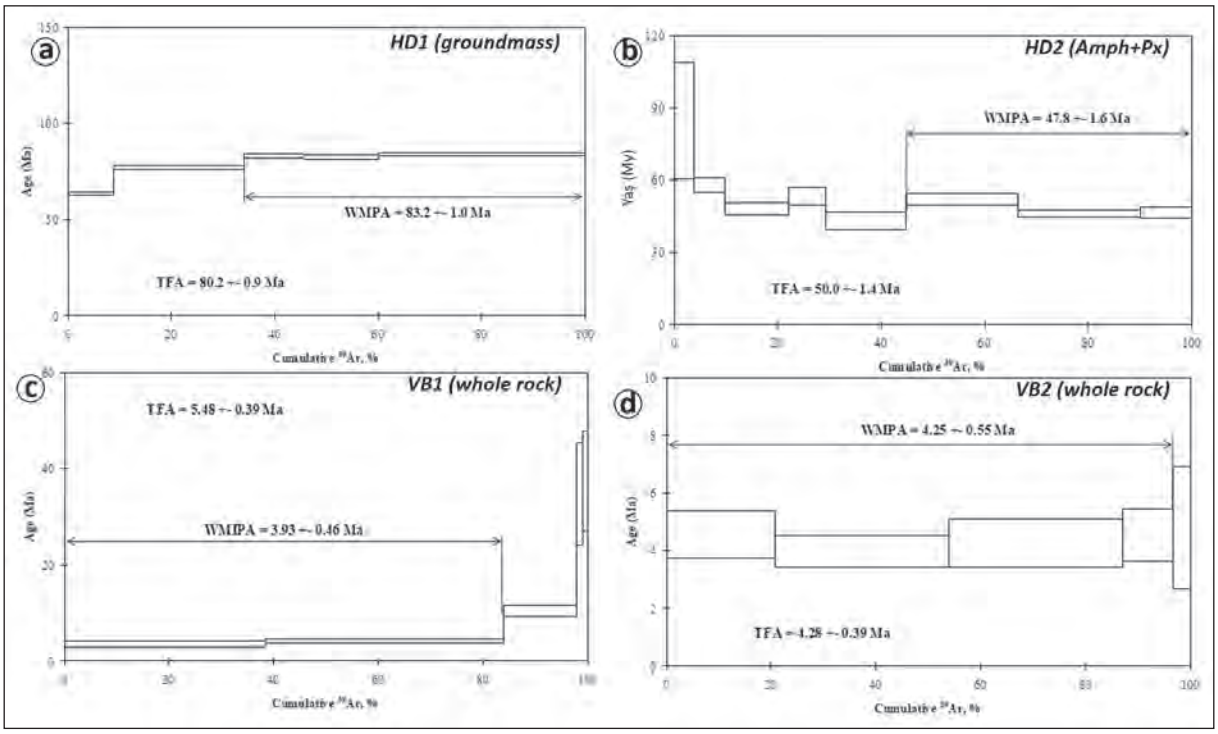

Figure 8- Ar-Ar plateau age for; (a) dacite of Çayırbağ formation, (b) basalt of Melyat formation, (c) dacite and (d) andesite of Handüzü formation.

The Çayırbağ formation was deposited in marine environment accompanied by the acidic volcanism. The deposition of micritic limestone occurred when the volcanism was inactive. The appearent thickness of this formation is between 150 and 200 m. The Çayırbağ formation can be correlated with the upper sections of the units investigated by Uğuz et al. (2011) below the Esiroğlu formation, the Tirebolu formation of Güven (1993) where the trachyandesitic lavas are dominant and the rock units introduced in the Eastern Pontides as second-phase dacitic series, the hematitic series defined by Kahraman et al. (1987) and with the dacitic lava and pyroclastics of mineralized sections defined by Güner et al. (1983).

3.1.6. Cankurtaran Formation (KTc)

The formation, which is mainly composed of sandstone, claystone and clayey limestone, was named as the Cankurtaran formation by Yılmaz et al. (1997). The Cankurtaran formation has small outcrops in the study area. It is possible to see the limited outcrops of the formation along the Kalkandere side road of Rize (F45 d4) and between the Derbent village and Başköy west (F46 b4) to the south of Arhavi.

The lower parts of the formation are mostly of clastic units. The succession begins with yellowish beige and greenish-colored, fine-to-medium bedded sandstone and claystone alternations and passes into marl, mudstone and carbonate levels in the upper layers (Figure 9). The upper levels of the formation are in the form of beige and burgundy colored, thin to medium bedded micritic limestones, with much fractures and micro faunas. The mudstones are also observed in the limestones in intermediate levels. Outside the study area, the presence of tuff, volcanic sandstone, agglomerate levels in the Cankurtaran formation is mentioned (Terlemez, 1986; F46 b3). The

Figure 9- View from the micritic limestones and sandstone layers in the upper levels of the Cankurtaran formation (southwest of the Rize provincial center, eastward view F45 d4).

folds in layers of the formation, slip-settlement and bottom structures are also seen.

The apparent thickness of the formation in the study area varies between 150 and 200 m. The thickness exceeds 250 m along the Hopa-Borçka road, in outside of study area. The Cankurtaran formation conformably overlies the Çayırbağ formation (Figure 3). However, the formation is unconformably overlain by the Erenler formation, which is the cover rock of the Maçka tectonic slice to the east of the study area, and by the Kaplıca formation to the near south of Rize.

The Campanian - Maastrichtian and Maastrichtian ages were obtained in the fossil determination of the samples collected from the Cankurtaran formation (Table 2). Kandemir et al. (2014) obtained Campanian-early Selandian age range from the formation to the east of the study area. In addition, Yılmaz et al. (1997) found Danian age at the upper levels of the formation in around the Hopa. According to data of previous studies, fossil contents and the gradational transition between the formation and the Çayırbağ formation at the bottom, and the unconformable contact with the Late Paleocene-Middle Eocene Erenler formation at the above, the age of the Cankurtaran formation should be late Maastrichtian-Danian.

The lithological and faunal characteristics of the Cankurtaran formation and its slip-and-settlement structures suggest that the unit may have been deposited under slope-basin conditions where the marine volcanism is effective. The environment is under the effect of the magmatic arc activity (Yılmaz et al., 1997). The Cankurtaran formation can be correlated with the Akveren formation (Badgley, 1959), Mescitli formation (Güven, 1993), one section of the Bakırköy formation (Güven, 1993), Fatsa formation (Terlemez and Yılmaz, 1980), Rize formation (Gedik and Korkmaz, 1987) and the Katila formation of Adamia et al. (1992).

3.2. Cover Units on the Maçka Tectonic Slice

The cover units, which unconformably overlie the Maçka tectonic slice are; the Late Paleocene-Middle Eocene Erenler Formation, the Early-Middle Eocene Kaplıca and Melyat formations, the Early-Middle Miocene Pazar formation, the Pliocene Handüzü volcanics, the Plio-Quaternary Hamidiye formation and the Quaternary Çağırankaya volcanics (Figure 3).

3.2.1. Erenler Formation (Tpee)

The sedimentary rocks, which are generally formed by the alternation of mudstone, claystone and sandstone in the east of the study area, Hopa and Borçka, were named as the Erenler formation by Yılmaz et al. (1997). The unit is observed in the vicinty of Aşağışahinler village in the southeast of Arhavi County in F46 b3 sheet and the Çatak Tepe (hill) in the southwest of Arılı in limited outcrops (Figure 2b). The large outcrops are located in the Hopa-Borçka region in east of the study area.

The unit is composed of greenish gray, brownish white, thin to medium bedded clastic rocks in turbiditic character such as mudstone, claystone and sandstone. It is possible to see the depositional traces like flute marks and canal structures in sandstones.

The formation unconformably overlies the Çağlayan, Çayırbağ and Cankurtaran formations in the study area (Figure 3). It is known that the unit, which its upper contact cannot be observed in the study area is transitional with the Middle Eocene Kabaköy formation in Hopa-Borçka region (Yılmaz et al., 1997). The apparent thickness of the unit, which has limited outcrops in the study area, is around 100-150 m. However, this thickness can vary between 500-750 m in east of the Hopa district (Yılmaz et al., 1997).

The Early Eocene age was obtained in the fossil determination of the samples collected from the Erenler formation (Table 3). However, Yılmaz et al. (1997) found that the formation was Middle Eocene in age, while Kandemir et al. (2014) found the Late Paleocene-Middle Eocene age for the same formation in east of the study area. Considering previous studies and fossil contents, the Late Paleocene-Middle Eocene age was given to the formation.

Faunal and lithological features indicate that the formation was deposited in a shallow marine and semi-pelagic environment. The sedimentary structures observed in the unit such as flute marks represent the semi-pelagic environment. The formation can be correlated with Erenler and Kaplıca formations (Gedik and Korkmaz, 1987), the lower levels of the Tonya formation (Kurt et al., 2006), one part of the Fındıkbeli formation (Pelin, 1977), Sarp formation (Adamia et al., 1992) and Yedigöze formation (Akdeniz et al., 1994).

Table 3- Fossil findings of the cover units on the Maçka tectonic slice (Cooridantes are UTM ED 1950).

Formation Name	Sample ID on Map (Figure 2b)	Sample Location	Age	Fossils
Erenler	R18	Y: 695484 X: 4569834	Early Eocene	**Nannoplankton***: Coccolithus crassus* Bramlette and Sullivan, *Ericsonia obruta* Perch-Nielsen, *Fasciculithus tympaniformis* Hay and Mohler, *Sphenolithus radians* Deflandre, *Sphenolithus anarrhopus* Bukry and Bramlette, *Neochiastozygus perfectus* Perch-Nielsen
Kaplıca	R19	Y: 630393 X: 4542704	Ypresian	**Nannoplankton***: Coccolithus crassus* Bramlette and Sullivan, *Ericsonia obruta* Perch-Nielsen, *Fasciculithus tympaniformis* Hay and Mohler, *Sphenolithus radians* Deflandre, *Sphenolithus anarrhopus* Bukry and Bramlette, *Neochiastozygus perfectus* Perch-Nielsen
	R20	Y: 630396 X: 4542692	Late Ypresian –Early Lutetian	**Nannoplankton***: Discoaster sublodoensis* Bramlette and Sullivan, *Reticulofenestra dictyoda* (Deflandre), *Discoaster kuepperi* Stradner, *Sphenolithus radians* Deflandre, *Tribrachiatus orthostylus* Shamrai, *Coccolithus crassus* Bramlette and Sullivan, *Calcidiscus protoannulus* (Gartner), *Rhabdosphaera truncata* Bramlette and Sullivan, *Rhabdosphaera tenuis* Bramlette and Sullivan, *Chiasmolithus grandis* (Bramlette and Riedel), *Blackites spinosus* (Deflandre and Fert), *Discoaster lodoensis* Bramlette Riedel, *Rhabdosphaera morionum* (Deflandre), *Lophodolithus nascens* Bramlette and Sullivan, *Neochiastozygus perfectus* Perch-Nielsen, *Pontosphaera multipora* (Kamptner), *Coronocyclus prionion* (Deflandre and Fert), *Imperiaster obscurus* (Martini), *Zygrhablithus bijugatus* (Deflandre), *Toweius? gammation* (Bramlette and Sullivan)
	R21	Y: 630486 X: 4542750	Late Ypresian	*Reticulofenestra dictyoda* (Deflandre), *Coccolithus crassus* Bramlette and Sullivan, *Tribrachiatus orthostylus* Shamrai, *Discoaster binodosus* Martini, *Sphenolithus radians* Deflandre
	R22	Y: 630409 X: 4542652	Ypresian–Lutetian	*Subbotina linaperta* (Finlay), *Subbotina* cf. *triangularis* (White), *Subbotina* sp.,*Acarinina* sp., *Globanomalina* sp., *Morozovella* cf. *subbotinae* (Morozova), *Morozovella* cf. *aragonensis* (Nuttall), *Acarinina* cf. *angulosa* (Bolli), *Acarinina* cf. *primitiva* (Finlay)
	R23	Y: 630000 X: 4542250	Middle Eocene	*Pseudohastigerina micra* (Cole), *Acarinina* cf. *bulbrooki* (Bolli), *Globigerinatheka* sp., *Acarinina* sp., *Morozovella* sp., *Globigerina* sp., *Hantkenina* sp., *Turborotalia* sp., Textularidae, *Nummulites* sp., *Truncorotaloides* sp.

3.2.2. Kaplıca Formation (Tek)

The unit, which consists of Early-Middle Eocene claystone, mudstone, sandstone, clayey limestone and volcanoclastic rocks in the northern part of the Kaçkar Mountains in the study area, was named as the Kaplıca formation by Gedik and Korkmaz (1987). The formation was distinguished and investigated only near the Rize provincial center in the study area.

The unit begins to deposit with alternation of sandstone, claystone and limestone, and continues upward in the form of mudstone and clayey limestone interlayers. It then passes in to the Melyat formation with alternating claystone and volcanoclastics in upper layers (Figure 10). The sandstones at the bottom are yellowish beige colored, medium to thick bedded with thicknesses sometimes reaching up to one meter, hard and fragile. Sandstones have greenish-gray colored claystones. The limestones located in intermediate levels are beige-colored, medium bedded and rarely outcrop. The upper levels of the formation consist of greenish, brownish and burgundy colored, thin bedded volcanoclastic, claystone, sandstone and mudstone. The Eocene aged volcanics are more alkaline than the Cretaceous volcanics. However, they sometimes show calc-alkaline characteristics (Gedik et al., 1992).

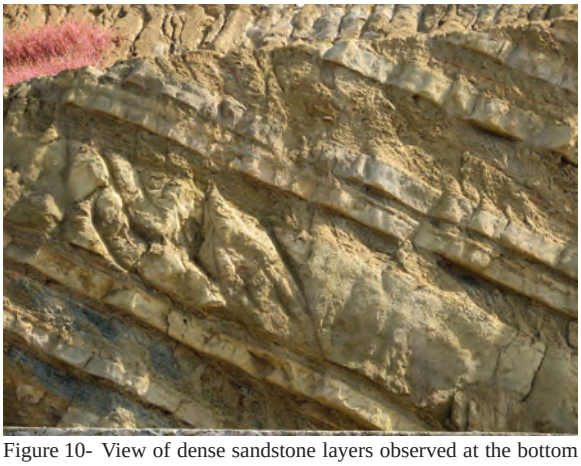

Figure 10- View of dense sandstone layers observed at the bottom of the Kaplıca formation (Rize province, Kaplıca district, to southeasterly view, F45 d4).

The Kaplıca formation unconformably overlies the Cankurtaran formation (Figure 3). It is both vertically and laterally transitional with the overlying Early-Middle Eocene Melyat formation. The apparent thickness of the unit varies between 250-300 m.

The fossil determinations of the samples collected from the Kaplıca formation yielded Ypresian, late Ypresian-early Lütetian, late Ypresian and Middle Eocene ages (Table 3), and the age of the formation was given as Early-Middle Eocene. The lithological characteristics and fossil contents of the Kaplıca formation indicate that it was deposited in a shallow marine environment. The formation can be correlated with the Foldere formation of Korkmaz (1993), the lower levels of Tonya formation of Kurt et al. (2006), the Erenler formation of Yılmaz et al. (1997) and with one section of the Fındıkbeli formation of Pelin (1977).

3.2.3. Melyat Formation (Tem)

The unit, which is generally composed of andesitic and basaltic lavas, pyroclastic rocks and sandstone and claystone, was named as the Melyat formation by Gedik and Korkmaz (1987). The formation extends along the slopes facing the seaside in NE-SW directions between Rize city center and the Pazar district in the study area.

The dominant lithology of the formation is andesite, basaltic lavas, tuffs and agglomerates. Rarely, it is possible to find clastics between the volcanic levels. Basaltic and andesitic lavas often show a color change ranging from a som, grayish smoked to a brownish purple. In basalts, there is sometimes observed an alteration from inside towards outside. It is possible to see yellowish, gray altered areas in the outcrops in south of the Çayeli County. Basaltic lavas rarely show columnar and sometimes pillow structures. The clastic layers between the lavas are composed of grayish sandstone, claystone and shales. The apparent thickness of the formation in the study area is between 600 and 700 m.

The formation is laterally and vertically transitional with the Early-Middle Eocene Kaplıca formation at the bottom and unconformably overlain by the Pazar formation (Figure 3). It unconformably overlies the Campanian-Maastrichtian Çayırbağ formation among the Aşıklar, Derinsu, Suçatı and Sivrihisar (F45 c3, c4) villages in south of Çayeli and Pazar districts, and has a fault contact relationship with the Late Santonian-Campanian Çağlayan formation among Pazarköy, Yenihisar and Musadağı villages in Rize province center and south of the Çayeli district (F45 d3, d4).

Paleontological data was not taken from the formation. Radiometric age determinations by Ar/Ar method from andesites in the lower levels of the formation gave the age of 47.8 ± 1.6 Ma (Figure 8b) (HD2, F45 d3, 946000; 4545000). Barbieri et al. (1985) and Akıncı et al. (1991) performed radiometric determination by K/Ar method in seven samples between Trabzon-Arhavi and obtained 45.2 to 54.3 My age. In addition, the Melyat formation is both laterally and vertically transitional with the underlying Early-Middle Eocene Kaplıca formation. Therefore this formation was given the same age.

Aydınçakır and Şen (2013) stated that the similar aged volcanics developed under the post-collisional extensional tectonic regime in their investigation in the vicinity of Borçka to the east of the study area. Considering also the environmental characteristics of the Kaplıca formation, which is transitional both in lateral and vertical directions, it can be said that the formation was formed in the shallow marine conditions. The Melyat formation can be correlated with the Yeşilce formation of Terlemez and Yılmaz (1980) around Ordu, upper part of of the Fındıkbeli formation of Pelin (1977), the Kabaköy formation of Güven 1993) and upper part of the Tonya formation of Kurt et al. (2006).

3.2.4. Pazar Formation (Tmp)

The unit is composed of the intercalations of sandstone, marl, conglomerate and claystone and was named as the Pazar formation by Gedik and Korkmaz (1987). The unit, which has very limited exposures in the study area, is observed only around Çayeli (F45 d3) and Pazar (F45 c1, c2) districts.

The formation begins with the deposition of conglomerate at the bottom then continues upward with sandstone, sandy limestone, marl and claystone (Figure 11). The conglomerates are poorly sorted and mainly of volcanic origin. The claystones are thin bedded and reddish. Sandstone layers are beige, grayish, thin bedded, much macrofossilliferous. Gastropod and lamellibranch shells are widely observed.

The apparent thickness of the formation ranges between 50 and 100 m, and the formation was

Figure 11- View from macrofosilliferous sandstone layers in the Pazar formation (Rize province, Çayeli county, road of Abdullahhoca village, F45 c4).

deposited in shallow marine environment. The formation unconformably overlies the Early-Middle Eocene Melyat formation and unconformably underlies the Plio-Quaternary Hamidiye formation (Figure 3). No fossil assemblage was obtained from the samples in the formation. Abundant quantities of gastropods and lamellibranch shells are observed in the sandstones. However, Özsayar (1980) determined from this formation the microfossil of Elphidium reginum which gave the Early-Middle Miocene age. Due to previous studies and stratigraphic location of the formation the age of the unit was given as Early-Middle Miocene. The Pazar formation can be correlated with the Sarıkum formation defined in the vicinity of Sinop (Sinan, 1959) and the Sinop formation (Gedik and Korkmaz, 1984).

3.2.5. Hamidiye Formation (plQh)

Pliocene units composed of the alternations of conglomerate and sandstone were named as the Hamidiye formation by Gedik and Korkmaz (1987). The unit has very limited exposures in the study area and is well observed along the Ardeşen - Çamlıhemşin crossroad.

The unit, which mainly consists of the alternation of pebbles and sandstones, are thick and cross-bedded in places. Layers have lateral transitions with each other and form lenses. The beds are nearly horizontal. Pebbles are well rounded and well sorted in the formation, which is observed in grayish white color range. Most of the gravels were derived from the underlying volcanic rocks and exhibit well gradation. Conglomerate and sandstone layers forming the formation show lateral transitions in them.

The Hamidiye formation unconformably overlies Pazar, Melyat and Çayırbağ formations in the study area and overlain by the Quaternary forms (Figure 3). The Ardeşen-Çamlıhemşin road cut is a good type section for the formation and its apparent thickness ranges between 40-50 m. The Hamidiye formation must have been deposited in a continental environment characterized by the flood plain.

No fossils for the age determination were found in the formation. Considering the stratigraphic location, the age of the formation was estimated as the Plio-Quaternary. The formation is not widely observed in the region. However, it can be correlated with the units around the Trabzon Airport studied by Uğuz et al. (2011) outside the study area.

3.2.6. Handüzü Volcanics (Tplhd)

These volcanics are composed of basalt, andesite and dacites and were named in this study the first time. The basalt and andesite defined within the Çağırankaya formation in previous studies (Güven, 1993) and crosscutting dacites were investigated as the Handüzü volcanics in this study and the age ranges were re-assessed.

It is understood from the studies of Ağar (1977) that the unit of which its exposures are observed in the Han yayla (valley) (G45 a2), Kafkuma yayla and the south of Büyük yayla had also distributions around Trabzon.

In the lowermost part of the volcanics, the basalts, andesites and rarely observed crosscutting dacites are seen (Figure 12). In the Han valley, the pinkish red and occasionally grayish basalt and andesitic sections with flow structures are present. Whereas the domal type, grayish dacitic sections are observed in the southern part other valley. The apparent thickness of the Handüzü volcanics is about 150-200 m.

The Handüzü volcanics show characteristics varying from basic to acidic, and are considered to have been exposed through cracks and fractures. This volcanics are above the Çatak formation and the Kaçkar granitoid I and there was not observed any unit in the upper contact. The radiometric dating of dacites from volcanics was estimated as 3.93 ± 0.46 My (VB1, G45 a3, 643650; 4519250) and 4,25 ± 0,55 My (VB2, G45 a2, 638750,4527250) based on the Ar/Ar method (Figure 8c, d) and the age of Handüzü volcanics was

Figure 12- View from dacites in the Handüzü volcanics (Rize province, İkizdere county, southeast of Büyükyayla, southward view G45 a3).

Figure 13- View from obsidians within the Çağırankaya volcanics (Rize province, İkizdere county, southwest of Büyükyayla, G45 a3).

evaluated as Pliocene. This unit can be correlated with the Çağırankaya formation of Güven (1993).

3.2.7. Çağırankaya Volcanics (Qç)

The volcanics composed of rhyolite, rhyodacite, dacite, obsidian and ignimbrites were redefined in this study and investigated under the name of Çağırankaya volcanics. Güven (1993) in his study defined the unit under the name of Çağırankaya volcanics including also the basic volcanics (Handüzü volcanics) located in the lower part. The Çağırankaya volcanics give outcrops throught the fracture and crack systems around the Büyük yayla (G45 a3; figure 2b).

The Çağırankaya volcanics are of an acidic volcanic product and consist of rhyolite, rhyodacite, dacite, ignimbrite and obsidian (Figure 13). Rhyolite and dacites are in banded flowing structure. The obsidians, which are seen as hillocks, alternate with rhyolites in places. Rhyolites and dacites are whitish gray and obsidians are black, brownish red, red, black banded and somewhat mottled, and exhibit columnar and brecciated views. The apparent thickness of the Çağırankaya volcanics is about 75-100 m, and overlie the Çatak formation, Handüzü volcanics and the Kaçkar granitoid I.

There was not detected any age from the volcanics. However, Hanedan (2008) performed the radiometric dating to obsidians in the Çağırankaya volcanics by using Ar/Ar method and determined their ages as ranging between 1.7 My and 2 My and gave the Quaternary age to the unit. The age of the Çağırankaya volcanics was evaluated as Quaternary also in this study. The Çağırankaya volcanics can be correlated with the Çağırankaya formation of Güven (1993) and the Büyükyayla obsidian of Hanedan (2008).

3.3. Taşköprü Tectonic Slice

The Turonian - Maastrichtian Yağmurdere formation section consisting of the basic volcanic and clastic-carbonate interlayers outside the study area of the slice, which is formed by the clastic, carbonate and volcanogenic rocks between Paleocene-Maastrichtian age intervals, is observed (Figure 14). This formation is unconformably overlain by the Early-Middle Eocene Yedigöze and Çoruh formations. The Kaçkar granitoid I and the Yağmurdere formation are in contact with each other. The Güllübağ monzonite is in contact with the Early-Middle Eocene units, which are the cover rocks of the Taşköprü tectonic slice, and is in Late Eocene age (Figure 14). It is possible to correlate the Taşköprü tectonic slice with the Kadırga tectonic slice of Uğuz et al. (2011).

3.3.1. Yağmurdere Formation (Ky)

The Turonian-Maastrichtian unit, which consists of basalt, andesite, lava, pyroclastics, micritic limestone, sandstone and claystone, was named as the Yağmurdere formation by Duygu et al. (2013). It is possible to see the widespread exposures of the formation on the southern slopes of the Kaçkar Mountains, on the Ovit mountain section of the İkizdere-İspir road (G45 c4),

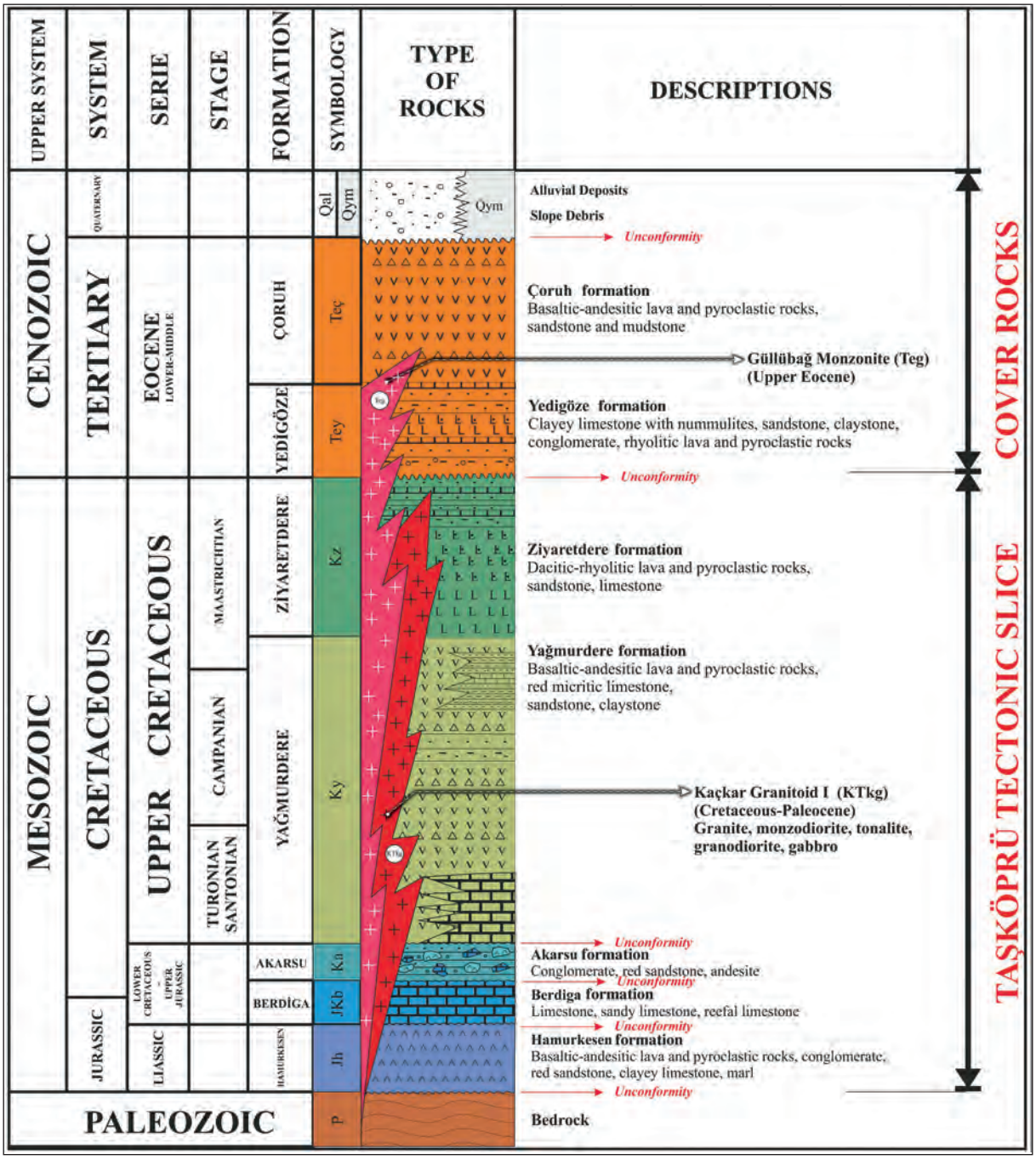

Figure 14- Generalized stratigraphic section of the Taşköprü tectonic slice and cover rocks (Duygu et al., 2013).

in the vicinity of the Orso Mountain (G45 d4) and the Karaduman Mountain, between the Büyükdere village and the Abros Yayla (valley) (G45 d3), between the Moryayla village (G45 c3) and the Tetos Mountain (G45 c2).

With the sedimentary deposits generally formed by basalt, andesite, pyroclastic, limestone, sandstone and claystone in the formation and the alternating basalts in places are grayish black and green colored and have pillow structures in occasion. Andesites are

grayish-green, hard, brittle and massive in appearance. Pyroclastic rocks are grayish, greenish, very thick and massive. These volcanic levels consist of grayish, green and burgundy sandstone, claystone and micritic limestone layers. The micritic limestones are burgundy and thin to medium bedded, whereas the sandstone and claystones are thin bedded. The topography, in which basalt and andesitic lavas are present, is in the form of steep cliffs.

The formation unconformably overlies the Akarsu formation outside the study area. It has crosscutting relationship with the Kaçkar granitoid I in the area. The formation is unconformably overlain by the Early-Middle Eocene Yedigöze and Çoruh formations, which are laterally and vertically transitional with each other (Figure 14). The apparent thickness of the formation in the study area is between 750 and 800 m around the Büyükdere village.

The age of Yağmurdere formation determined as Turonian-Maastrichtian according to fossil determination (Table 3) of the samples taken from the near north of the Ulutaş village. Uğuz et al. (2011) obtained the Cenomanian age from the units that can be correlated with this formation in the investigation carried out to the west of the study area. Duygu et al. (2013) made detailed paleontological studies from widespread carbonates in the western part of the same unit. The authors' found ages as Turonian-Santonian in samples collected from the Karameşe locality (G43 c2) in east of the Çatak valley; as Campanian-Maastrichtian in samples taken from the upper levels of the unit in the vicinity of the Aytaş village (Table 4) . Depending on all these data, they suggested the age of the Yağmurdere formation as ranging between Turonian-Maastrichtian. Considering the stratigraphic position and the data given above, the age of the unit was suggested as Turonian-Maastrichtian.

The existence of turbiditic and pelagic sediments intercalating with volcanic rocks and faunal assemblage indicate that the formation may have been deposited in slope environments where the basic volcanism is effective. The Yağmurdere formation can be correlated with the Çatak and Çağlayan formations of Güven (1993) and the Esiroğlu and Ayeserdere formations of Uğuz and others (2011).

3.4. The Cover Units on the Taşköprü Tectonic Slice

3.4.1. Yedigöze Formation (Tey)

The unit mainly consists of limestone, sandstone, claystone, conglomerate, rhyolitic lava and pyroclastic rocks and is defined by Akdeniz et al. (1994) as the Yedigöze formation. The units belonging to the formation can be seen around Moryayla, Ulutaş villages and Vank valley (G45 c3) in the study area (Figure 2b).

The unit is represented with conglomerate at the bottom then passes into yellowish beige, greenish-brown, fine to medium bedded limestone, sandstone and claystone alternation (Figures 15 and 16). Among these marine facies; white, whitish green rhyolites and

Table 4- Fossil findings both of the units belonging to Taşköprü tectonic slice and its cover units ([1] and [2] taken from Duygu et al., 2013; [3] Uğuz et al., 2011, Coordiantes are UTM ED 1950).

Formation Name	Sample ID on Map (Figure 2b)	Sample Location	Age	Fossils
Yağmurdere	R24	Y: 659000 X: 4496700	Turonian-Maastrichtian	Globotruncanidae, *Globigerinelloides* sp.
		[1]Çatak plateau, Karameşe avenue	Turonian–Santonian	*Marginotruncana coronata* Bolli, *Marginotruncana renzi* (Gandolfi), *Marginotruncana pseudollinneiana* Pessegno, *Marginotruncana* sp., *Dicerinella* sp.
		[2]Aytaş village	Campanian–Maastrichtian?	*Globutruncana arca* (Cushman), *Globutruncana* cf. *linneiana* (d'Orbigny), *Globutruncana bulloides* Vogler, *Stomiosphaera sphaerica* (Kaufmann), *Marginotruncana* sp., *Globigerinelloides* sp., *Heterohelix* sp
Yedigöze	R25	Y: 662650 X: 4493500	Middle Eocene (probably Bartonian)	Globotruncanidae, *Globigerinelloides* sp.
		[3]Yazlık village (Aydıntepe-Bayburt)	Early Eocene	*Discocyclina* sp., *Asterocyclina* sp., *Nummulites* sp., *Lockhartia* sp., *Sphaerogypsina* sp., *Rotalia* sp., Gypsinidae, Rotaliidae, Textularidae, Miliolidae, Algae, Bryozoa

ignimbrites are observed. These levels continue in the lateral direction as clastic carbonate facies. Very large nummulites are encountered in the nodular limestones on conglomerates. The apparent thickness of the formation in the study area is between 100 and 150 m.

The Yedigöze formation unconformably overlies the Kaçkar granitoid I and Yağmurdere formation in the study area. It is both laterally and vertically transitional with the overlying same aged Çoruh formation (Figure 14). The lower layers of the Çoruh formation are distinguished from the Yedigöze formation with purple andesites and clastic alternations.

The Middle Eocene (Bartonian ?) age was obtained from fossil determination of samples taken in the study area, and Early Eocene age was obtained from fossil determination of the samples (Table 4) taken by Uğuz et al. (2011) from westward extension of the Yedigöze formation in outside of the study area (Yazlık village, Aydıntepe county, Bayburt province), Thus the Yedigöze formation was aged as the Early-Middle Eocene.

The formation should have been deposited in a shallow marine environment ranging from the terrestrial environment, where red conglomerates are deposited, to the tidal environment where the energy occasionally falls and rises. The Yedigöze formation can be correlated with the Eocene volcanic flysch of Yalçınlar (1952) and the Nişantaşı member of Yazyurdu formation of Keskin et al. (1989).

Figure 15- View from conglomerates observed at the bottom of the Yedigöze formation (Erzurum province, İspir county, east of the Ulutaş village, G45 c3).

Figure 16- View of the nummulitic limestones belonging to the Yedigöze formation (Erzurum province, İspir county, east of the Ulutaş village, G45 c3).

3.4.2. Çoruh Formation (Teç)

The unit, which its lower layers are composed of the alternation of clastic and basalt, and lower layers are composed of basalt, andesite and pyroclastic rocks, was described by Akdeniz et al. (1994) as the Çoruh formation. The formation widely outcrops in the southern part of the study area, along the eastern and western lines on the southern slopes of the Kaçkar Mountains and in the vicinity of the Kemer Mountain, Akdağ (G45 d4), Taşlıyayla, Güneydere (G45 c3), Kızıldağ (G45 c4, d3), Soğuksu (G45 c4), Özlüce, Çayırözü and Kaynakbaşı villages (Figure 2b; G45 c3).

The grayish green, purple and sometimes pinkish gray colored unit begins to deposit at the bottom with clastics then transitionally passes into grayish purple and pink andesitic lavas with pyroclastics in the upper layers (Figure 17). Lava fragments are commonly observed in pyroclastics. The succession continues upward in the form of purple basalt, andesite, tuff, agglomerate and red mudstone. Sandstones are dirty white to gray in color and thin to medium bedded. Lavas are dominant at the topmost layers of the succession. Basalts are red to smoke colored, gas-filled with pillow structures occasionally. Andesites are in the form of blue layers between gray, bluish-gray, purple clastics and pyroclastics. Tuffs are in the form of whitish gray, purple colored, disintegrated crystal and lithic. In the alteration zones where the vein or semi-plutonic rocks intrude in the form of dikes along cracks and fractures, a considerable amount of pyrite is encountered and these areas are important in terms of mineralization.

Figure 17- View from lavas and pyroclastics located in the Çoruh formation which show alternation with clastics (Erzurum province, Pazaryolu county, west of the Çaydere village, southward view G45 d3).

In the study area, it is both laterally and vertically transitional with the same aged Yedigöze formation under the Çoruh formation (Figure 14). Besides, it unconformably overlies the Kaçkar granitoid I without having the Yedigöze formation in lateral direction. The Late Eocene Güllübağ monzonite in south of Özlüce and Yukarı (Upper) Fındıklı villages in G45c3 sheet (Figure 2b) cuts the Çoruh formation.

The fossil content could not be detected in the Çoruh formation. However, the age of the formation was considered to be Early-Middle Eocene as the stratigraphic position and the age of the Yedigöze formation is Early-Middle Eocene.

The apparent thickness of the Çoruh formation is more than 1000 m, and is the last phase products of the arc volcanism corresponding to the calc-alkaline and alkaline subduction zone (Tokel, 1973). The formation can be correlated with the Yazyurdu formation of Keskin et al. (1989) and the Kabaköy formation defined by Güven (1993) which covers the Early-Mid Early Eocene volcanic units in the study area.

3.5. Plutonic Rocks

3.5.1. Kaçkar Granitoid I (KTkg)

Granitoids, which cut a part of the Late Cretaceous units and are transgressively covered by the Early-Middle Eocene units, are called as the Kaçkar granitoid I by Güven (1998). It is possible to see the widespread outcrops of the Kaçkar granitoid I (G45 a3, a4, b4, c1, c2 and d series) on Kaçkar Mountains extending in SW-NE directions from the south of the İkizdere District in the study area. The exposures belonging to these granitoids are well observed along the road that runs from İkizdere district (Rize) to İspir district (Figure 2b; Erzurum).

The Kaçkar granitoid I is observed as greenish, greyish beige and pink colored, compact, in massive structure and arenized in most places. In general, the Kaçkar granitoid I consist of granite, granodiorite, diorite, tonalite and monzonite. The granitoids consisting of granite and monzonite are beige to pink colored, and have large visible orthoclase grains. Alkaline feldspar granites are mostly light greenish and grayish in color. It is possible to encounter the enclaves in the rocks of the Kaçkar granitoid I. The gabbro is greenish-gray in color and macroscopically has granular texture.

Lithologies belonging to the Cretaceous-Paleocene Kaçkar granitoid I, one section of the Late Jurassic-Early Cretaceous, the Late Cretaceous sedimentary and volcanic rocks (Berdiga and Çatak formations) have cross cutting relationship. It is unconformably overlain by the Early-Middle Eocene units in the upper contact (Figure 3). It outcrops as magmatic complex on large areas along the ascension of Kaçkar Mountains.

The Campanian age with 80.7 My by Taner (1977), the Late Cretaceous and Paleocene age by Boztuğ et al. (2001, 2006), the Campanian age with 79 My by Karslı et al. (2010*a*) (Harşit pluton) in similar units and the Campanian age with 80 my by Evcimen et al. (2013) were taken from the areas corresponding to the Kaçkar granitoid I. Therefore; when field observations of the Kaçkar granitoid I and the radiometric age data was considered, the Cretaceous-Paleocene age was given to the Kaçkar granitoid.

The rocks of the Kaçkar granitoid I are the; I-type granitoids formed by the northward subduction of the oceanic crust of Neotethys beneath the Pontide continent (Gedik et al., 1992, Yılmaz and Boztuğ, 1996, Okan and Şahintürk, 1997; Okay and Tüysüz, 1997; Boztuğ et al., 2006; Karslı et al., 2007, 2010*a*, 2010*b*).The units of the Kaçkar granitoid I can be correlated with the Harşit pluton located at east of the study area (Karslı et al., 2010*a*), the Kaçkar batholith (Altınlı, 1970), Ayder, Ortaköy, Kaptanpaşa plutons

(Gedik et al., 1992), one part of the Composite Kaçkar batholith (Boztuğ et al., 2001, 2006) and the Rize granite (Çoğulu, 1970).

3.5.2. Kaçkar Granitoyid II (Tekg)

The Eocene intrusive rocks in the Kaçkar Mountains were described by Güven (1998) as the Kaçkar granitoid II. The granitoids observed in the vicinity of Güneysu, Hemşin, Ardeşen, Fındıklı districts, which are composed of tonalite, granite, diorite, granodiorite, gabbro and gabroporphyry were investigated under the name of Kaçkar granitoid II in this study too. The units belonging to the Kaçkar granitoid II outcrop mostly at lower elevations on the north-facing slopes of Kaçkar Mountains (Figure 2b). The gabbro in south of the Kurtuluş village (F46 d1), the granite on the road of Ardeşen-Çamlıhemşin and in Hemşin, and the gabbro porphyries on the road to Derinsu and Erenler villages from the Pazar district (F45 c4) in the Çayırbağ formation are well observed in small outcrops (Figure 2b) which cannot be mapped. Granodiorite and diorite are well observed in south of Fındıklı and Arhavi districts (F46 c1, d2) and in the near south of Güngören, Taşköprü and Söğütözü districts (Figure 2b).

When looking at the nomenclatures and mineral associations of rocks of the Kaçkar granitoid II, there is not observed much difference than the Kaçkar granitoid I. The rocks in the petrographic descriptions of the Kaçkar granitoid II are granite, tonalite, diorite, gabbro and gabbro porphyry (Figure 18). The enclaves are also seen in all these rocks. The surface colors are mostly blackish in gabbroic rocks, greenish gray in granites, and greenish gray and black in diorites, and they have very hard and compact appearance. The fractured structure is well developed in gabbroic rocks.

Figure 18- View from the gabbro porphyry belonging to the Kaçkar granitoid II intruded in the rocks of the Campanian-Maastrichtian Çayırbağ formation (Rize province, Pazar county, north of Derinsu village, northward view, F45 c3).

The Kaçkar granitoid II has generally crosscutting relationship with the Late Cretaceous units. The porphyritic units of granitoid is intruded the Ipresian levels of the Erenler formation only in one locality (southwest of the Arılı village). The intrusions in south of Ardeşen, Fındıklı and Arhavi in units of the Kaçkar granitoid II are observed in the form of crosscutting relationship with Çağlayan, Çayırbağ and Cankurtaran formations (Figure 3).

The units of the Kaçkar granitoid II have crosscutting relationship with the Late Santonian, Campanian, Maastrichtian, Danian and Ipresian units in different areas. According to the radiometric dating for the samples taken from the gabbro porphyries intruded into the Çayırbağ formation the Ipresian age (50,5±0,8 My) was detected using the Ar/Ar method. In addition, Boztuğ et al. (2001, 2006) reported that the units belonging to the Kaçkar granitoid II were of the Eocene age. Evcimen et al. (2013) obtained 43,81 My age based on radiometric dating from the sample they collected in these units. The age of the unit was given as the Eocene by Keskin (2013) and younger than Eocene by Kahraman et al. (1987).

Both the data regarding the age and boundary relationships and the interpretations for the geodynamic evolution show that the units of the Kaçkar granitoid II indicate the continuous plutonism from Early Eocene to the beginning of Late Eocene. The rocks of the Kaçkar granitoid II form the post collisional products (Okay and Tüysüz, 1999, Topuz and others 2005, 2011, Karslı et al., 2007, 2010*a*, 2010*b*, 2011). These granitoids can be correlated with Asniyor leucogranite, Ayder granitoid and the Samistal microgranite of Boztuğ et al. (2001, 2006), the Tertiary granitoid of Evcimen et al. (2013) which they investigated under the name of the Kaçkar batholith and with one section of the Harşit pluton of Karslı et al. (2010*a*).

3.5.3. Güllübağ Monzonite (Teg)

Monzonites located in the north of İspir district (Erzurum) towrads the south of the Kaçkar Mountains were defined by Boztuğ et al. (2001, 2006) under the name of Güllübağ monzonite. It is possible to observe

the outcrops in the south of Özlüce and Yukarı Fındıklı villages (G45 c3) in the study area (Figure 2b).

Güllübağ monzonites are magmatic rocks which intruded into the Early-Middle Eocene rocks (Figure 14) in the form of stocks and dykes (Boztuğ et al., 2001, 2006). It is grayish pink, massive and somewhat altered and arenitized. It is composed of plagioclase, orthoclase, amphibole, augite and biotite and is typical with its porphyritic texture.

The Güllübağ monzonite is observed in the form of stocks and dykes in the study area. It has crosscutting relationship with the Early-Middle Eocene lithologies (Boztuğ et al., 2001, 2006). There was not observed any unit overlying this intrusion in the study area.

Boztuğ et al. (2001, 2006) detected that these units were of Late Eocene in age by using the radiometric dating. The Güllübağ monzonite was accepted as Late Eocene in this study. The Güllübağ monzonite expresses the opening environment which formed due to the gravitational collapse of the thickening crust after collision in the Late Eocene (Boztuğ et al., 2001, 2006).

The Güllübağ monzonite has been investigated in many studies under the name of Kaçkar batholith. In terms of indicating that it corresponds to the opening in geodynamic evolution (Boztuğ et al., 2001, 2006) it was deemed appropriate to introduce this monzonite with a different name than Kaçkar granitoids in this study.

3.5.4. Ardeşen Gabbro (Tea)

The greenish black Late Eocene gabbro, which outcrops in a narrow area to the south of the Ardeşen district in the study area, was defined by Boztuğ et al. (2001, 2006) as the Ardeşen gabbro. Ardeşen gabbro is greenish black, occasionally fractured and massive in appearance and intruded into the Campanian-Maastrichtian Çayırbağ formation (Figure 3) in the form of stocks and veins. Based on radiometric dating the age of the Ardeşen gabbro was determined by Boztuğ et al. (2001, 2006) as the Late Eocene. The Ardeşen gabbro was intruded due to the gravitational collapses of the thickening crust during the collision in the Late Eocene (Boztuğ et al., 2001, 2006).

3.6. Quaternary Units

Quaternary units observed in the study area are mainly alluvial, terrace and slope debris. Terraces (Qt) are often observed in suspended river beds. The slope debris (Qym) develops on the hill slopes of intensive faults which developed by the effect of tectonism in the study area and steep slopes. The alluvial (Qal) is formed along river beds formed by the rivers flowing to the black Sea.

4. Geodynamic Evolution

There are different opinions about the subduction in the Eastern Pontides where the study area is located. A group of researchers suggested that the lithosphere belonging to Paleotethys subducted northward beneath the Pontides starting from Paleozoic to Eocene (Adamia et al., 1977; Tokel, 1981; Ustaömer and Robertson, 1996; Rice et al., 2009; Dilek et al., 2010). There have also been reports on the formation of the Eastern Pontide magmatic arc by the northern subduction of the northern branch of Neotethys beneath the Sakarya continent in Cretaceous (Şengör and Yılmaz, 1981; Okay, 1989; Okay and Şahintürk, 1997; Yılmaz et al., 1997; 2003, Şengör et al., 2003). According to another view, the lithosphere belonging to Paleotethys has been subducted from north to south under the Eastern Pontides in Paleozoic-Eocene interval (Dewey et al., 1973; Bektaş et al., 1999; Eyüboğlu et al., 2007). The most commonly accepted opinion with controversy is that the northern branch of Neotethys subducted northward benath the Eastern Pontides through Cretaceous period and formed the arc magmatism in Late Cretaceous.

The basement of the Eastern Pontides, which is also included in the study area, is formed by the Devonian-Early Carboniferous Pulur metamorphic rocks and Carboniferous Gümüşhane granodiorites. The Pulur metamorphic rocks are unconformably overlain by the Late Carboniferous-Early Permian clastic carbonate deposits. The presence of Liassic deposits and the absence of Triassic deposits with a transgression after the Early Permian caused this period to be interpreted as terrestrial. The presence of transgression in Liassic is expressed by the opening of the northern branch of Neotethys and accordingly; the clastic and carbonated sediments have been deposited in the environment deepening starting from Liassic (Görür et al., 1983; Şengör and Yılmaz, 1981; 1983; Yılmaz, 1995; Bektaş et al., 1987). However, the presence of the Late Triassic

age determined based on the fossils collected from the İzmir-Ankara-Erzincan Zone, which is considered to have been opened in Liassic as the northern branch of Neotethys (Uğuz et al., 1999; Tekin et al., 2002), the presence of the Middle-Late Triassic volcanic seamounts in OIB (Oceanic Island Basalts) character and the Late Permian metamorphism in basic rocks belonging to the oceanic crust of the Ankara mélange (Sarıfakıoğlu et al., 2011; 2014) in basal rocks of the oceanic crust within the Ankara melange have made all these claims contradictory.

In this study, geodnamic evolution model of the region comprising between the Turonian and Middle Eocene range is presented (Figure 19). This model was depicted by evaluating of the data both obtained at this study and at literature. The environment to become continental in the Early Cretaceous then the subduction of the Neotethys oceanic lithosphere beneath the Pontide have initiated a new transgression and caused the deposition of a Turonian-Maastrichtian volcanic succession (Figure 19a). The late Maastrichtian-Danian Cankurtaran formation in the study area was formed in an environment where the activity of the arc volcanism had continued and the back arc basin had begun to develop (Figure 19b). The Yağmurdere formation belonging to the Taşköprü tectonic slice should be the product of the environment where the arc volcanism has been partially effective relatively in the character of axial sediments in the arc and the southern face of the arc volcanism (Figures18 b, c). The lack of volcanic activity in southern areas outside the study area reinforces this idea. The continent to continent collision has occurred starting from the Late Paleocene by the depletion of the Mesozoic ocean during Cretaceous. In the close southern parts of the study area the Danian depositions should have probably been subjected to pre Early Eocene erosion while the Danian deposition has been detected in the study area and the close vicinity of the back arc region. The pebbles of the outcropping granitoid rocks (Kaçkar granitoid I) are observed at the bottom of the Early-Middle Eocene units. The age of the Maçka tectonic slice range until Danian before Eocene. The first pre Eocene age is the Maastrichtian obtained from the Taşköprü tectonic slice which is observed below the thrust contact outside the study area. The absence of Paleocene can be explained by the fact that while the sedimentation was continued in Danian in the Maçka tectonic slice before the thrust, at that time the area where the Taşköprü tectonic slice is located is in the land. After Danian, the Maçka tectonic slice should probably have thrusted on the Taşköprü tectonic slice during the pre-Late Paleocene period (Figure 19c). The disappearance of these traces and being erased by the overlying Kaçkar granitoid I in the study area, the observation of the gravels of these granitoids at the bottom of the Early-Middle Eocene can be explained in such a way that the units of the Kaçkar granitoid I outcropped and was eroded probably in late Thanethian period.

By the exposure of units of the Kaçkar granitoid I in the study area, the Kaçkar Mountains separated the region as the form of ridge in pre Early-Middle Eocene as north, south and east. Thus, Erenler in the east, Kaplıca and Melyat in the north, and Yedigöze and Çoruh formations in the south were deposited (Figure 19 d). It is possible to see the continental deposits in the same period in the near south of the Kaçkar mountains highs while the marine deposits are observed in the north in Miocene. During Pliocene and Quaternary periods, the Handüzü and Çağırankaya volcanoes were formed under the control of the E - W extending joint and fracture systems. The lithologies of the Plio-Quaternary units and their appearance as coarse pebbles in the region indicate that the uplift continued in this time.

5. Conclusions

The results of this study covering the area of approximately 4200 km^2 between the east and south of Rize, Çayeli, Arhavi, İspir and İkizdere in Eastern Black Sea Region are presented below.

1. In the study area, the first detailed stratigraphy compatible geological mapping was made for 1/25000 scaled 29 sheets (F45 c1, c2, c3, c4, d3, d4, G45 a1, a2, a3, a4, b1, b2, b3, b4, c1, c2, c3, d2, d3, d4, F46 a3, b4, c1, d1, d2, d3, d4).

2. The Kızılkaya formation, which includes Kuroko-type Cu deposits commonly observed in Eastern Pontides, is confused with Çayırbağ formation containing similar lithologies. This confusion is removed by (i) a clear definition of the stratigraphic location of the Çağlayan formation consisting of volcanosedimentary deposits dominated by basic volcanics between both formations and (ii) re-evaluation the age of Çayırbağ formation as Kampanian - Maastrichtian according to 83.2 ± 1.0 My (Ar / Ar method) radiometric age obtained first time at this study and fossil descriptions.

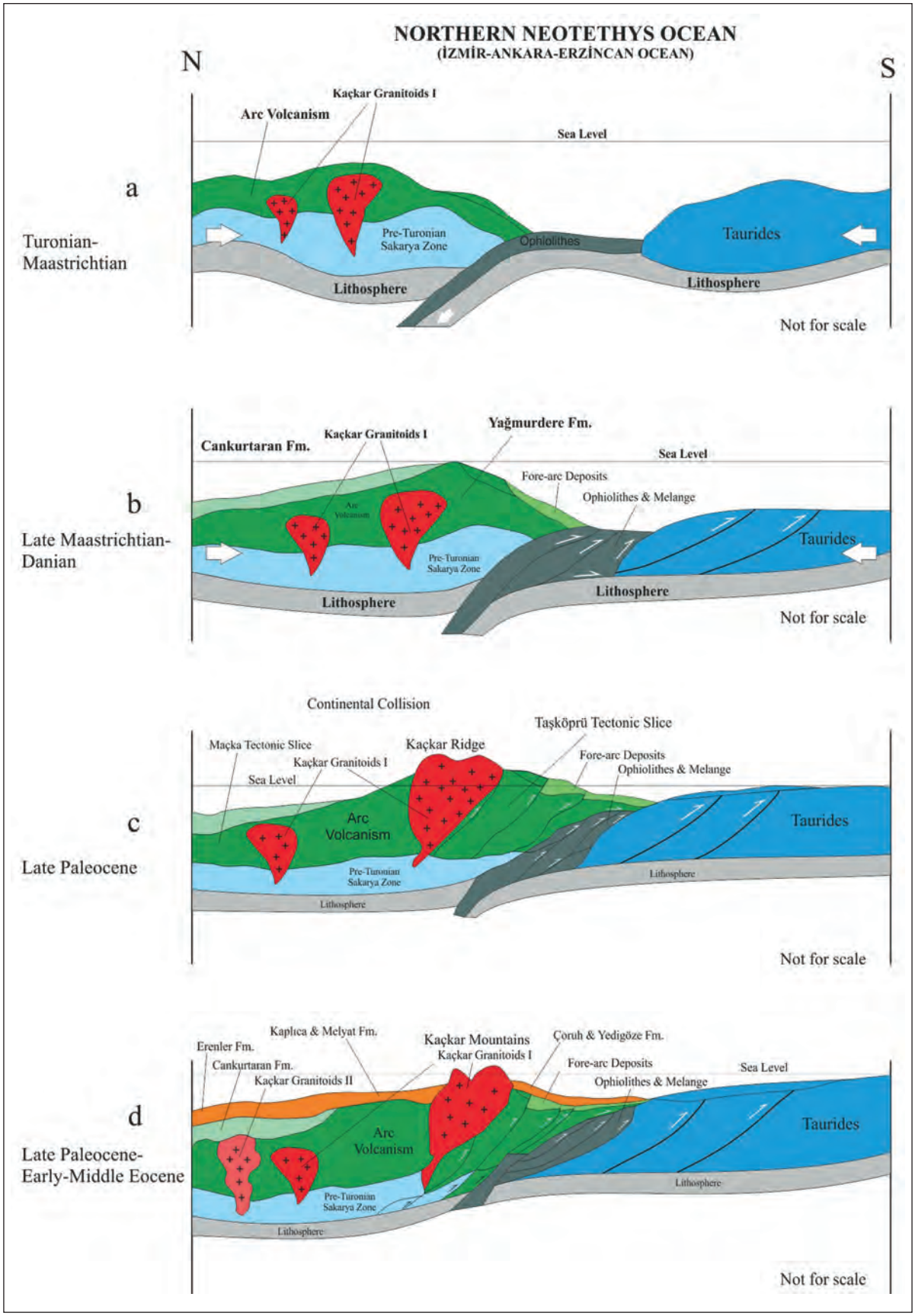

Figure 19- Model sections showing the regional tectonic evolution of the Eastern Pontides between Late Cretaceous and Early-Middle Eocene.

3. Within the scope of this study, it was observed that the products of arc volcanism in the Maçka tectonic slice were more dominant than the Taşköprü tectonic slice. The contact relation of both tectonic slice which is stated as tectonic in outside of study area in Çankaya village (Araklı-Trabzon) by Duygu et al., (2013) disappeared with the rise of Kaçkar granitoid I in Late Paleocene.

4. The extend of the granitoid rocks which are defined in restricted area by Boztuğ et al. (2001, 2006) named as (i) Cretaceous-Paleocene aged Kaçkar granitoid I product of arc magmatism, (ii) Eocene aged Kaçkar granitoid II product of collision, and (iii) Late Eocene aged Güllübağ monzonit and Ardeşen gabbro product of extentional were mapped for the first time in the study area.

5. It has been determined that the deposition of the Cankurtaran formation, which has been reported to have deposited in back-arc basin in Campanian to the east of the study area (Kandemir et al., 2014), have started in Maastrichtian.

6. It has been determined that the Early-Middle Eocene deposits in and around the study area were developed in three different areas. With the beginning of the continent to continent collision in the Late Paleocene, the units of Kaçkar granitoid I were uplifted in this part of the Eastern Pontides and formed a ridge dipping eastward (Hopa-Borçka) in NE-SW direction. The Eocene sediments should be deposited in the form of two branches in different area in the Eocene sea, most likely started to move in Late Paleocene from east to west. Late Paleocene and Eocene sediments were formed by showing small differences between each others, and these units were defined in the study area as Kaplıca, Melyat, Çoruh,Yedigöze and Erenler formations.

7. The ages of the units belonging to between Late Cretaceous and Eocene were re-assessed on the basis of detailed paleontological data. In addition, it was determined by radiometric datings (^{40}Ar / ^{39}Ar) that the age of Çayırbağ formation is Campanian (83.2 ± 1.0 Ma), the age of Melyat formation is Lutetian (47.8 ± 1.6 Ma) and the age of Handüzü volcanics are Pliocene (andesite, 55 Ma; dacite, for example, 3.93 ± 0.46 Ma).

8. According to ages obtained from the arc volcanism and clastic and carbonates of Late Cretaceous, its concluded that the volcanic products of (i) first basic stage are located in the Çatak formation, (ii) first asidic stage are located in the Kızılkaya formation, (iii) second basic stage are located in the Çağlayan formation, and (iv) second asidic stage are located in the Çayırbağ formation. Especially, determination of the stratigraphic relations of these Late Cretaceous volcanic rocks will also contribute to the exploration of Kuroko-type deposits in the region.

Acknowledgements

This article consists of the studies carried out within scope of the project titled as “Geology of the Area between Çayeli (Rize) - İspir (Erzurum)” conducted by the Department of Geological Researches, MTA Directorate General. We would like to thank to paleontologists Dr. Burcu Coşkun Tunaboylu, Dr. Birkan Alan, Dilek Tokatlı, Ayşegül Aydın, Füsun Danacı and to petrograph Meltem Kadınkız who described the samples collected in the field study during this work.

References

Adamia, S. H., Lordkipanidze, M. B., Zakariadze, G. S. 1977. Evolution of an active continental margin as exemplified by the Alpine history of the Caycasus. Tectonophysics 40, 183-199.

Adamia, S. H., Bayraktutan, S., Lordkipanidze, M., Kuloshvili, S., Maisuradze, G., Chkhotua, T. 1992. Geology of Eastern Pontides (Artvin and Erzurum Districts). Geol. Inst. Ac. Sci. Georgia, 124 p.

Ağar, Ü. 1977. Demirözü (Bayburt) ve Köse (Kelkit) Bölgesinin Jeolojisi: Doktora Tezi, İstanbul Üniversitesi, Fen Fakültesi, 595. s. İstanbul.

Akdeniz, N. 1988. Demirözü Permo-Karboniferi ve bölgesel yapı içindeki yeri: Türkiye Jeoloji Bülteni, 31/1, 70-80.

Akdeniz, N., Akçaören, F., Timur, E. 1994. Aşkale-İspir arasının jeolojisi. Maden Tetkik ve Arama Genel Müdürlüğü, Derleme Rapor No. 9731, Ankara (unpublished).

Akıncı Ö. T., Barbieri, M., Calderoni, G., Delita, C., Ferrini, V., Masi, U., Nicoletti, M., Petrucciani, C., Tolomeo, L. 1991. The Geochemistry of hydrothermaly altered rocks of the lower volcanic cycle from the Eastern Pontides (Trabzon, NE Turkey). Chem, Erde, 51, 173-186.

Altınlı, İ., E. 1970. İkizdere granit karmaşığı (İkizdere granite complex). İstanbul Üniversitesi, Fen Fakültesi Mecmuası, Tabii İlimler, Seri B, XXXV, 3-4, 161-167.

Arni, P. 1939. Tektonische Grundzüge Ostanatoliens und Benachbarter Gebiete: Maden Tetkik ve Arama Enstitüsü. Veröff. Ser. B, No. 4, Ankara.

Aydınçakır, E., Şen, C. 2013. Petrogenesis of the post-collisional volcanic rocks from the Borçka (Artvin) area: implications for the evolution of the Eocene magmatism in the Eastern Pontides (NE Turkey), Lithos 172-173, 98-117.

Badgley, P. C. 1959. Stratigraphy and petroleum possibilities of the Sinop Region: Tidewater Atlantic-Texaco Exploration Group., Petrol Dairesi Başkanlığı Teknik Arşivi, Ankara.

Barbieri, M., Calderoni, G., Ferrini, V., Masi, U., Nicoletti, M., Petrucciani, C., Tolomeo, L. 1985. Geochemistry and geochronology of volcanic rocks from Eastern Pontides (Trabzon, NE Turkey). Terra Cognita 5, 280.

Bektaş, O., Van A., Boynukalın S. 1987. Doğu Pontitlerde (Kuzeydoğu Türkiye) Jura volkanizması ve tektoniği , Türkiye Jeoloji Bülteni, 30, 9-18.

Bektaş, O., Yılmaz, C., Taşlı, K. 1995. Doğu Pontid yay gerisi havzasında derin yayılma çukurlarının oluşumu (KD Türkiye): Neo-Tetis'in pasif kıta kenarı evrimi, KTÜ Jeoloji Mühendisliği Bölümü 30. Yıl Sempozyumu Bildiriler Kitabı, I, 263-274.

Bektaş, O., Şen, C., Atıcı, Y., Köprübaşı, N. 1999. Migration of the Upper Cretaceous subduction-related volcanism towards the back-arc basin of the eastern Pontide magmatic arc (NE Turkey). Geol. J., 34, 95-106.

Boztuğ, D., Erçin, A.İ., Göç, D., Er, M., İskenderoğlu, A., Kuruçelik, M.K., Kömür, İ. 2001. Petrogenesis of the Composite Kaçkar Batholith along a North–South Geotraverse Between Ardeşen (Rize) and İspir (Erzurum) Towns, Eastern Black Sea Region, Turkey: Fourth International Turkish Geology Symposium (ITGS IV), Adana/Turkey, September 24– 28, 2001, Abstracts, p. 210.

Boztuğ, D., Erçin, A.İ., Kuruçelik, M.K., Göç, D., Kömür, İ., İskenderoğlu, A. 2006. Geochemical Characteristics of the Composite Kackar Batholith Generated in a Neo- Tethyan Convergence System, Eastern Pontides, Turkey: Journal of Asian Earth Sciences 27, 286–302.

Çağatay, M.N. 1993. Hydrothermal alteration associated with volcanogenic massive sulfide deposits: Examples from Turkey. Econ. Geol. 88:606–621.

Çağatay, M.N., Boyle, D.R. 1977. Geochemical Prospecting for Volcanogenic Sulphide Deposits in the Eastern Black Sea Ore Province, Turkey. Developments in Economic Geology, Volume 9, 1977, Pages 49-71.

Çekiç Y., Gümüşel, A., Topcu, T., Yağcı, A., Özdoğan, K., Yılmaz, H. Kırcı, M. 1984. Artvin- F 47 a1, a2, a3, a4, b1, b2, b3, b4, c3, c4, d1, d3, d4 paftalarının polimetalik masif sülfit cevheri prospeksiyon raporu. Maden Tetkik ve Arama Genel Müdürlüğü Rapor No: 7940, Ankara (unpublished).

Çoğulu, H. E. 1970. Gümüşhane ve Rize granit plütonlarının mukayeseli petrolojik ve jeokronolojik etüdü (Doktora Tezi): İstanbul Teknik Üniversitesi Kitaplığı, 150 s., İstanbul.

Dewey, J. F., Pitman, W. C., Ryan, W. B. F., Bonin, J. 1973. Plate tectonics and the evolution of the Alpine system: Geol. Soc. Am. Bul., 84, 3137-3180.

Dilek, Y., Imamverdiyev, N., Altunkaynak, S. 2010. Geochemistry and tectonics of Cenozoic volcanism in the Lesser Caucasus (Azerbaijan) and the peri-Arabian region: collision-induced mantle dynamics and its magmatic fingerprint. International Geology Review 52 (4-6), 536-578.

Duygu, L., Bakırhan, B., Tunçdemir, V., Evcimen, Ö. 2013. Doğu Pontidler' in orta-kuzey kesiminin tektonostratigrafik özellikleri. 66. Türkiye Jeoloji Kurultayı Bildiri Özleri, Ankara.

Evcimen, Ö., Bakırhan, B., Karslı, O., Duygu, L., Tunçdemir, V., Demirbağ, H. 2013. Uzungöl intrüzif kompleksinin jeokronolojisi ve petrolojisi, KD Türkiye: Geç Mesozoyik yitim safhasından Erken Senozoyik kıtasal incelme ortamına geçiş için kanıtlar. 66. Türkiye Jeoloji Kurultayı Bildiri Özleri, Ankara.

Eyüboğlu, Y., Bektaş, O., Pul, D. 2007. Mid-Cretaceous olistostromal ophiolitic melange developed in the back arc basin of the eastern Pontide magmatic arc (NE Turkey). International Geology Review 49 (12), 1103e1126.

Eyüboğlu, Y., Santosh, M., Yi, K., Tüysüz, N., Korkmaz, S., Akaryalı, E., Dudas, F., Bektaş, O. 2014. The Eastern Black Sea-type volcanogenic massive sulfide deposits: geochemistry, zircon U–Pb geochronology and an overview of the geodynamics of ore genesis. Ore Geology Reviews, 59, 29–54.

Gattinger, T. E. 1956. Trabzon, Rize, Gümüşhane, Erzurum, Artvin ve Kars Vilayetlerinin bulunduğu sahadaki Doğu Pontidler'de yapılan jeolojik löve revizyon çalışmaları hakkında rapor: Maden Tetkik ve Arama Enstitüsü Derleme Rapor No: 280, Ankara (unpublished).

Gayle, R. B. 1959. Geology of the Sinop Basin: Petrol İşleri Genel Müdürlüğü Arşivi, Ankara.

Gedik, A., Korkmaz, S. 1984. Sinop Havzası'nın jeolojisi ve petrol olanakları. Jeoloji Mühendisliği Dergisi, Sayı 19, 53-79.

Gedik, A., Korkmaz, S. 1987. Rize- Fındıklı- Çamlıhemşin arasında kalan bölgenin jeolojisi ve petrol oluşumları. Maden Tetkik ve Arama Genel Müdürlüğü Rapor No: 8283, Ankara (unpublished).

Gedik, A., Ercan, T., Korkmaz, S., Karataş, S. 1992. Rize-Fındıklı-Çamlıhemşin arasında (Doğu Karadeniz) yer alan magmatik kayaçların petrolojisi ve Doğu Pontidlerdeki bölgesel yayılımları, Türkiye Jeoloji Kurumu Bülteni, C.35. 15-38, Ankara.

Gökçe, A., Spiro, B. 2000. Sulfur-isotope characteristics of the volcanogenic Cu–Zn–Pb deposits of the eastern Pontide region, Northeastern Turkey. Int. Geol. Rev. 42, 565–576.

Görür, N., Şengör, A.M.C., Akkök, R., Yılmaz, Y. 1983. Pontidlerde Neo - Tetis'in kuzey kolunun açılmasına ilişkin sedimantolojik veriler, Türkiye Jeoloji Kurumu Bülteni, C. 26, 11-20, Ankara.

Güner, S., Gülibrahimoğlu, İ., Saraloğlu, A., Akıncı, S., Topçu, T., Konak, O. 1983. Rize-Çayeli-Fındıklı yöresinin jeolojisi. Maden Tetkik ve Arama Genel Müdürlüğü Rapor No: 7688, Ankara (unpublished).

Gürsoy, H., Öztürk, A., İnan, S. 1993. Kelkit (Gümüşhane) ve yakın dolayının il tektonostratigrafik gelişimi: A. Suat Erk Sempozyumu, Bildiriler, 53-64, Ankara.

Güven, İ. H. 1993. Doğu Pontidler'in jeolojisi ve 1/250 000 ölçekli kompasyonu: Maden Tetkik ve Arama Genel Müdürlüğü, Ankara (unpublished).

Güven, İ. H. 1998. 1/100 000 ölçekli açınsama nitelikli Türkiye Jeoloji Haritaları, No. 58, Trabzon C29 ve D29 paftaları: Maden Tetkik ve Arama Genel Müdürlüğü, Jeoloji Etütleri Dairesi Yayını, Ankara.

Hamilton, W.J. 1842. Researchs in Asia Minor, Pontus, and Armenia; with Some Account of their Antiquities and Geology. Volume I, p. 545, London: John Murray, Albemarle Street.

Hanedan, A. 2008. Büyük Yayla obsidiyenlerinin petrografik, mineralojik, mineral kimyası ve jeokimyasal özellikleri, Doktora Tezi, Karadeniz Teknik Üniversitesi, 143 s., Trabzon.

Iğdır, A. 1971. Sürmene, Araklı, Arsin ve Yomra Bölgesinin jeolojisi: Maden Tetkik ve Arama Enstitüsü, Bölge Rapor No: 109, Trabzon (unpublished).

Kahraman, İ., Çağlar, O., Şatır, F., Çakır, M., Yılmaz, T., Türkmen, İ., Karanis, H. A. 1987. Rize-Fındıklı, Artvin-Arhavi-Hopa-Yusufeli kuzeyi yörelerinin jeolojisi ve cevherleşmeleri raporu, Maden Tetkik ve Arama Genel Müdürlüğü Rapor No: 8406, Ankara (unpublished).

Kandemir, Ö., Kanar, F., Pehlivan, Ş., Tok, T., Çobankaya M., Akbayram, K. 2014. Doğu Pontid Magmatik Yayının Gelişimi: Yay ardında Doğu Karadeniz havzasının açılması ve Doğu Pontid yayının Anatolid-Torid Levhası ile çarpışması. 66. Türkiye Jeoloji Kurultayı Bildiri Özleri, Ankara.

Karslı, O., Chen, B., Aydın, F., Şen, C. 2007. Geochemical and Sr-Nd-Pb isotopic compositions of the Eocene Dölek and Sarıçiçek plutons, Eastern Turkey: Implications for magma interaction in the genesis of high-K calc-alkaline granitoids in a post-collision extensional setting. Lithos 98, 67-96.

Karslı, O., Dokuz, A., Uysal, I., Aydin, F., Chen, B., Kandemir, R., Wijbrans, J.R. 2010*a*. Relative contributions of crust and mantle to generation of Campanian high-K calc-alkaline I-type granitoids in a subduction setting, with special reference to the Harşit Pluton, Eastern Turkey." Contributions to Mineralogy and Petrology 160, 467-487.

Karslı, O., Dokuz, A., Uysal, I., Aydın, F., Kandemir, R., Wijbrans, J.R. 2010*b*. Generation of the Early Cenozoic adakitic volcanism by partial melting of mafic lower crust, Eastern Turkey: Implications for crustal thickening to delamination, Lithos, v. 114, p. 109-120.

Karslı, O., Ketenci, M., Uysal, I., Dokuz, A., Aydın, F., Chen, B., Kandemir, R., Wijbrans, J.R. 2011. Adakitelike granitoid porphyries in the Eastern Pontides, NE Turkey: Potential parental melts and geodynamic implications, Lithos, v. 127. p. 354-372.

Keskin, İ. 2013. 1/100.000 ölçekli Türkiye Jeoloji Haritaları, Artvin-F 46 paftası, No: 178, Maden Tetkik ve Arama Genel Müdürlüğü, Jeoloji Etütleri Dairesi, Ankara.

Keskin, İ., Korkmaz, S., Gedik, İ., Ateş, M., Gök, L., Küçümen, Ö., Erkal, T. 1989. Bayburt dolayının jeolojisi, Maden Tetkik ve Arama Genel Müdürlüğü Derleme Rapor No: 8995, Ankara (unpublished).

Keskin, İ., Özbek, T., Dönmez, M., Küçümen, Ö. 1991. Köse-Gökçedere (Gümüşhane), Demirözü

(Bayburt) dolayının jeolojisi, Maden Tetkik ve Arama Genel Müdürlüğü Derleme Rapor No: 9450, Ankara (unpublished).

Ketin, İ. 1951. Bayburt bölgesi jeolojisi: İstanbul Üniversitesi Fen Fakültesi Mecmuası, seri B, cilt XVI, sayı. 2, İstanbul.

Konak, N., Ercan, T., Bilgin, Z. R. 1991. Artvin-Oltu arasındaki Jura öncesi kayaların tanımı ve yapısal özellikleri: Ankara Üniversitesi, Suat Erk Jeoloji Sempozyumu, Bildiri özleri.

Konak, N., Hakyemez, H. Y., Bilgiç, T., Ercan, Bilgin, Z. R., Hepşen, N., Ercan, T. 2001. Kuzeydoğu Pontidlerin (Oltu - Olur - Şenkaya - Narman - Tortum - Uzundere - Yusufeli) jeolojisi: Maden Tetkik ve Arama Genel Müdürlüğü, Rapor no: 10489, Ankara (unpublished).

Korkmaz, A. 1993. Tonya-Düzköy (GB Trabzon) yöresinin stratigrafisi, Türkiye Jeoloji Kurumu Bülteni, C. 36, 151-158, Ankara.

Kovenko, V. 1943. Bakırlı pirit madenleri bölgesi Giresun vilayetinde, Espiye ve Görele dolaylarındaki Karaerik, Ağlık madenleri: Maden Tetkik ve Arama Enstitüsü Mecmuası, 2/30, Ankara.

Kurt, İ., Özkan, M. K., Karslı, Ş., Çolak, T., Topçu, T. 2006. Doğu Karadeniz Bölgesinin jeodinamik ve metalojenik evrimi: Maden Tetkik ve Arama Genel Müdürlüğü Derleme Rapor No. 10875, Ankara (unpublished).

Okay, A. I. 1989. Tectonic units and sutures in the Pontides, northern Turkey, In: Şengör, A., M., C. (Ed.)-Tectonic evolution of the Tethyan region, pp. 109-115, Kluwer Academic Publications, Dordrecht.

Okay, A. İ., Şahintürk, Ö. 1997*a*. Pulur bölgesi stratigrafisi ve tektoniği (Bayburt, Doğu Pontidler). MTA Dergisi, 119, 1-22.

Okay, A.I., Şahintürk, Ö. 1997*b*. Geology of the Eastern Pontides. In "Regional and Petroleum Geology of the Black Sea and Surrounding Region" (ed. A.G. Robinson), American Association of Petroleum Geologists (AAPG) Memoir No. 68, 291-311.

Okay, A.İ., Tüysüz, O. 1999. Tethyan sutures of northern Turkey. In "The Mediterranean Basins: Tertiary extension with in the Alpine orogen" (eds. B. Durand, L. Jolivet, F. Horvath and M. Séranne), Geological Society, London, Special Publications 156, 475-515.

Özsayar, T. 1980. Pazar (Rize) yöresi Sarmasiyen Elphidium'ları: TJK Bülteni, c. 23, 87-92, Ankara.

Özsayar, T., Pelin, S., Gedikoğlu, A., Eren, A. A., Çapkınoğlu, Ş. 1982. Ardanuç (Artvin) yöresinin jeolojisi: Karadeniz Teknik Üniversitesi Yerbilimleri Dergisi, c. 2, 21-38, Trabzon.

Pelin, S. 1977. Alucra (Giresun) güneydoğu yöresinin petrol olanakları bakımından jeolojik incelemesi: Karadeniz Teknik Üniversitesi yayını, No. 87, 103 s., Trabzon.

Rice, S.P., Robertson, A.H.F., Ustaömer, T., İnan, N., Taşlı, K. 2009. Late Cretaceous-Early Eocene tectonic development of the Tethyan suture zone in the Erzincan area, Eastern Pontides, Turkey: Geological Magazine, v. 146, n. 4, p. 567-590.

Robertson A.H.F., Ustaömer, T. 2009. Upper Palaeozoic Subduction/Accretion Processes In The Closure Of Palaeotethys: Evidence From The Chios Melange (E Greece), The Kara-burun Melange (W Turkey) And The Teke Dere Unit (Sw Turkey)", Sedimetary Geolo-gy, 201: 29-59

Sarıfakıoğlu, E., Sevin, M., Esirtgen, E., Duran, S., Parlak, O., Bilgiç, T., Dönmez, M., Dilek, Y. 2011. Çankırı-Çorum havzasını çevreleyen ofiyolitik kayaçların jeolojisi: Petrojenezi, tektoniği ve içerikleri. Maden Tetkik ve Arama Genel Müdürlüğü Rapor No. 11449, Ankara (unpublished).

Sarıfakıoğlu, E., Dilek, Y., Sevin, M. 2014. Jurassic-Paleogene intraoceanic magmatic evolution of the Ankara Melange, North-central Anatolia, Turkey. Solid Earth 5, 1-32.

Schultze-Westrum, H.H. 1960. Giresun-Aksudere (Doğu Pontos cevher bölgesi) hinterlandında yapılan prospeksiyon ve jeoloji harita çalışmaları hakkında rapor. Maden Tetkik ve Arama Enstitüsü, Rapor No: 3184, Ankara (unpublished).

Şengör, A. M. C., Yılmaz, Y. 1981. Tethyan evolution of Turkey: a plate tectonic approach: Tectonophysics, 75, 181-241.

Şengör, A. M. C., Yılmaz, Y. 1983. Türkiye'de Tetis'in evrimi: Levha tektoniği açısından bir yaklaşım: Türkiye Jeoloji Kurumu, Yerbilimleri Özel Dizisi, No. 1, Ankara.

Şengör, A. M. C., Yılmaz, Y., Ketin, İ. 1980. Remmants of a Pre - Late Jurassic Ocean in Northern Turkey: Fragments of Permian-Triassic Paleo - Tethys: Geological Society America Bulletin, 91, Part I, 599-609.

Şengör, A. M. C., Yılmaz, Y., Ketin, İ. 1981. Kuzey Türkiye'de Jura sonu öncesi okyanus kalıntıları: Permiyen-Triyas Paleotetis parçaları: Yeryuvarı ve İnsan, 6, 1-2, 6-16, Ankara.

Şengör, A., M., C., Özeren, S., Genç, T., Zor, E. 2003. East Anatolian high plateau as a mantlesupported, North-south shortened domal structure. Geophysical Research Letters 30, 8045, doi: 10.1029/2003GL017858.

Taner, M. F. 1977. Etude geologique et petrographique de la region de Güneyce, İkizdere, situee au sud de Rize (Pontides orientales, Turquie): Ph.D these no. 1788, Geneve, 180 pp.

Tekin, U. K., Göncüoğlu, M. C., Turhan, N. 2002. First evidence of Late Carnian radiolarian fauna from the İzmir-Ankara-Sture Complex, Central Sakarya, Turkey: Implication for the opening age of the İzmir-Ankara branch of Neotethys. Geobios 35, 127-135.

Terlemez, İ. 1986. Fındıklı-Arhavi-Hopa-Ortacalar arasında kalan bölgenin jeolojisi (F46 a3, b2, b3, b4). Maden Tetkik ve Arama Genel Müdürlüğü, Jeoloji Etütleri Dairesi Rapor No: 250, Ankara (unpublished).

Terlemez, İ., Yılmaz, A. 1980. Ünye-Ordu-Koyulhisar-Reşadiye arasında kalan yörenin stratigrafisi. Türkiye Jeoloji Kurultayı Bülteni, 23/2, 179-182.

Tokel, S. 1973. Stratigraphical and volcanic history of Gümüşhane Region; NE Turkey: (Ph. D. Thesis), College University., London.

Tokel, S. 1981. Plaka tektoniğine magmatik yerleşimler ve jeokimya, Türkiye'den örnekler, Türkiye Jeoloji Kurumu, Yeryuvarı ve İnsan Dergisi, 6/3-4, 53-65, Ankara.

Topuz, G., Altherr, R., Schwarz W. H., Siebel, W., Satır, M., Dokuz, A. 2005. Post collisional plutonism with adakite-like signatures: the Eocene Saraycık granodiorite (Eastern Pontides, Turkey). Contrib Mineral Petrol 15: 441-451.

Topuz, G., Okay, A. I., Altherr, R., Schwarz W. H., Siebel, W., Zack, T., Satır, M., Şen, C. 2011. Post-collissional adakite- like magmatism in the Ağvanis Massive and implications for the evolution of the Eocene magmatism in the Eastern Pontides (NE Turkey). Lithos 125: 131-150.

Uğuz, M.F., Turhan, N., Bilgin, A.Z., Umut, M., Şen, A.M. ve Acarlar, M. 1999. Kulu (Konya), Haymana (Ankara) ve Kırıkkale dolayının jeolojisi. Maden Tetkik ve Arama Genel Müdürlüğü, Rapor No: 10399, Ankara (unpublished).

Uğuz, M.F., Bilgin, A.Z., Tunçdemir, V., Atıcı, G., Gündoğdu, E. A. 2011. Doğu Karadeniz bölgesinin jeolojisi (Bayburt-Gümüşhane-Trabzon), Maden Tetkik ve Arama Genel Müdürlüğü, Rapor No: 11452, Ankara (unpublished).

Ustaömer, T., Robertson, A.H.F. 1996. Paleotethyan tectonic evolution of the North Tethyan margin in the central Pontides, N Turkey. In: Erler, A., Ercan, T., Bingöl, E., Örçen, S. (Eds), International Symposium on the Geology of the Black Sea Region, Proceedings-I, 24-33.

Ustaömer, T., Robertson, A.H.F. 2010. Late Paleozoic-Early Cenozoic tectonic development of the Eastern Pontides (Artvin area), Turkey: Stages of closure of Tethys along the southern margin of Euresia. In M. Sosson, N. Kaymakçı, R. A. Stephenson, F. Bergerat & V. Starostenko (Eds.) Sedimantery basin tectonics from the Black Sea and Caucasus to the Arabian platform (Vol. 340, pp. 281-327), London: Geological Society, Special Publications.

Yalçınlar, İ. 1952. İspir, Pazar, Arhavi ve Yusufeli arasındaki bölgenin jeolojisi: Maden Tetkik ve Arama Genel Müdürlüğü Derleme Rapor No. 2022, Ankara (unpublished).

Yılmaz, A. 1985. Yukarı Kelkit Çayı ile Munzur Dağları arasının temel jeoloji özellikleri ve yapısal evrimi: Türkiye Jeoloji Kurultayı Bülteni, 28/2, 79-92.

Yılmaz, A., Adamia, S., Engin, T., Lazarashvili, T. 1997. Geoscientific studies of the area along Turkish-Georgian border. General Directorate of Mineral Research and Exploration Turkey, Maden Tetkik ve Arama Genel Genel Müdürlüğü, Rapor No: 10122, Ankara (unpublished).

Yılmaz, C. 1995. Gümüshane-Bayburt yöresindeki Alt Jura çökellerinin fasiyes ve ortamsal nitelikleri (KD Türkiye), Yerbilimleri, 26, 119-128.

Yılmaz, S., Boztuğ, D. 1996. Space and time relations of three plutonic phases in the Eastern Pontides, Turkey. International Geology Rewiew, 38, 10, 935-956.

Bull. Min. Res. Exp. (2019) 158: 31-47

Bulletin of the Mineral Research and Exploration

http://bulletin.mta.gov.tr

Structural properties and tectonic significance of a shear zone discovered within the Tauride orogen near Alanya, SW Turkey

Volkan ÖZAKSOY[a*]

[a]*Department of Geological Engineering, Faculty of Engineering, Akdeniz University, TR-07058 Konyaaaltı, Antalya, Turkey*
orcid.org/0000-0002-8126-8134

Research Article

Keywords:
Nappe, folds, foliation, transcurrent shear, kinematic indices, tectonic mèlange.

ABSTRACT

A major shear zone, referred to as the Yeşilöz Shear Zone, was discovered in the lower Mahmutlar Nappe of the Alanya Nappe Complex in Alanya region. The nappe shows early transposed folds with axial metamorphic foliation and upright open folds formed during emplacement. The NW-trending shear zone is around 2 km wide and mappable over a length segment of 10 km. The shear zone consists of the metamorphic rocks of the host nappe, but with the phyllite mylonitized by vertical shear foliation and the quartzite and marble dispersed as lenticular bodies. These brittle rock bodies show broken upright folds similar as in the nappe, and also the phyllite shear lenses bear relics of the nappe metamorphic foliation. Analysis of kinematic indices in the shear zone points to a dextral transcurrent deformation. The emplacement of Mahmutlar Nappe caused mild metamorphism of the upper part of underlying nappe and also affected it with the development of the shear zone that extended downwards. The nappe underwent no further translational movement during and after the shear zone formation, which suggests that the ductile transcurrent deformation probably accommodated a residual shortening induced by the emplacement of the next, younger nappe of the Alanya Nappe Complex.

Received Date: 13.06 2018
Accepted Date: 05.10 2018

1. Introduction

The Anatolian plate, located within the Alpine–Himalayan orogenic belt, is an assemblage of continental platelets derived from the northern Gondwana plate and accreted to the southern margin of the Laurasian plate in the latest Mesozoic and early Cenozoic (Şengör and Yılmaz, 1981; Leren et al., 2007; Okay, 2008). The present study is from the Tauride orogenic belt in SW Anatolia (Okay and Tüysüz, 1999), with the study area located in the eastern arm of the large-scale orocline structure known as the Isparta Bend or Angle (Figure 1; Blumenthal, 1947, 1951; Robertson et al., 2003, 2012; Nemec et al., 2018). The Tauride orogen in this region was mapped by several groups of researchers and its tectono-stratigraphy and petrology have long been studied (Blumenthal, 1951; Özgül, 1976, 1984; Okay and Özgül, 1984; Marcoux et al., 1989; Okay, 1989; Usta and Öztürk, 2000; Bedi and Öztürk, 2001; Bozkaya and Yalçın, 2004; Çetinkaplan et al., 2010; Şenel et al., 2016*a*, *b*).

The regional studies revealed that the orogen in this region consists of two nappe complexes – referred to herein as the Antalya Nappe Complex and Alanya Nappe Complex (Figure 1) – emplaced towards the NE in the latest Cretaceous to early Palaeocene; and a broader nappe complex emplaced towards the SSW in the Palaeogene and referred to as the Hoyran–Bozkir Nappe Complex (Figure 1). The lithology of nappes is highly varied: some nappes consist of non-metamorphic sedimentary rocks, siliceous and carbonate to siliciclastic; others show low-grade (greenschist facies) metamorphism at the base or throughout; yet others include high-grade metamorphic rocks. Except for the kinematic

* *Corresponding author: Volkan ÖZAKSOY, volkano@akdeniz.edu.tr*
http://dx.doi.org/ 10.19111/bulletinofmre.502054.

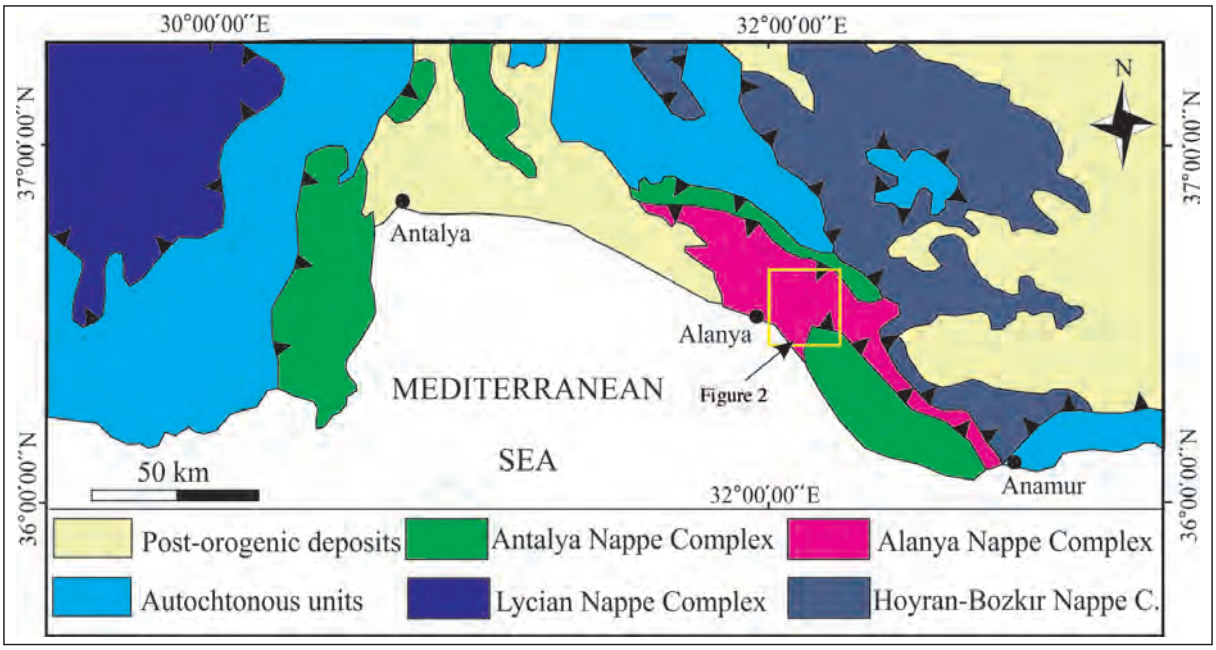

Figure 1- Simplified geological map of the Isparta Bend orocline at the transition of Central and Western Taurides (based on Okay and Özgül 1984).

analysis by Marcoux et al. (1989) from the Alanya Nappe Complex, the internal tectonic structure and emplacement kinematics of the nappes have thus far been little studied. The nappes are overlain by Neogene to Quaternary molasse deposits post-dating the orogeny (Figure 1).

The present paper reports on a large shear zone discovered by geological mapping of the lower component nappe of the Alanya Nappe Complex in the vicinity of Yeşilöz near Alanya (Figures 1 and 2). Detailed analysis of the structural and kinematic properties of this shear zone, hereby referred to as the Yeşilöz Shear Zone, contributes to a better understanding of the directional tectonics of nappe emplacement in this part of the Tauride orogen. At a broader level, this case study adds to a general understanding of the geological significance of tectonic shear zones within orogenic belts.

2. Regional Geological Setting

The Tauride orogen in the western arm of the Isparta Bend orocline (Figure 1) can be regarded as a large-scale antiformal stack of nappe complexes emplaced from two opposite directions (Figure 2). The NE-emplaced Antalya Nappe Complex was covered by a similarly emplaced Alanya Nappe Complex, and the latter was then overridden from the north by the Hoyran–Bozkır Nappe Complex (Figure 2).

2.1. The Antalya Nappe Complex

This nappe complex, referred to earlier variously as the Antalya nappes (Lefevre, 1967; Brunn et al., 1971), Antalya Unit (Lefevre, 1967; Brunn et al., 1971) or Antalya Complex (Woodcock and Robertson, 1977), occurs in both arms of the Isparta Bend orocline (Figure 1) and the lithology of its component nappes is highly varied. For example, ophiolites are involved only in the western arm of the Isparta Bend. The nappes consist generally of non-metamorphic sedimentary rocks that range from deep to shallow marine and comprise radiolarites, shales, siliciclastic sandstones and limestones, including reefal and oolitic carbonate varieties. The age of these deposits ranges from Cambro–Ordovician to Late Cretaceous (Senonian), with an apparent lack of Silurian–Lower Permian and Upper Jurassic (Özgül, 1984; see also Şenel et al., 2016*a*, *b*).

2.2. The Alanya Nappe Complex

This nappe complex occurs only in the eastern arm of the Isparta Bend (Figure 1) and was earlier referred to variously as the Alanya Massif (Blumenthal, 1951), Alanya Unit (Özgül, 1976) or Alanya Nappe (Okay and Özgül, 1984). This allochthon unit of low and high-grade metamorphic rocks consists of three nappes thrust upon one another (Figure 2; Okay and Özgül, 1982; Özgül, 1984) and hence is here in

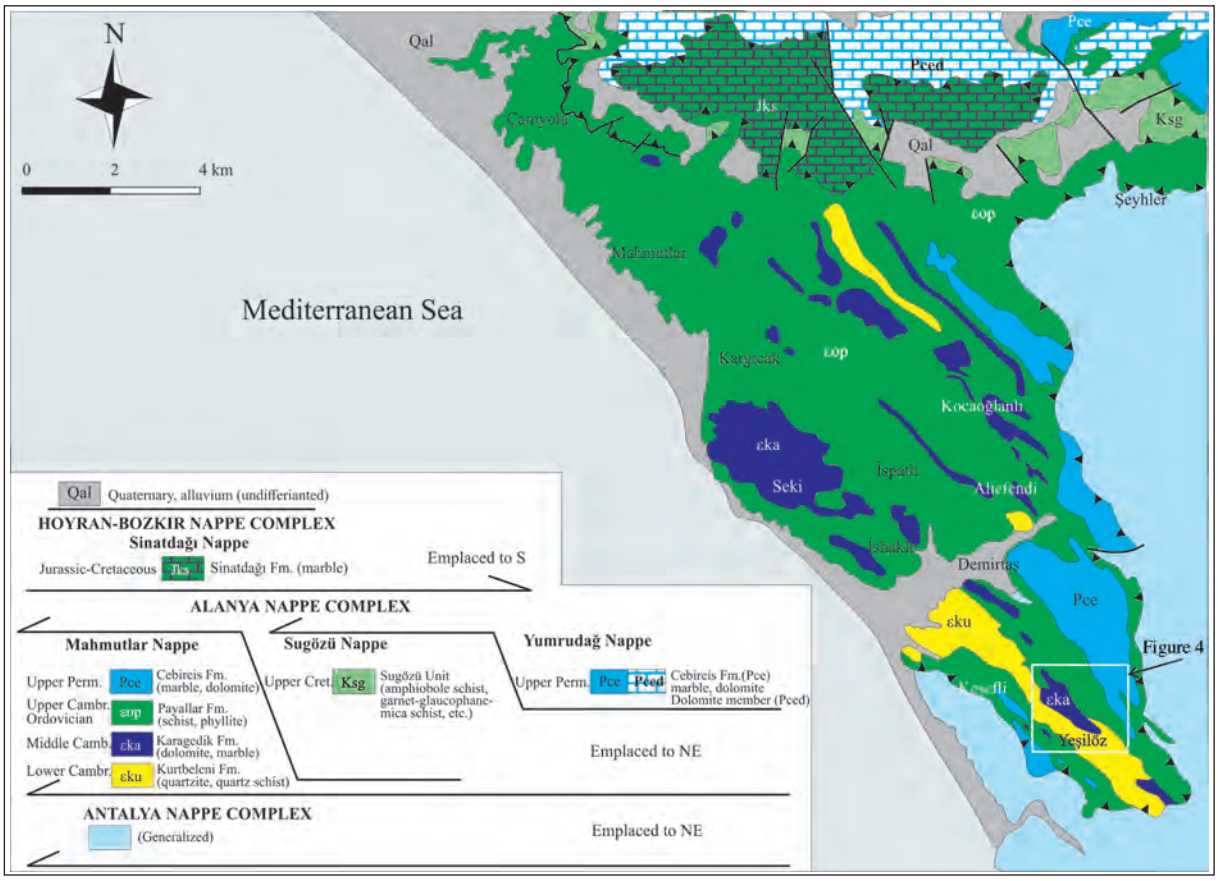

Figure 2- Geological map of the eastern arm of the Isparta Bend with the legend showing the local tectono-stratigraphy of the Tauride orogen (slightly modified from Şenel et al. 2016*a, b*).

regarded as a nappe complex. Öztürk et al. (1995) considered the rock suite of the Alanya Nappe Complex to be a metamorphic equivalent of the rock suite of the Antalya Nappe Complex.

The Alanya Nappe Complex is an assemblage of the following three nappes (Figure 2): the lower Mahmutlar Nappe, the middle Sugözü Nappe and the upper Yumrudağ Nappe, which were earlier referred to also as "units" or "formations" (Okay and Özgül, 1982; Özgül, 1984). The present study is from this nappe complex and hence the internal lithostratigraphy of its component nappes is reviewed briefly in the ensuing subsections. For more detailed descriptions, the reader is referred to Usta and Öztürk (2000) and Bedi and Öztürk (2001).

2.2.1. The Mahmutlar Nappe

This lower nappe is most extensively preserved (Figure 2) and consists of pelitic schists, quartzites, marbles and phyllites representing the green schist metamorphic facies. The basal part of the nappe is the Kurtbeleni formation of early Cambrian age, comprising quartzites and quartzitic schists (Usta and Öztürk, 2000; Bedi and Öztürk, 2001). It is covered conformably by the Karagedik formation of middle Cambrian age, composed of marbles ranging from meta-limestones and meta-dolomites (Usta and Öztürk, 2000). These fine-crystalline meta-carbonates are overlain conformably by the late Cambrian–Ordovician Payallar Formation comprising schists, phyllites and quartzites (Öztürk et al., 1995). A major stratigraphic unconformity separates this latter formation from the overlying Cebireis Formation of late Permian age (Özgül, 1984; Usta and Öztürk, 2000), which consists of phyllites, marbles, quartzites and quartzitic schists.

2.2.2. The Sugözü Nappe

This second nappe (Figure 2), distinguished originally by Özgül (1984) as the Sugözü formation/Nappe and labelled by Şenel et al. (2016*a, b*) as the Sugözü unit, shows a higher metamorphic grade and consists of metabasalts, eclogites and garnet mica-

schists. The age of these rocks has long remained uncertain (Özgül 1984) and controversial. Şenel et al. (2016*a, b*) have recently ascribed these rock assemblage to the Late Cretaceous.

2.2.3. The Yumrudağ Nappe

This third, upper nappe (Figure 2) was initially referred to by Özgül (1984) as the Yumrudağ Group or Yumrudağ Unit. It consists of fine-crystalline limestones and dolomites (marbles) and pelitic schists, representing a low-grade greenschist metamorphism. The rocks formed as sedimentary deposits in the Permian to early Triassic, and became metamorphosed in the Late Cretaceous (Özgül, 1984; Şenel et al., 2016*a, b*).

2.3. The Hoyran–Bozkır Nappe Complex

This S-emplaced non-metamorphic nappe complex is limited in its regional extent to the eastern arm of the Isparta Bend (Figure 1) and is only sparsely preserved as klippen-type outliers in the Alanya region (Figure 2). Özgül (1984) distinguished four component nappes comprising such rocks as neritic limestones and dolomites of Late Triassic to Early Jurassic age, and pelagic to cherty limestones with shales, minor sandstones, green tuffs, diabases and pillow-lava basalts of Middle Triassic to Late Cretaceous (Senonian) age.

3. The Yeşilöz Shear Zone

This shear zone, which is the main topic of the paper, was discovered within the Mahmutlar Nappe – the lower nappe of the Alanya Nappe Complex (Figure 2) – and the present study is the first ever literature report on this intra-orogen feature. The shear zone, striking N35°W, occurs about 20 km to the east of Alanya (Figure 1) and is best exposed in a valley between the villages of Yeşilöz and Hocalar (Figures 3 and 4). It nearly pinches out about 2 km to the SE of Yeşilöz, where the outcrop of Mahmutlar Nappe terminates and where it passes into a couple of unremarkable subvertical strike-slip faults in the Antalya Nappe Complex, but extends for at least 10 km to the NW of Yeşilöz, where its exposure abruptly deteriorates. The shear zone is about 2 km wide, and its best exposed 3-km segment (Figure 3) has been mapped at a scale of 1:5000 and studied in detail.

The Yeşilöz Shear Zone separates blocks the folded phyllites and marbles of the Mahmutlar Nappe (Figures 4 and 5). The dominant rock of the zone itself is a sheared phyllite with elongated lenticular bodies of quartzite and marble, ranging in length from a few decimetres to a couple of kilometres or more (Figure 4). These boudin-like rock bodies, drifted relative to one another within the shear zone, are mainly in a subvertical to vertical position and their long axes are aligned parallel to the zone's strike (Figures 4 and 5).

4. Deformation Structures

The deformation structures in the Mahmutlar Nappe are herein divided arbitrarily into relatively

Figure 3- Oblique photograph of the Yeşilöz Shear Zone (valley) with large lenticular bodies of quartzite (q) and marble (mb).

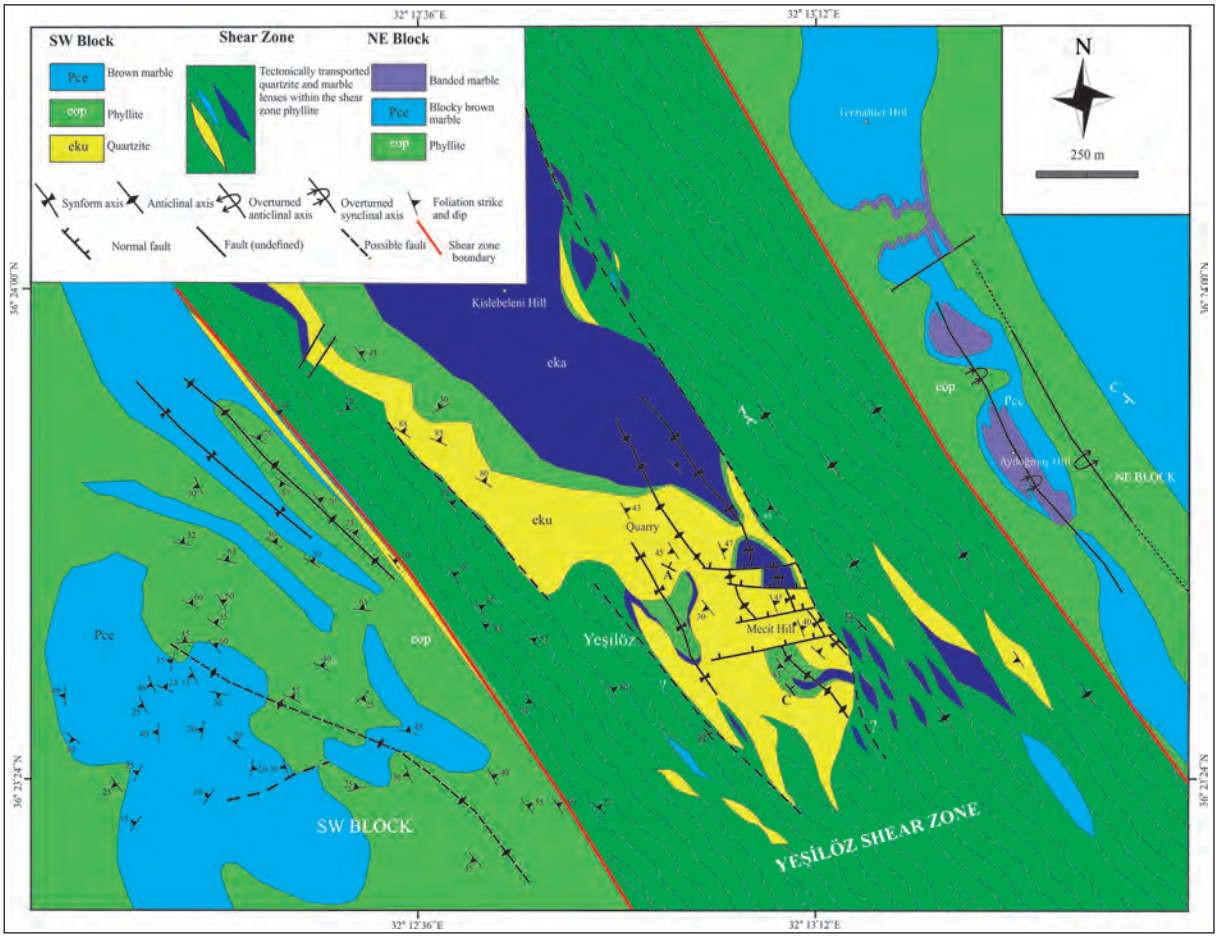

Figure 4- Geological map of the study area, showing the Yeşilöz Shear Zone and adjacent non-sheared parts of the Mahmutlar Nappe (referred to as blocks).

simple (D1), such as folds and faults, and tectonically more advanced (D2), involving metamorphism, recrystallization, pervasive shear and mylonitization.

4.1. Deformation D1: Folds and Faults

The most distinct deformation structures in the study area are folds and faults related to the nappe emplacement (Figures 4 and 5). Mappable folds occur in the Mahmutlar Nappe on both sides of the Yeşilöz Shear Zone, and as disrupted relics within the shear zone. Folds are generally tight, with horizontal or slightly plunging axes trending NW–SE and with upright axial planes (Figures 4 and 5). The folds evolved through two consecutive deformation phases (Figure 6). In the first phase, the competent rocks were transformed into boudins, or lenses, by the formation of isoclinal tight folds F_1 with metamorphic axial cleavage and a bulk transposition of primary bedding (Figure 6, diagrams 1–4). In the next phase of contractional deformation, upright open folds F_2 formed with those lenses of competent rocks preserved in the fold limbs (Figure 6, diagram 5).

Folds F_2 and F_1 have roughly parallel axes, and the spatial trend of the fold axes outside and within the shear zone is the same (Figure 4). Overturned, SW-verging folds F_2 up to a kilometre in axial extent are found within the nappe at the NE boundary of the shear zone (e.g., see the Aydoğmuş Hill area in figures 4 and 5, lower cross-section).

As documented and discussed further in the text, the Yeşilöz Shear Zone is basically a SE-trending dextral strike-slip fault zone – represented by only a couple of faults in the underlying Antalya Nappe Complex beyond the klippe limit of the Mahmutlar Nappe. However, there are also many perpendicular or oblique faults cutting the marble bodies in the Mahmutlar Nappe and the quartzite and marble bodies within the shear zone (Figure 4). They are mainly vertical or subvertical, normal and/or strike-slip faults,

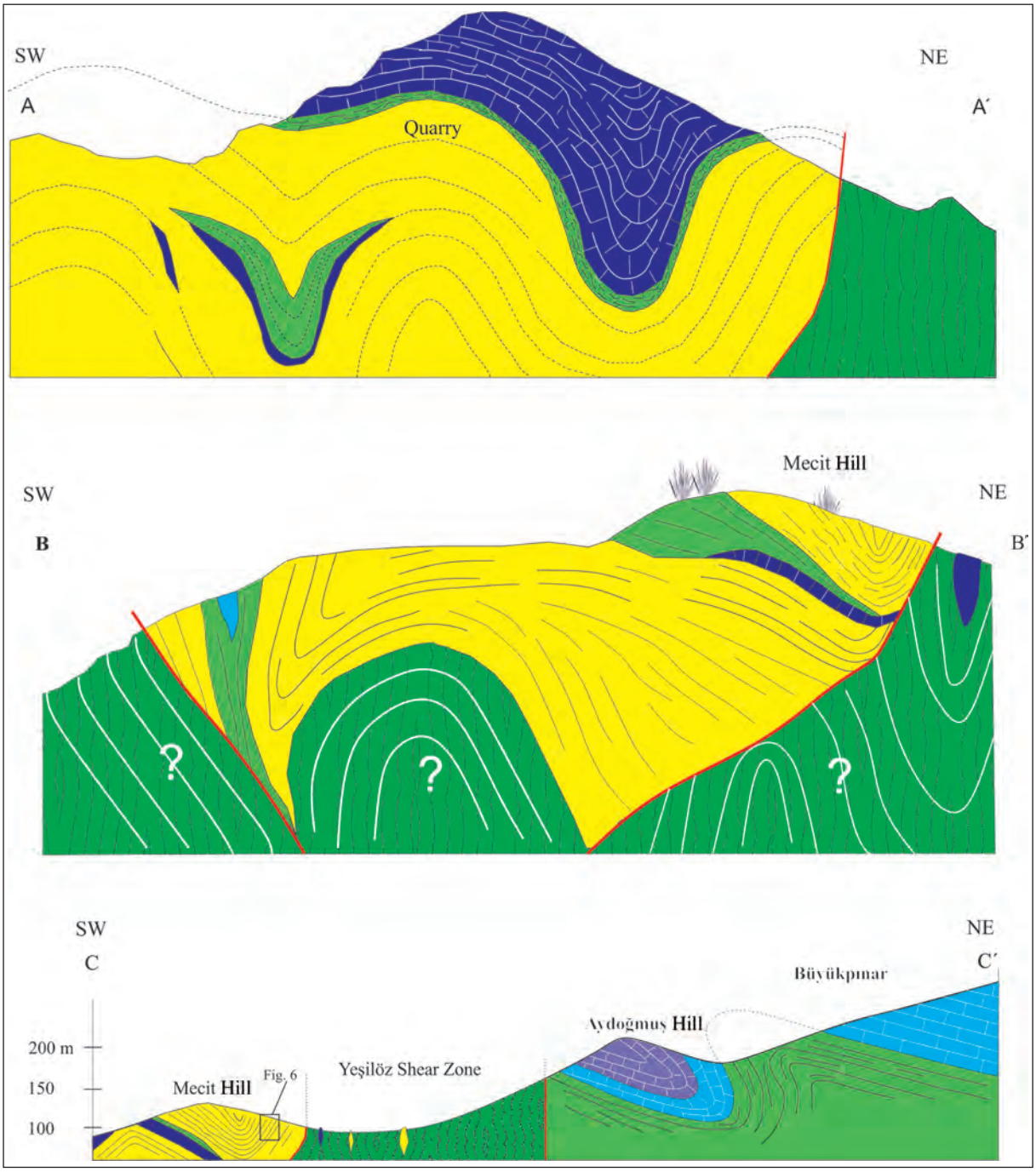

Figure 5- Geological sections across the Yeşilöz Shear Zone and its surroundings (see cross-section lines on the map in figure 4). Cross-sections AA' and BB' are not to scale.

but are difficult to recognize and trace within the rock mass of phyllites.

4.2. Deformation D2: Foliations and Lineation

Foliation in the non-sheared Mahmutlar Nappe generally follows the F_2 folds (Figure 6, diagram 5) and its dip varies, but is uniformly steep, subvertical to vertical, in the Yeşilöz Shear Zone (Figures 4 and 5). This striking difference helps recognize the shear-zone boundary where it runs through phyllites. Additional useful field criterion is the abundance of shear lenses (facoids) within the shear zone and their virtual lack outside its boundaries. The steep foliation and the

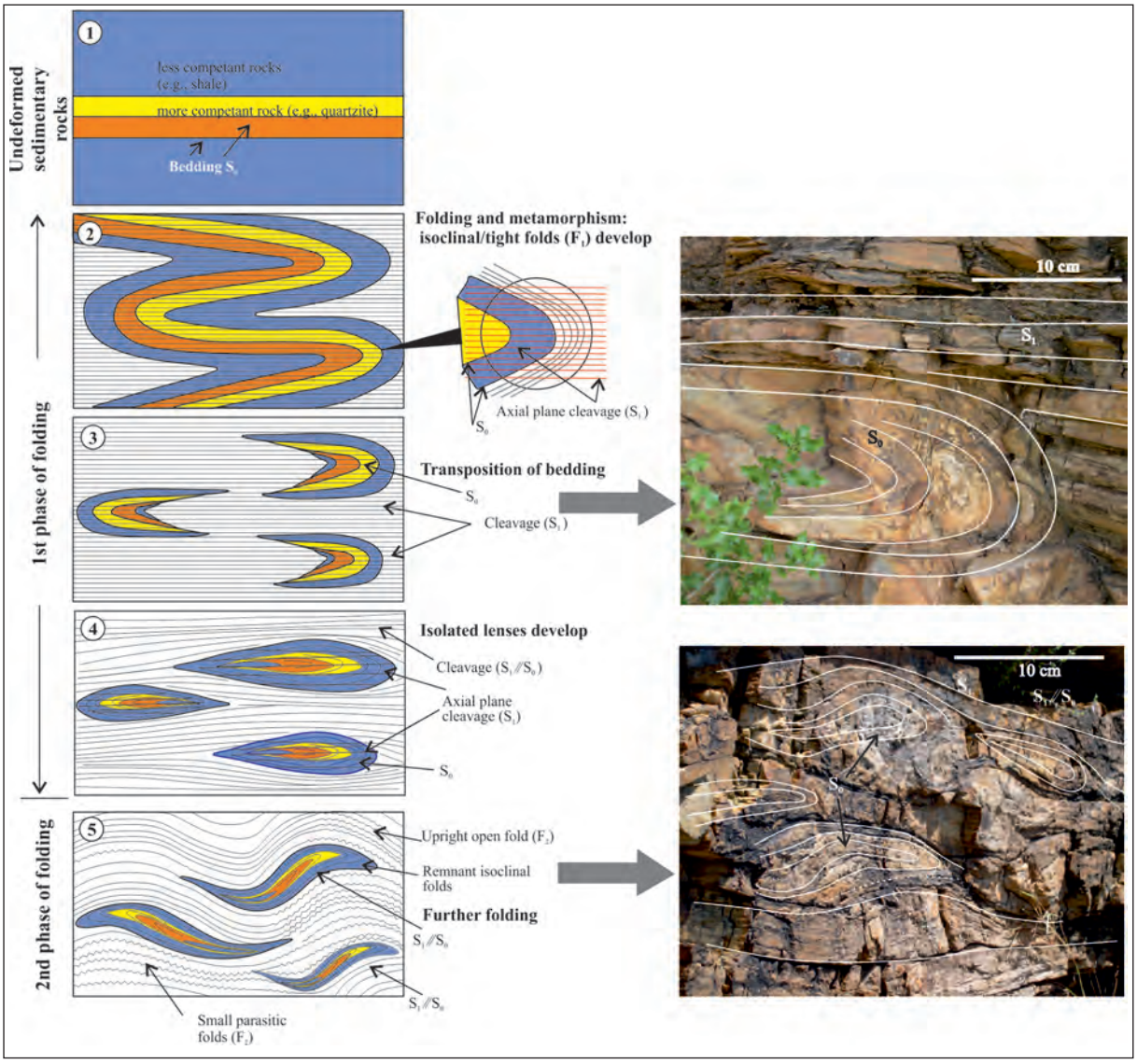

Figure 6- Schematic cartoon showing the development of folding in the Mahmutlar Nappe, illustrated with outcrop photographs from the village of Yeşilöz and the slope of Mecit hill (see localities in figure 4).

rectilinear shear-zone boundary (Figure 4) clearly indicate a steep, nearly vertical shear zone (Figure 5, section CC').

The steep foliation in the mylonitized phyllites of the shear zone has a mean strike N35°-40°W. This foliation (S_s) is younger than the foliation S_1 (Figure 6) in the phyllites outside this zone. Relics of foliation S_1 in the shear zone are recognizable within many of the facoidal lenses enveloped by steep foliation S_s (Figure 7A, B).

The subvertical to vertical foliation planes of the mylonitized phyllites of the shear zone show a genetically related lineation. Lineation is also observed on fault plane. As described further in the next section, these lineation structures served as an important kinematic indicator of tectonic deformation.

4.3. Kinematic Indicators

Mesoscopic kinematic structıres have been used to recognize the directional sense of shearing in the Yeşilöz Shear Zone. These indices include asymmetrical, rotational quartz grains, shear bands (c-s structures), fault slip lineation, foliation and mineral lineation.

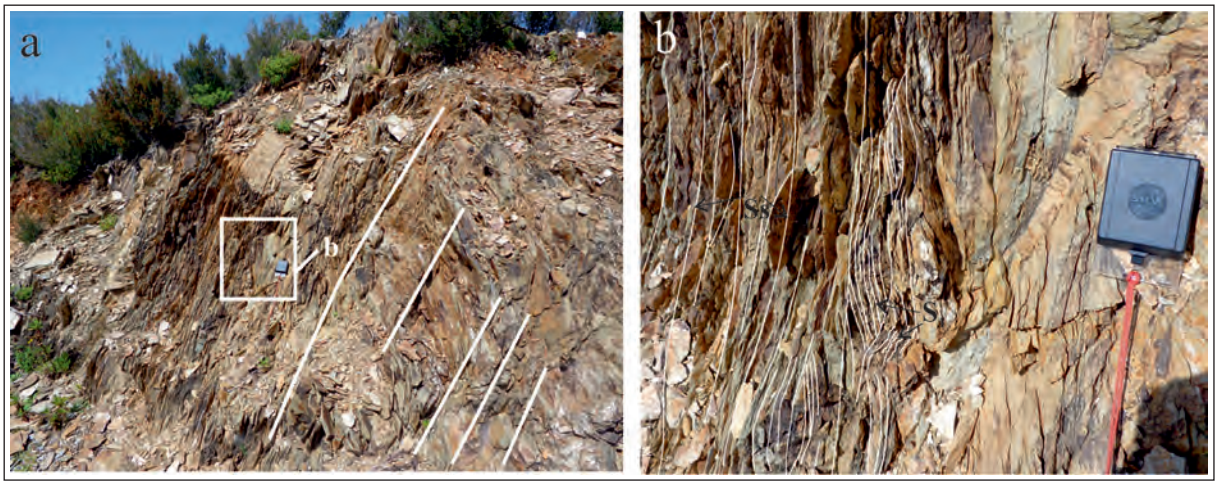

Figure 7- Shear-zone phyllites. (a) Outcrop photograph of the foliated phyllites and fault planes cutting them (white lines). (b) Close-up view of the steep foliation S_s with shear lenses preserving relics of the earlier foliation S_1. Compass for scale.

4.3.1. Asymmetrical Structures and Shear Bands

Asymmetrical, or monoclinic, structures (Figure 8a–c) are found at many localities in the shear zone. The asymmetry of quartz grains in mylonites is due to rotational deformation (Choukroune et al., 1987; Simpson and Schmidt, 1983) and in the present case indicates a dextral shearing. Measurements from several localities show that the azimuthal direction of dextral shearing was 130°–140°.

Shear bands are very common structure in the shear-zone mylonites (Figure 8d–f). Such bands, also known as c-s structures, are formed by the rotation of foliation in a shear zone and are generally a reliable kinematic indicator (Fossen, 2010). The shear bands in the present indicate consistently a dextral shearing in azimuthal direction of 140°.

4.3.2. Foliation and Lineation

Foliation planes and lineation on them were measured in the Yeşilöz Shear Zone within Mahmutlar Nappe (Figure 9) and in the underlying upper nappe of the Antalya Nappe Complex (Figure 10) exposed at the SE extension of the shear zone (see map in figure 2). The aim of these measurements was to verify the shear direction derived from other structures; to assess whether the shear zone is limited to the Mahmutlar Nappe or extends deeper; and to estimate on this basis the age of the shear zone relative to nappe emplacement. The data plotted on stereonet show that the directional trend of lineation is nearly parallel to the strike trend of foliation (Figure 9a). The parallelism and concordance of foliation and lineation in the Mahmutlar Nappe and the underlying nappe (Figure 9a) indicate that the development of the Yeşilöz Shear Zone in this former nappe had clearly affected the underlying older one.

4.3.3. Faults and Slip Lineation

The subvertical to vertical foliation S_s in the shear zone is cut obliquely or parallel by similarly steep fault planes (Figure 11c, d). Faults parallel to foliation indicate strike-slip faulting (Figure 11a), whereas the oblique ones are normal or oblique-slip faults (Figure 4). Some of the faults are dextral Riedel fractures formed in a right-lateral simple shear system (Figure 11b).

Another conspicuous feature in the axial part of the shear zone is a NW-trending ridge comprising quartzite and marble (Figures 4 and cross-section AA' and BB' in figure 5). Slip lineation indicating strike-slip faulting is found in the slopes of the ridge. This ridge is thought to be an uplifted positive flower structure within the shear zone (Figure 5, section BB').

5. Discussion

The Yeşilöz Shear Zone, trending N35°W and at least 2 km wide, can be followed over its length segment of more than 10 km (Figure 12) and is best exposed in a topographic valley between the towns of Yeşilöz and Demirtaş and between the villages of İspatlı and Aliefendi. The shear zone is unmappable farther to the NW, where its exposure in forested area is very poor. Mesoscopic kinematic indices point

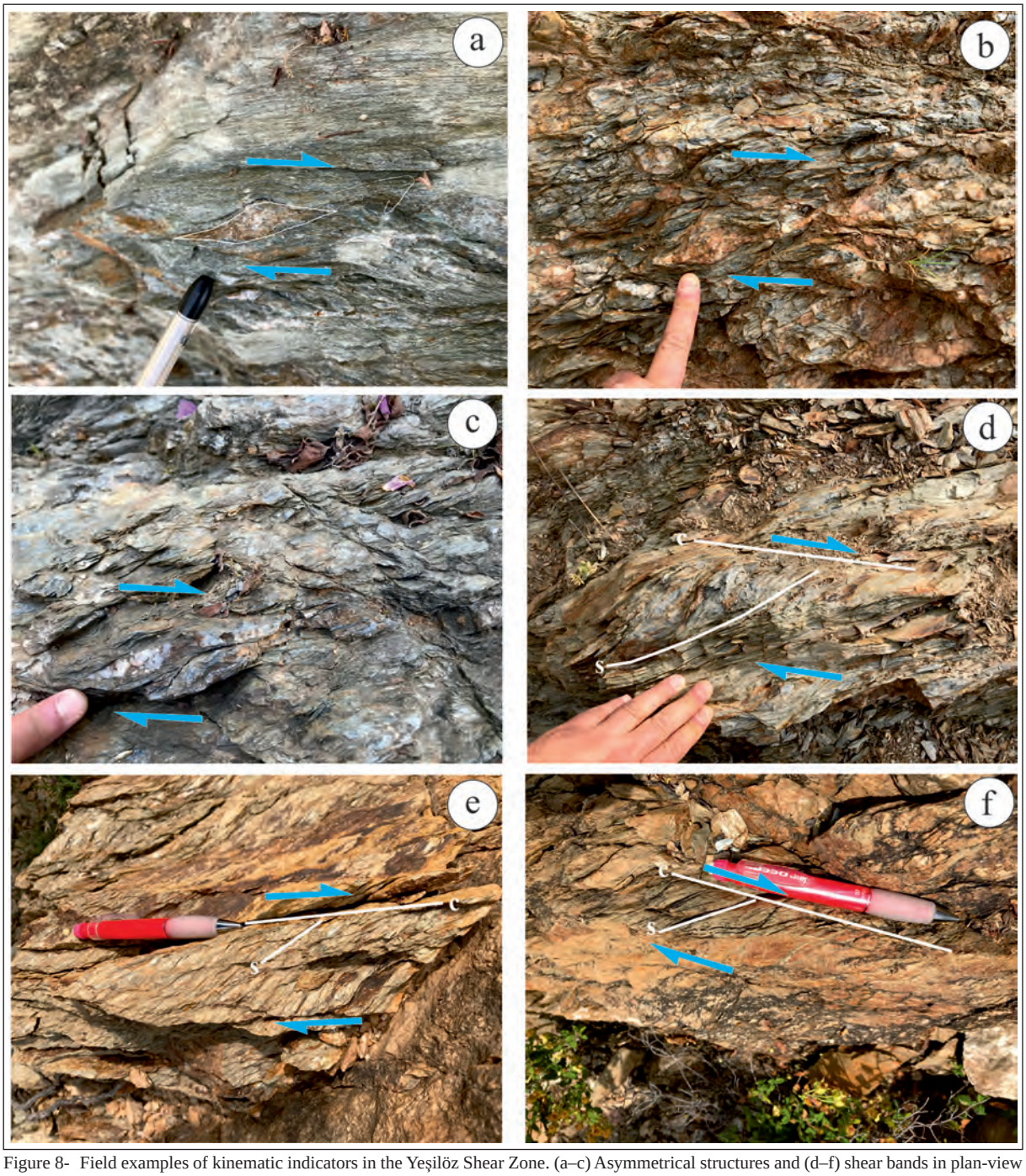

Figure 8- Field examples of kinematic indicators in the Yeşilöz Shear Zone. (a–c) Asymmetrical structures and (d–f) shear bands in plan-view outcrops.

unanimously to a dextral strike-slip deformation in the shear zone (Figures 8–11). The shear zone is in the lower Mahmutlar Nappe of the NE-emplaced Alanya Nappe Complex (Figure 2) and is narrower towards the SE, where it recognizably extends into the uppermost nappe of the underlying Antalya Nappe Complex (Figure 12), as evidenced by the parallelism of both their subvertical to vertical foliation and the lineation on foliation and fault planes (Figures 9, 11, 12 and 13).

The structural evidence from the Yeşilöz Shear Zone and the adjoining non-sheared parts of the Mahmutlar Nappe indicates two main stages of tectonic deformation (Figure 14). The deformation stage D1 occurred prior to and during the nappe emplacement

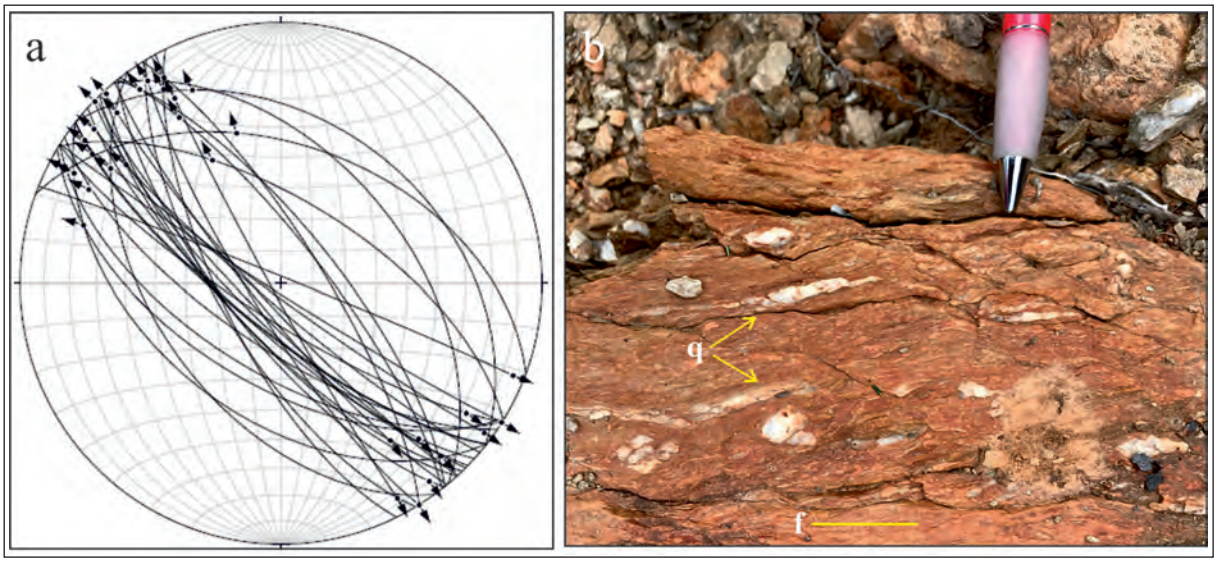

Figure 9- (a) Stereoplot of the foliation and lineation measurements from Yeşilöz Shear Zone. Equal-area lower hemisphere projection; plot made with the FaultKinWin Version 1.2.2 software (Marret and Allmendinger 1990; Allmendinger et al. 2012). (b) Plan-view outcrop photograph showing the planes of vertical foliation (f) and flattened, boudinaged quartz bands (q) in the shear-zone phyllite.

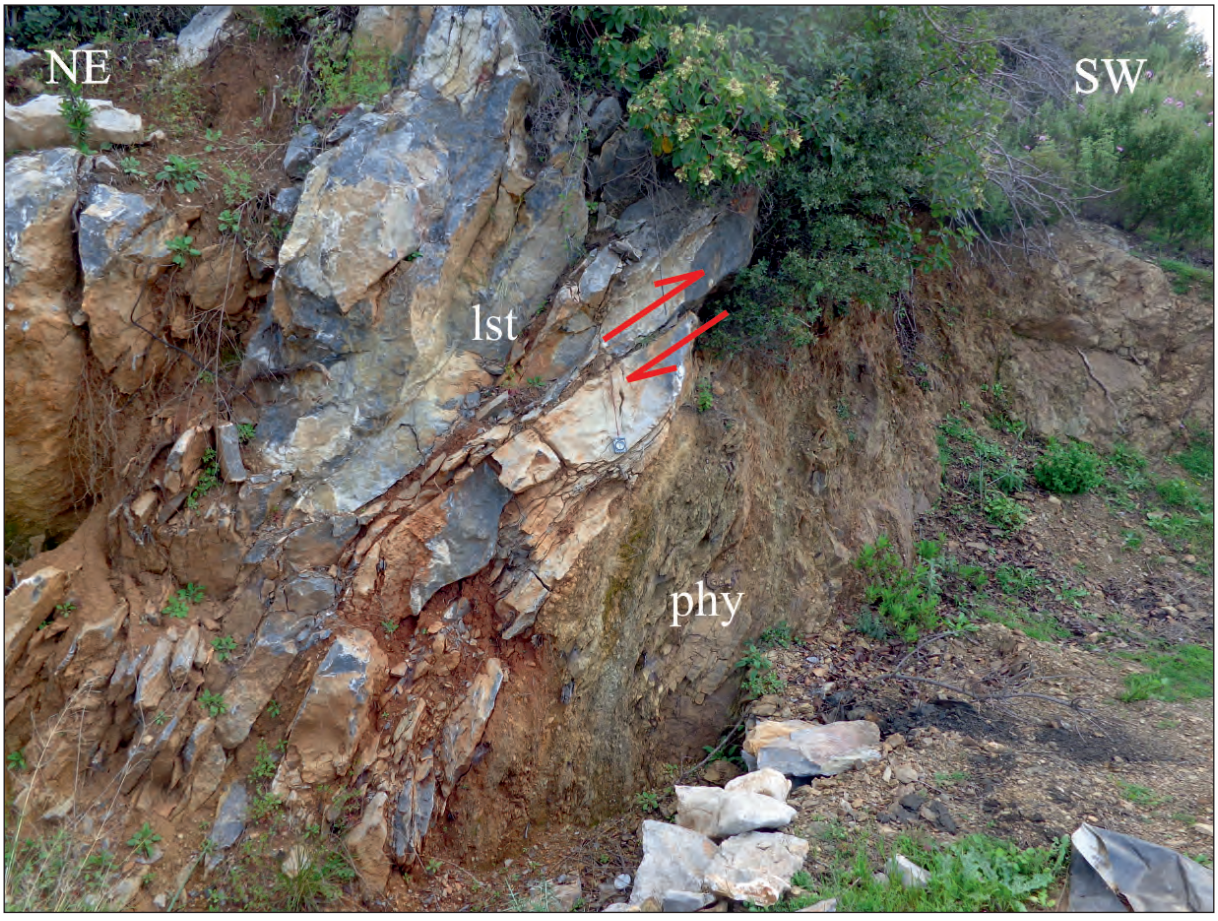

Figure 10- Outcrop photograph showing subvertically foliated phyllitic shale (phy) and recrystallized limestone (lst) in the topmost part of the Antalya Nappe Complex exposed about 2 km west of Uğrak at the SE extension of the Yeşilöz Shear Zone. This field evidence indicates that the uppermost part of the non-metamorphic Antalya Nappe Complex was not only mildly metamorphosed by the emplacement of Mahmutlar Nappe, but also structurally affected by the development of its shear zone.

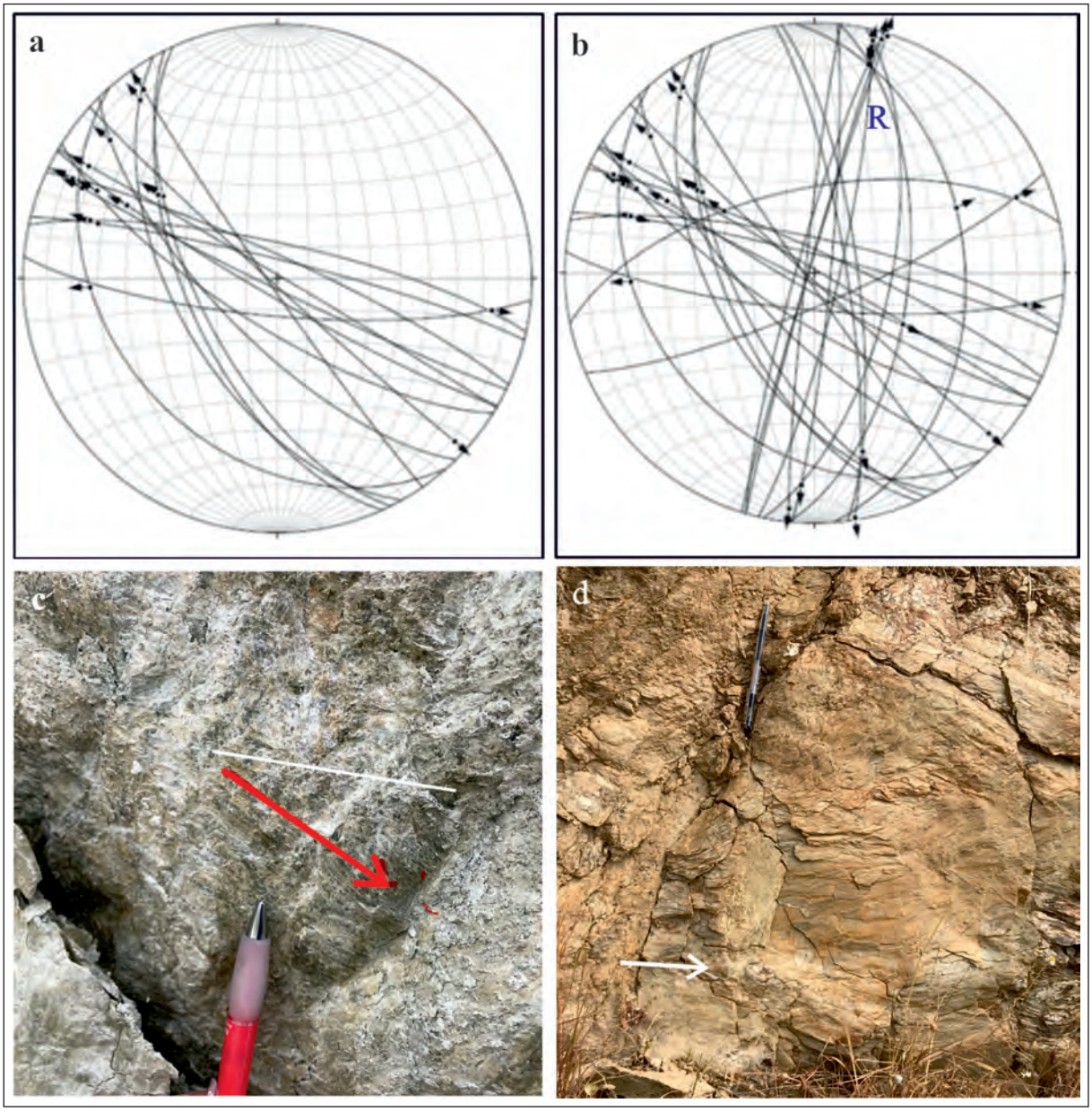

Figure 11- Equal-area lower hemisphere stereographic projection of fault planes and striae measurements from from the Yeşilöz Shear Zone. (a) Strike-slip faults parallel to the shear zone and (b) coeval Riedel fractures. Plot made with the FaultKinWin Version 1.2.2 software (Marret and Allmendinger 1990; Allmendinger et al. 2012). (c, d) Outcrop photographs of fault planes and slip lineation in the shear zone.

and included metamorphic folding (Figure 6) with the transposition of primary bedding S_0, development of folds F_1 with pervasive axial cleavage S_1, and formation of upright open folds F_2 with small local parasitic folds F_3. The axes of folds F_2 in the quartzite-marble bodies within the shear zone are parallel to the F_2 axes in the non-sheared nappe outside (Figure 4), which indicates a common origin of these folds – reflecting a NE–SW tectonic shortening (Figure 14a) and attributed to the thin-skinned nappe emplacement.

The Alanya Nappe Complex, like the underlying Antalya Nappe Complex in the study area, is widely considered to have been derived from the SW (e.g., Özgül, 1976, 1984; Okay and Özgül, 1984; Öztürk et al., 1995; Okay and Tüysüz, 1999; Nemec et al., 2018). Although the evidence of a SW-verging fold F_2 at the NE margin of the shear zone (see figure 4 and cross-section CC' in figure 5) might suggest an opposite direction of the Mahmutlar Nappe emplacement (cf. Marcoux et al., 1989), this vergence cannot be

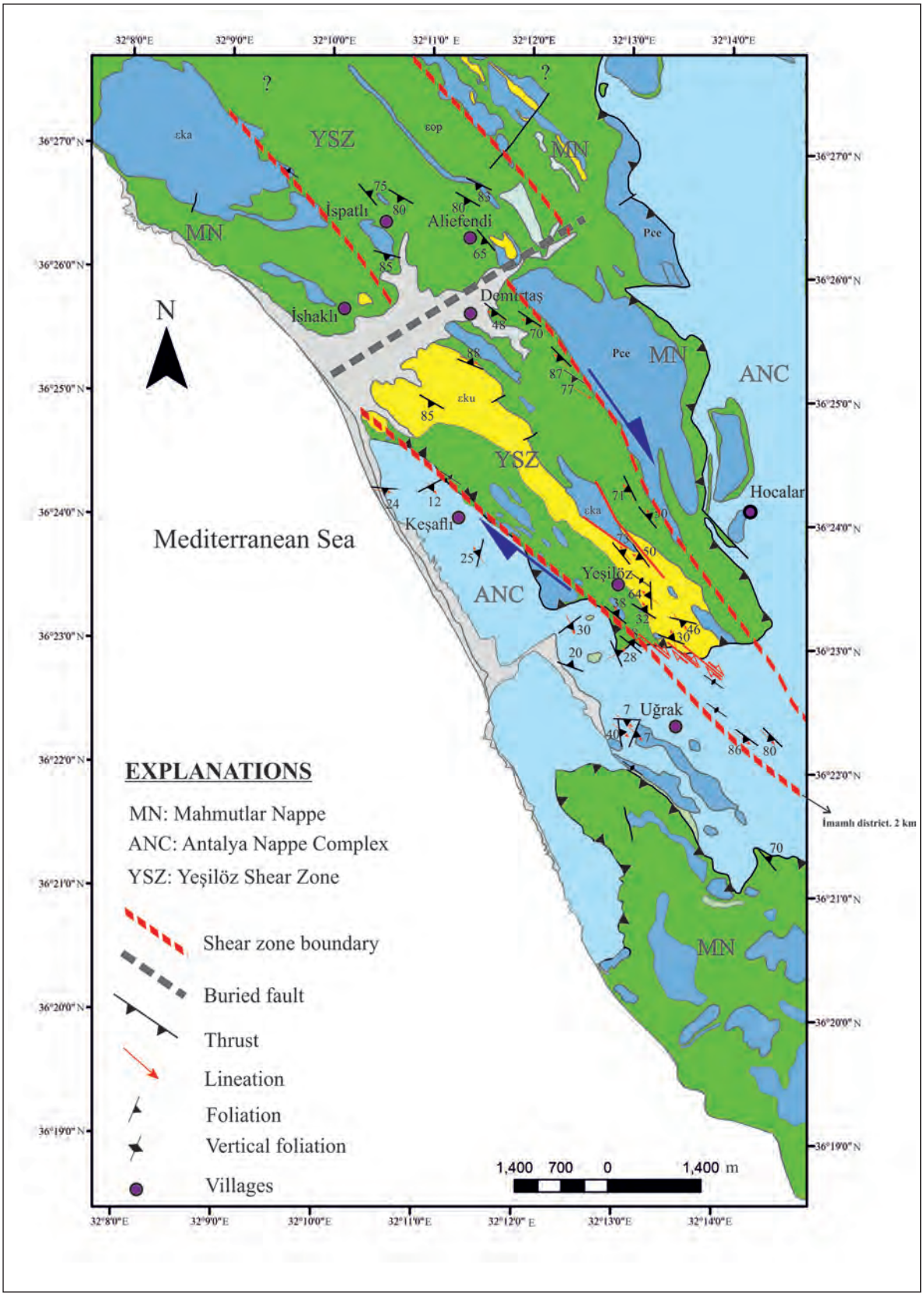

Figure 12- Geological map of the Yeşilöz Shear Zone, showing its offset by transverse fault near Demirtaş and its narrowing towards the SE with extension into the underlying Antalya Nappe Complex. The map is a simplified compilation from Özgül (1976, 1984) and Şenel et al. (2016*b*); legend as for figure 2.

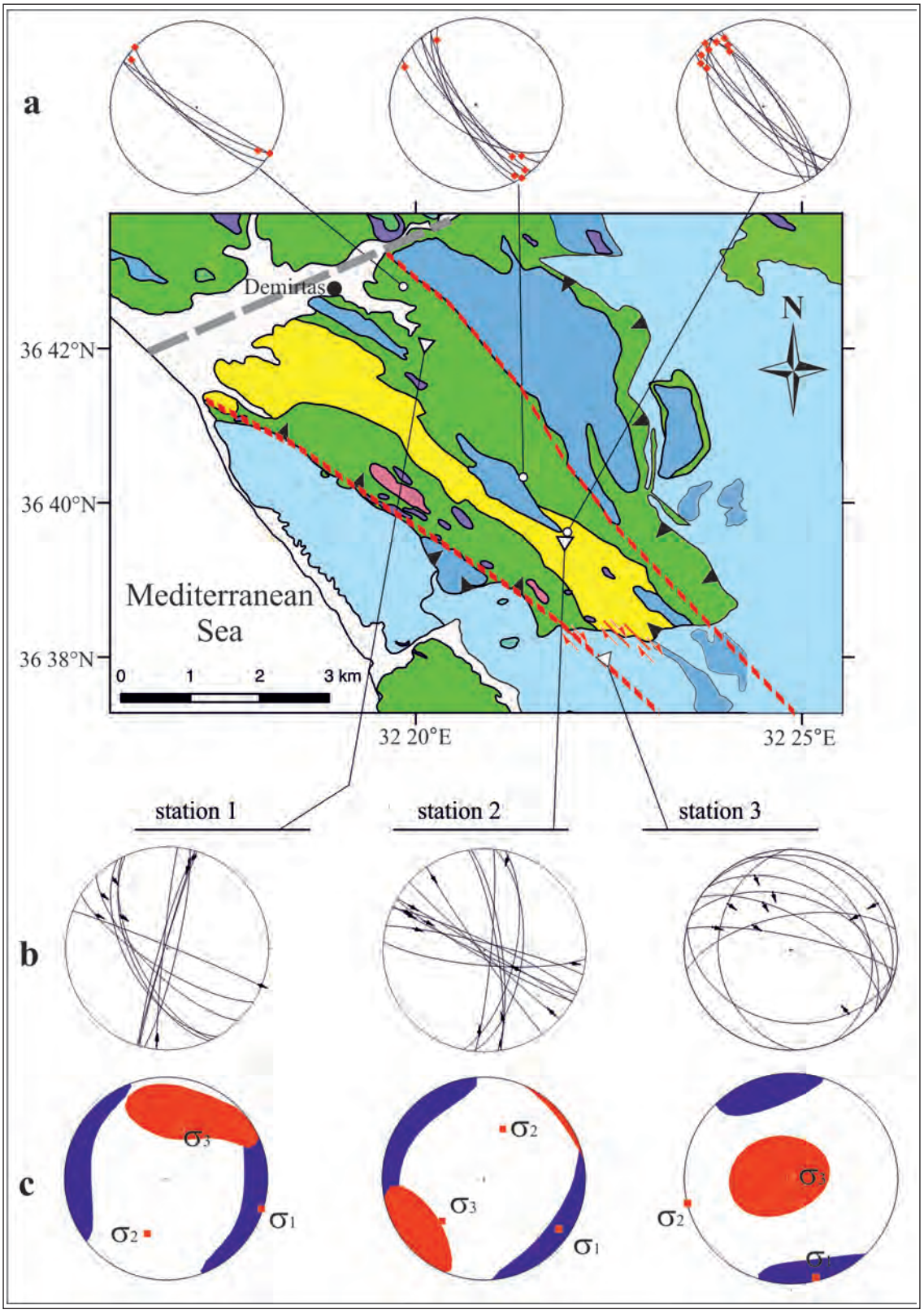

Figure 13 - A synthetic display of the whole dataset from the Yeşilöz Shear Zone in Mahmutlar Nappe and from the shear zone SE extension in the underlying Antalya Nappe Complex (see figure 12). (a) Foliation and lineation data, (b) fault data and (c) a contoured stereoplot of kinematic axes. The plot was made with the FaultKinWin Version 1.2.2 software (Marret and Allmendinger 1990; Allmendinger et al., 2012). The geological map is a simplified compilation from Özgül (1976, 1984) and Şenel et al. (2016*b*); legend as for figure 2.

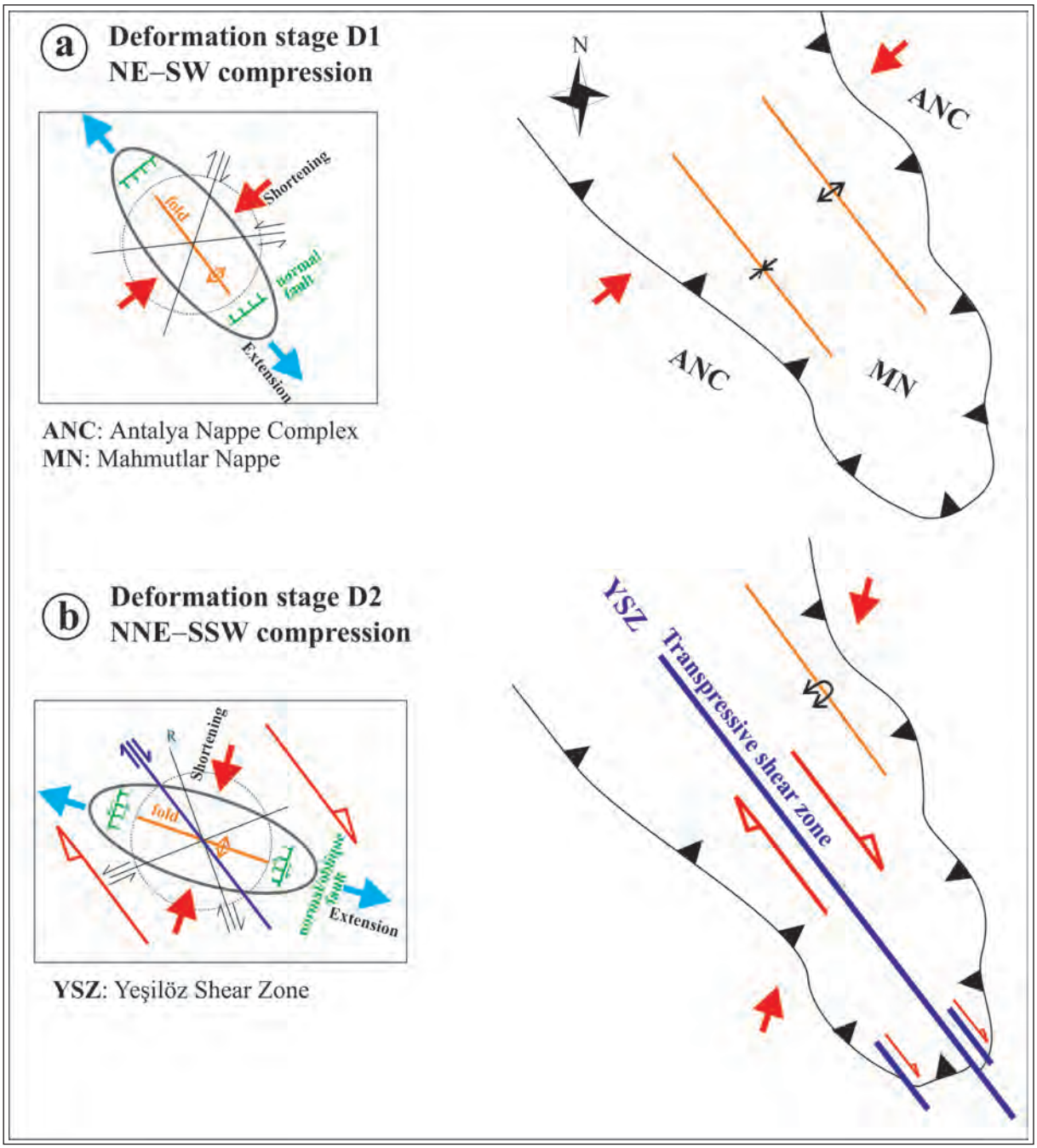

Figure 14- Interpretive cartoon summarizing the development of orogenic deformation as recognized in the study area, with the sketch map referring to figure 13. (a) The NE–SW contraction (pure shear) and formation of folds at stage D1. (b) The subsequent NNE–SSW contraction with dextral simple shear and the formation of Yeşilöz Shear Zone at stage D2.

regarded as representing the frozen movement and rotation that generated the nappe's system of F_2 folds. The inference of bulk movement direction from fault vergence is supposable where all folds in their regional system express a unique one-sided movement, with their vergence including the younging direction (cf. Fossen, 2010). Nothing like that is the case in the Mahmutlar Nappe, where – in contrast – the large F_2 folds preserved in the quartzite-marble bodies within the shear zone and those present on its SW side are all upright folds (Figures 4 and 5). The overturned fold is at the NE margin of the shear zone and hence is probably related genetically to the latter. For example, this overfold may be a shallow-level expression of the shear zone's sideways expansion (widening), perhaps at a restraining bend of parental strike-slip fault, with the tectonic drift of large rigid quartzite-marble bodies adding excess local rock volume at depth (Figure 4).

The deformation stage D2 (Figure 14b) occurred after the emplacement of Mahmutlar Nappe and involved a simple-shear strain system related to an anticlockwise-rotated compression stress axis. This transcurrent deformation was essentially ductile and resulted in the development of the transpressional Yeşilöz Shear Zone with subvertical to vertical foliation S_s paralleled by strike-slip faults and with a tectonic drift of lenticular, rigid quartzite/marble bodies. Phyllite shear lenses bear relics of foliation S_1 (Figure 7b) inherited from the original nappe. The N–S compression and dextral transcurrent deformation are best evidenced by the kinematic analysis of fault data from the shear zone (Figures 13b, c and 14b).

The emplacement of the Mahmutlar Nappe (deformation stage D1) caused a mild dynamic metamorphism of the underlying top part of the Antalya Nappe Complex, into which the transcurrent strain of the Yeşilöz Shear Zone then extended directly downwards (Figures 12 and 13). This evidence implies that no significant further translational movement of the Mahmutlar Nappe occurred during and after the shear zone formation. The shear zone formed in a different stress field, probably by the independent emplacement of the younger Sugözu Nappe or perhaps the Sugözü –Yumrudağ nappe set (Figure 2, legend) onto the Mahmutlar Nappe. The shear zone most likely accommodated the residual shortening induced by the younger nappe movement.

It is worth noting that the internal lithostratigraphy of the Mahmutlar Nappe (Figure 2, legend), as mapped and described in the regional literature (Özgül, 1976, 1984; Şenel et al., 2016*a*, *b*), was broken and virtually destroyed within the Yeşilöz Shear Zone – with the fragments of the individual formations turned into allochthonous blocks (Figure 4). The shear zone's mylonitized phyllite with dispersed quartzite/marble blocks, despite their consanguinity to the nappe lithostratigraphic units (cf. Figure 2, legend), should then be regarded as a tectonic mèlange, or "broken formation". The distinction between nappes and their derivative tectonic mèlanges is crucial to the reconstruction of the tectonic history and deformation dynamics of an orogen.

5. Conclusions

The NW-trending shear zone discovered in the Alanya region, labelled the Yeşilöz Shear Zone, occurs in the lower Mahmutlar Nappe of the NE-emplaced Alanya Nappe Complex. The nappe underwent early metamorphic folding and developed upright open folds during its movement. The shear zone is around 2 km wide and mappable over a length segment of 10 km. Its exposure in the forested area farther to the NW is poor to none, whereas to the SE, the shear zone is markedly narrowing at the nappe outcrop limit and shows direct downward extension into the underlying older nappe of the Antalya Nappe complex.

The shear zone consists of the component metamorphic rocks of the Mahmutlar Nappe, but with the phyllite strongly mylonitized and showing vertical shear foliation S_s and with the quartzites and marbles dispersed as lenticular bodies ranging in length from decimetres to more than 1 km. These brittle rock bodies show broken upright open folds similar as in the nappe, and also the phyllite facoidal shear lenses bear relics of the nappe metamorphic foliation S_1. Analysis of kinematic indices in the shear zone points to a dextral transcurrent deformation.

The nappe emplacement of Mahmutlar Nappe had mildly metamorphosed the upper part of the underlying nappe and also affected it with the development of the shear zone that reached directly downwards. The nappe thus showed no further translational movement during and after the shear zone formation, which suggests that the mylonitic ductile deformation probably accommodated a residual shortening induced by the emplacement of the next, younger nappe of the Alanya Nappe Complex.

Acknowledgements

The author appreciates stimulating field discussions with Øystein J. Jansen and Wojciech Nemec, and further helpful discussions with Yahya Çiftçi and Fuat Erkül. Constructive reviews by Yaşar Eren, Şule Gürboğa and Wojciech Nemec helped to improve the manuscript.

References

Allmendinger, R. W., Cardozo, N., Fisher, D. 2012. Structural Geology Algorithms: Vectors and Tensors in Structural Geology. Cambridge University Press, Cambridge, 302 p.

Bedi, Y., Öztürk, E.M. 2001. Alanya-Köprülü (Antalya) dolayının jeolojisi (Alanya-O 28-c1, d1, d2 ve d3 paftaları). Maden Tetkik ve Arama Genel Müdürlüğü Rapor no: 10488, Ankara (unpublished).

Blumenthal M. 1947. Geologie des Taurusketten im Hinterland von Seydisehir und Beyşehir. Mineral Research and Exploration Institute (MTA) of Turkey Publication, Series D2.

Blumenthal, M.M. 1951. Recherches géologiques dans le Taurus occidental dans l'arrière-pays d'Alanya. Mineral Research and Exploration Institute Publication, Series D5, Ankara.

Bozkaya, Ö., Yalçın, H. 2004. New mineralogic data and implications for the tectonometamorphic evolution of the Alanya Nappes, Central Tauride Belt, Turkey. Int. Geol. Rev., 46, 347–365.

Brunn, J.H., Dumont, J.F., Graciansky, P.C., Gutnic, M., Juteau, T., Marcoux, J., Monod, O., Poisson , A. 1971. Outline of the geology of the Western Taurides. In: Campbell A.S., editor, Geology and History of Turkey, p. 225–252. Petroleum Exploration Society of Libya, Tripoli.

Choukroune, P., Gapais, D., Merle, O. 1987. Shear criteria and structural symmetry. J. Struct. Geol., 9, 525–530.

Çetinkaplan, M., Candan, O., Koralay, O.E., Okay, A., Oberhänsli, R., Chen, F. 2010. Alanya Masifinin Petrolojisi, Jeokronolojisi ve Tektono-Metamorfik Evrimi. Tübitak Proje Raporu, Proje no: 107Y107, 215 p.

Fossen, H. 2010. Structural Geology. Cambridge University Press, Cambridge, 463 p.

Lefevre R. 1967. Un nouvel e´le´ment de la ge´ologie du Taurus Lycien: les nappes d'Antalya (Turquie). Comp. Rend. l'Acad. Sci. de Paris, 165, 1365–1368.

Leren, B. L. S., Janbu, N. E., Nemec, W., Kırman, E., Ilgar, A. 2007. Late Cretaceous to Early Eocene sedimentation in the Sinop–Boyabat Basin, north-central Turkey: a deep-water turbiditic system evolving into littoral carbonate platform. IAS Spec. Publ., 38, 401–456.

Marcoux, J., Ricou, L.E., Burg, J.P., Brun, J.P. 1989. Shear-sense criteria in the Antalya and Alanya thrustsystem (southwestern Turkey): Evidence for a southward emplacement: Tectonophysics, 161, 81–91.

Marrett, R.A., Allmendinger, R.W. 1990. Kinematic analysis of fault-slip data. J. Struct. Geol., 12, 973–986.

Nemec, W., Alçiçek, M.C., Özaksoy, V. 2018. Sedimentation in a foreland basin within synorogenic orocline: Palaeogene of the Isparta Bend, Taurides, SW Turkey. Basin Res., 30, 650–670.

Okay, A.I. 1989. An exotic eclogite/blueschist slice in a Barrovian-style metamorphic terrain, Alanya Nappes, Southern Turkey. J. Petrol., 30, 107–132.

Okay, A.I. 2008. Geology of Turkey: A synopsis. Anschnitt, 21, 19–42.

Okay, A.I., Özgül, N. 1982, Blueschist and eclogites from the Alanya Massif, Turkey. Conference Abstracts, Geological Evolution of the Eastern Mediterranean, Edinborough, p. 82.

Okay, A.I, Özgül, N. 1984. HP/LT metamorphism and structure of the Alanya Massif, southern Turkey: an allochthonous composite tectonic sheet. In: Robertson, A.H.F., Dixon, T.E., editors, The Geological Evolution of the Eastern Mediterranean. Geol. Soc. London Spec. Publ., 14, 429–439.

Okay, A.I., Tüysüz, O.1999. Tethyan sutures of northern Turkey. In: Durand, B., L. Jolivet, L., Horváth, F., Séranne, M., editors, The Mediterranean Basins: Tertiary Extension within the Alpine Orogen. Geol. Soc. London Spec. Publ., 156, 475–515.

Özgül, N. 1976. Torosların bazı temel jeolojik özellikleri. Türkiye Jeol. Kur. Bült., 19, 65–78.

Özgül, N. 1984. Stratigraphy and tectonic evolution of the Central Taurides. In: Tekeli, O., Göncüoğlu, M.C., editors, Geology of the Taurus Belt. Proc. International Symposium, Ankara, p. 77–90.

Öztürk, E.M., Akdeniz, N., Bedi, Y., Sönmez, İ., Usta, D., Kuru, K., Erbay, G. 1995. Alanya napının stratigrafisine farkli bir yaklaşım. Türkiye Jeol. Kur. Bült., 10, 2–10.

Robertson, A. H. F., Poisson, A., Akıncı, Ö. 2003. Developments in research concerning Mesozoic–Tertiary Tethys and neotectonics in the Isparta Angle, SW Turkey. Geol. J., 38, 195–234.

Robertson, A.H.F., Parlak, O., Ustaömer, T. 2012. Overview of the Palaeozoic–Neogene evolution of Neotethys in the Eastern Mediterranean region (southern Turkey, Cyprus, Syria). Petrol. Geosci., 18, 381–404.

Simpson, C., Schmid, S.M. 1983. An evaluation of criteria to deduce the sense of movement in sheared rocks. Geol. Soc. Am. Bull., 94, 1281–1288.

Şengör, A.M.C., Yılmaz, Y. 1981. Tethyan evolution of Turkey: a plate tectonic approach. Tectonophysics, 75, 181–241.

Şenel, M., Bedi, Y., Çörekçioğlu, E. 2016*a*. 1:100 000 Ölçekli Türkiye Jeoloji Haritaları Serisi, Alanya-O28 paftası. Maden Tetkik ve Arama Genel Müdürlüğü no: 232, Ankara.

Şenel, M., Bedi, Y., Usta, M. 2016*b*. 1:100 000 Ölçekli Türkiye Jeoloji Haritaları Serisi, Alanya-P28 paftası. Maden Tetkik ve Arama Genel Müdürlüğü no: 223, Ankara.

Usta, D., Öztürk, E.M. 2000. Gülendağı-Gündoğmuş dolayının (Alanya O27-a3, b4, O28-a4 paftalarının) jeolojisi. Maden Tetkik ve Arama Genel Müdürlüğü Rapor no: 10487, Ankara (unpublished).

Woodcock, N.H., Robertson, A.H.F. 1977. Imbricate thrust belt tectonics and sedimentation as a guide to emplacement of part of the Antalya Complex, S.W. Turkey. In: Izdar, E., Nakoman, E., editors, Proceedings of the 6th Colloquium on Geology of the Aegean Region. Contributions Series 2, Dokuz Eylul University, Bornova, İzmir.

Bull. Min. Res. Exp. (2019) 158: 49-119

Bulletin of the Mineral Research and Exploration

http://bulletin.mta.gov.tr

Selandian benthic foraminiferal assemblages of the Southwestern Burdur (South of Lake Yarışlı, Western Turkey) and some taxonomic revisions

Şükrü ACAR[a*]

[a]*General Directorate of Mineral Research and Exploration, Department of Geology, 06800, Ankara, Turkey. orcid.org/0000-0003-0204-152X*

Research Article

Keywords:
Lake Yarışlı, Burdur, foraminifera, selandian, SBZ 2, *neosistanites*, *parahaymanella*, *pseudohottingerina*.

ABSTRACT

In this study, new genera and species are described. These three new genera are *Neosistanites* (type species *Sistanites iranica*), *Parahaymanella* (type species *Parahaymanella hakyemezae*) and *Pseudohottingerina* (type species *Pseudohottingerina burdurensis*). *Neosistanites* new species and new genus (*N. sozerii, N. okuyucui, N. guvenci, N. dageri, N. catali, N. armagani, N. inali*) and *Neosistanites iranicus* are defined. *Parahaymanella* is the new genus and its new species *(P. hakyemezae, P. bozkurti* and *P. alanae*). New species of new genus *Pseudohottingerina* (*Ps. burdurensis* and *Ps. yarisliensis*). *Laffitteina anatoliensis, Laffitteina thraciaensis, Sirtina paleocenica, Ankaraella minima* new species and *Laffitteina erki, Laffitteina mengaudi, Ankaraella trochoidea* species are defined and illustrated. Known *Akbarina primitiva, Bolkarina aksarayi, Biloculinites* cf. *paleocenica, Miscellanea? globularis, Globoflarina? sphaeroidea* species and *Heterillina* sp., *Keramosphaera* sp., *Textularia* sp., *Chrysalidina?* sp., *Kolchidina?* sp., *Lockhartia?* sp., *Popovia?* sp. and *Thalmannita?* sp., genera, illustrated only. Only photographs of undescribed benthic foraminifera genera (miliolid, miscellanid, planulinid, rotaliid, mississippinid, aglutine) are given. The definition of a new family (Neosistanitidae), the classification of the *Neosistanites*, the type species and species transfers between the genera, the emendation of the *Ankaraella* genus and the corrections of the *Ankaraella trochoidea* were made. Photographs of some fossil algae are given in plates. All material (SBZ 2) belongs to the Selandian.

Received Date: 21.12.2017
Accepted Date: 27.03.2018

1. Introduction

The type localitiy of *Laffitteina erki* (Sirel, 1969) is in the Pontide belt (Gölköy-Mesudiye-Ordu). This species, in later studies (İnan, 1995, 1996; İnan and İnan, 1987, 2008; İnan et al., 1992, 2005; Özgen, 1997; Öztürk et al., 1984; Sirel 1994, 1996, 1998, 2004, 2009, 2015; Şengün et al., 1988), was reported also in various localities in the Pontide and the Anatolide belts. As a result of the MTA (General Directorate of Mineral Research and Exploration) survey conducted within the scope of the Yeşilova project, the presence of this foraminiferal species in the Mediterranean (Tauride) belt, has been determined (Bilgin et al., 1990). Therefore, locality of the sample bearing *L.* erki (just South of the Lake Yarışlı, SW Burdur) was visited in 1990 by the author of this study in order to contribute to knowledge of Paleocene paleogeography of Turkey and to examine benthic foraminiferal assemblage accompanied by *L. erki*, and five systematic limestone samples were taken from a very small outcrop of 3-5m thickness (Text Figure 1). Most of these benthic foraminifera are characterised by their porcelaneous tests and are organisms occuring in the shallow marine, back reef and restricted shelf environments.

The study area (just South of the Lake Yarışlı) is located in a place (West of Isparta Angle, Taurides) that tectonic is significantly active (Poisson, 1984; Price and Scott, 1994; Flecker et al., 2005) (Figure 1). Mamatlar formation, which is the subject of this study, outcrops in a small area and is rich in benthic foraminifera and algae especially in lower levels

* *Corresponding author: Şükrü ACAR, dr.sukru.acar@gmail.com*
https://dx.doi.org/10.19111/bulletinofmre.494620.

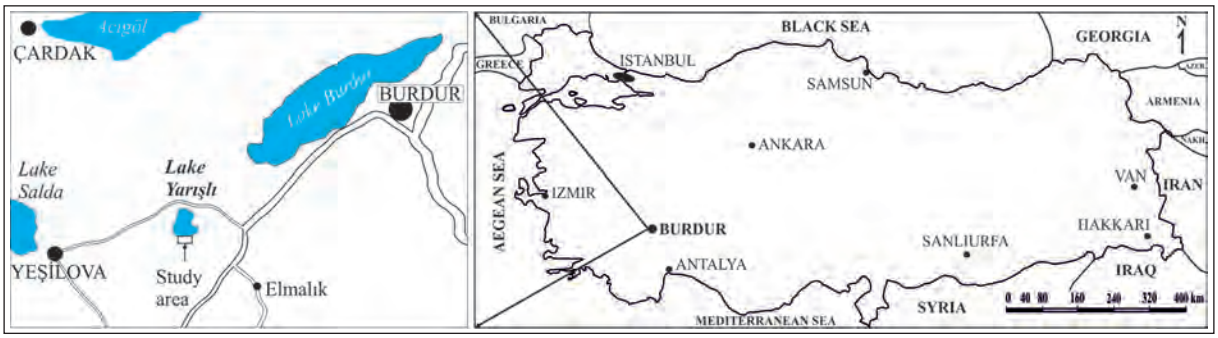

Figure 1- Location maps of the study area.

(Poisson, 1977) (Table 1). A limited number of studies were conducted in the region (Bilgin et al., 1990). Bilgin et al. (1990) prepared geological maps at 1: 25.000 scale in the area and used the name Mamatlar Formation, which had been defined by Poisson (1977), for this middle to late Paleocene ("Montian" – Thanetian) unit (Figure 2).

Sirel (1996, p.79) reported for the first time that the presence of the genus *Sistanites* Rahaghi (1983) in Turkey from "Yarışlı Village, West of Burdur" and determined the following benthic foraminifera: *Sistanites iranica* Rahaghi, 1983, *Bolkarina aksarayi* Sirel, 1981**,** *Miscellanea globularis* Rahaghi, 1983, *Miscellanea primitiva* Rahaghi, 1983, *Idalina sinjarica* Grimsdale, 1952, *Laffitteina mengaudi* (Astre, 1923), *Laffitteina erki* (Sirel, 1969), *Globoflarina sphaeroidea* (Fleury, 1982) and Miliolidae. Sirel (1998, p.29), referring to the Burdur region, stated that *L. erki, B. aksarayensis, M.? primitiva, M.? globularis, I. sinjarica, G. sphaeroidea* and *L.mengaudi* were determined from "Thanetian aged possibly exotic blocks in Yarışlı". Sirel (2004, p. 20, p. 57) indicated that, in Yarışlı region, Selandian limestones contain an assemblage with *B. aksarayensis, M.*? g*lobularis, M.*? *primitiva, S.iranica, G. sphaeroidea, Hottingerina anatolica* Sirel, 1999, *I. sinjarica,* keramospherid type, Miliolidae and algae.

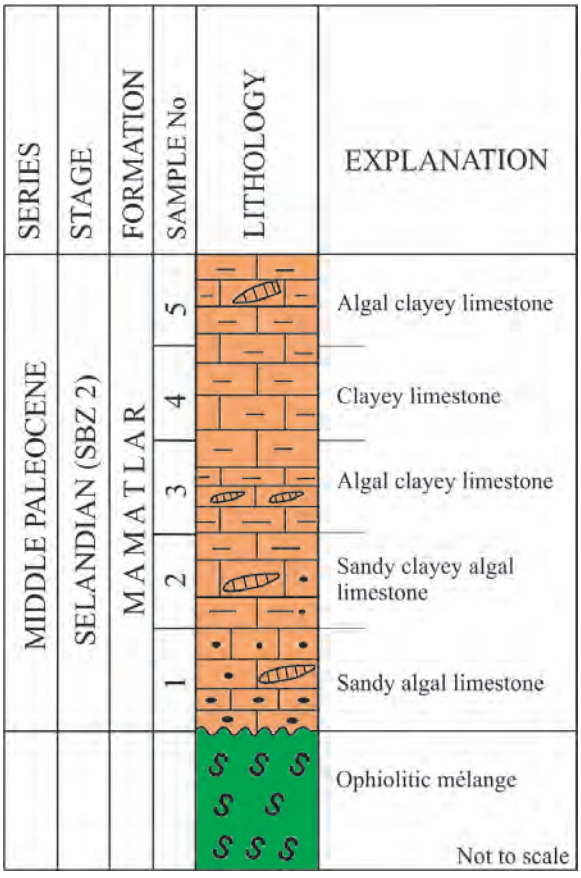

Figure 2- Stratigraphic section of the studied area.

2. Materials and Methods

In 1990, just south of Yarışlı Lake; five systematic limestone samples were taken from a very small outcrop of 3-5m thickness (Figure 1). These samples have been used in this current study. At first, two random thin section from each hard limestone samples were prepared. After a preliminary examin, several oriented thin sections (OTS) were obtained. To obtain OTS, each sample was divided into two pieces. The first one was divided into plates (ca. 4 mm thick) parallel to the bedding. The second one was divided into plates (ca. 4 mm thick) perpendicular to the bedding. Both sides of each plate were polished by grinding disc and examined under binocular microscope. During the examination, the specimens that would be prepared for OTS, were circled with a permanent marker. Plates of individuals (whose borders are drawn) are cut into small pieces. Each miniplate was re-examined under binocular microscope. Based on the examination

Table 1- Fossil assemblage of the South of Lake Yarışlı (SBZ 2).

PALEOCENE	SERIES	AGE
SELANDIAN	STAGE	
SBZ 2	SHALLOW BENTHIC ZONES (Serra-Kiel et al., 1998)	

ŞAY-1	ŞAY-2	ŞAY-3	ŞAY-4	ŞAY-5	SAMPLE NO	
●	●		●	●	*Akbarina primitiva*	FORAMINIFERA
●		●			*Ankaraella minima* n.sp.	
●		●			*Ankaraella trochoidea*	
●					*Biloculinites* cf. *paleocenica*	
●				●	*Bolkarina aksarayi*	
●					*Chrysalidina*? sp.	
●	●	●		●	*Globoflarina*? *sphaeroidea*	
●	●				*Heterillina* sp.	
	●				*Keramosphaera* sp.	
●					*Kolchidina*? sp.	
				●	*Laffitteina anatoliensis* n.sp.	
				●	*Laffitteina erki*	
●				●	*Laffitteina mengaudi*	
				●	*Laffitteina thraciaensis* n.sp.	
●					*Lockhartia*? sp.	
●	●	●			*Miscellanea*? *globularis*	
				●	*Neosistanites armagani* n.gen. n.sp.	
			●	●	*Neosistanites catali* n.gen. n.sp.	
●	●	●		●	*Neosistanites dageri* n.gen. n.sp.	
●	●	●			*Neosistanites guvenci* n.gen. n.sp.	
	●		●	●	*Neosistanites inali* n.gen. n.sp.	
●	●	●			*Neosistanites iranicus*	
●					*Neosistanites okuyucui* n.gen. n.sp.	
●	●	●			*Neosistanites sozeri* n.gen. n.sp.	
●	●	●			*Parahaymanella alanae* n.gen. n.sp.	
	●		●		*Parahaymanella bozkurti* n.gen. n.sp.	
●	●	●	●		*Parahaymanella hakyemezae* n.gen. n.sp.	
			●		*Popovia*? sp.	
●	●	●			*Pseudohottingerina burdurensis* n.gen. n.sp.	
●	●	●			*Pseudohottingerina yarisliensis* n.gen. n.sp.	
●	●			●	*Sirtina paleocenica* n.sp.	
				●	Agglutinated gen.1 indet.	
	●				Agglutinated gen.2 indet.	
●		●			Miliolid gen.1 indet.	
		●			Miliolid gen.2 indet.	
	●				Miliolid gen.3 indet.	
●		●			Miliolid gen.4 indet. sp.1	
●					Miliolid gen.4 indet. sp.2	
		●			Miliolid gen.4 indet. sp.3	
●	●	●			Miliolid gen.5 indet.	
●	●			●	Miliolid gen.6 indet.	
			●	●	Miliolid gen.7 indet.	
●				●	Miliolid gen.8 indet.	
				●	Miliolid gen.9 indet.	
●			●		Miscellanid gen.1 indet.	
	●	●			Mississippinid gen.1 indet.	
	●		●		Planulinid gen.1 indet.	
●	●				Rotaliid gen.1 indet.	
	●				Rotaliid gen.2 indet.	
●				●	Rotaliid gen.3 indet.	
●	●	●			Rotaliid gen.4 indet.	
		●			*Textularia* sp.	
●	●				*Thalmannita* sp.	
●		●			Algae gen.1 indet.	ALGAE
	●				Algae gen.2 indet.	
●	●			●	Algae gen.3 indet.	

result, each miniplate was orient during grinding according to which section (vertical, horizontal, axial, equatorial etc.) of the specimens had to be obtained. Thus, each specimen became ready for preferred OTS. However, only one plane had to be obtained on the surface. To obtain good OTS. Then the miniplates were left a bit thicker and controlled for thickness under a biological microscope. Some sections were prepared with different thickness according to the different foraminiferal walls. For instance, in order to take good photographs, thin sections of benthic foraminifera with hyaline calcareous test should be normal or a bit more in thickness, yet thin sections of the benthics with porcelaneous test should be thinner than normal. In this study, 219 OTSs were prepared. The benthic foraminifera and algae of the assemblage were determined and photographed by using 213 of these OTSs (Table 1). Oriented thin section used in this study, are deposited in the collection of Paleontology Division, Department of Geology, Mineral Research and Exploration (MTA).

3. Findings

3.1. Systematic Paleontology

In systematic paleontology, Loeblich and Tappan, 1964 and Acar, 1995 are followed.

Phylum: Protozoa GOLDFUSS, 1817,

Subphylum: Sarcodina SCHAMARDA, 1871,

Class: Rhizopoda von SIEBOLD, 1845,

Order: Foraminiferida EICHWALD, 1830,

Suborder: Rotaliina DELAGE AND HÉROUARD, 1896,

Superfamily: Rotaliacea EHRENBERG, 1839,

Family: Neosistanitidae ACAR, New family,

Genus: *Neosistanites* ACAR, n. gen.,

Type Species: *Sistanites iranica* RAHAGHI, 1983.

3.2. New Family *Neosistanitidae* ACAR, n. fam.

Type Genus: *Neosistanites* ACAR, n. gen. [Type Species: *Sistanites iranica* RAHAGHI, 1983].

Description: Test free, tochospirally-rotaliid type coiled and with two layers. Outer layer: thread-like hyaline calcareous; inner layer: dark and blackish coloured, microgranular or very fine granied (Rahaghi, 1983, p.54). Sieved vertical plates (vpl), sieved horizontal plates (hpl), sieved compound plates (cpl), dorsal pillars (dp) and ventral pillars (vnp) with two different shell structure are present but intraseptal canals are absent. First ventral pillars (vnp1) (in the umbilical cavity) are present in rotaliid stage and are hyaline calcareous. Second ventral pillars (vnp2) are also in umbilical cavity yet they are microgranular not hyaline. Besides, funnels (f) between dorsal pillars, umbilical flaps (uf) and umbilical holes (uh) are present. Aperture (a) is single as a basal slit. However, aperture is also present at the base of penultimate septa and of previous septum as an intercameral foramen.

Comparison and Remarks: Features of this new family (Neosistanitidae ACAR, n.fam.) is different from the ones of the family Rotaliidae Ehrenberg, 1839 and of all its subfamilies. In this new family, differently from Rotaliidae; in addition to its two layered (hyaline calcareous, blackish coloured, microgranular or very fine grained) wall structure, the presence of sieved vertical plates (vpl), sieved horizontal plates (hpl), sieved compound plates (cpl), two different type of ventral pillars (vnp1,vnp2), umbilical holes (uh). Due to these differences, the new family Neosistanitidae is introduced.

3.3. Explanation About the Classification of New Genus *Neosistanites*

Genus *Sistanites* Rahaghi (1983) and its type species "*Sistanites iranica* Rahaghi, 1983" were first described and figured by Rahaghi (1983, p.54) from the Thanetian of Iran. Sirel (1996, p.79), later on, described *S. iranica* from Turkey for the first time and Sirel (1998, p.79) again emended this genus. New genus *Neosistanites* is needed to be described in this study, due to inadequate description of the structural elements of *Sistanites* in the studies of Sirel and Rahaghi and due to large number of structural elements specified in this study. *Neosistanites* n. gen. has dorsal pillars (dp) and funnels (f), sieved vertical plates (vpl), sieved horizontal plates (hpl), sieved compound plates (cpl), imperforated umbilical flaps (uf), two different type of ventral pillars (vnpl1, vnpl2), umbilical holes (uh), and a row of apertures (a) or an intercameral foramen (if).

3.4. Species and Type Species Transferring Between Genera

Numerous examples of transferring a new species or a type species into a known species or a new genus are existed in the literature. New descriptions about

this issue (specimens described in this study) are presented below:

A- *Sistanites iranica* Rahaghi, 1983, type species of *Sistanites* Rahaghi (1983), is transferred to the new genus *Neosistanites* as its type species (Rahaghi, 1983, p.54, Pl.34, fig.4).

B- *Orduina erki* Sirel, 1969, type species of *Orduina* Sirel (1969), was transferred to some different genera; at the present time, it is accepted and used as *Laffitteina erki* (Sirel, 1969). In this study, *L. erki* is described and figured as well.

C- *Miscellanea primitiva* Rahaghi, 1983 which had been described and figured by Rahaghi (1983), was assigned to different genera as the type species by two different authors (Hottinger, 2009; Sirel, 2009). In this study, it is figured as *Akbarina primitive* Sirel, 2009.

Order: Foraminiferida EICHWALD, 1830,

Suborder: Rotaliina DELAGE AND HÉROUARD, 1896,

Superfamily: Rotaliacea EHRENBERG, 1839,

Family: Neosistanitidae ACAR, New Family,

Type genus: *Neosistanites* ACAR, n. gen. [Type Species: *Sistanites iranica* RAHAGHI, 1983].

New Genus: *Neosistanites* Acar, n.gen.

Derivation of name: The name of "Neosistanites" is derived by the combination of prefix "neo" meaning "new", and the name of former genus.

Type species: Subhorizontal section (Rahaghi, 1983, Pl. 34, fig. 4).

Type locality: South of Lake Yarışlı, SW Burdur, W Turkey (Text figure 1).

Type level: Selandian; SBZ 2 (Serra-Kiel et al., 1998).

Diagnosis: Test of this benthic foraminifera is small with two layers, free, and coiled in trochospiral-rotaliid manner. Septa, especially in early rotaliid whorl, are two-layered (Pl. 1, Figs. 1, 4-6). Trochospirally coiled septa in the last whorl are single layered. Outer layer is characterized with thread-like hyaline calcareous and inner layer with dark or blackish coloured, microgranular or very fine grained wall structure (Rahaghi, 1983, p.54). Two-layered wall structure of the genus can especially be better observed in vertical sections. Test of the new genus is small in size. However, species of the new genus can be differentiated into four groups as large, medium, small, and very small based on their size. The new genus could be spherical, subspherical, lobulated, asymmetrical inflated lenticular, lenticular, and asymmetrical flattened lenticular in shape (Pl.1, figs. 1, 4-6; Pl.2, figs. 1-3; Pl.3, figs. 3, 4, 7; Pl.4, figs. 2-4, 7-10; Pl.5, figs. 1, 2, 4-6, 8-11, Pl.6, figs. 1, 3-5, 8, 9). Horizontal diameter and height of the genus varies between 0.758 mm – 1.983 mm and 0.467 mm – 1.371 mm respectively.

In megalospheric generations (fA): protoconch (pr) is spherical in shape and deuteroconch (dt) has a unique shape (similar to a human ear) (Pl.1, fig.6; Pl.2, fig.1; Pl.3, fig.7; Pl.4, fig.4; Pl.5, fig.3; Pl.6., fig.6) (Text figures 3B, C). However, in some specimens, tritoconch (tr) is also present; such is called "triple embryonic structure" (Pl.2, fig.4; Pl.3, fig.7; Pl.4, fig.5) (Text figure 3C). Protoconch diameters of the megalospheric specimens varies between 0.047 mm – 0.262 mm (Pl.1, figs. 5, 6; Pl.2, figs. 1, 2, 4; Pl.3, figs. 3, 4, 6, 7; Pl.4. figs. 1, 4-8; Pl.5, figs. 1-3, 7-11; Pl.6, figs. 3-6) (Text figures 3B, C).

Protoconch (pr) diameters of microspheric generations (fB) varies between 0.009 mm – 0.023 mm (Pl.1, fig.1; Pl.2, fig.5; Pl.4, fig.3) (Text figure 3A). Test is two-layered, outer layer is thread-like hyaline calcareous and inner layer is dark, microgranular or very fine grained, and imperforate (Pl.1, figs. 1, 2, 4-6; Pl.2, figs. 1-6; Pl.3, figs. 2-7; Pl.4, figs. 1-8; Pl.5, figs. 1-12, Pl.6, figs. 1-9) (Text figures 3A-C) (Rahaghi, 1983, p.54). Index of elongation (i.e) which is calculated by "horizontal diameter / height" formula, varies depending on species. Intraseptal canals are absent. Large chamber lumen is subdivided into two parts by one or two plates (vertical plate and/or compound plate) (Pl.1, figs. 1, 4-6; Pl.2, figs. 1-3; Pl.3, figs. 4, 7; Pl.4, figs. 2-4, 7-10; Pl.5, figs. 1, 2, 4-6, 10) (Text figures 3A, B). Chambers are evolute in dorsal side. Quite narrow surfical openings called as sutural opening (so) (Pl.1, figs, 2, 7; Pl.2, figs. 4, 6) (Text figures 3C), dorsal pillars (dp), funnels (f) and central pillars (cp) are present in dorsal side (Pl.1, figs. 1, 4-6; Pl.2, figs. 1-3; Pl.3, figs. 4, 5, 7; Pl.4, figs. 1-4, 7-9; Pl.5, figs. 1-4, 5-11; Pl.6, figs. 1-5, 8, 9) (Text figures 3A, B).

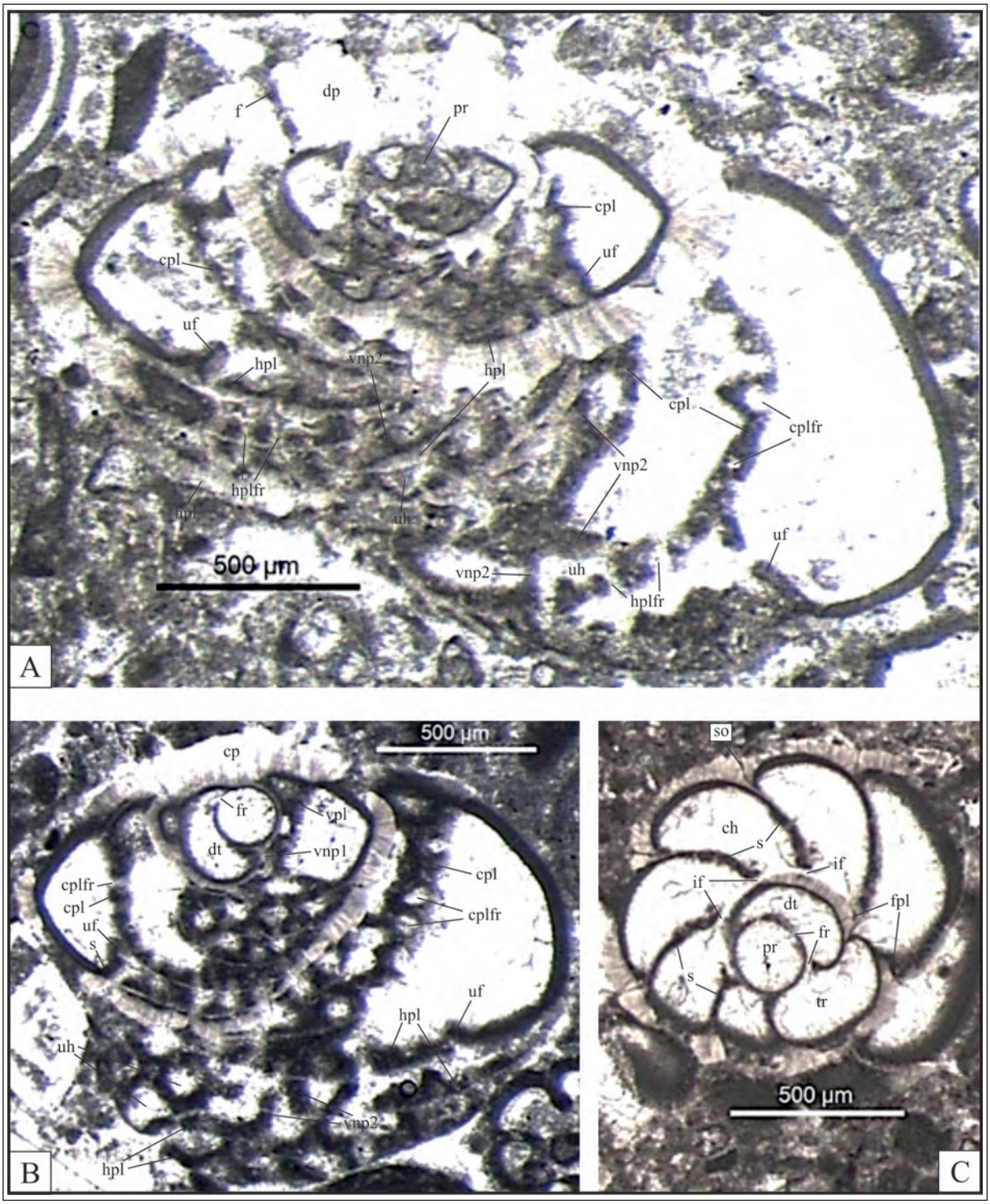

Figure 3- Some structural elements of *Neosistanites* ACAR n. gen. A: Vertical section; (fB) minute spherical protoconch (pr), dorsal pillars (dp), funnels (f), two-layered septum, compound plates (cpl), compound plate foramina (cplfr), umbilical flaps (uf), sieved horizontal plates (hpl), horizontal plates foramine (hplfr), second ventral pillars (vnp2), umbilical holes (uh). B: Vertical section; (fA), central pillar (cp), spherical protoconch (pr) and typical deuteroconch (dt), foramen (fr) between protoconch and deuteroconch, first ventral pillar (vnp1), vertical plate (vpl) (located to the immediate right side of the spherical protoconch), sieved (vertical) compound plate (cpl) (at the left) and compound plate foramina (cplfr), (inclined) compound plate (cpl) (at the right) and the compound plate foramina (at the right) (cplfr), umbilical flaps (uf),sieved horizontal plates (hpl), second ventral pillars (vnp2), umbilical holes (uh). C: Horizontal section; (fA), triple embrionic stage, [large spherical protoconch (pr), larger deuteroconch (dt), largest tritoconch (tr), and foramina (fr) between them], sutural / surfical opening (on the spire) (so), septa (s), chamber (ch), intercameral foramina (if), and foraminal plates (fpl).

Pseudospine-like (psp) structural elements are rarely observed (Pl.1, fig.2). Foraminal plates (fpl) located at the base of the intercameral foramina (if) or on the outer side of the underlying spire of the intercameral foramina (if), are present (Pl.1, figs. 2, 7; Pl.2, figs. 4, 6; Pl.3, fig. 5; Pl.5, figs. 7, 12; Pl.6, fig. 7) (Text figure 3C). Either sieved vertical plates (vpl) or sieved compound plates (cpl) divides chambers lumens into two parts. Horizontal plates (hpl), septa (s), umbilical flaps (uf) and second ventral pillars (vnpl2) are blackish, dark coloured, and microgranular or very fine grained in conformance with internal structure of the wall. All these structural elements fill up the umbilical cavity (Text figure 3A, B, C). Vertical plates (vpl) arise from the dorsal side of the test (from spire), and they divide the chamber lumen into two part as a very thick sieve plate in accordance with the anatomic structure (Pl.1, fig. 3), and then merge with the umbilical flap (uf) (Pl.1, figs.1, 4-6; Pl.2, figs. 1-3; Pl.3, figs. 2-4, 7; Pl.4, figs.2, 3, 7; Pl.4, figs. 2, 3, 7-10; Pl.5, figs. 1, 2, 4-6, 8-11; Pl.6. figs. 1, 3-5, 8, 9) (Text figures 3A, B). In other words, a very thick sieved vertical plate (vpl) contains a very short stage of microgranular and imperforate in the beginning, later on it becomes a sieve plate and finally merges with an umbilical flap (uf). Another vertical plate (vpl) gently curves down (towards the protoconch), and then merges with the umbilical flap (uf). These thick, gently curved concave vertical plates can be observed in some thin sections depending on the direction of the thin section. If the plane of the thin section do not cut this concave vertical plate; in other word, if the plane of the thin section passes through the space between a septum and a vertical plate, vertical plates can not be observed on the thin sections. Umbilical cavity is filled with sieved horizontal plates (hpl) and ventral pillars (vnp) that are located between those plates (hpl). These horizontal plates (hpl) are microgranular and sieved. Horizontal plates (hpl) are present on the ventral side (Pl.1, figs.1, 4-6; Pl.2, figs. 3-11; Pl.3, figs. 2-5, 7; Pl.4, figs. 1-4, 7-10; Pl.5, figs. 1-6, 8-11; Pl. 6, figs. 1-5, 8, 9) (Text figures 3A, B). Horizontal plates (hpl) also fill the umbilical cavity (uc), and one end of it conjoints with an umbilical flap (uf) and the other does with the preceding horizontal plate (hpl). Sometimes, two ends of a horizontal plate conjoint with the preceding horizontal plate (hpl). A large number of short, microgranular second ventral pillars (vnp2) are located between these thick, sieved horizontal plates (Pl.1, figs. 1, 4-6; Pl.2, figs. 1-3; Pl.3, figs. 3, 4, 7; Pl.4, figs. 2-4; Pl.5, figs. 1, 2, 4-6, 8-11; Pl.6, figs. 1, 3-5, 8, 9) (Text figures 3A, B). Compound plates (cpl) are sieved, microgranular and thick. These compound plates (cpl) are formed by merging of a sieve vertical plate (vpl) with a sieve horizontal plate (hpl) on an umbilical flap (uf). Besides, a compound plate (cpl) could be developed by a vertical plate evolving into a horizontal plate after it was attached to an umbilical flap (uf) (Pl.1, figs. 1, 4-6; Pl.2, figs. 1, 2; Pl.3, figs. 4, 7; Pl.4, figs. 2-4, 7-10; Pl.5, figs. 1, 2, 4-6, 10, 11; Pl.6, figs. 3, 5) (Text figures 3A, B). A compound plate (cpl) is located in the middle of a chamber lumen. It divides the chamber lumen into two part, and fills the ventral cavity. Sieve structure of thick vertical plates (vpl) and of thick compound plates (cpl) are clearly observed in oblique sections (Pl.1, figs. 3, 5; Pl.2, figs. 1-3; Pl.3, figs. 1-3; Pl.4, figs. 2, 7, 8) (Text figure 3B: at the right side and left side). In some cases, tissular thickness between foramina could be observed as pillars (p) in vertical parts of the tangential sections of thick compound plates (cpl). However, these are not pillars, only tissue/wall thickness between foramina (Pl.1, figs.1, 5; Pl.2, fig.1) (Text figure 3B: at the right side). Umbilical flap (uf) is a dark, blackish coloured, microgranular or very fine grained, imperforate plate (Pl.1, figs.1, 4-6; Pl.2, figs.1-3; Pl.3, figs.1-4, 7; Pl.4, figs.2-4, 7-10; Pl.5, figs.1-6, 8-11; Pl.6, figs.1-5, 8- 9) (Text figures 3A, B). Umbilical flap is either attached to or located at the end of a septum, and covers umbilical side (Hottinger, 1980, p.12, text figure 5). It especially is observed in the vertical sections of trochospirally / rotaliid coiled benthic foraminifera as an imperforate, small, gently curved plate (uf) at the end of a septum. New genus *Neosistanites* has also ventral and dorsal pillars. As is known, presence of the pillars in a benthic foraminifera is a very important criterion. Each anatomic structure determined above, leads to a specimen being described as different genus. Ventral pillars have two different structural types in its own (Figs. 3A, B). First ventral pillars (vnp1) are located in the umbilical cavity (uc) in first few whorls of the rotaliid stage (close to protoconch) of the test.

First ventral pillars (vnp1) are hyaline calcareous, plug-looking, monolithic, massive, short ventral pillars (Pl.1, fig.6; Pl.2, fig.1; Pl.3, fig.7; Pl.4, figs.8, 9; Pl.5, figs.2, 3, 5, 6, 10, 11, 12; Pl.6, figs.3, 5) (Text figure 3B). Second ventral pillars (vnp2) are also located in the ventral side. They are short, microgranular and located between the plates in accordance with the inner layer of the test wall (Pl.1, figs.4-6; Pl.2, figs.1-3; Pl.3, figs.3, 4, 7; Pl.4, figs.2-4, 7-9; Pl.5, figs.1, 2, 4-6, 8-10; Pl.6, figs.1, 3-5, 8, 9) (Text figures 3A, B). Dorsal pillars (dp) are located in the dorsal side, and they, in compatible with the outer structure of the test

wall, are radial and hyaline calcareous (Pl.1, figs.1, 4-6; Pl.2, figs.1-3; Pl.3, figs.3, 4; Pl.4, figs. 1-4, 7-10; Pl.5, figs. 1-6, 8-11; Pl.6, figs.1-5, 7-9). Funnels (f) are present between dorsal pillars. Umbilical holes (uh) or umbilical cavity (uc) are located between horizontal plates (hpl) and second ventral pillars (vnp2) in the ventral area (Pl.1, figs. 1, 4-6; Pl.2, figs. 1-3; Pl.3, figs.3, 4, 7; Pl.4, figs.2-4, 7-10; Pl.5, figs. 1, 2, 4-6, 8-10; Pl.6, figs. 1, 3-5, 8) (Text figures 3A, B, C). Intercameral foramina (if) are present at the base of setpa and can be observed in horizontal or subhorizontal sections (Pl.1, fig.7; Pl.2, figs.4-6; Pl.3, figs.2, 5, 6; Pl.5, figs. 7, 12; Pl.6, figs.6, 7) (Text figure 3C). Intercameral foramina (if) could be accepted as former apertures. Thus, we can describe apertures by examining intercameral foramina. Depending on this, we could say *Neosistanites* has one aperture which is located at the base of septum as a basal slit. Foraminal plate (fpl), observed in the horizontal or subhorizontal sections, is a dark coloured minute plate. It is present at the base of intercameral foramina, and located on the outer part of the preceding whorl (Pl.1, figs.2, 7; Pl.2, figs.4, 6; Pl.3, fig.5; Pl.4, figs.5, 6; Pl.5, figs.7, 12; Pl.6, fig.7). Fortyfive OTS and sixtythree specimen have been used in order to describe new genus *Neosistanites*. Dimorphism is present. Middle Paleocene, Selandian (SBZ 2) (Serra-Kiel et al., 1998).

Fossil Assemblage: It is associated with *Neosistanites iranicus* (Rahaghi, 1983), *Neosistanites sozerii* Acar, n.gen.,n.sp., *Neosistanites okuyucui* Acar, n.gen.,n.sp., *Neosistanites guvenci* Acar, n.gen.,n.sp., *Neosistanites dageri* Acar, n.gen.,n.sp., *Neosistanites catali* Acar, n.gen.,n.sp., *Neosistanites armagani* Acar, n.gen.,n.sp., *Neosistanites inali* Acar, n.gen.,n.sp., *Parahaymanella hahyemezae* Acar, n.gen., n.sp., *Parahaymanella bozkurti* Acar, n.gen., n.sp., *Parahaymanella alanae* Acar, n.gen., n.sp., *Pseudohottingerina burdurensis* Acar, n.gen.,n.sp., *Pseudohottingerina yarisliensis* Acar, n.gen.,n.sp., *Ankaraella minima* Acar, n.sp., *Laffitteina anatoliensis* Acar, n.sp., *Laffitteina thraciaensis* Acar, n.sp., *Sirtina paleocenica* Acar, n.sp., *Akbarina primitiva* (Rahaghi, 1983), *Ankaraella trochoidea* Sirel, 1998, *Bolkarina aksarayi* Sirel, 1981, *Laffitteina erki* (Sirel, 1969), *Laffitteina mengaudi* (Astre, 1923), *Biloculinites* cf. *paleocenica* Rahaghi, 1983, *Miscellanea*? *globularis* Rahaghi, 1978, *Globoflarina*? *sphaeroidea* (Fleury, 1982), *Heterillina* sp., *Keramosphaera* sp., *Textularia* sp., *Chrysalidina*? sp., *Kolchidina*? sp., *Lockhartia*? sp., *Popovia*? sp., *Thalmannita*? sp., *Periloculina* sp., undeterminated miliolid genera (Miliolid gen.1 indet, Miliolid gen.2 indet, Miliolid gen.3 indet; Miliolid gen.4 indet n.sp.1; Miliolid gen.4 indet n.sp.2; Miliolid gen.4 indet n.sp3; Miliolid gen.5 indet; Miliolid gen.6 indet; Miliolid gen.7 indet; Miliolid gen.8 indet or Idalinid gen.8 indet; Miliolid gen.9 indet), Aglutine gen. (1 and 2) indet., Miscellanid gen. indet., Planulinid gen.1 indet, Rotaliid gen.1 indet. (*Redmondoides?*), Rotaliid gen.2 indet., Rotaliid gen.3 indet., Rotaliid gen.4 indet. (with two layered test), Mississippinid gen. indet., algae gen.1 indet., algae gen.2 indet., algae gen.3 indet. Distrubition of the assemblage has been given in Table 1. Middle Paleocene, Selandian, SBZ 2 (Serra-Kiel et al., 1998).

Comparison with other genera: New genus *Neosistanites* has a two-layered test, and is trochospirally-rotaliid coiled. Evolute in dorsal side, intraseptal canals are absent (Pl.1, figs.1, 2, 4-6; Pl.2, figs.1-6; Pl.3, figs.2-7; Pl.4, figs.1-8; Pl.5, figs.1-12; Pl.6, figs.1-9) (Text figures 3A-C). Outer layer of the test is thread-like hyaline, and inner layer is dark, blackish coloured, microgranular or very fine grained and imperforate (Rahaghi, 1983, p.54). In megalospheric generation, spherical protoconch (pr) and unique shaped (similar to a human ear) deuteroconch (dt) (Pl.1, fig.6; Pl.2, fig.1; Pl.3, fig.7; Pl.4, fig.4; Pl.5, fig.3; Pl.6, fig.6) (Text figures 3B, C) and in some specimens tritoconch (tr) is observed (Pl.2, fig.4, Pl.3, fig.7; Pl.4, fig.5) (Text figure 3C). Protoconch diameters of megalospheric individuals (fA) vary between 0.047 mm – 0.262 mm (Pl.1, figs.5, 6; Pl.2, figs.1, 2, 4; Pl.3, figs.3, 4, 6, 7; Pl.4, figs.1, 4-8; Pl.5, figs. 1-3, 7-11; Pl.6, figs3-6) (Text figure 3B, C). Protoconch diatemeters of microspheric specimens vary between 0.009 mm – 0.023 mm (Pl.1, fig.1; Pl.2, fig.5; Pl.4, fig.3) (Text figure 3A). Large chamber lumina are divided by one or two plates which is a vertical plate (vpl) or a compound plate (cpl) (Pl.1, figs.1, 4-6; Pl.2, figs.1-3; Pl.3, figs.4-7; Pl.4, figs.2-4, 7-10, Pl.5, figs. 1, 2, 4-6, 10) (Text figures 3A, B). Very narrow sutural openings (so) (Pl.1, figs. 2, 7; Pl.2, figs. 4, 6) (Text figure 3C), dorsal pillars (dp) (Pl.1, figs. 1, 4-6; Pl.2, figs, 1-3; Pl.3, 3, 4, 7; Pl.4, 1-4, 7-10; Pl.5, figs. 1-6, 8-11; Pl.6, 1-5, 7-9) and funnels (f) (Pl.1, figs.1,4-6; Pl.2, figs.1-3; Pl.3, 4,5,7; Pl.4. figs.1-4,7,8; Pl.5, 1-4, 10; Pl.6, figs.1, 4, 5) (Text figures 3A, B) are present on the dorsal side. In some individuals, central pillars (cp) (Pl.2, fig.1; Pl.4, fig.9; Pl.5, figs. 5-11; Pl.6, figs.2, 3, 8, 9) (Text figure 3B) and pseudospines (psp) (Pl.1, fig.2) could be observed. A Vertical plate (vpl) arising from the dorsal side

(from the spire), divide chamber lumen into two parts, and merges with the umbilical flap (uf) which is attached to the septum (Pl.1, figs.1, 3, 4-6; Pl.2, figs.1-3; Pl.3, 2-4,7; Pl.4, figs. 2,3,7-10; Pl.5, figs. 1,2,4-6,8-11; Pl.6 figs.1,3-5,8,9) (Text figures 3A,B). These gently curved vertical plates (vpl) could only be observed in some sections (depending on the section plane). If the plane of the thin section doesn't cut the vertical plate; in other word, if the plane of the thin section passes through the space between a septum and a vertical plate, vertical plates can not observed on the thin sections. Compound plates (cpl) are microgranular, sieve, and divide the chamber lumine into two. They fill the umbilical cavity. A compound plate (cpl) is formed by merging of a vertical plate (vpl) with a sieved horizontal plate (hpl) on an umbilical flap (uf). Besides, a compound plate (cpl) could be developed by a vertical plate evolving into a horizontal plate after it was attached to an umbilical flap (uf) (Pl.1, figs.1,4-6; Pl.2, figs. 1,2; Pl.3, figs. 4,7; Pl.4, figs.2-4,7-10; Pl.5, figs. 1,2,4-6,10,11; Pl.6, figs. 3,5) (Text figures 3A, B). Especially, sieve structure of vertical and compound plates could be observed in oblique sections (Pl.1, figs.3,5; Pl.2, figs.1-3; Pl.3, figs.1-3; Pl.4, figs.2,7,8) (Text figure 3B). Interforaminal openings observed in the tangential sections of the thick compound plates (cpl), could be observed as if they were pillars (p), yet they are not pillars (Pl.1, figs.1,5; Pl.2, fig.1) (Text figure 3B). Because, interforaminal openings of the parts of thick vertical plates (vpl). Umbilical flaps (uf) are gently curved, minute plates and microgranular texture. They are either attached ot or located on a spetum (s) (Pl.1, figs. 1, 4-6; Pl.2, figs. 1-3; Pl.3, figs. 1-4,7; Pl.4, figs.2-4, 7-10; Pl.5, figs.1-6,8-11; Pl.6, figs.1-5,8,9) (Text figures 3A,B). An umbilical flap (uf) covers the umbilical side (Hottinger, 1980, p.12, text figure 5). Thick, sieved horizontal plates (hpl) and ventral pillars (vnp) are present in the vertical area. Ventral pillars (vnp) have two different structural types in its own (Text figures 3A, B). Horizontal plates are sieve and microgranular in accordance with the inner layer of the test wall. Horizontal plates (hpl) are located in the ventral side (Pl.1, figs. 1,4-6; Pl.2, figs. 11-3; Pl.3, figs. 2-5,7; Pl.4, figs. 1-4,7-10; Pl.5, figs. 1-6,8-11; Pl.6, figs. 1-5,8,9) (Text figures 3A, B). First ventral pillars (vnp1) are located in the umbilical cavity (uc) and in first few whorls of the rotaliid stage of the test (close to protoconch). First ventral pillars (vnp1) are hyaline calcareous, plug-looking, monolithic, massive, short ventral pillars (Pl.1, fig. 6; Pl.2, fig.1; Pl.3, fig. 7; Pl.4, figs. 8,9; Pl.5, figs. 2,3,5,6,10,11; Pl.6, figs. 3,5) (Text figure 3B). Second ventral pillars are microgranular and are located between plates (Pl.1, figs. 1,4-6; Pl.2, figs. 1-3; Pl.3, figs. 3, 4, 7; Pl.4, figs. 2-4, 7-10; Pl.5, figs. 1, 2, 4-6,8-11; Pl.6, figs. 1,3-5, 8, 9) (Text figures 3A, B). Umbilical holes (uh) are located between horizontal plates (hpl) and second ventral pillars (vnp2) in the ventral side (Pl.1, figs. 1,4-6; Pl.2, figs. 1-3; Pl.3, figs. 3,4,7; Pl.4, figs. 2-4,7-10; Pl.5, figs. 1,2,4-6,8-10; Pl.6, figs. 1,3-5,8) (Text figures 3A, B, C). New genus *Neosistanites* has only one foraminal plate (fpl) (Pl.1, figs. 2,7; Pl.2, figs. 4,6; Pl.3, fig. 5; Pl.5, figs. 7,12; Pl.6, fig. 7) (Text figure 3C) and only one aperture. *Sistanites* Rahaghi (1983) was first described and photographed by Rahaghi (1983, p.54) in Thanetian of Iran. *Sistanites* is differentiated from all other genera of Rotaliidae family by its two layered wall structure which is made of two different materials (Rahaghi, 1983, p.55 remarks). Rahaghi reported that subdivisions of septa were present in the ventral side of the genus *Sistanites*, yet it is not agreed in this study. Because, there is no subdivisions, meaning septula, belonging to septa in the ventral side. Both new genus and its type species have two layered wall structures. Rahaghi (1983, p.55) stated that, "septa are pierced by the intercameral foramen". This is to say, Rahaghi reported that *Sistanites* has one aperture and the author of this study is exactly agreed on. Sirel (1996, p.79) made first determination of *Sistanites iranica* Rahaghi (1983) in Turkey, and described the genus having cribrate aperture, its large umbilical side being filled with thick horizontal and vertical plates, and assigned the genus to Paleocene (Thanetian) age. The author of this study does not agree with the idea of Sirel (1996, p.79) on that the genus having cribrate aperture and being filled with vertical plate in its umbilical side. First of all, that specimen does not have cribrate aperture, but has one (Pl.1, fig. 7; Pl.2, figs. 4-6; Pl.3, figs. 2,5; Pl.4, figs. 5,6; Pl.5, figs. 7,12; Pl.6, figs. 6,7). As is known, position and the number of apertures in a benthic foraminifera is a very important criterion leading a specimen described as different genus. Besides, it was stated that the umbilical side was filled with vertical plates, yet they were not vertical plates, but second ventral pillars (vnp2) located between horizontal plates (hpl) (Pl.1, figs. 4-6; Pl.2, figs. 1-3; Pl.3, figs. 3,4,7; Pl.4, figs. 2-4,7-9; Pl.5, figs. 1,2,4-6,8-10; Pl.6, figs. 1,3-5,8,9) (Text figures 3A, B). The author agrees the statement of Sirel (1996, p.79) that "large umbilical side being filled with horizontal plates", and reports that these horizontal plates are not imperforate, contrarily sieved (Pl.1, figs 1,4-6; Pl.2, figs. 11-3; Pl.3, figs. 2-5,7; Pl.4,

figs. 1-4,7-10; Pl.5, figs. 1-6,8-11; Pl.6, figs. 1-5,8,9) (Text figures 3A, B). Deficiencies were eliminated for genus *Sistanites*, and the genus was emended by Sirel (1998, p.81). However, apart from the common generic characteristics of the genus described by Rahaghi (1983) and data reported by previous study of Sirel (Sirel, 1996, p.79), it was reported in that emendation of Sirel (1998, p.81): the genus had numerous vertical plates in the umbilical side and there were lots of holes in its umbilical cavity, and they were not true pillars as in *Locakhartia* Davies (Sirel, 1998: Pl. 39, figs. 1,4,7, 13; Pl. 40, figs. 1,6,12), and the aperture was sieve-plate with short subepidermal partititons (Sirel, 1998: Pl. 39, figs. 3,4,12; Pl. 40, figs. 2,5,8,9). But the author does not agree on the description of Sirel (1998, p.81) about apertures and subepidermal partitions. Because, that specimen has only one aperture (Pl.1, fig. 7; Pl.2, figs. 4-6; Pl.3, figs. 2,5; Pl.4, figs. 5,6; Pl.5, figs. 7,12; Pl.6, figs. 6,7). On the other hand, Sirel (1998, p.81) stated that there were lots of holes in the umbilical side, yet not explained how they were developed! The author accepts that there are lots of holes in the umbilical side, and reports that, these are developed between horizontal plates (hpl) and second ventral pillars (vnp2) (Pl.1, figs. 1,4-6; Pl.2, figs. 1-3; Pl.3, figs. 3,4,7; Pl.4, figs. 2-4,7-10; Pl.5, figs. 1,2,4-6,8-10; Pl.6, figs. 1,3-5,8) (Text figures 3A, B, C). The author believes that, pillars could be in different wall structure. As it is known, pillars are hyaline calcareous structured in *Lockhartia*, *Sakesaria* and rotaliids. However, as is known, interseptal pillars in *Archaias* de Montfort (1808) are in porcelaneous calcareous wall structure. Dorsal pillars (dp) and first ventral pillars (vnp1) of the new genus *Neosistanites* hyaline calcareous structured. However, second ventral pillars (vnp2) located in the umbilical side of the new genus *Neosistanites* are in microgranular wall structure. Consequently, presence or absence of pillars in a foraminiferal genus is highly important. As it is known, this leads individuals being described as different genera. Moreover, Sirel (1998, p.82) reported that protoconch diameters of microspheric generations varying between 0.090 mm – 0.130 mm. The author believes in that these measurements could be incorrect. As is known, protoconch diameter of any benthic foraminifera can not be between 0.090 mm – 0.130 mm. New genus *Neosistanites* has one aperture, central pillars (cp), pseudospines (psp), vertical plates (vpl), umbilical flaps (uf), compound plates (cpl), horizontal plates (hpl), first ventral pillars (vnp1), second ventral pillars (vnp2), umbilical holes (uh), and foraminal plates (fpl).

Fossil assemblage: Table 1; Age: Middle Paleocene, Selandian, SBZ 2 (Serra-Kiel et al, 1998).

Neosistanites iranicus (Rahaghi, 1983)

(Plate 1, Figures 1-7; Plate 2, Figures. 1-6; Plate 3, Figures 1,2) (Text figure 4/1)

1983 *Sistanites iranica* Rahaghi, p. 54, Pl. 34, figs. 1-4, 6-12, 14,15.

1996 *Sistanites iranica* Rahaghi; in Sirel: Drobne et al. (1996), p.79, Pl. 1, figs. 2,3,5,7-9,12-14.

1998 *Sistanites iranica* Rahaghi; Sirel, p.82, Pl. 39, figs. 1, 3, 4, 5, 11-13; Pl. 40, figs. 2, 3, 5, 6, 8-11, 13.

2008 *Sistanites iranica* Rahaghi, Pignatti et al., Pl. 6, figs. 4.

2009 *Sistanites iranica* Rahaghi; Sirel, Pl.5, figs. 6,7.

2015 *Sistanites iranica* Rahaghi; Sirel, Pl. 16, figs. 2,5,6,8-11,13.

Derivation of name: Former name of the species, "*iranica*", is made compatible with the name of the new genus (*Neosistanites*) and is changed "*iranicus*".

Type locality: South of Lake Yarışlı, SW Burdur, W Turkey (Figure 1).

Type level: Middle Paleocene, Selandian, SBZ 2 (Serra-Kiel et al., 1998).

Description: Test is free, small, trochospirally-rotaliid coiled, inflated lenticular (asymmetrical biconvex) or globular in general. Test of "*Neosistanites iranicus*" is larger among the species of the new genus. Chambers are evolute in dorsal side (Pl.1, figs. 1,4-6; Pl.2, figs. 1-3) (Text figure 4/1). Two layered wall structure is best observed in rotaliid stage. Outer layer is radially perforated calcareous in structure, and inner layer is blackish coloured, microgranular or very fine grained (Rahaghi, 1983, p.54). However, wall structure is generally microgranular in the last whorl or in last chambers. Diameter of protoconch in microspheric specimens is 0.009 mm (Pl.1, fig.1; Pl.2, fig. 5). Dorsal pillars (dp) are located on the dorsal side, and interpillar channels or funnels (f) are present as well (Pl.1, figs. 1,4-6; Pl.2, fig. 1-3) (Text figures 3A, B). Septa (s) are imperforate, gently curved, blackish coloured in accordance with structure of the inner layer of the test, microgranular or very fine granied (Pl.1, figs. 2,6,7; Pl.2, figs. 4-6; Pl.3, figs. 1,2)

(Text figure 3C). Intercameral foramina (if) are present at the base of imperforate septa, and the foramen located at the base of the ultimate septum forms the aperture (Pl.1, fig. 7; Pl.2, figs. 4-6) (Text figure 3C). Foraminal plate (fpl) which is present just above the spire located at the base of intercameral foramina, is a dark coloured, thin, minute plate (Pl.1, figs. 2,7; Pl.2, figs. 4,6) (Text figure 3C). Vertical plates (vpl) are found in chamber lumina and divide the chambers into two parts. They are sieved (Pl.1, figs. 3,5-7; Pl.2, figs. 1-3; Pl.3, fig. 1) (Text figure 3B), microgranular structured, and are slightly inclined towards the protoconch, and merges with the umbilical flap. Inner surface of horizontal plates, in ventral side, is slightly concave towards the dorsal side or protoconch, and is microgranular, sieved (Pl.1, figs. 1,4-6; Pl.2, figs. 1-3; Pl.3, figs. 1,2) (Rahaghi, 1983, Pl. 34, figs. 6, 8-12) (Sirel, 1996a, Pl. 1, figs. 2, 5, 7, 8; Sirel, 1998; Pl. 39, figs. 1, 3, 4, 7, 11, 12, 13). Horizontal plates (hpl) merges either with the preceding horizontal plate and the umbilical flap (uf) or with horizontal plates of both sides at the bottom. Horizontal plates (hpl) could be seen in vertical, subvertical and oblique sections depending on their geometrical structure and the section plane. A compound plate (cpl) is developed by merging of a sieve vertical plate (vpl) with a sieve horizontal plate (hpl) on an umbilical flap or developed by a sieve vertical plate evolving into a horizontal plate (hpl) after the umbilical flap (uf) (Pl.1, figs. 1, 4-6; Pl.2, figs. 1, 2; Pl.3, fig. 2) (Text figures 3A, B). Umbilical flap (uf), located at the end of septa, is a minute, microgranular, imperforate plate (Pl.1, figs. 1,4-6; Pl.2, figs. 1-3; Pl.3, figs. 1,2) (Text figures 3A,B). Ventral pillars (vnp1 and vnp2) are observed in vertical or subvertical sections, and are in two different types. First ventral pillars (vnp1) are hyaline calcareous, short, monolithic, plug-looking pillars. These pillars (vnp1) are located in the ventral side of rotaliid stage following embryonic chambers (Pl.1, figs. 1,4,6; Pl.2, figs. 1-3; Pl.3, figs. 1,2) (Text figures 3A,B). Second ventral pillars are, in accordance with the inner layer of the test wall, microgranular, short and are found between horizontal plates (hpl) (Pl.1, figs. 1,4-6; Pl.2, figs. 1-3; Pl.3, fig. 2) (Text figures 3A, B). Umbilical openings (uo) called umbilical hole (uh) or umbilical cavity (uc) are present in the present in the umbilical side, between horizontal plate and second ventral pillars (vnp2) (Pl.1, figs. 1,4-6; Pl.2, figs. 1-3; Pl.3, fig. 2) (Text figures. 3A, B). The new species "*N. iranicus*" is one of larger neosistanitids based on the dimensions (horizontal diameter and height) of its megalospheric individuals. Microspheric generations are some more flattened trochospirally coiled. Megalospheric specimens are more inflated. Dimorphism is present.

Biometric measurements of the megalospheric generation: Horizontal diameter is between 1.015 mm - 1.735 mm, height is 1.050 mm - 1.663 mm, protoconch diameter is 0.105 mm - 0.198 mm, deuteroconch diameter is 0.093 mm - 0.268 mm, and index of elongation 1.417 - 1.487 (Pl.1, figs. 5,6; Pl.2, figs. 1, 2,4,6) (Text figures 3B, C) (Text figure 4/1).

Biometric measurements of the microspheric generation: Horizontal diameter is between 1.867 mm - 2.246 mm, height 1.400 mm - 1.488 mm, protoconch diameter is 0.009 mm, index of elongation is 1.519 (Pl.1, fig. 1; Pl.2, fig. 5) (Text figure 3A)

Differential diagnosis: *N. iranicus* differs from such new species as *N. sozerii*, *N. okuyucui* and *N. catali*, in its convex shape in dorsal side and more convex shape in ventral side or its more inflated lenticular shape or its globular shape. *N. iranicus* is easily distinguished from such new species as *N. armagani*, *N. guvenci*, *N. dageri* and *N. inali* by its larger size and globular shape (Text figure 4/1).

Fossil assemblage: Table 1; Age: Middle Paleocene, Selandian; SBZ 2 (Serra-Kiel et al., 1998).

Neosistanites sozerii Acar, n.gen., n.sp.

(Plate 3, Figures 3-5) (Text figure 4/3)

Derivation of name: This species is dedicated to my first master, micropaleontologist Biler Sözeri, MSc. He was known as honest, helpful, hardworking person with his contributions on stratigraphy of Turkey in the years he worked for Directorate of Mineral Research and Exploration (MTA).

Holotype: Almost vertical section, megalospheric section (Pl.3, fig.4).

Type locality: South of Lake Yarışlı, SW Burdur, W Turkey (Text figure 1).

Type level**:** Middle Paleocene, Selandian, SBZ 2 (Serra-Kiel et al., 1998).

Diagnosis: Test is small, free, trochospirally-rotaliid coiled, almost spherical. Dorsal and ventral sides are strongly convex, chambers are evolute in dorsal side (Pl.3, figs.3,4) (Text figure 4/3). Especially rotaliid stage is not as developed as in *N. iranicus*

and is not strong (Pl.3, figs.3,4) (Text figure 4/3). Two layered wall structure is clearly observed (Pl.3, figs.3-5) (Text figure 4/3). Inner layer is blackish coloured, calcite, microgranular or very fine grained and imperforate. Outer layer is perforated hyaline calcareous and radially textured (Rahaghi, 1983, p.54). Ultimate whorl or chambers wall of the ultimate whorl is microgranular structured (Pl.3, figs. 3-5) (Text figure 4/3). Dorsal pillars (dp), funnels (f), first ventral pillars (vnp1), vertical plates (vpl) (Pl.3, figs.3-5), horizontal plates (hpl), compound plates (cpl), umbilical flaps (uf), second ventral pillars (vnp2), umbilical holes (uh) (Pl.3, figs. 3,4) (Text figure 4/3) are present. In this new species (*N. sozerii*), tritoconch is also observed. This type of embryon is called triplle embryonic structure (Pl.3, fig.4). Megalospheric individuals of this new species is among large neosistanitids.

Biometric measurements of the megalospheric generation: Horizontal diameter is between 0.91 0mm - 1.692 mm, height is 0.910 mm - 1.575 mm, protoconch diameter is 0.128mm-0.262mm, deuteroconch diameter is 0.117-0.286mm, index of elongation is 1.074-1.205 (Pl.3, figs. 3-5) (Text figure 4/3). Microspheric generation has not been determined yet. However, in the genus *Neosistanites*, advanced dimorphism is existed.

Differential diagnosis: *N. sozerii* is easily distinguished from other newly introduced species of *Neosistanites* by its spherical shape (Text figure 4/3).

Fossil assemblage: Table 1; Age: Middle Paleocene, Selandian; SBZ 2 (Serra-Kiel et al., 1998).

Neosistanites okuyucui Acar, n.gen., n.sp.

(Plate 3, Figures 6,7; Plate 4, Figures 1,2) (Text figure 4/2)

Derivation of name: In honour of Prof. Dr. Cengiz Okuyucu for his studies on Paleozoic benthic foraminifera in both national and international area.

Holotype: Vertical section, megalospheric form (Pl.3, fig.7).

Type locality: South of Lake Yarışlı, SW Burdur, W Turkey (Text figure 1).

Type level: Middle Paleocene, Selandian, SBZ 2 (Serra-Kiel et al., 1998).

Diagnosis: Test is small, free, trochospirally-rotaliid coiled, convex in dorsal side with ulttimate chamber hanging down or lobate structured or inflated biconvex or strongly asymmetric neosistanitid form (Text figure 4/2). In horizontal / subhorizontal sections: width and height of chambers are gradually increasing. Especially in vertical sections of adult specimens, hanging ultimate chamber or lobate structure is clearly seen, and margins of the chambers are rounded (Pl.3, figs. 6,7; Pl.4, figs. 1,2) (Text figure 4/2). Chambers are evolute in dorsal side and in especially inflated rotaliid forms, two layered wall structure is well observed (Pl.3, fig. 7; Pl.4, fig. 2). The wall of the inner layer is composed of blackish coloured calcite, microgranular or very fine grained texture, imperforate; though outer layer is perforated calcareous and radially structured (Rahaghi, 1983, p.54). Sieve vertical plates (vpl) (generally observed at the end of the septa in subhorizontal sections) (Pl3, fig.6; Pl.4, figs.1,2), sieve horizontal plates (hpl), sieve compound plates (cpl), umbilical flaps (uf), second ventral pillars (vnp2) (Pl.3, fig. 7; Pl.4, figs. 1,2), funnels (f) (Pl.3, fig. 7; Pl.4, fig. 1,2), thick and advanced first ventral pillars (vnp1) (Pl.3, fig.7), umbilical holes (uh) are present. Megalospheric generation of his new species (*N. okuyucui*) is among larger neosistanitids.

Biometric measurements of the megalospheric generation: Horizontal diameter is between 1.190 mm-1.575 mm, height is 1.225 mm-1.400 mm, protoconch diameter is 0.082 mm-0.175 mm, deuteroconch diameter is 0.076mm - 0.233mm, and index of elongation is 1.104-1.119 (Pl.3, figs. 6,7; Pl.4, figs. 1,2) (Text figure 4/2). Microspheric generaion has not been determined yet. However, in the genus *Neosistanites*, advanced dimorphism is existed.

Differential diagnosis: *N. okuyucui* differs from *N. iranicus, N. sozerii* ve *N. catali* in having larger test, hanging ultimate chamber or lobate structure, most inflated biconvex shape and rounded chamber margins. It is, by its larger size, also easily distinguished from the middle sized species such as *N. armagani*, *N.guvenci* and small sized *N. dageri* and the smallest sized *N. inali* (Text figure 4/2).

Fossil assemblage: Table 1; Age: Middle Paleocene, Selandian; SBZ 2 (Serra-Kiel et al., 1998).

Neosistanites guvenci Acar, n.gen., n.sp.

(Plate 4, Figures 3-8; Plate 5, Figures 1-4) (Text Figure 4/6)

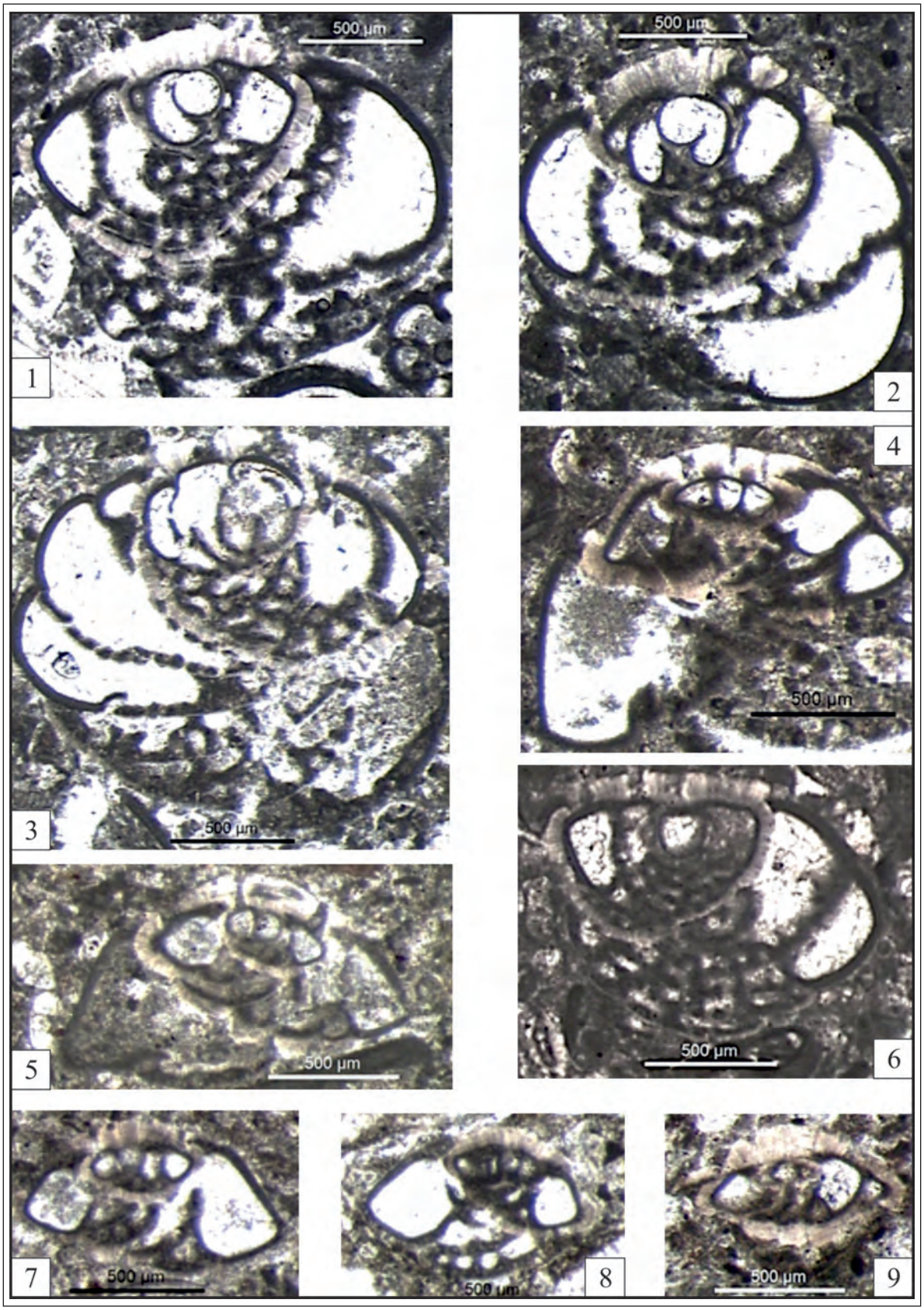

Figure 4- Species of the new genus *Neosistanites*: 1- *Neosistanites iranicus*. 2- *Neosistanites okuyucui* n.sp. 3- *Neosistanites sozerii* n.sp. 4- *Neosistanites catali* n.sp. 5- *Neosistanites armagani* n.sp. 6- *Neosistanites guvenci* n.sp. 7, 8- *Neosistanites dageri* n.sp. 9- *Neosistanites inali* n.sp.

1983 *Sistanites iranica* Rahaghi, p. 54, Pl. 34, figs. 5,13.

1996 *Sistanites iranica* Rahaghi; in Sirel, Drobne et al. (1996), p. 79, Pl. 1, figs. 1, 11.

1998 *Sistanites iranica* Rahaghi; Sirel, p. 82, Pl. 39, fig. 8; Pl. 40, figs. 7, 12.

2015 *Sistanites iranica* Rahaghi; Sirel, Pl. 16, figs. 7,12.

Derivation of name: This species is dedicated to Prof. Dr. Tuncer Güvenç who had undertaken studies on Paleozoic algae and continental shelf.

Holotype: Vertical section, microspheric form (Pl.4, Fig. 3).

Type locality: South of Lake Yarışlı, SW Burdur, W Turkey (Text figure 1).

Type level: Middle Paleocene, Selandian, SBZ 2 (Serra-Kiel et al., 1998).

Diagnosis: Test is small, free, asymmetric trochospirally-rotaliid coiled. Dorsal side is generally flattened or flattened convex, and chabers are evolute in dorsal side (Pl.4, figs. 3,4,7,8; Pl.5, figs. 1,2,4) (Text figure 4/6). Two layered wall structure is well seen in rotaliid stage (Pl.4,figs. 3,4,7,8; Pl.5, figs. 1-4). Even though inner layer of the wall is blackish coloured calcite, microgranular or very fine grained, imperforate, outer layer is perforated calcareous and microgranular textured (Rahaghi, 1983, p.54). Mıcrogranular structure is observed in the last whorl or in structure of wall or septum of the last whorl (Pl.4, figs. 3,5,6; Pl.5, figs. 2,3). Curved vertical plates (vpl) are seen by having small perforations in vertical sections. However, they are seen as pierced in slightly oblique sections (Pl.4, figs. 5,6). Horizontal plates (hpl), compound plates (cpl), umbilical flap (uf), second ventral pillars (vnp2) are in microgranular structure (Pl.4, figs. 3,4,7,8). Dorsal pillars (dp) and short first ventral pillars (vnp2) are hyaline calcareous, and funnels (f) are present (Pl.4, figs. 3,4,7,8; Pl.5, fig. 14). This new species has also tritoconch (tr) (Pl.4, fig.5). Umbilical holes (uh), horizontal plates (hpl), short second ventral pillars (vnp2) are present (Pl.4, figs. 3,4,7,8; Pl.5, figs. 1,2,4). The new species *N. guvenci* could be counted in middle sized neosistanitids. Dimorphism in this new species is existed.

Biometric measurements of the megalospheric generation: Horizontal diameter is between 0.688 mm-1.283 mm, height is 0.595 mm-1.003 mm, protoconch diameter is 0.070 mm-0.215 mm, deuteroconch diameter is 0.082mm -0.222 mm, tritoconch diameter is 0.093 mm-0.198 mm and index of elongation is 1.156-1.589 (Pl.4, figs. 4-8; Pl.5, figs. 1-4) (Text figure 4/6)

Biometric measurements of the microspheric generation: Horizontal diameter is 2.100 mm, height is 1.167 mm, protoconch diameter is 0.025 mm, and index of elongation is 1.799 (Pl.4, fig.3).

Differential diagnosis: *N. güvenci* is easily distinguished from all other species of *Neosistanites* by being flattened in dorsal side, and convex in ventral side (Text figure 4/6).

Fossil assemblage: Table 1; Age: Middle Paleocene, Selandian; SBZ 2 (Serra-Kiel et al., 1998).

Neosistanites dageri Acar, n.gen., n.sp.

(Plate 4, Figures 9,10; Plate 5, Figures 5-12) (Text figure 4/7, 8)

1996 *Sistanites iranica* Rahaghi; in Sirel, Drobne et al. (1996), p. 79, Pl.1, figs. 4, 10.

1998 *Sistanites iranica* Rahaghi; Sirel, p. 82, Pl. 39, figs. 2,6,7, 9, 10, 14, Pl. 40, fig. 4.

2015 *Sistanites iranica* Rahaghi; Sirel, Pl. 16, figs. 3,4.

Derivation of name: This species is dedicated to micropaleontologist Dr. Zeki Dağer since his contributions on the geology and micropaleontology of Turkey with his studies on Mesozoic benthic foraminifera and for his sincere personality.

Holotype: Almost vertical section, microspheric form (Pl.5, fig. 5).

Type locality: South of Lake Yarışlı, SW Burdur, W Turkey (Text figure 1).

Type level: Middle Paleocene, Selandian, SBZ 2 (Serra-Kiel et al., 1998).

Differential diagnosis: Test is small, free, almost lenticular (Pl.4, figs. 9,10; Pl.5, figs. 5,6,8-10), trochospirally-rotaliid coiled. Chambers are evolute in dorsal side. Two layered wall structure is well observed especially in rotaliid stage (Pl.4, figs. 9,10; Pl.5, figs. 5-12) (Text figures 4/7,8). Inner layer of the wall is blackish calcite, microgranular or very fine grained and imperforate. Outer layer is radial hyaline

calcareous in structure (Rahaghi, 1983, p.54). Last wohorl or the septa and their wall structure in the last whorl are microgranular (Pl.5, figs. 6,7,9,10,12). Vertical plates (vpl) (Pl.4, fig.9), horizontal plates (hpl), compound plates (cpl), umbilical flap (uf) and short second ventral pillars (vnp2) are identical to inner layer of the test wall (Pl.4, figs. 9,10; Pl.5, figs. 5,6,8-11). Dorsal pillars (dp), funnels (f) (Pl.4, fig. 10; Pl.5, figs. 10,11) and central pillars (Pl.4, fig. 9; Pl.5, figs. 5,6,8,9) are present. First ventral pillars (vnp1) are hyaline calcareous structured (Pl.4, fig. 9; Pl.5, figs. 5,6,10,11). Umbilical holes (uh) are located between sieve horizontal plates (hpl) and ventral pillars (Pl.4, figs. 9,10; Pl.5, figs. 5,6,8-11). Septa, intercameral foramina (if) and foraminal plate (fpl) are observed in oblique subhorizontal sections (Pl.5, figs. 7,12). The new species *N. dageri* could be accepted as small sized neosistanitids depending on its dimensions (Text figures 4/7, 8). Dimorphism is distinct.

Biometric measurements of the megalospheric generation: Horizontal diameter is between 0.758mm-1.143mm, height is 0.513mm-0.630mm, protoconch diameter is 0.047mm-0.089mm, and index of elongation is 1.530mm-1.850mm (Pl.4, fig. 10; Pl.5, figs. 7-11).

Biometric measurements of the microspheric generation: Horizontal diameter is between 0.933mm-1.202mm, height is 0.490mm-0.618mm, protoconch diameter is 0.014mm-0.023mm, and index of elongation is 1.904mm-1.945mm (Pl.4, fig. 9; Pl.5, figs. 5,6,12).

Differential diagnosis: *N. dageri* is distinguished from all other species of *Neosistanites*, especially from the smallest one *N. inali*, by its small size and almost symmetrical lenticular shape (Text figures 4/7,8).

Fossil assemblage: Table 1; Age: Middle Paleocene, Selandian; SBZ 2 (Serra-Kiel et al., 1998).

Neosistanites catali Acar, n.gen., n.sp.

(Plate 6, Figures 1-3) (Text figure 4/4)

1996 *Sistanites iranica* Rahaghi; in Sirel, Drobne et al. (1996), p.79, Pl. 1, fig. 6.

1998 *Sistanites iranica* Rahaghi; Sirel, p.82, Pl. 40, fig. 1.

2015 *Sistanites iranica* Rahaghi; Sirel, Pl. 16, fig.1.

Derivation of name: This species is dedicated to Erol Çatal, MSc, for his contribution to geology of Turkey with his studies on Paleozoic benthic foraminifera.

Holotype: Almost vertical section, megalospheric form (Pl.6, fig. 1).

Type locality: South of Lake Yarışlı, SW Burdur, W Turkey (Text figure 1).

Type level: Middle Paleocene, Selandian, SBZ 2 (Serra-Kiel et al., 1998).

Diagnosis: Test is small, free, asymmetric trochospirally-rotaliid coiled, convex. Ultimate chambers of adult specimens are very large (height and width of the chambers are quite large in size). Especially margins of the hanging final chambers are truncate (Pl.6, fig. 1,2) (Text figure 4/4). Chambers are evolute in rotaliid stage and two layered wall structure is apparent (Pl.6, figs. 1-3). Last whorl or wall and septal structure of the last whorl is microgranular (Pl.6, figs.1,2). Inner wall of the test is blackish coloured calcite, microgranular or very fine grained, and imperforate. Outer wall is perforated radial hyaline calcareous (Rahaghi, 1983, p.54). Curved vertical plates (vpl) are observed in vertical plates (Pl.6, fig.3) and umbilical flaps (uf) are observed as being attached to septa (Pl.6, figs.1-3). Horizontal plates (hpl) (Pl.6, figs.1-3), compound plates (cpl) and second ventral pillars (vnp2) are in same structure with the inner layer of the wall (Pl.6, figs.1,3). Central (cp) (Pl.6, figs.2,3) and dorsal pillars (dp) belonging to the outer wall of the test are in hyaline calcareous structure, and funnels (f) are also present (Pl.6, fig.1). These larger dorsal pillars can be observed on well preserved and well cleaned free specimens like a central granule (Pl.6, figs. 2,3). Umbilical holes (uh), are found between sieve horizontal plates and second ventral pillars in the ventral area (Pl.6, figs.1,3).). The new species *N. catali* could be incorporated into larger neosistanitids depending on its size (Text figure 4/4).

Biometric measurements of the megalospheric generation: Horizontal diameter is between 1.138mm-1.517mm, height is 0.846mm-0.933mm, protoconch diameter is 0.117mm, and index of elongation is 1.793-1.862 (Pl.6, fig.3). Microspheric generaion has not been determined yet.

Differential diagnosis: Chambers in the final whorl of *N. catali* are very larger and the last chamber is lobate or hanging-down. Its chambers are truncate

(Pl.6, figs.1,2) (Text figure 4/4). This species is distinguished from all other species of the genus especially from *N. okuyucui* by its shape and larger test.

Fossil assemblage: Table 1; Age: Middle Paleocene, Selandian; SBZ 2 (Serra-Kiel et al., 1998).

Neosistanites armagani Acar, n.gen., n.sp.

(Plate 6, Figures 4-6) (Text figure 4/5)

Derivation of name: This species is dedicated to Fahrettin Armağan, MSc, who has contributed to geology of Turkey with his studies on Mesozoic benthic foraminifera.

Holotype: Vertical section, megalospheric form (Pl.6, fig. 4).

Type locality: South of Lake Yarışlı, SW Burdur, W Turkey (Text figure 1).

Type level: Middle Paleocene, Selandian, SBZ 2 (Serra-Kiel et al., 1998).

Diagnosis: Test is small, free, asymmetric trochospirally-rotaliid coiled, convex in dorsal side, inflated and asymmetrical lenticular, but ventral side is almost flattened, and especially last whorls are sharp-edged. Two layered test wall is well observed in rotaliid stage (Pl.4, figs.4,5) (Text figure 4/5). Last whorl, or septa or wall structure of the last whorl is microgranular (Pl.6, figs.4-6). While inner layer of the test is blackish calcite, microgranular or very fine graied and imperforate; outer layer of the test is hyaline calcareous and radial structured (Rahaghi, 1983, p.54). Spherical shaped protoconch (p) and deuteroconch (dt) are present (Pl.6, fig.5). Vertical plates (vpl) (Pl.6, fig.5), horizontal plates (hpl), umbilical flap (uf), and second ventral pillars (vnp2) are identical structure to inner structure of the test (Pl.6, figs.4,5). First ventral pillars (vnp1) (Pl.6, fig.5), dorsal pillars (dp) and funnels (f), septa (s), intercameral foramina (if) (Pl.6, fig.6) are also present (Pl.6, figs.4,5). Umbilical holes (uh) and short second ventral pillars (vnp2) are located in the ventral side (Pl.6, figs.4,5). This new species could be counted in middle sized neosistanitids.

Biometric measurements of the megalospheric generation: Horizontal diameter is between 0.793mm-1.370mm, height is 0.642mm-0.735mm, protoconch diameter is 0.089mm-0.107mm, and index of elongation is 0.642mm-0.735mm (Pl.6, figs.4-6). Microspheric generaion has not been determined yet.

Differential diagnosis: *N. armagani* is distinguished from *N. iranicus*, *N. catali*, *N. okuyucui* by its inflated, middle sized, asymmetric lenticular test, regular coiling, and being almost flattened in ventral side. Being middle sized differs this species from smaller ones (*N. dageri* ve *N. inali*).

Fossil assemblage: Table 1; Age: Middle Paleocene, Selandian; SBZ 2 (Serra-Kiel et al., 1998).

Neosistanites inali Acar, n.gen., n.sp.

(Plate 6, Figures 7-9) (Text figure 4/9)

Derivation of name: This species is dedicated to Erdoğan İnal, MSc. who has contributed to geology of Turkey with his studies on Tertiary benthic foraminifera.

Holotype: Vertical section, microspheric form (Pl.6, fig. 8).

Type locality: South of Lake Yarışlı, SW Burdur, W Turkey (Text figure 1).

Type level: Middle Paleocene, Selandian, SBZ 2 (Serra-Kiel et al., 1998).

Diagnosis: Test is free, small, trochospirally-rotaliid coiled, flattened lenticular (Pl.6, figs.8,9) (Text figure 4/9). Chambers are evolute in dorsal side. Two layered wall structure is well observed in especially rotaliid stage (Pl.6, figs.7-9). This new species is the smallest one (Pl.6, figs.7-9) (Text figure 4/9). While, inner layer of the test is blackish calcite, microgranular or very fine grained, imperforate; outer layer is perforated calcareous and radial structured (Rahaghi, 1983, p.54). Horizontal plates (hpl), umbilical flaps (uf) and second ventral pillars (vnp2) are in same structure with inner layer of the test (Pl.6, figs.8,9). Central pillars (cp) (Pl.6, figs.8,9) and dorsal pillars (dp) are hyaline calcareous. Funnels (f) are present (Pl.6, figs. 7-9). Umbilical holes (uh) and short second ventral pillars (vnp2) are observed in vertical (Pl.6, figs. 8,9); septa and intercameral foramina (if) are observed in oblique subhorizontal sections (Pl.6, fig. 7). This new species could be included in smallest sized neosistanitids (Text figure 4/9). Dimorphism is evident.

Biometric measurements of a broken megalospheric individual: Horizontal diameter is between 0.852mm, height is 0.583mm, index of elongation is 1.411, and protoconch diameter is 0.070mm (Pl.6, fig.9).

Biometric measurements of the microspheric generation: Horizontal diameter is between 0.758mm-

0.968mm, height is 0.583mm, protoconch diameter is between 0.014mm-0.023mm, and index of elongation is 1.660 (Pl.6, figs.7,8).

Differential diagnosis: *N. inali* is the smallest species of *Neosistanites* (Text figure 4/9). It is easily distinguished by its small and flattened lenticular shape from all other species of *Neosistanites*, especially from *N. dageri*.

Fossil assemblage: Table 1; Age: Middle Paleocene, Selandian; SBZ 2 (Serra-Kiel et al., 1998).

Order: Foraminiferida EICHWALD, 1830,

Superfamily: Miliolacea EHRENBERG, 1839,

Family: Soritidae EHRENBERG, 1839,

Subfamily: Soritinae EHRENBERG, 1839;

Genus: *Parahaymanella* ACAR, n.gen.,

Type species: *Parahaymanella hakyemezae* ACAR, n.gen., n.sp.

New genus *Parahaymanella* Acar, n.gen.,

Derivation of name: Name of the genus is derived from the combination of prefix "para" meaning "almost" or "approximate" and the name of genus "*Haymanella*" which the new genus resembles to.

Type species: Longitudinal horizontal section, megalospheric form (Pl.7, fig. 1).

Type locality: South of Lake Yarışlı, SW Burdur, W Turkey (Text figure 1).

Type level: Middle Paleocene, Selandian, SBZ 2 (Serra-Kiel et al., 1998).

Diagnosis: Test is small, elongated, asymmetric and free. Shape of the new genus *Parahaymanella* (*Prh.*) is like a golf club as in *Haymanella* (Pl.7, figs. 1-12), (Sirel, 1998, p.36; Sirel, 1999, p.122; Sirel, 2004, p.65; Sirel, 2015, Pl.4, fig. 10). Elongated test is composed of two parts and its length reaches to 0.478-1.313mm. First or spirally coiled part is composed of regular, spiral coiling undivided chambers following triloculine chambers after spherical protoconch. Diameter of this spirally coiled part varies between 0.327 mm-0.595mm (Pl.7, figs. 1,3-5, 8-10). Two types of uniserial chambers are present.

A- Chambers of uniserial stage of *Parahaymanella hakyemezae* n.gen., n.sp. or *Parahaymanella bozkurti* n.gen., n.sp. are composed of irregularly aligned chambers (different height and length) (Pl.7, figs. 1,2,6-8).

B- Chambers of uniserial stage of *Parahaymanella alanae* n.gen., n.sp. are regularly aligned chambers (almost same height and length) (Pl.7, figs. 9-12). Besides, the new genus *Parahaymanella* has imperforate porcelaneous calcareous test with one aperture. Intercameral foramina (if) are located at the base of spirally aligned chambers and in the middle of uniserial chambers (Pl.7, figs. 1-3,6,7,11,12). Dimorphism is faint.

Fossil assemblage: Table 1; Age: Middle Paleocene, Selandian; SBZ 2 (Serra-Kiel et al., 1998).

Comparison with other genera: Only similarity between the new genus *Parahaymanella* (*Prh.*) and *Haymanella* Sirel (1999) is the shape of uniserial part of their tests (like an elongated golf club). Irregular milioline arrangement following protoconch is present in megalospheric (fA) and microspheric (fB) generations of *Haymanella* Sirel (Sirel, 1999, Pl. 4, figs. 1,11,13,16; Pl. 5, figs. 5,9,11; Sirel, 2015, Pl. 4, figs. 7,8,13,14). Width of uniserial chambers of *Haymanella* Sirel is regular, gradually increasing and these chambers are triangular (Sirel, 1999, Pl. 4, figs. 1-4,8-10,12,14-16; Pl. 5, figs. 1,3,4,8-10; Sirel, 2015, Pl. 4, fig. 10). Test wall of the genus *Haymanella* Sirel is vacuolar and coarsely agglutinated (Sirel, 1999, Pl. 4, figs. 2-6, 8-10,12-18; Pl. 5, figs. 1-5,9-11,13; Sirel, 2015, Pl. 4, figs. 7,8,10-12,14,17,18). Aperture is terminal, and ribs extending from the apertural periphery towards the center, are present (Sirel, 1999, Pl. 4, figs. 1-5,7, 10,12,14,15,17,18; Pl. 5, figs. 1-4,6-10,12,13; Sirel, 2015, Pl. 4, figs. 9,15,16,18). The genus *Haymanella* with these features is far different from the new genus *Parahaymanella*. Because, in both generations (fA, fB), the new genus *Parahaymanella* has single aperture, imperforate porcelaneous calcareous wall structure, regular spirally aligned undivided chambers after milioline arranged chambers following protoconch. Besides, new genus *Parahaymanella* differs from all other foraminifera with agglutinated wall such as *Acruliammina* Loeblich and Tappan (1964), *Haplophragmium* Reuss (1860) and *Cribratina* Sample (1932), by its imperforated porcelaneous calcareous wall structure. On the other hand, alignment, coiling, and porcelaneous calcareous wall structure of spiral and uniserial stages of the new genus *Parahaymanella* is in common with *Kayseriella*

Sirel (1999, p.126). However, apertural structure is different in each. *Parahaymanella* has single, simple aperture; but *Kayseriella* has toothed (t) aperture with ribs (r). The new genus *Parahaymanella* and *Kolchidina* Morozova (1976) are in common with their planispirally coiled first stage chambers. However, the latter differs from the new genus by its agglutinated wall structure and cribrate aperture.

Fossil assemblage: Table 1; Age: Middle Paleocene, Selandian; SBZ 2 (Serra-Kiel et al., 1998).

Parahaymanella hakyemezae Acar, n.gen., n.sp.

(Plate 7, Figs. 1-5)

Derivation of name: This species is dedicated to (micropaleontologist) Dr. Aynur Hakyemez who has contributed to many geological projects with her studies on planctonic foraminifera.

Holotype: Oblique equatorial section, megalospheric form (Pl.7, fig. 1).

Type locality: South of Lake Yarışlı, SW Burdur, W Turkey (Text figure 1).

Type level: Middle Paleocene, Selandian, SBZ 2 (Serra-Kiel et al., 1998).

Diagnosis: Test is small, elongated, asymmetric and free. This new species (holotype) is the largest one among the species of the new genus *Parahaymanella* (*Prh.*).It resembles a golf club (Pl.7, figs. 1,2) (Sirel, 1998, p.36; Sirel, 1999, p.122; Sirel, 2004, p.65; Sirel, 2015, Pl. 4, fig. 10). Elongated test of the genus is consisting of two parts. First part is consist of regular spirally coiled chambers following triloculine stage after protoconch and the diameter of these chambers reach to 0.408-0.455 mm (Pl.7, figs.3-5). Length of the second part which is uniserial (handle of the golf club), reaches to 1.050-1.313 mm (Pl.7, figs.1,2). Height and width of triangular chambers of this uniserial stage are different, and these are lined up in an irregular pattern. Chamber width and chamber height of the chamber which is both the largest and the highest chamber of the uniserial stage, are 0. 222 mm and 0.257 mm respectively (Pl.7, fig.1). *Prh. hakyemezae* has imperforate porcelaneous calcareous test and single central aperture. Intercameral foramina or these "former apertures" are located at the base of spirally coiled undivided chambers (Pl.7, figs.3-5) in the first part; and are located in the middle of chambers (Pl.7, figs.1,2) in the second (uniserial) part. A slight flattening is observed in one side of the spirally coiled stage following protoconch (Pl.7, figs.2-4). Dimorphism is faint. Age: Middle Paleocene-Selandian; SBZ2 (Serra-Kiel et al., 1998).

Biometric measurements of the megalospheric generation: In the first part (fA), spherical and large protoconch (0.089-0.175mm) is followed by triloculine chambers which are followed by undivided spirally / planispirally enrolled chambers and intercameral foramina or "former apertures" (Pl.7, figs.3,4). Chambers of the second (uniserial) part are observed in longitudinal or oblique longitudinal sections cutting through the tubular, undivided, irregularly aligned chambers (Pl.7, figs.1,2). Height and length of chambers of this uniserial part are not isometric, or they are irregular (Pl.7, figs.1,2).

Biometric measurements of the microspheric generation: It has been observed in a broken specimen: in the first part, protoconch (0.022mm) is followed by at first cryptoquinqueloculine, then triloculine chambers which are finally followed by undivided spirally/planispirally enrolled chambers with intercameral foramina (Pl.7, fig.5). Second part is absent in this broken specimen.

Differential diagnosis: *Haymanella paleocenica* Sirel, 1999 has irregularly coiled chambers following protoconch (Sirel, 1999, Pl. 4, figs. 11, 16; Pl. 5, figs. 5, 11; Sirel, 2015, Pl. 4, figs. 7,8,13,14) and regularly arranged isometric chambers with gradually increasing height and width in second or uniserial stage (Sirel, 1999, Pl.4, figs.1-4,9,10,12,14-16, Pl.5, figs. 1,3,4,8-10; Sirel, 2015, Pl. 4, figs. 10,12). Besides, *H. Paleocenica* has agglutinated wall structure and extensions in its aperture or ribs (Sirel, 2015, Pl. 4, figs. 9,15,16). *H. Paleocenica* is easily distinguised from *Prh. hakyemezae* by these structural elements. Moreover *Prh. hakyemezae* Acar, n.gen., n.sp. is easily distinguished by its long and irregularly arranged chambers (triangular chambers of uniserial stage) from the smallest species of the genus, *Parahaymanella bozkurti* Acar, n.gen., n.sp., , and from the middle sized *Prh.. alanae* Acar, n.gen., n.sp. having regularly arranged chambers (uniserial).

Fossil assemblage: Table 1; Age: Middle Paleocene, Selandian; SBZ 2 (Serra-Kiel et al., 1998).

Parahaymanella bozkurti Acar, n.gen., n.sp.

(Plate 7, Figures 6-8)

Derivation of name: This species is dedicated to young micropaleontologist candidate Alper Bozkurt,

MSc., who is a successful field geologist, for his contributions to many geological projects.

Holotype: Oblique equatorial section, megalospheric (Pl.7, fig. 8).

Type locality: South of Lake Yarışlı, SW Burdur, W Turkey (Text figure 1).

Type level: Middle Paleocene, Selandian, SBZ 2 (Serra-Kiel et al., 1998).

Diagnosis: Test is free, minute, elongated, asymmetrical. This new species is the smallest species of *Parahaymanella* (*Prh.*). It resembles a golf club (Sirel, 1998, p.36; Sirel, 1999, p.122; Sirel, 2004, p.65). Test of the species is consisting of two parts. First part is consist of triloculine chambers following protoconch and of regular, spirally coiled undivided chambers (Pl.7, fig.8). Diameter of this (first part) regular, spirally coiled chambers vary between 0.327-0.408mm. Length of uniserial part of *Prh. bozkurti* varies between 0. 478-0.618mm and this part is quite short (Pl.7, figs.6-8). Height and width of (triangular) chambers of the uniserial stage are different, and these chambers are arranged in an irregular manner. Chamber width and chamber height of the chamber which is both the largest and the highest chamber of the uniserial stage, are 0. 175mm and 0.187mm respectively (Pl.7, fig.7). The species has imperforate porcelaneous calcareous test and single aperture. Intercameral foramina or these "former apertures" are located at the base of spirally coiled undivided chambers (Pl.7, fig.8) in the first part; and are located in the middle of chambers (Pl.7, figs.6,7) in the second (uniserial) part. A slight flattening is observed in one side of the spirally coiled stage following protoconch (Pl.7, figs.2-4). Dimorphism is faint. Age: Middle Paleocene- Selandian; SBZ2 (Serra-Kiel et al., 1998).

Biometric measurements of the megalospheric generation: First part is comprised of spherical protoconch of 0.107mm, following triloculine chambers and regular spirally coiled undivided chambers (Pl.7, fig.8). Chamber diameter of this first part (regular, spirally enrolled part) is 0.408mm. Microspheric generation has not been determined yet.

Differential diagnosis: This new species is easily distinguished from *H. paleocenica, Prh. hakyemezae* and *Prh. alanae* by smallest (spirally coiled) first stage and uniserial second stage with the smallest handle part.

Fossil assemblage: Table 1; Age: Middle Paleocene, Selandian; SBZ 2 (Serra-Kiel et al., 1998).

Parahaymanella alanae Acar, n.gen., n.sp.

(Plate 7, Figures 9-12)

Derivation of name: This species is dedicated to Dr. Birkan Alan, who has contributed to many geological projects with her studies on benthic foraminifera.

Holotype: Longitudinal equatorial section, megalospheric form (Pl.7, fig.10).

Type locality: South of Lake Yarışlı, SW Burdur, W Turkey (Text figure 1).

Type level: Middle Paleocene, Selandian, SBZ 2 (Serra-Kiel et al., 1998).

Diagnosis: Test is small, free, elongated, asymmetric. This new species is a middle sized species of *Parahaymanella* (*Prh*). It resembles stalk of a golf club (Sirel, 1998, p.36; 1999, p.122; 2004, p.65). The elongated test is consisting of two parts. First part is consisting of triloculine chambers following protoconch and of regular, spirally coiled undivided chambers. Diameter of this spirally coiled part reaches to 0.373-0.572mm (Pl.7, figs.9,10). Length of uniserial part of *Prh. alanae* is 0.700-1.050 mm (Pl.7, figs.9-11). However, length of uniserial part is longer than in *Prh. bozkurti* and shorter than in *Prh. hakyemezae*. Besides, roof of the chambers of *Prh. alanae* are dome-shaped and its chambers are isometric. They are regular in arrangement. Its wall structure is imperforate porcelaneous calcareous and the species has single aperture. Former apertures or intercameral foramina (if) are located in the center or in the middle of the chambers of second (uniserial) part (Pl.7, figs.9,11,12). A slight flattening is observed in both sides of the spirally coiled stage in longitudinal sections (Pl.7, fig.10). Dimorphism is faint. Age: Middle Paleocene- Selandian; SBZ2 (Serra-Kiel et al., 1998).

Biometric measurements of the megalospheric generation: Diameter of the spherical protoconch in first part varies between 0. 047-0.163mm. Diameters of undivided triloculine chambers following protoconch and regular spirally coiled chambers vary between 0. 373-0. 572mm (Pl.7, figs.9,10). Microspheric generation has not been determined yet.

Differential diagnosis: Height, width and arrangement of dome-shaped chambers of uniserial

part of *Prh. alanae* is regular (Pl.7, figs.9-11). The species, with these features, differs from *Prh. hakyemezae* and *Prh. bozkurti*. However, length of the uniserial part of *Prh. alanae* is shorter than in *Prh. hakyemezae* and longer than in *Prh. bozkurti*. *H. Paleocenica* is similar to *Prh. alanae* in terms of having regular and gradually increasing chambers in uniserial adult stage, but differs by apertural openings, ribs, and triangular chambers of uniserial stage (Sirel, 1999, Pl. 4, figs. 1-4,8-10,12,14-16, Pl. 5, figs. 1, 3,4,8-10).

Fossil assemblage: Table 1; Age: Middle Paleocene, Selandian; SBZ 2 (Serra-Kiel et al., 1998).

Order: Foraminiferida EICHWALD, 1830,

Suborder: Miliolina DELAGE VE HEROUARD, 1896,

Superfamily: Miliolacea EHRENBERG, 1839,

Family: Miliolidae EHRENBERG, 1839,

New genus: *Pseudohottingerina* ACAR, n.gen.,

Type species: *Pseudohottingerina burdurensis* ACAR, n.gen. n.sp.

New genus: *Pseudohottingerina* Acar, n.gen.

Derivation of name: This genus is dedicated to honest, helpful, respectable scientist and grand master, paleontologist Prof. Dr. Lukas Hottinger (passed away in 4th Sept. 2011) who the author refers as his only master. The name of this new genus is derived by combination of the prefix “Pseudo” (meaning false or fake in Latin) and the name of the genus *Hottingerina* Drobne (1975) in order to make Prof. Hottinger’s name eternal one more time.

Type species: Oblique equatorial section, megalospheric form (Pl.8, fig. 1).

Type locality: South of Lake Yarışlı, SW Burdur, W Turkey (Text figure 1).

Type level: Middle Paleocene, Selandian, SBZ 2 (Serra-Kiel et al., 1998).

Diagnosis: Test is small, subcylindirical or inflated discoidal shape, slightly depressed in the middle, rounded in the poles, and has radial septal filaments (just as in *Nummulites*) (Pl.7, figs.14-19). Biometric measurements of megalospheric generations (fA) as follows: protoconch diameter is between 0.083-0.115 mm; equatorial diameter is 0.520-1.771 mm; and axial diameter varies between 0.563 - 0.962 mm (Pl.8, figs.1,5). Subepidermal plates are absent between septal filaments (sfl) (Pl.7, figs.14,15,19) of *Pseudohottingerina* (*Psh)*. Subepidermal plate is one of the structural elements in foraminifera. Hence, absence or presence of this element leads the individuals being defined as different genera. In megalospheric generation (fA), spherical protoconch is followed by triloculine chambers (Pl.8, figs. 1-3,6-9), planispirally coiled undivided chambers, thick and curved septa (s) (Pl.8, fig. 1), counters septum (cs) (Pl.8, figs. 1-4,9), advanced lips (lp) (Pl.8., figs.1-3), large intercameral foramina (if) (Pl.8, fig. 18; Pl.8, figs. 1,2,4) respectively. Flaring chambers (fch) of the flaring whorls (fw) of some specimens are very large, high and undivided. These individuals might be passing to a uniserial stage (Pl.8, fig.3). The ultimate chamber of only one specimen appears like being divided into chamberlets (cht) (Pl.8, fig.3). However, this structure has not been observed in any other specimens yet. Chambers of the ultimate whorl of this new genus are evolute in subaxial sections (Pl.7, figs.14-16). Both sides of the test are observed as slightly depressed in subaxial sections (Pl.7, figs.14-16). This depression is caused by being more inflated of biserial evolute last chambers of ultimate whorl. Spherical protoconch, triloculine chambers, undivided planispiral chambers, thick and curved septa (s), counters septa (cs), intercameral foramina (if), lips (lp), penultimate flaring chambers (fch), and flaring whorls (fw) are present in a oblique equatorial section of the holotype (Pl.8, fig.1). Test wall, basal layer, whorls, septa (s) are in imperforate porcelaneous calcareous structure (Pl.7, figs. 14-19; Pl.8, figs. 1-9). Single and large aperture is located close to the middle of a septum, not at the base (Pl.7, fig.18). Periphery of this large aperture is bordered by a thick lip (lp) (Pl.8, figs.1-3). Occurrence of this aperture almost in the middle of a septum provides the formation of this structural element described as counter septum (cs) by Hottinger (2006: p.70, figs. 33, A-G) (Pl.7, fig. 18; Pl.8, figs. 1-4,9). If the aperture were at the base of the septum, counter septum would not be developed. There must be an interval or a bulge between the underlying whorl/spire and the aperture for the occurrence of counter septum. Therefore, aperture of the new genus is located almost in the middle of the septum (Pl.7, fig.18). The counter septum (cs) is observed, in equatorial sections of *Pseudohottingerina*, beneath the aperture or above the spire. Since the microspheric individuals of *Pseudohottingerina* has not been determined yet, dimorphism is absent in *Pseudohottingerina*. Age:

Middle Paleocene, Selandian, SBZ2 (Serra-Kiel, et al., 1998).

Comparison with other genera:

1- It has been reported that radial septal filaments and the septula between these filaments are present in *Hottingerin*a Drobne (1975, p.250) (Drobne, 1975: Pl.1, fig. 1, Pl. 2, figs. 1,2; Pl. 4, figs. 1-4,6,8,9; Pl. 5, figs. 1-4; Pl. 6, figs. 1-5). However, these are not septula, and beacuse of this reason, these can not form chamberslets (as in Alveolinids). Abovementioned elements actually are subepidermal plates. These subepidermal plates are identical to the one in *Malatyna* and in this genus, they are well developed (Sirel and Acar, 1993: Pl. 1, figs. 1-3,5-7,10,13,15; Pl.2, figs. 1-5,8-10). These subepidermal plates are the short, triangular shape, planar plates hanging down from the ceiling of the chambers but generally not reaching to the base of the chambers (Sirel and Acar, 1993: Pl.1, figs. 1-3,5-7,10,13,15; Pl.2, figs. 1-5,8-10). It has been reported that the aperture of *Hottingerina* is single, simple and is located at the base of septum in planispiral stage (Drobne, 1975: Pl. 3, fig. 1; Pl. 4, figs. 5,7,8; Pl. 6, figs. 1,3,4), yet is cribrate in uniserial stage (Drobne, 1975: pl.6, fig.4; Pl.9, fig.1 top-right). Uniserial stage of the new genus *Pseudohottingerina* has not been clearly observed thus far. Counter septum (cs) described by Hottinger (2006, p.70,fig.33, A-G), is well developed in the new genus *Pseudohottingerina* (Pl.8, figs. 1-9) and the presence of this structural element in *Hottingerina* is agreed as well (Drobne,1975: p.250, Pl.3, fig.1; Pl.4, figs.5,7,8; Pl.5, fig.2; Pl.6, figs.1,3-5). Counter septum (cs) is well developed in *Pseudohottingerina burdurensis* n.sp. (Pl.8, figs.1-4). Subepidermal plates are absent in the new genus *Pseudohottingerina* (Pl.7, figs. 14-19; Pl.8, figs. 1-9). However, counter septum (cs) (Pl.8, figs.1-4), lips (lp); and in megalospheric generations, triloculine chambers following protoconch, and succeeding planispiral chambers are present (Pl.8, figs.1-3,6-9). Briefly, except the common features (apertures, coiling, etc.) of *Pseudohottingerina* and *Hottingerina*; key difference between these genera is the presence or absence of subepidermal plates.

2- Hottinger (2006, p.70, figs. 33, A-G) made the description of counter septum (cs) by examining equatorial sections of the species *Amphistegina tuberculata* (Cushman, 1919) of the hyaline calcareous walled genus *Amphistegina* d'Orbigny (1826). Although the new genus and *Amphistegina* differ in wall structure (porcelaneous calcareous vs. hyaline calcareous), they are in common with the presence of counter septum.

3- *Kayseriella* Sirel (1998, 1999, 2004) differs from the new genus by its toothed (t) and ribbed (r) aperture. Septal filaments (sfl) (Pl.7, figs.14-19), counter septum (cs) (Pl.8, figs.1-4) and lips (lp) are present in the new genus, and the new genus has single aperture. Triloculine chambers following the spherical protoconch, and succeeding planispirally coiled undivided chambers (ch), thick septa (s), thick whorls/ spire are existed in both megalospheric generations of *Kayseriella* Sirel (1999) and of the new genus (*Pseudohottingerina*). Both genera have porcelaneous calcareous wall structure. These genera are similar, with those common features (Pl.8, figs. 1-3,6-9), (Sirel, 2004: Pl. 55, figs. 2,5-7; Pl. 56, figs. 9-11).

4- *Nurdanella* Özgen (2000) differs from the new genus by the presence of cribrate aperture and by the absence of counter septum. However, the new genus differs from *Nurdanella*, by having septal filaments (sfl) on its test (Pl.7,figs. 14-19), counter septum (cs) (Pl.8, figs. 1-4), lips (lp) and single aperture. Both genera are in common with the absence of subepidermal plates; and by the presence of triloculine chambers following protoconch, succeeding planispiral chambers, imperforate porcelaneous calcareous test structure (Özgen, 2000).

5- *Raoia* Matsumaru and Sarma (2010, p.560) has sieve or cribrate aperture. Peripheral zones of its chambers are divided by main radial septula. *Raoia* has septal filaments on its test, but no subepidermal plates. *Raoia* is similar to the new genus *Pseudohottingerina*, by these features (Pl.7, figs. 14-19) (Matsumaru and Sarma, 2010: p.560, Pl. 2, figs. 9,10). However, these features of *Raoia* was not reported by the authors of the genus (Matsumaru and Sarma, 2010, Pl. 2, figs. 10). Subepidermal plates are absent (Pl.7, figs.14-19); but counter septum (cs) (Pl.8, figs. 1-4), lip structure and single aperture are present in *Pseudohottingerina*. Peripheral zones of the chambers of *Pseudohottingerina* are not divided by main radial septula. Besides, each genera has different apertural openings. *Pseudohottingerina* and *Raoia* are in common with the features of having septal filaments (sfl) on their tests, having imperforate porcelaneous calcareous tests, having chambers arranged in some planes (milioline?), and having planispirally coiled, undivided, involute chambers.

Fossil assemblage: Table 1; Age: Middle Paleocene, Selandian; SBZ 2 (Serra-Kiel et al., 1998).

Pseudohottingerina burdurensis Acar, n.gen., n.sp.

(Plate 7, Figures 14-19; Plate 8, Figures 1-4)

Derivation of name: Burdur is city in the SW Turkey.

Holotype: Oblique equatorial section, megalospheric form (Pl.8, fig. 1).

Type locality: South of Lake Yarışlı, SW Burdur, W Turkey (Text figure 1).

Type level: Middle Paleocene, Selandian, SBZ 2 (Serra-Kiel, et al., 1998).

Diagnosis: Test is small, subcylindrical or inflated discoidal shape, slightly depressed in the middle, rounded in poles. The test has radial septal filaments (as in *Nummulites*), has no subepidermal partitions (Pl.7, figs.14-19). Biometric measurements are as follows: protoconch diameter is between 0.083-0.115mm; equatorial chamber is 1.124 - 1.771 mm; and axial diameter varies between 0.563 - 0.962 mm. Holotype is an oblique equatorial section. 37 chambers could be counted in 3.5 whorls (except the large and single aperture of penultimate whorl), and the diameter is measured as 1.574 mm (Pl.8, fig.1). Septa (s) and spire are very thick, loosely coiled beginning from the protoconch; whorls are higher, so are the chambers (Pl.7, figs.14-19; Pl.8, figs. 1-4). Counter septum (cs) of *Psh. burdurensis* is very thick (Pl.8, figs. 1-4). Especially the septum between the ultimate chamber and the penultimate chamber of holotype, is the thickest one (Pl.8, fig. 1). Single and large aperture of the species is not at the base of the septum; but located close to the middle of the septum; and the aperture is bordered by a thick lip (lp) around the aperture (Pl.7, fig. 18; Pl.8, figs. 1-4). Wall is imperforate, porcelaneous calcareous. Age: Middle Paleocene, Selandian, SBZ2 (Serra-Kiel, et al., 1998).

Differential diagnosis:

1- *Hottingerina lukasi* Drobne (1975) and the new species *Pseudohottingerina burdurensis* both are in common with having single aperture and counter septum (Pl.8,figs. 1-4) (Drobne,1975: Pl. 3, fig. 1; Pl. 4, figs. 5,7,8; Pl. 5, fig. 2; Pl. 6, figs. 1,3-5).

2- Aperture of *Hottingerina anatolica* Sirel, (1999) was reported by Sirel (1998, 1999) as a basal slit. Sirel (2004, p.57) again, reported the same element as single opening at the base of the septum (Sirel, 1998: Pl. 24, figs. 1-7; Pl. 25, figs. 5,8; Sirel, 1999: Pl. 8, figs. 1,7; Pl. 9, figs. 5,8; Sirel, 2004: Pl. 53, figs. 5,8). Counter septum (cs) can not be present or developed between the aperture and the preceding whorl or spire, in the aperture type named as basal slit or opening. Because, the aperture of *H. anatolica* is not basal slit type, but in the middle of the septum. Therefore, *H. anatolica* has counter septum (cs) (Sirel, 1998: Pl. 24, figs. 1,5,7; Pl. 25, figs. 1,2,4,5,8,9; Sirel, 1999: Pl. 8, figs. 1,2,4,5,7; Pl. 9, figs. 1,2,4,5,8,9; Sirel, 2004: Pl. 52, figs. 1,2,4,5,7; Pl. 53, figs. 1,2,4,5,8, 9; Sirel, 2015: Pl. 26, figs. 1-5,8,9). However, this structural element (cs) was not described by Sirel (Sirel, 1999, p.134: Pl.8, figs. 1,4,7; Pl. 9, figs. 2,5,8,9; Sirel, 2015: Pl. 26, figs. 1-5,8,9). Besides, in the equatorial section of this specimen figured as *Peneroplis* sp. by Sirel (2004), planispiral chambers following the protoconch (pr) and counter septum (cs) are clearly observed since subepidermal partitions can not be observed. Because of this reason, this individual may be *Hottingerina anatolica*, *Hottingerina* sp./(n.sp)?, or a new species of *Pseudohottingerina* Acar, n.gen. (Sirel, 2004: Pl. 40, fig. 6). Natural size of *Psh. burdurensis* is larger, its whorls are looser, its apertures are larger, and it has an advanced lip (lp) structure (Pl.7, fig. 18; Pl.8, figs. 1-9). Moreover, whorl, septum and counter septum thickness in *Psh. burdurensis* are thicker than in *Psh. yarisliensis*. While six chambers are counted in a *Psh. burdurensis* specimen of 0.438 mm diameter (Pl.8, fig.1), 16 chambers are counted in the *Psh. yarisliensis* of the same diameter (Pl.8, fig.5).

Fossil assemblage: Table 1; Age: Middle Paleocene, Selandian; SBZ 2 (Serra-Kiel et al., 1998).

Pseudohottingerina yarisliensis Acar, n.gen., n.sp.

(Plate VIII, Figures 5-9)

Derivation of name: Yarışlı is a village in SW Burdur, SW Turkey.

Holotype: Equatorial section, megalospheric form (Pl.8, fig. 8).

Type locality: South of Lake Yarışlı, SW Burdur, W Turkey (Text figure 1).

Type level: Middle Paleocene, Selandian, SBZ 2 (Serra-Kiel, et al., 1998).

Diagnosis: Test is small. Biometric measurements of equatorial and subequatorial sections: protoconch

diameter varies between 0.041-0.104 mm, and equatorial diameter varies between 0.510-0.916 mm. 16 chambers are present in a *Pseudohottingerina yarisliensis* specimen of 0.438 mm diameter (Pl.8, fig.5). Holotype: low sparitised, slightly oblique equatorial section. 27 chambers have been counted in an specimen of 0.755 mm equatorial diameter (Pl.8, fig.8). Smallest protoconch diameter of *Psh. yarisliensis* is 0.041 mm. Cryptotriloculine chambers, undivided spirally coiled chambers and oblique septa, counter septa and intercameral foramina are present (Pl.8, fig.8).

Differential diagnosis: Test of this small species is smaller and spire of the species is shorter than in *Psh. burdurensis*. Its counter septum and intercameral foramina are narrower or limited; septum and spire/ whorls are thinner than in *Psh. burdurensis*.

Fossil assemblage: Table 1; Age: Middle Paleocene, Selandian; SBZ 2 (Serra-Kiel et al., 1998).

Superfamily: Rotaliacea EHRENBERG, 1839,

Family: Rotaliidae EHRENBERG, 1839,

Subfamily: Laffitteininae HOTTINGER, 2014

Genus: *Laffitteina* MARIE, 1946,

Type species: *Nummulites mengaudi* ASTRE, 1923.

Laffitteina anatoliensis Acar, n.sp.

(Plate 8, Figure 15; Plate 9, Figures 1-4) (Text figure 5/2)

Derivation of name: Lands of the Turkish Republic founded by Atatürk in 1923, take place on the Asian and European continents. The name of the big peninsula located on Asian continent, is known as “Anadolu” in republic. Anadolu is derived from “Anatolia” in Latin. Anadolu is also referred as “Asia minör” in French. The name of this new species is derived from “Anatolia” in Latin.

Holotype: Slightly oblique vertical section, megalospheric form (Pl.8, Fig. 15).

Type locality: South of Lake Yarışlı, SW Burdur, W Turkey (Text figure 1).

Type level: Middle Paleocene, Selandian, SBZ 2 (Serra-Kiel et al., 1998).

Diagnosis: Test is small. However, this species has a very large horizontal diameter among the species of *Laffitteina* Marie (1946). Test is hyaline calcareous, low trochospirally coiled, convex in dorsal side, flattened in ventral side, and asymmetrical inflated lenticular (Pl.8, fig.15; Pl.9, figs. 1-3) (Text figure 5/2). Chambers of the new species (*L. anatoliensis*) are truncate in vertical sections (Pl.8, fig.15; Pl.9, figs. 1-3). Dorsal pillars (dp) are weak, ventral pillars (vnp) are stronger and longer, funnels (f) are larger in the *L. anatoliensis* (Pl.8, fig. 15; Pl.9, figs. 1-3). Short pustules (ps) are also present (Pl.9, fig.3). Embryonic apparatus of this species (in axial sections) is located on the dorsal side of the test or a place close to dorsal part (Pl.8, fig. 15; Pl.9, figs. 1-3).Biometric measurements are as follows: horizontal diameter is between 1.744 –2.952 mm, height is 0.884 - 1.279 mm, index of elongation is 1.973 – 2.630, protoconch diameter is 0.070 - 0.117 mm (Pl.8, fig. 15; Pl.9, figs. 1,2). Horizontal diameter or equatorial diameter of a juvenile specimen (in equatorial section) is measured as 1.286mm, and three whorls were counted. Number of the chambers in these three whorls are 10, 19, and 29 respectively (Pl.9, fig.4). Diameter of flattened protoconch (pr) is 0.119-0.155mm, diameter of deuteroconch (dt) is 0.071-0.095mm (Pl.9, fig.4). Intraseptal canal (isc), rectangular chambers formed by septa, spiral canal (spc) and umbilical flap (uf) are present in vertical sections (Pl.9, fig.4). Ventral pillars are present in the ventral area, and the pillars fill the umbilical cavity. Width of the area formed by the ventral pillars, is significant for the description of species. This width has been named as width of ventral pillars (wvp). Width of ventral pillars (wvp) in this new species varies between 1.605-1.714mm (Pl.8, fig. 15; levha IX, şekil 1-3). Width of ventral pillars (wvp) commences from the point that ultimate chamber and penultimate chamber merges at (after pustules if present); and this interval is measured from the base of the test. Ventral pillars can be observed in vertical sections, tangential sections through the base, and bottom view of free specimens. Width and shape of ventral pillars area (vnpa) is important. When looking to the ventral side of the species of *Laffitteina* Marie (1946) (in vertical sections or bottom view of free specimens), it can be observed that the ventral pillars area (vnpa) is flattened, strongly convex or dome-like (Pl.8, fig. 15; Pl.9, figs. 1-3; Pl.10, figs. 1-5; Pl.11, figs. 1-4) (Text figure 5). Key differences between the species of this genus are as follows: shape of dorsal side (flattened or convex), shape of ventral pillars area (flattened, convex, dome-like), position of the embryonic apparatus (distant from dorsal side / close to dorsal side), horizontal diameters, height, index of elongation.

Differential diagnosis: The new species *Laffitteina anatoliensis* differs from the new species *Laffitteina thraciaensis* by widely conical/low trochospiral or asymmetrical inflated lenticular shape. Besides, the former is flattened in dorsal side and its chambers are sharper in periphery (Pl.8, fig. 15; Pl.9, figs. 1-3) (Text figure 5/2). The new species *L. anatoliensis* and *L. erki* (Sirel, 1969) arein common with their natural sizes and convex shape in dorsal side. However, *L. anatoliensis* is both flattened in ventral side and the bottom. The bottom, ventral side and ventral pillars area of *L. erki* is strongly concave. For today, the latter is the most concave species (in ventral side) among the species of *Laffitteina* Marie (1946) (Pl.10, figs. 5,6; Pl.11, fig. 1) (Loeblich and Tappan, 1987: Pl. 760, figs. 6,7; Sirel, 1969: Pl.2, 1 (Holotype), 2; Sirel, 1994: Pl.1, figs. 4,6, Pl.2, figs. 1-7,11; Sirel, 1998: Pl. 51, figs. 4,5,7; Sirel, 2004: Pl. 22, figs. 4,5,7; Sirel, 2015: Pl. 9, figs. 3-5). Horizontal diameters of *L. anatoliensis* and *L. erki* are approximate. However, *L. erki* has the largest horizontal diameter (with a horizontal diameter of 3.743 mm) among species of its own genus (Sirel, 2004: Pl. 22, fig. 4; Sirel, 2015: Pl..9, fig.5). The bottom or ventral pillars area (vnpa) of *Laffitteina mengaudi* Astre, 1923 is also flattened (Pl.11, figs.2-4) (Text figure 5/1).

Fossil assemblage: Table 1; Age: Middle Paleocene, Selandian; SBZ 2 (Serra-Kiel et al., 1998).

Laffitteina thraciaensis Acar, n.sp.

(Plate 9, Figure 11; Plate 10, Figures 1-3) (Text figure 5/4)

1994, *Laffitteina erki* (Sirel), Sirel, p.47, Pl.1, figs. 1-3,5,9,10.

1998 *Laffitteina* cf. *erki* (Sirel), Sirel, Pl.22, fig.1.

1999 *Laffitteina* sp., Sirel, Pl.3, fig.1.

Derivation of Name: "Thrac" is the name of a community in Greek. The name of the land where Thracian People lived, was "Thracia". Today, the part of the land of Turkish Republic in European Continent, is called in Turkish as "Trakya". The name of this species is derived from "Thracia".

Holotype: Slightly oblique vertical section, megalospheric form (Pl.9, fig.11).

Type locality: South of Lake Yarışlı, SW Burdur, W Turkey (Text figure 1).

Type level: Middle Paleocene, Selandian, SBZ 2 (Serra-Kiel et al., 1998).

Diagnosis: Test is small, hyaline calcareous; whorls are involute in both dorsal and ventral sides. Dorsal side is strongly convex; ventral side is flattened (Pl.9, fig. 11) (Text figure 5/4), very slightly convex (Pl.10, figs.1,2) or very slightly concave (Pl.10, figs.1,2), strongly asymmetrical, strongly inflated lenticular or high conical or triangular shape, and its chambers are slightly rounded. Embryonic apparatus of this species (in axial section) is found at the dorsal side or very close to the dorsal side of the test (Pl.9, fig. 11; Pl.10, figs. 1-3) (Text figure 5/4). While dorsal pillars (dp) are weak and short; funnels (f) are narrow in the new species *L. thraciaensis*; ventral pillars (vnp) are very strong, very long, and funnels (f) are large (Pl.9, fig. 11; Pl.10, figs. 1-3). This new species is the highest conical species among the Paleocene species of *Laffitteina* Marie (1946) (Pl.9, fig. 11; Pl.10, figs. 1-3) (Text figure 5/4). Index of elongation (horizontal diameter/height) of the new species is 2.019, which means its horizontal diameter is almost double of its height.

Biometric measurements of the megalospheric generation: Horizontal diameter is between 1.767-2.349mm, height is 1.023-1.233mm, protoconch diameter is 0.093- 0.116mm. Witdth of ventral pillars (wvp) or ventral pillars area (vnpa) varies between 1.047-1.302 mm.

Differential diagnosis: *Laffitteina thraciaensis*; is a very high conical, strongly asymmetric and strongly inflated lenticular species. Its chambers are rounded, and its ventral side is mainly flattened (Pl.9, fig. 11; Pl.10, figs. 1-3) (Text figure 5/4). On the other hand, the new species *Laffitteina anatoliensis* is (in vertical sections), depressed trochospiral, asymmetrical lenticular shape, and its chambers are truncate (Pl.8, fig. 15; Pl.9, figs. 1-3) (Text figure 5/2). Ventral side of *Laffitteina erki* (Sirel, 1969) is strongly concave (Text figure 5/3). The height of *L. thraciaensis*; is much more than the heights of *L. erki*, *L. thraciaensis*; and *L. mengaudi*, and the former is strongly inflated or much more asymmetrical lenticular in shape.

Fossil assemblage: Table 1; Age: Middle Paleocene, Selandian; SBZ 2 (Serra-Kiel et al., 1998).

Laffitteina erki (Sirel, 1969)

(Plate 10, Figures 4,5; Plate 11, Figure 1) (Text figure 5/3)

1969 *Orduina erki* n.gen., n.sp., Sirel, p.160, Pl.2, figs. 1,2.

1969 *Orduina erki* var. *conica* n. var., Sirel, p.160, Pl.3, figs. 1,2,4.

1986 *Laffitteina mengaudi* (Astre), Sirel, Pl.3, fig. (La_2).

1987 *Kathina erki* (Sirel), Loeblich and Tappan, p.661, Pl. 760, figs. 6,7.

1994 *Laffitteina erki* (Sirel), Sirel, p.47, Pl.1, figs. 4,6-8; Pl.2, figs. 1-11.

non *Laffitteina erki* (Sirel), Sirel, 1994, p.47, Pl.1, figs. 1-3,5,9,10.

1996 *Laffitteina erki* (Sirel), Sirel, p.22, Pl.2, figs. 12,20; Pl.8, figs. 1,4,5,7.

non *Laffitteina erki* (Sirel), Sirel, 1996, p.22, Pl.8, figs. 2,6,8.

1996 *Laffitteina erki* (Sirel), İnan, 1996, Pl.4, figs. 1,2.

non *Laffitteina erki* (Sirel), İnan, 1996, Pl.4, figs. 3-10.

1998 *Laffitteina erki* (Sirel), Sirel, p.91, Pl. 51, figs. 1,4,5,7.

non *Laffitteina* cf. *erki* (Sirel), Sirel, 1998, Pl. 22, figs. 1;

non *Laffitteina erki* (Sirel), Sirel, 1998, Pl. 51, figs. 2,6,8.

2004 *Laffitteina erki* (Sirel), Sirel, p.18, Pl. 22, figs. 1,4,5,7.

non *Laffitteina erki* (Sirel), Sirel, 2004, p.18, Pl. 22, figs. 2,6,8.

2009 *Laffitteina erki* (Sirel), Sirel, Pl.5, fig. 8.

non *Laffitteina erki* (Sirel), Sirel, 2009, Pl.5, fig. 9.

2015 *Laffitteina erki* (Sirel), Sirel, Pl. 9, figs. 1,3-5.

non *Laffitteina erki* (Sirel), Sirel, 2015, Pl.9, figs. 2,6.

Diagnosis: Test is small, hyaline calcareous, low trochospiral, convex in dorsal side, ventral side is concave and asymmetrical lenticular shaped. Its chamber margins are slightly rounded (Pl.10, figs. 4,5; Pl.11, fig. 1) (Text figure 5/3). Its identical to Sirel's low conical individuals (Sirel, 1969: Pl.2, fig. 1 (Holotype), 2; Sirel, 1994: Pl.1, figs. 4,6, Pl.2, figs. 1-7,11; Sirel, 1998: Pl. 51, figs. 4,5,7; Sirel, 2004: Pl. 22, figs. 4,5,7; Sirel, 2015: Pl. 9, figs. 3-5; Loeblich and Tappan, 1987: Pl. 760, figs. 6,7). Embryonic apparatus of this species (in vertical sections) is located on the dorsal side or very close to the dorsal side (Pl.10, figs. 4,5; Pl.11, fig. 1). Dorsal pillars (dp) of this species are weak and short, and its funnels (f) are narrow. However, its ventral pillars (vnp) are strong, long and its funnels are large (Pl.10, figs. 4,5; Pl.11, fig. 1). Pustules (ps) and tubercules (tb) are observed between ventral pillars and test channel in the ventral side of some individuals (Pl.10, fig. 4: at the left). It was reported (Sirel, 2004, p.20) that *Laffitteina erki* is the species with the largest horizontal diameter among the species of Laffitteina Marie (1946). However, any of the specimens' horizontal diameter, in the measurements which was taken and accepted in the synonym list by the Sirel (2004), is not 5.4 mm (Sirel, 1969: Pl.2, fig. 1 (Holotype)). For example, the largest horizontal diameter in Sirel (2004: Pl. 22, fig. 4 or 2015: Pl. 9, fig. 5) is 3.714 mm. Biometric measurements are as follows: horizontal diameter is between 2.558-2.628mm, height is 0.791-0.884mm, index of elongation is 2.973-3.234, protoconch diameter is 0.070 -0.081mm (Pl.10, figs. 4,5; Pl.11, fig. 1). Width of ventral pillars varies between 1.000-1.813mm (Pl.10, figs. 4,5; Pl.11, fig. 1).

Differential diagnosis: *Laffitteina erki* is a species with the largest horizontal diameter (3.714mm) among the species of *Laffitteina* Marie (1946) (Sirel, 2004: Pl. 22, figs. 4; Sirel, 2015: Pl. 9, fig. 5) (Text figure 5/3). This species also has, among the species of *Laffitteina*, the most concave ventral side (Pl.10, figs. 4,5; Pl.11, fig. 1) (Loeblich andTappan, 1987: Pl. 760, figs. 6,7; Sirel, 1969: Pl.2, figs. 1,2; Sirel, 1994: Pl.1, figs. 4,6, Pl.2, figs. 1-7,11; Sirel, 1998: Pl. 51, figs. 4,5,7; Sirel, 2004: Pl. 22, figs. 4,5,7; Sirel, 2015: Pl. 9, figs. 3-5) (Text figure 5/3). *L. erki* and *L. anatoliensis* are similar to each other by their natural sizes and convex dorsal sides. While the ventral side of *L. anatoliensis* is flattened, the ventral side of *L. erki* is strongly concave (Text figure 5/3). *L. erki* is easily distinguished from the new species *L. thraciaensis* and the other species of *Laffitteina* by its size and shape.

Fossil assemblage: Table 1; Age: Middle Paleocene, Selandian; SBZ 2 (Serra-Kiel et al., 1998).

Laffitteina mengaudi (Astre, 1923)

(Plate 11, Figures 2-4) (Text figure 5/1)

1923 *Nummulites mengaudi* n.sp., Astre, p. 360-368, Pl. 12, figs. 1-23.

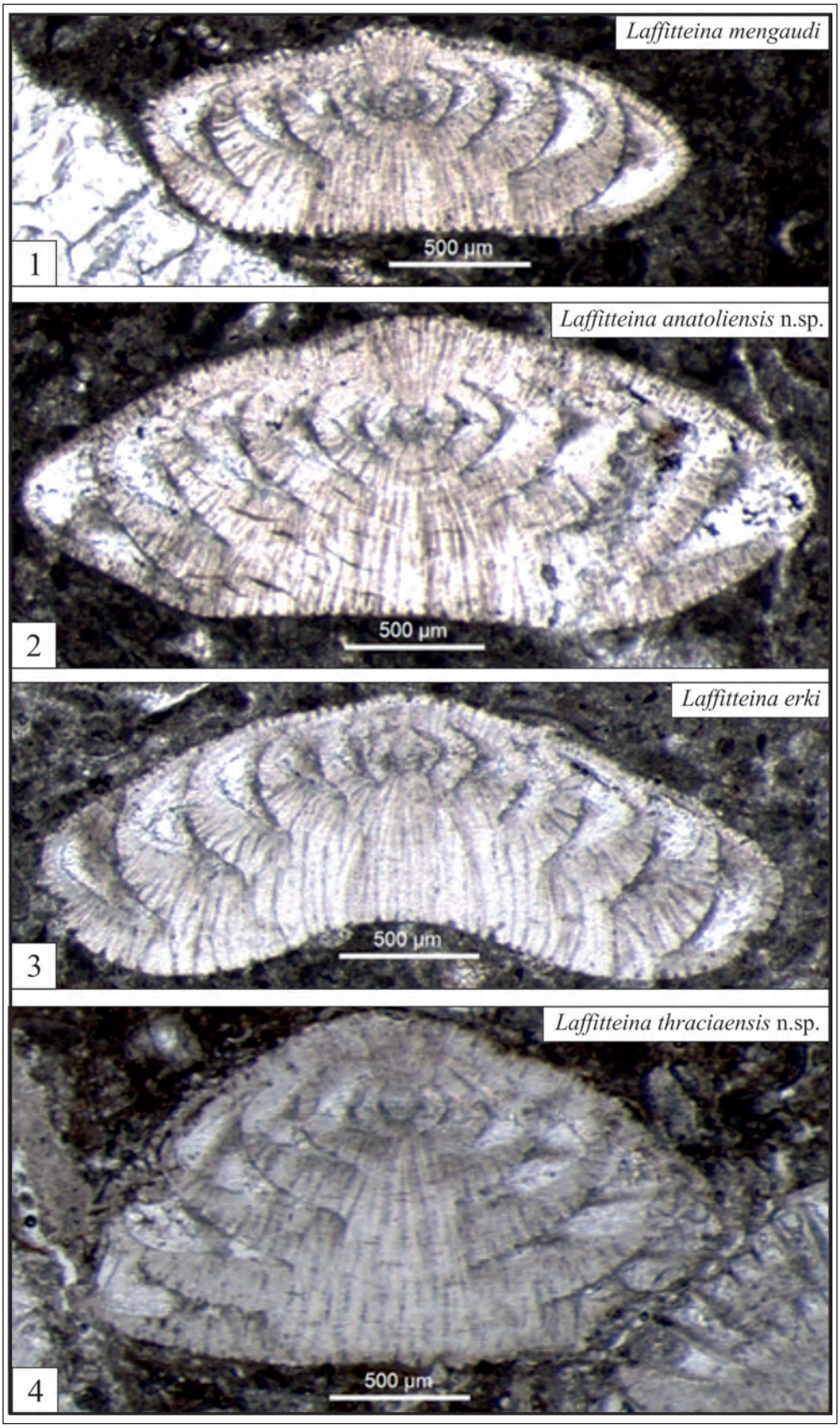

Figure 5- New and some known species of the genus *Laffitteina*. 1- *Laffitteina mengaudi*. 2- *Laffitteina anatoliensis* n.sp. 3- *Laffitteina erki* (Sirel, 1969). 4- *Laffitteina thraciaensis* n.sp.

non *Laffitteina mengaudi* (Astre); Sirel, 1986, Pl. 3 (La_2).

1996 *Laffitteina mengaudi* (Astre); Sirel, p. 12, Pl.1, figs. 6,10-13,17,18; Pl.2, figs. 1-4,6-8,10,11,14,15,17,19,21; Pl.3, figs. 1-6,9,10; Pl.4, fig. 19.

non *Laffitteina mengaudi* (Astre); Sirel, 1996, Pl.2, figs. 12,20; Pl.3, fig. 8.

1996 *Laffitteina bibensis* Marie; İnan, Pl.3, figs. 4,5.

1996 *Laffitteina erki* (Sirel); İnan, Pl.4, figs. 4-8.

1987 *Laffitteina mengaudi* (Astre); Loeblich and Tappan, p. 661, Pl. 759, fig.4.

1998 *Laffitteina mengaudi* (Astre); Sirel, Pl. 46, figs. 6-8,10,12,13; Pl. 47, figs. 2-4,6-8,10,11, 14,17,18,19,21.

non *Laffitteina mengaudi* (Astre); Sirel, 1998, Pl. 46, figs. 9,11,14-23; Pl. 47, figs. 1, 5, 12, 13,15,20; Pl. 48, fig.1.

2009 *Laffitteina erki* (Sirel), Sirel, Pl.5, fig. 10.

2015 *Laffitteina mengaudi* (Astre); Sirel, Pl. 2, figs. 6-11, 16, 23.

Diagnosis: Test is small and hyaline calcareous, asymmetric or slightly asymmetric, lenticular shaped. Dorsal and ventral sides are flattened. Chambers are rounded except in the last whorl (Pl.11, figs. 2-4) (Text figure 5/1). Embryonic apparatus of the species (in axial sections) is located in the middle of or very close the test (Pl.11, figs. 2-4) (Text figure 5/1) (Sirel, 2015: Pl. 2, figs. 6-11,15-17). However, in vertical sections of some trochospiral Paleocene species (*Laffitteina anatoliensis* n.sp., *Laffitteina thraciaensis* n.sp. and *Laffitteina erki*) of the genus *Laffitteina*; embryonic apparatus is observed as located on the dorsal side or close to dorsal side (Pl.8, fig. 15; Pl.9, figs. 1-3,11; Pl.10, figs. 1-5; Pl.11, fig. 1). Dorsal pillars (dp) are weak, short; and funnels (f) are very narrow in this species (Pl.11, fig. 4). However, ventral pillars (vnp) are very strong, very long; and funnels (f) are larger (Pl.11, figs.2-4). Biometric measurements are as follows: horizontal diameter is between 1.348 (broken)-1.907mm, height is 0.721-0.837mm, index of elongation is 1.87-2.278, protoconch diameter is 0.105 -0.140mm. Width of ventral pillars varies between 0.721-0.977mm.

Differential diagnosis: Dorsal and ventral sides are flattened in *Laffitteina mengaudi*. Dorsal side is convex, but ventral side is flattened in the new species *Laffitteina anatoliensis*. Both species (*L. mengaudi* ve *L. anatoliensis*) are identical in their ventral sides (flattened). Diameter and height of *L.mengaudi* are much smaller than in either *L. anatoliensis* or in *L.erki*. The subspecies *Laffitteina mengaudi mengaudi* (Astre) and *Laffitteina mengaudi trochoidea* Sirel, 2015 are very similar to each other. However, the test of the subspecies *L. mengaudi trochoidea* is slightly larger than of *L. mengaudi mengaudi*, and the former has a depressed trochospiral and low conical test (Sirel, 2015: Pl. 2, figs. 19-22,24). Besides, *L. mengaudi trochoidea* is slightly concave in ventral side (Sirel, 2015: Pl. 2, figs. 19,20,21,24). Strongly depressed trochospiral appearance (in vertical sections) of *L.mengaudi trochoidea* is provided by its last chambers in both sides (Sirel, 2015: Pl. 2, figs. 19,20,21,24). The individuals in which those last chambers are not present or not developed (younger specimens), is the juvenile forms of *Laffitteina mengaudi mengaudi* (Astre). Besides, *L. mengaudi* and *Laffitteina bibensis* Marie (1946) are in common with their flattened dorsal and ventral sides. However, *Laffitteina bibensis* is much thinner than *L. mengaudi*.

Fossil assemblage: Table 1; Age: Middle Paleocene, Selandian; SBZ 2 (Serra-Kiel et al., 1998).

Super Family: Orbitoidacea SCHWAGER, 1876,

Family: Lepidorbitoididae VAUGHAN, 1933, _

Genus: *Sirtina* BRÖNNIMANN AND WIRZ, 1962, _

Type Species: *Sirtina orbitoidiformis* BRÖNNIMANN AND WIRZ, 1962,

Sirtina paleocenica Acar, n.sp.

(Plate 8, Figures 10-14; Plate 9, Figures 5-10; Plate 10, Figures 7,8)

Derivation of Name: The name of this species is derived from Serie “Paleocene” of Tertiary time.

Holotype: Almost vertical section, microspheric form (Pl.9, fig.9)

Type locality: South of Lake Yarışlı, SW Burdur, W Turkey (Text figure 1).

Type level: Middle Paleocene, Selandian, SBZ 2 (Serra-Kiel et al., 1998).

Diagnosis: Test is minute, trochospirally coiled, slightly convex in dorsal side or rarely flattened. Dorsal pillars (dp) are very short and thin, lateral chambers in dorsal side are very narrow or finely perforated. However, ventral side of the newly introduced Paleocene species of genus *Sirtina* Brönnimann and Wirz (1962) is strongly inflated asymmetrical lenticular (Pl.8, figs. 10-14; Pl.9, figs. 5-10; Pl.10, figs. 7,8). Ventral side of the test is strongly inflated; and its ventral pillars (vnp) are well developed and coarse, funnels (f) are advanced. Whorls are involute in both dorsal and ventral sides (Pl. 10, fig.7). Periphery of the shell is sharp and angular (Pl.8, figs. 11,12,14; Pl.9, figs. 5-8). Although the orbitoidal or orbitoidiform structured-very narrow lateral chambers of *Sirtina paleocenica* are well observed in vertical sections, these lateral chambers are not clearly observed in oblique or slightly oblique sections (Pl.8, figs. 13,14; Pl.9, fig. 10). Biometric measurements are as follows: horizontal diameter is between 0.300-0.860mm, height is 0.240-0.600mm, index of elongation is 1.25-1.433, protoconch diameter (measured in only one specimen) is 0.040mm (Pl.8, fig.12). Measurements of the holotype are as follows: horizontal diameter is 0.780 mm, height is 0.520 mm, index of elongation is 1.433 (Pl.9, fig.9). Dimorphism is present.

Differential diagnosis: *Sirtina orbitoidiformis* Brönnimann and Wirz, 1962 and *Sirtina granulata* Rahaghi, 1976 are lenticular shaped specimens with thick dorsal pillars and well developed-orbitoidal lateral chambers. However, the new species *Sirtina paleocenica* is trochospirally coiled, slightly convex but rarely flattened in dorsal side. Its dorsal pillars are very thin and weak, lateral chambers are very narrow with tiny space, ventral side is strongly inflated or strongly asymmetrical lenticular (Pl.8, figs. 10-14; Pl.9, figs. 5-10; Pl.10, figs. 7,8) (Loeblich and Tappan,1987: Pl. 735, figs. 9,10; Pl. 736, figs. 5,6,10).

Fossil assemblage: Table 1; Age: Middle Paleocene, Selandian; SBZ 2 (Serra-Kiel et al., 1998).

Super Family: Miliolacea EHRENBERG, 1839,

Family: Miliolidae EHRENBERG, 1839,

Subfamily: Miliolininae EHRENBERG, 1839,

Genus: *Ankaraella* SİREL, 1998,

Type species: *Ankaraella trochoidea* SİREL, 1998.

Ankaraella minima Acar, n.sp.

(Plate 11, Figures 5-9)

1998 *Ankaraella trochoidea* Sirel, p.51, Pl. 14, figs. 6,8-10.

2004 *Ankaraella trochoidea* Sirel; Sirel, p.208, Pl. 63, figs. 6,10.

2004 *Ankara**ra**ella* sp. Sirel, p.208, Pl. 63, figs. 5,7-9.

Derivation of Name: The word “minima” is derived from “Minutus” in Latin. This species has been named by “minima” due to its small size.

Holotype: Almost vertical section, microspheric form (Pl.11, fig.5)

Type locality: South of Lake Yarışlı, SW Burdur, W Turkey (Text figure 1).

Type level: Middle Paleocene, Selandian, SBZ 2 (Serra-Kiel et al., 1998).

Diagnosis: Test is small, trochospirally coiled, slightly convex in both dorsal and ventral sides. Septa are thick, chambers are evolute in dorsal/spiral side, but involute in ventral side; umbilical cavity (uc) is narrow (Pl.11, figs.5-7). Short ribs (r) are found in intercameral foramina (if) (Pl.11, figs. 6,8) and in some chambers (Pl.11, figs. 5,6,8). Biometric measurements are as follows: horizontal diameter is between 0.921-1.079mm, height is 0.526-0.658 mm, index of elongation is 1.640-1.751 (Pl.11, figs.5-7), protoconh diameter of megalospheric specimens is 0.066-0.099mm and the protoconch is spherical (Pl.11, figs. 5-7). Protoconch of the microspheric generations could not be measured. In the holotype: dorsal side is convex, chambers are truncate in dorsal side and curved in ventral side. Biometric measurements of the holotype are as follows: horizontal diameter is between 1.053mm, height is 0.448mm, index of elongation is 2.350 (Pl.11, fig. 5). Test wall is porcelaneous calcareous, and dimorphism is present.

Differential diagnosis: *Ankaraella minima* Acar, n.sp. differs from *Ankaraella trochoidea* with smaller natural size.

Fossil assemblage: Table 1; Age: Middle Paleocene, Selandian; SBZ 2 (Serra-Kiel et al., 1998).

Ankaraella trochoidea Sirel, 1998

(Plate 11, Figures 10-12)

1998 *Ankaraella trochoidea* Sirel, p. 51, Pl. 14,

figs. 1-4.

2004 *Ankaraella trochoidea* Sirel; Sirel, p.68, Pl. 63, figs. 1-4.

2009 *Ankaraella trochoidea* Sirel; Sirel, Pl.2, figs. 8-10.

2010 *Ankaraella trochoidea* Sirel; Sirel, Pl. 5, figs. 8-10.

2015 *Ankaraella trochoidea* Sirel; Sirel, Pl. 22, figs. 8-10.

Diagnosis: Test is small, trochospirally coiled, flattened or slightly convex in dorsal side, convex in ventral side. Septa are thick, chambers are evolute in dorsal/spiral side, but involute in ventral side (Pl.11, figs. 10-12). Intercameral foramina (if) are present in a broken, almost horizontal section (Pl.11, fig.10). Ribs (r) can be observed depending on the section plane (Pl.11, fig.11). However, presence of these ribs (r) was not reported in the first description of the genus *Ankaraella* (Sirel, 1998: p. 51, Pl. 14, figs. 1-3). Ribs (r) are present in the chambers of *Ankaraella* Sirel (1998) (Pl.11, fig. 11) (Sirel, 1998: Pl. 14, figs. 1-3). Biometric measurements are as follows: horizontal diameter is between 1.25-1.5 mm, height is 0.625-1.125 mm, index of elongation is 1.333-2.000. Protoconch diameter could not be measured.

Fossil assemblage: Table 1; Age: Middle Paleocene, Selandian; SBZ 2 (Serra-Kiel et al., 1998).

4. Discussions

4.1. Some Mistakes and Emendations on *Ankaraella trochoidea* Sirel, 1998

A- Sirel (2004, s.68) erroneously wrote "*Ankaraella trochoidea* Sirel, n.gen.n.sp., 1998" in the text. He should have written "*Ankaraella trochoidea* Sirel, 1998" instead. Because, new genus description of this specimen was made in 1998 (Sirel, 1998).

B- In the same paper, Sirel (2004, s.68) wrote "(Plate 63, figures 1-10)". He should have written "(Plate 63, figures 1-4, 6, 10)" instead. Because, Sirel (2004, s.208) explained only (figures 1-4,6,10) for *Ankaraella trochoidea* in the plate explanations of Plate 63.

C- Again in the same place, "*Ankararaella sp*." was written for "(Plate 63, figures 5,7-9)" and was explained by Sirel (2004, p.208). This implies that the specimens in "(Plate 63, figures 5,7-9)" are not belonging to the species *Ankaraella trochoidea*. Therefore in the text, "(şekil 1-4,6,10)" should have been written instead of "(levha 63, şekil 1-10)". In this current study, figures of "*Ankararaella sp*." have been transferred to the synonym list of *Ankaraella minima* Acar, n.sp. (Sirel, 2004: Pl. 63, figs. 5,7-9).

4.2. Species and Type Species Transferring Between Genera

There must be a type species for an accepted genus or an accepted subgenus, based on the zoological nomenclature. If a genus (or a subgenus) has only its type species, this is called as monotypic. This means, that genus (or subgenus) has no species except its type species. For this reason, if the type species of a monotypic genus (or subgenus) is transferred to another known genus (or subgenus) or a new genus (or subgenus), the genus can not be used anymore. Because, no representatives of this genus (or subgenus), including its type species, is present from then on. In other saying, a genus with no species (even type species) perishes and is invalid. However, type species are never die out, yet they are used in other genera (or subgenera). Many examples could be given about the transferring of a known species or a type species to a new genus (or a subgenus). Regarding this issue, nomenclature and new descriptions made for the specimens in this current study, are presented below:

A- In this current study, "*Sistanites iranica* Rahaghi, 1983" (type species of *Sistanites* Rahaghi (1983)) which was inadequately described by Rahaghi (1983), has been transferred to the new genus *Neosistanites* as type species in this study (Rahaghi, 1983: p.54, Pl. 34, fig. 4). Therefore, monotypic genus *Sistanites* Rahaghi (1983) can not be used anymore since there is no representatives, including the type species.

B- *Laffitteina erki* (Sirel, 1969) which is described and figured in this study, was the type species of *Orduina* Sirel, (1969) (as *Orduina erki* Sirel, 1969). Systematics of this species was changed. *Orduina* Sirel, 1969 was a monotypic genus. At first, the genus *Orduina* Sirel (1969) was transferred to the genus *Kathina* Smout, 1954 by Loeblich and Tappan (1987, s.661) due to its inadequate description, and became *Kathina erki* (Sirel, 1969). Thereafter, the same species (*Orduina erki*) was transferred to *Laffitteina*

Marie, 1946 by Sirel (1994) and the species has being used as *Laffitteina erki* (Sirel, 1969) (Sirel, 1994: p.106). However, *Orduina* Sirel (1969) can not be used anymore by the reason of its type species was transferred to another genus (*Laffitteina* Marie, 1946). Hereafter, there is no representatives (including type species) for the genus *Orduina* just as in *Sistanites* Rahaghi, 1983.

C- Some changes for the systematics of *Miscellanea primitiva* Rahaghi, 1983, which is figured as *Akbarina primitiva* (Rahaghi, 1983) in this study, have been made. *Miscellanea primitiva* Rahaghi, 1983, which was first described by Rahaghi, 1983, was transferred to two different genera by two different authors (Hottinger, 2009; Sirel, 2009) in the later years.

a- Hottinger (2009) transferred *Miscellanea primitiva* Rahaghi, 1983, which had been ineaduqualtely described by Rahaghi, 1983 but having the characteristics of Hottinger's new genus, to his new genus (*Miscellanites* Hottinger, 2009) as the type species; and presented it to the scientific community as *Miscellanites primitivus* (Rahaghi, 1983).

b- Sirel (2009) transferred *Miscellanea primitiva* Rahaghi, 1983 to his new genus as the type species during describing the new genus *Akbarina*; and presented to the scientific community as *Akbarina primitiva* (Rahaghi, 1983). The name *Akbarina primitiva* has been adopted in this study.

5. Conclusions

In this study, some new benthic foraminifera from the SBZ 2 (Selandian) have been described (yet some benthic foraminifera and algae could not be described). Benthic foraminiferal genera and species, which have been determined in this study, are as follows: *Neosistanites iranicus* (Rahaghi, 1983), *Neosistanites sozerii* Acar, n.gen.,n.sp., *Neosistanites okuyucui* Acar, n.gen.,n.sp., *Neosistanites guvenci* Acar, n.gen.,n.sp., *Neosistanites dageri* Acar, n.gen.,n.sp., *Neosistanites catali* Acar, n.gen.,n.sp., *Neosistanites armagani* Acar, n.gen.,n.sp., *Neosistanites inali* Acar, n.gen.,n.sp., *Parahaymanella hahyemezae* Acar, n.gen., n.sp., *Parahaymanella bozkurti* Acar, n.gen., n.sp., *Parahaymanella alanae* Acar, n.gen., n.sp., *Pseudohottingerina burdurensis* Acar, n.gen.,n. sp., *Pseudohottingerina yarisliensis* Acar, n.gen.,n. sp., *Ankaraella minima* Acar, n.sp., *Laffitteina anatoliensis* Acar, n.sp., *Laffitteina thraciaensis* Acar, n.sp., *Sirtina paleocenica* Acar, n.sp. Besides, *Akbarina primitiva* (Rahaghi, 1983), *Ankaraella trochoidea* Sirel, 1998, *Bolkarina aksarayi* Sirel, 1981, *Laffitteina erki* (Sirel, 1969), *Laffitteina mengaudi* (Astre, 1923), *Biloculinites* cf. *paleocenica* Rahaghi, 1983, *Miscellanea*? *globularis* Rahaghi, 1978, *Globoflarina*? *sphaeroidea* (Fleury, 1982), *Heterillina* sp., *Keramosphaera* sp., *Textularia* sp., *Chrysalidina*? sp., *Kolchidina*? sp., *Lockhartia*? sp., *Popovia*? sp., *Thalmannita*? sp. have been described among known benthic foraminiferal genera and species. *Periloculina* sp, has been determined but could not be figured. However, some benthic foraminiferal genera and algae could not be described. Undetermined genera here figured are as follows: undetermined miliolid genera (Miliolid gen.1 indet, Miliolid gen.2 indet, Miliolid gen.3 indet; Miliolid gen.4 indet n.sp.1; Miliolid gen.4 indet n.sp.2; Miliolid gen.4 indet n.sp3; Miliolid gen.5 indet; Miliolid gen.6 indet; Miliolid gen.7 indet; Miliolid gen.8 indet or Idalinid gen.8 indet; Miliolid gen.9 indet), Agglutineted gen. (1 and 2) indet., Miscellanid gen. indet., Planulinid gen.1 indet, Rotaliid gen.1 indet. (*Redmondoides?*), Rotaliid gen.2 indet., Rotaliid gen.3 indet., Rotaliid gen.4 indet. (with two layered test), Mississippinid gen. indet., algae gen.1 indet., algae gen.2 indet., algae gen.3 indet. The presence of fifty seven specimens have been reported in this study. Moreover, introduction of a new family (Neosistanitidae), some explanations on the classification of the new genus *Neosistanites*, transferring of type species or species between genera and emendation (about the presence of ribs) of the genus A*nkaraella* Sirel (1998), and some emendations about *Ankaraella trochoidea* Sirel, 1998 have been made in this study.

Acknowledgements

This study was supported by the General Directorate of Mineral Research and Exploration. The author would like to thank Alper Bozkurt (MSc.) for taking photomicrograps and drawing in computer, Prof. Dr. Güner Ünalan for the translations, Prof. Dr. Tuncer Güvenç for the helps about affixes in Latin and Dr. Erdal Herece for helping the drawings. Orhan Sazlı is also thanked for the preparation of thin sections.

References

Acar, Ş. 1995. Türkiye'nin Değişik Bölgelerinin Paleojen'inden Bazı Alveolin Cinslerinin (*Alveolina (Alveolina), Alveolina (Glomalveolina), Borelis* ve *Praebullalveolina*) Sistematik Tanımları ve Stratigrafik Dağılımları. Selcuk University, PhD Thesis, 166p., 38 pls., Konya-Turkey.

Bilgin, Z.R., Karaman, T., Öztürk, Z., Şen, M.A., Demirci, A.R. 1990. Yeşilova-Acıgöl Civarının Jeolojisi. General Directorate of Mineral Research and Exploration, Report No: 9071.

Boudagher-Fadel, M.K. 2008. Evolution and Geological Significance of Larger Benthic Foraminifera. (Elsevier Science) Development in Paleontology & Stratigraphy, 21, 544 p.

Drobne, K. 1975. La succesion des Alveolines Paleogenes Nord-Quest de la Yugoslavıe, Bull. Soc. Geol., France, 7, XVII, 123-266.

Drobne, K. 1977, Alvéolines paléogenes de la Slovénie et de I'Istrie. Schweizerische Paläontologische Abhandlungen 99, 1-175, 96 figs., 21 pls., Basel.

Flecker, R., Poisson, A., Robertson, A.H.F. 2005. Facies and paleoogeographic evidence for the Miocene evolution of the Isparta Angle in its regional eastern Mediterranean context. Sedimantary Geology, 173, 277-314.

Hottinger, L. 2006. Illustrated glossary of terms used in foraminiferal research. Carnets de Géologie / Notebooks on Geology- Memoir 2006/2 (CG2006_M02), 126s.

Hottinger, L. 2009. The Paleocene and earliest Eocene foraminiferal Family Miscellaneidae: neither nummulitids nor rotaliids. Carnets de Geologie/ Notebooks on Geology Article 2009/06 (CG 2009-A06).

İnan, N. 1995. The importance of Laffitieina (Foraminifera) Genus at the Symposium on the Geology of the Black Sea Region. 109-118, Ankara.

İnan, N. 1996. Türkiye'de Laffitteina türlerinin coğrafik yayılımı ve stratigrafik dağılımı. Geological Bulletin of Turkey, 39 (1), 43-53.

İnan, N., İnan, S. 2008. Türkiye'nin kuzeydoğu kesiminde Selandiyen (Üst Paleosen) bentik foraminifer toplulukları ve stratigrafik dağılımları. Bulletin for Earth Sciences, 29 (3), 147-158.

İnan N. , Kurt, I., Demirbaş, M. 1992. Kretase – Paleosen geçişinde yeni paleontolojik bulgular: iğdi Kireçtaşı (Koyulhisar - Sivas), 45. 45th Geological Congress of Turkey, Abstracts, p.28, Ankara.

İnan, N., Taslı, K., İnan, S. 2005. Laffitteina from the Maastrichtian-Paleocene shallow marine carbonate successions of the Eastern Pontides (NE Turkey) biozonation and microfacies. Journal of Asian Earth Sciences 25, 367–378.

İnan, S., İnan, N. 1987. Tecer Kireçtaşı Formasyonunun stratigrafik tanımlaması: Cumhuriyet University., Science Journal, Serie A - Earth sciences, 3 - 12, Sivas.

Loeblich, A.R., Tappan, H. 1964, Treatise on invertebrate Paleontology, Part C, Protista 2, 900p., 653 figs., Lawrence, Kansas (Kansas Univ. Press).

Loeblich, A.R., Tappan, H. 1987. Foraminiferal genera and their classification. Vol. 1, 1-970; 2, 212p.,.847 pls., New

York (Von Nostrand Reinhold).

Marie, F. 1946. Sur Laffitteina bibensis et Laffitteina monodi nouveau genre et nouvelles especes de foraminiferes du Montien Bull..Soc. Geol. France Ser.5, tome 15, (1945), fasc.7-8, 430p. Paris.

Matsumaru, K., Sarma, A. 2010. Larger foraminiferal biostratigrapy of the lower Tertiary of Jaintia Hills, Meghalaya, NE India. Micropaleontology, 56 (6), 539-565.

Özgen, N. 1997. Batı Pontid'lerde Paleosen / Eosen Yüzlekleri ve Bentik Foraminiferleri. Cumhuriyet University, Institute for Science, PhD Thesis, 255 p.

Özgen, N. 2000. Nurdanella boluensis n.gen., n.sp., a Miliolid (Foraminifera) from the Lutetian of the Bolu Area (Northwestern Turkey). Revue Paléobiol., Genève 19 (1), 79-85.

Öztürk, A., İnan, S., Tutkun, Z. 1984. Abant – Yeniçağ (Bolu) yöresinin stratigrafisi: Cumhuriyet Univ. Science Journal. Serie A – Earth sciences, 1 (1), 1 - 18, Sivas.

Pignatti J., Massimo, C., Andrea, B., Cecilia, B., Antonino, B., Manuela, F., Ruggero, M., Gianluca, P., Michela, Ragusa 2008. SBZ 2-6 Larger Foraminiferal assemblages from the Apulian and pre-Apulıan domıans. Atti Mus. Civ. Stor. Nat. Trieste, Suppl. al 53, 131-146.

Poisson, A. 1977. Recherhes geologiques dans les Taurides occidentales (Turquie). These, Univ. Paris-Sud. Orsay, 795p.

Poisson, A.,1984. The extention of the Ionian trough into southwesternTurkey. In: Dixon, j:E. ve Robertson, A.H.F. (Eds) The jeological Evolution of the Eastern Mediterraean, spec. Publ., Geol. Soc. Londra 17, 241-250.

Price, S.P., Scott, B. 1994. Fault-block rotations at the edge of a zone of continental extention; southwest Turkey. J. Structure Geol. 16, 381-392.

Rahaghi, A. 1983. Stratigraphy and Faunal assemblage of Paleocene-Lower Eocene in Iran. N.I.O.C., Geological Lab. Pub. No.10, 73p.,49 pls., Tehran.

Serra-Kiel, J., Hottinger, L., Drobne, K., Ferrandez, C., Jauhri, A. K., Less, G., Pavlovec, R., Pignatti, J., Samso, J. M., Schaub, H., Sirel, E., Strougo, A., Tambareau, Y.,Tosquella, J., Zakrevskaya, E. 1998. Larger foreminiferal biostratigraphy of the Tethyan Paleocene and Eocene. Bull. Soc. geol. France, 169 (2), 281-299.

SireL, E. 1969. Rotaliidae Familyasına ait, yeni bir cins Orduina n.gen. ve türü hakkında. Bulletin of the Mineral Research and Exploration, 73, 160-162.

Sirel, E. 1981. Bolkarina, new genus (Foraminiferida) and some associated species from the Thanetian limestone (Central Turkey). Eclogae geol. Helv., 74/1: 75-95.

SireL, E. 1994. Ordu ve Burdur (Türkiye) Paleoseninde Bulunmuş Orduina erki Sirel, 1969, in Laffitteina erki Olarak Yeniden Adlandırılması. Bulletin of the Mineral Research and Exploration, 116, 105-106.

Sirel, E. 1996. Occurrence of the genus Sistanites Rahaghi, 1983 (Foraminiferida) in two localities of Turkey: in: Drobne, K.; Gorican, S.; Kotnic, B. (Ed.) The role of impact Processes in the Geological and biological Evolution of planet Earth. Guide, 79-81.

Sirel, E. 1998. Foraminiferal description and biostratigraphy of the Paleocene-Lower Eocene shallow-water limestones and discussion on the Cretaceous-Tertiary boundary in Turkey. General Directorate of Mineral Research and Exploration Monography 2, 117p.

Sirel, E. 1999. Four new genera (Haymanella, Kayseriella, Elazıgella and Orduella) new species of Hottingerina from the Paleocene of Turkey. Micropaleontology, 45 (2), 113-137.

Sirel, E. 2004. Türkiye'nin Mesozoyik ve Senozoyik Yeni Bentik Foraminiferleri. UCTEA Chamber of Geological Engineer of Turkey (Special Edition 1).

Sirel, E. 2009. Reference sections and key localities of the Paleocene Stages and their very shallow/shallow-water three benthic foraminifera in Turkey. Revue de Paleontologie, Geneve, 28 (2), 413-435.

Sirel, E. 2010. Haymana-Polatlı Basin. Chamber of Geological Engineer of Turkey, Series of Technical Visit 6 p.18,19.

Sirel, E. 2015. Referece Sections and Key localities of the Paleogene Stages and Discusstion C-T, P-E and E-O Boundaries by the Very Shallow-Shallow Water Foraminifera in Turkey (Ankara University Faculty of Engineering, Department of Geological Engineering). Ankara University Press No: 461, 171p., 53 pls.. Ankara-Turkey.

Sirel, E., Acar, Ş. 1993, Malatyna, a new foraminiferal genus from the Lutetian of Malatya region. Geol. Croat. 46 (2), 181-188.

Şengün, M., Akçaören, F., Keskin, H., Akat, U., Altun, I.E.,Deveciler, E., Sevin, M. 1988. Daday - Kastamonu- İnebolu yöresinin Jeolojisi. General Directorate of Mineral Research and Exploration, Report No: No. 8994, Ankara.

FIGURE AND PLATE EXPLANATIONS

(In alphabetical order)

a: aperture
adch: additional chamber
bl: basal layer
bfs: bifurcating septum
ch: chamber
chl: chamberlet
cp: central pillar
cpl: compound plate
cplfr: compound plate foramen
cs: counter septum
dp: dorsal pillar
dt: deuteroconch/deuteroculus
ems: embryonic stage
f: funnel
fch: flaring chamber
fpl: foraminal plate
fr: foramen
fw: flaring whorls
g: goulot
hp: horizontal plate
hpfr: horizontal plate foramen
if: intercameral foramen
isc: intraseptal canal
kha: keyhole aperture
lp: lip
lch: lateral chamber (in dorsal side)
p: pillar
pr: protoconch/proloculus
prp: preseptal passege
ps: pustules
psp: pseudospine
r: rib
s: septum
sfl: septal filaments/septal traces
sl: septulum
so: sutural opening
spc: spiral canal
t: tooth
tnch: transation chamber
to: test ornamentations
tr: tritoconch/triloculus
trch: truncate chamber
trms: trematophoric structure
uc: umbilical cavity
uf: umbilical flap
uh: umbilical holes
upl: umbilical plate
uplfr: umbilical plate foramen
vnp: ventral pillar
vnp_1: first ventral pillar
vnp_2: second ventral pillar
vpl: vertical plate
vplfr: vertical plate foramen
ws: whorl suture

PLATES

PLATE - I

Neosistanites iranicus (Rahaghi, 1983), n.gen.,

(Selandian, SBZ 2, South of Lake Yarışlı, SW Burdur, W Turkey)

(megalospheric specimens 5,6; microspheric specimen 1)

Figure 1- Slightly oblique vertical section showing minute protoconch, dorsal pillars, funnels, two layered septum, compound plates (cpl), compound plate foramina (cplfr), umbilical flaps, sieve horizontal plates, horizontal plates foramina, second ventral pillars and umbilical hole or umbilical openings (ŞAY-1/S-1-2).

Figure 2- Oblique section showing very narrow sutural opening (so), pseudospine (psp), imperforate septum (s), foraminal plate (fpl) and umbilical flap (uf) (ŞAY-3/I-31-3).

Figure 3- Tangential section showing sieve vertical plate (vpl) and vertical plates foramina (vplfr) (ŞAY-2/I-8-3).

Figure 4- Slightly oblique broken vertical section showing dorsal pillars (dp), large funnels (f), vertical plate, compound plates, umbilical flaps, horizontal plates (hpl), thick second ventral pillars (vnp2) and large umbilical hole (uh) (ŞAY-1/ S-3-1).

Figure 5- Slightly oblique vertical section showing spherical protoconch, dorsal pillars, funnels, septum (two layered), vertical plates (vpl), sieve compound plates (cpl), compound plates foramina (cplfr), umbilical flaps (uf) sieve horizontal plates (hpl), second ventral pillars (vnp2) and umbilical hole (uh) (ŞAY-1/N-8-1S).

Figure 6- Vertical section showing spherical protoconch, typical deuteroconch, dorsal pillars, large funnels, imperforate septa (s), vertical plates (vpl) (at both left and right side of the protoconch), compound plates, umbilical flaps (uf), sieve horizontal plates, second ventral pillars (vnp2) and umbilical hole (uh) (ŞAY-2/S-12-1).

Figure 7- Oblique subhorizontal section showing very narrow sutural opening, single layered septa (microgranular and imperforate) (s), vertical plates (vpl) with narrow perforations at the end of the septa, narrow foramina of vertical plates (vplfr), intercameral foramina (if) and foraminal plate (fpl) (ŞAY-3/I-25-1S).

PLATE - I

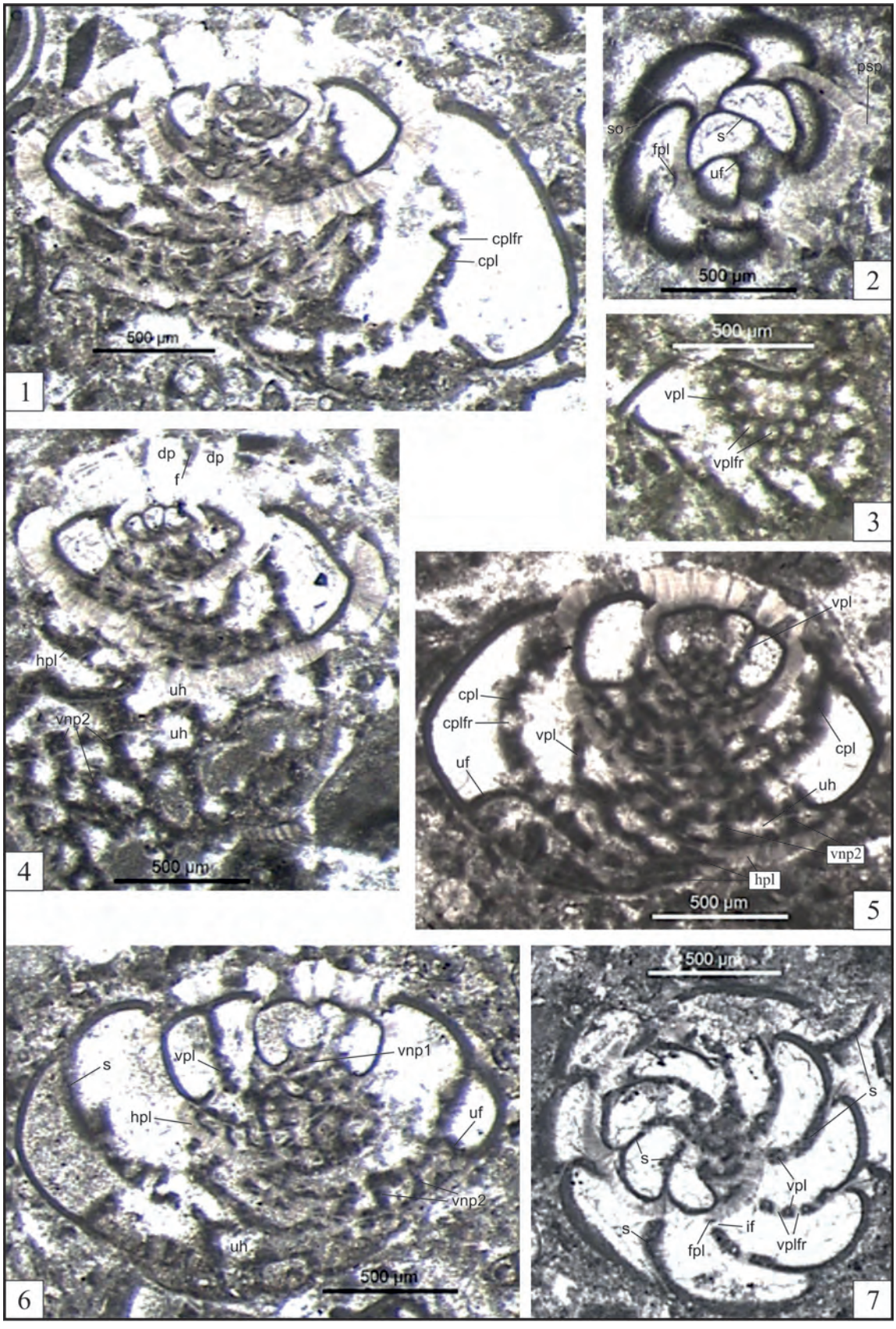
cplfr
cpl
500 µm
1
psp
so
s
fpl
uf
500 µm
2
500 µm
vpl
vplfr
3
dp
dp
f
hpl
uh
uh
vnp2
500 µm
4
vpl
cpl
cplfr
vpl
uf
cpl
uh
vnp2
hpl
500 µm
5
s
vpl
vnp1
hpl
uf
vnp2
uh
500 µm
6
500 µm
s
s
vpl
s
if
fpl
vplfr
7

PLATE - II

Neosistanites iranicus (Rahaghi, 1983), n.gen.,

(Selandian, SBZ 2, South of Lake Yarışlı, SW Burdur, W Turkey)

(megalospheric specimens 1,2,4; microspheric specimen 5)

Figure 1- Broken vertical section (with rotaliid form) showing central pillar (cp), spherical protoconch (pr) and typical deutreoconch (dt), foramen between protoconch and deuteroconch, first ventral pillar (vnp1), septa, vertical plate (vpl) (just right side of protoconch), vertical compound plate (cpl) (at left side) (interforaminal tissue seems as if being thick pillars but not), compound plates foramina (cplfr), imperforate umbilical flaps (uf), horizontal plates (hpl), vertical or inclined second ventral pillars (vnp2) and large umbilical hole (uh) (ŞAY-1/A-2-1S).

Figure 2- Vertical section showing dorsal pillars, narrow funnels, protoconch, vertical plate (microgranular) (vpl), inclined compound plate (sieve, at right side) (cpl), compound plate foramina (cplfr), imperforate umbilical flaps (uf), perforated horizontal plates (hpl), second ventral pillars (vnp2) and large umbilical hole (uh) (ŞAY-3/G-17-4BS).

Figure 3- Subvertical section showing dorsal pillars, narrow funnels, septa, tangential section of the sieve vertical plate (at left) (vpl), vertical plate foramina (vplfr), imperforate umbilical flaps (uf), sieve horizontal plates (hpl), thick and well developed second ventral pillars (vnp2) and large umbilical hole (uh) (ŞAY-1/S-8-1).

Figure 4- Horizontal section showing tripple embryonic stage and the foramina, large protoconch (p), large deuteroconch (dt), and the largest tritoconch (tr), sutural opening (on the spire), septa and chambers, intercameral foramina (if), foraminal plate (ŞAY-3/I-20-1S).

Figure 5- Slightly oblique almost horizontal section showing two layered spire, septa (imperforate, microgranular, inclined or gently curved) (s), intercameral foramina (if), irregular chambers of the last whorl (ŞAY-1/S-16-2).

Figure 6- Poorly preserved slightly oblique subhorizontal section showing two layered whorl or spire, surfical or sutural opening (so), septa (inclined, imperforate and microgranular), foraminal plate (fpl), and intercameral foramina (if) (ŞAY-2/S-14-3).

PLATE - II

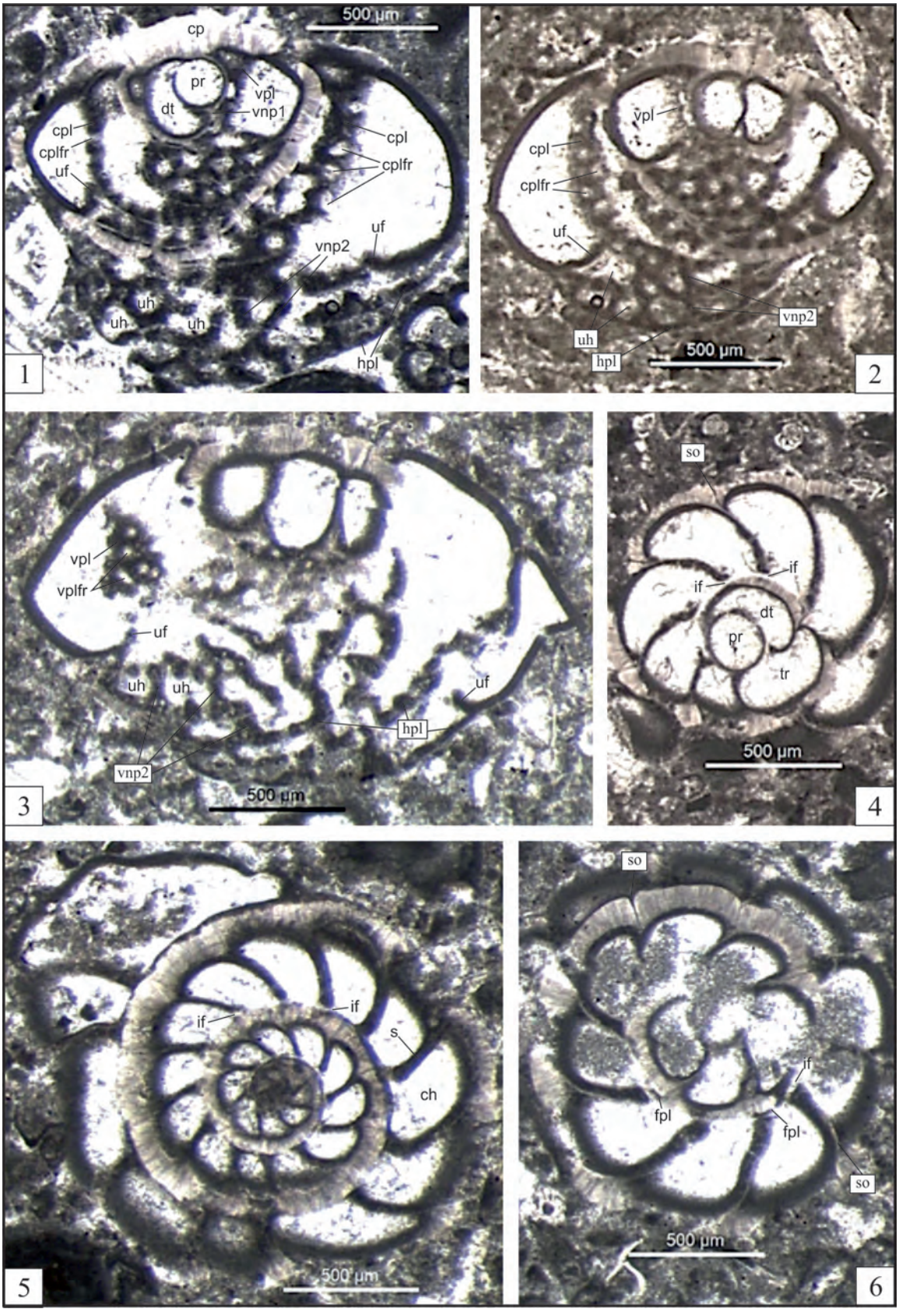
500 µm
cp
pr
vpl
dt
vnp1
cpl
cplfr
uf
cpl
cplfr
uf
vnp2
uh
uh
uh
hpl
1
vpl
cpl
cplfr
uf
vnp2
uh
hpl
500 µm
2
vpl
vplfr
uf
uh
uh
uf
hpl
vnp2
500 µm
3
so
if
if
dt
pr
tr
500 µm
4
if
if
s
ch
500 µm
5
so
if
fpl
fpl
so
500 µm
6

PLATE - III

(Selandian, SBZ 2, South of Lake Yarışlı, SW Burdur, W Turkey)

(megalospheric specimens 3-7)

Neosistanites iranicus (Rahaghi, 1983), n.gen.,

Figure 1- Oblique marginal section (towards umbilical area) showing septa (microgranular and imperforate) (s), umbilical flaps (uf), slightly inclined vertical plate (initially imperforate) (vpl) and vertical plate foramina (vplfr) (ŞAY-2/M-5S).

Figure 2- Oblique subhorizontal section (through umbilical area) showing septa (s), intecameral foramen (if), vertical plate (vpl), compound plate, umbilical flaps (uf), horizontal plates (at the center, attached to umbilical flap at the base) (hpl), second ventral pillars (at the center) and umbilical hole (uh) (at the center) (ŞAY-3/I-23-1S).

Neosistanites sozerii Acar, n. gen., n.sp.

Figure 3- Vertical section showing large spherical protoconch, septa (s), vertical plate (tangential section, in the left side of protoconch) (vpl), vertical plate foramina (vplfr), horizontal plates (hpl), horizontal plates foramina (hplfr), umbilical flaps (uf), second ventral pillars (vnp2) and umbilical hole (uh) (ŞAY-3/M-13-3s).

Figure 4- Vertical section showing embryonic chambers (ems), dorsal pillars, funnels, vertical plate (vpl), compound plates (cpl), horizontal plates (hpl), horizontal plates foramina (hplfr), umbilical flaps (uf), second ventral pillars (vnp2) and larger umbilical hole (uh), Holotype, (ŞAY-2/S-9-2).

Figure 5- Oblique horizontal section showing embryonic chambers [protoconch (pr), deuteroconch (dt), tritoconch (tr)], septa, umbilical flaps, foraminal plate (fpl), vertical plate (vpl), (ŞAY-1/K-2S).

Neosistanites okuyucui Acar, n.gen., n.sp.

Figure 6- Slightly oblique horizontal section showing spherical protoconch, horizontal plates, second ventral pillars (at the center, around protoconch), septa (s), umbilical flaps (uf), vertical plates (vpl) (ŞAY-1/K-1-1S).

Figure 7- Vertical section showing protoconch (p), typical deuteroconch (dt), tritoconch (tr), large passage between protoconch and deuteroconch, dorsal pillars, funnels, first ventral pillars (vnp1), compound plate (cpl), umbilical flaps (uf), horizontal plates (hpl), horizontal plates foramina (hplfr), second ventral pillars (vnp2), umbilical hole (uh), Holotype, (ŞAY-1/N-8-2).

PLATE - III

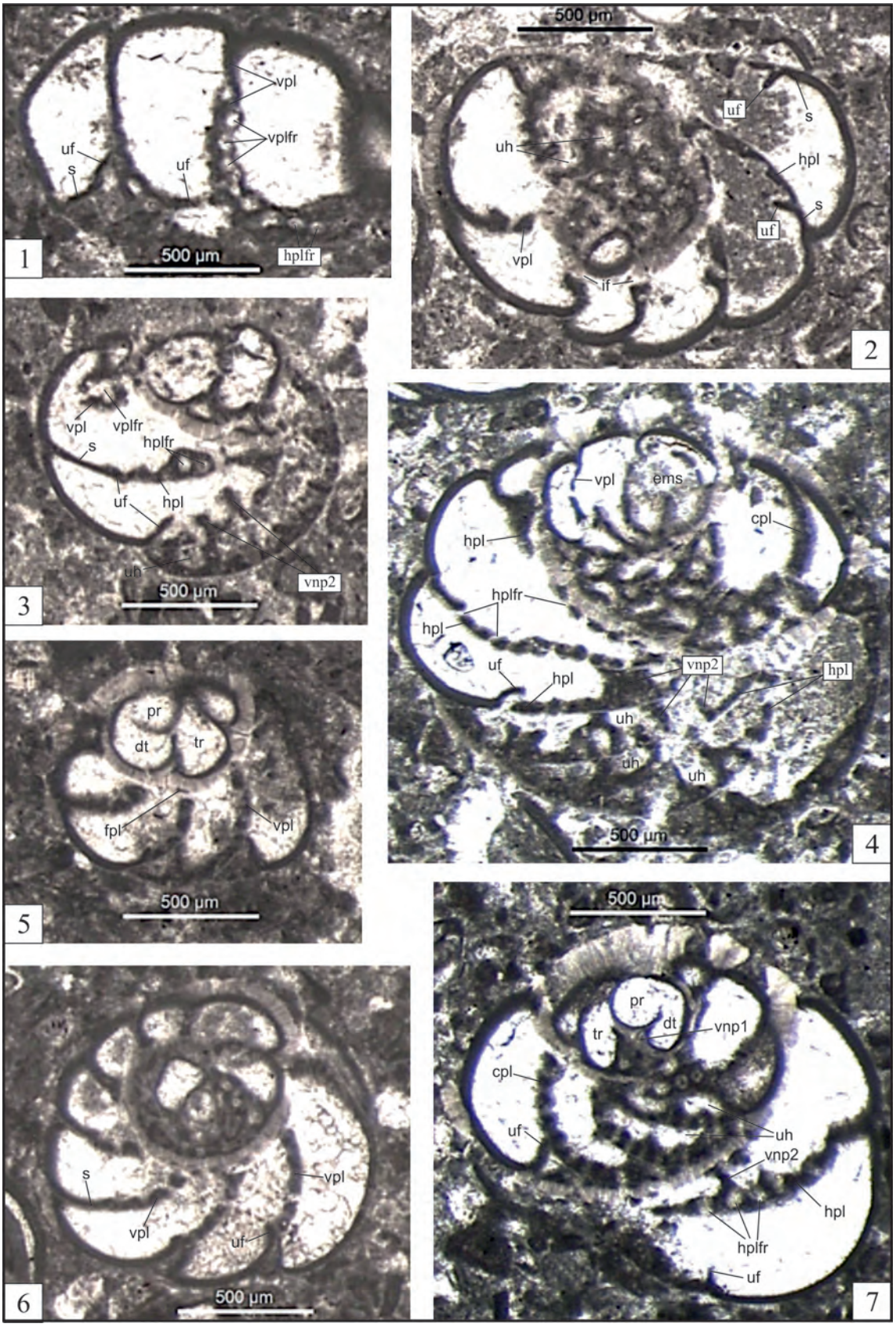
1
vpl
vplfr
uf
s
uf
500 µm
hplfr
2
500 µm
uf
s
uh
hpl
s
uf
vpl
if
3
vpl
vplfr
hplfr
s
uf
hpl
uh
500 µm
vnp2
4
vpl
ems
cpl
hpl
hplfr
hpl
uf
hpl
vnp2
hpl
uh
dh
uh
500 µm
5
pr
dt
tr
fpl
vpl
500 µm
6
s
vpl
vpl
uf
500 µm
7
500 µm
pr
dt
tr
vnp1
cpl
uf
uh
vnp2
hpl
hplfr
uf

PLATE - IV

(Selandian, SBZ 2, South of Lake Yarışlı, SW Burdur, W Turkey)

(megalospheric specimens 1, 4-8; microspheric specimens 3, 9)

Neosistanites okuyucui Acar, n.gen., n.sp.

Figure 1- Vertical section showing spherical protoconch, dorsal pillars, funnels, septa (s), horizontal plates (hpl), horizontal plates foramina (hplfr), umbilical flaps (uf) (ŞAY-1/B-2-4 Ns).

Figure 2- Subvertical section showing dorsal pillars, funnels, vertical plate (at right) (vpl), umbilical flaps (uf), horizontal plates (hpl), second ventral pillars (vnp2) and large umbilical hole (uh) (ŞAY-1/P-2-3S).

Neosistanites guvenci Acar, n.gen., n.sp.

Figure 3- Vertical section showing minute spherical protoconch, dorsal pillars (dp), funnels (f), compound plate, umbilical flap (uf), horizontal plates (hpl), second umbilical pillars and umbilical hole, Holotype, (ŞAY-1/S-2-1a).

Figure 4- Oblique section showing spherical protoconch, deuteroconch (dt), foramen between protoconch and deuteroconch (fr), dorsal pillars, vertical plate (at left of protoconch) (vpl), compound plate, horizontal plates, second ventral pillars (vnp2), umbilical hole (ŞAY-2/G-9-6s).

Figure 5- Slightly oblique horizontal section showing embryonic chambers (pr, dt, tr) foramen between tritoconch and protoconch (fr), first whorl (two layered) and ultimate whorl (single layered, microgranular), septa (s), vertical plates (with narrow foramina) (vpl), vertical plates foramina (vplfr) (ŞAY-2/S-11-2).

Figure 6- Slightly oblique horizontal section showing spherical protoconch, deuteroconch, foramen between protoconch and deuteroconch (fr), vertical plates with narrow foramina, foraminal plate (fpl) (ŞAY-3/S-6-2).

Figure 7- Almost vertical section of a young specimen showing spherical protoconch, dorsal pillars, funnels, horizontal plates (hpl), second ventral pillars (vnp2), umbilical hole (uh) (ŞAY-1/M-18-9s).

Figure 8- Vertical section showing spherical protoconch, dorsal pillar, funnels, compound plate (cpl), first ventral pillar (vnp1), umbilical flaps, horizontal plates, second ventral pillars and umbilical hole (uh) (ŞAY-3/G-17-1).

Neosistanites dageri Acar, n.gen., n.sp.

Figure 9- Vertical section showing small spherical protoconch (pr), central pillar (cp), funnels, umbilical flaps, vertical plate, compound plate (cpl), horizontal plate (hpl), first ventral pillar (vnp1), second ventral pillar (vnp2) and umbilical hole (ŞAY-1/S-2-1b).

Figure 10- Subvertical section showing central pillar, septum, compound plate (cpl), umbilical flaps (uf), horizontal plates (hpl), second ventral pillars and umbilical hole (ŞAY-5/M-6-1s).

PLATE - IV

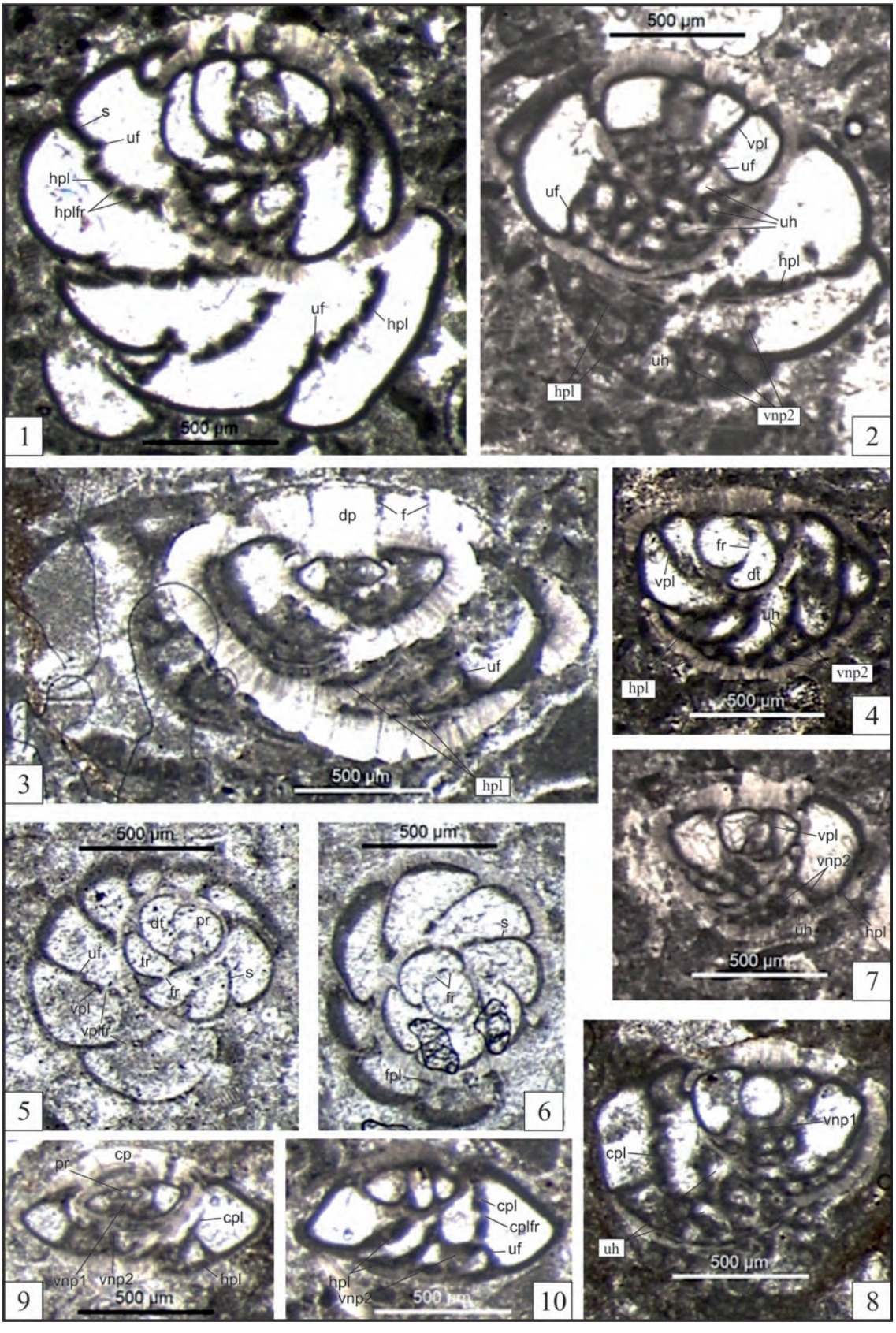
1
s
uf
hpl
hplfr
uf
hpl
500 µm
2
500 µm
vpl
uf
uf
uh
hpl
uh
hpl
vnp2
3
dp
f
uf
500 µm
hpl
4
fr
vpl
dt
uh
vnp2
hpl
500 µm
5
500 µm
dt
pr
uf
tr
s
fr
vpl
vplfr
6
500 µm
s
fr
fpl
7
vpl
vnp2
uh
hpl
500 µm
8
vnp1
cpl
uh
500 µm
9
pr
cp
cpl
vnp1
vnp2
hpl
500 µm
10
cpl
cplfr
uf
hpl
vnp2
500 µm

PLATE - V

(Selandian, SBZ 2, South of Lake Yarışlı, SW Burdur, W Turkey)

(megalospheric specimens 1-3,7-11; microspheric specimens 5,6,12)

Neosistanites guvenci Acar, n.gen., n.sp.

Figure 1- Vertical section showing protoconch, dorsal pillars, large funnels, compound plate (cpl), umbilical flaps (uf), horizontal plates, second ventral pillars (vnp2) and umbilical hole (uh) (ŞAY-1/G-7-3s).

Figure 2- Poorly preserved vertical section showing large spherical protoconch, foramen of protoconch (fr), first ventral pillar (vnp1), second ventral pillar (vnp2), compound plate (cpl), horizontal plate (hpl) and umbilical hole (uh) (ŞAY-2/S-3-4).

Figure 3- Oblique section showing spherical protoconch, dorsal pillars, funnels, horizontal plates with small foramina (hpl), umbilical flaps (uf), first ventral pillars (vnp1) and second ventral pillars (short) (ŞAY-1/S-1-2b).

Figure 4- Subvertical section showing dorsal pillars, funnels, compound plate (cpl), umbilical flaps, horizontal plate (hpl), second ventral pillars and umbilical hole (uh) (ŞAY-1/M-18-10s).

Neosistanites dageri Acar, n.gen., n.sp.

Figure 5,6- Vertical and subvertical sections showing protoconch (pr), very thick central pillars (cp), compound plates (cpl), umbilical flaps (uf), horizontal plates, first ventral pillar (vnp1), second ventral pillars (vnp2) and umbilical hole (uh), Holotype, (ŞAY-1/S-2-2) and (ŞAY-1/S-1) respectively.

Figure 7- Oblique horizontal section showing spherical protoconch (pr), deuteroconch (dt), inclined imperforate septa, intercameral foramina (if) and foraminal plate (fpl) (ŞAY-1/S-3-1).

Figure 8- Almost vertical section showing very thick central pillar (cp), narrow funnels, umbilical flaps (uf), horizontal plates (hpl), second ventral pillars and umbilical hole (ŞAY-2/G-11-2s).

Figure 9,10- Vertical sections showing spherical protoconchs, central pillar (cp), dorsal pillars (dp), narrow funnels, sparitised compound plates (cpl), umbilical flaps, horizontal plates, second ventral plates (vnp2), umbilical hole (uh); (ŞAY-1/S-2-3) and (ŞAY-3/G-14-2s) respectively.

Figure 11- Broken vertical section showing spherical protoconch, very thick dorsal pillar (dp), funnel, compound plate (cpl), umbilical flap, horizontal plate and second ventral pillar (vnp2) (ŞAY-5/Ml-10-2s).

Figure 12- Oblique, almost horizontal section showing septa (s), intercameral foramina (if), foraminal plates (ŞAY-1/M-1-2s).

PLATE - V

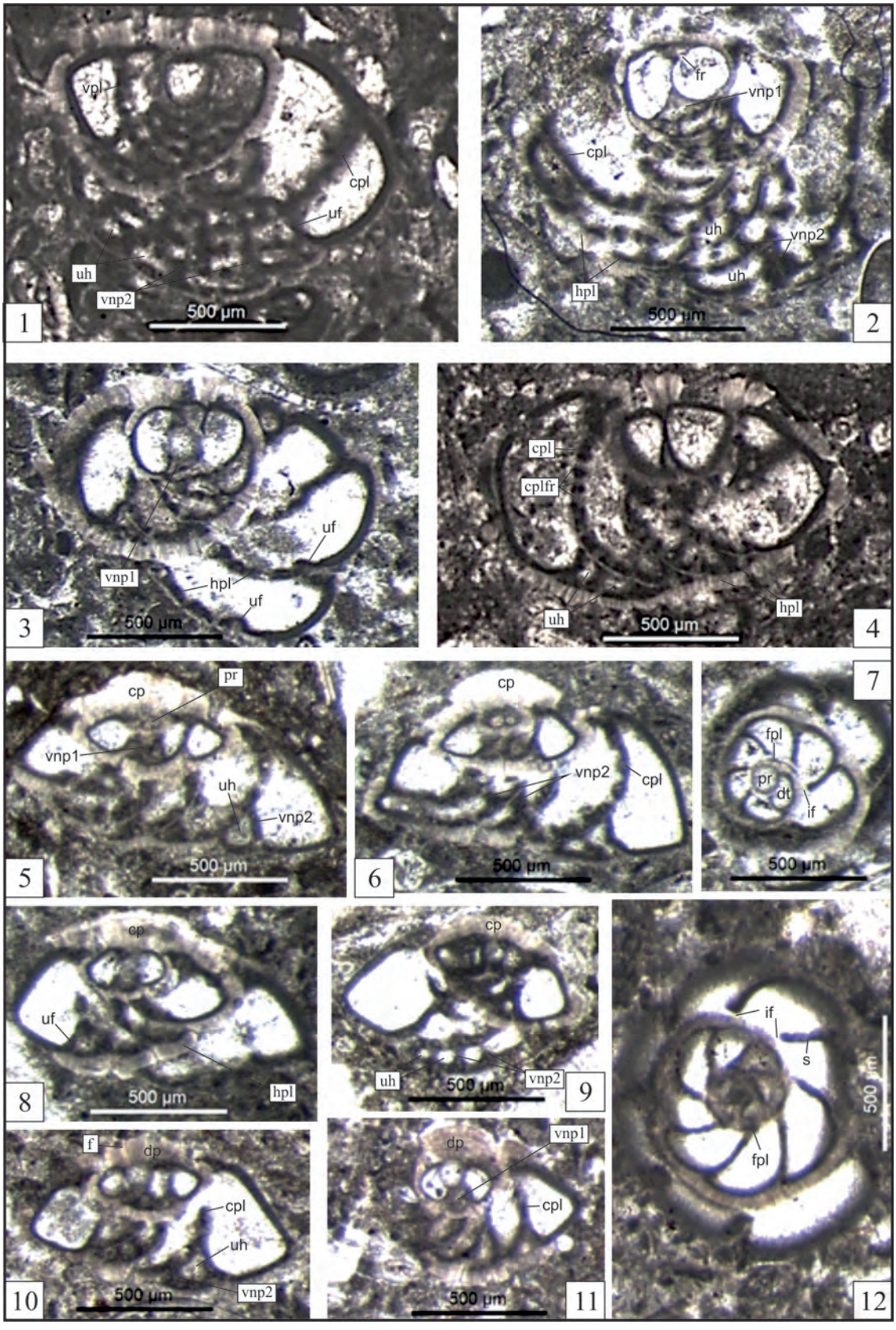
vpl
cpl
uf
uh
vnp2
500 µm
1
fr
vnp1
cpl
uh
vnp2
uh
hpl
500 µm
2
uf
vnp1
hpl
uf
500 µm
3
cpl
cplfr
uh
hpl
500 µm
4
pr
cp
vnp1
uh
vnp2
500 µm
5
cp
vnp2
cpl
500 µm
6
7
fpl
pr
dt
if
500 µm
cp
uf
hpl
500 µm
8
cp
uh
vnp2
500 µm
9
if
s
fpl
500 µm
f
dp
cpl
uh
vnp2
500 µm
10
dp
vnp1
cpl
500 µm
11
12

PLATE - V I

(Selandian, SBZ 2, South of Lake Yarışlı, SW Burdur, W Turkey)

(megalospheric specimens 3-6,9; microspheric specimens 7,8,10; scale bars: 500μm and 2mm)

Neosistanites catali Acar, n.gen., n.sp.

Figure 1- Subvertical section showing dorsal pillars (dp) and funnels (f), compound plate (cpl), umbilical flaps (uf), horizontal plate (hpl), second ventral pillar (vnp2) and umbilical hole (uh), Holotype, (ŞAY-5/L-2-3).

Figure 2- Oblique section showing very large central pillar (cp) and funnel, imperforate septa (s), horizontal plates (hpl), umbilical flaps (uf) and second ventral pillars (at the center) (ŞAY-5/L-5-3).

Figure 3- Vertical section of a broken specimen showing spherical protoconch (pr), large central pillar (cp), first ventral pillar (vnp1), vertical plates (vpl), imperforate compound plate?, umbilical flap (uf), horizontal plates (vnp2), second ventral pillars and large umbilical hole (uh) (ŞAY-4/L-1-1).

Neosistanites armagani Acar, n.gen., n.sp.

Figure 4- Vertical section showing spherical protoconch, large dorsal pillars (dp), large funnels (f), umbilical flaps (uf), horizontal plates (hpl), second ventral pillars (vnp2) and umbilical hole (uh), Holotype, (ŞAY-5/L-17-2A).

Figure 5- Vertical section of a broken specimen showing spherical protoconch (pr), deuteroconch (dt), dorsal pillar, funnels, umbilical flaps (uf), vertical plates (vpl), compound plate, horizontal plates, thick second ventral pillars (vnp2) and large umbilical hole (uh) (ŞAY-5/L-2-4).

Figure 6- Oblique section showing spherical protoconch (pr), deuteroconch (dt), septa (s) and intercameral foramina (if) (ŞAY-5/Rt-2-3).

Neosistanites inali Acar, n.gen., n.sp.

Figure 7- Oblique horizontal section showing spherical protoconch (pr), dorsal pillars (dp), funnel, imperforate septa, intercameral foramina (if) and foraminal plate (fpl) (ŞAY-2/G-11-1S).

Figure 8- Vertical section showing small spherical protoconch (pr), large central pillar (cp), horizontal plates (hpl), umbilical flaps, second ventral pillars (vnp2) and large umbilical hole, Holotype, (ŞAY-5/L-17-4).

Figure 9- Subertical section of a broken specimen showing spherical protoconch (pr), large dorsal pillar (dp), funnel, umbilical flaps (uf), horizontal plates, second ventral pillars and umbilical hole (ŞAY-4/M-2-1S).

Bolkarina aksarayi Sirel, 1981,

Figure 10- Oblique section of a broken specimen showing spiral-like or rotaliid coiling at the center, bilateral pillars and interpillar passages (ŞAY-1 /B-1-1).

Figure 11- Subaxial section showing bilateral pillars, interpillar passages and irregular equatorial chambers (at right) (ŞAY-1/B-3-1).

PLATE - VI

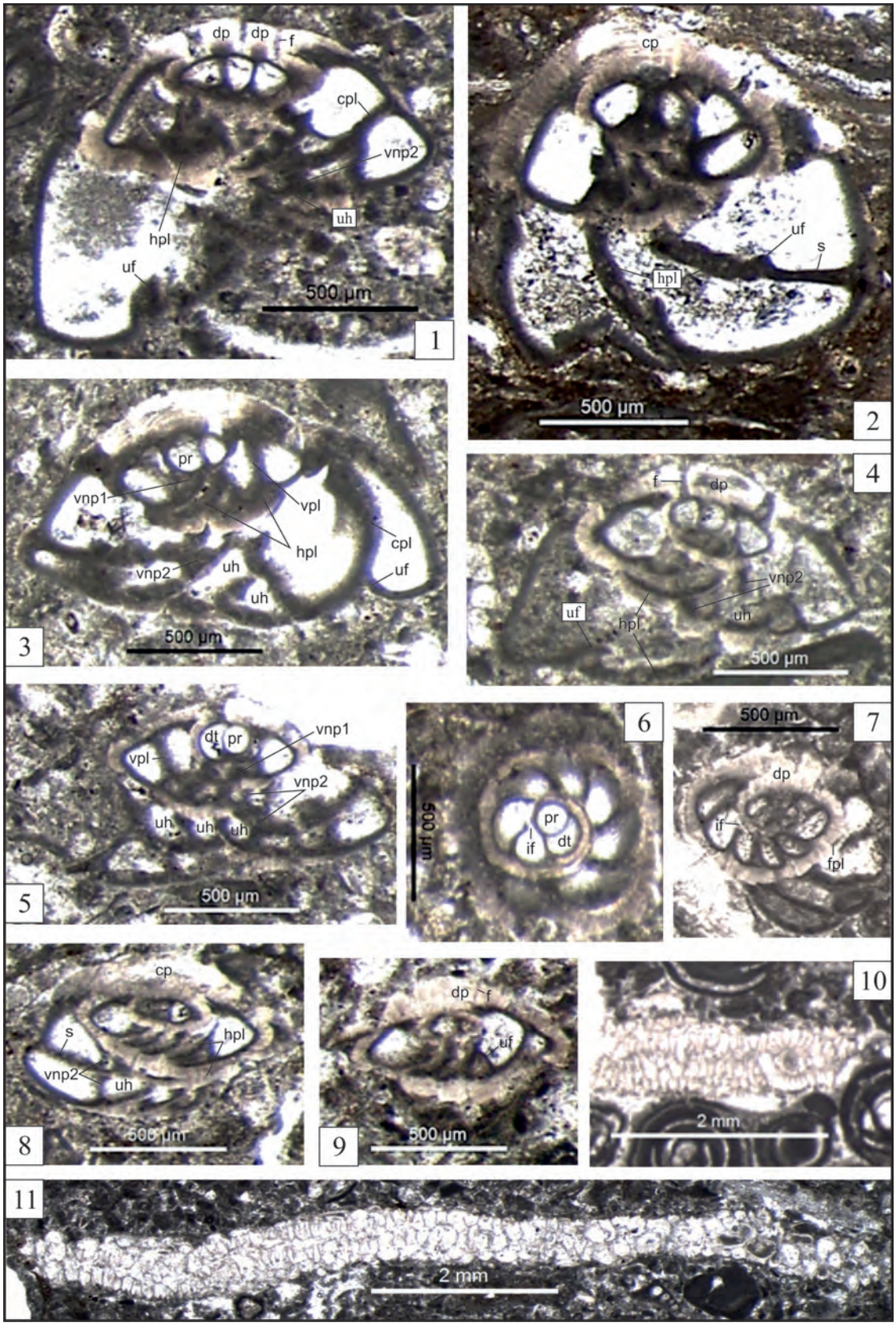
dp
dp
f
cpl
vnp2
uh
hpl
uf
500 µm
1
cp
uf
s
hpl
500 µm
2
pr
vnp1
vpl
hpl
cpl
vnp2
uh
uf
uh
500 µm
3
f
dp
vnp2
uf
hpl
uh
500 µm
4
dt
pr
vnp1
vpl
vnp2
uh
uh
uh
500 µm
5
500 µm
pr
if
dt
6
500 µm
dp
if
fpl
7
cp
s
hpl
vnp2
uh
500 µm
8
dp
f
uf
500 µm
9
2 mm
10
2 mm
11

PLATE - VII

(Selandian, SBZ 2, South of Lake Yarışlı, SW Burdur, W Turkey)

(megalospheric specimens 1,3,4,8-10,12; microspheric specimen 5)

Parahaymanella hakyemezae Acar, n.gen., n.sp.

Figure 1,2- Broken, longitudinally equatorial or subequatorial sections showing spherical protoconch (pr), triloculine chambers, spiral chambers, uniserial irregular chambers, septum (s) and intercameral foramina (if), Holotype; (ŞAY-4/H-1-2) and (ŞAY-1/G-5-1) respectively.

Figure 3,4- Slightly oblique equatorial sections showing milioline and spiral chambers and intercameral foramen (if); (ŞAY-1/G-3-1) and (ŞAY-2/G-11-3) respectively.

Figure 5- Oblique equatorial section showing protoconch, milioline chambers and spiral chambers (ŞAY-2/S-13-6).

Parahaymanella bozkurti Acar, n.gen., n.sp.

Figure 6,7- Longitudinal sections showing chambers of first stage; variable-sized, irregular chambers of second (uniserial) stage, and intercameral foramina (if); (ŞAY-2/N-2-4) and (ŞAY-2/K-7-1) respectively.

Figure 8- Slightly oblique longitudinally equatorial section showing large spherical protoconch (pr), chambers of first stage (triloculine and regular-spiral), variable-sized and irregularly arranged chambers of uniserial (second) stage, intercameral foramina (if), Holotype, (ŞAY-4/M-3-2).

Parahaymanella alanae Acar, n.gen., n.sp.

Figure 9- Longitudinally equatorial sections showing very large spherical protoconch (pr), triloculine and regular-spiral chambers of first stage, and regularly arranged (uniserial) chambers second stage (ŞAY-2/S-9-1).

Figure 10- Longitudinal sections showing spherical protoconch (pr), evolute chambers of first stage; regularly arranged, equally spaced and equidimensional chambers of second (uniserial) stage, Holotype, (ŞAY-1/M-1-2).

Figure 11,12- Longitudinal sections showing regularly arranged chambers of second (uniserial) stage, septum (s) and intercameral foramina (if); (ŞAY-1/K-3-1A) and (ŞAY-3/P-5-2Nh) respectively.

Biloculinites* cf. *paleocenica Rahaghi, 1983

Figure 13- Oblique, almost axial section showing short-vertical particles at the bottom (ŞAY-1/P-9-3).

Pseudohottingerina burdurensis Acar, n.gen., n.sp.

Figure 14-19- Tangential sections showing thick and radial septal filaments on the test (sfl) (without subepidermal partitions), thick septa (s), intercameral foramina (if), counter septum (cs) and single aperture (a), (ŞAY-1/G-6-2); (ŞAY-1/B-3-3), (ŞAY-1/G-5-1), (ŞAY-2/G-12-1), (ŞAY-2/G-9-7) and (ŞAY-2/G-11-1) respectively.

PLATE - VII

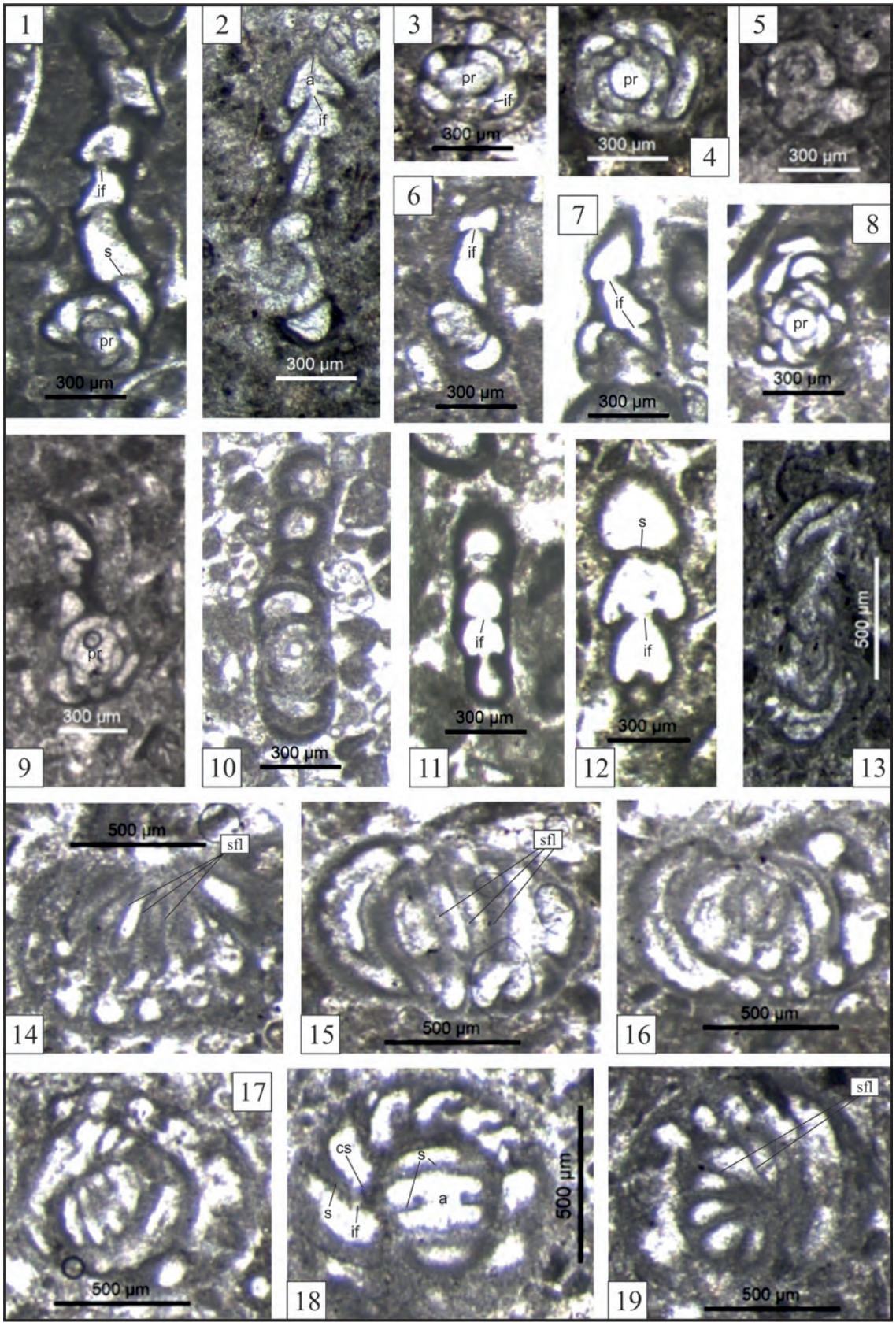
1
if
s
pr
300 µm
2
a
if
300 µm
3
pr
if
300 µm
4
pr
300 µm
5
300 µm
6
if
300 µm
7
if
300 µm
8
pr
300 µm
9
pr
300 µm
10
300 µm
11
if
300 µm
12
s
if
300 µm
13
500 µm
14
500 µm
sfl
15
sfl
500 µm
16
500 µm
17
500 µm
18
cs
s
s
a
if
500 µm
19
sfl
500 µm

PLATE - VIII

(Selandian, SBZ 2, South of Lake Yarışlı, SW Burdur, W Turkey)

(megalospheric specimens 1-9,12; microspheric specimens 10,14)

Pseudohottingerina burdurensis Acar, n.gen., n.sp.

Figure 1- Oblique equatorial section showing spherical protoconch, triloculine chambers, undivided spiral chambers; thick, inclined and curved septa (s), counter septa (cs), intercameral foramina (if), curved lip structure (lp), penultimate flaring whorls (fw) and undivided flaring chambers (fch), Holotype, (ŞAY-1/G-8-5).

Figure 2- Almost equatorial section showing triloculine chambers, undivided spiral chambers, thick and curved septa, counter septa (cs), intercameral foramina (if), curved lip structure (lp) (ŞAY-3/G-13-2).

Figure 3- Almost equatorial sparitised section showing undivided spiral chambers, septa, counter septa (cs), intercameral foramina, curved lip structure (lp), undivided flaring chambers (fch), septulum? (sl) and chamberlets? (chl) (ŞAY-1/G-4-1).

Figure 4- Slightly oblique equatorial sparitised section showing spherical protoconch, cryptotriloculine chambers, undivided spiral chambers, septa, counter septa (cs), intercameral foramina (if), curved lip structure (ŞAY-1/G-2-1)

Pseudohottingerina yarisliensis Acar, n.gen., n.sp.,

Figure 5-9- Slightly oblique subequatorial sparitised sections showing spherical protoconch, slightly curved septa, undivided spiral chambers, counter septa (cs), intercameral foramina and curved lip structure; (ŞAY-1/G-4-2), (ŞAY-1/N-5-4), (ŞAY-2/G-10-1) and (8) Holotype (ŞAY-3/G-17-4), (ŞAY-3/I-18-3B) respectively.

Sirtina paleocenica Acar, n.sp.

Figure 10-14- Vertical or subvertical sections showing thin dorsal pillars (dp), funnels (f), very narow lateral chambers (lch) and large ventral pillars (vnp); (ŞAY-3/I-22-1Sr),(ŞAY-2/Sr-2-4), (ŞAY-2/K-10-1Sr) (ŞAY-3/G-17-6), (ŞAY-3/M-9-1Sr) respectively.

Laffitteina anatoliensis Acar, n.sp.

Figure 15- Vertical section showing spherical protoconch, dorsal pillars (dp), funnels (f) and ventral pillars (vnp), Holotype, (ŞAY-5/L-14-1).

PLATE - VIII

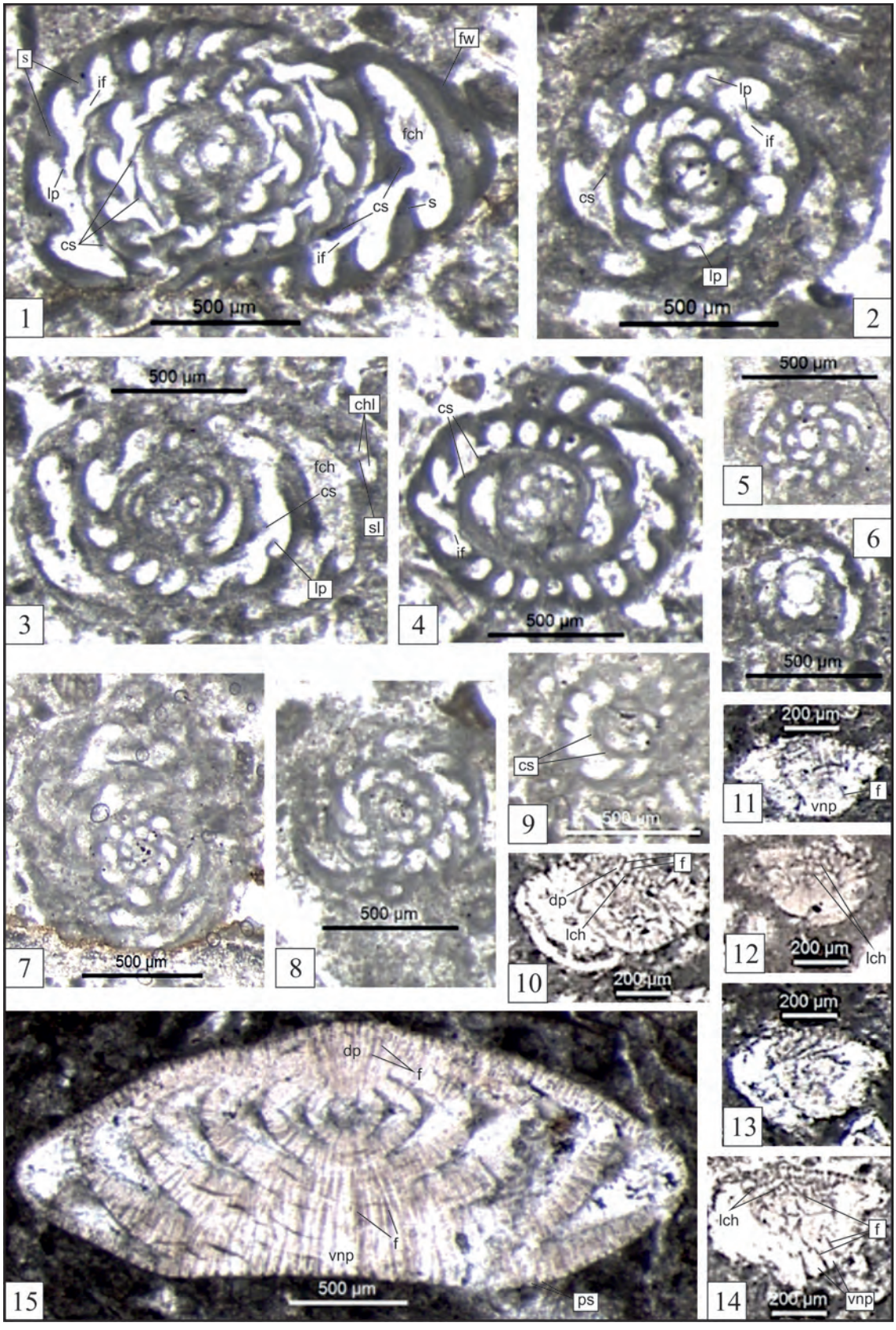
s
if
lp
cs
fw
fch
cs
s
if
500 µm
1
lp
if
cs
lp
500 µm
2
500 µm
chl
fch
cs
sl
lp
3
cs
if
500 µm
4
500 µm
5
6
500 µm
7
500 µm
8
cs
500 µm
9
200 µm
f
vnp
11
f
dp
lch
200 µm
10
200 µm
lch
12
200 µm
13
dp
f
f
vnp
500 µm
ps
15
lch
f
200 µm
vnp
14

PLATE - IX

(Selandian, SBZ 2, South of Lake Yarışlı, SW Burdur, W Turkey)

(megalospheric specimens 1-7, 11; microspheric specimens 8-10)

Laffitteina anatoliensis Acar, n.sp.

Figure 1-3- Almost vertical sections showing dorsal pillars (dp), narrow funnels (f) and ventral pillars (vnp); (ŞAY-5/L-17-1A), (ŞAY-5/L-16-1), (ŞAY-5/L-17-1B) respectively.

Figure 4- Slightly oblique horizontal section showing embryonic chambers (protoconch and deuteroconch), regular spiral coiling and rectangular chambers, straight or slightly inclined septa, umbilical flaps (uf), intraseptal canal (isc), spiral canal (spc), (ŞAY-5/M-3-1L).

Sirtina paleocenica Acar, n.sp.

Figure 5-10- Vertical or subvertical sections showing protoconch (pr), thin/weak dorsal pillars (dp), narrow funnels (f), lateral dorsal chambers (lch), ventral pillars (vnp) and pustules; (ŞAY-5/K-9-12Sr), (ŞAY-2/S-9-3Sr), (ŞAY- 2/He-2-3Sr), (ŞAY-2/S-4-2Sr); 9 Holotype (ŞAY-2/Sr-2-3A), (ŞAY-1/B-2-Sr) respectively.

Laffitteina thraciaensis Acar, n.sp.

Figure 11- Slightly oblique vertical section showing spherical protoconch, septa (s), dorsal pillars, ventral pillars, funnels and pustules (ps), Holotype (ŞAY-5/L-6-1).

PLATE - IX

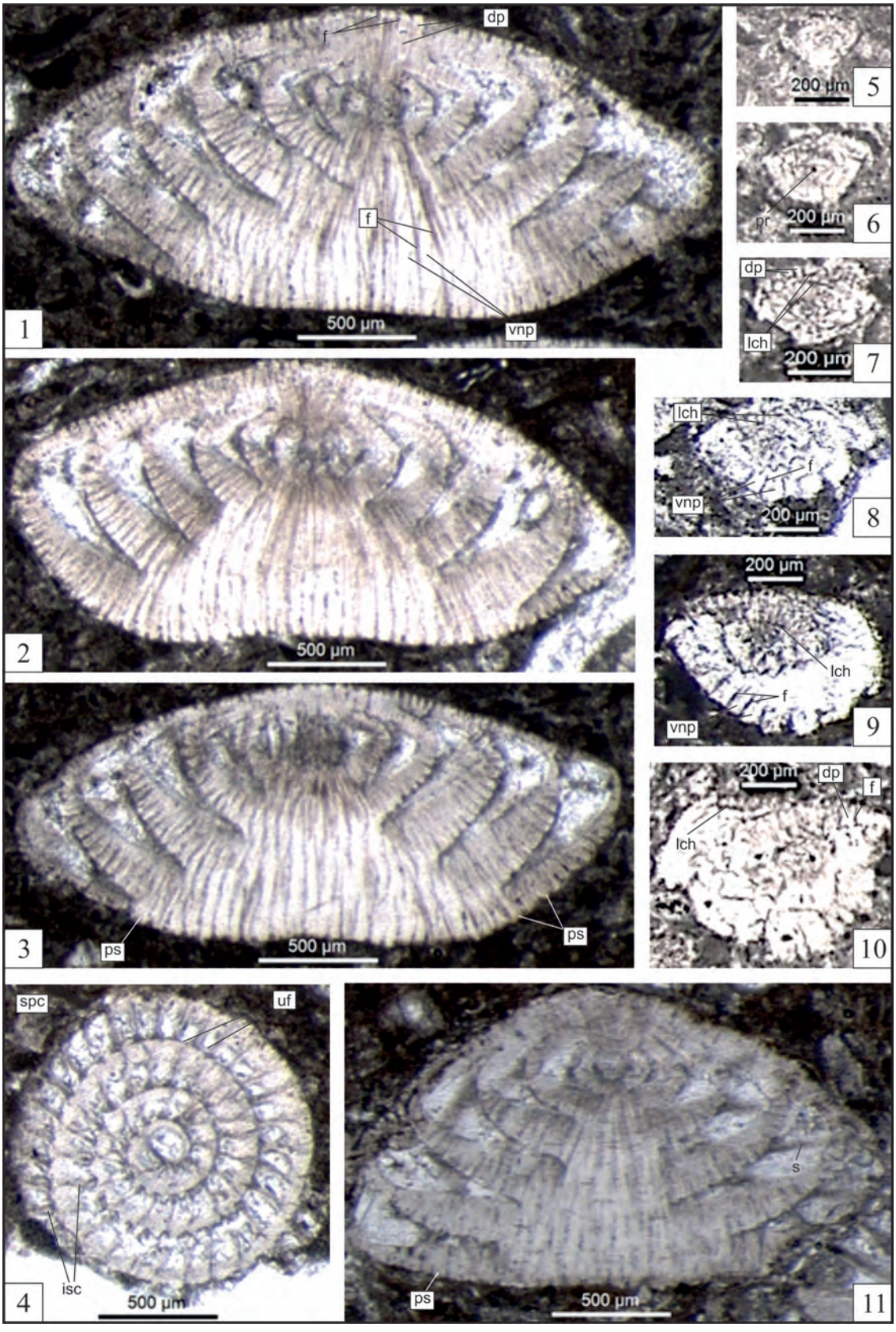
dp
f
f
500 µm
vnp
1
200 µm
5
pr
200 µm
6
dp
lch
200 µm
7
lch
f
vnp
200 µm
8
500 µm
2
200 µm
lch
f
vnp
9
ps
ps
500 µm
3
200 µm
dp
f
lch
10
spc
uf
isc
500 µm
4
s
ps
500 µm
11

PLATE - X

(Selandian, SBZ 2, South of Lake Yarışlı, SW Burdur, W Turkey)

(megalospheric specimens 1-4,9,10; microspheric specimens 7,8?)

Laffitteina thraciaensis Acar, n.sp.

Figure 1-3- Vertical, slightly oblique vertical and subvertical sections showing spherical protoconch, septa (s), dorsal pillars, funnels (f), ventral pillars (vnp); (ŞAY-5/G-14-1B), (ŞAY-5/L-15-1L), (ŞAY-5/L-13-1) respectively.

Laffitteina erki (Sirel, 1969)

Figure 4,5- Vertical and slightly oblique subvertical sections showing spherical protoconch, dorsal pillars, funnels, ventral pillars and marginal pustules (slightly curved) (ps); (ŞAY-5/L-13-1), (ŞAY-5 /L-18-1A1) respectively.

Bolkarina aksarayi Sirel, 1981

Figure 6- Oblique subaxial section showing bilateral pillars and interpillar passages (ŞAY-5/B-4-3).

Figure 10- Oblique equatorial section of a broken specimen showing protoconch (pr) and rectangular chambers (ŞAY-5/I-21-1).

Sirtina paleocenica Acar, n.sp.

Figure 7- Oblique section showing small spherical protoconch (pr), thin dorsal pillars, narrow funnels, very narrow lateral chambers, septa, chambers, ventral pillars (vnp) and pustules (ps) (at left) (ŞAY-5/I-16-Sr).

Figure 8- Almost horizontal section showing loosely coiling, inclined septa, rectangular chambers (ŞAY-5/P-8-7Sr).

***Popovia*? sp.**

Figure 9- Centered longitudinal section showing protoconch (pr) and following planispiral chambers, and uniserial chambers (ŞAY-5/S-16-1).

PLATE - X

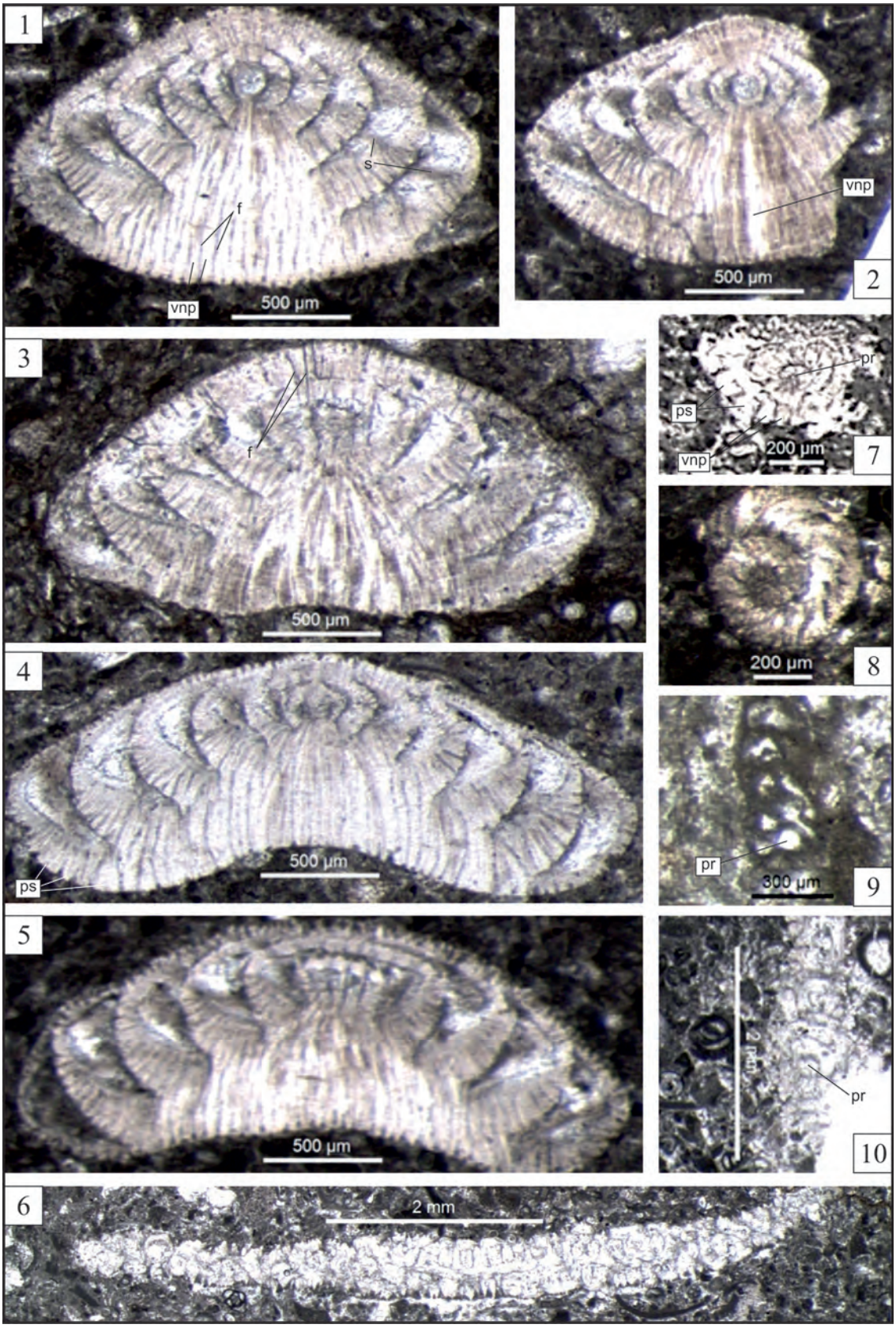
1
s
f
vnp
500 µm
2
vnp
500 µm
3
f
500 µm
4
ps
500 µm
5
500 µm
6
2 mm
7
pr
ps
vnp
200 µm
8
200 µm
9
pr
300 µm
10
2 mm
pr

PLATE - XI

(Selandian, SBZ 2, South of Lake Yarışlı, SW Burdur, W Turkey)

(megalospheric specimens 1-5,7,9; microspheric specimens 8,10)

Laffitteina erki (Sirel, 1969)

Figure 1- Vertical section showing spherical protoconch, weak dorsal pillars (dp), narrow funnels (f) and ventral pillars (vnp) (ŞAY 5/L-1-2).

Laffitteina mengaudi (Astre, 1923)

Figure 2-4- Vertical sections showing spherical protoconch, dorsal pillars, narrow funnels and ventral pillars; (ŞAY 5/S-3-2), (ŞAY-5/L-5-4), (ŞAY-1/G-1-2**)** respectively.

Ankaraella minima Acar, n.sp.

Figure 5-7- Vertical, subvertical and slightly eroded sections showing depressed spherical protoconch (pr), convex or flattened dorsal side, trochospirally coiled curved chambers, ribs (r), umbilical cavity, (5) Holotype; (ŞAY-1/A-1-2), (ŞAY-1/A-2-3), (ŞAY-3/P-6-2) respectively.

Figure 8,9- Vertical and almost horizontal section showing spherical protoconch (pr), trochospirally coiled milioline chambers at the center (8), intercameral foramina (if), hook-structured and convex ribs (r) and triloculine chambers (9): (ŞAY-1/G-6A), (ŞAY-1/K-4-2) respectively.

Ankaraella trochoidea Sirel, 1998

Figure 10- Almost horizontal section of a broken and eroded specimen showing quinqueloculine (at the center) and triloculine chambers, convex ribs and intercameral foramen (ŞAY-3/P-5-2).

Figure 11- Tangential or subvertical section showing trochospirally arranged chambers which are flattened in dorsal side and concave in ventral side, thick convex ribs (r), umbilical cavity (ŞAY-1/M-1-3).

Figure 12- Subvertical section showing flattened dorsal side and very large umbilical cavity (uc) (ŞAY-3/M-9-2).

PLATE - XI

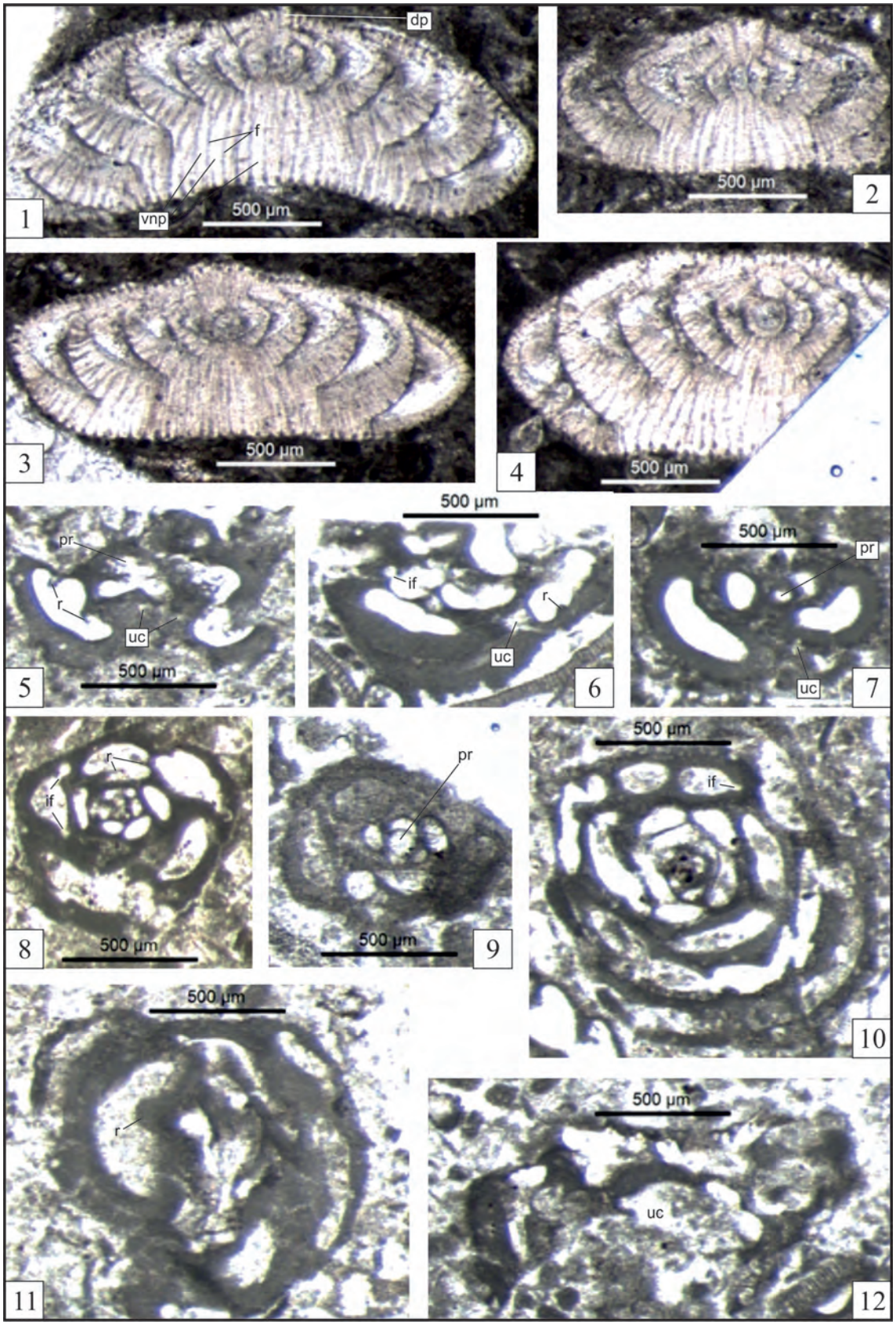
dp
f
vnp
500 µm
1
500 µm
2
500 µm
3
500 µm
4
500 µm
pr
r
uc
500 µm
5
if
r
uc
6
500 µm
pr
uc
7
r
if
500 µm
8
pr
500 µm
9
500 µm
if
10
500 µm
r
11
500 µm
uc
12

PLATE - XII

(Selandian, SBZ 2, South of Lake Yarışlı, SW Burdur, W Turkey)

(megalospheric specimens 3-7; microspheric specimens 1,8,9)

Globoflarina*? *sphaeroidea (Fleury, 1982)

Figure 1- Poorly preserved almost axial section showing septa (s), septulum (sl), chamberlet (chl), axis of coiling and flaring whorls (asymmetrical) (fw) (ŞAY-1/G-5-2A).

Figure 2- Poorly preserved, broken, slightly oblique tangential section showing flaring whorls (fw), septula (sl), chamberlets (chl) and preseptal passage (prp) (ŞAY-1/G-8-1).

Figure 3- Almost equatorial oblique section showing depressed spiral chambers which follow protoconch, and chambers (ŞAY-5/Ml-3-1B).

Figure 4- Slightly oblique equatorial section showing the largest protoconch, foramen between protoconch and goulot (fr), depressed spiral chambers (ch), key hole aperture (kha) or main aperture, secondary or main aperture, and key hole aperture or dome-like alveol opening into secondary aperture (ŞAY-5/G-9-1).

Figure 5- Slightly oblique equatorial section showing large, rectangular protoconch, succeeding depressed spiral chambers intercameral foramen (if) (ŞAY-1/G-6-2).

Figure 6- Equatorial section showing very large protoconch, foramen between protoconch and goulot, goulot (g), depressed spiral chambers (ch) and flaring whorls (fw) (ŞAY-2/G-10-1A).

Figure 7- Equatorial section showing very large protoconch, goulot (g), septa (s), depressed spiral chambers (ch) and intercameral foramina (if) (ŞAY-3/G-14-1).

***Keramosphaera* sp.**

Figure 8, 9- Almost centered sections; (ŞAY-2/K-6-3), (ŞAY-2/K-5-1) respectively.

PLATE - XII

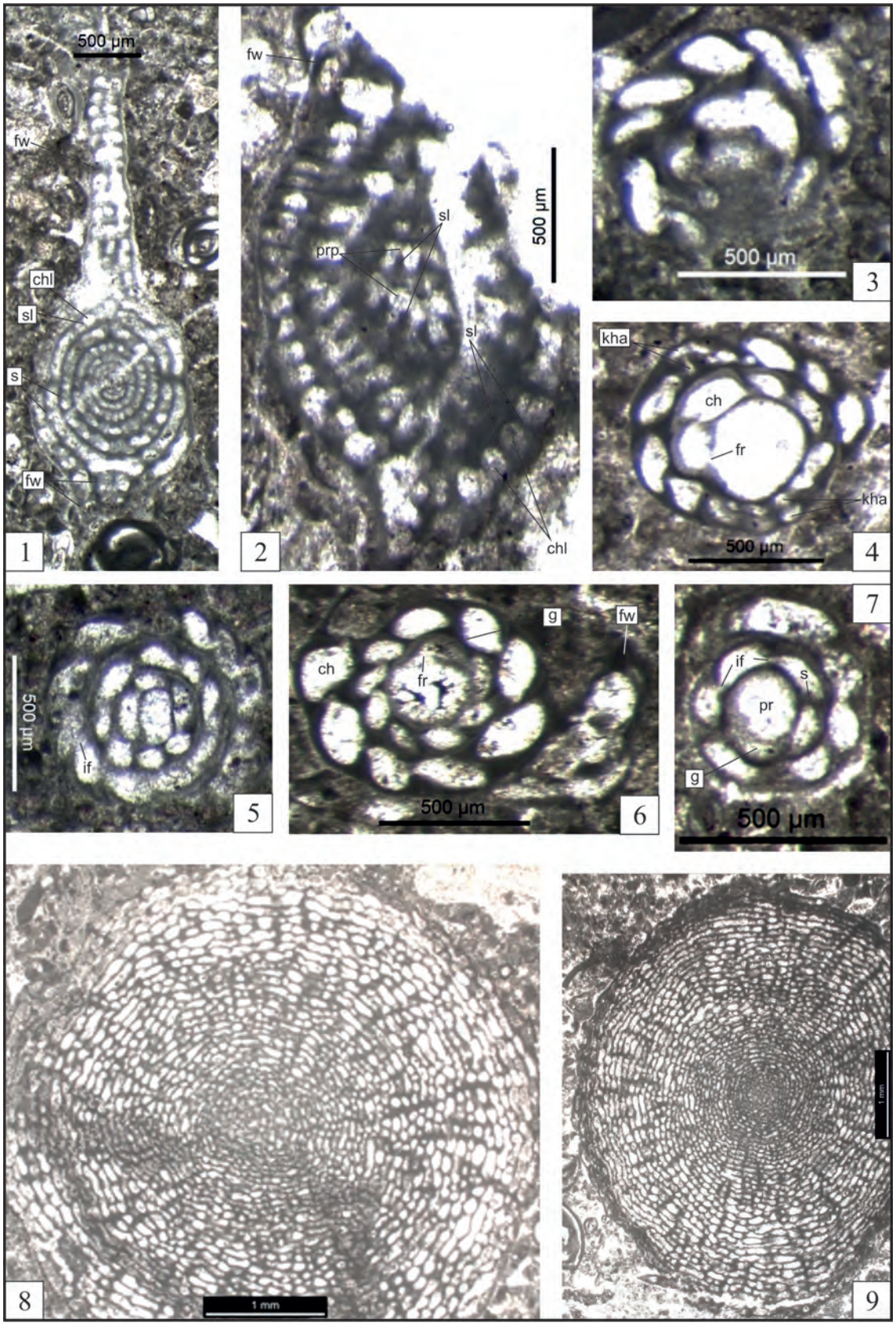
500 µm
fw
chl
sl
s
fw
1
fw
sl
prp
500 µm
sl
chl
2
500 µm
3
kha
ch
fr
kha
500 µm
4
500 µm
if
5
g
fw
ch
fr
500 µm
6
7
if
s
pr
g
500 µm
8
1 mm
1 mm
9

PLATE - XIII

(Selandian, SBZ 2, South of Lake Yarışlı, SW Burdur, W Turkey)

(megalospheric specimens 1-8, 10-15, 17?)

Miscellanea*? *globularis Rahaghi, 1978

Figure 1-4- Slightly oblique and centered axial sections showing spherical protoconch, deuteroconch, bilateral pillars (p), funnels (f) and test ornamentations; (ŞAY-1/M-12-1), (ŞAY-2/M-8-1), (ŞAY-2/G-9-5), (ŞAY-2/P-8-4M) respectively.

Figure 5-8- Slightly oblique or equatorial sections showing spherical protoconch (pr), deuteroconch (dt), septa (s), narrow intraseptal canals (isc), weak spiral canals (spc) and test ornamentations (ŞAY-2/He-2-1), (ŞAY-1/M-1-6), (ŞAY-3/M-13-2), (ŞAY-1/M-2-1) respectively.

Figure 9- Tangential section showing septa (s), one row of apertures (a) on septa and vertical sections of test ornamentations (to) (ŞAY-3/I-25-3).

Akbarina primitiva (Rahaghi, 1983)

Figure 10- Equatorial sections showing protoconch and deuteroconch, inclined septa (s), intraseptal canal (isc) and weak spiral canal (spc) (ŞAY-4/M-3-2).

Figure 11-15- Slightly oblique or centered axial sections showing bilateral pillars (p), funnels (f), test ornamentations. 12: young specimen, and 15: slightly oblique subaxial section; (ŞAY-2/M-5-2), (ŞAY-1/M-1B), (ŞAY-5/M-4-3), (ŞAY-5/M-2-1), (ŞAY-5/L-5-4M) respectively.

Figure 16- Oblique equatorial section showing septum, intraseptal canal (isc) and spiral canal (spc) (ŞAY-5/L-17-2M).

***Kolchidina*? sp.**

Figure 17- Almost equatorial oblique section showing microgranular or fine grained agglutinated test, spiral chambers following embryonic stage, and succeeding operculinid chambers (ŞAY-1/B-2-6).

Algae gen.3 indet.

Figure 18-20- Vertical? Sections showing prayer beads-shaped or celled algal chambers (spherical or slightly oblique ovoid). 20: various type of flaring chambers/cells on periphery; (ŞAY-2/G-11-4), (ŞAY-1/G-1-3), (ŞAY-5/Al-1-1), respectively.

PLATE - XIII

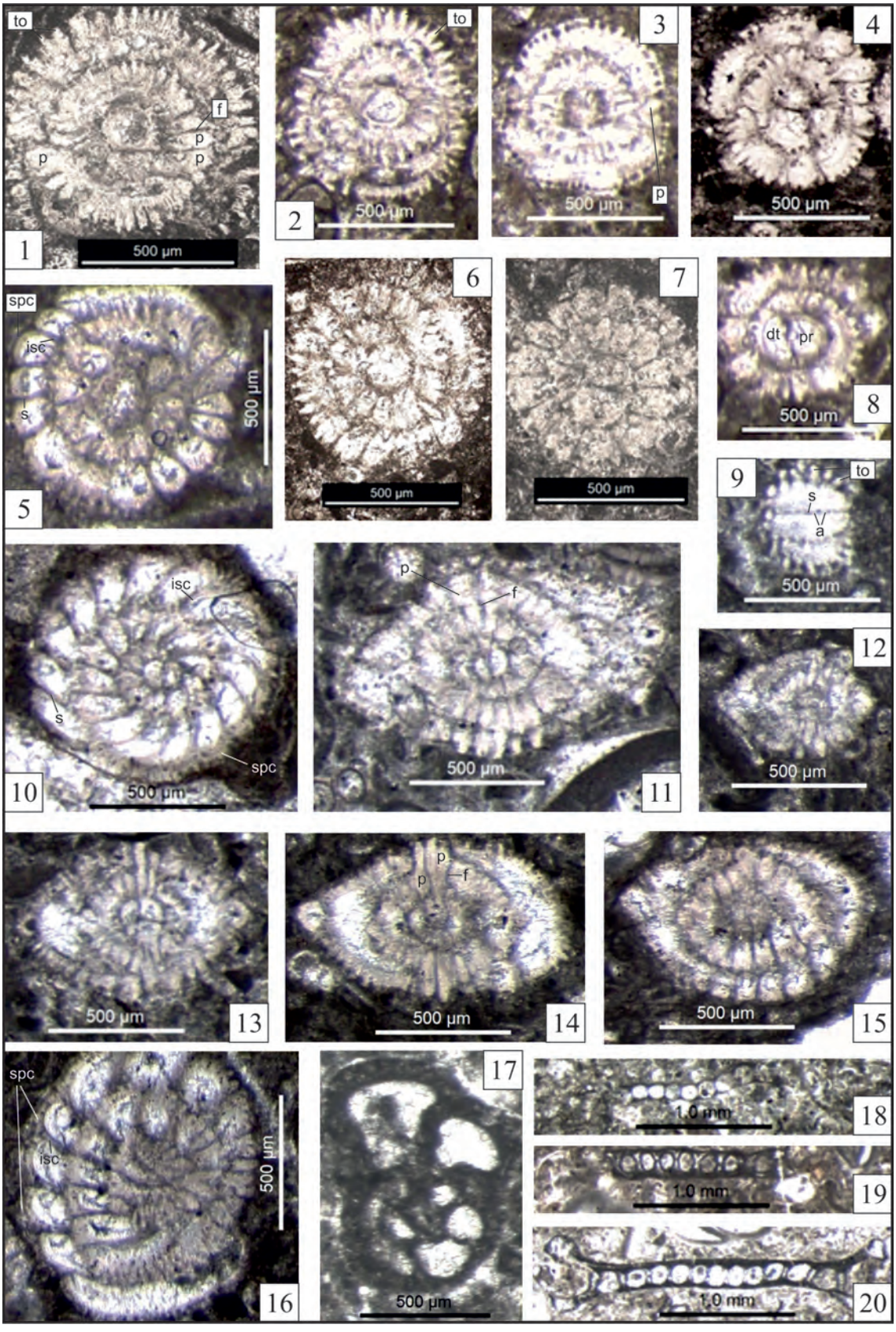
to
f
p
p
p
1
500 µm
to
2
500 µm
3
p
500 µm
4
500 µm
spc
isc
s
500 µm
5
6
500 µm
7
500 µm
dt
pr
8
500 µm
9
to
s
a
500 µm
isc
s
spc
10
500 µm
p
f
500 µm
11
12
500 µm
500 µm
13
p
p
f
500 µm
14
500 µm
15
spc
isc
500 µm
16
17
500 µm
1.0 mm
18
1.0 mm
19
1.0 mm
20

PLATE - XIV

(Selandian, SBZ 2, South of Lake Yarışlı, SW Burdur, W Turkey)

(megalospheric specimens 2,3,5; microspheric specimens 1,4,6,7)

Miliolid gen.1 indet.

Figure 1- Almost axial section showing ovoid embryonic stage (quinqueloculine? chambers), ribs (r), triloculine and biloculine chambers with very thick basal layer, simple tooth in the last whorl and simple trematophoric structure (trms) with weak pillar (ŞAY-3/I-20-2).

Figure 2,3- Axial section showinglarge spherical protoconch, large and long goulot (g), foramen between protoconch and goulot (fr), triloculine and biloculine chambers, ribs (r), simple tooth (t) and polar enlargement in some chambers; (ŞAY-3/B-6-1M), (ŞAY-1/M-2-4M) respectively.

Miliolid gen.2 indet.

Figure 4- Almost axial oblique section showing fusiform embryonic stage (fusiform shaped, irregular, quinqueloculine? and triloculine chambers) and ovoid biloculine chambers with thick basal layer, short ribs (r) and single teeth (t) (ŞAY-3/I-34-Sg1).

Figure 5- Broken axial? Section showing fusiform shaped protoconch with ragged edge; triloculine chambers with irregular thick basal layer (bl), teeth (t) and ribs (r) (ŞAY-3/I-20-4M).

Miliolid gen.3 indet.

Figure 6- Almost equatorial section showing spherical quinqueloculine chambers of embryonic stage, triloculine chambers, bifurcating biloculine chambers (bfs) and cyclic chambers (ŞAY-2/I-6).

Figure 7- Almost axial slightly oblique section showing spherical quinqueloculine chambers of embryonic stage, triloculine chambers, bifurcating biloculine chambers (bfs) and cyclic chambers (ŞAY-2/I-6).

PLATE - XIV

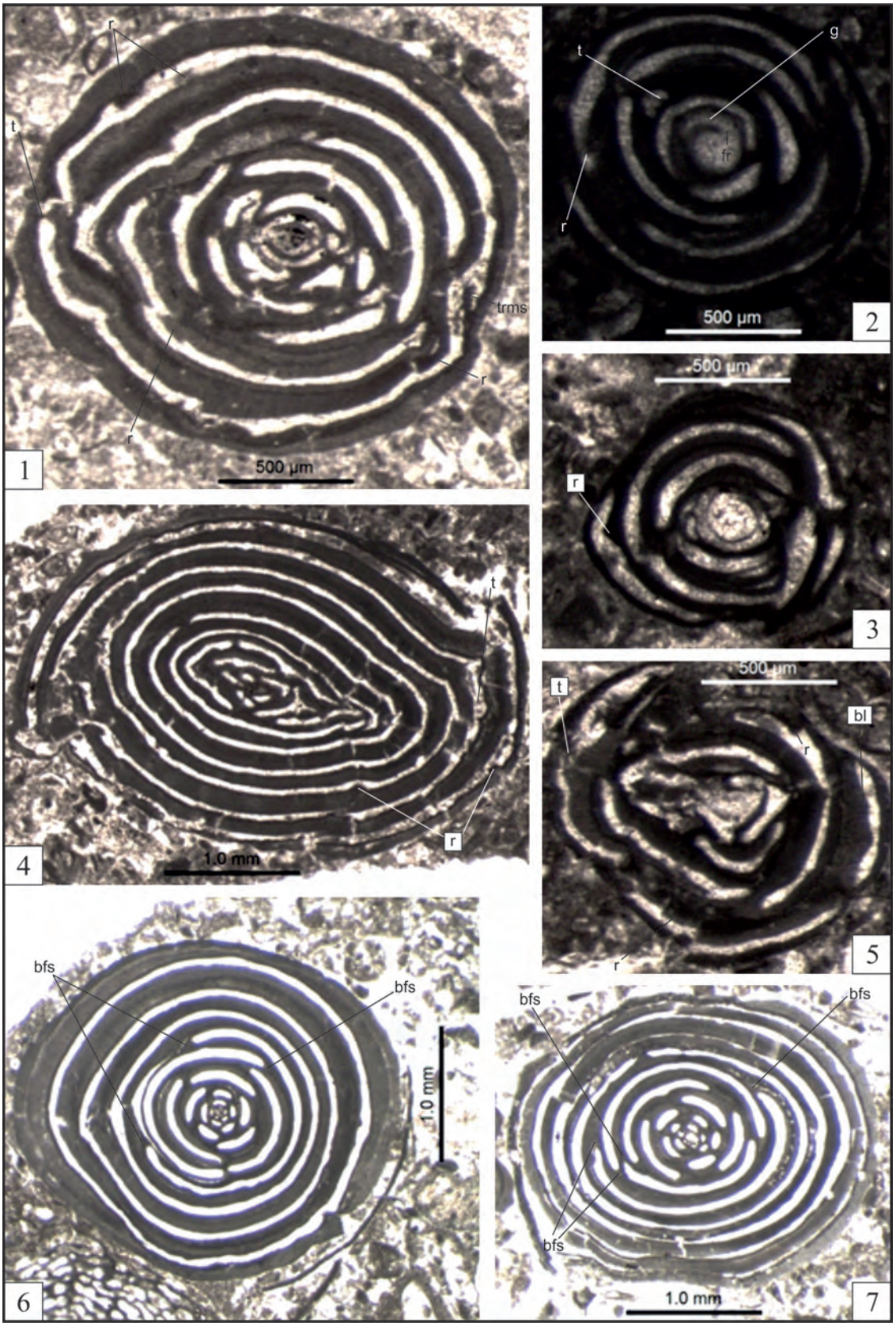
r
t
trms
r
r
500 µm
1
t
g
fr
r
500 µm
2
500 µm
r
3
t
r
1.0 mm
4
500 µm
t
bl
r
r
5
bfs
bfs
1.0 mm
6
bfs
bfs
bfs
1.0 mm
7

PLATE - XV

(Selandian, SBZ 2, South of Lake Yarışlı, SW Burdur, W Turkey)

(megalospheric specimens 3,4,6,9-13, 15; microspheric specimens 1,5?,7, 14?)

Miliolid gen.4 indet. sp.1

Figure 1- Almost axial oblique broken section showing quinqueloculine? chambers, triloculine truncate chambers (tnch), transition chamber (tnch), broken chambers and irregular penultimate chamber (at left) (ŞAY-3 /I-31-4M).

Figure 2- Almost euqatorial oblique section showing truncate chambers (trch) at the center and succeeding whorls, transition chamber (tnch) and simple tooth (t) (ŞAY-1/B-2-2M).

Miliolid gen.4 indet. sp.2

Figure 3- Axial section of a lenticular form (with sharp edge) showing spherical protoconch, triloculine chambers, biloculine truncate chambers (trch) and tooth? (ŞAY-1/Pl-1-3A).

Figure 4- Oblique section showing spherical protoconch, goulot? and transition chamber (tnch) (ŞAY-1/Ms-1-2M).

Miliolid gen.4 indet. sp.3

Figure 5,6- Broken and centered axial sections showing limited chambers of embryonic stage, truncate chambers (trch), transition chamber (tnch) and simple tooth structure; (ŞAY-3/I-35-2Sg), (ŞAY-3/I-25-2Sg) respectively.

Miliolid gen.5 indet.

Figure 7- Equatorial section showing spherical chambers of embryonic stage (minute spherical protoconch, quinqueloculine and triloculine chambers), short and thick septa, spiral chambers of 1.5 cycle, simple tooth (t), intercameral foramina (if) and ultimate chamber with irregular internal structure (ŞAY-3/N-3-1).

Figure 8- Non-centered oblique section showing triloculine? And irregular spiral chambers, short and thick septa, intercameral foramen (if), simple tooth (t), and aperture (a), (ŞAY-2/N-2-3).

Figure 9,10- Axial sections showing spherical protoconch, triloculine and evolute biloculine chambers, simple tooth (t), (ŞAY-2/M-11-1Q), (ŞAY-3/N-7-4A) respectively.

Figure 11- Slightly oblique equatorial section showing spherical protoconch, triloculine chambers, spiral chambers, intercameral foramen (if), simple tooth (t), (ŞAY-1/I-3-2).

***Thalmannita*? sp.**

Figure 12-15- Axial sections; (ŞAY-1/G-8-2T), (ŞAY-2/N-6-1Ra), (ŞAY-1/G-5T), (ŞAY-1/N-8-3T) respectively.

PLATE - XV

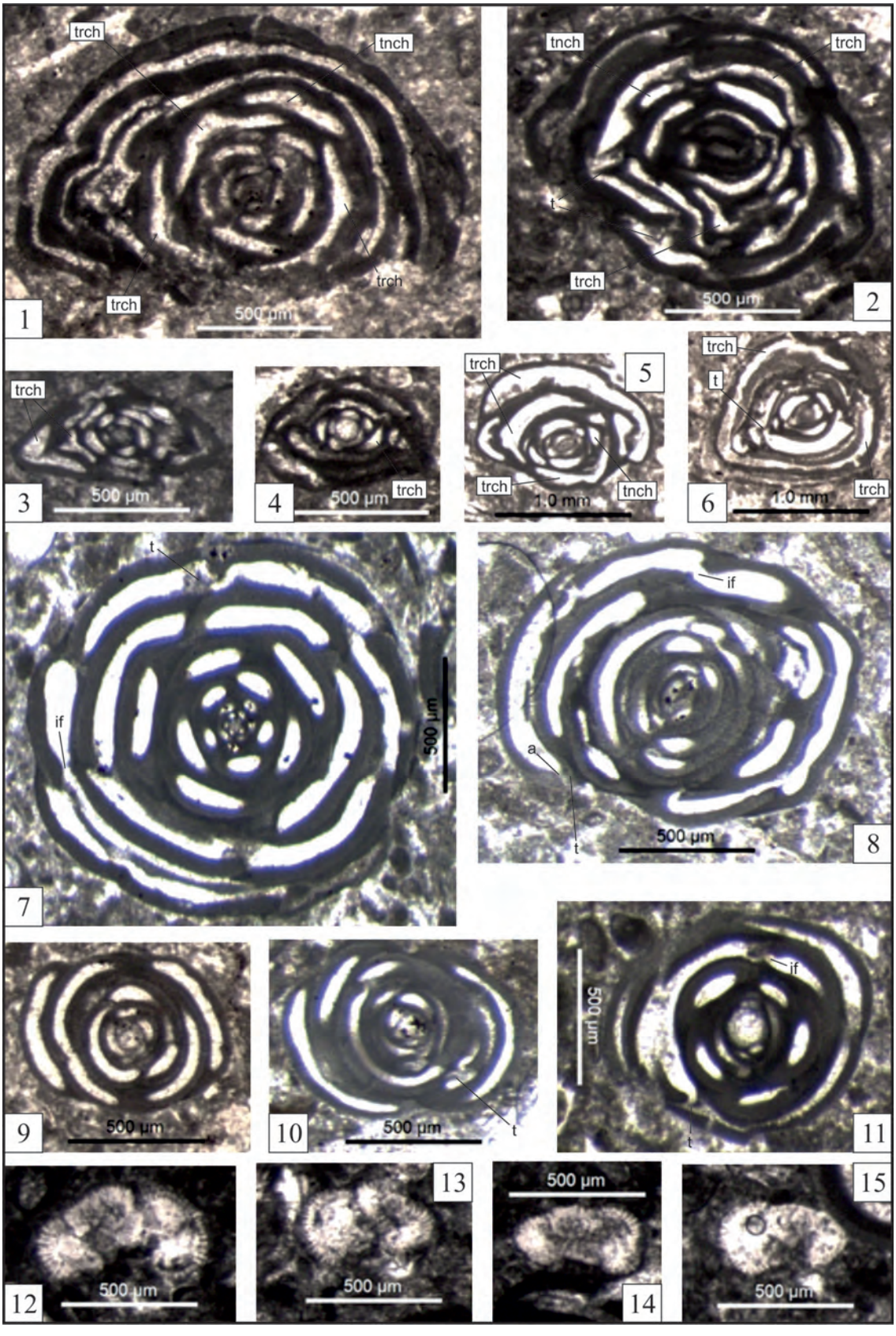
trch
tnch
trch
500 µm
1
tnch
trch
t
trch
500 µm
2
trch
500 µm
3
500 µm
trch
4
trch
5
trch
tnch
1.0 mm
trch
t
6
trch
1.0 mm
t
if
500 µm
7
if
a
t
500 µm
8
500 µm
9
500 µm
t
10
if
500 µm
t
11
500 µm
12
13
500 µm
500 µm
14
500 µm
15

PLATE - XVI

(Selandian, SBZ 2, South of Lake Yarışlı, SW Burdur, W Turkey)

(megalospheric specimens 2,3,5,6,8,9; microspheric specimens 1,4,7)

Miliolid gen.6 indet.

Figure 1- Axial sections showing spherical embryonic quinqueloculine (in two planes) and triloculine (in three planes) chambers, ovoid (evolute) biloculine chambers (1.5 whorls), transition chambers (tnch), whorl sutures (ws) and thick basal layer (bl), (ŞAY-2/N-4-1).

Figure 2,3- Axial sections showing spherical protoconch, spherical triloculine chambers and irregularly coiled ovoid (evolute) biloculine chambers (1 – 1.5 whorls) and goulot (g), (ŞAY-1/M-2-1Ml) (ŞAY-5/Ml-5-1C) respectively.

Miliolid gen.7 indet.

Figure 4- Axial sections showing ovoid embryonic chambers (minute spherical protoconch and succeeding ovoid biloculine chambers) and succeeding irregular (quinqueloculine? and triloculine) chambers, additional chambers (adch), whorl suture (ws) and interlocular microgranular fillings? (in the bottom, on the penultimate chambers) (ŞAY-5/Ml-1-1B).

Figure 5,6- Axial sections showing spherical protoconch, irregular triloculine chambers and additional chamber (adch), (ŞAY-5/M-4-2) (ŞAY-4/M-3-2A) respectively.

Miliolid gen.7 indet. or Idalinid genus 1

Figure 7- Poorly preserved, almost axial section showing ovoid embryonic chambers (minute spherical protoconch) and following biloculine chambers and a simple tooth (t), (ŞAY-5/Ml-4-2).

Figure 8,9- Oblique axial sections showing spherical protoconch, goulot (g), biloculine chambers and simple tooth? (ŞAY-5/Ml-5-1B) (ŞAY-1/G-4-2) respectively.

PLATE - XVI

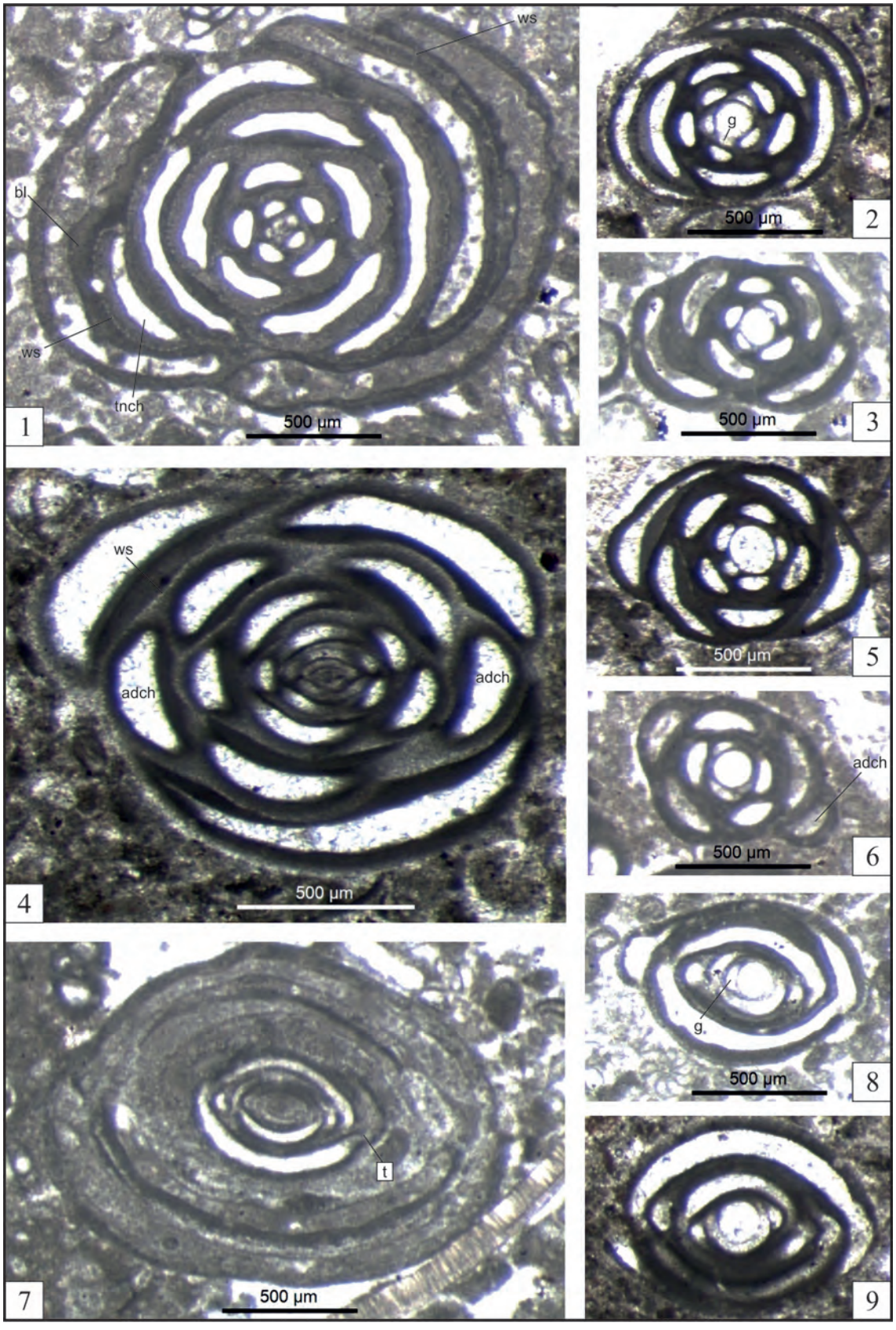
ws
bl
ws
tnch
500 µm
1
g
500 µm
2
500 µm
3
ws
adch
adch
500 µm
4
500 µm
5
adch
500 µm
6
t
500 µm
7
g
500 µm
8
9

PLATE - XVII

(Selandian, SBZ 2, South of Lake Yarışlı, SW Burdur, W Turkey)

(megalospheric specimens 2-5,7,9-14; microspheric specimens 1,6)

Miliolid gen.9 indet.

Figure 1- Almost axial sections showing spherical quinqueloculine chambers and triloculine chambers, thick basal layer (bl), ribs (r), whorl suture (ws), transition chamber (tnch) and irregular biloculine chambers (ŞAY-5/Ml-9-1).

Figure 2- Axial sections showing large spherical protoconch, elongated goulot (g), irregular triloculine chambers and biloculine chambers, thick basal layer (bl), and a very thick rib (r) dividing the ultimate chambers (ŞAY-5/Ml-6-1).

Agglutinated gen. 1 indet.

Figure 3,4,6- Poorly preserved vertical sections showing conical agglutinated shell, inflated triserial chambers, spherical protoconch (pr), septum (s), umbilical flap (uf), umbilical plate (upl), umbilical plate foramina (uplfr) and pillar? (ŞAY-2/I-11-2Tx) (ŞAY-2/P-8-5Tx) (ŞAY-3/I26-2Tx) respectively.

***Textularia* sp.**

Figure 5- Vertical section showing small spherical protoconch and textulariid chambers (ŞAY-3/I-23-2Tx).

Agglutinated gen. 2 indet.

Figure 7,9- Slightly oblique vertical sections showing globular, agglutinated shell, depressed triserial chambers, spherical protoconch (pr), strongly depressed and large chambers, septum (s), umbilical plate (upl), umbilical plate foramina (uplfr) and pillar? (p); (ŞAY-2/G-11-2) (ŞAY-2/Sr-2-6Gf) respectively.

Figure 8- Slightly oblique horizontal sections showing triserial chambers, septum (s), chamber lümen, thick umbilical flaps (uf) and umbilical plate foramina (uplfr) (ŞAY-2/G-9-Gf).

***Heterillina* sp.**

Figure 10,11- Almost axial sections showing triloculine and biloculine chambers, (ŞAY-1/C-1-2) (ŞAY-2/He-2 3).

Miscellanid gen. 1 indet.

Figure 12,13- Axial sections showing spherical protoconch (pr), pillars (p), funnels (f), lenticular chambers preceding the last whorl, and truncate chambers of the last whorl (trch), (ŞAY-2/M-2-2) (ŞAY-1/M-1-1) respectively.

Figure 14- Slightly oblique equatorial sections showing protoconch and deuteroconch (dt), spiral canal (spc), intraseptal canal (isc), irregular planispirally coiled rectangular (with a bigger height) chambers (ŞAY-4/M-3-1).

PLATE - XVII

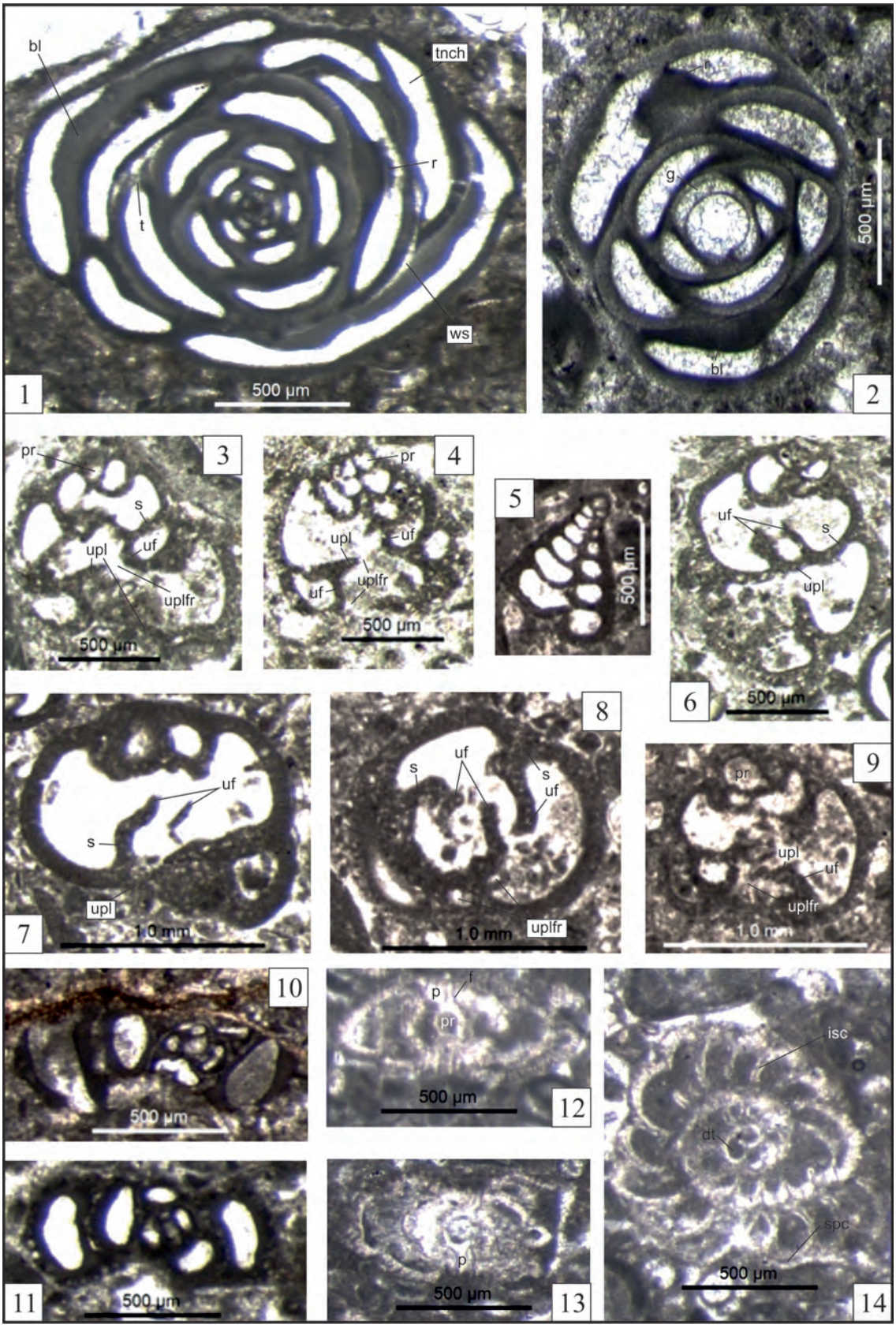
bl
tnch
r
t
ws
500 µm
1
h
g
500 µm
bl
2
pr
s
upl
uf
uplfr
500 µm
3
pr
4
upl
uf
uplfr
uf
500 µm
5
500 µm
uf
s
upl
6
500 µm
uf
s
upl
7
1.0 mm
s
uf
uf
8
s
uf
uplfr
1.0 mm
pr
9
upl
uf
uplfr
1.0 mm
10
500 µm
p
f
pr
500 µm
12
isc
dt
spc
500 µm
14
11
500 µm
p
500 µm
13

PLATE - XVIII

(Selandian, SBZ 2, South of Lake Yarışlı, SW Burdur, W Turkey)

(megalospheric specimens 2,4-7,10,14-18,21,22,25-29; microspheric specimens 11,24)

Note that, the scale bar is 500μm for figure 13

Figure 1- ***Chrysalidina?*** **sp**.; Subvertical section showing a conic form (ŞAY-1/C-1- 13A).

Figure 2-4- Planulinid gen. 1 indet.: 2,3- Vertical and subvertical or axial sections (ŞAY-2/B-4-2Pl)**,** (ŞAY-2/P-8-3Pl) respectively; 4- Slightly oblique or equatorial section (ŞAY-4/M-1-1Pl)

Figure 5,6- ***Lockhartia*****? sp.**: Vertical sections, (ŞAY-1/R-1-3L), (ŞAY-1/M-18-2L) respectively.

Figure 7-10, 13,14- Rotaliid gen. 1 indet. ***(Redmondoides?)*****:** 7-10,13- Vertical or subvertical sections, (ŞAY-1/M-18-10A), (ŞAY-1/M-18-12R), (ŞAY-1/M-18-8R), (ŞAY- 1/G-7-1R) (ŞAY 2/G-9-3R) respectively; 14- oblique section, (ŞAY-1/I-4-2R)

Figure 11,12- Rotaliid gen. 2 indet.: 11- Almost horizontal section, (ŞAY-2/P-8-7R); 12- Vertical section, (ŞAY-2/M-7-1R).

Figure 15-18- Rotaliid gen. 3 indet.; (15-17)- Vertical sections, (ŞAY-5/Ml-10-2Pk) (ŞAY-5/M-6-1APk) (ŞAY-5/L-1-1M) respectively; 18- Horizontal section, (ŞAY-1/G-3-1Pk).

Figure 19-24- Rotaliid gen. 4 indet. (with two layered test): (19-22)- Vertical or subvertical sections, (ŞAY-2/I-8-2Rc) (ŞAY-2/P-8-1Rc) (ŞAY-3/I-17-1Rc) (ŞAY-1/M-12-1Rc) respectively; 23,24- Horizontal or subhorizontal sections, (ŞAY-1/M-18-11Rc2) (ŞAY-1/M-18-7Rc) respectively.

Figure 25-29- Mississippinid gen. 1 indet.: Vertical or subvertical sections, (ŞAY-3/I-23-3), (ŞAY-2/I-39-Ms), (ŞAY-3/I-28-3Ms), (ŞAY-3/I-29-3Ms), (ŞAY-2/I-11-3Ms) respectively.

Figure 30,31- Algae gen. 1 indet.: 30- Oblique vertical section, (ŞAY-3/B-6-1Al); 31- Oblique horizontal section, (ŞAY-1/M-2-2Al).

Figure 32- Algae gen. 2 indet.: Vertical? section (ŞAY-2/G-11-Al).

PLATE - XVIII

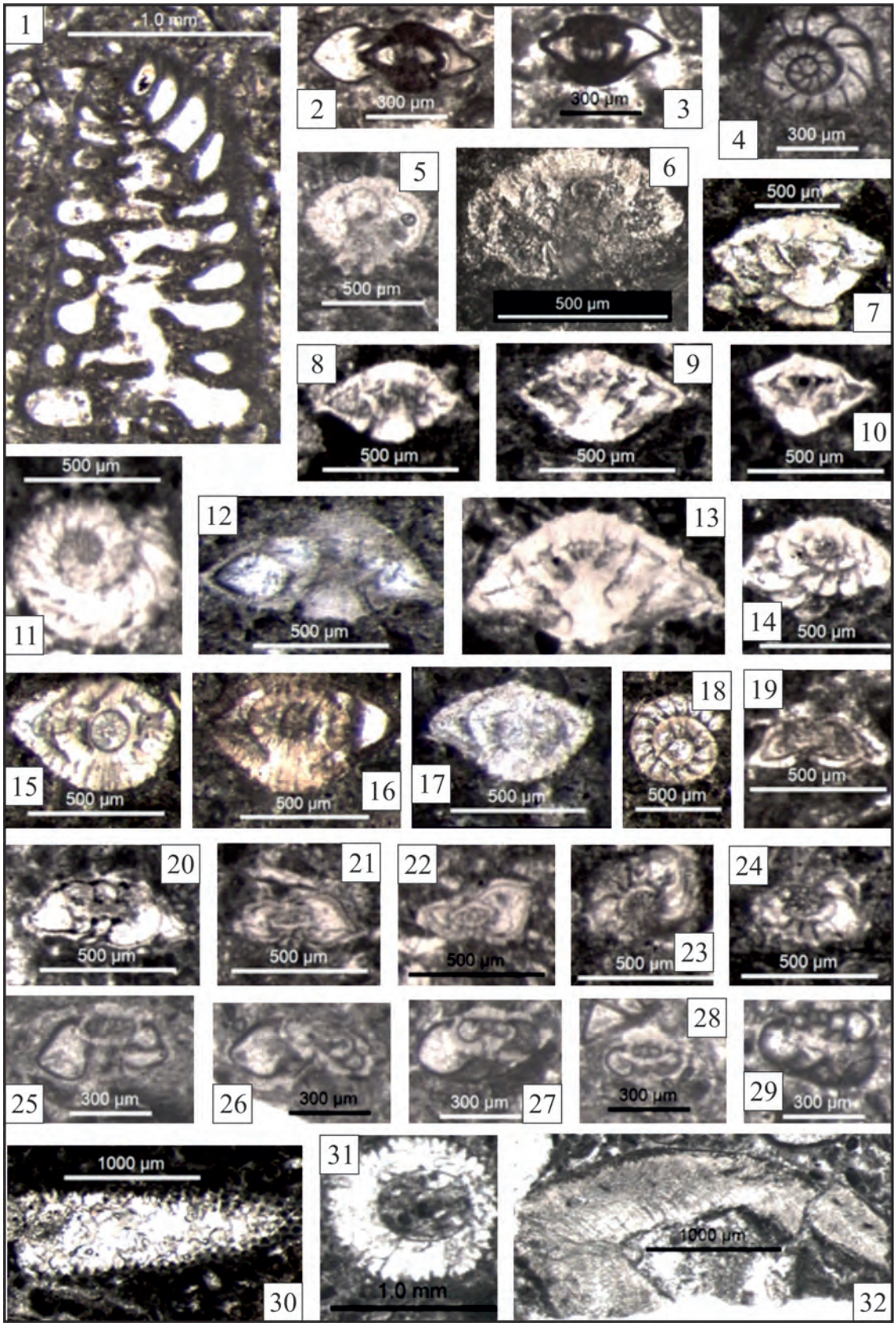
1
1.0 mm
2
300 µm
3
300 µm
4
300 µm
5
500 µm
6
500 µm
500 µm
7
8
500 µm
9
500 µm
10
500 µm
500 µm
11
12
500 µm
13
14
500 µm
15
500 µm
16
500 µm
17
500 µm
18
500 µm
19
500 µm
20
500 µm
21
500 µm
22
500 µm
500 µm
23
24
500 µm
25
300 µm
26
300 µm
300 µm
27
28
300 µm
29
300 µm
1000 µm
30
31
1.0 mm
1000 µm
32

Bull. Min. Res. Exp. (2019) 158: 121-139

Bulletin of the Mineral Research and Exploration

http://bulletin.mta.gov.tr

A new species of *Nummulites* Lamarck (Nummulitidae, Foraminiferida) from Central Turkey

Ali DEVECİLER[a*]

[a]*Department of Geological Engineering, Ankara University, 06830, Ankara, Turkey*

Research Article

Keywords:
Foraminiferida, nummulitidae, middle eocene, *nummulites sireli* n. sp., Turkey.

Received Date: 01.01.2018
Accepted Date: 26.03.2018

ABSTRACT

A new nummulitid species Nummulites sireli n. sp. is described from the middle Lutetian of the Çayraz section, North of Haymana, South of Ankara, Turkey. The new species is referred to the *N. distans* group, of which six other species from the Haymana and Çiçekdağ regions of Central Anatolia are identified.

1. Introduction

Nummulites Lamarck, 1801 is one of the most studied larger benthic foraminiferal genus since the first paleontological investigations. In particular, the variations in its species and geographic distribution over Tethys region maket his genus an important index taxon for the late Thanetian to early Oligocene age (d'Archiach, 1850; Boussac, 1911; Doncieux, 1926; Lluca, 1929; Roveda, 1970; Blondeau, 1972; Schaub, 1981; Racey, 1995; Serra-Kiel et. al., 1998, Sirel and Deveciler, 2018)

The main purpose of this study is to describe *Nummulites sireli* n. sp. from the middle Lutetian (SBZ 14-15; Serra-Kiel et al., 1998) of the Çayraz section (north of Haymana, south of Ankara, central Turkey). In addition, four other relative species from the same locality (*Nummulites kaufmanni* Mayer-Eymar, 1877; *Nummulites polygyratus* Deshayes, 1838; *Nummulites nemkovi* Schaub, 1966; *Nummulites somaliensis* Nuttall and Brighton, 1931) and two others from the Çiçekdağ region (*N. distans* Deshayes, 1838; *Nummulites pratti* d'Archiac and Haime, 1853) are identified and compared in detail with *N. sireli* n. sp.. These species are considered to belong to the *N. distans* group *sensu* Schaub (1981) for their lateral and equatorial characteristics.

The Çayraz section (Figure 1-A, B), which is mainly composed of clayey limestone, marl, sandstone and sandy limestone, has been chosen as the reference section of Cuisian-Lutetian in Anatolian Peninsula by Sirel (2015) for its accessibility, completeness and rich benthic foraminiferal content (Figure 2). Because of these characteristics, it has been studied by many authors such as Hottinger (1960 a, b), Schaub (1962), Dizer (1964), Yüksel (1970), Gökçen (1976a, b), Sirel and Gündüz (1976), Ünalan et al. (1976), Toker (1979, 1980), Schaub (1981), Sirel et al. (1986), Koçyiğit (1991), Çiner et al. (1996), Özcan (2002), Özcan et al. (2007), Deveciler (2010), Sirel and Deveciler (2017) and Sirel and Deveciler (2018). Despite the abundance and diversity of nummulitids, only two species *Nummulites lehneri* Schaub (1962) and *Nummulites haymanensis* Schaub (1981) have their type locality here.

The other sampling area is located in the Çiçekdağ region of central Anatolia, Turkey (Figure 1-A). The general geological setting of this region can be divided into three main parts: Kırşehir massif, Ankara melange and post-Lower Cretaceous sediments (Şenalp, 1980). These different rock groups have been investigated by Birgili et. al. (1975), Erdoğan et. al. (1996), Akgün et. al. (2002), Akkiraz et. al. (2007) and Schweitzer et. al. (2007). The larger benthic foraminiferal content has not been studied in detail yet.

* *Corresponding author: Ali DEVECİLER, adeveci@eng.ankara.edu.tr*
https://dx.doi.org/10.19111/bulletinofmre.413708

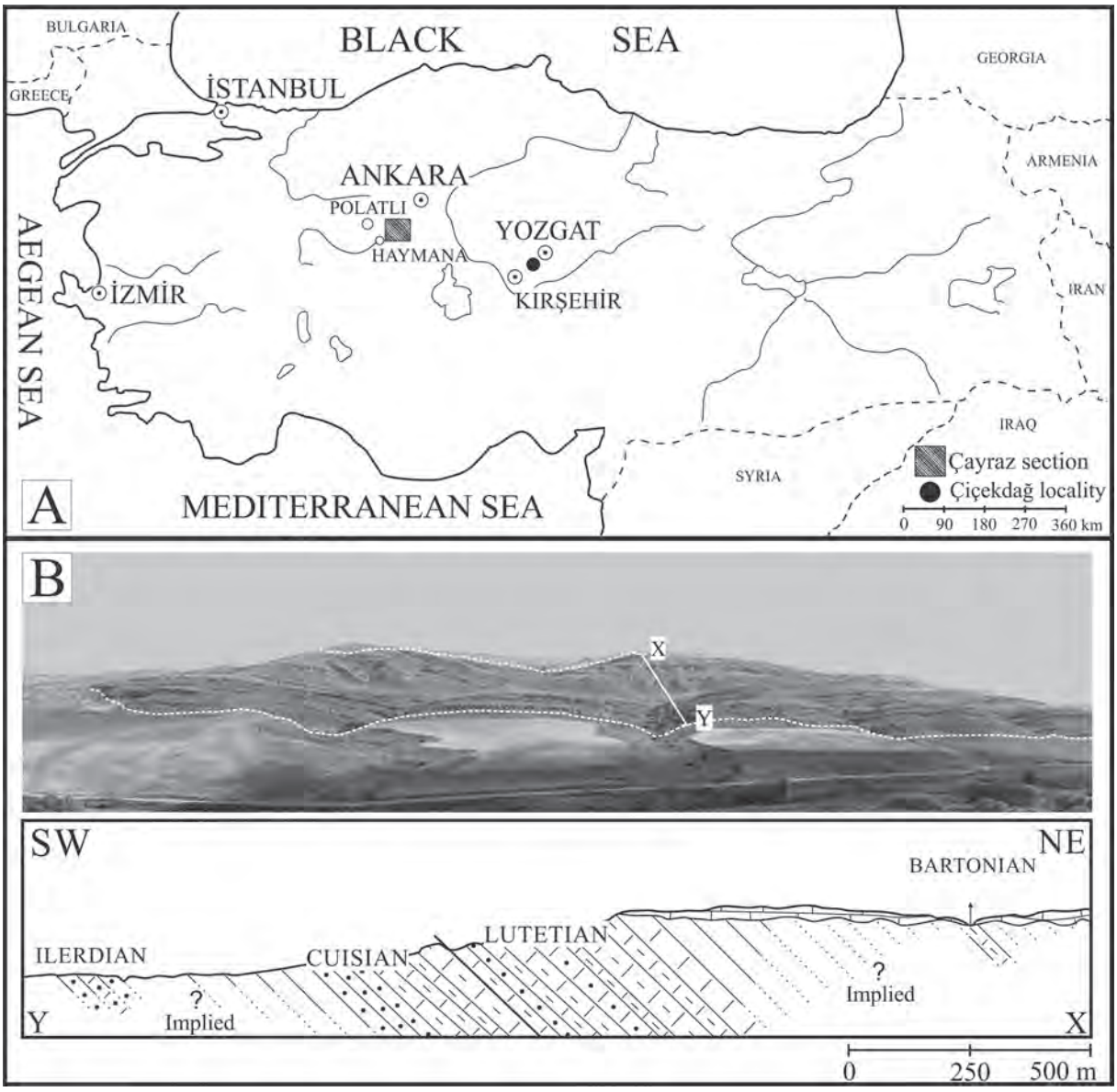

Figure 1- Location map of Çayraz section and Çiçekdağ locality (A) and the cross section of Çayraz succession (B).

2. Materials and Methods

All materials used in this study, except for *N.* distans and *N. pratti*, were collected from the argillaceous limestone and limestone series of the Çayraz locality (Figure 1-B; GPS reference: 36S 460078E – 4370296N) within the scope of the author's PhD Thesis (Deveciler, 2014). Specimens of *N. distans* and *N. pratti* from the Çiçekdağ region (GPS reference: 36S 641643E – 4382508N) were collected as a spot sample by Dr. Ercüment Sirel. Also, some of these materials except the specimens of *N. sireli* are discussed and illustrated in detail by Sirel and Deveciler (2018).

The twentytwo oriented thin sections were made from the free specimens of nummulitids of Çayraz and Çiçekdağ regions. Photographs were taken via Leica binocular microscope mounted Leica camera in Paleontology Laboratory of Ankara University Geological Engineering. All the individual samples and oriented thin sections are deposited in the collection of Ankara University, Faculty of Engineering, Department of Geological Engineering.

3. Systematic Paleontology

Order: Foraminiferida Eichwald, 1830

Family: Nummulitidae Blainville, 1825

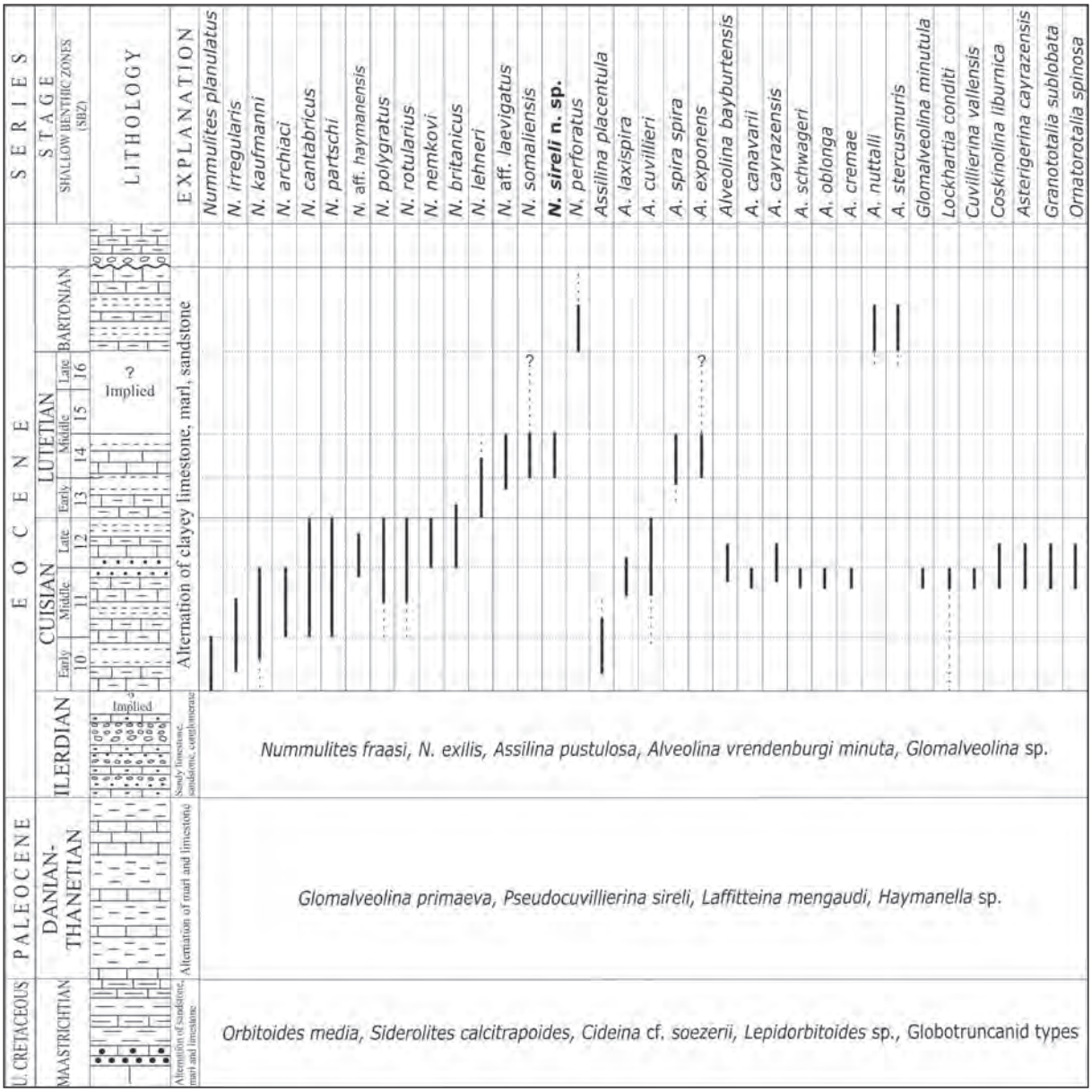

Figure 2- Biostratigraphic distributions of the nummulitid species in Çayraz section, modified after Sirel and Gündüz (1976), Deveciler (2010, 2014), Sirel (2015) and Sirel and Deveciler (2017) (not to scale).

Genus: *Nummulites* Lamarck, 1801

Type species: *Camerina laevigata* Bruguiére, 1792

Group: *Nummulites distans* sensu Schaub, 1981

Description: This group is characterized by lenticular to flat test with an undulated margin (Plate 1, Figures 2-4; Plate 2, Figures 4, 6; Plate 3, Figures 5, 11; Plate 4, Figures 2-3; Plate 5, Figure 3). Septal filaments are thin, curved, turbulanted and mostly meandric (Plate 1, Figure 6; Plate 2, Figures 2, 7; Plate 4, Figure 5; Plate 5, Figure 2). The surface is covered by small granules. Some species have a central knob in the center of the test (Plate 1, Figures 2-4, 11; Plate 4, Figures 2-3; Plate 5, Figures 3). The spire is irregular (Plate 2, Figures 1) or semi-irregular (Plate 2, Figures 5, 8). The septa are observed as thin, curved and undulated as from adult stage. Schaub (1981) defined nine species under *N. distans* group including *N. haymanensis*, *N. nemkovi*, *N. kaufmanni*, *N. distans*, *N. alponensis*, *N. polygyratus*, *N. millecaput*, *N. maximus* and *N. dufrenoyi* of Cuisian-Lutetian age. Unlike in Schaub (1981) *N. pratti* d'Archiac and Haime and in addition *N. somaliensis* Nuttal and

Bringhton are counted in this group because of their lateral and equatorial characteristics.

Nummulites sireli n. sp.

(Plate. 1, Figures 1-12)

1948 *Nummulites montefriensis* Douvillé, Doncieux, page 21, plate 2, figures 17-22.

2014 *Nummulites* sp. 3, Deveciler, page 63-64, plate 11, figures. 12-22; plate 12, figures 1-6.

Derivation of name: After Dr. Ercüment Sirel (Ankara University), for his seminal contributions on the systematics of larger benthic foraminifera fossil.

Holotype: Equatorial section of microspheric form illustrated in Plate 1, Figure 1. (label Cay 2/3/15).

Paratypes: Five microspheric and six megalospheric forms (Plate 1, Figures 2-12; labels are given in Plate 1).

Material: Twentyfour oriented thin sections and free specimens of holotype and paratypes from the Çayraz section.

Depository: Holotype and paratypes are deposited in the collection of Ankara University Department of Geological Engineering (Ankara, Central Turkey).

Type locality: Çayraz section, NW of Çayraz village, NE of Haymana, SW of Ankara, Central Turkey.

Type level: Middle Lutetian (SBZ 14-15).

Description: The microspheric (B-form) generation has a flat test and rounded periphery. The surface is generally straigth but, in some specimens it can be slightly undulated. Small granules are barely visible on abraded samples. Meandering septal filaments continue towards the periphery as slightly curved (Plate 1, Figure 6). The central knob disappears after the adult stage and than it cannot be observed on the surface (Plate 1, Figure 2-4). The equatorial diameter ranges between 16.6-23 mm, and the axial thickness is between 2.5-3.2mm. The first four whorls of the nepionic stage are 1.9-1.6 mm. After this stage the gap between the whorls increases gradualy and stays constant. The spire is thick and slightly irregular. There are 14-15 whorls in diameter of 10 mm. Curved septa are thin and undulated in the adult stage. Average height-length ratio (h/l) of the chambers is between 1.5-2. The septa count in the first 10 whorls of four specimens: 2nd- 25; 3rd- 28-32; 4th- 33; 5th- 34-38; 6th- 36-40; 7th- 45; 8th- 48-50; 9th- 54; 10th- 58-62.

The megalospheric (A-form) generation has a lenticular test with a pointed periphery (Plate 1, Figure 12). The central knob can be observed on the surface (Plate 1, Figure 7). Septal filaments are slightly curved. The equatorial diameter is between 2.5-3mm, the axial thickness is 1.3-1.4mm. The ovoid proloculus has a diameter between 0.25-0.35mm. After the proloculus, whorl height increases slowly. The spire is regular. There are four whorls in a diameter of 1.2 mm. Slightly bent septa join to the previous whorl upright. Average height-length ratio (h/l) of the chambers is between 1-1.76. The septa count in three whorls of four specimens: 1st, 11; 2nd, 23; 3rd, 26.

Remarks: *N. sireli* n. sp. shows the main characteristics of *N. distans* group by its size, outher view and coiling properties. *N. sireli* n. sp. differs from *N.somaliensis* Nuttal and Bringhton (Plate 2, Figures 1-4) with its flat test, much regular and tight spire and apparent central knob in its axial sections. *N. kaufmanni* Mayer-Eymar (Plate 3, Figures 1-5) is more irregular in coiling and lenticular in shape than *N. sireli* n. sp.. *N. nemkovi* has the similar equatorial characteristics with *N. sireli*, however it has a lenticular test with swollen center, and curved-turbulented septal filaments (Plate 2, Figures 5-8). *N. polygyratus* Deshayes (Plate 3, Figures 6-11) is different from *N. sireli* n. sp. with its multiple spire growth, tight coiling, elongated lenticular test and closely aligned curved septa. *N. distans* Deshayes (Plate 4, Figures 1-10) and *N. pratti* d'Archiac and Haime (Plate 5, Figures 1-7) are distinguished from *N. sireli* n. sp. because of their lax and irregular spire and their larger equatorial diameters. (Figure 3, Table 1).

In addition to the foregoing species, *N. haymanensis*

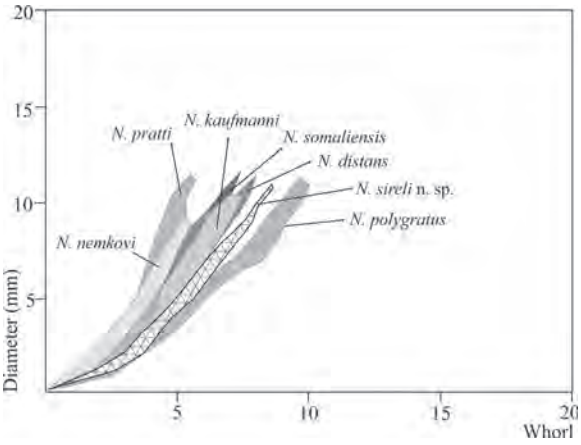

Figure 3- The spiral graph of the microspheric forms in this study.

Table 1- Comparison of the microspheric generations of *N. distans* group [the characteristics and biostratigraphic ranges of *Nummulites* species in the table is based on Nuttall and Brighton (1931), Schaub (1981), Racey (1995) and Serra-Kiel et al. (1998)].

Species	*N. kaufmanni* Mayer and Eymar, 1877	*N. nemkovi* Schaub, 1966	*N. distans* Deshayes, 1838	*N. pratti* d'Archiach and Haime, 1853	*N. polygyratus* Deshayes, 1838	*N. somaliensis* Nuttal and Brington, 1931	***N. sireli* n. sp.**
Shape of Test	Lenticular, sligtly pointed periphery	Lenticular, sligtly pointed periphery	Flat, thin lenticular, rounded periphery	Flat, thin lenticular, rounded periphery	Discoid lenticular, pointed perphery	Discoid lenticular, pointed perphery	Flat, thin lenticular rounded perihery
Granulation	Absent	Very small	Very small	Very small	Very small	Very small	Very small
Central Knob	Absent	Absent	Prensent	Prensent	Absent	Absent	Present
Diameter/Thickness	**22.8 mm** (lectotype in Schaub, 1981) 17.6-22.6/5.8-7 mm (present work)	**14.8 mm** (holotype in Schaub, 1981) 14.7-18.2/3.2-4.5 mm (present work)	**38.4 mm** (lectotype in Schaub, 1981) 32-35/2.8-3.2 mm (present work)	**39.2 mm** (neotype in Schaub, 1981) 35-36/2.52 mm (present work)	**32 mm** (lectotype in Schaub, 1981) 28.8-30.4/4.4 mm (present work)	**23 mm** (average) (lectype in Nut. and Br., 1931) 19.5-25/3-4mm (present work)	**23 mm** (holotype) 19.5-25/3-4 mm (paratypes)
Count of Whorls	**14 (in 20 mm diam.)** (lectotype in Schaub, 1981) 13-14 (in 20 mm diam.) (present work)	**10 (in 14 mm diam.)** (holotype in Schaub, 1981) 9-10 (in 14 mm diam.) (present work)	**12 (in 20 mm diam.)** (lectotype in Schaub, 1981) 12-13 (in 20 mm diam.) (present work)	**8 (in 20 mm diam.)** (neotype in Schaub, 1981) 8-10 (in 20 mm diam.) (present work)	**15 (in 20 mm diam.)** (lectotype in Schaub, 1981) 18-19 (in 20 mm diam.) (present work)	**12-13 (in 22.8 mm diam.)** (cotype in Nut. and Br., 1931) 11-12 (in 20 mm diam.) (present work)	**15 (in 20 mm diam.)** (holotype) 14-15 (in 20 mm diam.) (paratypes)
Stratigraphic Distribution	early-middle Cuisian SBZ 10-11 Present work: SBZ 10-11	late Cuisian SBZ 12 Present work: SBZ 12	middle-late Cuisian SBZ 11-12 Present work: SBZ 11-12	middle-late Cuisian SBZ 11-12 Present work: SBZ 11-12	middle-late Cuisian SBZ 11-12 Present work: SBZ 11-12	middle-late Lutetian SBZ 14-16 Present work: SBZ 14	middle Lutetian SBZ 14

Schaub (1981, plate 66, figure 11 (holotype)) from *N. distans* group differs from *N.* sireli n. sp. with its test shape and surface ornamentation. Furthermore other larger representatives of *N. distans* group including; *N. alponensis* Schaub (Schaub, 1981; plate 68, figure 14 (holotype)), *N. dufrenoyi* d'Archiac and Haime (Schaub, 1981; plate 69, figure 22 (lectotype)), *N. millecaput* Boubeé [Schaub, 1981; plate 68, figure 24 (neotype)] and *N. maximus* d'Archiac [Schaub, 1981; plate 69, figure 28 (lectotype)] are distinguished from *N. sireli* n. sp. with their tight spire.

N. sireli n. sp. shows identical characteristics with the figures of *Nummulites montefriensis* Douvillé (1906; page 212, plate XV, figures 1-8) in Doncieux (1948; plate II, figures 17-22) by its outer surface and equatorial sections. However, the equatorial section of the specimens figured by Doncieux (1948; figures 20-22) differ from that of the holotype of *N. montefriensis* Douvillé (plate XV, figure 7) because of their more regular and tight spire. Thus, the specimens figured by Doncieux (1948) are referred to here to *N. sireli* n. sp.

Stratigraphic distribution: Due to the co-occurrence of *N. lehneri*, *N.* aff. *laevigatus*, *N. somaliensis*, *Assilina exponens* and *A. spira spira* in the yellowish, hard clayey limestone beds of upper most of Çayraz section, the biostratigraphic age of *N. sireli* is considered in the middle Lutetian (SBZ 14-15).

4. Conclusions

The new nummulitid species here described as *Nummulites sireli* n. sp. is distinguished by its flat test with rounded periphery, small granules, a thin central knob and slightly irregular spire. It is associated with *N. lehneri*, *N.* aff. *laevigatus*, *N. somaliensis*, *Assilina exponens*, *A. spira spira* and *A. spira abrardı* in yellow colored clayey limestone beds of the middle Lutetian (SBZ 14) in the Çayraz section. Also the other five species of the *N. distans* group; *N. kaufmanni*, *N. distans*, *N. pratti*, *N. polygyratus*, *N. nemkovi* and *N. somaliensis* are identified for the first time from the middle Cuisian-middle Lutetian of central Anatolia, Turkey. These data are particularly significant for providing new paleobiogeographic and stratigraphic distributions of the *N. distans* group.

Acknowledgement

The author thanks to Prof. Dr. Johannes Pignatti for his valuable contributions and the linguistic improvement of the manuscript.

References

Akgün, F, Akay, E., Erdoğan, B. 2002. Tertiary terrestrial to shallow marine deposition in Central Anatolia: A palynological approach. Turkish Journal of Earth Science 11, 127-160.

Akkiraz, S.M., Sezgül, M., Akgün, F. 2007. Paleoecology of Coal-Bearing Eocene Sediments in Central Anatolia (Turkey) Based on Quantitive Palynological Data. Turkish Journal of Earth Science 17, 317-360.

Archiac, E. J. A. D. d'. 1850. Description des fossiles du groupe nummulititique recueillis par M.S.P. Pratt et M. J. Delbos aux environs de Bayonne et de Dax. Mémoires de la Société Géologie de France 2, 3, 397-456.

Birgili, S., Yoldaş, R., Ünalan, G. 1975. Çankırı-Çorum havzasının jeolojisi ve Petrol olanakları. Maden Tetkik ve Arama Genel Müdürlüğü Raporu Rapor No: 5621, 78 p Ankara (unpublished).

Blondeau, A. 1972. Les Nummulites. De l'enseigment a la recherche des sciences de la terre, Paris: Vuibert 254 p, France.

Boussac, J. 1911. Etudes paléontologiques sur le Nummulitique Alpin. Carte Géologique Détaillées de France 9, 437 p. Paris.

Çiner, A., Deynoux, M., Ricou, S., Koşun, E. 1996. Cyclicity in the Middle Eocene Çayraz carbonate formation, Haymana Basin, Central Anatolia, Turkey. Palaeogeography, Palaeoclimatology, Palaeoecology 121, 313-329.

Deveciler, A. 2010. The first appearance of the Bartonian benthic foraminifera at the Çayraz Section (north of Haymana, south Ankara, central Turkey). Yerbilimleri 31, 3, 191-203.

Deveciler, A. 2014. Haymana-Polatlı havzası Nummulites Lamarck ve Assilina d'Orbigny (Nummulitidae familyası) türlerinin tanımlaması ve bunların biyostratigrafisi. PhD thesis, Ankara Üniversitesi Fenbilimleri Enstitüsü, 132 p. Ankara (unpublished).

Dizer, A. 1964. Sur quelques Alveolines de l'Eocene de Turquie. Revue de Micropaléontologie 7, 4, 265-279.

Doncieux, L. 1926. Catalogue descriptif des fossiles nummulitiques de l'Aude et de l'Hérault. Deuxième partie (Fascicule 3) Corbières septentrionales. Annales de l'Université de Lyon I, 45, 80 p. France.

Doncieux, L. 1948. Les foraminiféres Éocénes et oligocénes de l'ouest de Madagascar. Annales Géologiques du Service des Mines 13, 8-33.

Douvillé, R. 1906. Esquisse géologique des Préalpes subbétiques (partie centrale). Paris, H. Bouillant. 215 p France.

Erdoğan, B., Akay, E., Uğur, M. S. 1996. Geology of Yozgat region and evolution of the collisional Çankırı Basin. International Geology Review 38, 788-806.

Gökçen, S.L. 1976*a*. Ankara-Haymana güneyinin sedimantolojik incelemesi I: Stratigrafi birimleri ve tektonik. Yerbilimleri, 2, 161-200.

Gökçen, S.L. 1976*b*. Ankara-Haymana güneyinin sedimantolojik incelemesi II: Sedimantoloji ve paleoakıntılar. Yerbilimleri, 2, 201-236.

Hottinger, L. 1960*a*. Recherches sur les Alveolines du Paleocene et de Eocene. Mémoires Suisses de Paléontologie. 242 p.

Hottinger, L. 1960*b*. Über Paleocaene und Eocaene Alveolinen. Eclogae Geologicae Helvetiae 53, 1, 265-283.

Koçyiğit, A. 1991. An example of an accretionary forearc basin from northern Central Anatolia and its implications for the history of subduction of Neo-Tethys in Turkey. Geological Society of America Bulletin 103, 22-36.

Llueca, G. F. 1929. Los Numulítidos de España. Comisión de Investigaciones Paleontológicas y Prehistóricas 36, 8, 1-400, Madrid.

Nuttall, W.L.F., Bringhton, A.G. 1931. Larger foraminifera from the Tertiary of Somaliland. Geological Magazine 68, 49-65.

Özcan, E. 2002. Cuisian orthophragminid assemblages (Discoctclina, Orbitoclypeus, Nemkovella) from Haymana-Polatlı basin (central Turkey): biometry and description of two new taxa. Eclogae Geologicae Helvetiae 95, 75-97.

Özcan, E, Less, Gy., Kertesz, B. 2007. Late Ypresian to middle Lutetian orthophragminid record from central and northern Turkey: taxonomy and remarks on zonal scheme. Turkish Journal of Earth Science 16, 281-321.

Racey, A. 1995. Lithostratigraphy and larger foraminiferal (nummulitid) biostratigraphy of the Tertiary of northern Oman. Micropaleontology 41, 1-123.

Roveda, V. 1970. Revision of the Nummulites (Foraminiferida) of the N. fabianii-fichteli group. Rivista Italiana di Paleontologia e Stratigrafia 76, 2, 235-324.

Schweitzer, C.E., Shirk, A.M., Cosovic, V., Okan, Y., Feldman, R.M., Hoşgör, İ. 2007. New species of Harpactocarcinus from the Tethyan Eocene and their paleoecological settings. Journal of Paleontology 81, 5, 1091-1100.

Serra-Kiel, J., Hottinger, L., Caus, E., Drobne, K., Ferrandez, C., Jauhri, A.K., Pavlovec, R., Pignatti, J., Samso J. M., Schaub, H., Sirel, E., Strougo, A., Tambareau, Y., Tosquella, J., Zakrevskaya, E. 1998. Larger foraminiferal biostratigraphy of the Tethyan Paleocene and Eocene. Bulletin de la Societe Géologique de France 169, 2, 281-299.

Schaub, H. 1962. Über einige stratigraphich wichtige Nummuliten-Arten. Eclogae Geologicae Helvetiae 55, 2, 529-551.

Schaub, H. 1981. Nummulites et assilines de la Tethys Paleogene: taxonomie, phylogenese et biostratigraphie. Mémoires Suisses de Paléontologie, Muséum d'Histoire Naturelle. 104/105/106, 1-236.

Sirel, E. 2015. Reference sections and key localities of the Paleogene Stage and Discussion C-T, P-E and E-O boundaries by the very shallow-shallow water Foraminifera in Turkey. Ankara Üniversitesi Basımevi. 171 p.

Sirel, E., Gündüz, H. 1976. Haymana (G Ankara) yöresi İlerdiyen, Küiziyen ve Lütesiyen' deki Nummulites, Assilina ve Alveolina cinslerinin bazı türlerinin tanımlamaları ve stratigrafik dağılımları. Türkiye Jeoloji Kurumu Bülteni 19, 31-44.

Sirel, E., Dağer, Z., Sözeri, B. 1986. Some biostratigraphic and paleogeographic observations on the Cretaceous/Tertiary boundary in the Haymana Polatlı region (Central Turkey). Walliser O. (Ed.). Global Bio-Events: Lecture Notes in Earth Sciences 385-396.

Sirel, E., Deveciler, A. 2017. A new late Ypresian species of Asterigerina and the first records of Ornatorotalia and Granorotalia from the Thanetian and upper Ypresian of Turkey. Rivista Italiana di Paleontologia e Stratigrafia 123, 1, 65-78.

Sirel, E., Deveciler, A. 2018. Description and some revision of Ranikothalia Caudri, Nummulites Lamarck and Assilina d'Orbigny species from Thanetian – early Chattian of Turkey. Ankara Üniversitesi Yayınevi. 182 p.

Şenalp, M. 1980. Çankırı-Çorum havzasının Sungurlu bölgesindeki Eosen yaşlı türbidit, olistostrom ve olistolit fasiyesleri. Maden Tetkik ve Arama Enstitüsü Dergisi, 93/94, 27-53.

Toker, V. 1979. Haymana yöresi (GB Ankara) Üst Kretase Planktonik Foraminifera' ları ve biyostratigrafi incelemesi. Türkiye Jeoloji Kurumu Bülteni 22, 121-134.

Toker, V. 1980. Nannoplankton biostratigraphy of the Haymana region (SW Ankara). Bulletin of Geological Society of Turkey 23, 165-177.

Ünalan, G., Yüksel, V., Tekeli, T., Gönenç, O., Seyirt, Z., Hüseyin, S. 1976. Haymana Polatlı yöresinin (GB Ankara) Üst Kretase-Alt Tersiyer stratigrafisi ve paleocoğrafik evrimi. Türkiye Jeoloji Kurumu Bülteni 19, 159-176.

Yüksel, S. 1970. Etude géologique de la région d' Haymana (Turquie Centrale). PhD thesis, Faculté des Sciences de L'Université de Nancy, 179 p. France.

PLATES

PLATE - I

Nummulites sireli n. sp.; all figures from middle Lutetian of Çayraz section, compiled from Deveciler (2014);

Figure 1- Centred equatorial section of B-form (Cay 2/3/15-holotype).

Figure 2- Axial section of B-form showing the central knob at the center of the test and the thin pillars (Cay 2/3/11).

Figure 3- Centred axial section of B-form (Cay 2/2/12).

Figure 4- Axial section of B-form (Cay 2/2/13).

Figure 5- Centred equatorial section of B-form (Cay2/3/16).

Figure 6- Lateral view of B-form showing meandering septal filaments and small granules on the edge of the surface (Cay 2/2/5).

Figure 7- Outer view of A-form showing radial septal filaments and central knob on the surface (Cay 2/2/1a).

Figure 8- Centred equatorial section of A-form showing proloculus (Cay 2/2/14).

Figure 9- Equatorial section of A-form (Cay 2/2/4).

Figure 10- Equatorial section of A-form (Cay 2/2/90).

Figure 11- Equatorial section of A-form (Cay 2/2/91).

Figure 12- Axial section of A-form showing central pillar (Cay 2/2/1b).

PLATE - I

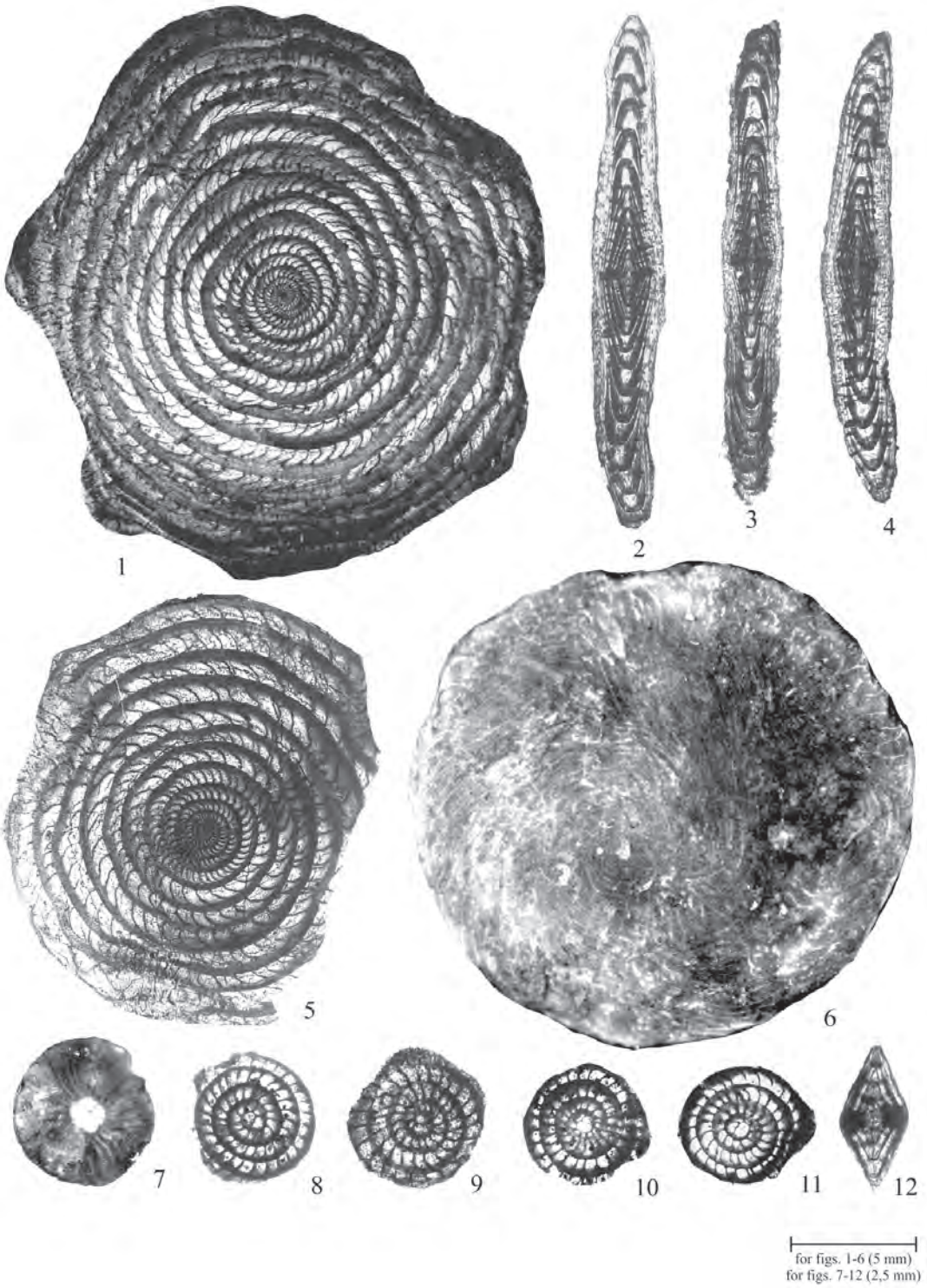

PLATE - II

Nummulites somaliensis Nuttall and Bringhton, 1931; all figures from middle Lutetian of Çayraz section, compiled from Deveciler (2014);

Figure 1- Centred equatorial section of B-form (Cay 2/3/7).

Figure 2- Outher view of B-form showing meandering septal filaments and thin granules on the surface (Cay 2/1/66).

Figure 3- Equatorial section of B-form (Cay 2/1/69).

Figure 4- Axial section of B-form (Cay 2/3/10).

Nummulites nemkovi Schaub, 1966; all figures from late Cuisian of Çayraz section, compiled from Deveciler (2014);

Figure 5- Equatorial section of B-form (Cyzd 10/17).

Figure 6- Axial section of B-form (Cyzd 10/21b).

Figure 7- Lateral view (Cyzd8/1).

Figure 8- Equtorial section (Cyzd 8/5).

PLATE - II

PLATE - III

Nummulites kaufmanni Mayer-Eymar, 1877; all figures from early-middle Cuisian of Çayraz section, figure 1, 5 from Deveciler (2014), figure 2-4 from Sirel and Deveciler (2018);

Figure 1- Equatorial section of B-form (Cyzd17-6).

Figure 2- Equatorial section of A-form (ka6/3).

Figure 3- Equatorial section of A-form (ka5/2).

Figure 4- Axial section of A-form (ka/7).

Figure 5- Axial section of B-form (Cyzd17-8).

Nummulites polygyratus Deshayes, 1838; all figures from middle-late Cuisian of Çayraz section, figure 6, 11 from Deveciler (2014), figure 7-10 from Sirel and Deveciler (2018);

Figure 6- Equatorial section of B-form (Cyzd9/18).

Figure 7- Equatorial section of A-form, (Ç. 17/6).

Figure 8- Equatorial section of A-form, (Ç. 17/7).

Figure 9- Equatorial section of A-form, (Ç. 17/8).

Figure 10- Equatorial section of A-form, (Ç. 17/9).

Figure 11- Axial section of B-form (Cyzd12/31b).

PLATE - III

PLATE - IV

Nummulites distans Deshayes, 1838; all figures are from middle-late Cuisian of Çiçekdağ region, compiled from Sirel and Deveciler (2018);

Figrue 1- Equatorial section of B-form (K-11).

Figure 2- Axial section of B-form showing central knob (K-12).

Figure 3- Axial section of B-form (K-4).

Figure 4- Equatorial section of B-form (K-13).

Figure 5- Lateral view of A-form (K-5).

Figure 6- Equatorial section of A-form (K-8).

Figure 7- Equatorial section of A-form (K-6).

Figure 8- Equatorial section of A-form (K-8).

Figure 9- Axial section of A-form (K-9).

Figure 10- Axial section of A-form (K-10).

PLATE - IV

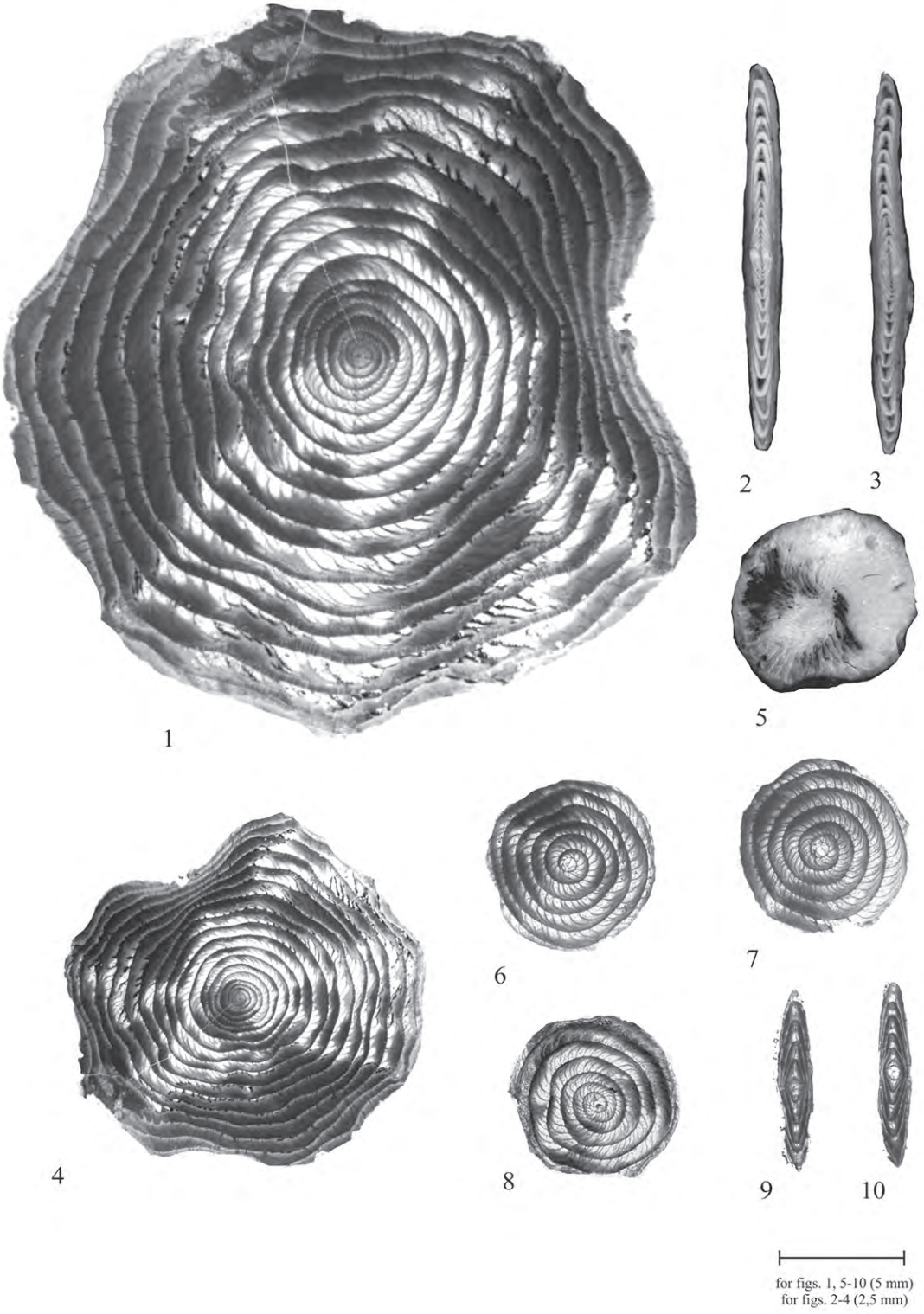

PLATE - V

Nummulites pratti d'Archiac and Haime, 1853; all figures are from middle-late Cuisian of Çiçekdağ region, compiled from Sirel and Deveciler (2018);

Figure 1- Equatorial section of B-form (Y-11).

Figure 2- Axial section (Y- 14).

Figure 3- External shape, showing turbulonant septal flaments (Y-17).

Figure 4- Equatorial section of A-form, (Y-15).

Figure 5- Axial section of A-form (Y-16).

Figure 6- Equatorial section of A-form (Y-12).

Figure 7- Equatorial section of A-form (Y-18).

PLATE - V

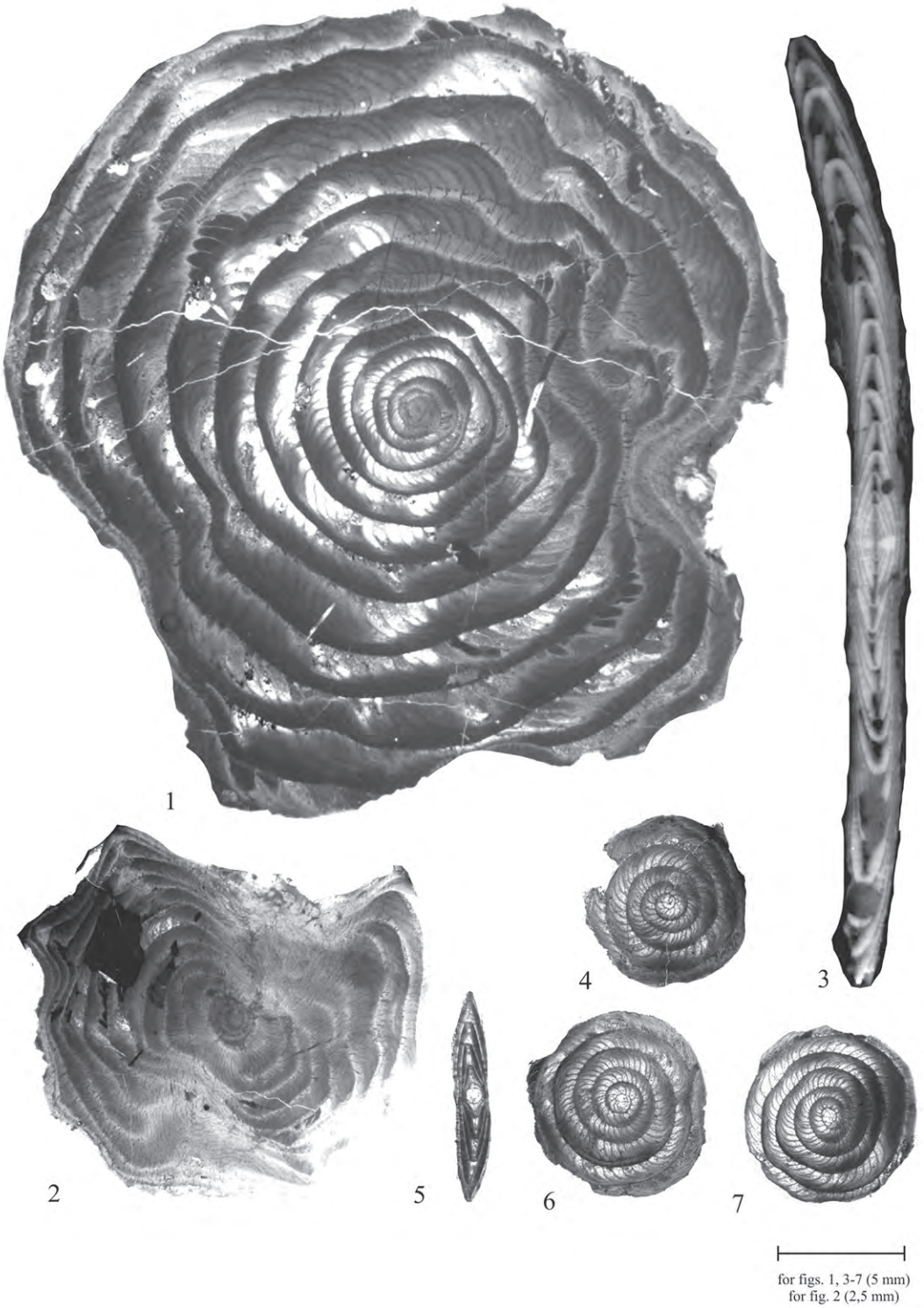

Bull. Min. Res. Exp. (2019) 158: 141-164

Bulletin of the Mineral Research and Exploration

http://bulletin.mta.gov.tr

Mineralogy, petrography and origin of hydrothermal alteration in Eocene magmatites in Central Anatolia (Sivas-Turkey)

Zeynel BAŞIBÜYÜK[a*] and Hüseyin YALÇIN[b]

[a] *Ahi Evran Üniversitesi Mühendislik Mimarlık Fakültesi Jeoloji Mühendisliği Bölümü Kırşehir, orcid.org/0000-0003-2845-148X*
[b] *Cumhuriyet Üniversitesi Mühendislik Fakültesi Jeoloji Mühendisliği Bölümü Sivas, orcid.org/0000-0001-9539-281*

Research Article

Keywords:
Alteration zones and types, plutonic, volcanic, XRD, SEM.

ABSTRACT

Three different types of hydrothermal alterations have occurred in the Eocene magmatics of the northern part of Sivas-Turkey which include propylitic phyllic / sericitic and argillic. Hydrothermal alteration affected both Karataş volcanites and Kösedağ syenite. The clay formations are concentrated in two major zones; extending in NE-SW direction and intersecting both plutonic and volcanic rocks with circular opening cracks within the volcanics parallel to the plutonic-volcanic contact. Hypogene and supergene hydrothermal alteration products occurring on surface and/or near surface conditions represent the primary and secondary minerals that develop directly and mostly from feldspars with the mechanisms of neoformation and/or degradation. The hypogene minerals are formed in two stages of early (kaolinite, pyrophyllite, illite, I-S (illite-smectite), smectite, quartz and opal-CT) and late (barite, ore minerals, alunite, goyazite, jarosite, chlorite and C-S). Tourmaline, epidote and carbonates (calcite, dolomite, azurite and malachite) are considered as metasomatic and supergeneous minerals, respectively. The most common mineral paragenesis are kaolinite + quartz + goethite + goyazite or alunite, kaolinite + quartz + jarosite + feldspar ± goethite and/or goyazite in the argillic alteration zone, I-S + quartz + jarosite ± goethite ± feldspar as well as I-S + quartz + feldspar minerals in the sericitic alteration zone. Kaolinite (T) is mostly in the form of pseudohexagonal platies, I-S (R1, R3 as argillic alteration origins, $1M_d$, 2M1, 1M and R3 as sericitic alteration origins) forming fiber-acicular bundles parallel to each other.

Received Date: 16.11.2017
Accepted Date: 04.02.2018

1. Introduction

The reason why hydrothermal alterations that occur in magmatic rocks are important is not only for their scientific meaning but also the fact that they form important clay deposits that can be used as industrial raw materials. In the study area, there is a wide range of hydrothermal alteration zone (propylitic, phyllic/sericitic and argillic) that affects both Karataş volcanites and Kösedağ syenite. The argillic alteration zone contains kaolinite formations, which is an industrial raw material with a wide range of applications in the industry. In addition to the hydrothermal alteration of kaolinite, it can also form important deposits in sedimentary formations (Murray and Smith, 1973; Murray, 1988; Murray and Keller, 1993; Domínguez and Murray, 1995; 1997; Karakaya et al., 2001; Arslan et al., 2006; Cravero et al., 2010; Yıldız and Başaran, 2015; Ariana et al., 2016; Ünal Ercan et al., 2016). Turkey has many kaolinite deposits formed as a result of hydrothermal alteration (Gençoğlu et al., 1989; Yalçın, 1991; Şener and Gevrek, 2000; Karakaya-Çelik et al., 2001; Yalçın and Bozkaya, 2003; Ece and Nakagawa, 2003; Ece et al., 2003; Ece and Schroeder, 2007; Ece et al., 2008; Kadir and Akbulut, 2009; Kadir et al., 2011, 2014; Acarlıoğlu et al., 2013; Ece et al., 20013; Kadir and Erkoyun, 2013).The kaolinite formations in the study area show differences from sedimantary and metamorphic rocks-hosted other formations with respect to hydrotermal alteration variety and whole rock and clay mineral assemblages.

** Corresponding author: Zeynel BAŞIBÜYÜK, zbasibuyuk@ahievran.edu.tr*
http://dx.doi.org/10.19111/bulletinofmre.461255

In order to better understand the mechanism of the hydrothermal alteration of the Eocene magmatics in the Sivas basin, it is necessary to look at the geological evolution of Anatolia and hence the area studied. The Central Anatolian region in which the study area is located consists of continental blocks separated from each other by ophiolitic suture zones. These tectonic belts are, from the north to the south, Pontide Continent, Intra-Pontide Suture, Sakarya Continent, Ankara-Yozgat-Erzincan Suture (Central Anatolian Metamorphites) and the Kırşehir Continent (Central Anatolian Metamorphics) (Figure 1), and the continental blocks developed as a result of Pan-African, Hercynian and Cimmerian orogenies and remained as the continental basement during the Neo-Tethyan evolution (Tüysüz, 1993).

The Neo-Tethys Ocean was opened by rifting of these continental bases along two lines in Lias, so that the Intra-Pontide and Ankara-Yozgat-Erzincan Ocean branches developed (Şengör and Yılmaz, 1981). At the beginning of the Late Cretaceous, a subduction started along the entire Pontide belt (Şengör and Yılmaz, 1981); in other words, the northern branch

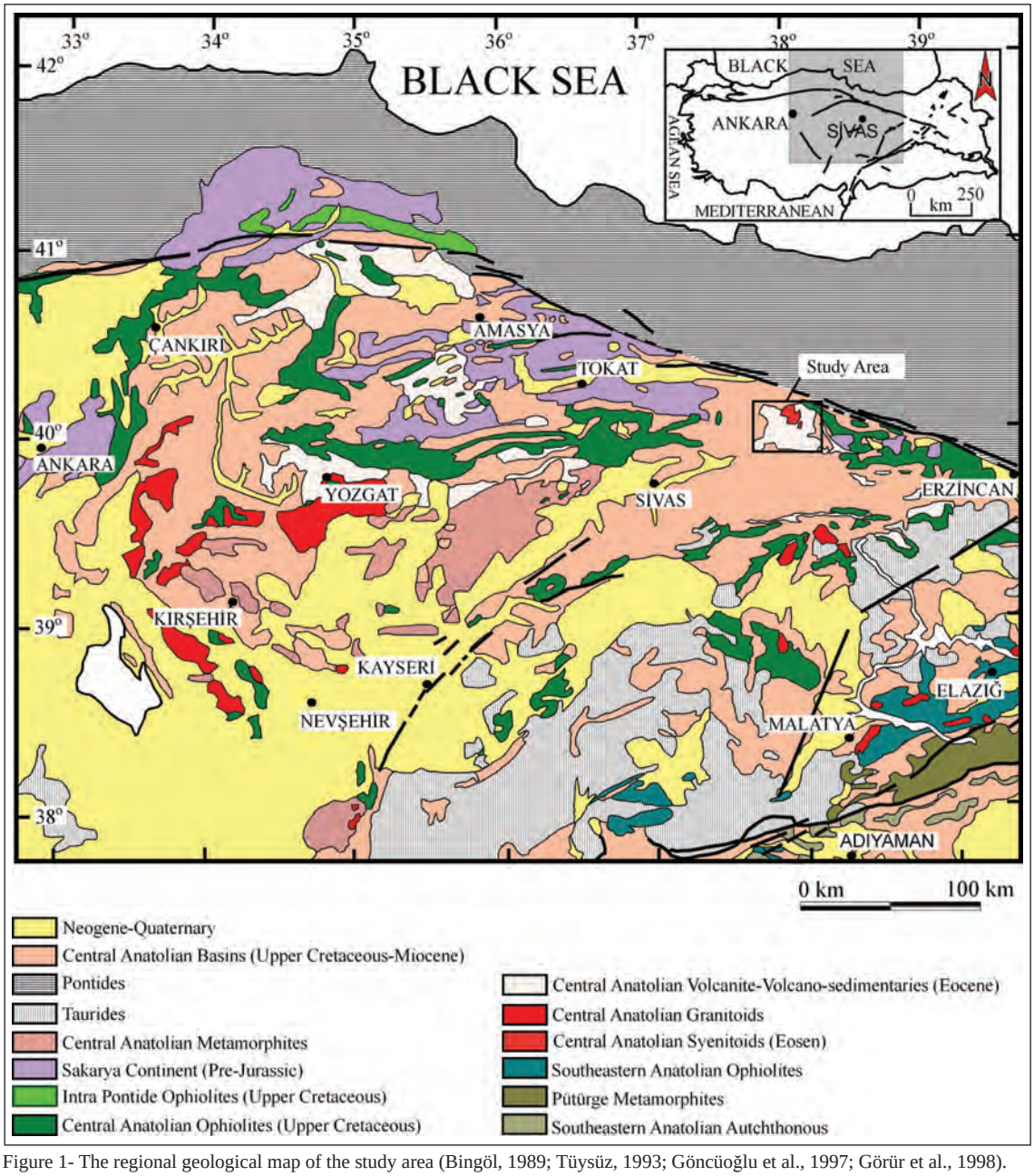

Figure 1- The regional geological map of the study area (Bingöl, 1989; Tüysüz, 1993; Göncüoğlu et al., 1997; Görür et al., 1998).

of Neo-Tethys began to subduct under the Pontide. During this period, the greatest ophiolitic nappes including Refahiye Complex, which is the oldest unit of the study area, was settled on Anatolide-Tauride continent (Şengör and Yılmaz, 1981, Göncüoğlu et al., 1997). In the Paleocene-Early Eocene, the northern branch of the Neo-Tethys was completely closed and the continent-continent collision (Şengör and Yılmaz, 1981) took place.

After the continent-continent collision, while the cold and high density oceanic crust is subducing into the asthenosphere producing a great force downward, the continental crust showed resistance to subduction and produce a stress effect in the bending zone (the subducting lithosphere and continental crust merging zone) (Davies and Blanckenburg, 1995). As a result, a thin opening occurred at the region where tension was effective, and the asthenosphere ascended into this opening, which continued until the oceanic crust had completely detached (Kusznir and Park, 1987, Davies and Blanckenburg, 1995). When previous researchers explain the geodynamic evolution of the study area and its immediate surroundings (Boztuğ and Jonckheere, 2007; Boztuğ et al., 2007), they claim that this phenomenon has created extensional tectonics in the region and caused horst and graben formation in the continental crust, lastly the Middle-Late basin was developed as a result of this. In the Middle-Late Eocene volcanism (Karataş volcanites) is derived from upper mantle at the syn- and/or post-collision and mostly contaminated by upper mantle continental crust and Kösedağ volcanites which is related with extensional regime and belong to same magmatic sequence of events with hot-hot contact. During the settlement of Kösedağ syenite, extensive hydrothermal alterations occurred in both plutonic and volcanic rocks that it intruded.

2. Geology

The Upper Cretaceous-Paleocene aged Refahiye complex composed of peridotite and serpentinites (Figure 2) is the oldest unit in the region (Yılmaz

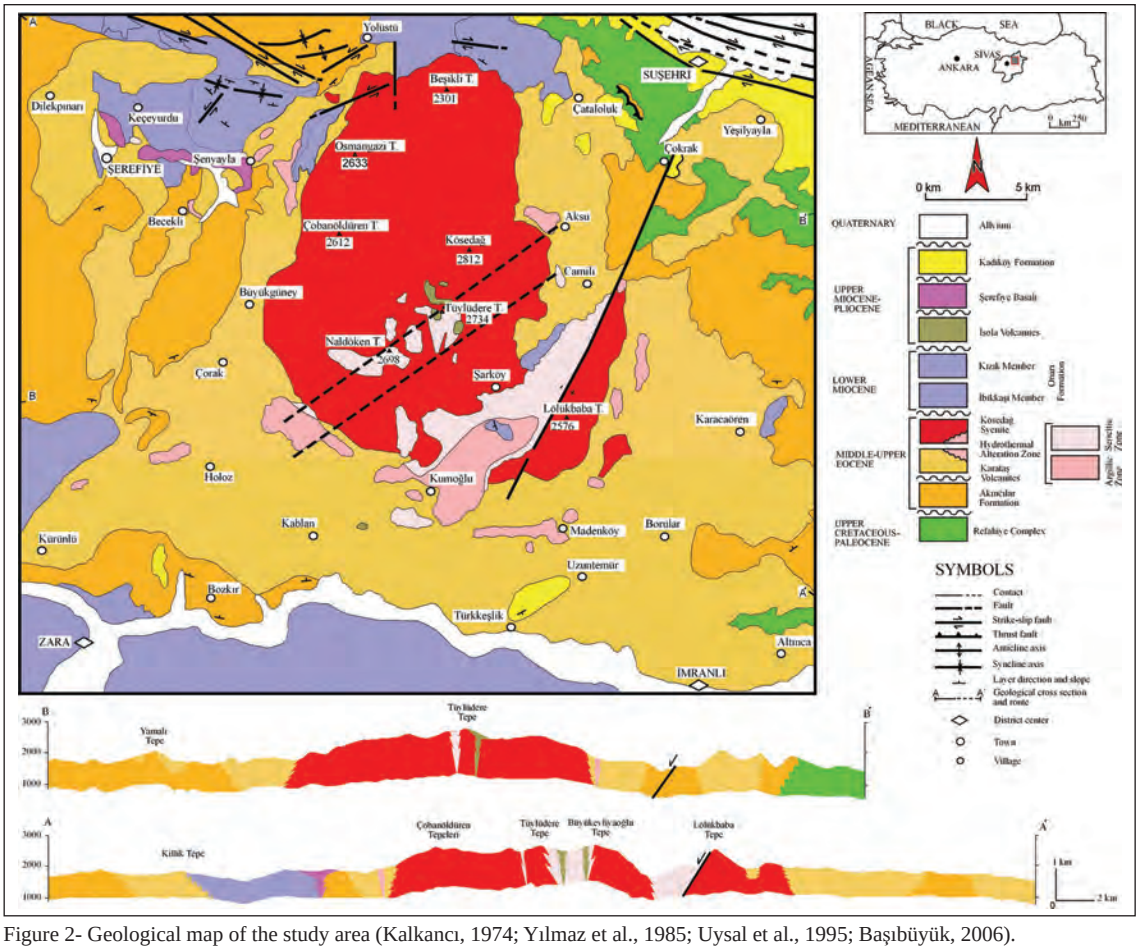

Figure 2- Geological map of the study area (Kalkancı, 1974; Yılmaz et al., 1985; Uysal et al., 1995; Başıbüyük, 2006).

et al., 1985). The Eocene magmatism in which the hydrothermal alteration occurred begins with Akıncılar formation with pyroclastic products. It continues with basaltic-trachytic lava flows belonging to Karataş volcanites, and ends up with Kösedağ syenite in shallow depths with hot-hot contact relation with alkaline feldspar syenite, syenite and quartz alkaline feldspar syenite, and partly monzonitic composition.

Plutonics with alkaline character, large scale upper continental crustal contamination and fractional crystallization of the upper mantle material, representing syn- or post-collisional plate magmatism, were found as 42 ± 4 m.a. for quartz syenite and 37 ± 2.6 m.a. for pegmatitic biotite syenite by previous researchers by analyzing Rb-Sr age determination (Kalkancı, 1974, 1978). The evaporation age of Kösedağ Syenite is determined with single zircon $^{207}Pb/^{206}Pb$ method as 52.1 ± 6.4 m.a. (Boztuğ et al., 2007). Hydrothermal alteration affected only Karataş volcanites and Kösedağ syenite. The age of the alteration was found to be 38.0 ± 0.9 million years with K/Ar radiometric dating from the alunite mineral (Başıbüyük, 2006). The clay formations are concentrated in two major zones. One of them is circle-shaped extending fractures in volcanics which are parallel to plutonic-volcanic contact. The second one is the zone that intersecting both NE-SW trending plutonics and volcanics. The age of alteration and the situation of the zones suggest that the alteration has occurred in the pegmatitic phase of the plutonic intrusion. Three types of hydrothermal alteration, propylitic, phyllic/serizitic and argillic, were distinguished in Kösedağ syenite and Karataş volcanites (Başıbüyük et al., 2007). Hydrothermal alteration levels are usually observed in zones of several km^2 (up to 30 km^2).

3. Material and Methods

376 samples were taken from the field studies in order to determine mineralogy of the alteration. 337 samples which are prepared in Cumhuriyet University Geological Engineering Department Thin Section Laboratory are studied to determine the rock-forming components and their textural features. 3 samples from altered levels are studied in Scanning Electron Microscope in Turkish Petroleum Cooperation in order to specify their textural relations and origin of clay minerals.

X-ray diffraction (XRD) analyzes were carried out with Rigaku DMAX IIIC model X-ray diffractometer to determine the polymorphic changes in the minerals and whole rock mineralogical compositions and clay size components of the submicroscopic rocks so small that they could not be studied with Optical microscope (OM) (XRD-TK: 356 samples, XRD-KF 283 samples). The whole rock and clay-size components (<2 mm) of the samples are defined with these analyzes and the semi-quantitative percentages are calculated based on the external standard method (Brindley, 1980). When determining the polytypes of pure or near pure kaolinite, illite, chlorite and pyrophyllite minerals, the identifier peaks which are suggested by Bailey (1980, 1988) and Fawcett et al. (1989) are used (kaolinite 4, chlorite 3, illite 2, pyrophyllite 1 sample). An alunite sample formed in the argillic alteration zone for K-Ar dating, with the aim of determining the age of the hydrothermal alteration, is analyzed in Activation Laboratories Ltd. (Actlabs) in Canada.

4. Research and Findings

4.1. Field Observations

4.1.1. Propylitic Alteration

Its distribution is very small and developed only in a few-meter zone within the volcanics at the plutonic-volcanic contact (Figure 3a). The plutonic rocks are observed in pinky skin colour, and they have very fine grain and holocrystalline texture, and the volcanic rocks are found in grayish light green with porphyritic texture.

4.1.2. Sericitic (Phyllic) Alteration

Such alterations have been extensively developed in Kösedağ syenite and rarely in Karataş volcanites. Its spread in the volcanics is not very much and observed as telescoping levels in the argillic alteration (Figure 3b). The outer appearance of the altered zones is light greenish yellowish color, soft and crumbly, and their thickness reaches up to 10 m.

Serizitic alteration has a very wide spread in syenites. It is characterized by a white-yellow-light brown appearance (Figure 3c). Sericitic alterations in the syenites includes NE-SW trending parallel barites with 0.15-1 m thick, light gray and black colored tourmaline veins rarely intersecting each others with 0.05-20 cm thick, yellowish red colored Fe-oxide coating levels, and orange-red colored oxidations (goethite) and sulphatization (jarosite) which are developed through fractures (Figure 3d).

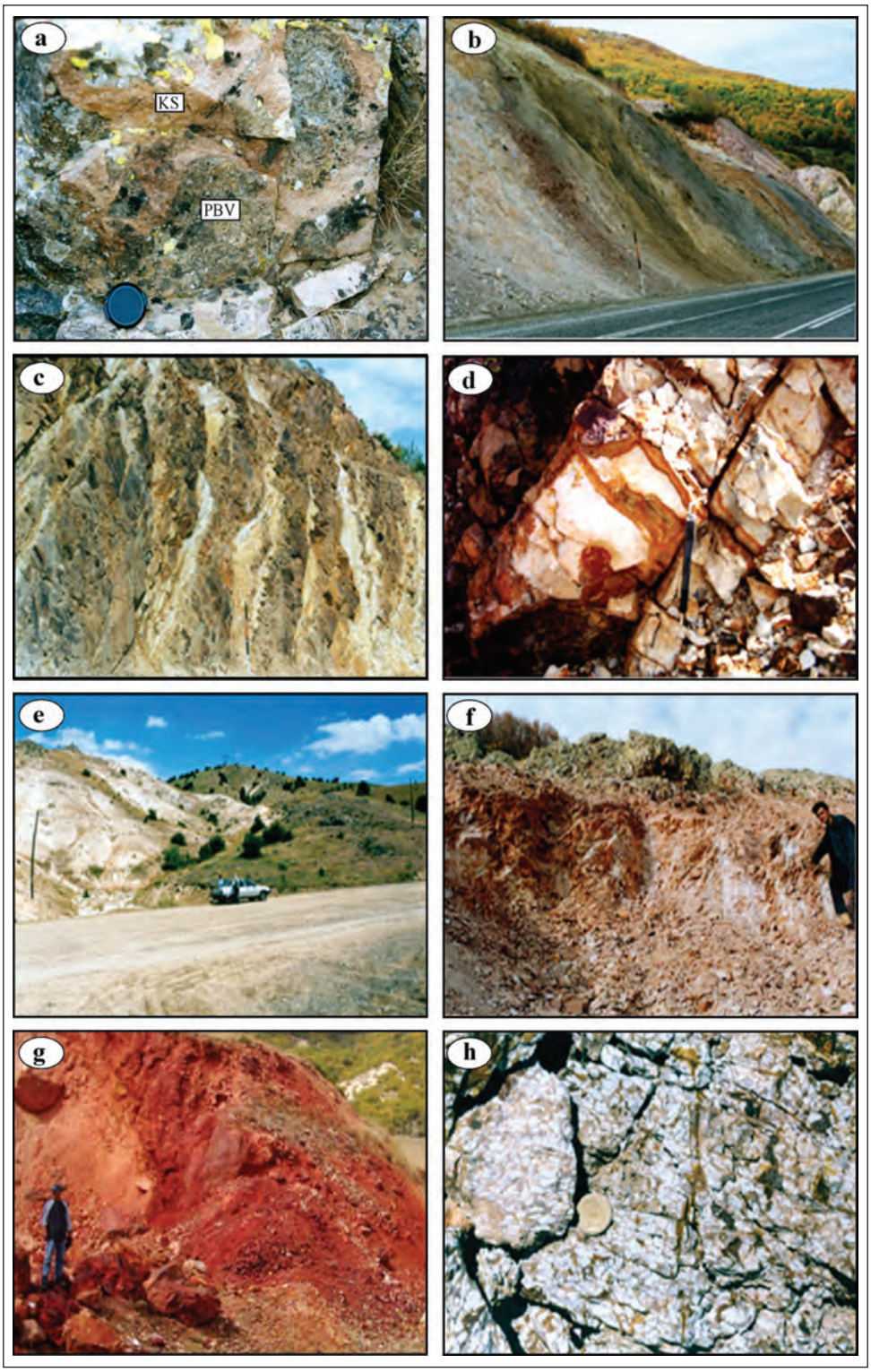

Figure 3- Field photographs of different hydrothermal alterations in the study area, a) Volcanic-plutonic contact in which propylitic alteration developed (KS=Kösedağ syenite, PBV=Propylitic altered volcanics), b) White argillic and green-yellow sericitic alteration zones within the volcanics, c) Lİght Brown-yellow sericitic alteration zone within the syenites, d) Oxidation (goethite) and sulphatization (jarosite) types of alterations developed within the cracks of sericitic alteration zones from syenites, e) Argillic alteration-volcanic contact observed within the Karataş volcanites, f) Silica hat observed at the upper part of argillic alteration in the volcanics, g) White argillic and green-yellow sericitic alteration zones within the volcanics, h) Argillic alteration with relic porphyritic texture in the volcanics.

4.1.3. Argillic Alteration

It is the most widespread and widest alteration zone in the region. It is usually observed in volcanics (Figure 3e); In syenites it is very small in amount and it is found in the sericitic alteration zone. Considering the topographic distributions, brecciated silica flats (Figure 3f) and iron oxides (Figure 3g) are represented in the upper sections with kaolinitic levels below this zone. They are not differentiated with clear boundaries. In some of these, rich levels of alunitic other clay minerals (illite, I-S and smectite) are in the form of telescoping zones.

In the field its yellowish-white appearance is characteristic. The kaolinites in the alteration zone is dominant and contain mostly cracks and fracture planes originating from the primary rock, and Fe-oxides are observed on the surfaces in very thin plasters. In argillic alteration which is developed from porhyritic textured volcanic rocks, porphyritic texture is not dissapeared. Feldspar phenocrystals turned into white color and matrix is turned into light brown kaolinite minerals (Figure 3h). In altered levels rarely 1-2 m wide unaltered rough and nodular levels which belong to primary rock are found.

4.2. Optical Microscopic Studies

4.2.1. Propylitic Alteration

It has been observed that biotitization, chloritization, sericitization, opacification (pyrite), carbonatization, epidotization and Fe-oxidation types of alteration develop in the microfractures and matrix of the propylitic altered andesites and also within the fine-grained matrix (Figure 4a-b).

4.2.2. Sericitic (Phyllic) Alteration

As a result of OM analysis coarse grained fibrous calcedonic quartz, very fine grained muscovite (illite, I-S) and in little quantity barite, tourmaline, kaolinite, smectite, chlorite, jarosite, goethite, pyrite and topaz minerals are defined in sericitic alteration zone of syenites.

In feldspar minerals, completely sericitization (sometimes coarse ~ 100 μm), argillization, rarely kaolinization, and silicification (fine-coarse-grained quartz) are observed (Figure 4c-d). As for mafic minerals, they are entirely iron oxidized within the microfractures in brecciated levels are observed to be filled with iron oxide formations (hematite, goethite) and brown-greenish jarosite.

4.2.3. Argillic Alteration

OM investigations have identified the silisic, alunitic and oxydic subzones as intergrown levels within this alteration zone. Quartz, goethite, goyazite, alunite, hematite, pyrite, jarosite, opal-CT, barite and other clay minerals are also accompanied by varying abundances of kaolinite in these parts. In the totally altered volcanic rocks, the initial porphyritic texture has not completely disappeared and can be observed as a residue (Figure 4e-f).

Feldspars can only be identified from their shapes in completely kaolinitized specimens. In addition, microlites accompanying Fe-oxidation in the matrix appear to be completely transformed into kaolinite minerals (Figure 4g). The kaolinite booklets that replace feldspar phenocrysts can be easily recognized in the optical microscope with cross polarized light by first serie colours of interference and shapes. The kaolinite minerals developed from the feldspar minerals are observed to be overlaid as large booklets reaching 50-100 μm in size (Fig. 4h). Only 4 samples of pyrophyllite minerals were identified from the altered parts; they are usually fine-grained and developed from the matrix. Pyrophyllites with yellowish-gray interference colors are accompanied by clusters of kaolinite minerals.

4.3. XRD Studies

4.1.2. Sericitic (Phyllic) Alteration

Feldspar, quartz, clay, biotite, hematite, jarosite, goethite, tourmaline, goyazite, hornblende, pyroxene, pyrite, calcite, dolomite and barite minerals were determined as the result of the XRD-WR analyzes of samples taken from altered plutonic rocks (Figure 5) In clay mineral content increasing samples, the amount of quartz mineral is also increasing. The most common mineral paragenesis is clay + quartz + jarosit ± goethite ± feldspar and clay + quartz + feldspar.

The common clay mineral paragenesis in the sericitic alteration zone are composed of I-S + chlorite, illite + I-S + chlorite + C-S, pure I-S, I-S + kaolinite and illite + smectite + kaolinite associations (Figure 6).

The illite or smectite ratio (Moore and Reynolds, 1997) in the I-S from the most common clay minerals

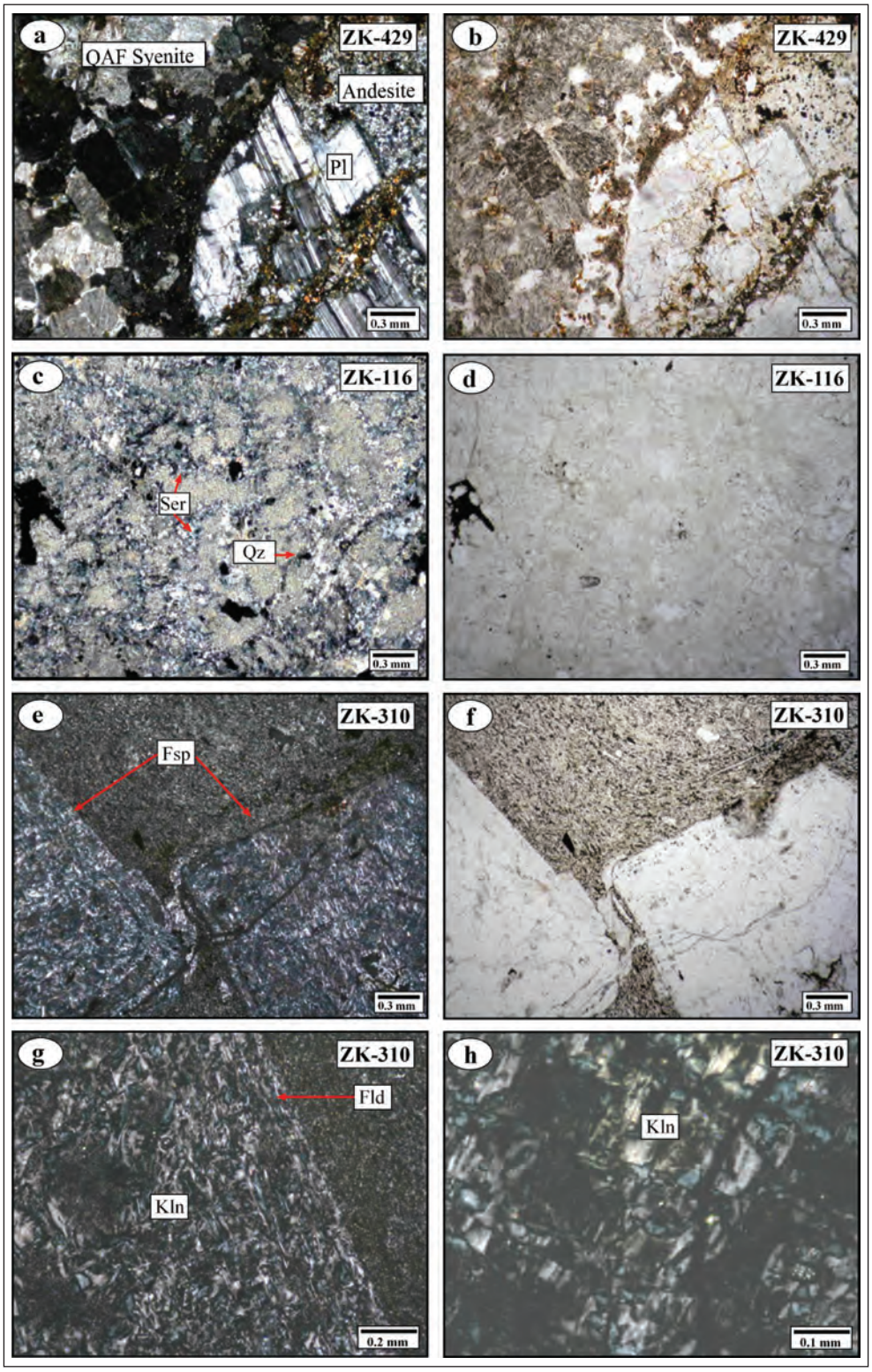

Figure 4- Thin-section images of the propylitic, sericitic/phyllic and argillic alteration zones in the study area (a-c-e=crossed polarized light, b-d-f=plane polarized light), a-b) Epidotization and Fe-oxidation in the propylitic altered volcanics within the Kösedağ syenite-Karataş volcanites contact (Pl=Plagioclase, QAF=Quartz alkali feldspar), c-d) Completely sericitization in feldspars and fine-grained quartzs in the sericitic/phyllic alteration zone within the Kösedağ syenite, (Ser=Sericite, Qz=Quartz), e-f-g-h) Relic porphyritic texture, completely kaolinitization in feldspar and matrix in the argillic alteration zone within the Karataş volcanites, (Fsp=Feldspar, Kln=Kaolinite).

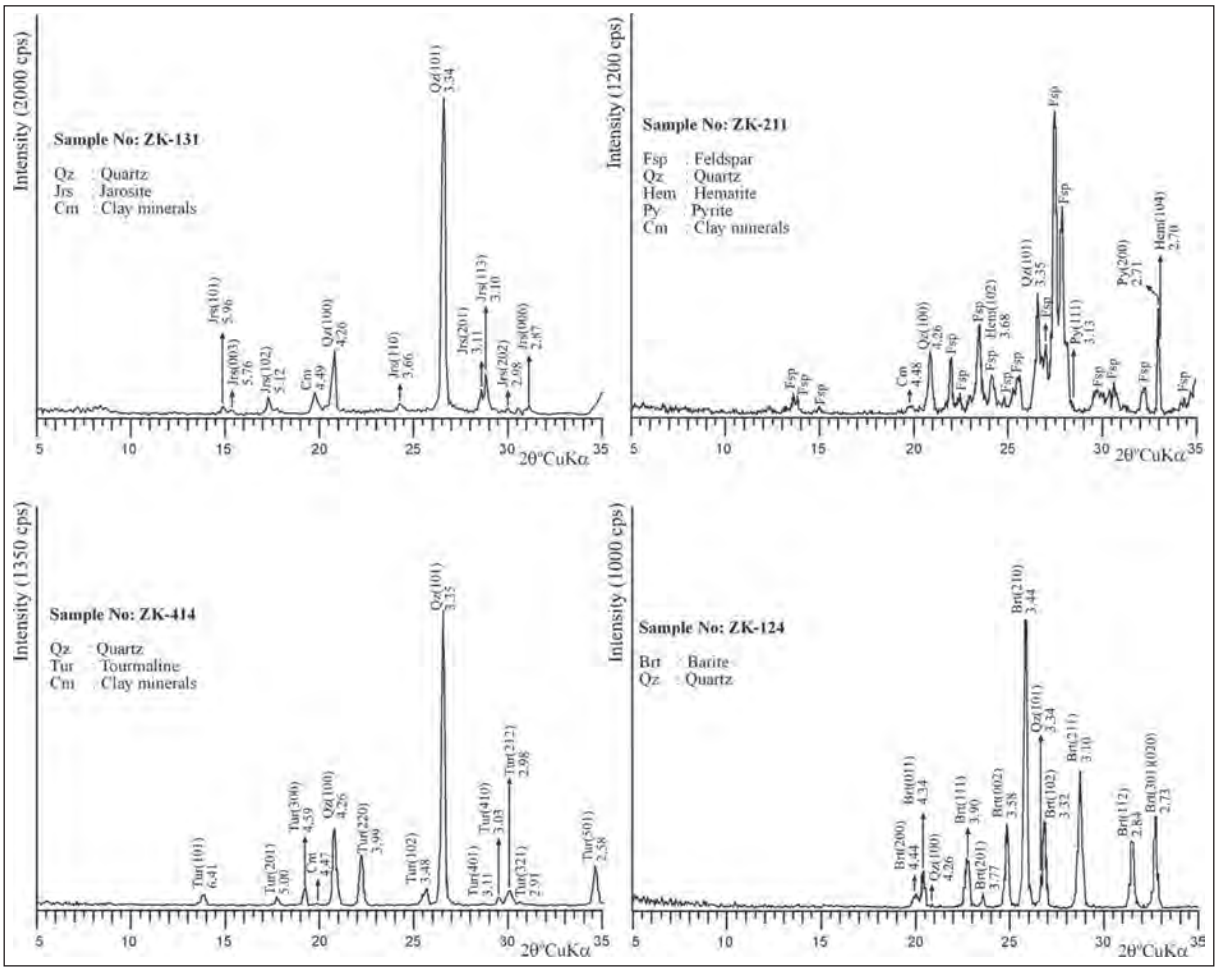

Figure 5- XRD-WR diffractograms of samples in the sericitic alteration zones in the study area..

in this alteration zone was calculated in 24 samples with illite content ranging from 84 to 95 % (smectite content 5 to 16 %), type of arrangement is observed as R=3 (Başıbüyük et al., 2010). In addition, it was determined that I-S had dioctahedral composition as a result of $d_{(060)}$ measurements of 11 pure or near-pure samples (Table 1).

As a result of the analysis of two polytype samples which prepared from pure I-S with illite high component, the illite in the I-S mineral is determined as type of 1Md+2M1+1M. In the XRD diffractogram of illite polytypes given in figure 7 as d (A˚) peaks, 3.88, 3.73, 3.49, 3.20, 2.98, 2.86, 2.79 and 2.58 peaks for 2M1; 4.34, 3.64, 3.07, 2.91 and 2.68 peaks for 1M, and the humpback between 2θ° 22-34 for 1Md are distictive.

It was observed that the $d_{(060)}$ measurement from one smectite and two C-S samples in the alteration zone had dioctahedral and trioctahedral compositions, respectively (Table 2). The chlorite content in C-S is in the range of 50-52 % (smectite content 48-50 %) and the arrangement type is determined as R=1.

4.3.2. Argillic Alteration

According to the order of abundance, quartz, goyazite, goethite, feldspar, alunite, jarosite, hematite, pyrite, calcite, opal-cristobalite/trydimite, biotite, dolomite, tourmaline and barite are determined by XRD-WR investigations, from samples taken from the argillic alteration zone.

The most common paragenesis minerals are formed of clay + quartz + goethite + goyazite, clay + quartz + alunite + goethite and clay + quartz + jarosite + feldspar + goethite and/or goyazite (Figure 8). Carbonate minerals (calcite and dolomite) are less likely to be found in high alteration grade, and opal-

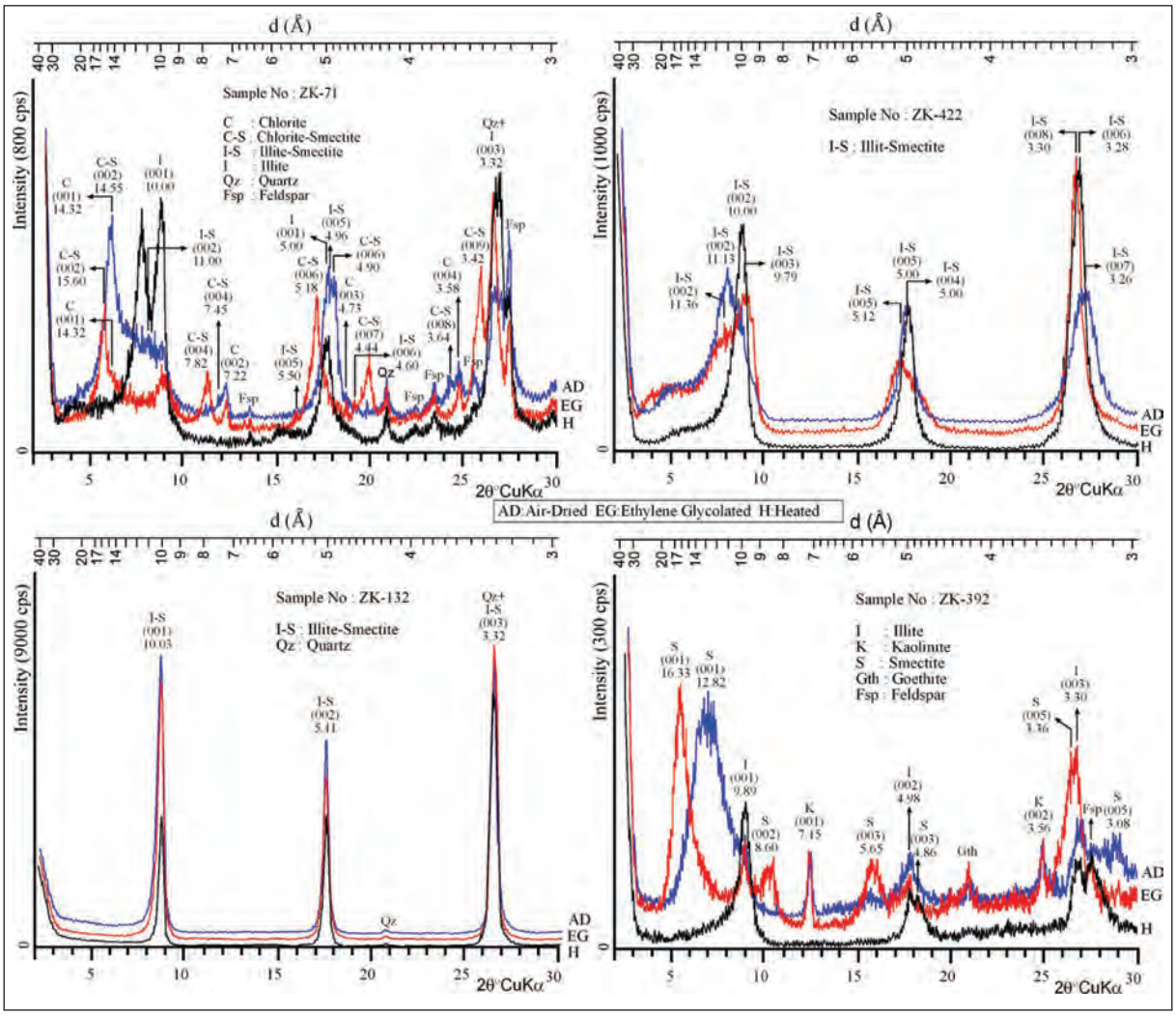

Figure 6- XRD-CF diffractograms of samples in the sericitic/phyllic alteration zones in the study area.

CT and barite are rarely present in the totally altered rocks.

As a result of the XRD analyzes of the samples taken from the alteration zone, it was observed that the clay fraction is consisted of kaolinite, I-S, smectite, illite, C-S, chlorite and pyrophyllite minerals (Figure 9). In the samples taken from the argillic alteration zone, kaolinite is very common and in most cases clay fractions are formed alone, whereas chlorite and C-S minerals are very common in rocks with less aleration. In this alteration zone only C-V mineral was observed in one specimen. The most common clay mineral associations in the altered samples are kaolinite + smectite + I-S ± illite, kaolinite + smectite and kaolinite + I-S ± illite, and pyrophyllite accompanies kaolinite in five samples.

The most common clay mineral in the alteration zone is kaolinite. It is found in 197 of 218 samples. 95 of them are clay fraction alone. As a result of polytype investigations made from four kaolinite samples, it was determined that all of them were T (triclinic)-type (Collins and Catlow, 1991) (Figure 10). Unlike monoclinic types (Toraya et al., 1980), d (A °), which is distinctive for T-polytype; 2.75, 2.34, 2.19, 1.99, 1.84 and 1.54 peaks were determined. Crystallinity measurements are performed from unoriented 7 samples (Hinckley, 1963). Hinckley Crystallization Index values were determined as 3 kaolinite samples (Sayın, 1987) with an index value between 1.30 and 1.0 as medium and lower than 1.0 as poorly crystallized (Table 3).

Another clay mineral, I-S, which is commonly observed in the zone of the argillic alteration zone, is

Table 1- The $d_{(060)}$ values and illite or smectite ratio and ordering type of the I-S minerals in the sericitic alteration zones of Kösedağ syenite.

Sample no	$d_{(060)}$ Å	Description	I %	S %	Type of ordering
ZK-52	1.498	Dioctahedral	88	12	R=3
ZK-63			93	07	R=3
ZK-64			93	07	R=3
ZK-116	1.495	Dioctahedral	92	08	R=3
ZK-117	1.497	Dioctahedral	86	14	R=3
ZK-118	1.497	Dioctahedral	90	10	R=3
ZK-122	1.497	Dioctahedral	88	12	R=3
ZK-125	1.498	Dioctahedral	84	16	R=3
ZK-126	1.498	Dioctahedral	84	16	R=3
ZK-131	1.497	Dioctahedral	85	15	R=3
ZK-132			93	07	R=3
ZK-133			94	06	R=3
ZK-136	1.498	Dioctahedral	90	10	R=3
ZK-212			92	08	R=3
ZK-334			94	06	R=3
ZK-387			94	06	R=3
ZK-390			94	06	R=3
ZK-394			92	08	R=3
ZK-395			92	08	R=3
ZK-396			92	08	R=3
ZK-397			87	13	R=3
ZK-412			95	05	R=3
ZK-416	1.494	Dioctahedral	84	16	R=3
ZK-422	1.496	Dioctahedral	86	14	R=3

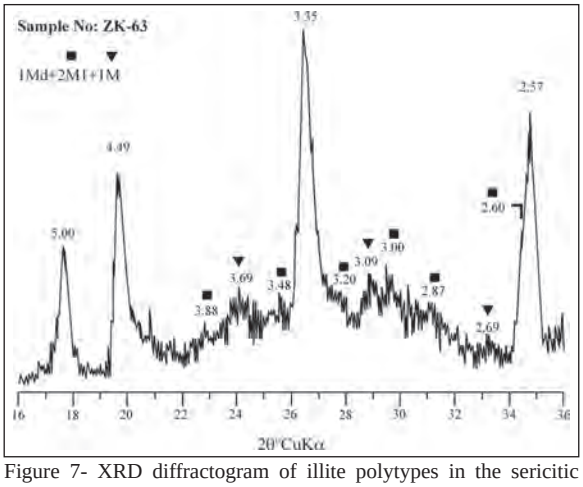

Figure 7- XRD diffractogram of illite polytypes in the sericitic alteration samples.

found in about one third of the samples and is usually observed together with kaolinite, smectite and illite. The illite or smectite ratio (Moore and Reynolds, 1997) in I-S, which was determined to have dioctahedral composition as a result of $d_{(060)}$ measurements made from 6 samples, was calculated for 21 altered volcanic rocks (illite content 54-91 %, smectite content 9-46). Arrangement types are determined as R=1 in 17 samples, R=3 in 4 samples (Table 4). The percentage of illites vary from 54 to 88 % in the case of the R=1 arrangement type, and from 84 to 91 % in the case of the R=3 arrangement type. In other words, as the degree of ordering increases the amount of illite increases.

Table 2- The $d_{(060)}$ values and chlorite or smectite ratio and ordering type of the smectite and C-S minerals in the sericitic alteration zones of Kösedağ syenite.

Sample no	Rock type	Mineral	$d_{(060)}$ Å	Description	C %	S %	Type of ordering
ZK-392	Altered quartz alkaline feldspar syenite	Smectite	1.497	Dioctahedral	0	100	
ZK-57	Quartz alkaline feldspar syenite	C-S	1.543	Trioctahedral	50	50	R=1
ZK-388	Altered granite	C-S			52	48	R=1

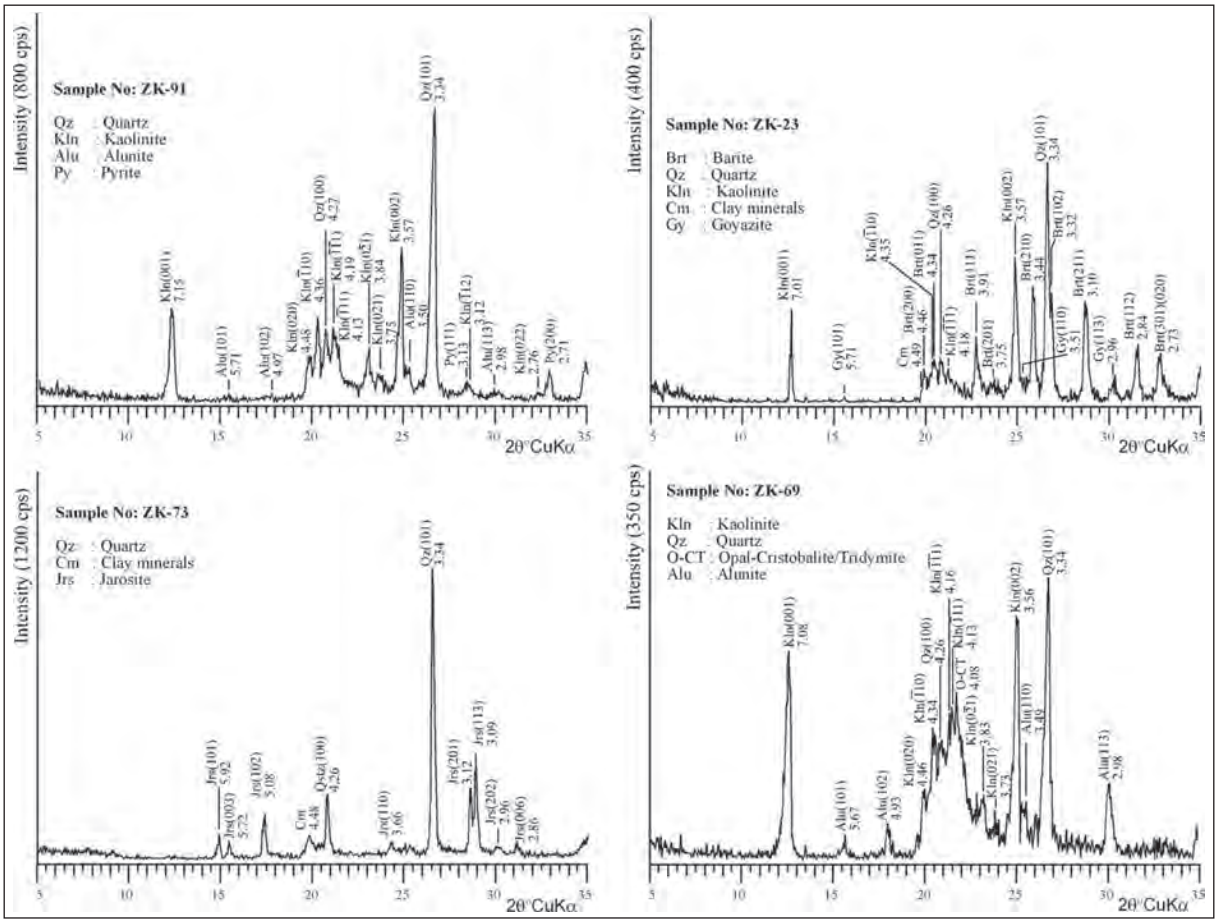

Figure 8- XRD-WR diffractograms of the argillic alteration zones in the study area.

The smectites in the alteration zone were found to have dioctahedral character as a result of $d_{(060)}$ measurements, and the illite content varied between 0 and 7 % (Table 5). The percentage chlorite and smectite content of C-S in this zone are calculated by using 3 samples. Its chlorite content is determined as 48-59 %, smectite content is found to be 20° 41-52. Arrangement type is determined as R=1 (Moore and Reynolds, 1997).

As a result of the $d_{(060)}$ measurements made on the two samples, it was found that C-S had trioctahedral composition (Table 6). The chlorite content of the C-S minerals in the andesites, which have not been too much altered, are higher than those of altered ones

Chlorites are one of the least observed clay minerals in the alteration zone, but they are present in 9 samples and are usually observed in less altered volcanics. They are mostly found with C-S and illite. However, kaolinite in two samples, smectite and I-S in three samples are accompanied by this mineral. The unit-cell compositions of the chlorites in the altered andesite samples, calculated from XRD data (Brown and Brindley, 1980; Chagnon and Desjardins, 1991), are given in table 7 and named as brunsvigite (Foster, 1962), (Figure 11). As a result of the polymorphism analysis of one sample, it was determined that chlorite has IIb polytope (Figure 12).

Pyrophyllite mineral is the least found clay mineral in the argillic alteration zone. It asociated with kaolinite and it formed of 57-71 % in three samples and 8-9 % in two samples of clay fractions. As a result of the polytype studies (Brindley and Wardle, 1970), d (A°); 3.76, 3.49, 3.17, 2.95, 2.75, 2.54, 2.34 and 1.89 peaks were observed. So it is differentiated from monoclinic-type and concluded that it has 1Tc polytype (Figure 13).

4.4. SEM Studies

Scanning electron microscope (SEM) studies were carried out involving Energy-dispersive X-ray

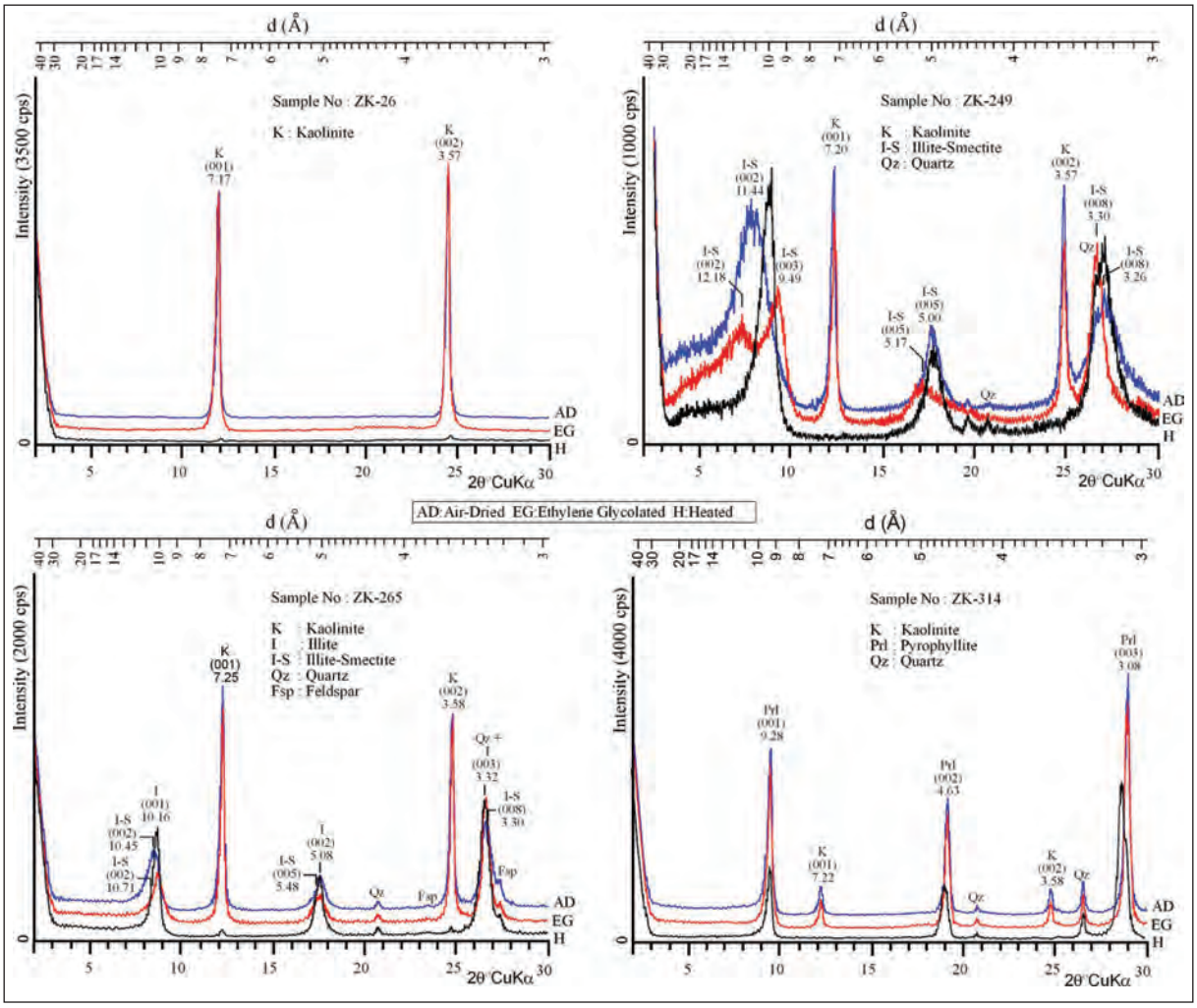

Figure 9- XRD-CF diffractograms of the argillic alteration zones in the study area.

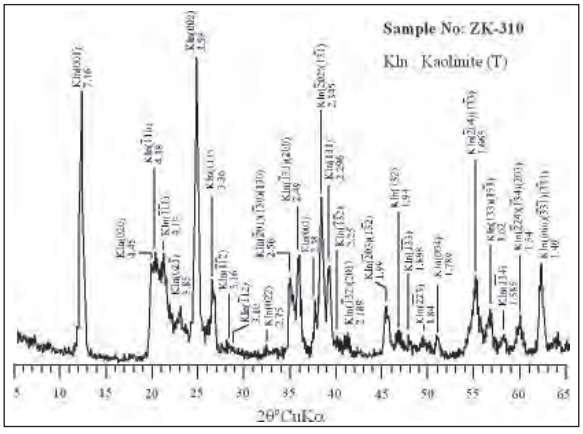

Figure 10- XRD diffractogram of kaolinite polytype in the argillic alteration zone of altered volcanic rocks.

spectroscopy (EDS) from three samples (ZK-169, ZK-314B, ZK-325) in the argillic alteration zone.

In the altered volcanic rock sample (ZK-169), I-S minerals are seen besides the anhedral kaolinite plates (Figure 14a). I-S minerals form fibrous-acicular bundles with 1 to 5 μm length which are partly parallel to each others. Jarosites often form single, rarely combined crystals. Trigonal-rombohedral jarosites with approximately equal dimension are similar to hexahedra and 1-2 μm in size (Figure 14b). The EDS spectra of the matrix of this example rich in jarosite and I-S show that semi-quantitative chemical composition on the anhydrous oxygen base varies between (%) Si 69.48-11.12, K 4.00-9.23 and Fe 26.52-79.65. These elements reflect the mineralogical composition of the rock, in other words to a large extent, a mixture of quartz, jarosite and Fe-oxide/hydroxide.

Table 3- Hinckley Crystallization Index values of kaolinite minerals in altered samples of Karataş volcanites.

Sample no	ZK-25	ZK-26	ZK-27	ZK-36	ZK-42/B	ZK-42/C	ZK-310
Hinckley K.İ.D.	1.10	1.22	0.71	0.96	1.15	0.78	0.73

Table 4- The $d_{(060)}$ values, illite or smectite ratio and ordering type of I-S minerals in the altered samples of the argillic alteration zones of Karataş volcanites.

Sample no	d(060) Å	Description	% I	% S	Type of ordering
ZK-41			61	39	R=1
ZK-50			76	24	R=1
ZK-73			67	33	R=1
ZK-74	1.500	Dioctahedral	84	16	R=3
ZK-75	1.495	Dioctahedral	69	31	R=1
ZK-149	1.494	Dioctahedral	88	12	R=1
ZK-159	1.500	Dioctahedral	84	16	R=3
ZK-161	1.496	Dioctahedral	74	26	R=1
ZK-223			64	36	R=1
ZK-225			67	33	R=1
ZK-227			54	46	R=1
ZK-228			61	39	R=1
ZK-229			74	26	R=1
ZK-233			78	22	R=1
ZK-234			74	26	R=1
ZK-249	1.497	Dioctahedral	74	26	R=1
ZK-258			91	09	R=3
ZK-265			91	09	R=3
ZK-283			76	24	R=1
ZK-322			66	34	R=1
ZK-377			70	30	R=1

Table 5- The $d_{(060)}$ values of the smectites in the altered samples in the argillic alteration zones of Karataş volcanites.

Sample no	d(060) Å	Description	I %	S %
ZK-177	1.501	Dioctahedral	7	93
ZK-188	1.500	Dioctahedral	2	98
ZK-297	1.499	Dioctahedral	2	98
ZK-329	1.494	Dioctahedral	0	100
ZK-359	1.491	Dioctahedral	0	100
ZK-410	1.500	Dioctahedral	2	98
ZK-417	1.496	Dioctahedral	0	100

In the SEM examinations of the altered volcanic sample (ZK-314B) consisting of clay (pyrophyllite and kaolinite), quartz and goyazite, platy pyrophyllite-kaolinite sheets are observed (Figure 14c). These minerals do not have typical morphologies and stacked up on top of each others; pyrophyllite is thicker and has angular edges, whereas kaolinite is composed of thinner and bended lamellas. The thickness of pyrophyllite ranges from 0.2 to 0.5 μm and the length varies from 3 to 5 μm. The morphological

Table 6- The $d_{(060)}$ values, illite or smectite ratio and ordering type of C-S minerals in the altered samples of the argillic alteration zones of Karataş volcanites.

Sample no	Rock type	$d_{(060)}$ Å	Description	C %	S %	Type of ordering
ZK-82	Andesite	1.538	Trioctahedral	59	41	R=1
ZK-172	Altered andesite	1.529	Trioctahedral	48	52	R=1
ZK-383	Alterered volcanic			52	48	R=1

Table 7- (002)/(001) and (004)/(003) peak intensity ratios and the octahedral Fe contents in the talc and brucite sheets of the chlorites in the argillic alteration zones of Karataş volcanites (B&B=Brown and Brindley, 1980; C&D=Chagnon and Desjardins, 1991).

Sample	$d_{(001)}$	Al^{IV}	(003)/ (001)	002+004/ 001+003	(002)/ (001)	(004)/ (003)	Fe^{+2} Talc		Fe^{+2} Brusite		SFe^{+2}			Mg
							B&B	C&D	B&B	C&D	B&B	C&D	Ort.	
ZK-258	14.25	1.04	1.00	2.36	2.68	2.04	2.3	1.3	1.9	1.1	4.2	2.4	3.3	1.66
ZK-259	14.23	1.10	0.86	2.32	2.54	2.07	2.2	1.3	1.9	1.1	4.1	2.4	3.3	1.60

characteristics of pyrophyllite are similar to the occurrences from hydrothermal alteration of volcanic material in Japan (Sudo et al., 1981); however, it differs from those of Pütürge (Malatya) in that it is smaller in size than the pyrophyllites formed by the hydrothermal alteration of the kyanites (Bozkaya et al., 2007).

In addition, pyrophyllite-kaolinite plates were observed, enclosing a material with a round amorphous-gel appearance (Figure 14d). The semi-quantitative chemical composition from EDS spectra of pyrophyllite and amorphous silicon-aluminum material were determined on the anhydrous oxygen base of pyrophyllite as (%) Si 74.23, Al 25.77. The chemical composition of the gel material (Si 74.01, Al 25.99) is almost identical to pyrophyllite. This is an important indicator of primarily kaolinite and/or pyrophyllite formation, followed by development of an aluminum-silica gel in the alteration process.

Fine-grained kaolinite plates are observed in the altered volcanic sample (ZK-325) containing quartz, clay (kaolinite), alunite and goyazite (Figure 14e). Equant kaolinite sheets are usually 1 to 5 μm in size, and their edges are not uniform. The thickness of kaolinite sheets are around 0.1 μm.

Alunites are found in micropores in the form of rhombohedral single and combined crystals, similar to hexaeder, with pseudohexagonal kaolinite plates about 2 μm in diameter (Figure 14f). Alunites are represented by euhedral crystals with a length of 5-10 μm. As a result of the EDS spectra and semi-quantitative chemical analyzes of this rock, the chemical composition (%) on the basis of anhydrous oxygen was determined as Si 61.15 and Al 38.85

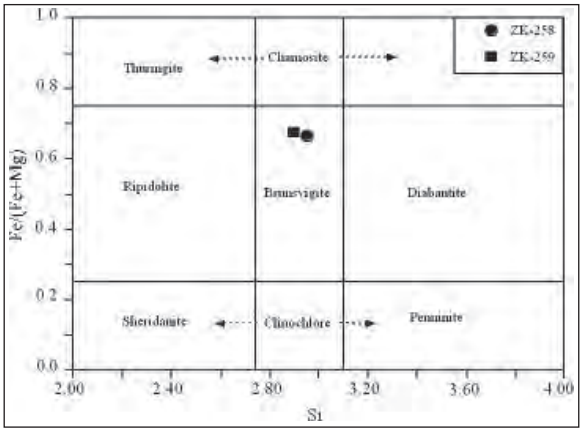

Figure 11- The settings on the Si^{IV} and octahedral Fe/(Fe+Mg) diagram of the chlorites in the altered andesites of the argillic alteration zone from Karataş volcanites (Foster, 1962).

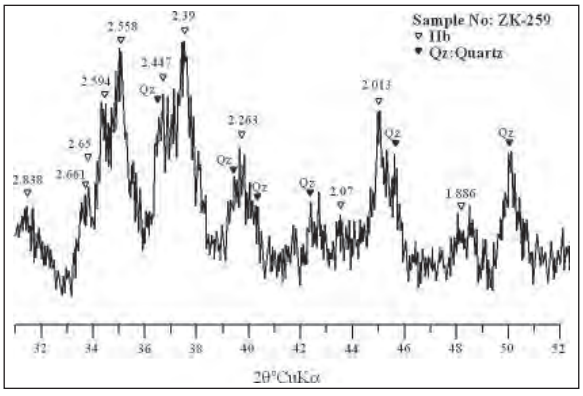

Figure 12- XRD diffractogram of chlorite polytype in the altered volcanic rocks in the argillic alteration zone from Karataş volcanites.

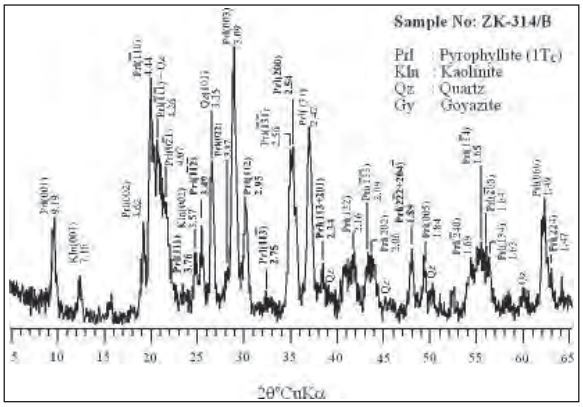

Figure 13- XRD diffractogram of 1Tc polytype of pyrophyllite in the altered volcanic rocks in the argillic alteration zone from Karataş volcanites.

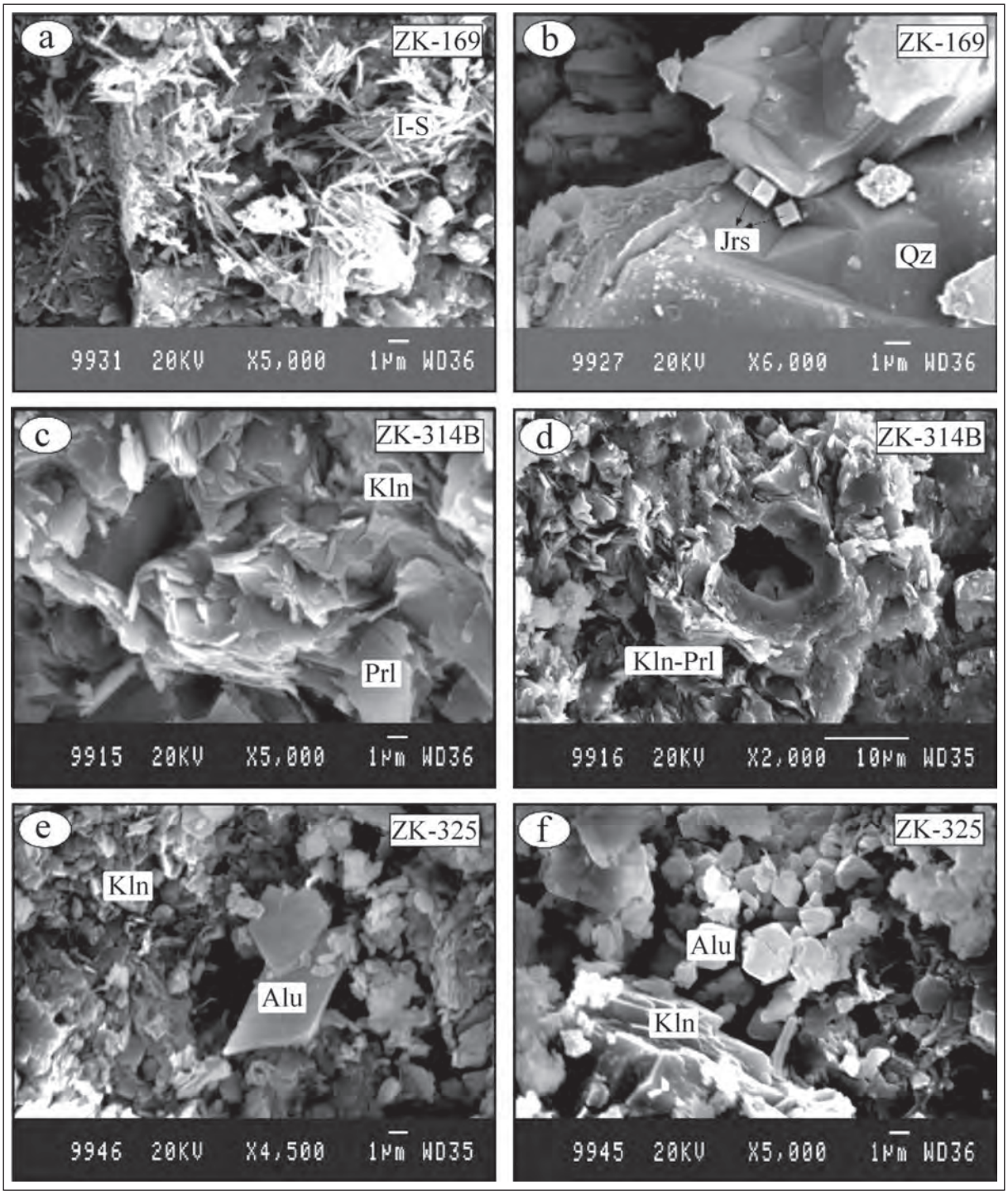

Figure 14- SEM microphotographs of samples in the argillic alteration zone (Qz=Quartz, Jrs=Jarosite, Prl=Pyrophyllite, Kln=Kaolinite, Alu=Alunite), a) Fibrous/acicular I-S minerals, b) Jarosite on euhedral quartz, c) Lamella of large pyrophyllite and thin kaolinite, d) Pyrophyllite-kaolinite plates developed from AlSi-gel, e) Weakly stacked euhedral kaolinite, and alunite minerals, f) Euhedral alunite minerals.

for kaolinite. Then percent values obtained for the groundmass (Si 19.92, Al 29.89, S 33.36, K 8.95, P 7.88) indicate the existence of minerals with silicate, sulphate and phosphate. The fact that kaolinite and pyrophyllite have weakly stacked texture indicates that the aqueous Al-silicate minerals are formed on the surface and/or near-surface conditions and they show a large similarity to those derived from the same type of rocks in literature (Keller, 1976, Gençoğlu et al., 1989; Yalçın, 1991).

5. The Formation and Origin of Hydrothermal Alteration Minerals

The formation of the minerals determined in the sericitic (phyllic) and argillic alteration levels in the Karataş volcanites and Kösedağ syenite are discussed below:

The formation of kaolinite and pyrophyllite which is found in studied area is discussed as follows. Liquid inclusion studies on quartz in the investigated area have determined that the solutions have a homogenization temperature ranging from 182-389 °C and a salinity equivalent to 2.8-10.5 NaCl (Efe and Gökçe, 1999). Pyrophyllite is a mineral which is stable at 275-350 °C in the Al_2O_3-SiO_2-H_2O system (Evans and Guggenheim, 1988). However, according to the same authors; when water is diluted with other components such as CH_4 and CO_2, the temperature of pyrophyllite formation can be reduced to lower values. In addition, silica-saturated fluids can cause pyrophyllite instead of kaolinite during hydrothermal alteration of silicates at low temperatures of up to 100°C (Hemley et al., 1980; Berman, 1988).

In this study, the presence of common silica, sulphur (alunite, jarosite, pyrite) and arsenic (goyazite) minerals from hydrothermal alteration and/or neoformation minerals; the fluids are rich in H_4SiO_4 and SO_2; but it is poor in terms of CO_2. Also; kaolinites are associated with other clay minerals (illite, I-S, smectite) and pyrophyllite is not widely developed, suggesting that the temperature of the solutions causing the alteration of the magmatics and/or the occurences of the neoformation minerals in the study area may be quite low.

Kaolinite is formed from both phenocrysts/microlites of feldspar, and the alteration of volcanic glass. Kaolinite-pyrophyllite sheets developed from aluminum-silica gel are observed in EDS investigations and SEM photographs taken from altered volcanic sample (ZK-314B). This fact suggests that an intermediate stage has happened (Yalçın and Bozkaya, 2003):

(Volcanic glass → Hydrous Al-silica gel → Kaolinite)

$4SiO_2.2Al_2O_3 + 14H_2O \rightarrow 2Al_2(OH)_6.4Si(OH) \rightarrow Al_4[Si_4O_{10}](OH)_8 + 10H_2O$

(Sanidine/Orthoclase → Hydrous Al-silica gel → Kaolinite + Quartz

$4KAlSi_3O_8 + 28H_2O + 4H^+ \rightarrow 2Al_2(OH)_6.12Si(OH)_4 + 4K^+ \rightarrow Al_4[Si_4O_{10}](OH)_8 + 8SiO_2 + 4K^+ + 26H_2O$

(Plagioclase → Hydrous Al-silica gel → Kaolinite)

$2(Na,Ca)Al_2Si_2O_8 + 12H_2O + 4H^+ \rightarrow 2Al_2(OH)_6.4Si(OH)_4$ ® $Al_4[Si_4O_{10}](OH)_8 + 10H_2O + 2(Na^+,Ca^{+2})$

(Feldspar → Kaolinite)

$2(Na,K,Ca)Al_2Si_2O_8 + 2H_2O + 4H^+ \rightarrow Al_4[Si_4O_{10}](OH)_8 + 2(Na^+,K^+,Ca^{+2})$

Excess silica during feldspar minerals transforming into kaolinite, Ca^{+2} and Na^+ from plagiclase, K^+ from sanidine/orthoclase are used in the formation of calcedonic quartz and other clay minerals, respectively. The low ratio of Si/Al in the system led to the formation of kaolinite, but pyrophyllite synthesis could only take place when this ratio rises rarely:

(Volcanic glass → Hydrous Al-silica gel → Pyrophyllite)

$4SiO_2.Al_2O_3 + 11H_2O \rightarrow Al_2(OH)_6.4Si(OH)_4 \rightarrow Al_2[Si_4O_{10}](OH)_2 + 10H_2O$

(Sanidine/Orthoclase → Hydrous Al-silica gel → Pyrophyllite + Quartz)

$2KAlSi_3O_8 + 14H_2O + 2H^+ \rightarrow Al_2(OH)_6.6Si(OH)_4 + 2K^+ \rightarrow Al_2[Si_4O_{10}](OH)_2 + 2SiO_2 + 2K^+ + 14H_2O$

It is thought that Na^+, K^+, Ca^{+2}, Mg^{+2} and Fe^{+2} cations, which are not used in the formation of kaolinites formed by the alteration of volcanic glass and/or feldspar, lead to the formation of illite/muscovite (sericite), I-S and/or smectites (Yalçın and Gümüşer, 2000 , Yalçın and Bozkaya, 2003, Yalçın et al., 2005):

(Volcanic glass → Hydrous Al-Silica gel → Illite/Muscovite)

$3SiO_2.2Al_2O_3 + 12H_2O \rightarrow 2Al_2(OH)_6.3Si(OH)_4 + K^+ \rightarrow KAl_3(Si_3AlO_{10})(OH)_2 + 10H_2O + 2OH^-$

(Sanidine/Orthoclase → Illite/Muscovite)

$4KAlSi_3O_8 + 6H^+ \rightarrow KAl_3(Si_3AlO_{10})(OH)_2 + 9SiO_2 + 2H_2O + 3K^+$

(Volcanic glass → Hydrous Al-silica gel → I-S)

$6SiO_2.3Al_2O_3.Na_2O.K_2O + 19H_2O + 4H^+ \rightarrow 6Al(OH)_3.6Si(OH)_4 \rightarrow KNaAl_4[Al_2Si_6O_{20}](OH)_4 + 18OH^-$

(Sanidine/Orthoclase → I-S + Quartz)

$6KAlSi_3O_8 + Na^+ + 4H_2O \rightarrow KNaAl_4[Al_2Si_6O_{20}](OH)_4 + 12SiO_2 + 5K^+ + 4OH^-$

(Plagioclase → I-S)

$3(Na,Ca)Al_2Si_2O_8 + 2H_2O + K^+ + 2H^+ \rightarrow KNaAl_4[Al_2Si_6O_{20}](OH)_4 + 2(Na^+,Ca^{+2}) + 2OH^-$

(Volcanic glass → Hydrous CaMgAl-silicate gel → Smectite)

$8SiO_2.3Al_2O_3.MgO.Na_2O.CaO + 25H_2O \rightarrow Na_2O.CaO.MgO.6Al(OH)_3.8Si(OH)_4 \rightarrow$

$NaCa(MgAl_5)[Si_8O_{20}](OH)_4.H_2O + 16H_2O + 12OH^- + Na^+ + Al^{+3}$

(Plagioclase → Smectite)

$5(Na,Ca)Al_2Si_2O_8 + 6Si(OH)_4 + 2Mg^{+2} + 2H^+ \rightarrow 2NaCa(MgAl_5)[Si_8O_{20}](OH)_4.2H_2O + 3(Na^+,Ca^{+2}) + 14OH^-$

OM studies indicate that chlorite and C-S have developed as a consequence of the alteration of biotite and/or volcanic glass (Yalçın et al., 2005):

(Volcanic glass → Hydrous MgFeAl-silicate gel → Chlorite)

$7SiO_2.Al_2O_3.2MgO.2FeO + 24OH^- + 10H^+ \rightarrow 9MgO.2FeO.2Al(OH)_3.7Si(OH)_4 \rightarrow Mg_9Fe_2Al[AlSi_7O_{20}](OH)_{16} + 9H_2O$

(Volcanic glass → Hydrous MgFeAl-silicate gel → Chlorite)

$7SiO_2.Al_2O_3.7MgO.FeO + 11H_2O + 12H^+ \rightarrow 7MgO.FeO.2Al(OH)_3.7Si(OH)_4 \rightarrow Mg_7FeAl[AlSi_7O_{20}](OH)_{12} + 4H_2 + 14H^+$

Jarosite is a secondary mineral that occurs in the conditions of superficial conditions in arid climates (Duda and Rejl, 1990). Jarosite in the study field are mostly accompanied by goethite. Here, it is possible that it can be occured by the Fe-containing minerals (pyrite, magnetite etc.) and/or biotite alteration, as well as the synthesis of solution according to the data obtained from the SEM examinations. Here, K which is released by the alteration of volcanic glass, sanidine/orthoclase and/or biotite, is also needed and is formulated as follows (Yalçın and Bozkaya, 2003; Yalçın et al., 2005):

(Biotite → Jarosite)

$KFe_3[AlSi_3O_{10}](OH)_2 + 2SO_2 + 4H_2O \rightarrow [(KFe_3(SO_4)_2(OH)_6] + 3SiO_2 + Al^{+3} + 4H^+$

(Biotite + Magnetite → Jarosite + Goethite)

$KFe_3[AlSi_3O_{10}](OH)_2 + Fe_3O_4 + 2SO_2 + 9H_2O \rightarrow [(KFe_3(SO_4)_2(OH)_6] + 3FeO(OH)_2 + 3SiO_2 + Al^{+3} + 8H^+$

(Pyrite → Jarosite)

$3FeS_2 + 22H_2O + K^+ \rightarrow [(KFe_3(SO_4)_2(OH)_6] + 4SO_2 + 38H^+$

(Ions → Jarosite)

$K^+ + 3Fe^{+3} + 2SO_2 + 10H_2O \rightarrow [(KFe_3(SO_4)_2(OH)_6] + 14H^+$

The other sulfate mineral observed in the study area is alunite and it can be suggested that jarosite has a similar formation mechanism. However, here, instead of Fe, Al has to enter the structure and this cation must be provided especially during the kaolinization (Yalçın and Bozkaya, 2003):

(Sanidine → Alunite + Quartz)

$KAl_3Si_3O_8 + 2SO_2 + 8H_2O \rightarrow KAl_3(SO_4)_2(OH)_6] + 3SiO_2 + 10H^+$

(Ions → Alunite)

$K^+ + 3Al^{+3} + 2SO_2 + 10H_2O \rightarrow [(KAl_3(SO_4)_2(OH)_6] + 14H^+$

Goyazite has a general formula of [(Sr,Ca,Ba) $Al_3[(P,As)O_4]_2(OH)_5.H_2O$], and it is member of the krandallite group. A similar formation of jarosite and alunite for this mineral is possible:

(Feldspar → Goyazite + Quartz)

$3(SrCaBa)Al_2Si_2O_8 + 2P^{+5} + 2As^{+6} + 16H_2O \rightarrow$

$2[(SrCaBa)Al_3[(P,As)O_4]_2(OH)_5H_2O] + 6SiO_2 + (Sr^{+2},Ca^{+2},Ba^{+2}) + 18H^+$

(Ions → Goyazite)

$(Sr^{+2},Ca^{+2},Ba^{+2}) + 2P^{+5} + 2As^{+5} + 3Al^{+3} + 10H_2O \rightarrow [(Sr,Ca,Ba)Al_3[(P,As)O_4]_2(OH)_5.H_2O] + 14H^+$

In barite neomineralization observed in fractures of syenites and kaolinites, Ba, which is released during kaolinization, is the most important source:

Feldspar → Barite + Quartz)

$(Ca,Ba)Al_2Si_2O_8 + SO_2 + 2H^+ \rightarrow BaSO_4 + 2SiO_2 + 2Al^{+3} + Ca^{+2} + 2OH^-$

Consequently, the type of clay mineral (kaolinite, I-S or/and smectite) in argillic zone formed by hydrothermal alteration of volcanic material is seemed to be controlled by folowing parameters (Bohor and Triplehorn, 1993; Gündoğdu et al., 1996; Yalçın and Bozkaya, 2003): pH of hydrothermal solutions (kaolinite if acidic, I-S and smectite in medium-basic), salinity and/or alkalinity of hydrothermal solutions (kaolinite in low salinity, I-S and smectite in high salinity), degree of leaching in open and closed system (kaolinite in open system, I-S and smectite in closed system), silica saturation (kaolinite in high, I-S and smectite in low), activities of ions (H^+, H_4SiO_4, $[Al(OH)_4]$ etc.) and water (kaolinite in high activity, I-S and smectite in less), dissolution speed and quantity (kaolinite in high, I-S and smectite in low) and also composition of volcanic material (kaolinite if Fe and/or Mg, K, Na and Ca are poor, I-S and smectite if rich), alkali cation ratios (for kaolinite Na/K=0, for smectite 0.5, for I-S K/Na=1).

6. Formation Model of Kaolinite Deposits

It has been observed that a pyroclastic material, which is concentrated at intervals from the lowest levels of the Middle-Upper Eocene Akıncılar formation to the upper parts, is observed. At the highest levels, it passes to Karataş volcanites with agglomeratic level. A volcanic activity starting from Middle Eocene in the region continued until the end of Eocene in the form of lava flows. The composition of magma forming these volcanics is differentiated by fractional crystallization. Before Karataş volcanites have yet not completely cooled, the syenites have settled by ascending up to shallow depths with hot-hot contact (Figure 15a).

In the solidification of syenite and the volcanics around it, fractures and cracks were formed by the increase of the pressure of the volatile components in the pluton, and along these weak zones hydrothermal solutions formed alteration zones of interaction with magmatics (Figure 15b-c). As a result of the field observations, altough there is no definite zoning distinction of hydrothermal alteration types; in the main alteration zone (Kumoğlu Village) starting from unaltered syenites, sericitic and argillic + sericitic altered syenites; argillic + sericitic and argillic altered volcanics can be followed. In the volcanics, compared with the syenites, the reason for the argillic alteration zones are wider and also types of hydrothermal alteration are different; volcanics are finer grained (volcanic glass and microlites in the matrix) than syenites so it interacts with hydrothermal fluids faster.

These alteration zones are concentrated in the volcanics surrounding the plutonics and in two main zones with NE-SW trending where cut the pluton. In the main alteration zones, argillic, sericitic and propylitic and Fe-Pb-Zn ± Cu ± Mo-ore minerals were developed (Efe and Gökçe, 1999). Considering the environment and mechanism occured minerals, two different origins can be suggested (Esquevin, 1956; Millot, 1970). First is hydrothermal neoformation (direct formation from solution) and the other is hydrothermal degradation (the negative alteration of previously formed minerals in solid-solid phase). The boundary between mechanisms in the evolution of the minerals is not certain and neoformation mechanism can develop after degradation. Based on this classification; tourmaline, barite, ore minerals, quartz, opal-CT, alunite, goyazite, jarosite, calcite, dolomite, azurite and malachite were formed by neoformation; chlorite and C-S by degradation; and epidote, kaolinite, pyrophyllite, illite, I-S and smectite by both neoformation and degradation mechanisms. Considering only the environment, these minerals are secondary; when the mechanism is considered, it can be stated that the neoformation minerals are primary and the degradation minerals are secondary.

According to types of hydrothermal alteration (hypogen, metasomatism, supergene); barite, ore minerals, quartz, opal-CT, alunite, goyazite, jarosite from neoformation minerals; chlorite and C-S from degradation minerals; kaolinite, pyrophyllite, illite, I-S and smectite minerals formed by both neoformation and degradation mechanism are hypogene. As to carbonate minerals such as calcite, dolomite, azurite and malachite from other neoformation minerals, they are supergene. Tourmaline and epidote are thought to be metasomatic minerals. According to their mineral assemblages, textural properties, and macroscopic

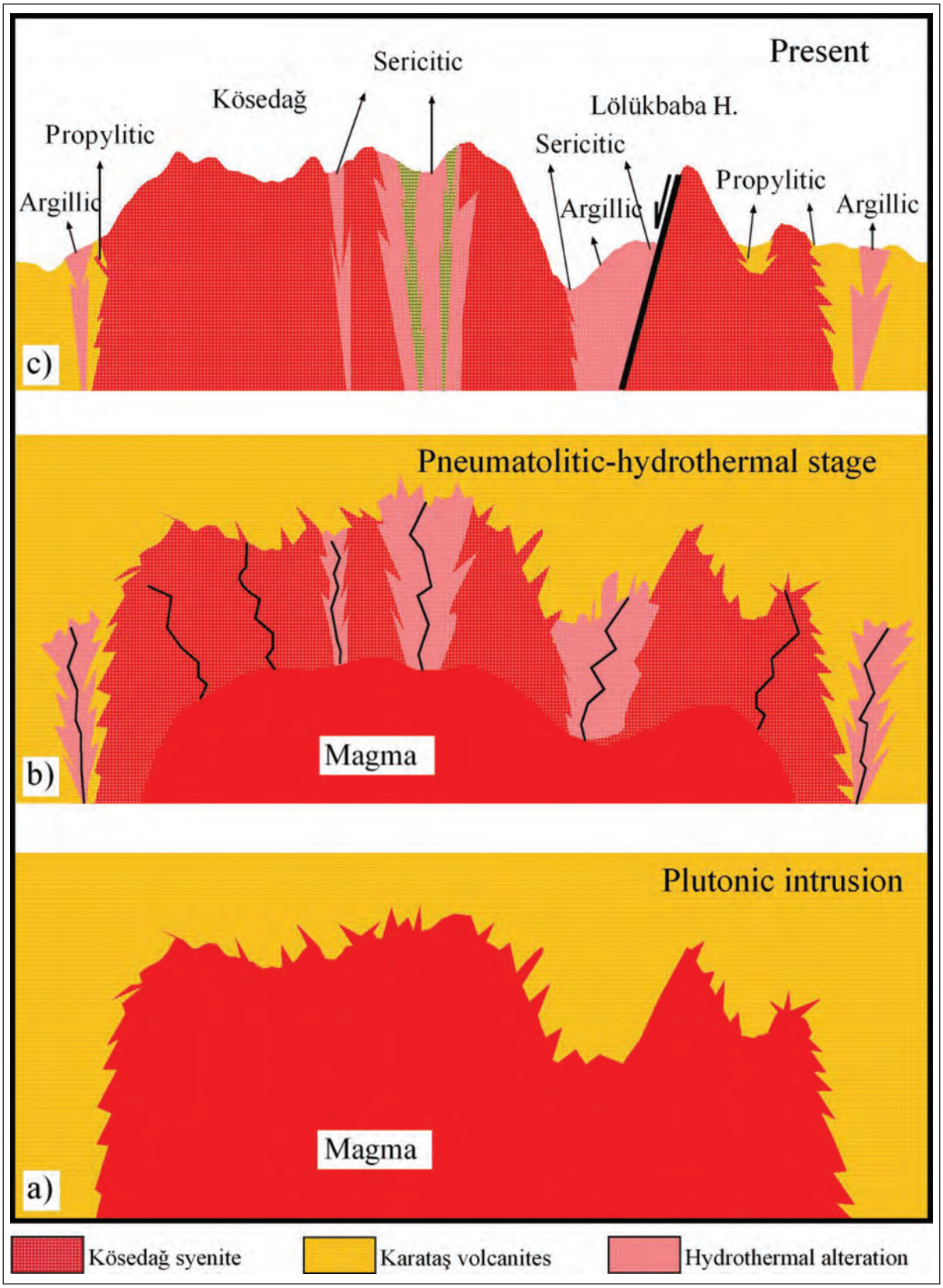

Figure 15- Hydrothermal alteration evolution model in Kösedağ syenite and volcanics, a) Upper shallow depth of Kösedağ pluton and intrusion into Karataş volcanites, b) Hydrothermal phase, c) Present location of magmatic and alteration products.

positions, hypogeneous hydrothermal minerals can be divided into two groups as early and late stages minerals. Of these, kaolinite, pyrophyllite, illite, I-S, smectite, quartz and opal-CT are early-; barite, ore minerals, alunite, goyazite, jarosite, chlorite and C-S are late-stage minerals.

7. Conclusions

The conclusions obtained from the lithological and mineralogical studies of the Kösedağ syenite and Karataş volcanites, where the hydrothermal alterations of the propylitic, phyllic/sericitic and argillic alteration in the study area develop, are presented below:

Upper Cretaceous-Paleocene Refahiye Complex is represented by serpentinized ultramafic rocks; Akıncılar formation of Middle-Late Eocene aged marine magmatism by clastic-volcanoclastic; Karataş volcanites the of Middle-Upper Eocene by of basaltic trachyandesite-trachyandesite volcanics in compositon; Kösedağ syenite of the Middle-Upper Eocene by quartz alkaline feldspar syenite. The Akıncilar formation was found to have widespread volcanosedimentary character; in other words, the unit reflects the first signs of the volcanism in region in the form of pyroclastics. In the region lava flows (Karataş volcanites) followed the agglomerate products of the magmatism for a short time, and then plutonics (Kösedağ syenite) intruded the lavas at shallow depths with hot-hot contact before they totally cooled.

Hydrothermal alteration affected only Middle-Upper Eocene Karataş volcanites and Kösedağ syenite. The age of the alteration was found to be 38.0 ± 0.9 million years as a result of K/Ar radiometric age dating from alunite mineral. The alteration zones are concentrated in two major zones. One of them is circle-shaped extending fractures in volcanics which are parallel to plutonic-volcanic contact. The second one is the zone that cutting both NE-SW trending plutonics and volcanics. The system that brings the alterations, solidification of syenite by the placement of Karataş volcanites into syenite with hot-hot contact before it cooled, the formation of the crack and fractures as a result of the increase of the pressure of the volatile components in the pluton and the interaction of hyrdrothermal solutions with magmatics through these weak zones. According to the syenites around volcanics, the reason for the argillic alteration zones is wider and the type of hydrothermal alteration is different; volcanics are finer grained than syenites (volcanic glass and microlites in the matrix) and interacted with hydrothermal fluids faster.

Although kaolinite occurrences are observed in both Kösedağ syenite and Karataş volcanites, the kaolinite deposit formations that can be operated have developed only in the argillic alteration zone of Karataş volcanites; it has been revealed that the region has an important potential for kaolinitic industrial raw materials. Hydrothermal altered levels are usually observed in a few km^2 zones; only the extent of the alteration zone observed in Gemin Beli is about 30 km^2. Kaolinite deposits with no sharp boundaries contain rich in iron oxide, alunite and other clay minerals (mostly I-S), and its upper parts are covered by a silica cap. As a result of the hydrothermal alteration, enrichment of ore minerals has occured in addition to clay minerals. In the contact of Kösedağ syenite and Karataş volcanites and generally within the plutonics perpendicular to dominant alteration trend, vein type of Pb-Zn deposits which are related to NW-SE-oriented fracture systems are observed. In Kösedağ syenite there are tourmaline-quartz (between a few mm and about 20 cm) and barite veins (0.3-1 m) in altered levels.

As a result of hydrothermal alteration, diferentiated as propylitic, phyllic/sericitic and argillic types, starting from Kösedağ syenite and Karataş volcanites, phyllosilicate/clay minerals (kaolinite, illite, smectite, chlorite, I-S, C-S and pyrophyllite), oxides and hydroxides (hematite, goethite), sulfides (galenite, sphalerite, pyrite, calcopyrite, molybdenite, covellite), carbonates (calcite, dolomite, malachite, azurite), sulphates (barite, alunite, jarosite), phosphate (goyazite), quartz and opal-CT minerals are formed. The most common hydrothermal mineral paragenesis in the Karataş volcanites, where argillic alteration is observed, are clay + quartz + goethite + goyazite, clay + quartz + alunite + goethite and clay + quartz + jarosite + feldspar + goethite and/or goyazite.

The kaolinite minerals formed by the alteration of volcanics in the argillic zone show moderate to poor crystallinity values according to the Hinckley Crystallization Indices. I-S minerals with volcanic origin are in dioctahedral composition and their illite content ranges from 54 to 91 % (smectite content 9 to 46 %). Smectites are dioctahedral; C-S minerals are trioctahedral and 48-59 % chlorite (41-52 % smectite) in content. Kaolinite has T (triclinic), pyrophyllite $1T_c$ and chlorite IIb polytope.

The most common mineral paragenesis are clay + quartz + jarosit ± goethite ± feldspar and clay + quartz + feldspar in the rocks formed by alteration of Kösedağ syenite. Illite or smectite contents in the I-S minerals from the altered products of the plutonics range from 84 to 95 % and from 5 to 16 %. I-S minerals have dioctahedral composition and 1Md + 2M1 + 1M polytype. The chlorite or smectite content of C-S minerals with trioctahedral composition in the rocks formed by alteration of the Kösedağ syenite is in the range of 50-52 % or 48-50 %. As for smectites, they are dioctahedral composition.

Field observations, OM and SEM studies show that hypogene and supergene hydrothermal alteration products are represented by the primary and secondary minerals formed directly or mostly from feldspars by neoformation and/or degradation mechanisms. Hypogene minerals are formed in two stages: early (kaolinite, pyrophyllite, illite, I-S, smectite, quartz and opal-CT) and late stage (barite ore minerals, alunite, goyazite, jarosite, chlorite and C-S). Tourmaline and epidote are considered as metasomatic and carbonates (calcite, dolomite, azurite and malachite) as supergene minerals. In other words, all of these minerals have formed in the surface and/or near-surface conditions.

The fluids forming the hydrothermal alteration have the salinity of 2.8-10.5 % NaCl and a homogenization temperature of 182-389 ° C. The presence of common silica, sulphur (alunite, jarosite, pyrite) and arsenic (goyazite) minerals from hydrothermal alteration and/or neoforming minerals indicate that the solutions rich in in H_4SiO_4 and SO_2 but poor in CO_2. Furthermore, the fact that clay minerals (illite, I-S, smectite) accompanying kaolinite, and low development of pyrophyllite, consider that solutions that cause alteration in the magmatics and/or occurence of neoformation minerals, have low temperature values. Kaolinite-pyrophyllite platies from aluminum-silica gel are observed in EDS investigations and SEM photographs. This fact suggests that an intermediate stage has happened.

The cations Na^+, K^+, Ca^{+2}, Mg^{+2} and Fe^{+2} which are not used in the structure of kaolinites from hydrothermal alteration of volcanic glass and/or feldspars lead the occurences of other clay minerals such as illite/muscovite, I-S and/or smectite. The low ratio of Si/Al in the system has caused the formation of kaolinite; pyrophyllite synthesis is occured in cases where this ratio rarely increases.

Jarosite in the field of study are mostly accompanied by goethite. It has been concluded that this mineral can be formed from Fe-containing minerals (pyrite, magnetite etc.) and/or biotite alteration, or it is possible to synthesize from solution in the light of the data from SEM. There is also a need for K, which is released by the decomposition of volcanic glass, sanidine/orthoclase and/or biotite.The alunite mineral has also a similar formation mechanism like jarosite, in which Al instead of Fe enters the structure and this cation must be provided from sanidine especially during the kaolinization.

Goyazite from a member of the krandallite group has a general formula of $[(Sr,Ca,Ba)Al_3[(P,As)O_4]_2(OH)_5.H_2O]$ and it is found with kaolinites. It seems that a similar formation as jarosite and alunite is possible for this mineral. Ba is the most important source released during kaolinization in the barite neomineralization within the fractures of the syenites and kaolinites,

The type of clay minerals (kaolinite, I-S or/and smectite) in argillic zone formed by hydrothermal alteration of volcanic material is seemed to be controlled by folowing parameters: pH of hydrothermal solutions (kaolinite if acidic, I-S and smectite in medium-basic), salinity and/or alkalinity of hydrothermal solutions (kaolinite in low, I-S and smectite in high), degree of leaching in open and closed systems (kaolinite in open, I-S and smectite in closed), silica saturation (kaolinite in high, I-S and smectite in low), activity of ions (H^+, $H_4SiO_4^{-4}$, $[Al(OH)_4]^-$ etc.) and water (kaolinite in high, I-S and smectite in less), dissolution speed and quantity of volcanic material (kaolinite in high, I-S and smectite in low), composition of volcanic material (kaolinite if Fe and/or Mg, K, Na and Ca are poor, I-S and smectite if rich), alkali cation ratios (for kaolinite Na/K=0, for smectite 0.5, for I-S K/Na=1).

References

Acarlioğlu, S., Kadir, S., Abdioğlu, E., Arslan, M. 2013. Epithermal-alteration geology, mineralogy and geochemistry of Eocene volcanic rocks in the Hasandağ (Giresun) area, eastern Pontides, NE Turkey. Neues Jahrbuch für Mineralogie Abhandlungen, 190, 79-99.

Ariana, Z., Par ,W., Mario, B., Vladimir, M. 2016. Geological, mineralogical and chemical characterization of Devonian kaolinite-bearing sediments for further applications in the ceramic (tiles) industry in La Paz, Bolivia. Environ Earth Sci, 75:546, 1-15.

Arslan, M., Kadir, S., Abdioğlu, E., Kolaylı, H. 2006. Origin and formation of kaolinite minerals in saprolite of Tertiary alkaline volcanic rocks, Eastern Pontides, NE Turkey. Clay Minerals, 41(2), 597-617.

Başıbüyük, Z. 2006. Eosen volkaniklerinin hidrotermal alterasyon mineralojisi-petrografisi ve jeokimyası: Zara-İmranlı-Suşehri-Şerefiye Dörtgeni'nden bir örnek (Sivas Kuzeydoğusu, İç-Doğu Anadolu, Türkiye). Doktora Tezi, C.Ü. Fen Bil. Enst. Sivas, 269s.

Başıbüyük, Z., Yalçın, H., Bozkaya, Ö. 2007. Eosen yaşlı Kösedağ magmatiklerinin hidrotermal alterasyonla ilişkili kil mineralojisi (Sivas Kuzeydoğusu). 13. Ulusal Kil 2007 Sempozyumu, Süleyman Demirel Üniversitesi, Isparta, 12-14 Eylül, Bildiriler Kitabı, s. 44-64.

Başıbüyük, Z., Yalçın, H., Bozkaya, Ö. 2010. Zara-Suşehri (KD Sivas) Yöresi Magmatik Kayaçlarında Hidrotermal Karışıkı Tabakalı İllit-Smektit Oluşumları. IV. Ulusal Jeokimya Sempozyumu, 26-28 Mayıs, Elazığ, Bildiriler ve Özetler Kitabı, s.29-30.

Bailey, S. W. 1988. X-ray diffraction identification of the polytypes of mica, serpentine, and chlorite. Clays and Clay Minerals, 36(3), 193-213.

Berman, R.G. 1988, Internally-consistent thermodynamic data for minerals in the system Na_2O-K_2O-CaO-MgO-FeO-Fe_2O_3-Al_2O_3-SiO_2-TiO_2-H_2O-CO_2: Journal of Petrology, v. 29, p. 445-522.

Bingöl, E. 1989. 1/2.000.000 ölçekli Türkiye Jeoloji Haritası. Maden Tetkik ve Arama Genel Müdürlüğü Yayını, Ankara.

Bohor, B.F., Triplehorn, D.M. 1993. Tonsteins: Altered volcanic ash layers in coal bearing sequences. Geological Society of America, Special Paper, 285, 44 pp.

Bozkaya, Ö., Yalçın, H., Başıbüyük, Z., Bozkaya, G. 2007. Metamorphic-hosted pyrophyllite and dickite occurrences from the hydrous Al-silicate deposits of the Malatya-Pütürge region, Central Eastern Anatolia, Turkey. Clays and Clay Minerals, 55, 4, p. 423-442.

Boztuğ, D., Jonckheere, R. C. 2007. Apatite fission track data from central Anatolian granitoids (Turkey): Constraints on Neo-Tethyan closure. Tectonics, 26(3).

Boztuğ, D., Tichomirowa, M., Bombach, K. 2007. $^{207}Pb/^{206}Pb$ single-zircon evaporation ages of some granitoid rocks reveal continent-oceanic island arc collision during the Cretaceous geodynamic evolution of the central Anatolian crust, Turkey. Journal of Asian Earth Sciences, 31(1), 71-86.

Brindley, G.W. 1980. Quantitative X-ray mineral analysis of clays: In: Crystal Structures of Clay Minerals and Their X-ray Identification, G.W.Brindley and G.Brown (eds.), Mineralogical Society, London, 411-438.

Brindley, G.W., Wardle R. 1970. Monoclinic and triclinic forms of pyrophyllite and pyrophyllite anhydride. Am. Miner., 48, 42-61.

Brown, G., Brindley, G.W. 1980. X-ray diffraction procedures for clay mineral identification. In Crystal Structuresof Clay Minerals ang their X-ray Identification, Mineralogical Society, London, 305-360.

Chagnon, A., Desjardins, M. 1991. Détermination de la composition de la chlorite par diffraction et microanalyse aux rayons X. Canadian Mineralogist, 29, 245-254.

Collins, D.R., Catlow, C.R.A. 1991. Energy-minimized hydrogen-atom positions of kaolinite. Acta Cryst., Vol.47, pp.678-682.

Cravero, F., Marfil, S., Maiza, P. 2010. Statistical analysis of geochemical data: A tool: to discriminate between kaolinite deposits of hypogene and supergen origin. Patagonia, Argentina. Clay Minerals, 183-196.

Davies, J. H., Von Blanckenburg, F. 1995. Slab breakoff: a model of lithosphere detachment and its test in the magmatism and deformation of collisional orogens. Earth and Planetary Science Letters, 129(1), 85-102.

Domínguez, E., Murray, H.H. 1995. Genesis of the Chubut river valley kaolinite deposits, and their industrial applications. Pp. 129-134 in: Proceedings of the 10th International Clay Conference, 1993 (G.J. Churchman, R.W. Fitzpatrick & R.A. Eggleton, editors) CSIRO Publishing, Melbourne, Australia.

Domínguez, E., Murray, H.H. 1997. The Lote 8 Kaolin Deposit, Santa Cruz, Argentina. Genesis and paper industrial application. Pp. 57-64 in: Proceedings of the 11th International Clay Conference (H. Kodama, A.M. Mermut & J.K. Torrance, editors) Ottawa, Canada.

Duda, R., Rejl, L. 1990. Minerals of The World. Arch Cape Press, New York, 520 p.

Ece, O.I., Nakagawa, Z.E. 2003. Alteration of volcanic rocks and genesis of kaolinite deposits in the Şile region, northern İstanbul, Turkey. Part II: differantial mobility of elements. Clay Minerals, 38, p.529-550.

Ece, Ö.I., Schroeder, P.A. 2007. Clay mineralogy and chemistry of halloysite and alunite deposits in the Turplu area, Balıkesir, Turkey. Clays and Clay Minerals, 55, 18-35.

Ece, O.I., Nakagawa, Z.E., Schroeder, P.A. 2003. Alteration of volcanic rocks and genesis of kaolinite deposits in the Şile region, northern İstanbul, Turkey. I: Clay Mineralogy. Clays and Clay Minerals, Vol.51, No.6, p.675-688.

Ece, Ö.I., Schroeder, P.A., Smilley, M.,Wampler, M. 2008, Acid-sulfate alteration volcanic rocks and genesis of halloysite and alunite deposits in the Biga Peninsula, NW Turkey. Clay Minerals, 43, 281-315.

Ece, Ö.İ., Ekinci, B., Schroeder, P.A., Crowe, D., Esenli, F. 2013. Origin of the Düvertepe kaolinite-alunite deposits in Simav Graben, Turkey: Timing and Styles of hydrothermal mineralization. Journal of Volcanology and Geothermal Research, 255, 57-18.

Efe, A., Gökçe, A. 1999. Maden köyü (İmranlı-Sivas) çevresindeki Pb-Zn yataklarının jeolojisi ve sıvı kapanım incelemeleri. C.Ü. Mühendislik Fakültesi Dergisi Seri A-Yerbilimleri, 16, 29-38.

Esqueviv, J. 1956. Synthèse des phyllites zincifères. Bull. Gr. Fr. Argilés, 8, 3, pp. 23-27.

Evans, B.W., Guggenheim, S. 1988. Talc, pyrophyllite, and related minerals, *in* Hydrous Phyllosilicates (exclusive of micas): Bailey, S.W. ed., Washington DC, Reviews in Mineralogy, Mineralogical Society of America, v.19, p. 225-294.

Fawcett, T. G., Crowder, C. E., Brownwell, S. J., Zhang, Y., Hubbard, C., Schreıner, W., Hamıll, G. P., Huang, T. C., Sabıno, E., Langford, J. L., Hamılton, R., Lou~R, D. 1989. In Methods and Practices in X-ray Powder Diffraction, edited by R. Jenkins, Section 13.3. International Centre for Diffraction Data, Swathmore, USA.

Foster, M.D. 1962. Interpretation of the composition and a classification of the chlorites. U.S. Geological Survey Professional Paper, 414-A, 1-33 p.

Gençoğlu, H., Bayhan, H., Yalçın, H. 1989. Bilecik-Söğüt yöresi kaolinite yataklarının mineralojisi ve kökeni. IV. Ulusal Kil Sempozyumu, C.Ü. Sivas, 20-23 Eylül, Bildiriler Kitabı (Eds. D.Boztuğ and H.Yalçın), 97-112.

Göncüoğlu, M.C., Dirik, K., Kozlu, H. 1997. Pre-Alpine and Alpine Terranes in Turkey: Explanatory notes to the Terrane Map of Turkey. Ed.D. Papanikolaou, F.P. Sassi, IGCP Project No:276 Final Volume: Terrane Maps and Terrane Descriptions. Annales. Géol.Pays Helléniques, 37, 515-536.

Görür, N., Tüysüz, O., Şengör, A.M.C. 1998. Tectonic evolution of the Central Anatolian Basins. International Geology Review, 40, 831-850.

Gündoğdu, M.N., Yalçın, H., Temel, A., Clauer, N. 1996. Geological, mineralogical and geochemical characteristics of zeolite deposits associated with borates in the Bigadiç, Emet and Kırka Neogene lacustrine basins, Western Turkey. Mineralium Deposita, 31, 492-513.

Hemley, J.J., Montoya, J.W., Marinenko, J.W., Luce, R.W. 1980. Equilibria in the system Al_2O_3-SiO_2-H_2O and some general implications for alteration/ mineralization processes: Economic Geology, v. 75, p. 210-228.

Hinckley, D.N. 1963. Variability in “crysallinity” values among the kaolinite deposits of the coastal plain of Georgia and South Carolina. Clays and Clay Minerals, 11, 22-235.

Kalkancı, Ş. 1974. Etüde geologique et petrochimique du sud de la region de Suşehri. Geochronologie du massif syenitique de Kösedağ (Sivas Turquie). These de doctoral de 3e cycle, L’universite de Grenoble, 135 p.

Kalkancı, Ş. 1978. Suşehri güneyinin jeolojik ve petrokimyasal etüdü. Kösedağ siyenitik masifinin jeokronolojisi (NE Sivas-Türkiye). TJK 32. Bilimsel ve Teknik Kurultayı, Bildiri Özetleri, 33-34.

Kadir, S., Akbulut, A. 2009. Mineralogy, geochemistry and genesis of the Taşoluk kaolinite deposits in pre-Early Cambrian metamorphites and Neogene volcanites of Afyonkarahisar, Turkey. Clay Minerals, 44, 89-112.

Kadir, S., Erman, H., Erkoyun, H. 2011. Mineralogical and geochemical characteristics and genesis of hydrothermal kaolinite deposits within Neogene volcanites, Kütahya (western Anatolia), Turkey. Clays and Clay Minerals, 59(3), 250-276.

Kadir, S., Erkoyun, H. 2013. Genesis of the hydrothermal Karaçayır kaolinite deposit in Miocene volcanics and Palaeozoic metamorphic rocks of the Uşak-Güre Basin, western Turkey. Turkish Journal of Earth Sciences, 22(3), 444-468.

Kadir, S., Külah, T., Eren, M., Önalgil, N., Gürel, A. 2014. Mineralogical and geochemical characteristics and genesis of the Güzelyurt alunite-bearing kaolinite deposit within the Late Miocene Gördeles ignimbrite, central Anatolia, Turkey. Clays and Clay Minerals, 62, 486-508.

Karakaya, M.Ç., Karakaya, N., Temel, A. 2001. Kaolin occurrences in Erenler Dağı volcanics, southwest Konya Province, Turkey. Int. Geol. Rev. 43/8, 711-722.

Karakaya N., Karakaya-Çelik, M. 2001. Şaplıca (Şebinkarahisar, Giresun) volkanitlerinin hidrotermal alterasyon türlerinin mineralojik ve jeokimyasal özellikleri. Türkiye Jeoloji Bülteni, 44, 75-89.

Keller, W.D. 1976. Scan electron micrographs of kaolins collected from diverse environments of origin-I: Clays and Clay Minerals, v. 24, p. 107-113.

Kusznir, N. J., Park, R.G. 1987. The extensional strength of the continental lithosphere: its dependence on geothermal gradient, and crustal composition and thickness. In: Coward, M.P., Dewey, J.F., Hancock P.L., (eds.) Continental Extensional Tectonics, Blackwell, Oxford, pp. 35-52.

Millot, G. 1970. Geology of Clays. (trans. W.R.Farrand and H.Paquet). Springer Verlag, New York, Berlin, 429pp.

Moore, D.M., Reynolds, R.C.JR. 1997. X-ray diffraction and the identification and analysis of clay minerals. Oxford University, 378 p.

Murray, H. H. 1988. Kaolin minerals: their genesis and occurrences. In: Bailey SW (ed) Reviews in mineralogy, hydrous phyllosilicates. Mineralogical Society of America Publication no. 19

Murray, H. H., Smith J. M. 1973. The geology and mineralogy of the Grahamstown, South Africa kaolinite deposit. In: Programs and abstracts, 22nd annual clays minerals conference, Clay Minerals Society

Murray, H.H., Keller, D. W. 1993. Kaolins, kaolins and kaolins; In Kaolin genesis and utilization. Special publication no. 1. The Clay Minerals Society, pp 1-24

Sayın, Ş.A. 1987. Türkiye'nin farklı bölgelerine ait kaolinitlerde kristalleşme derecesi. III. Ulusal Kil Sempozyumu Bildiriler Kitabı, 21-27 Eylül 1987, s. 57-72.

Sudo, T., Shimoda, S., Yotsumoto, H., Aita, S. 1981. Electron Micrographs of Clay Minerals: Elsevier, Tokyo, Developments in Sedimentology, v. 31, 203 p.

Şener, M., Gevrek, A. I. 2000. Distribution and significance of hydrothermal alteration minerals in the Tuzla hydrothermal system, Çanakkale, Turkey. Journal of Volcanology and Geothermal Research, 96(3), 215-228

Şengör, A.M.C., Yılmaz, Y. 1981. Tethyan evolution of Turkey: A plate tectonic approach. Tectonophysics, 75, 181-241.

Tüysüz, O. 1993. Karadeniz'den Orta Anadolu'ya Bir Jeotravers: Kuzey Neo-Tetisin Tektonik Evrimi. Türkiye Petrol Jeolojları Derneği Bülteni, 5, 1-33.

Toraya, H., Iwai, S., Marumo, F. 1980. The structural investigation of a kaolinite mineral by X-ray powder pattern-fitting. Mineralogical Journal (Japan). 10, 4, 168-180

Uysal, Ş., Bedi, Y., Kurt, İ., Kılınç, F. 1995. Koyulhisar (Sivas) dolayının jeolojisi. Maden Tetkik ve Arama Genel Müdürlüğü Rapor No: 9838, 120 s Ankara (unpublished).

Ünal, Ercan, H., Işik, Ece, Ö., Schroeder, P. A., Karacık, Z. 2016. Differentiating Styles of Alteration Within Kaolin-Alunite Hydrothermal Deposits of Çanakkale, NW Turkey. Clays and Clay Minerals, 64(3), 245-274.

Yalçın, H. 1991. Hidrotermal kaolinitlerin morfolojisi ve kimyası : Eskişehir ve Malatya yörelerinden örnekler. V. Ulusal Kil Sempozyumu, Anadolu Üniversitesi, Eskişehir, 16-20 Eylül, Bildiriler Kitabı (Ed. M.Zor), 74-86.

Yalçın, H., Gümüşer, G. 2000. Mineralogic and geochemical characteristics of of Late Cretaceous bentonite deposits at the north of Kelkit valley, Northern Turkey. Clay Minerals, 35, 807-825.

Yalçın, H., Bozkaya, Ö. 2003. Sivas Batısındaki (Yıldızeli-Akdağmadeni) hidrotermal kaolinite ve I-S oluşumlarının mineralojisi ve jeokimyası. Türkiye Jeoloji Bülteni, 46, 1-23.

Yalçın, H., Bozkaya, Ö., Tetiker, S. 2005. Kangal kömür yatağının kil mineralojisi ve jeokimyası. 12. Ulusal Kil Sempozyumu, Yüzüncüyıl Üniversitesi, Van, 5-9 Eylül, Bildiriler Kitabı, s. 16-31.

Yılmaz, A., Okay A., Bilgiç T. 1985. Yukarı Kelkit Çayı yöresi ve güneyinin temel jeoloji özellikleri ve sonuçları. Maden Tetkik ve Arama Genel Müdürlüğü Rapor No: 7777, 124 s. Ankara (unpublished).

Yıldız, A., Başaran, C. 2015. Sediment-Hosted Kaolin Deposit from Çakmaktepe (Uşak, Turkey): its Mineralogy, Geochemistry, and Genesis. Clays and Clay Minerals, 63(4), 235-261.

Bull. Min. Res. Exp. (2019) 158: 165-194

Bulletin of the Mineral Research and Exploration

http://bulletin.mta.gov.tr

Geological, mineralogical and geochemical properties of the Dağbaşı skarn ores (Araklı-Trabzon, NE Turkey)

Yılmaz DEMİR[a*]

[a] *Recep Tayyip Erdoğan University, Department of Geological Engineering, 53100 Rize/Turkey orcid.org 0000-0001-6608-4823*

Research Article

Keywords:
Dağbaşı skarn ore, skarn mineralogy, skarn geochemistry, Dağbaşı granitoid, Araklı-Trabzon.

ABSTRACT

The Dağbaşı skarns have developed as an exoskarn type along the nearest border of Upper Cretaceous Dağbaşı Granitoid and block- and lens-shaped limestones of Berdiga formation located in the Liassic volcanics. The early garnets are predominantly grossular type ($And_{0–0.81}Grs_{59.69–78.65}Prs_{21.35–38.11}$), while pyroxenes have a composition between diopside and hedenbergite ($Hed_{24.44–31.81}Diy_{67.3–76.99}Joh_{0.52–0.88}$). The late garnets are characterized by high andradite ($And_{74.67–100}Grs_{0–22.8}Prs_{0–4.51}$), and late pyroxenes by increasing johannsenite content ($Hed_{22.17–62.63}Diy_{0–36.2}Joh_{31.86–76.69}$). High andradite content of late garnets is similar to Cu–Fe-type skarns, whereas the higher johannsenite and Mn/Fe ratios of pyroxenes are similar to Zn-type skarns. Higher andraditic garnets indicate an oxidized-type skarn and association with the shallow emplacement of intrusion. Increasing And/Grs ratios of garnets, from core to rim, also point out to increasing degree of oxidation. The retrograde skarn minerals are epidote, tremolite-actinolite, quartz, calcite, and chlorite. The ore minerals are composed of magnetite, hematite, pyrrhotite, pyrite, chalcopyrite, sphalerite, and galena. The Ag content of the galena (1.18-1.43wt%) suggests significant silver potential. Dağbaşı Granitoid shows high-K (2.38–3.75wt.% K_2O), calc-alkaline, metaluminous–peraluminous transitional (A/CNK=0.88–1.23) and volcanic arc type granitoid. The various main and trace element contents of the granodiorite observed along the skarn zones show similarities with Fe–Cu–Zn type skarn-related granitoids, whereas there is no clear relation between the skarn type and composition of outher granitoids. Therefore, the presence of sulfur phases, in addition to the oxide ore suggests that geochemical characteristics of granitoid had a large effect on the mineral composition.

Received Date: 09.01.2018
Accepted Date: 25.05.2018

1. Introduction

The northeast Black Sea Region is an important metallogenic province of Turkey containing different types of ore deposits. In addition to the predominantly observed massive sulfide-type deposits, hydrothermal, skarn, and porphyry deposits are the other main types of ore mineralizations in the region. The region contain a large number of skarn-type ore deposits, due to the widespread outcrop of carbonate rocks (Berdiga formation) and granitic intrusions which cut these carbonate rocks. Çambaşı, Kotana, Kirazören, Ögene, Özdil, Dağbaşı, Kartiba, Sivrikaya, Demirköy, Eğrikar, Camiboğazı, and Arnastal are some of these well-known skarn occurrences (Demir et al., 2017) (Figure 1).

Some studies performed on the skarn-type deposits of the region (Aslan, 1991; Hasançebi, 1993; Saraç, 2003; Çiftçi and Vıcıl, 2003; Çiftçi, 2011; Sipahi, 2011; Kurt, 2014; Sipahi et al., 2017; Demir et al., 2017) have demonstrated that these deposits show many differences in terms of ore types, alteration products, and formation conditions. According to these studies, while exoskarn-type mineralization has been reported from Özdil, Kartiba, Sivrikaya, Çambaşı, Kotana, Arnastal, and Camiboğazı deposits, both endoskarn- and exoskarn-type deposits have been

* *Corresponding author: Yılmaz DEMİR, yilmaz.demir@erdogan.edu.tr*
http://dx.doi.org/10.19111/bulletinofmre.457070

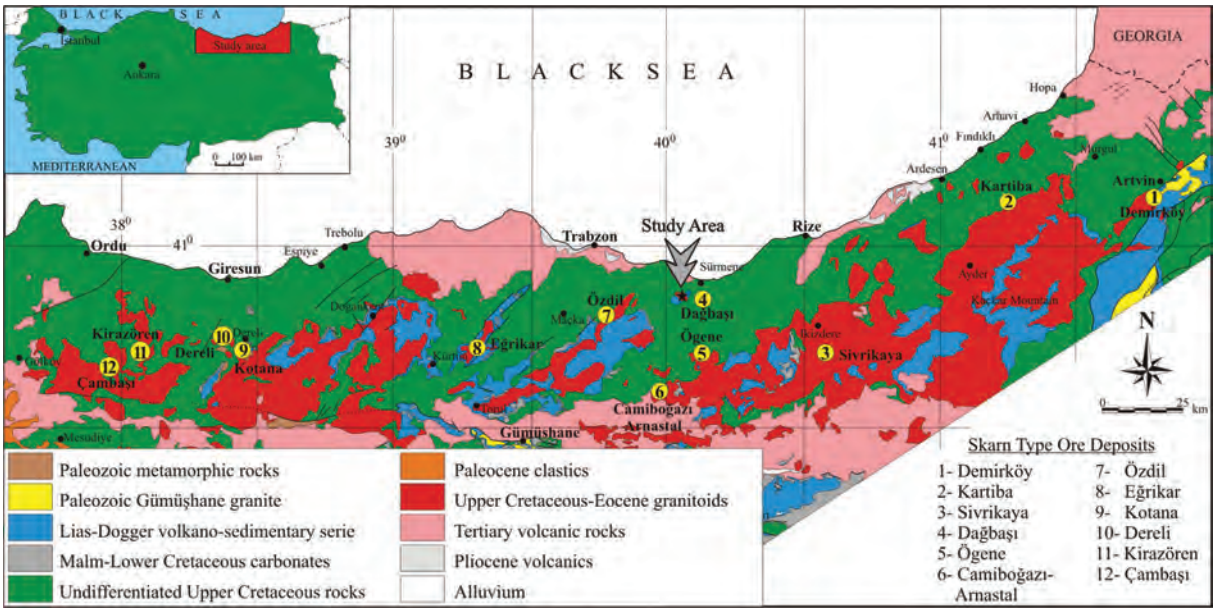

Figure 1- Geological map of the Eastern Black Sea Region and distribution of some skarn type deposits (Modified after Güven et al., 1998).

reported from Kirazören, Ögene, and Eğrikar deposits. Ore in the Özdil, Kartiba, Camiboğazı, and Sivrikaya deposits consists of oxide minerals (magnetite and hematite) while sulfur minerals accompany oxide phases in the Arnastal, Kotana, Kirazören, Eğrikar, and Dağbaşı deposits (Demir et al., 2017). In terms of host rocks, the age of carbonates ranges from Early Jurassic to Late Cretaceous and the age of intrusions from Jurassic to Eocene (Sipahi et al., 2017; Demir et al., 2017). In spite of these studies, it is understood that skarn-type deposits are less well investigated in comparison with the other types of deposits in the region, so the geological, mineralogical, and geochemical differences between these deposits have not been sufficiently clarified.

Dağbaşı skarn ores, the subject of this study, have been studied by Gülibrahimoğlu (1986) and Hasançebi (1993). In these studies, the presence of magnetite, specularite, pyrite, chalcopyrite, and sphalerite has been reported, but the skarn mineralogy has not been investigated. Granitic rocks in the region which played an important role in the skarn developments have been studied by Kaygusuz (1992), Aydınçakır (2006), and Kaygusuz and Aydınçakır (2011). They reported that these granites are I-type with low to medium K content and show properties of volcanic-arc-type calc-alkaline granitoids. They also reported that fractional crystallization and magma mixing were the main processes for these granite occurrences.

Skarn-type deposits occur as a result of the metasomatic process between granitoid and carbonate host rocks. At the early stage of this process, prograde skarn minerals develop due to the high temperature of intruding granites, whereas retrograde skarn minerals develop at the late stage with decreasing temperatures. Previous studies have shown that the anhydrous silicate minerals (such as garnet and pyroxene) develop in the prograde stage while the hydrous silicate minerals (such as epidote, amphibole, and chlorite) develop in the retrograde stage (Einaudi et al., 1981; Meinert, 1992; Orhan and Mutlu, 2009; Oyman, 2010).

Previous researchers showed a relationship between the garnet, pyroxene composition, and metal content of the skarn and the oxidation degree, and the classification was made accordingly (Einaudi et al., 1981; Einaudi and Burt, 1982; Nakona et al., 1994; Nakona, 1998; Meinert et al., 2005). In this classification, pyroxenes with high Mn content (johannsenite) correspond to the Zn-type skarns, while pyroxenes ranging between diopside and hedenbergite compositions correspond to the Cu–Fe-type skarns. According to these studies, oxidized skarns have high andradite and low spessartine and almandine contents. Some other studies have also shown that the increasing And/Grs ratios, from core to rim, reflect increasing oxidation degree in the zoned garnet crystals (Collins, 1977; Newberry, 1983; Abu el Enen et al., 2004). Newberry (1991) pointed out that in the reduced skarns, pyroxene is more commonly observed than

garnet and has a hedenbergite composition, whereas in the oxidized skarns pyroxene is less commonly observed and has a composition between diopside and hedenbergite.

The relationships between chemical compositions of granitoids and skarn types and their metal contents have been investigated by many researchers (Kwak and White, 1982; Newberry and Swanson, 1986; Meinert, 1995; Meinert et al., 2005). In these studies, it was shown that skarn-related granitoids are mostly associated with normal calc-alkaline intrusions, W, Sn, and Mo skarns are associated with intra-continental granitoids, and Fe, Cu, Zn, and Au containing skarns are associated with I-type island arc granitoids. With respect to the Al saturation, Sn skarns are associated with peraluminous plutons which develop as a result of melting of sedimentary rocks of continental crust. On the other hand, calcic Fe skarns are associated with metaluminous island arc plutons and other types of skarns are associated with granitoids of metaluminous–peraluminous transitions.

In this study, four different skarn locations have been defined around the Dağbaşı area. The geological and mineralogical properties of these skarn zones have been studied by systematic sampling. Garnet and pyroxene compositions have been studied in detail, because they give critical information on the classification of skarn deposits, developments of formation conditions, and determination of their metal content. The geochemical characteristics of Dağbaşı granitoid were also investigated because of the relationship between the geochemical features of the granitoids and skarn types and the metal contents. In addition, the compositions of sulfur minerals (pyrrhotite, pyrite, chalcopyrite, sphalerite, and galena) in skarn zones were measured by mineral chemistry analysis and the main and trace element contents were evaluated.

2. General Geology

The oldest units in the study area are volcano-sedimentary rocks consisting of andesite, basalt, and their pyroclastics including sandstone, marl, claystone, and sandy limestone intercalations. This unit is highly fractured and altered and covers a wide area around the Ipekçili, Köprüüstü, Kükürtlü, Çakırınsırt, and Kalaycıoğlu districts and Güney Hill. Andesites and basalts consist of plagioclase, amphibole, biotite, augite, and opaque minerals and display brecciated, glassy, microlitic, microlitic porphyritic, amygdaloidal, and void textures. According to the microscopic study, the anorthite content of the plagioclases is $An_{21–29}$ in andesite and $An_{52–58}$ in basalt. In some cases, quartz, calcite, epidote, and chlorite, which are secondary in origin, accompany these minerals. In general, these secondary minerals are found along the fractures or gas cavities and are mostly accompanied by opaque minerals.

Pyroclastic rocks composed of tuff and volcanic breccia are observed as sedimentary intercalations in the volcanic rocks and are observed around the Çimenli, Akrut, and Ustaoğlu districts. Tuffs are mainly composed of very small crystals and cementing ash, and breccias are made of relatively larger crystals, rocks fragments, and cementing ash material. Tuffs are classified as crystal and lithic crystal tuffs according to various mineral and rock fragments. In this unit, there are thin to medium laminated sandstone, marl, sandy limestone, and red biomicrite layers. They are a few metres in thickness and not more than several hundred metres in length.

This unit containing andesite, basalt, pyroclastics, and some sedimentary intercalations has been dated as Jurassic by Schultze-Westrum (1961), Köprübaşı (1992), and Çamur et al. (1994). Based on the *Involitina liassica, Trocholina* sp., *Lenticulina* sp., *Spirillina* sp., *Vidalina martana Farinacci, Lingulina* sp., *and Lagenidea* sp. *fossil species* found in the red biomicrite layer of the same unit, Liassic age was determined by Güven et al. (1998). On the other hand, Aydınçakır (2006) argues that volcano-sedimentary rocks may be Jurassic–Lower Cretaceous in age, taking into account the overlying Malm–Lower Cretaceous Berdiga formation.

Oldest volcanic rock units covering large areas around the Dağbaşı Granitoid (Figure 2) and extending along the eastern Black Sea metallogenic belt have been defined as Lower Basic Series by some researchers (Schultze-Westrum, 1961; Gedikoğlu et al., 1979; Aslaner, 1977; Şen, 1988; Kaygusuz, 1992; Aydınçakır, 2006). On the other hand, different names have been given to this volcano sedimentary unit, such as Telmeyaylası formation by Yüksel (1976), Hamurkesen formation by Ağar (1977), Balkaynak formation by Kesgin (1983), Zimonköy formation by Eren (1983), and Şenköy formation by Kandemir (2004), although all these names refer to the Liassic same unit in the region according to

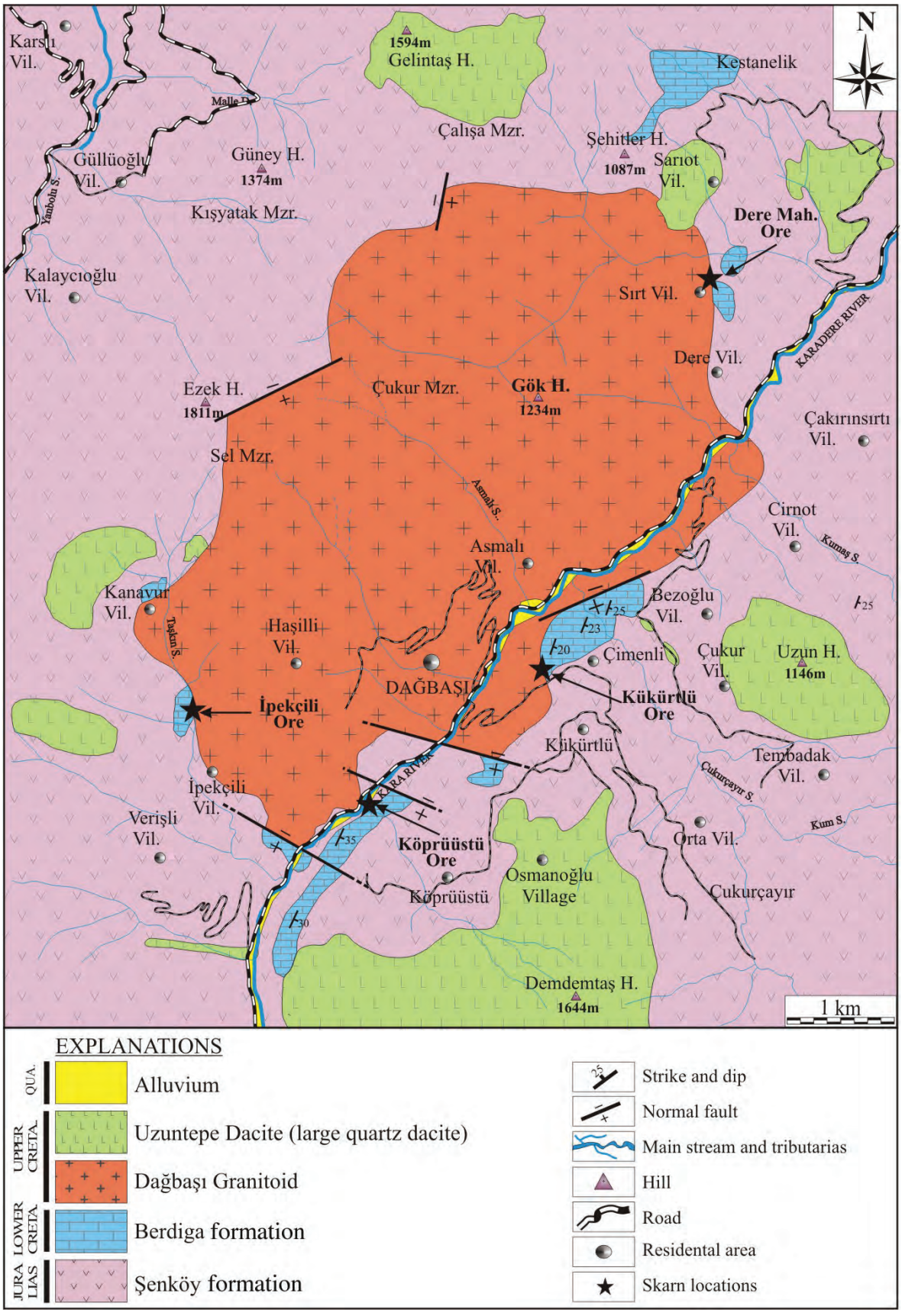

Figure 2- Geological map of the Dağbaşı area (Modified after Aydınçakır, 2006).

the palaeontological data. In this study, the name "Şenköy formation", proposed by Kandemir (2004), is preferred, observing all the facies of this unit from bottom to top.

There are numerous dolomitic limestone lenses and blocks at the upper level of Şenköy formation, reaching up to 300 m in thickness and a kilometre in length. The thicknesses of the limestone layers cropping out around Sırt, Çiftepınar, Kestanelik, Kükürtlü, and Köprüüstü districts and Sel field vary between 10 and 30 cm. The colours of the limestones vary from dark grey to light grey far from the border, but the colours change in light colour tones from grey to beige near the granitoid contact, and calcite crystals become larger along the contact. These massive limestones, present in the northern part of the eastern Black Sea Region with limited lateral extensions, were considered as the products of platform carbonates and named as the Berdiga formation by numerous researchers (Kırmacı et al., 1996, 2018; Yılmaz et al., 2008). Limited lateral extension of these limestones was explained by active rifting tectonics during the Cretaceous by some studies (Yılmaz and Kandemir, 2006; Koch et al., 2008).

Carbonate and volcanic rock fragments, shell pieces, fine-grained quartz, plagioclase, and disseminated opaque minerals were observed in the thin section of the limestones. Significant lamination was observed at the levels containing clay-siltstone. Micritic cemented limestones were named as a biomicrite according to Folk (1962) and greywacke according to Dunham (1962). Although some *Globotruncana* and *Radiolarian* remnants were observed in some thin sections (the definition was given by Dr. Raif Kandemir), reliable palaeontological data could not be obtained in this study for the age determination. But it is understood that this unit was aged as Jurassic–Lower Cretaceous in some studies (Köprübaşı, 1992; Güven et al., 1998; Çamur et al., 1994), and this age was also accepted by some other researchers (Şen, 1988; Kaygusuz, 1992; Hasançebi, 1993; Aydınçakır, 2006; Kırmacı et al., 2018).

An outcrop of granitic rocks with an area of about 25 km^2, around Dağbaşı region, was named as Dağbaşı Granitoid by Şen (1988). This granitoid was emplaced into volcano-sedimentary rocks of the Şenköy formation and crystallized limestones of the Berdiga formation (Figure 2). Quartz, plagioclase, alkali feldspar, pyroxene and amphibole minerals could be observed in the granitic rocks macroscopically. Orthoclase ratios increase quite noticeably in the central part of the granitoid. Therefore, dark pink and pink-like grey colours become noticeable. The large crystal size in this central part becomes smaller towards the edge of the granitoid. Accordingly, the orthoclase contents decrease in the outer part of the granitoid while the quartz and plagioclase contents increase. Dağbaşı Granitoid contains some mafic microgranular enclaves, a few centimeters to a meter scale, along the contact with volcanic rocks. The age of the pluton was determined as 88.1–86.0 million years by Kaygusuz and Aydınçakır (2011) by the U–Pb SHRIMP method conducted on the zircon minerals. This time interval corresponds to the Upper Cretaceous period.

Dağbaşı Granitoid was divided into four different zones according to its modal mineralogical composition by Aydınçakır (2006). According to this study, monzogranite composition is dominant in central parts, while granitoid becomes granodiorite, tonalite, and diorite composition towards the outher zone. Because of the irregular distribution of these zones, additional sampling has been carried out to determine the petrographic and geochemical properties of the granitoids around the skarn contacts. In addition to macroscopically determined quartz, plagioclase, and alkali feldspar, hornblende and biotite were extensively observed in the prepared thin sections. Apatite and zircon are relatively less common and have euhedral crystal forms. Epidote and chlorite, observed especially around the biotites, are secondary in origin. Porphyritic and myrmekitic textures are quite common in thin sections. In some cases, biotite and hornblende inclusions in orthoclase minerals display poikilitic textures.

The dacitic rocks cutting Dağbaşı Granitoid and volcanic rocks of Şenköy formation around the study area were described as "coarse crystal dacites" by some studies (Şen, 1988; Kaygusuz, 1992; Hasançebi, 1993). On the other hand, as these dacites have characteristic columnar structure around Uzuntepe area, they were called "Uzuntepe Dacites" and Senonian age was appointed by Aydınçakır (2006) and Kaygusuz and Aydınçakır (2011).

3. Analytical Method

In this study, skarn zones around the Dağbaşı area have been systematically sampled. Preparations of thin and polished sections, mineralogical studies, and

sample preparation for the whole rock analyses have been carried out in the laboratories of the Department of Geological Engineering at the Recep Tayyip Erdoğan University.

Chemical analyses of 20 samples from the Dağbaşı Granitoid have been analysed for major, trace, and lanthanum group elements in the ACME analytic laboratory in Canada. Major and trace elements of the samples were analysed by ICP-AES (Inductively Coupled Plasma – Atomic Emission Spectrometry), and lanthanum group elements were analysed by the ICP-MS (Inductively Coupled Plasma – Mass Spectrometry) method. For the major and trace element analyses, 0.2 g of powdered sample was mixed with 1.5 g of LIB_2, then dissolved in 5% HNO_3-containing liquid, and then analysed. For lanthanum group element analyses, 0.25 g powdered samples were dissolved in various acidic solutions and then analysed. The results of the major element analyses are given as weight percentages, while trace and lanthanum group elements are given parts per million (ppm).

Silicate and sulfur mineral analyses have been carried out using a CAMECA-SX100 electron microprobe at the Mineralogy and Petrology Institute of Ludwig Maximilian University. Measurements were performed under conditions of 15 kV and 20 nA, and the electron beam diameter was chosen to be 1 μm. The counting time was 30 s for Al, Ni, and Ca, 20 s for Ti, and 10 s for all the other elements. Natural and synthetic standards have been used for the calibration. The detection limit of the measured elements (in wt%) of the oxide samples was determined as 0.01 for Si, Al, K, Ti, Ca, and Na; 0.02 for Mg; 0.03 for Cr; 0.04 for Fe and Ni; and 0.06 for Mn. The detection limit for the sulfide samples was determined as 0.08 for the Fe, Pb, and S; 0.06 for the Cu; 0.05 for the As, Co, and Ni; 0.04 for Zn; 0.03 for Cd; and 0.02 for Ag.

4. Studies in Skarn Zones

4.1. Skarn Zones and Skarn Mineralogy

Four different skarn-type mineralizations were described around the Dağbaşı area including İpekçili, Köprüüstü, Kükürtlü, and Dere districts (Figure 3). There are some abandoned adits left from the old mining activities, all of which are closed. All the skarn mineralizations have developed in the sides of the lens- and block-shaped limestones closest to the pluton. The contact between granitoid and limestones is not observable in the area (Figure 3). There are no skarn developments in the granite itself, so all of the skarns have developed as exoskarn. Considering the mineralogy and texture of the skarn, four zones have been studied accordingly. As İpekçili and Köprüüstü skarns have similar characteristics, they have been considered together. In these locations, a progressive stage is represented by the presence of garnets and pyroxenes. According to their textures, they have been divided into early and late stages and the minerals of both stages have been defined in the distal zone limestones. Early progressive stage garnets and pyroxenes together show massive (Figure 4a), rhythmically banded (Figure 4b), nodular (Figure 4c), and granular (Figure 4d) textures representing primary developments. These first stage garnets show zoned growth structures under the microscope (Figure 4e) and in the BSE pictures (Figure 4f). Late progressive stage garnets and pyroxenes have developed as veins along the cracks in the limestones (Figure 4g) and they also show zoned growth under the microscope (Figure h) and in the BSE pictures (Figure 4i). Early stage garnets do not have any relation with the ore-forming minerals; on the other hand, late stage garnets accompany to magnetite and hematite in their growth zones (Figure 4j), indicating that ore mineralizations started in the late stage. Quartz and calcite always accompany to the prograde stage garnets and pyroxene in thin sections.

In these two locations, retrograde stage skarn minerals of epidote, quartz and calcites have developed along the fractures of volcanic host rocks (Figure 4k, l). In some locations, retrograde stage epidote and quartz are also present as disseminations in the volcanic rocks (Figure 5a). In the Köprüüstü location only, retrograde stage minerals, that is, tremolites and actinolites, have garnet and pyroxene as macro-lenses (Figure 5b) and as micro-inclusions (Figure 5c).

In the Kükürtlü and Dere Mahalle districts, garnet and pyroxene developments, representing prograde stage, are not seen in thin sections or macroscopically in the field. The signs of retrograde skarn developments are present in these locations. Developments of epidote, chlorite, quartz, and calcite veins are commonly present (Figure 5d) in these two locations along the cracks in the limestones and volcanic rocks. In some cases, banded structures are present (Figure 5e) between quartz and epidote. In addition, there are

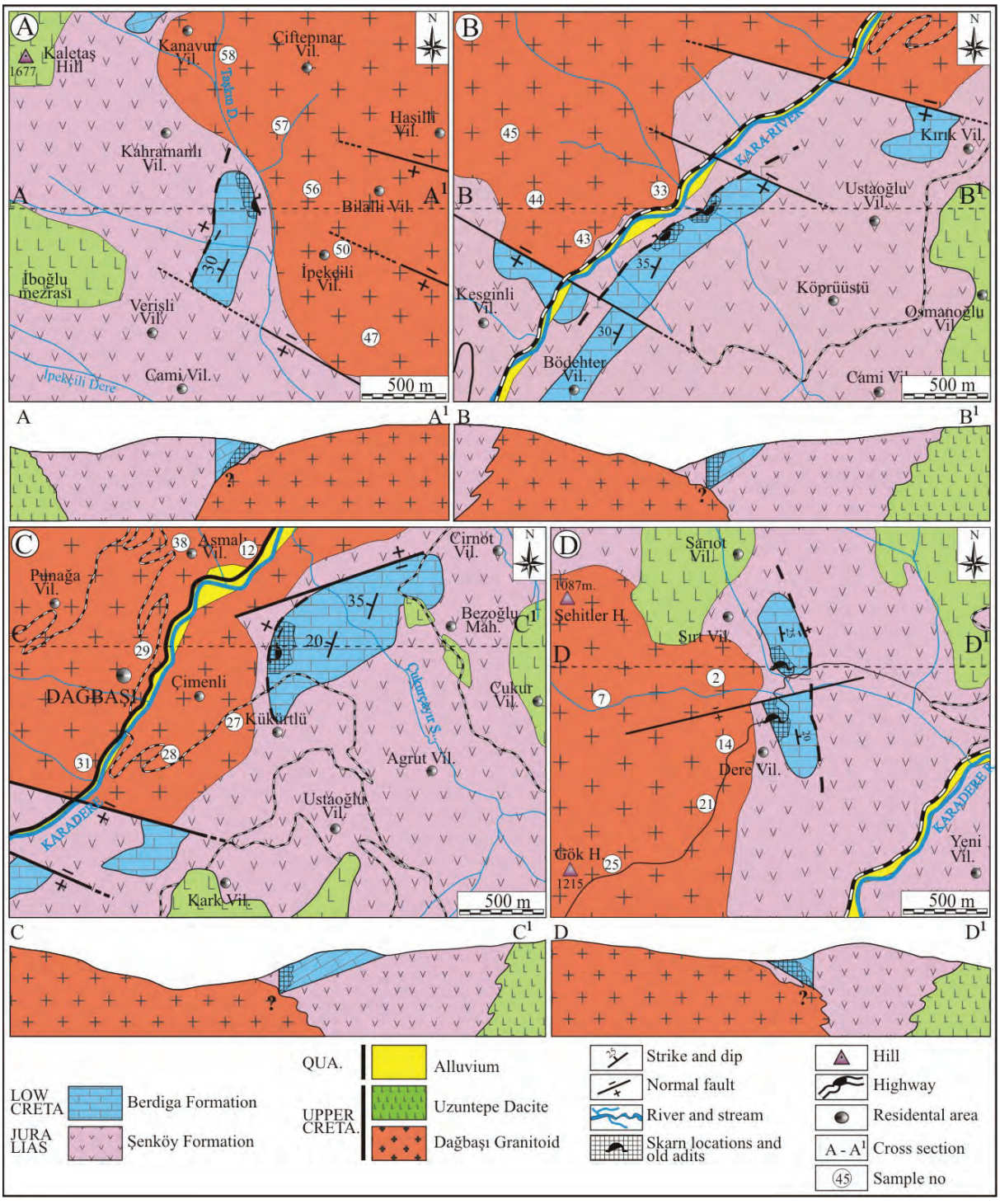

Figure 3- a) Geological map and cross sections of the skarns in İpekçili, b) Köprüüstü, c) Kükürtlü, d) Dere Mahalle locations (Modified after Aydınçakır, 2006).

quartz inclusions, reaching up to 1 cm in size, in both limestones and volcanic rocks (Figure 5f). In the thin sections, early epidotes always accompany the quartz (Figure 5g), and the quartz was enclosed by later stage epidotes. In the thin sections, quartz and calcite are commonly observed in the fractures (Figure 5h) and gas voids (Figure 5i) of volcanic host rock.

Oxide and sulfur minerals in the outcrops in the İpekçili and Köprüüstü locations have different

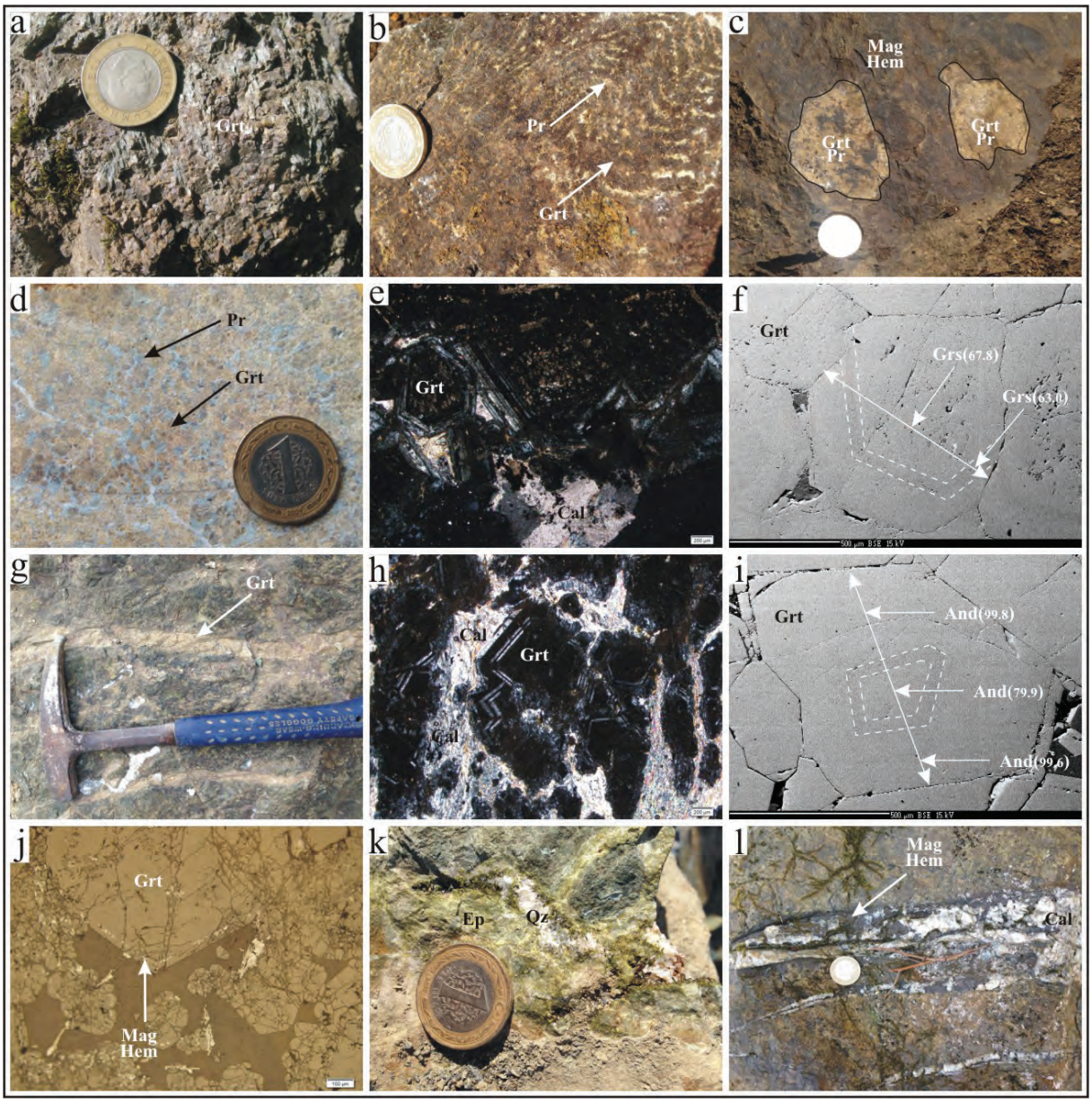

Figure 4- a) Massive garnet texture in the İpekçili skarn; b) rhythmically banded texture between garnet and pyroxenes; c) nodular garnet and pyroxenes in the Köprüüstü carbonates; d) granular texture showing that garnet and pyroxenes developed together; e, f) microphotograph and BSE photograph of early stage zoned garnet crystal (X nicol); g) late stage garnet veins developed along the cracks in the limestones (rarely including pyroxene); h, i) microphotograph (X nicol) and BSE photograph of zoned late stage garnet (X nicol); j) magnetite and hematite developments along the growth zone of late stage garnets; k) epidote and quartz developments in the volcanic rocks during the retrograde skarn stage; l) magnetite- and hematite-bearing calcite veins in the volcanic host rocks (Grt: garnet; Pr: pyroxene; Mag: magnetite; Hem: hematite; Qz: quartz; Cal: calcite; Trm: tremolite; Act: actinolite; Ep: epidote).

structures. These are irregularly shaped piles (Figure 6a) and lenses in the limestones, banded along the weak zones of limestone layers with a thickness of up to 30 cm in size (Figure 6b), irregularly shaped fracture-filling type in the limestones with a thickness not exceeding 10 cm (Figure 6c), and fracture-filling and breccia-filling structures in the volcanic host rock (Figure 6d). Along these zones, epidote, quartz, and calcite accompany ore minerals. However, magnetite and hematite developments in growth zones in the late stage garnets indicate that ore mineralization started towards the end of the prograde stage (Figure 4j). On the other hand, both the ore shape and the presence of epidote, quartz, and calcite accompanying ore mineralization indicate that the main ore mineralization developed at the retrograde skarn stage.

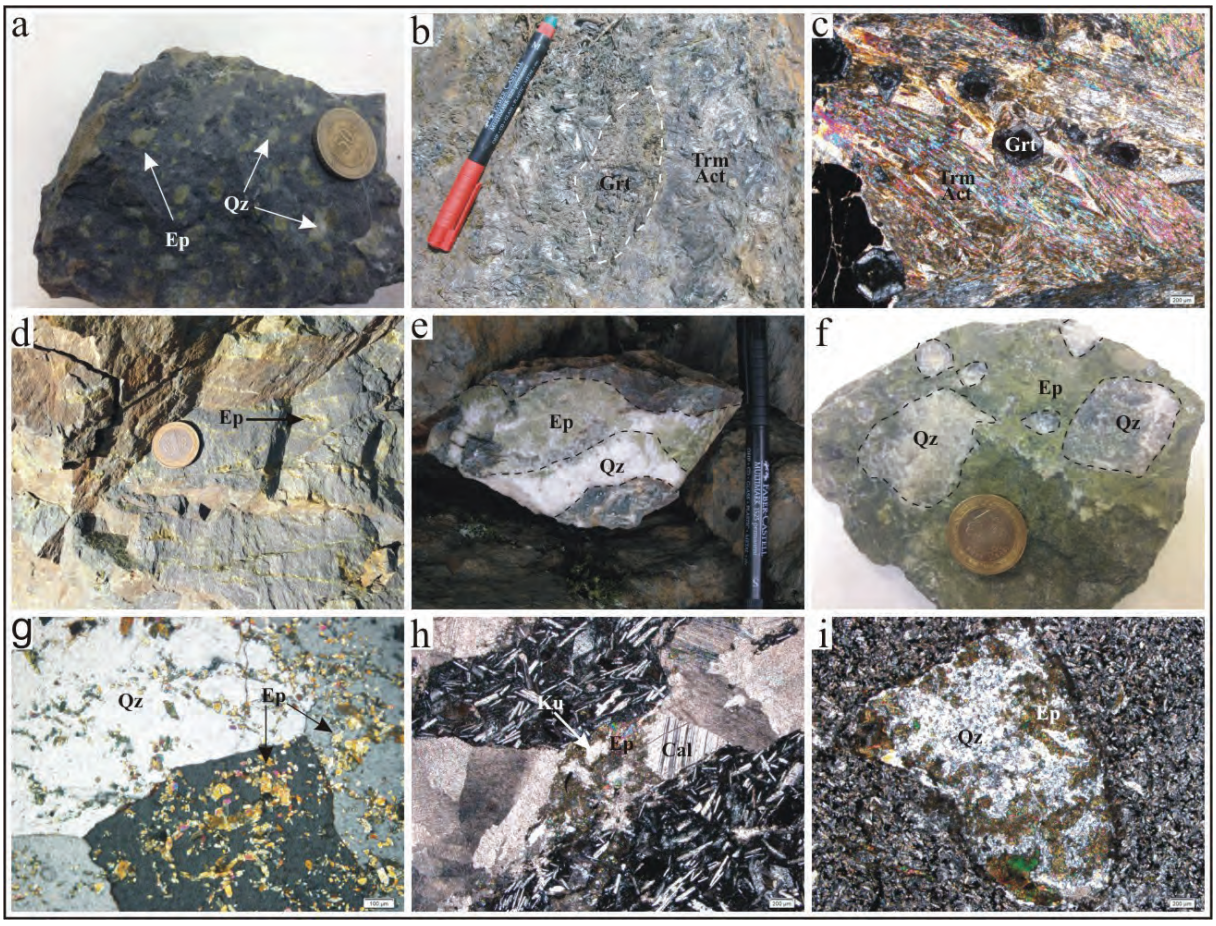

Figure 5- a) Epidote and quartz disseminations in the volcanic host rocks; b) garnet and pyroxene inclusions in the tremolites and actinolites of the Köprüüstü skarn; c) microphotograph of (X nicol) garnet inclusions in the tremolites and actinolites; d) epidote, quartz, and calcite veins developed along the cracks of the volcanic host rock around the Kükürtlü and Dere mahalle districts; e) banded texture of quartz and epidote; f) quartz inclusions in the highly epidotized volcanic rocks; g) microphotograph (X nicol) of quartz and epidote development; h and i) microphotograph (X nicol) of epidote, quartz, and calcite developments along the cracks and gas voids in the volcanic rocks (Qz: quartz; other symbols are same as it is in figure 4).

In the Kükürtlü and Dere Mahalle locations, in addition to magnetite and hematite veins formed along the fractures of limestone and volcanic host rock, ellipsoidal magnetite and hematite piles, up to meter in size, were also observed (Figure 6e). Apart from these, disseminated magnetites and hematites can be seen in thin sections as well as in the hand specimens (Figures 6f, g). Replacement remnants of magnetite and hematite accompany quartz fillings seen in Figure 5f (Figure 6h). Ore mineralization in the Kükürtlü and Dere Mahalle locations developed at the retrograde stage, because evidence for a prograde skarn stage has not been identified. However, quartz and epidote are found to be filling fractured ore fragments, indicating that ore mineralization started before these minerals (Figure 6i).

Magnetites and hematites (in some cases as specularite) are the main ore-forming minerals in each location. Magnetites and hematites seen in the growth zones (Figure 4i) of the late stage garnets indicate that ore mineralizations started together with these late stage garnets. However, the presence of these garnets as inclusions in magnetites and hematites indicates that the main ore development takes place after these garnets (Figure 6j). Apart from magnetite and hematite, there is some difference in terms of the sulfur mineral content between locations. Pyrrhotite, pyrite, and chalcopyrite are the sulfur minerals present in the skarn zone in the İpekçili location. In this location, pyrrhotites are characteristic with a “bird’s eye structure” (Figure 6k) and have been replaced by late stage sphalerites (Figure 6l). In the Köprüüstü location, galena accompanies pyrite,

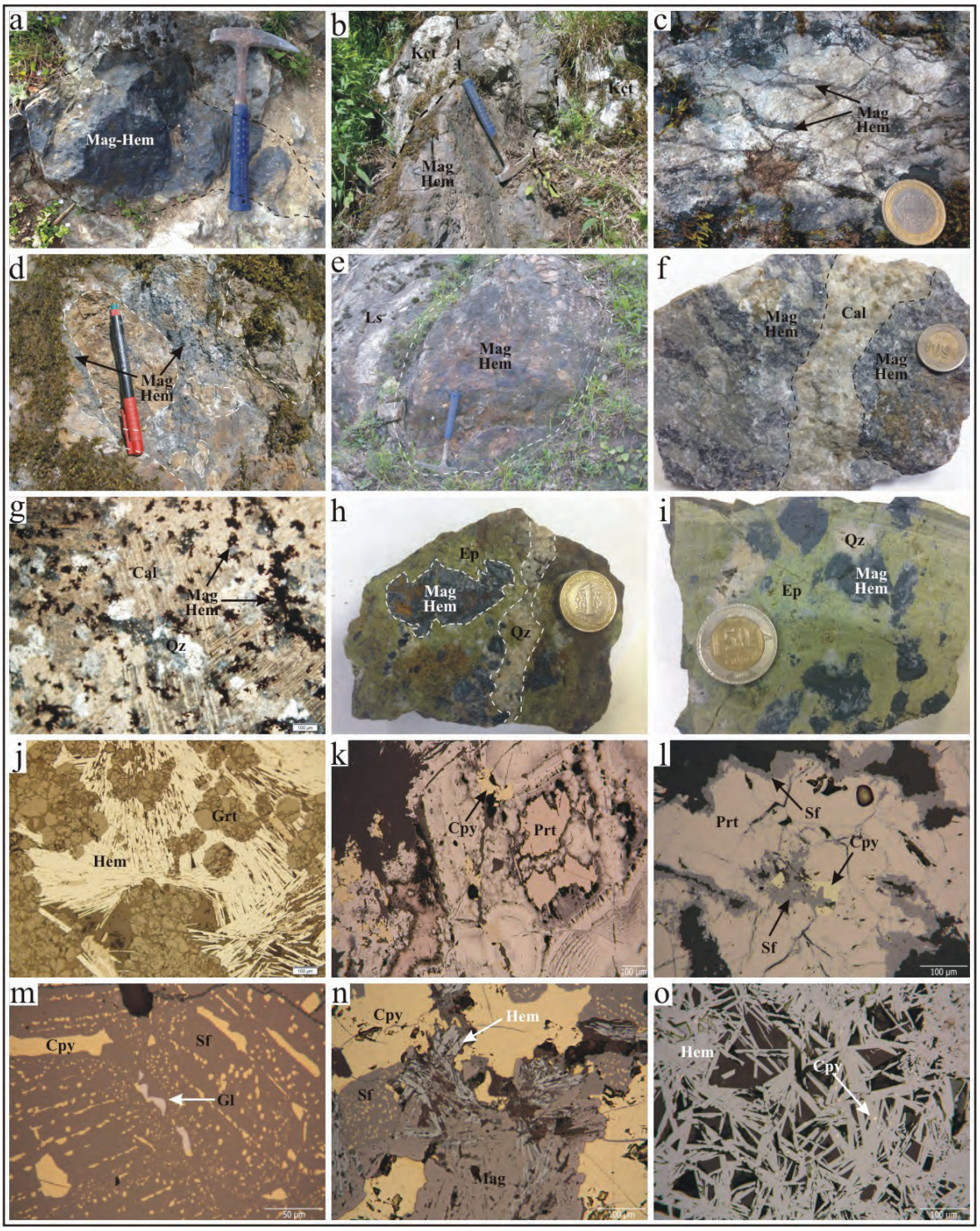

Figure 6- a) Ore pile containing unsystematically developed magnetite and hematite; b) magnetite and hematite development in the weak zones along the bedding planes in the limestones; c) ore veins developed along the fracture zones in the limestones; d) volcanic breccia filling structure along the skarn zones; e) ellipsoidal ore piles in the limestones reaches up to meter size; f, g) macro and micro (X nicol) photograph of magnetite and hematite disseminations along the calcite veins in the limestones; h) partly replaced ore inclusions in the epidotes; i) epidote and quartz filling the interspaces in the ore fragments; j) late stage garnet inclusions in the hematites; k) pyrrhotites with characteristic bird's eye texture, commonly found in the İpekçili skarn; l) replacements of pyrrhotites by sphalerites; m) exsolution texture between chalcopyrite and sphalerite is commonly present in the Köprüüstü skarn. Galena inclusion in the sphalerite; n) coexistence of oxide and sulfur minerals in the Köprüüstü skarn; o) pyrite and chalcopyrite inclusions in the hematites of the Kükürtlü skarn (Cpy: chalcopyrite; prt: pyrrhotite; sf: sphalerite; gl: galena; other symbols are same as it is in figure 4).

chalcopyrite, and sphalerite (Figure 6m) which is much less common than the others. Magnetites and hematites also accompany sulfide ore mineral (Figure 6n). However, these magnetites and hematites are in the form of mineral inclusions in the sulfur minerals. Alteration products of covellite, chalcocite, digenite, and goethite are present in both locations.

Magnetite and hematites are the main ore minerals in both Kükürtlü and Dere Mahalle locations. Pyrite and chalcopyrite inclusions, a few microns in size, are observed rarely in these minerals (Figure 6o). Apart from these, no other sulfide minerals are present. Abundances of the sulfide minerals in Kükürtlü and Dere Mahalle locations are much lower compared with the İpekçili and Köprüüstü ores. With all the information given on the skarn mineralogy, paragenesis and successions of the Dağbaşı skarn ore have been established as shown in figure 7.

4.2. Geochemical Characters of the Dağbaşı Granitoid and Their Relations with the Skarn Types

Dağbaşı Granitoid has different mineralogical and geochemical zonings (Aydınçakır, 2006). Because of irregular distribution of these zones, additional sampling and geochemical analyses were performed. For this purpose, 20 samples were collected from the skarn zone granitoids and were analysed for their major, trace, and LGE elements (Table 1) and results have been correlated with the skarn types. Chemical compositions of the granitoids along the skarn zones have been correlated with the chemical compositions of the granitoids in other parts and the results were evaluated from the viewpoints of skarn types. SiO_2, CaO, and Na_2O values of the granitoid samples are in the following order: 61.76–71.69%, 2.32–4.88%, and 2.77–4.30%. Al_2O_3 changes from 13.12 to 16.72% and K_2O changes (apart from samples 12 and 38, which show variations from 0.45 to 0.82%) from 2.28 to 3.75%. Based on these values, A/NK and A/CNK ratios of 1.51–2.45 and 0.88–1.23, respectively, have been calculated.

Considering the major element content, granitoid samples show compositions between granodiorite and tonalite compositions (Figure 8a) in the P–Q diagram (Debon and Le Fort, 1988). However, granodiorite, monzogranite and tonalite samples collected from various and parts of the granitoid by Aydınçakır (2006) have tonalite compositions. Analyses of the samples collected by Aydınçakır (2006) and samples in this study fall into the calc-alkaline area in the AFM classification diagram (Figure 8b) of Irvine and Baragar (1971). While skarn-zone granitoids fall into the high-potassium calc-alkaline area in the SiO_2–K_2O diagram (Figure 8d), analyses of the samples collected from other parts of the granitoid fall into medium calc-alkaline and tholeiitic areas. According to the molar A/NK and A/CNK ratios, samples from the skarn zones have metaluminous–peraluminous compositions, while samples from the other parts have peraluminous compositions (Figure 8e). Comparing the major element analyses of the skarn-zone granitoids with the skarn-producing granitoids of different types (Figures 8c, d), all the samples have compositions between the Fe–Cu–Zn type skarn (Meinert et al., 2005). On the

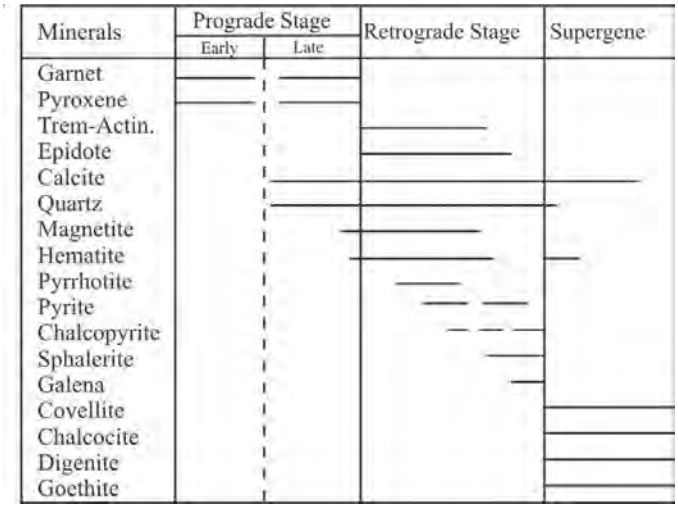

Figure 7- Generalized mineral paragenesis and succession in the skarn ores around Dağbaşı area.

Table 1- Major oxide (wt%), trace and LGE elements (ppm) content of the samples from the skarn zone granitoid.

Sample No	2	7	12	14	21	25	27	28	29	31	33	38	43	44	45	47	50	56	57	58
Major oxid (%)																				
SiO_2	62.94	63.69	71.69	62.86	63.18	65.10	64.25	63.26	65.66	65.19	64.62	71.21	63.15	61.76	63.30	63.70	64.53	65.48	63.04	62.73
TiO_2	0.39	0.38	0.30	0.39	0.38	0.34	0.37	0.39	0.33	0.32	0.37	0.33	0.40	0.40	0.37	0.38	0.39	0.36	0.40	0.38
Al_2O_3	16.10	15.70	14.54	16.18	15.65	14.99	15.66	15.45	15.32	15.21	16.72	13.12	15.40	15.37	16.01	15.59	16.37	14.91	14.66	15.92
Fe_2O_3	4.62	4.42	2.07	4.73	4.48	3.92	4.26	4.50	4.14	3.93	4.32	3.79	4.62	4.66	4.43	4.54	4.42	4.15	4.69	4.50
MnO	0.13	0.11	0.02	0.13	0.11	0.10	0.11	0.11	0.11	0.10	0.11	0.08	0.12	0.12	0.11	0.11	0.13	0.11	0.12	0.11
MgO	1.92	1.96	1.17	2.04	2.00	1.64	1.83	1.97	1.61	1.65	1.70	0.86	2.51	2.73	2.14	2.35	1.72	1.79	2.14	2.01
CaO	4.88	4.25	4.30	3.71	4.12	4.13	4.31	4.47	3.81	3.89	2.32	3.00	2.70	3.95	3.46	3.74	4.61	2.70	3.89	3.22
Na_2O	3.38	3.07	3.68	3.65	3.83	3.16	3.13	3.38	3.54	3.70	3.47	4.30	4.03	3.26	4.00	3.44	3.64	2.77	3.09	4.26
K_2O	2.41	3.03	0.45	3.07	2.78	2.68	2.55	2.71	2.38	2.89	2.43	0.82	3.19	3.24	3.38	3.20	2.47	3.75	2.28	3.45
P_2O_5	0.13	0.13	0.07	0.14	0.13	0.11	0.12	0.13	0.11	0.12	0.13	0.07	0.13	0.14	0.13	0.14	0.13	0.13	0.13	0.13
LOI	2.80	3.00	1.50	2.80	3.00	3.50	3.10	3.30	2.70	2.70	3.60	2.30	3.40	4.00	2.30	2.50	1.30	3.60	5.30	3.00
Total	99.70	99.68	99.78	99.68	99.69	99.68	99.66	99.67	99.71	99.71	99.75	99.83	99.69	99.61	99.68	99.67	99.69	99.70	99.72	99.73
A/NK	2.17	2.45	1.72	1.74	1.68	1.94	1.96	1.85	1.77	1.71	1.79	1.53	1.58	1.81	1.59	1.75	1.70	1.97	1.86	1.51
A/CNK	0.88	1.06	0.90	0.97	0.91	0.99	0.98	0.93	0.98	0.96	1.21	1.00	1.06	0.99	0.98	1.01	0.90	1.23	1.03	0.99
Tra. Ele.(ppm)																				
Ni	1.80	1.70	0.60	1.10	1.50	1.70	1.70	1.60	1.00	1.00	1.60	<0.1	8.10	8.90	6.60	7.40	1.40	1.40	2.10	2.30
V	94.00	99.00	50.00	104.00	102.00	85.00	93.00	100.00	84.00	89.00	87.00	27.00	96.00	107.00	99.00	107.00	85.00	93.00	99.00	103.00
Cu	8.40	9.00	1.10	9.40	12.50	12.80	12.60	13.60	9.80	9.20	10.00	1.00	8.20	2.50	12.90	14.30	8.00	16.30	24.30	14.70
Pb	2.50	2.60	0.50	5.20	3.30	13.10	10.40	2.80	7.70	2.50	10.20	1.30	4.00	4.50	7.50	6.40	5.70	19.50	72.80	5.30
Zn	46.00	43.00	6.00	33.00	46.00	37.00	43.00	42.00	37.00	37.00	46.00	40.00	47.00	50.00	36.00	38.00	27.00	46.00	118.00	47.00
W	254.00	375.80	749.90	283.70	234.60	275.70	224.10	296.10	163.20	129.40	207.60	555.50	157.50	299.60	172.60	272.10	359.00	159.50	156.00	230.10
Rb	57.10	74.70	6.10	81.30	67.30	73.40	64.20	59.50	62.30	64.30	75.10	14.70	84.90	85.70	85.50	79.40	61.60	123.80	69.10	84.90
Ba	1136.00	1129.00	143.00	1206.00	1205.00	1379.00	1494.00	1317.00	1297.00	1317.00	782.00	230.00	1275.00	1604.00	1331.00	1223.00	1115.00	1468.00	1043.00	1029.00
Sr	523.20	520.70	385.70	596.30	530.40	509.70	553.70	515.50	501.60	527.20	495.40	229.00	413.40	518.00	568.60	574.80	556.30	388.00	273.50	393.00
Ta	0.60	0.70	0.50	0.60	0.60	0.60	0.60	0.70	0.70	0.60	0.60	0.20	0.70	0.70	0.60	0.60	0.60	0.60	0.50	0.50
Nb	8.00	7.60	5.20	7.80	7.60	7.50	8.10	7.50	7.80	6.60	8.10	2.80	7.40	7.00	6.80	7.00	7.90	7.10	7.20	7.20
Hf	2.60	2.90	2.90	2.90	2.80	2.50	2.60	2.60	2.50	2.50	3.00	3.00	2.90	2.70	2.60	2.50	2.70	2.60	2.40	2.60
Zr	106.20	106.80	98.00	104.90	104.10	87.60	94.50	93.60	96.40	81.50	104.20	120.10	96.90	103.30	96.30	90.70	100.50	104.30	95.00	91.30
Y	12.50	11.30	17.20	15.60	12.10	10.80	12.10	11.80	11.00	9.40	13.40	27.90	15.20	12.60	12.00	12.10	13.00	12.40	11.10	11.60
Th	6.70	8.80	6.60	8.80	8.60	9.90	8.70	8.60	7.90	9.30	6.70	2.00	9.90	9.20	9.70	9.30	7.10	6.70	9.30	9.40
U	2.70	2.60	1.80	2.70	2.90	2.90	2.90	3.10	2.60	2.70	2.20	0.70	2.60	2.80	2.80	2.90	2.40	2.30	2.90	2.70
LGE (ppm)																				
La	26.40	28.00	19.50	29.00	26.80	27.80	27.20	27.90	28.50	25.00	28.00	10.10	33.10	24.20	28.50	28.60	31.30	22.90	23.60	22.90
Ce	46.40	45.50	34.50	47.50	45.80	46.20	45.60	45.10	47.60	42.50	46.90	21.10	51.10	42.60	47.30	48.70	55.60	43.50	42.30	42.50
Pr	4.73	4.68	3.60	5.12	4.50	4.47	4.58	4.73	4.71	4.07	5.18	2.60	5.38	4.48	4.60	4.78	5.51	4.32	4.40	4.18
Nd	16.70	16.20	13.50	19.10	15.60	15.70	15.90	16.10	16.10	13.80	18.50	12.00	20.30	16.10	15.40	16.70	18.60	14.70	16.30	14.70
Sm	2.90	2.83	2.41	3.19	2.66	2.63	2.64	2.71	2.67	2.38	3.18	2.94	3.02	2.67	2.77	2.79	2.93	2.51	2.62	2.50
Eu	0.80	0.74	0.71	0.86	0.77	0.70	0.80	0.80	0.80	0.70	0.91	1.05	0.94	0.82	0.81	0.83	0.85	0.65	0.63	0.71
Gd	2.71	2.46	2.71	3.19	2.57	2.20	2.34	2.61	2.18	2.10	2.68	3.91	3.08	2.59	2.62	2.56	2.71	2.37	2.14	2.17
Tb	0.35	0.31	0.40	0.43	0.35	0.32	0.33	0.35	0.33	0.29	0.40	0.65	0.40	0.36	0.32	0.35	0.37	0.34	0.32	0.31
Dy	2.22	1.94	2.66	2.52	2.06	1.94	2.02	1.89	1.80	1.70	2.22	4.31	2.22	2.16	1.87	2.16	2.11	1.95	1.99	1.90
Ho	0.42	0.39	0.56	0.51	0.41	0.39	0.38	0.43	0.40	0.34	0.45	1.02	0.45	0.39	0.38	0.39	0.44	0.39	0.40	0.34
Er	1.31	1.12	1.71	1.52	1.15	1.18	1.12	1.24	1.10	1.12	1.18	2.99	1.46	1.26	1.18	1.20	1.33	1.20	1.13	1.11
Tm	0.21	0.18	0.27	0.22	0.17	0.18	0.17	0.18	0.17	0.15	0.21	0.46	0.21	0.19	0.18	0.20	0.21	0.20	0.18	0.18
Yb	1.27	1.26	1.80	1.40	1.33	1.14	1.35	1.38	1.24	0.98	1.30	2.93	1.28	1.16	1.20	1.32	1.33	1.25	1.15	1.13
Lu	0.22	0.20	0.29	0.23	0.19	0.19	0.20	0.21	0.20	0.20	0.24	0.49	0.23	0.21	0.21	0.18	0.22	0.19	0.19	0.19

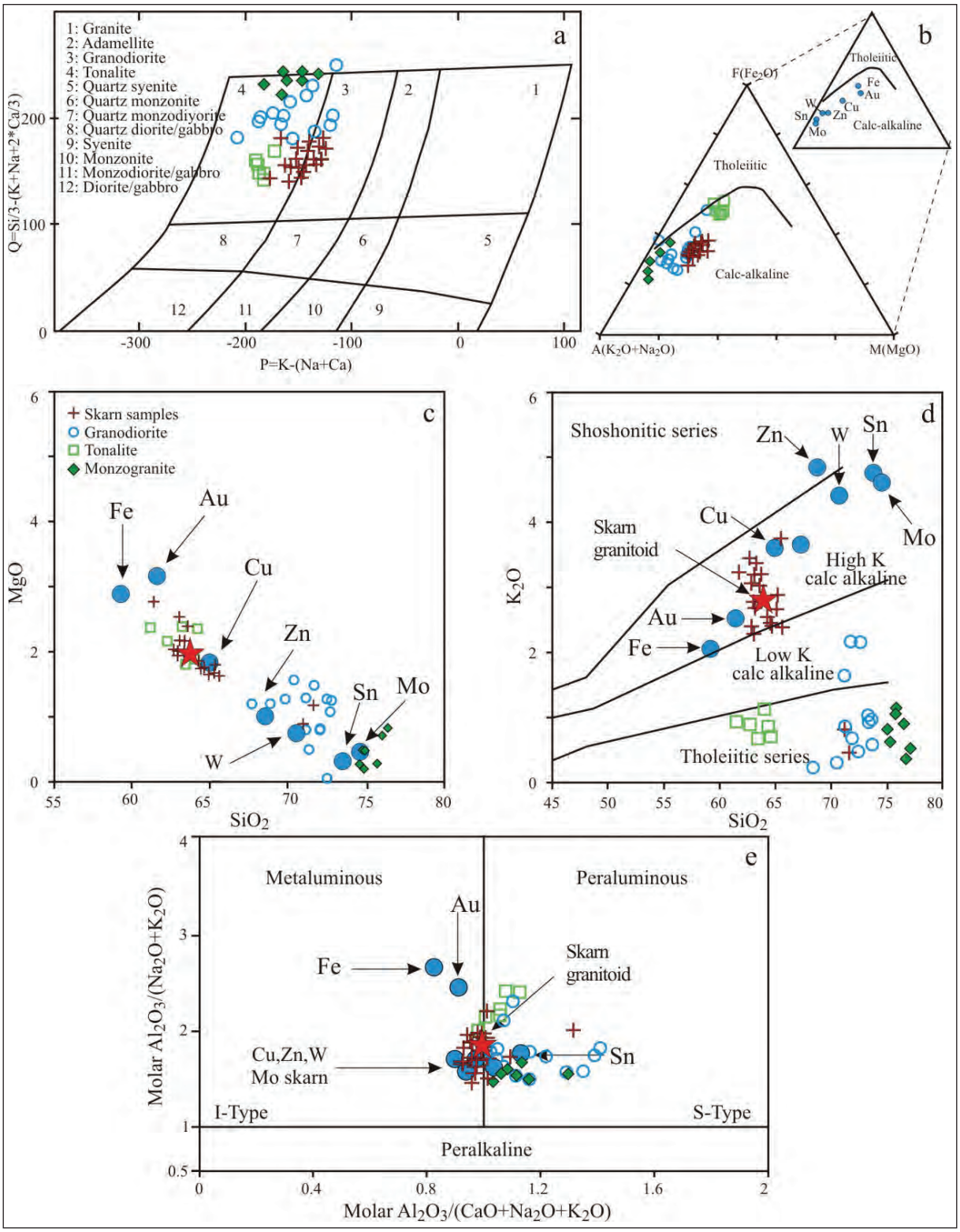

Figure 8- a) Distribution pattern of the skarn zone granitoid samples and samples from the other part of the Dağbaşı Granitoid plotted together on the P–Q diagram (Debon and Le Fort, 1983); b) distribution of these samples on the AFM diagram and comparison of these samples with the skarn-related granitoids (tholeiitic-calk-alkali curve according to Irvine and Baragar, 1971); c, d) MgO and K_2O variations of these samples versus SiO_2 and comparison of these samples with the skarn-related granitoids; e) classification based on molar A/NK versus A/CNK transition (Maniar and Piccoli, 1989). The star symbol is the average of the skarn granitoid samples.

other hand, the results of the samples from the other parts of the Dağbaşı Granitoid collected by Aydınçakır (2006) show quite different composition from the skarn-producing granitoids.

Changes in major element contents of the skarn zone granitoids have been correlated with the SiO_2 contents. There was no meaningful outcome. However, when the results of this study were evaluated together with the results of Aydınçakır (2006), the increase in SiO_2 contents showed negative correlations with the K_2O, CaO, MgO, Al_2O_3, Fe_2O_3, P_2O_5, and TiO_2 contents (Figure 9a, c–h.) On the other hand, there is a positive correlation between the SiO_2 and Na_2O contents (Figure 9b). The negative correlation between SiO_2 and MgO, CaO, and Al_2O_3 represents the fractional crystallization of plagioclase, hornblende, and biotite; the correlation between SiO_2 and Fe_2O_3 and TiO_2 represents the magnetite and Ti-oxide fractions; and the correlation between SiO_2 and P_2O_5 represents the apatite fractions. All of the negative correlations for the major elements indicate that the granitoid originated from the parent reservoir by fractional crystallization.

Granitoid samples from the skarn zones fall into the volcanic-arc-type granitoid (VAG) field in the tectonic setting classification diagrams of Nb–Y and Rb–Y+Nb (Figures 10a, b). Nb–Y, Rb–Y+Nb, and Rb–Sc diagrams show that the trace element content of the skarn granitoid has a similar composition to the Fe–Cu–Zn-type skarn-producing granitoids (Figures 10a, b, and d). On the other hand, the distribution of the samples from the other parts of the granitoid displays a quite independent composition pattern. Based on the analyses of the samples of the zoned Dağbaşı Granitoid, near to skarn zones, these graphics show that an association could be drawn between the skarn types and the compositions of the Dağbaşı Granitoid. On the other hand, samples from the other parts of the granitoid do not have any compositional similarities with the skarn types. Both granitoid samples close to the skarn zones and samples from other parts of the granitoid have similarities with the Fe–Cu–Zn-type skarn composition on the Rb/Sr–Zr diagram (Figure 10c).

4.3. Compositions of the Skarn Minerals

Skarn-type deposits develop by metasomatic processes along the contacts between carbonate rocks and granitic intrusions. The mineralogical properties of the skarn show differences according to the chemical composition of the magma, type of carbonate host rock, depth of the skarn development, and degree of oxidation of skarn minerals (Meinert et al., 2005). Because of this, the mineralogical properties of the skarns have to be taken into account when defining and classifying skarn-type deposits. Additionally, the chemical compositions of the minerals and their zonations give valuable information on the process and environment of skarn development.

Garnets and pyroxenes are the most common minerals present in the skarn zones. Studies on skarn deposits showed that there is a systematic connection between the compositions of these minerals and the metal contents of the deposits. So classifications have been carried out on the basis of the compositions of these minerals (Burt, 1972, 1982; Einaudi et al., 1981; Nakona et al., 1994, 1998; Meinert et al., 2005). The stoichiometric compositions of these minerals determined by analysing their compositions are commonly shown as end members on the triangular diagrams. In these studies (pyrope+spessartine+almandine)–grossular–andradite are used as end members for garnet, and johannsenite–hedenbergite–diopside are used as end members for pyroxenes.

In this study, the compositions of the garnet and pyroxenes in the skarn zones have been analysed by electron-probe micro analyser (EPMA) and their chemical stoichiometric compositions and end members have been calculated. Skarn types have been determined by plotting these data on triangular diagrams. Additionally, the chemical variations of petrographically determined early and late stage minerals and variations on the zoned crystals have been studied. Those, evoluations of the solutions caused skarns have been investigated. The calculations are based on a total of 24 oxygens for garnets and six oxygens for pyroxenes. The ferric iron calculation for garnets has been carried out according to Droop (1987).

4.3.1. Garnet

Analyses of garnets from Köprüüstü and İpekçili locations have been evaluated and early and late stage garnet compositions have been interpreted separately. Analyses of the garnets from these two locations are given in table 2. Early garnets from the Köprüüstü location are dominantly of grossular type and have the

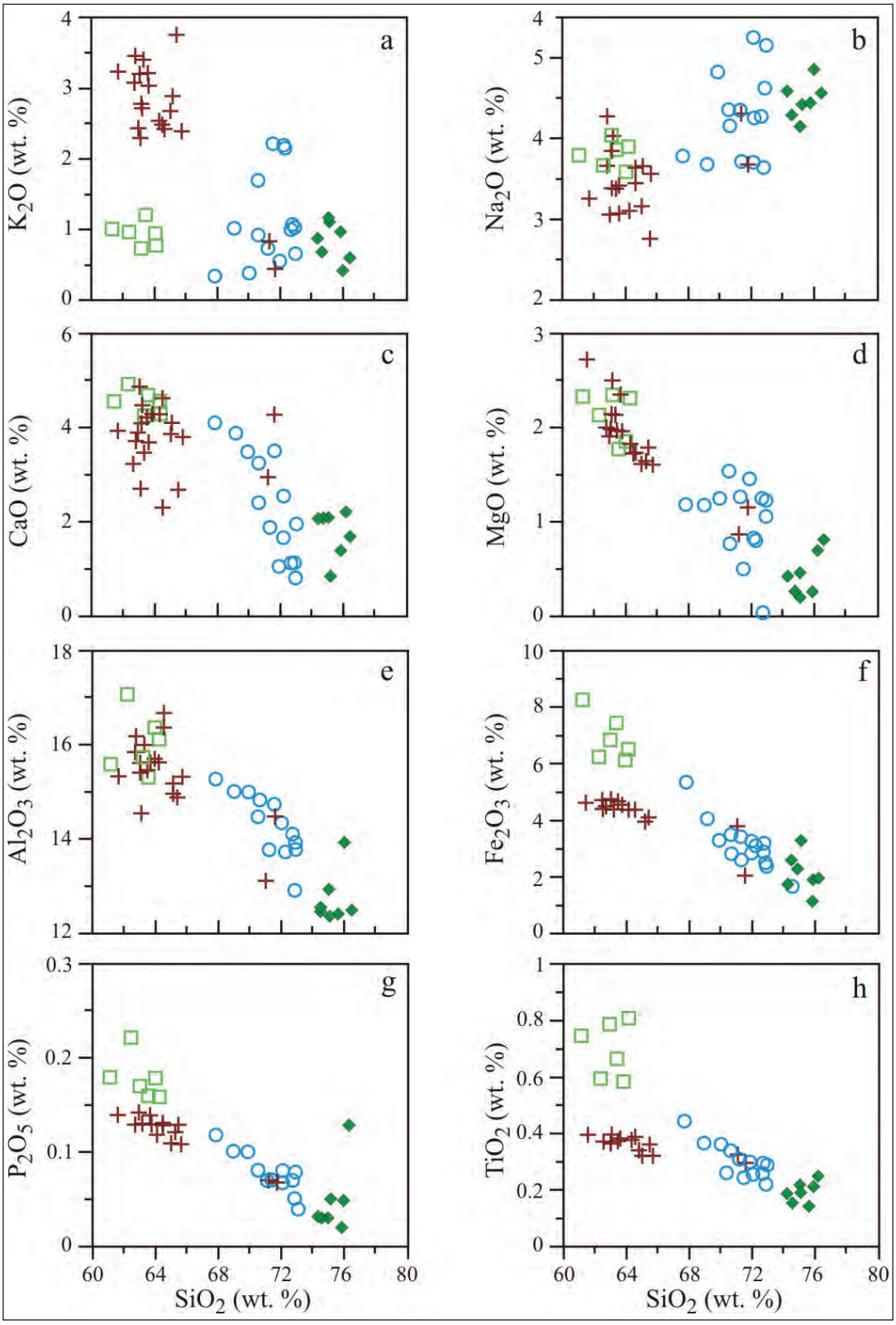

Figure 9- SiO_2 versus major element variation diagrams of the samples from the skarn zones and other parts of the granitoid (symbols are same as it is in figure 8c).

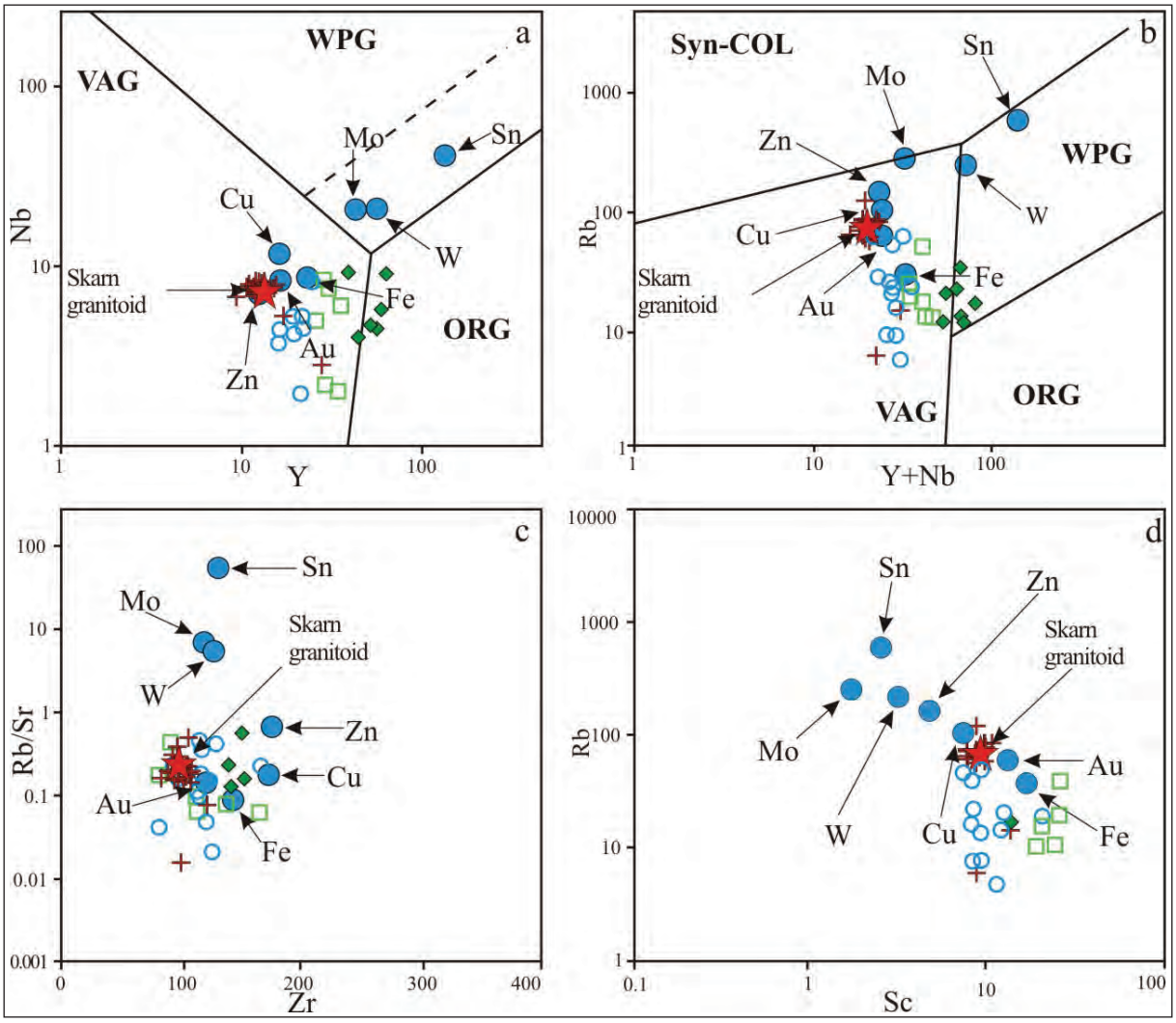

Figure 10- a, b) Distribution pattern of the skarn zone and the Dağbaşı granitoid samples plotted together on the Nb–Y and Rb–(Nb–Y) trace element diagrams used in defining tectonic settings (Pearce et al., 1984) and comparison of these with the granitoids causing different types of skarns (WPG: within plate granitoids, ORG: ocean ridge granitoids, VAG: volcanic arc granitoids, syn-COL: collision granitoids; dashed lines show the upper limit of the ORG anomaly values); c, d) distribution pattern of the Dağbaşı Granitoid samples on the Zr–Rb/Sr and Sc–Rb diagrams and comparison of them with the compositions of plutonic rocks with different skarn types (Meinert, 1995; symbols same as in figure 8c).

composition $And_{0–8.81}Grs_{59.69–78.65}Prs_{21.35–38.11}$, whereas late garnets are of andradite type with a composition of $And_{74.67–100}Grs_{0–22.81}Prs_{0–2.52}$. Accordingly, early and late stage garnets from the İpekçili locations have similarities with the dominant grossular type at the early stage ($And_{0–8.81}Grs_{55.67–66.53}Prs_{32.40–38.00}$) and dominant andradite type at the late stage ($And_{75.71–99.96}Grs_{0–21.80}Prs_{0–4.41}$).

It is possible to show the ideal stoichiometric compositions of the minerals by plotting their analyses on triangular diagrams as end members (Meinert, 1992). The chemical compositions of early and late stage garnets from Köprüüstü and İpekçili locations have been plotted on a (pyrope+spessartine+almandine)–grossular–andradite triangular diagram separately (Figure 11a). According to this, late stage garnets have high andradite and low grossular contents. On the other hand, both grossular and almandine contents are high in the early stage garnets.

Microscopic studies show that garnets in the limestones have zonation from core to rim. Mineral chemistry analyses performed on these zoned crystals from core to rim confirm that there are some variations in the element concentrations which reflect the changes in the chemistry of solutions. In both Köprüüstü and İpekçili locations, the Al_2O_3 content of the early

Table 2- EPMA analyses representing early and late stage garnets from the Köprüüstü and İpekçili skarns (bdl: below detection limit).

Sample No	E27	E27	E27	E27	E27	E71	E71	E71	E71	E71	49	49	49	49	49	KL2	KL2	KL2	KL2	KL2
Analyses No	1	2	3	4	5	7	8	9	10	11	1	2	3	4	5	12	13	14	15	16
SiO_2	36.58	37.25	37.36	37.23	37.23	34.06	34.54	33.99	34.17	33.96	37.49	37.78	38.11	37.61	38.19	34.94	34.93	34.91	35.60	35.06
TiO_2	bdl	0.11	0.11	0.10	0.17	bdl	bdl	0.01	bdl	bdl	0.05	0.03	0.20	0.11	0.12	bdl	bdl	0.02	bdl	bdl
Al_2O_3	20.66	23.01	23.35	23.22	23.15	0.72	0.95	0.34	0.15	1.48	20.47	21.23	20.79	20.95	23.56	0.41	0.84	1.74	0.38	1.05
Fe_2O_3	16.30	13.46	12.95	13.02	13.30	30.15	29.50	30.38	30.08	28.17	17.56	16.24	16.83	16.34	13.57	31.40	30.56	29.82	31.45	30.54
MnO	0.06	0.06	0.01	bdl	0.04	0.43	0.62	0.40	0.35	0.48	0.37	0.17	0.12	0.32	0.23	0.58	0.68	0.83	1.43	0.61
MgO	0.01	0.05	0.04	0.06	0.05	bdl	0.01	bdl	bdl	bdl	0.03	0.02	0.46	0.54	0.05	0.01	0.01	0.01	bdl	bdl
CaO	23.17	23.51	23.62	23.55	23.55	31.76	31.66	31.58	31.44	30.79	22.96	22.93	23.25	22.74	23.71	32.81	32.12	32.34	32.51	32.88
Na_2O	0.02	bdl	0.01	bdl	bdl	0.01	0.02	0.01	bdl	bdl	0.01	bdl	bdl	bdl	0.01	0.01	bdl	bdl	0.02	bdl
K_2O	bdl	bdl	0.01	bdl	bdl	bdl	bdl	bdl	0.01	bdl	bdl	bdl	0.15	0.20	bdl	bdl	bdl	0.01	0.02	bdl
Total	96.80	97.45	97.46	97.18	97.49	97.12	97.30	96.71	96.21	94.88	98.93	98.40	99.89	98.82	99.43	100.16	99.14	99.69	101.40	100.15
Si	2.954	2.920	2.913	2.915	2.913	2.953	2.979	2.962	3.024	2.992	2.970	2.990	2.979	3.017	2.927	2.944	2.976	2.940	2.964	2.944
Al iv	0.046	0.080	0.087	0.085	0.087	0.047	0.021	0.037	-	0.008	0.030	0.010	0.021	-	0.073	0.044	0.024	0.060	0.036	0.056
Al vi	1.925	2.062	2.080	2.077	2.066	0.031	0.082	-	0.016	0.156	1.888	1.973	1.900	1.956	2.073	-	0.067	0.125	0.003	0.056
Ti	-	-	0.007	0.006	0.010	-	-	0.006	-	-	0.003	0.002	0.012	0.006	0.007	-	-	0.001	-	-
Fe^{3+}	0.067	-	-	-	-	1.634	1.592	1.657	1.671	1.535	0.096	0.023	0.078	0.060	-	1.668	1.623	1.561	1.655	1.615
Fe^{2+}	1.035	0.973	0.963	0.962	0.969	0.552	0.536	0.557	0.414	0.541	1.067	1.053	1.022	0.850	0.974	0.544	0.503	0.539	0.535	0.530
Mn	0.004	0.004	0.001	-	0.002	0.031	0.045	0.030	0.027	0.036	0.025	0.012	0.008	0.022	0.015	0.041	0.049	0.059	0.101	0.043
Mg	0.001	0.006	0.005	0.007	0.006	-	0.001	-	-	-	0.003	0.002	0.053	0.065	0.005	0.002	0.001	0.002	-	-
Ca	2.005	1.975	1.974	1.976	1.974	2.950	2.926	2.949	2.981	2.907	1.949	1.945	1.947	1.954	1.947	2.962	2.933	2.918	2.900	2.959
Total	8.036	8.026	8.029	8.027	8.027	8.199	8.183	8.194	8.133	8.174	8.031	8.008	8.019	7.931	8.021	8.205	8.176	8.204	8.193	8.203
Prop	0	0.2	0.2	0.2	0.2	0	0	0	0	0	0.1	0.1	1.8	2.2	0.2	0.1	0.1	0.1	0	0
Spessartine	0.1	0.1	0	0	0.1	1.2	1.8	1.1	0.9	1.4	0.8	0.4	0.3	0.8	0.5	1.6	1.9	2.3	2.2	1.7
Almandine	32.0	32.1	32.0	32.0	31.9	0	0	0	0	0	33.4	34.5	32.6	29.4	32.8	0	0	0	0	0
Andradite	3.4	-	-	-	-	95.7	94.3	98.0	99.1	90.9	4.9	1.1	3.9	3.1	-	97.6	95.0	90.0	97.8	93.9
Grossular	64.5	67.6	67.8	67.8	67.8	3.1	3.9	0.9	0.0	7.7	60.8	63.9	61.4	64.5	66.5	0.7	3.0	7.6	-	4.4

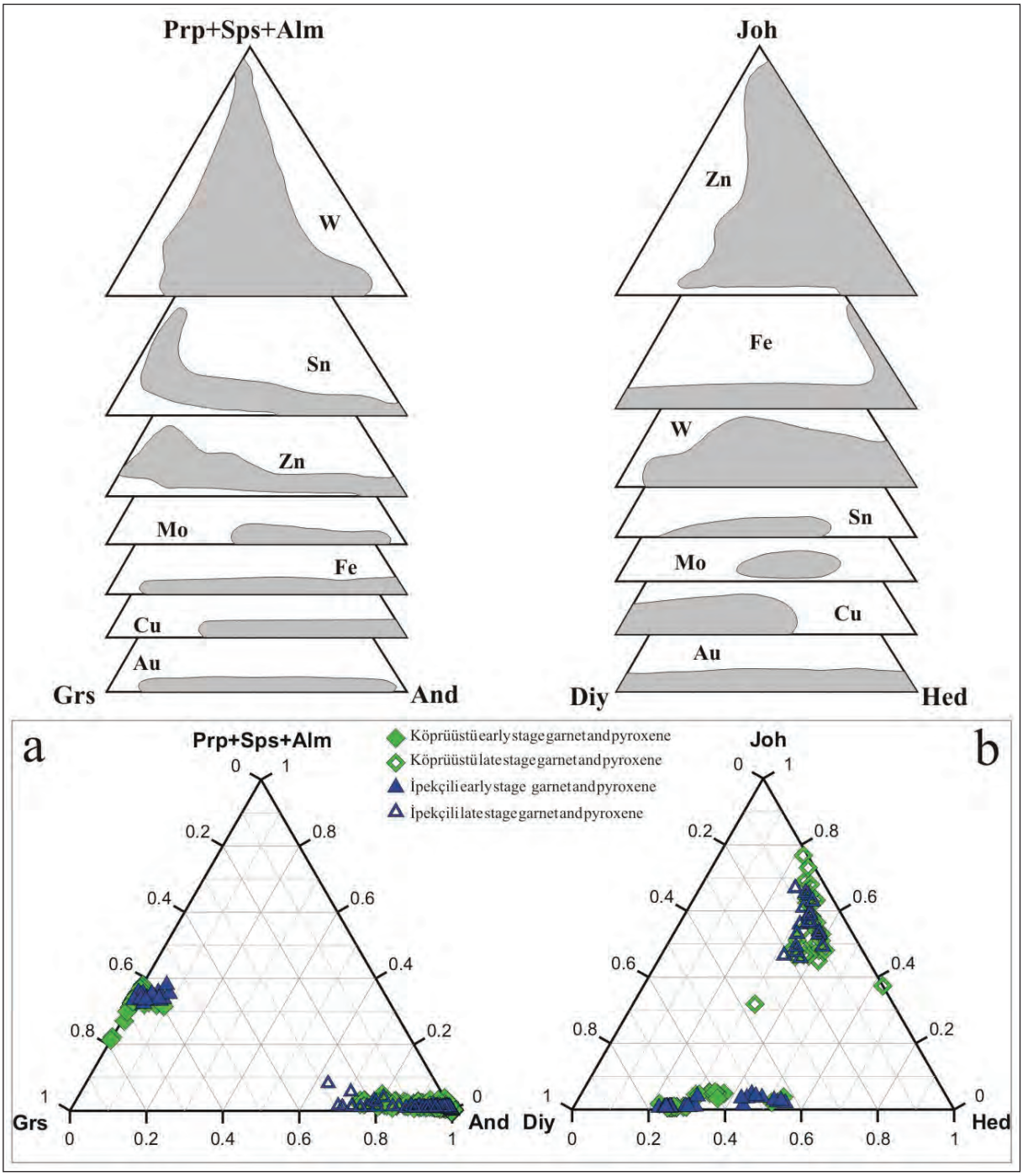

Figure 11- Skarn type classifications based on the garnet and pyroxene compositions (Einaudi et al., 1981; Meinert, 1983, 1982): a, b) compositional variations in the early- and late-stage garnets and pyroxenes in the Köprüüstü and İpekçili skarns (Prp: pyrope, Sps: spessartine, Alm: almandine, Grs: grossular, And: andradite; Joh: johannsenite, Diy: diopside, Hed: hedenbergite).

stage grossular-type garnet (X_{Grs}: 0.60–0.79 and X_{Grs}: 0.56–0.67, respectively) decreases in zoned crystals from core to rim while FeO increases (Figure 12). This zonation indicates that the garnet composition changes from grossular type $Ca_3Al_2(SiO_4)_3$ to andradite $Ca_3Fe_2(SiO_4)_3$.

Profile analyses of garnet with andradite (X_{And}: 0.75–1) composition shows zonation from core to rim (Figure 13). In these minerals, the Al_2O_3 contents decrease while FeO contents increase from core to rim. According to this, in garnets with andradite composition, the And/Grs ratio shows a greater increase from core to rim.

4.3.2. Pyroxene

In the Köprüüstü and İpekçili locations, pyroxenes have been classified into two groups, representing early and late stage developments. The results of the pyroxene analyses are given in table 3. According to these analyses, the pyroxene compositions are given in the hedenbergite–diopside–johannsenite triangular diagram (Figure 11b). The composition of early stage pyroxenes in the Köprüüstü location has been calculated as $Hed_{24.59–29.57}Diy_{69.65–74.76}Joh_{0.6–0.88}$, while the late pyroxene composition is $Hed_{22.17–62.63}Diy_{0–36.2}Joh_{31.86–76.69}$. In the İpekçili location, the composition of early stage pyroxenes is $Hed_{22.44–31.81}Diy_{67.3–76.99}Joh_{0.52–0.88}$ and the late stage pyroxenes have a composition of $Hed_{24.95–40.97}Diy_{5.62–21.25}Joh_{45.76–66.93}$. In both locations, the early stage pyroxenes have compositions between hedenbergite–diopside. In the late stage pyroxene, there is an increase in the johannsenite content (Figure 11b). In the late stage pyroxenes, the increase in johannsenite content is related to the increase in Mn^{2+}. Since the increase in manganese would increase the Mn/Fe ratio, in the late stage pyroxenes containing johannsenite, this ratio would be quite high, reaching 0.78–3.42. On the other hand, in the early stage pyroxenes, this ratio ranges between 0.02 and 0.15.

To study skarn types and classifications, the compositions of garnets and pyroxenes have been plotted on the triangular diagrams proposed by Einaudi et al. (1981) and Meinert (1983, 1992). According to these diagrams, early stage garnets with high grossular

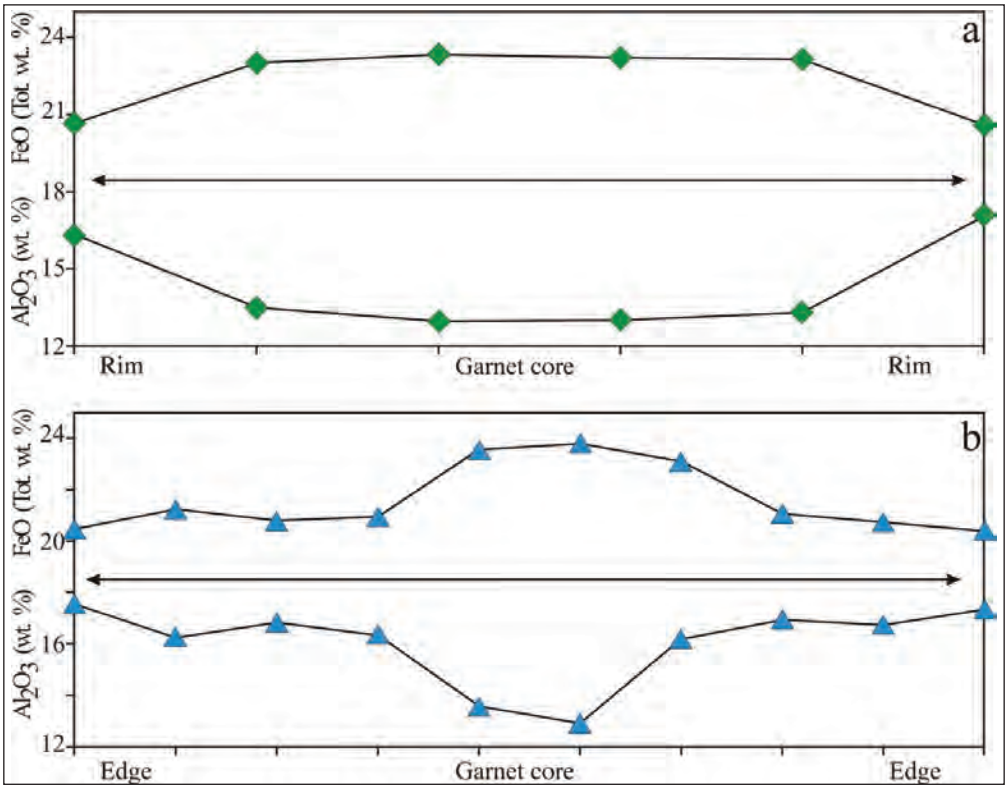

Figure 12- FeO and Al_2O_3 variations along the zoned garnet crystals, from core to rim, in the early stage garnet (grossular type) of the Köprüüstü (a) and İpekçili (b) locations.

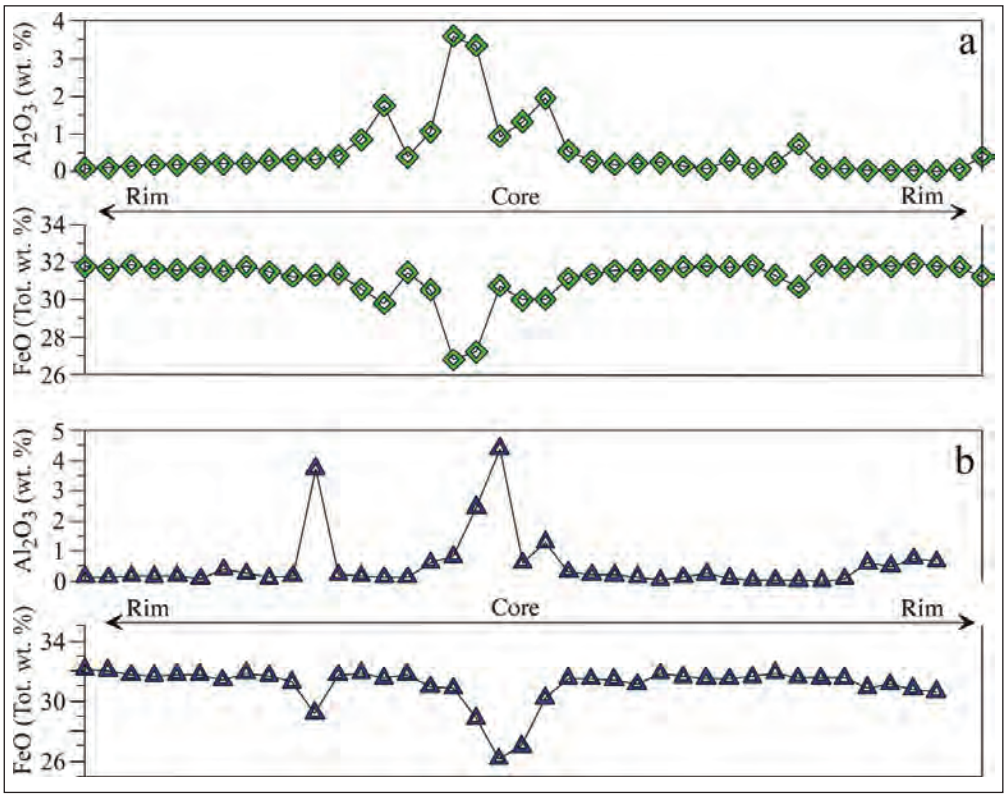

Figure 13- FeO and Al_2O_3 variations along the zoned garnet crystals, from core to rim, in the late stage garnets (andradite type) of the Köprüüstü (a) and İpekçili (b) locations.

and almandine contents do not have any relation with the skarn types but late stage garnets with high andradite contents have compositions similar to those of the Fe-, Cu-, and Zn-type skarns. On the other hand, early stage pyroxenes with compositions changing between diopside and hedenbergite have similar compositions to the Au, Cu, Sn, and W skarn types. But the late stage pyroxenes with high johannsenite contents are in close characteristic association with Zn-type skarns (Figure 11a, b).

4.4. Mineral Chemistry of Sulfurs

In the Kükürtlü and Dere Mahalle districts in the Dağbaşı area, magnetite and hematite are the main skarn ore minerals. There are some micron-sized pyrite and chalcopyrite inclusions in the magnetites and hematites in some of the polished sections of the samples from these locations (Figure 6o). On the other hand, in the İpekçili and Köprüüstü skarn locations, there is a significant amount of sulfur minerals in addition to the magnetites and hematites. The major and trace element contents of sulfur minerals of pyrrhotite, pyrite, sphalerite, and galena are given in tables 4 and 5.

Pyrrhotite is not a common mineral in other locations but it is a common mineral in the İpekçili ores. In the chemical analyses of the pyrrhotites, some high concentrations of elements are as follows: Pb 1.30%, As 0.39%, Cd 0.12%, and Ag 0.13%. According to the analyses, pyrrhotites show up to 10% deviation from the stoichiometric composition (FeS), and the chemical formula is calculated as $Fe_{(1-0.1)}S_{(1+0.1)}$. In the pyrrhotite analyses carried out along the profile from core to the rim, the Fe content decreases while the S content increases (Figures 14a, b). Therefore, pyrrhotites are close to the stoichiometric composition in the core, but towards the rim they show deviation from the stoichiometric composition depending on decreases in Fe.

Pyrites accompany pyrrhotite, chalcopyrite, and sphalerite in the İpekçili ore, while they accompany chalcopyrite, sphalerite, and galena in the Köprüüstü ore. According to the mineral chemistry analyses, pyrites include up to 4.31 wt% Pb, 1.4 wt% Zn, 1.29 wt% Cu, 0.78 wt% As, and 0.25 wt% Cd. Apart from these, four out of 46 analyses contain Co, varying between 0.06 and 0.47 wt%, and Ni is always below detection limit.

Table 3- EPMA analyses representing ealy and late stage pyroxens from the Köprüüstü and İpekçili skarns.

Sample No	68	68	68	68	68	38	38	38	38	38	49	49	49	49	49	KL2	KL2	KL2	KL2	KL2
Analyses No	4	5	6	7	8	6	7	8	9	10	4	5	6	7	8	3	4	5	12	15
SiO_2	47.32	47.49	47.37	47.91	46.87	51.46	51.65	51.99	51.70	51.26	48.07	47.10	99.02	93.38	47.06	58.49	53.32	53.19	54.27	54.01
TiO_2	0.01	bdl	bdl	bdl	bdl	0.53	0.47	0.43	0.40	0.51	bdl	bdl	bdl	0.01	bdl	bdl	bdl	bdl	bdl	0.01
Al_2O_3	0.29	0.14	0.09	0.08	0.55	2.16	2.16	1.77	2.37	2.41	1.09	1.04	0.04	0.29	1.19	1.66	0.32	0.51	0.49	0.10
Fe_2O_3	8.80	8.75	7.84	10.91	10.49	11.58	11.12	10.51	9.95	11.39	12.70	10.47	0.28	0.94	11.44	9.28	10.20	12.70	12.54	11.59
MnO	18.68	18.91	20.21	15.98	17.87	0.30	0.30	0.28	0.22	0.32	14.87	16.75	0.22	1.20	16.41	0.78	1.48	1.76	1.89	1.06
MgO	1.11	0.86	0.76	1.48	1.40	15.18	15.23	15.68	15.75	15.11	1.98	2.15	bdl	0.78	1.54	19.31	11.85	12.63	12.27	10.78
CaO	21.22	21.22	21.09	21.56	20.01	19.48	19.76	20.00	20.16	19.55	20.47	20.34	0.06	1.08	20.96	0.43	24.59	15.79	18.66	24.58
Na_2O	0.04	0.01	0.02	0.05	0.07	0.27	0.29	0.25	0.23	0.28	0.14	0.11	0.00	0.02	0.13	0.01	0.12	0.10	0.15	0.07
K_2O	bdl	bdl	bdl	bdl	bdl	bdl	bdl	bdl	bdl	bdl	bdl	0.01	bdl	0.02	bdl	bdl	bdl	0.02	0.02	0.01
Total	97.47	97.38	97.38	97.97	97.27	100.95	100.98	100.91	100.78	100.83	99.31	97.97	99.62	97.72	98.73	89.96	101.88	96.69	100.29	102.20
Si	1.986	1.999	1.996	1.995	1.971	1.900	1.903	1.913	1.900	1.893	1.968	1.953	3.979	3.815	1.942	2.384	1.980	2.089	2.057	2.014
Ti	0.000	-	-	-	-	0.015	0.013	0.012	0.011	0.014	-	-	-	0.000	-	-	-	-	-	0.000
Al	0.015	0.007	0.004	0.004	0.027	0.094	0.094	0.077	0.103	0.105	0.052	0.051	0.002	0.014	0.058	0.080	0.014	0.024	0.022	0.005
Fe^{3+}	0.016	0.000	0.005	0.010	0.036	0.097	0.094	0.091	0.092	0.101	0.023	0.054	-	-	0.068	-	0.035	-	-	-
Fe^{2+}	0.292	0.308	0.271	0.370	0.333	0.261	0.249	0.232	0.214	0.251	0.412	0.309	0.009	0.032	0.326	0.316	0.282	0.417	0.398	0.361
Mn	0.664	0.674	0.721	0.564	0.637	0.009	0.009	0.009	0.007	0.010	0.515	0.588	0.007	0.042	0.574	0.027	0.047	0.058	0.061	0.033
Mg	0.069	0.054	0.048	0.092	0.088	0.835	0.837	0.860	0.863	0.832	0.121	0.133	-	0.047	0.095	1.173	0.656	0.739	0.693	0.599
Ca	0.954	0.957	0.952	0.962	0.902	0.771	0.780	0.788	0.794	0.774	0.898	0.903	0.002	0.047	0.927	0.019	0.978	0.664	0.758	0.982
Na	0.003	0.001	0.002	0.004	0.006	0.019	0.020	0.018	0.017	0.020	0.011	0.009	0.000	0.002	0.010	0.001	0.009	0.008	0.011	0.005
K	-	-	-	-	-	-	-	-	-	-	-	0.001	-	0.001	-	-	-	0.001	0.001	-
Total	4	4	4	4	4	4	4	4	4	4	4	4	4	4	4	4	4	4	4	4
Joh	63.7	65.0	69.0	54.5	58.3	0.8	0.8	0.7	0.6	0.9	48.2	54.3	37.4	31.9	54.1	1.7	4.6	4.8	5.3	3.4
Hed	29.6	29.7	26.4	36.7	33.7	29.6	28.7	27.0	25.8	29.3	40.5	33.4	62.6	31.9	37.0	22.0	31.0	34.7	34.8	36.4
Diy	6.7	5.2	4.6	8.9	8.1	69.6	70.5	72.3	73.6	69.9	11.3	12.3	-	36.2	8.9	76.3	64.4	60.5	60.0	60.2

Table 4- Results of the representative mineral chemistry analyses of the pyrrhotite, pyrite and chalcopyrite.

	Pyrrhotite						Pyrite							Chalcopyrite						
	İpekçili						İpekçili			Köprüüstü				İpekçili				Köprüüstü		
Sample No	D6-13	D6-59	D6-59-8	D5-19	D5-22	D5-24	D6-2-1	D6-2-2	D6-2-8	K10-8	K10-9	K10-11	KL1-20	D6-11	D6-22	K11-13	K11-13-2	K10-11	K10-16	K10-29
Fe	57.70	60.16	59.55	64.22	63.45	63.46	45.82	45.44	45.21	45.66	46.80	46.33	46.06	30.16	30.50	30.18	30.31	29.65	29.61	29.40
Pb	0.82	bdl	0.67	bdl	0.18	bdl	1.30	0.82	bdl	bdl	0.34	0.64	bdl	1.37	1.54	0.68	1.30	0.51	0.74	bdl
As	bdl	bdl	bdl	bdl	bdl	0.13	0.28	0.36	0.29	bdl	bdl	0.08	0.28	bdl	0.06	0.22	0.24	0.35	bdl	0.30
Zn	bdl	bdl	bdl	bdl	bdl	bdl	bdl	bdl	bdl	1.42	0.94	0.73	bdl	bdl	bdl	0.07	bdl	0.40	1.35	1.73
Cd	0.07	bdl	bdl	bdl	0.08	0.07	0.10	bdl	bdl	bdl	0.17	0.15	bdl	bdl	bdl	0.08	bdl	bdl	bdl	0.15
Ag	bdl	0.10	bdl	0.11	bdl	bdl	bdl	bdl	0.07	bdl	0.15	0.08	bdl	0.07	bdl	bdl	bdl	bdl	bdl	bdl
Cu	0.07	0.06	bdl	bdl	bdl	bdl	bdl	bdl	bdl	0.13	0.08	0.05	0.44	32.89	32.53	34.12	33.94	34.67	34.10	33.61
Co	bdl	bdl	bdl	bdl	bdl	bdl	bdl	bdl	bdl	0.47	bdl	0.06	0.34	bdl	bdl	bdl	bdl	bdl	bdl	bdl
S	40.08	39.64	39.60	36.93	36.81	37.38	53.23	54.01	54.03	52.13	52.51	52.30	53.39	34.37	33.99	34.81	34.56	33.94	34.97	35.15
Total	98.59	99.71	99.41	100.99	100.77	100.44	100.54	100.45	99.45	99.81	100.20	100.37	99.37	98.99	98.37	100.09	100.41	99.02	99.99	98.84
Fe	0.903	0.930	0.925	0.998	0.994	0.986	0.988	0.974	0.972	0.991	1.007	1.004	0.987	1.011	1.027	0.996	1.003	0.989	0.972	0.964
Pb	0.003	-	0.003	-	0.001	-	0.008	0.005	-	-	0.002	0.004	0.004	0.012	0.014	0.006	0.012	0.005	0.007	-
As	-	-	-	-	-	0.001	0.005	0.006	0.005	-	-	0.001	0.004	-	0.001	0.005	0.006	0.009	-	0.007
Zn	-	-	-	-	-	-	-	-	-	0.026	0.017	0.014	-	-	-	0.002	-	0.012	0.038	0.048
Cd	0.001	-	-	-	0.001	0.001	0.001	-	-	-	0.002	0.002	-	-	-	0.001	-	-	-	0.002
Ag	-	0.001	-	0.001	-	-	-	-	0.001	-	0.002	0.001	-	0.001	-	-	-	-	-	-
Cu	0.001	0.001	-	-	-	-	-	-	-	0.003	0.001	0.001	0.008	0.969	0.963	0.989	0.987	1.016	0.984	0.969
Co	-	-	-	-	-	-	-	-	-	0.010	-	0.001	0.007	-	-	-	-	-	-	-
S	1.092	1.068	1.071	1.000	1.004	1.011	1.998	2.015	2.022	1.970	1.968	1.973	1.993	2.006	1.993	2.000	1.991	1.970	2.000	2.008
Total	2.000	2.000	2.000	2.000	2.000	2.000	3.000	3.000	3.000	3.000	3.000	3.000	3.000	4.000	4.000	4.000	4.000	4.000	4.000	4.000

Table 5- Results of the representative mineral chemistry analyses.

	Sphalerite											Galena						
	İpekçili					Köprüüstü						Köprüüstü						
Sample No	K11-5	K11-6	K11-9	K11-13	K11-14	K10-16	K10-17	K10-18	K10-20	K10-22	K10-24	K10-3	K10-7	K10-8	K10-10	K10-12	K10-3-9	K10-3-10
Fe	2.42	2.81	3.16	4.64	3.70	4.76	2.19	2.73	2.75	3.08	2.58	bdl	0.15	0.18	0.42	0.23	0.42	0.49
Pb	bdl	0.11	0.32	0.28	0.92	bdl	0.37	2.03	bdl	1.01	bdl	82.89	83.15	82.11	82.74	83.52	81.23	82.76
As	bdl	0.12	bdl	bdl	0.22	bdl	bdl	bdl	0.05	0.26	bdl	bdl	bdl	bdl	bdl	bdl	bdl	bdl
Zn	65.25	64.95	63.13	59.95	62.74	59.19	65.57	64.30	65.19	64.03	65.77	0.18	0.55	0.19	bdl	0.35	0.91	0.47
Cd	0.45	0.41	0.18	0.08	0.39	0.28	0.19	0.11	0.13	0.23	0.32	bdl	bdl	bdl	bdl	0.06	0.13	0.22
Ag	bdl	0.06	bdl	bdl	0.15	bdl	bdl	bdl	0.13	bdl	0.06	1.39	1.22	1.28	1.37	1.30	1.43	1.26
Cu	0.53	0.36	1.23	2.07	0.69	2.67	0.36	0.19	0.43	0.62	0.28	0.05	0.26	0.83	0.10	0.37	1.14	0.72
Co	bdl	bdl	bdl	0.09	bdl	bdl	0.05	bdl	bdl	bdl	0.05	bdl	0.06	bdl	bdl	bdl	bdl	bdl
S	30.96	30.85	32.35	31.45	31.61	32.59	31.54	31.77	31.58	31.45	31.83	13.88	13.59	13.41	13.42	13.28	13.71	14.23
Total	99.41	99.62	100.15	98.55	100.65	99.42	100.12	100.72	100.01	100.14	100.49	98.41	98.98	98.04	98.11	99.12	99.02	100.18
Fe	0.043	0.050	0.055	0.082	0.065	0.083	0.039	0.048	0.048	0.054	0.045	-	0.006	0.008	0.018	0.010	0.017	0.020
Pb	-	0.001	0.002	0.001	0.004	-	0.002	0.010	-	0.005	-	0.942	0.941	0.937	0.950	0.954	0.897	0.903
As	-	0.002	-	-	0.003	-	-	-	0.001	0.003	-	-	-	-	-	-	-	-
Zn	0.988	0.984	0.939	0.909	0.942	0.882	0.985	0.965	0.976	0.962	0.979	0.006	0.020	0.007	-	0.013	0.032	0.016
Cd	0.004	0.004	0.002	0.001	0.003	0.002	0.002	0.001	0.001	0.002	0.003	-	-	-	-	0.001	0.003	0.004
Ag	-	0.001	-	-	0.001	-	-	-	0.001	-	0.001	0.030	0.027	0.028	0.030	0.029	0.030	0.026
Cu	0.008	0.006	0.019	0.032	0.011	0.041	0.006	0.003	0.007	0.010	0.004	0.002	0.009	0.031	0.004	0.014	0.041	0.026
Co	-	-	-	0.003	-	-	0.001	-	-	-	0.001	-	0.002	-	-	-	-	-
S	0.956	0.953	0.982	0.973	0.969	0.991	0.966	0.972	0.965	0.963	0.967	1.019	0.994	0.989	0.996	0.980	0.978	1.003
Total	2.000	2.000	2.000	2.000	2.000	2.000	2.000	2.000	2.000	2.000	2.000	2.000	2.000	2.000	2.000	2.000	2.000	2.000

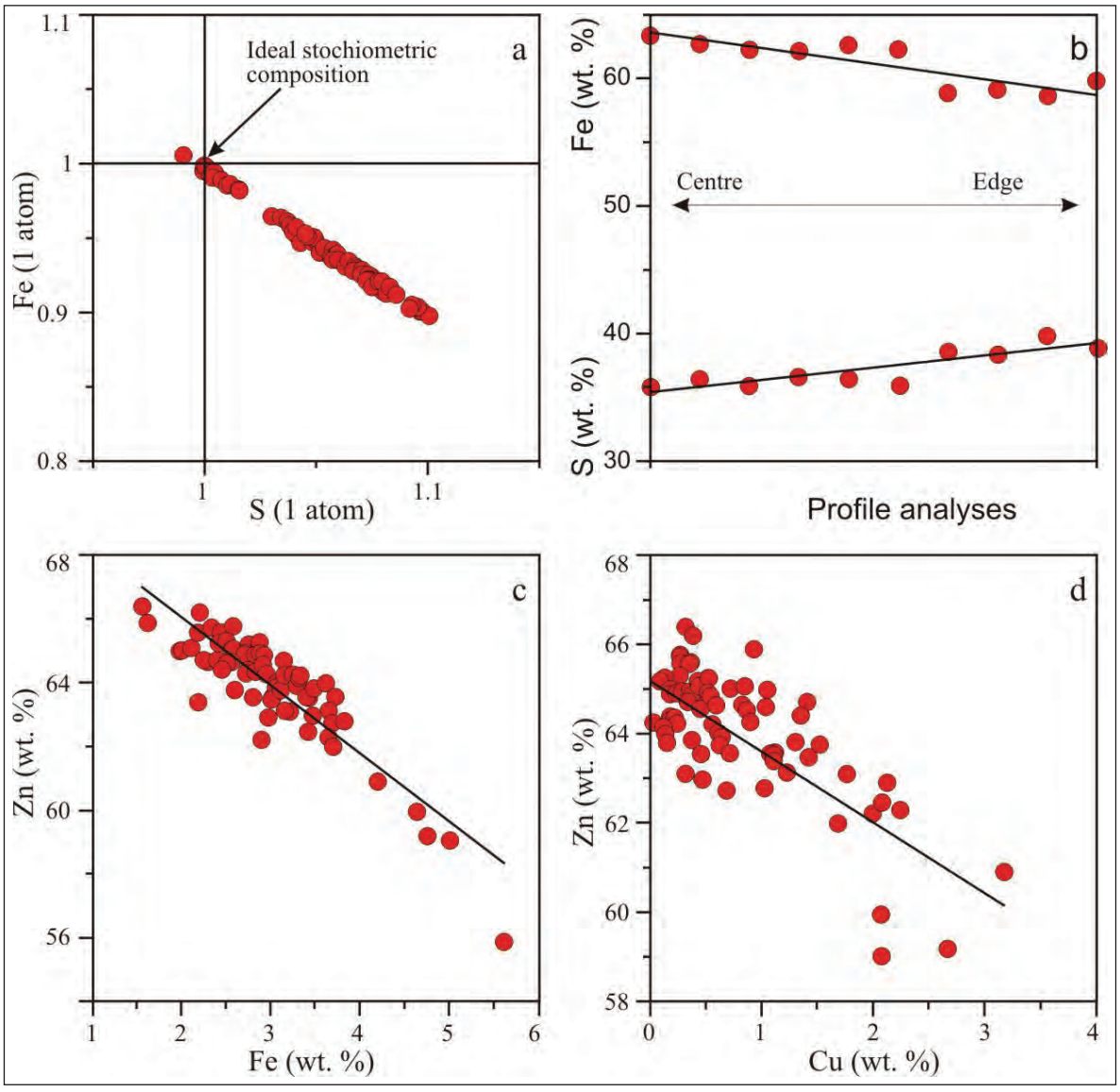

Figure 14- a) Stoichiometric compositional changes of the pyrrhotites in the İpekçili ore; b) Fe versus S variations on the profile analyses of pyrrhotites; c, d) correlations showing element substitution in sphalerites of the Köprüüstü ore.

Chalcopyrites in both İpekçili and Köprüüstü locations contain up to 1.82 wt% Pb, 2.6 wt% Zn, and 0.47 wt% As. The general formula of these chalcopyrites has been calculated as $Fe_{0.96–1.05}Cu_{0.97–1.04}S_{1.95–2.02}$. No differences were detected between different locations in terms of trace element concentrations.

Sphalerites always accompany to other sulfides in both locations but are more abundant in the Köprüüstü ore than in the İpekçili location. In the analyses of sphalerite, apart from the main element of Zn, higher concentrations of some other elements are 5.01 wt% Fe, 3.18 wt% Cu, 2.04 wt% Pb, and 0.45 wt% Cd. The negative correlations between Fe and Zn and between Cu and Zn indicate elemental substitution between these elements (Figures 14c, d).

Galena is only present in the Köprüüstü location. It is always observed as inclusions in sphalerites, and modal abundances are less than 1% in the ore. The highest concentrations of some elements measured in galena are 1.43 wt% Ag, 1.14 wt% Cu, 0.91 wt% Zn, and 0.49 wt% Fe. On the basis of mineral chemistry analyses, the formula of galena is calculated as $Pb_{(0.94–0.95)}S_{(0.98–1.02.)}$. Apart from Ag, the concentrations of the other elements show variations between the detection limits and the higher concentrations given above. On

the other hand, nine separate galena analyses show that the Ag contents are always higher than 1 wt%, showing very close variations of between 1.18 and 1.43 wt%. This suggests that galena minerals may have silver potential in the study area.

5. Discussion and Results

5.1. Host Rocks' Relations and Skarn Mineralogy

The Dağbaşı skarn ores have developed as an exoskarn type along the nearest border of the Upper Cretaceous Dağbaşı Granitoid and block- and lens-shaped limestones of Berdiga formation which are located in the Liassic volcanics. In the field studies, neither contact between limestones and granitoid nor the development of skarn minerals in the granitoid has been observed. Since skarn-type deposits develop with metasomatic processes between granitoid and limestone, the absence of a contact relationship makes it difficult to explain the skarns in the region. However, although no contact relations were found in the field, as marked in the cross-sections (Figure 3), it is quite possible to claim that the granitoid and limestones may have contact below the surface. In this case, hydrothermal solutions interacting with the limestones along the underground contact reached the surface by spreading through the weak zones of the limestones. According to this explanation, the main skarn contact and ore zones are below the surface. The presence of numerous old adits and mine waste around them supports the idea that the main ore zone is below the surface.

The prograde stage is represented by garnet and pyroxene occurrences in the field, but in detail it is subdivided into early and late stages. The early prograde stage is represented by garnets and pyroxenes in the limestones forming massive, rhythmically banded, granular, and nodular textures. Garnet and pyroxene veins developed along the fractures in the limestones are considered to be the products of the late-prograde stage. Mineral chemistry analyses have also shown that these garnets and pyroxenes from both stages have different compositions. On the other hand, tremolite-actinolite, epidote, quartz, and calcites are products of the retrograde stage. The presence of magnetites and hematites in the growth zones in the garnets may indicate that ore mineralizations started in the late prograde stage, but the main ore mineralization developed in the retrograde stage. In addition to the fracture-filling-type ore veins in the limestones and volcanic rocks, the presence of banded ore along the limestone layers indicates that oxide and sulfide ore mineralization developed in the retrograde stage.

5.2. Skarn Types and Formation Conditions

Chemical analyses of the garnets from the Köprüüstü and İpekçili locations indicate that garnet compositions change between grossular and andradite. Early stage garnets have higher grossular compositions and have a total of up to 38% pyrope+spessartine+almandine in the chemical formula ($And_{0–8.81}Grs_{55.67–78.65}Prs_{32.40–38.00}$). According to Einaudi et al. (1981), reducing skarns are characteristic with their low andradite (Fe^{3+}) and high spessartine (Mn^{2+}) and almandine (Fe^{2+}) contents. According to this explanation, the high grossular and almandine contents of early prograde stage garnets indicate the reducing skarn type. On the other hand, late stage garnets with higher andradite contents indicate oxidized skarn types (Jamtveit, 1991; Jamtveit and Hervig, 1994; Clechenko and Valley, 2003; Ciobanu and Cook, 2004; Meinert et al., 2005; Orhan and Mutlu, 2009). Einaudi (1981) also suggests that Fe^{3+}-rich garnets (andradite) are quite common in oxidized skarns and also suggest that andradite-rich garnets may be an indication of the shallow emplacement of granitoids.

Taking into account the explanation given above, grossular-type early stage garnets and andradite-type late stage garnets show a transition from reduced to oxidized skarn. These type changes in the oxidation degree of skarn have been explained by the fracturing of overlying rocks along the skarn contact due to the increasing hydraulic pressure (Yardley and Lioyd, 1995; Dipple and Gerdes, 1998; Clechenko and Valley, 2003; Meinert et al., 2005). According to this, increased permeability and porosity of the host rocks allow the circulation of meteoric water through the skarn environments. Similar findings were also reported by Orhan (2017), who noted that the garnet composition of the early stage changes from grossular type to the andradite one in the Kozbudaklar skarn. In this study, the transition from grossular to andradite has also been explained by the introduction of meteoric water into the skarn zone.

In this study, analyses conducted along the profile line of the grossular- and andradite-type zoned garnet crystals showed increases in the And/Grs ratios from core to rim. In similar studies, researchers indicate that zoned garnet crystals can be used to understand the formation condition of skarns (Collins, 1977;

Newberry, 1983; Abu el Enen et al., 2004). These researchers have argued that the zoning from the centre to the rim reflects the evolution of fluids. According to this explanation, increased And/Grs ratios in the zoned garnets are related to the increase in the degree of oxidation f (O_2) of the skarns. In this study, the increase of the And/Grs ratio in the skarn minerals from the centre towards the rim could be explained by the increase in the oxidation rate.

There is a systematic relation between the element content of the pyroxene and the metal content of the skarn-type deposits (Burt, 1972; Einaudi et al., 1981; Newberry; 1991; Nakona et al., 1994; Nakona, 1998). Depending upon the skarn type, the Mg, Mn, and Fe contents of pyroxenes show variations (Einaudi and Burt, 1982). According to this explanation, Mn-containing pyroxenes (johannsenite) represent Zn-type skarns, while diopside- and hedenbergite-containing pyroxenes represent Cu–Fe-type skarns. Plotting the element contents of pyroxenes on the triangular diagrams showed that late stage pyroxenes from the Köprüüstü and İpekçili locations with their high Mn contents fall into the Zn-type skarn area (Figure 11b). On the other hand, early stage pyroxenes from these two locations fall into the Cu–Fe-type skarn area (Figure 11b).

Studies on skarn-type deposits showed that in addition to the Mn content of pyroxenes, Mn/Fe ratios could also be used in the classification of skarn-type deposits (Nakano et al., 1994; Nakano, 1998). In these studies, it is suggested that the Mn/Fe ratios of pyroxenes are < 0.1 for Cu–Fe skarns, 0.1–0.2 > for W-type skarns, and > 0.2 for Pb–Zn-type skarns. In this study, the Mn/Fe ratios of early stage pyroxenes from the Köprüüstü and İpekçili locations show variation between 0.02 and 0.15, while late stage pyroxenes show variation between 0.78 and 3.42. Although the calculated Mn/Fe ratios of early stage pyroxenes show a little deviation from the value of 0.1, the data are mostly compatible for Cu–Fe-type skarns. On the other hand, Mn/Fe ratios ranging between 0.78 and 3.42 are characteristic for Zn-type skarns. The presence of sphalerite in the skarn paragenesis supports this approach.

5.3. Granitoid Geochemistry and Its Relation to Skarn Types

The compositions of magmatic rocks and their relations with skarn types and metal contents have been studied by a number of researchers (Kwak and White, 1982; Meinert, 1983, 1995; Newberry and Swanson, 1986; Meinert et al., 1991, 2005; Kuşçu et al., 2001; Öztürk et al., 2005). According to these studies, granitoids associated with skarns have calc-alkaline compositions (Figure 8b). The Mg contents are higher in the granitoids associated with Fe, Au, and Cu-type skarn than in those associated with W, Sn, and Mo-type skarn (Figure 8c). On the other hand, plutons related to the Fe, Au, and Cu skarns have lower K_2O contents than the granitoids associated with W, Sn, and Mo skarns (Figure 8d). From the point of view of aluminium saturation, skarn-related plutons mostly have metaluminous–peraluminous transitional composition, except for the Sn skarns, which have a peraluminous composition, indicating granitoids of sedimentary origin (S-type). In addition, Fe-type skarn-related granitoids have metaluminous composition, indicating magmatic plutons of island arc origin (I-type) (Figure 8e).

Dağbaşı Granitoid is divided into four different zones by Aydınçakır (2006), namely granodiorite, monzogranite, tonalite, and diorite. Due to the heterogeneous composition of Dağbaşı Granitoid, the geochemical characteristics of the granitoid along the skarn zones have also been studied and correlated with skarn-related granitoids elsewhere. While samples collected from the granitoid along the skarn zones have compositions between granodiorite and tonalite, samples from the other parts have tonalite composition (Figure 8a). Based on the major element contents, all of the granitoid samples have calc-alkaline composition. While the K_2O contents of the granitoid samples from the skarn zones point to Fe–Cu skarns, granitoid samples from the other parts do not have a connection with the skarn types. The MgO contents of the skarn-zone granitoids have close similarity with Fe–Cu skarns, while samples from the other parts have a resemblance with W, Sn, and Mo skarns. In terms of the aluminıum saturation, granitoids along the skarn zones have metaluminous–peraluminous transition, whereas granitoids from the other parts in general have peraluminous compositions.

On the basis of the tectonic setting and their various trace element contents, plutonic rocks have been classified in relation to the skarn types in previous studies (Meinert et al., 1991, 2005; Kuşçu et al., 2002; Öztürk et al., 2005). In those studies, Fe, Au, Cu, and Zn skarns were associated with volcanic arc granitoids, and Sn, W, and Mo skarns with within-

plate granitoids. In this study, analyses of the granitoid samples from the skarn zones have been plotted on the Nb–Y, Rb–Y+N trace element variation diagrams which were used for the determination of the tectonic setting of the granitoid. The result shows that they are of volcanic arc type (VAG) (Figures 10a, b). Comparing the trace element contents of the Dağbaşı granitoids with the others, Dağbaşı granitoids have compositions similar to those of the granitoids related to Fe–Cu–Zn-type skarns. Along with these, the Rb/Sr ratios and Rb contents of the Dağbaşı granitoids are considerably lower than those of the Sn-, Mo-, and W-related granitoids and resemble the Fe–Cu–Zn-producing granitoids in figure 10c and d.

In conclusion, major and trace element contents of Dağbaşı Granitoid along skarn zones have similar compositions with the granitoids producing Fe–Cu–Zn-type skarns. On the other hand, the other parts of the granitoid showing zonation with different mineralogy have quite different compositions. Accordingly, the presence of sulfide minerals (pyrrhotite, pyrite, chalcopyrite, sphalerite, and galena), in addition to oxide phase (magnetite and hematite), indicates that the skarn mineralogy is controlled by the geochemical properties of the granitoid.

Acknowledgements

This study was supported by TÜBİTAK through project number 112Y331. Special thanks are due to Melanie Kaliwoda for providing the microprobe analyses for this study at the Mineralogy and Petrology Institute of Ludwig Maximilian University. Sincere thanks are offered to İbrahim Uysal for his help during the microprobe analyses. Raif Kandemir is thanked for his help during the microscopic studies. Great thanks are due to Emin Çiftçi and two anonymous reviewers whose comments improved the paper. Ali Dişli, Kadir Bayraktar, Mustafa Aksu and Mehdi İlhan are thanked for their assistance during the fieldwork and laboratory studies.

References

Abu El-Enen, M.M., Okrusch, M., Will, T.M. 2004. Contact metamorphism and metasomatism at a dolerite-limestone contact in the Gebel Yelleq area, Northern Sinai, Egypt. Mineralogy and Petrology 81, 135-164.

Ağar, Ü. 1977. Demirözü (Bayburt) ve Köse (Kelkit) Bölgesinin Jeolojisi. Doktora Tezi, İÜ, Fen Fakültesi, İstanbul.

Aslan, Z. 1991. Özdil (Yomra-Trabzon) Yöresinin Petrografisi Skarn Oluşukları ve Granat-Piroksen Ritmikleri. Yüksek Lisans Tezi, KTÜ Fen Bilimleri Enstitüsü, 72s, Trabzon.

Aslaner, M. 1977. Türkiye bakır-kurşun-çinko yataklarının jeolojik ve bölgesel sınıflamasıyla plaka tektoniği yönünden incelenmesi. KTÜ, Yerbilimleri Fakültesi, Yayın No: 12, Trabzon.

Aydınçakır, E. 2006. Dağbaşı (Araklı-Trabzon) granitoyidi ve çevresinin petrografik, jeokimyasal ve petrolojik özelliklerinin incelenmesi. Yüksek Lisans Tezi, KTÜ, Fen Bilimleri Enstitüsü, 120s.

Burt, D.M. 1972. Mineralogy and Geochemistry of Ca-Fe-Si Skarn Deposits. Ph.D. Thesis, Harvard University, 256p.

Burt, D.M. 1982. Skarn deposits-historical bibliography through 1970. Economic Geology 77, 755-763.

Ciobanu, C.L., Cook, N.J. 2004. Skarn texture and a case study: the Ocna de Fier- Dognecea orefield, Banat, Romania. Ore Geology Reviews 24, 315-370.

Clechenko, C.C., Valley, J.W. 2003. Osciallatory zoning in garnet from the Willsboro Wollastonite Skarn, Adirondacks Mts, New York: a record of shallow hydrothermal processes preserved in granulite facies terane. Journal of Metamorphic Geology 21, 771-784.

Collins, B.I. 1977. Formation of scheelite-bearing and scheelite-barren skarns of Lost Creek, Pioneer Mountains, Montana. Economic Geology 72, 1505-1523.

Çamur, M.Z., Tüysüz, N., Güven, İ.H., Arıkal, T., Er, M. 1994. Eastern Pontides Volcanism and Related Ore Deposits, Internatonal Volcanologıcal Congress, IAVCEI, Ankara.

Çiftçi, E. 2011. Sphalerite associated with pyrrhotite-chalcopyrite ore occurring in the Kotana Fe-skarn deposit (Giresun, NE Turkey): exolutions or replacement. Turkish Journal of Earth Science 20, 307-320.

Çiftçi, E., Vıcıl, M. 2003. Kurtulmuş iron mineralization – an example to the skarn-type ore deposits from Eastern Pontides (Giresun, NE Turkey). Geosound, 26, 79-92.

Debon, F., Le Fort, P. 1983. A chemical-mineralogical classification of common plutonic rocks and associations, Trans, Roy, Soc., Edinburg, Earth Science 73, 135-149.

Demir, Y., Uysal, I., Kandemir, R., Jauss, A. 2017. Geochemistry, fluid inclusion and stable isotope constraints (C and O) of the Sivrikaya Fe-skarn mineralization (Rize, NE Turkey). Ore Geology Reviews 91, 153-172.

Dipple, G.M., Gerdes, M.L. 1998. Reaction-infiltration feedback and hydrodynamics at the skarn front. Mineral. Assoc. Can., Short Course Series 26, 71-97.

Droop, G.T.R. 1987. A general equation for estimating Fe+3 concentrations in ferromagnesian silicates and oxides from microprobe analyses, using stochiometric criteria. Mineralogical Magazine 51, 431-435.

Dunham, R.J. 1962. Classification of carbonate rocks according to depositional textures in W.E. Ham. (ed), Classification of carbonate rocks. Amerikan Association of Petroleum Geologist 1, 108-121.

Einaudi, M.T, Meinert, L.D., Newberry, R.J. 1981. Skarn Deposits. Economic Geology 75, 317-391.

Einaudi, M.T., Burt, D.M. 1982. A Special Issue Devoted to Skarn Deposits, Introduction-Terminology, Classification and Compositionof Skarn Deposits. Economic Geology 77, 4, 745-754.

Eren, M. 1983. Gümüshane-Kale Arasının Jeolojisi ve Mikrofasiyes incelemesi. Yüksek Lisans Tezi, KTÜ, Fen Bilimleri Enstitüsü, 197s, Trabzon.

Folk, R.L. 1962. Spectral subdivision of limestone types in W.E. Ham. (Ed)classification of carbonate rocks. AAPG Bulletion 1, 62-82.

Gedikoğlu, A., Pelin, S., Özsayar, T. 1979. The main lines of the geotectonic evolution of the eastern pontides in mesozoik era. Geocome 1, 555-580.

Gülibrahimoğlu, İ. 1986. Araklı güneyinin jeolojik etüt raporu, Maden Tetkik ve Arama Genel Müdürlüğü Rapor No: 2086, Ankara (unpublished).

Güven, İ.H, Nalbantoğlu, A.K., Takaoğlu, S. 1998. 1/100.000 Ölçekli Açınsama Nitelikli Türkiye Jeoloji Harita Serisi, Maden Tetkik ve Arama Genel Müdürlüğü Yayını.

Hasançebi, N. 1993. Dağbaşı (Araklı-Trabzon) granitoyidine bağlı cevherleşmelerin incelenmesi. Yüksek Lisans Tezi, KTÜ Fen Bilimleri Enstitüsü, 65s, Trabzon.

Irvine, T.N., Baragar, W.R.A. 1971. A guide to chemicla classification of the common volcanic rocks. Canadian Journal of Earth Science 8, 523-548.

Jamtveit, B. 1991. Oscillatory zonation patterns in hydrothermal grossular-andradite garnet: Nonlinear dynamics in regions of immiscibility. American Mineralogist 76, 1319-1327.

Jamtveit, B., Hervig, R.L. 1994. Constraints on transport and kinetics in hydrothermal systems from zoned garnet. Science 263, 505-508.

Kandemir, R. 2004. Gümüşhane Yakın Yörelerindeki Erken-Orta Jura Yaşlı Şenköy Formasyonu'nun Çökel Özellikleri ve Birikim Koşulları. Doktora Tezi, KTÜ Fen Bilimleri Enstitüsü, 274s, Trabzon.

Kaygusuz, A. 1992. Dagbası (Araklı-Trabzon) ve Çevresinin Minerolojik ve Petrografik Olarak İncelenmesi. Yüksek Lisans Tezi, KTÜ Mimarlık-Mühendislik Fakültesi, 63s, Trabzon.

Kaygusuz, A., Aydınçakır, E. 2011. U-Pb zircon SHRIMP ages, geochemical and Sr-Nd isotopic compositions of Cretaceous plutons in the eastern Pontides (NE Turkey): The Dağbaşı pluton. Neues Jahrbuch für Mineralogie 188, 211-233.

Kesgin, Y. 1983. Bayburt (Gümüşhane) İlçesi, Akşar Köyü ve Güneybatısının Jeolojik İncelemesi, Yüksek Lisans Tezi, KTÜ Fen Bilimleri Enstitüsü, 94s, Trabzon.

Kırmacı, M.Z., Koch, R., Bucur, J.I. 1996. An Early Cretaceous section in the Kırcaova area (Berdiga Limestone, NE-Turkey) and its correlation with platform carbonates in W-Slovenia. Facies 34, 1-22.

Kırmacı, M.Z., Yıldız, M., Kandemir, R., Eroğlu-Gümrük, T. 2018. Multistage dolomitization in late Jurassic-Early Cretaceous platform carbonates (Berdiga formation), Başoba Yayla (Trabzon), NE Turkey, Implication of the generation of magmatic arc on dolomitization. Marine and Petroleum Geology 89, 515-529.

Koch, R., Bucur, I.I., Kırmacı, M.Z., Eren, M., Taslı, K. 2008. Upper jurassic and lower cretaceous carbonate rocks of the Berdiga limestone- sedimentation on an onbound platform with volcanic and episodic siliciclastic influx. Biostratigraphy, facies and diagenesis (kırcaova, kale-gümüşhane area; NE-Turkey). Neues Jahrb. für Geol. Palaontologie 247, 23-61.

Köprübaşı, N. 1992. Aşağı Harşit bölgesinin magmatik petrojenezi ve masif sülfitlerde jeokimyasal hedef saptama uygulamaları, Doktora Tezi, KTÜ Fen Bilimleri Enstitüsü, Trabzon.

Kurt, Y. 2014. Giresun, Bulancak Kirazören bölgesi skarn tipi demir yataklarının jeolojik ve jeokimyasal incelenmesi. Yüksek Lisans Tezi, İstanbul Üniversitesi, Fen Bilimleri Enstitüsü, 111s, İstanbul.

Kuşçu, İ., Gençalioğlu, G., Erler, A. 2001. Geochemical signatures of granitoids associated with skarn in central Anatolia. International Geology Review 43, 8, 722-735.

Kuşçu, İ., Gençalioğlu, G., Meinert, D., Floyd, A. 2002. Tectonic setting and petrogenesis of the Çelebi granitoid, (Kırıkkale-Turkey) and comparison with skarn granitoids. Journal of Geochemical Exploration 76, 3, 175-194.

Kwak, T.A.P., White, A.J.R. 1982. Contrasting W-Mo-Cu and W-Sn-F skarn types and related granitoids. Mining Geology 32, 4, 339-351.

Maniar, P.D., Piccoli, P.M. 1989. Tectonic discirimination of granitoids. Geological Society of Amerika Bulletion 101, 635-643.

Meinert, L.D. 1983. Variability of skarn deposits-guides to exploration, S.J. Boardman (Ed.), Revolution in the earth sciences: Kendal-Hunt Publishing, 301-316.

Meinert, L.D. 1992. Skarn and skarn deposits. Geoscience Canada 19, 145-162.

Meinert, L.D. 1995. Compositional variation of igneous rocks associated with skarn deposits, chemical evidence for a genetic connection between petrogenesis and mineralization. Mineralogical Association of Canada, Short Course Series 23, 401-418.

Meinert, L.D., Brooks, J.W., Myers, G. L. 1991. Whole rock geochemistry and contrast among skarn types, in Bufa, R.H. and Coyner, A.R. (ed), Geology and ore deposits of the Great Basin: Reno, Nevada, Geological Society of Nevada, Fieldtrip Guidebook Compendium 1, 72-80.

Meinert, L.D., Diple, G.M., Nicolescu, S. 2005. World skarn deposits, society of economic geologist. Economic Geology 100th Anniversary Volume 299-336.

Nakano, T. 1998. Pyroxene Geochemistry as an Indicator for Skarn Metallogenesis in Japan, Mineralized Intrusion-Related Skarn Systems, D.R Lentz. (Ed.), Mineralogical Association of Canada, Short Course Series 26, 147-167.

Nakona, T., Yoshino, T., Shimazaki, H., Shimizu, M. 1994. Pyroxene Composition as an Indicator in the Classification of Skarn Deposits. Economic Geology 89, 1567-1580.

Newberry, R.J. 1983. The formation of subcalcic garnet in scheelite-bearing skarns. Canadian Mineralogist 21, 529-544.

Newberry, R.J. 1991. Scheelite-bearing skarns in the Sierra Nevada region, California: Contrast in zoning and mineral compositions and tests of infiltration metasomatism theory. In skarns - Their Genesis and Metallogeny, A. Barto- Kyriakidis (Ed.), Theophrastus Publications, Atkens, Greece 343-384.

Newberry, R.J., Swanson, S.E. 1986. Scheelite skarn granitoids: An evaluation of the roles of magmatic source and process. Ore Geology Reviews 1, 57-81.

Orhan, A. 2017. Evolution of the Mo-rich scheelite skarn mineralization at Kozbudaklar, Western Anatolia, Turkey: Evidence from mineral chemistry and fluid inclusions. Ore Geology Reviews 80, 141-165.

Orhan, A., Mutlu, H. 2009. Susurluk (Balıkesir) skarn yatağının mineralojik ve petrografik Özellikleri. Eskişehir, Osmangazi Üniversitesi Mühendislik Fakültesi Dergisi 12, 2, 65-90.

Oyman, T. 2010. Geochemistry, mineralogy and genesis of the Ayazmant Fe-Cu skarn deposit in Ayvalık, (Balıkesir), Turkey. Ore Geology Reviews 37, 75-101.

Öztürk, Y.Y., Helvacı, C., Satır, M. 2005. Genetic relations between skarn mineralization and petrogenesis of the Evciler Granitoid, Kazdağ, Çanakkale, Turkey and comparison with world skarn granitoids. Turkish Journal of Earth Science 14, 255-280.

Pearce, J.A., Harris, N.B.W., Tindle, A.G. 1984. Trace elements discrimination diagram for the tectonic interpretation of granitic rock. Journal of Petrology 25, 43-63.

Saraç, S. 2003. Doğu Karadeniz Fe-Skarn Yataklarının karşılaştırmalı mineralojik ve jeokimyasal özellikleri. Doktora Tezi, KTÜ Fen Bilimleri Enstitüsü, 259s, Trabzon.

Schultze-Westrum, H.H. 1961. Giresun Civarındaki Aksu Deresinin Jeolojik Profili, Kuzeydoğu Anadolu'da Doğu Pontus Cevher ve Mineral Bölgesinin Jeolojisi ve Maden Yatakları ile İlgili Mütaalalar. Maden Tetkik ve Arama Genel Müdürlüğü Dergisi 57, 63-71.

Sipahi, F. 2011. Formation of skarns at Gümüşhane (Northeastern Turkey). Neues Jahrbuch für Mineralogy 188, 2, 169-190.

Sipahi, F., Akpınar, İ., Eker, Ç.S.,Kaygusuz, A., Vural, A. 2017. Formation of the Eğrikar (Gümüşhane) Fe-Cu skarn type mineralization in NE Turkey: U-Pb zircon age, lithogeochemistry, mineral chemistry, fluid inclusion, and O-H-C-S isotopic compositions. Journal of Geochemical Exploration 182, 32-52.

Şen, C. 1988. Dağbaşı (Trabzon) bölgesinde yüzeyleyen alt bazik (Jura)-Granitoid (Üst Kretase) formasyonlarının petrografik özellikleri. Yüksek Lisans Tezi, KTÜ Fen Bilimleri Enstitüsü, 92s, Trabzon.

Yardley, B.W.D., Lioyd, G.E. 1995. Why metasomatic fronts are really metasomatic sides. Geology 23, 53-56.

Yılmaz, C., Kandemir, R. 2006. Sedimentary records of the extensional tectonic regime with temporal cessation: Gümüşhane Mesozoic Basin (NE Turkey). Geologica Carpathica 57, 1, 3-13.

Yılmaz, C., Carannante, G., Kandemir, R. 2008. The rift-related Late Cretaceous drowning of the Gümüşhane carbonate platform (NE Turkey). Italian Journal of Geoscience 127, 1, 37-50.

Yüksel, S. 1976. Şiran Batı yöresi Mesozoik karbonat kayaçları ve eosen flisinin petrografik ve sedimantolojik incelenmesi, Doçentlik Tezi, KTÜ, Trabzon.

Bulletin of the Mineral Research and Exploration

http://bulletin.mta.gov.tr

Evaluation of soil geochemistry data of Canca Area (Gümüşhane, Turkey) by means of Inverse Distance Weighting (IDW) and Kriging methods-preliminary findings

Alaaddin VURAL[a*]

[a] *Gümüşhane University, Faculty of Engineering and Natural Sciences, Department of Geological Engineering, 29000, Gümüşhane, Turkey*
orcid.org/0000-0002-0446-828X

Research Article

Keywords:
Soil geochemistry, inverse distance weighting (IDW), kriging, Gümüşhane.

ABSTRACT

The purpose of this study is to assess soil geochemical data of the Canca alteration area (Gümüşhane-Turkey) using statistical methods and investigate potential gold mineralizations of the area. With this purpose, 288 soil samples were collected and analyzed for gold and associated pathfinder elements. The concentrations ranged (Au and Hg: in µg/kg, others in mg/kg) between 0,68-19,20; 0,02-28,97; 2-314; 7-857; 2,1-394; 4-199,5; 0,59-49,29; 5-89; 0,04-37; 0,52-16,30; 1,25-91,9 for Au, Ag, Cu, Pb, Zn, As, Sb, Bi, Mo, Sn and Hg respectively. According to Sperman's rho correlation coefficients, although not very strong, correlation was observed between Cu and Au; Zn and Cu; Sb and Pb and As; Mo and Pb and As and Sb; Sn and As; Sb and Mo. The threshold values of the elements were obtained by median+2 the median absolute deviation. The prediction maps of the elements were formed by using the Inverse Distance Weighting and Kriging methods. According to prediction maps; especially in the western part of the study area and also related to tectonic lines, elemental enrichments, (gold and silver) were determined. Therefore, it is suggested to give importance to the west of the area in exploration drilling, geophysics, etc. Since the element prediction maps produced by the Inverse Distance Weighting method has higher resolution in anomaly contrast, it is suggested that maps produced with this method can preferably be used to give an idea at first sight in soil geochemistry studies.

Received Date: 29.12.2017
Accepted Date: 29.05.2018

1. Introduction

Canca (Gümüşhane, NE Turkey) hydrothermal alteration area is approximately 10 km northwest of the Gümüşhane city center in the Black Sea Tectonic Unit in the Eastern Black Sea Region. There are many mineral deposits in various types such as porphyry, skarn and epithermal in the area where the study area is located (Koza gold mine, Gümüştaş zinc-lead copper mine, Yıldızlar zinc-lead copper mine, Arzular gold mine, Ünlüpınar lead mine, Kösdere copper-lead-zinc mine, Karadağ skarn, porphyry and vein type ores, Istala skarn type zinc-copper mine and etc.). There are many investigations carried out in Gümüşhane and its close vicinity mainly by the General Directorate of Mineral Research and Exploration (MTA), public and private organizations beginning from the second half of the 20th century because of its geological richness and host many mineral deposits. Many studies are in general geology, but most of them are in mineral exploration. Especially after the 1980s, such studies continued with acceleration.

Prospection studies on mineral exploration covering generally the whole Turkey and especially in the region were carried out mainly in the form of rock geochemistry and mining geology. As the rock geochemistry studies is directly related with mineralization they possess a significant place in exploration geochemistry studies and have a bigger role in detailed geochemistry studies.

General prospecting studies, one of the most important shortcomings of our country, are in fact

* *Corresponding author: Alaaddin VURAL, alaaddinvural@hotmail.com*
https://dx.doi.org/10.19111/bulletinofmre.430531

the most important and initial stages of detailed geochemical studies such as rock geochemical studies. Almost all developed countries in the world have completed their general prospection studies and have made great progress in detailed geochemical studies. Therefore, especially in recent years, the general prospection studies (soil, plant, water geochemistry) have been initiated by MTA.

As mentioned above, the rock geochemistry studies are more suitable for detailed prospection studies, however they are time consuming and do not always give any desired results when used in general prospections and/or in detailed studies alone. They also cause mineralizations to be missed in occasion in precious mineral deposits especially such as epithermal gold deposits. Especially in searching such mineral deposits; there are many encouraging mineral exploration stories and good results belonging to soil geochemistry and biogeochemistry studies which are carried out with the next stage of general prospection and even with the rock geochemistry.

The purpose of this study is to investigate the possible gold mineralization buried in the Canca (Gümüşhane-Turkey) hydrothermal alteration site, which was discovered during the prospection studies by MTA, using soil geochemistry by statistical methods. There, the mineral geochemistry studies were also performed from time to time as it was considered to be important in mineralization.

Works in the field seem to extend until 1980s when report records are taken into consideration. The preliminary studies are general mineral prospection studies carried out by Çınar et al. (1982) in the region. In this study, hydrothermal alterations in the area were pointed out. Güner et al. (1985) have mapped the hydrothermal alteration areas of the Canca area during the 1/5000 scale mapping studies of the Hazine Cave and Kırkpavli mineralizations located near the Canca site.

During the detailed study of the entire region within scope of the Turkish-Japanese Joint Project (MTA, 1986) co-operated with the Japan Cooperation Agency (JICA) in the 1980s the studies were carried out in order to determine the alterations in the Canca area, and attention was paid to hydrothermal alterations and scattered pyrite mineralizations.

Kansız et al. (1994) carried out prospection and geological investigations on a wide area in 1/5000 scale, including the study area, in 1989, 1990 and 1991. Within the scope of these studies, they carried out 1/10 000 scale geology and alteration mapping studies in the Canca area and detected values of 85-167 mg/kg Cu, 146 mg/kg Pb, 165 mg/kg Zn, 5-24 mg/kg Sb, 80-200 mg/kg As, 1.2-2 mg/kg Ag and 1 mg/kg Au in rock samples. In rock geochemical studies conducted by Güner and Yazıcı (2008), high Ag values of 1.2-5.1 mg/kg were reported. In another study conducted by the same researchers the values of 761 mg/kg As, 80 ppb Au and 2.7 mg/kg Ag (Yazıcı et al., 2014) were reported. In the context of the remarkable pathfinder element and other metals obtained, the silver and gold values are the data obtained from rock geochemistry studies.

No studies on soil and/or plant geochemistry have been found on the Canca alteration area. Despite the fact that mineral exploration studies were carried out in the area, the lack of soil geochemistry studies were noticed. Therefore; the soil geochemistry study was also carried out. There are many studies in the literature that use soil geochemistry in gold explorations. For example; Reis et al. (2001) showed that soil geochemistry studies had been effectively used in the exploration of gold mineralization in their studies. They also detailed the study area increasing the anomaly contrast resolution of the element distribution maps, which were formed by the soil geochemistry, using the method they suggested in the calculation of threshold value also benefiting especially from pathfinder elements.

In Çanakkale-Ayvacık and its close vicinity, the gold exploration was carried out by using soil geochemistry studies and the Kısacık gold field with a capacity of 10 tons of gold were found (Vural, 2006) by means of appropriate well sites given with soil geochemical studies. The soil geochemistry as well as plant geochemical studies has been an important method used in mineral explorations since 1950s. Satisfactory results have also been obtained with plant geochemical studies.

The soil geochemistry study in gold enrichments in the Arzular town (Gümüşhane province) located in the close vicinity of the study area was carried out by Yaylalı-Abanuz et al. (2012). Suggestions for suitable drilling locations for the area were also made with the study in which the element distribution maps were formed especially using the Kriging method. Soil geochemistry studies on the Kırkpavli alteration site were carried out by Vural and Erdoğan (2014),

which is located at 1.5-2 km SSW of the Canca area. In this study; they asserted that elements of Ba, Zn, Pb, Ni, Mn, Cu, Cr and As could be used as pathfinder elements for gold, formed the anomaly maps of these elements for the area by the Kriging interpolation method and suggested suitable drilling locations for gold exploration. At the moment, a private company has completed drillings for gold exploration and initiated operational processes.

The purpose of this study is to investigate possible gold mineralization buried in the Canca (Gümüşhane) hydrothermal alteration site, which was discovered during the prospection studies by MTA, using soil geochemistry study by statistical methods. There, the mineral geochemistry studies were also performed from time to time as it was considered to be important in the mineralization.

In this context, the total of 288 soil samples collected for soil geochemistry from the Canca area were analyzed in the Central Laboratory of the Gümüşhane University and various statistical analyzes of the obtained data were performed. The threshold values of the elements were calculated benefiting from the Median Absolute Deviation (MAD) values of which their excessive values are attenuated and the potential of buried gold mineralization of the area was investigated by means of the produced element distribution maps.

2. General Geology of the Area

The study area is located at 10 km north-west of the Gümüşhane province and covers an area of approximately 1.5-2 km^2 (Figures 1 and 2). The geology of Gümüşhane and its surroundings, including the study area, is like a small summary of the geology of a significant part of the Eastern Black Sea Region. The investigation of the geological elements by these researchers here significantly contributes to the understanding of the Eastern Black Sea Tectonic Union (Ketin, 1966), which is known as the Eastern Pontides.

The basement of the Eastern Black Sea Tectonic Union in Gümüşhane and its surroundings is formed by the Kurtoğlu Metamorphics and the cutting unmetamorphosed granitic plutons (Gümüşhane Granitoid) (Dokuz, 2011; Topuz et al., 2007; Yılmaz, 1972). These metamorphic basement rocks outcrop in southwest of Gümüşhane outside the study area. The Gümüşhane Granitoid outcrops in many places, mainly in the Gümüşhane city center and is overlain by the Early-Middle Jurassic volcanoclastic unit (Şenköy formation) (Kandemir, 2004). The volcanoclastic unit grades into the carbonate rocks of the Late Jurassic and the Early Cretaceous formations of Pelin (1977) called the Bergida formation in the upper layers. The carbonate rocks are then conformably overlain by the Late Cretaceous clastic units (Kermutdere formation) (Tokel, 1972) (Figure 1).

The Kermutdere formation, which begins with the deposition of sandy limestone at the bottom, grades into red pelagic limestones and a turbiditic series consisting of sandstone, siltstone, marl and limestones in the upper layers. All these units are then cut by the Late Cretaceous intrusions in the northwestern part of the study area (Kaygusuz et al., 2008). Late Cretaceous plutonic, volcanic and sedimentary rocks are stratigraphically overlain by the Middle-Late Eocene volcanic and volcanoclastic rocks (Arslan and Aliyazıcıoğlu, 2001; Güven, 1993). These units are called as the Alibaba formation in the region (Tokel, 1972). Alibaba formation is cut by the synchronous calc-alkaline granitoids (Eyüboğlu et al., 2011; Karslı et al., 2013) called the Gözeler granite (Vural, 2017, 2014) which outcrops in close vicinity of the study area.

2.1. Stratigraphy of the Study Area and Alteration Development Process

The Middle-Late Eocene Alibaba formation outcrops in the study area. The unit is formed by basalt and andesite in the study area and is occasionally cut by andesite-dolerite dykes which are the final product of the Eocene volcanism. In close vicinity of the study area the Gözeler granite, which is considered to be Upper Eocene (?) is observed in south of the area (Figure 1). It is predicted that the alteration in the area and possibly buried mineralization might have developed due to the Upper Eocene granitic intrusive rocks which outcrop in many areas such as Gözeler (Old Gümüşhane), Avliya (Torul-Gümüşhane), Demirören-Sarıçiçek-Dölek (Gümüşhane-Center) in the region and the Upper Cretaceous granitic rocks in northwest of the study area. Hydrothermal fluids, mainly the products of the Upper Eocene processes, have reached shallow geochemical environments along the tectonic lines developed as a result of the neotectonic evolution of the region and altered the predominantly andesitic rocks in the Canca area.

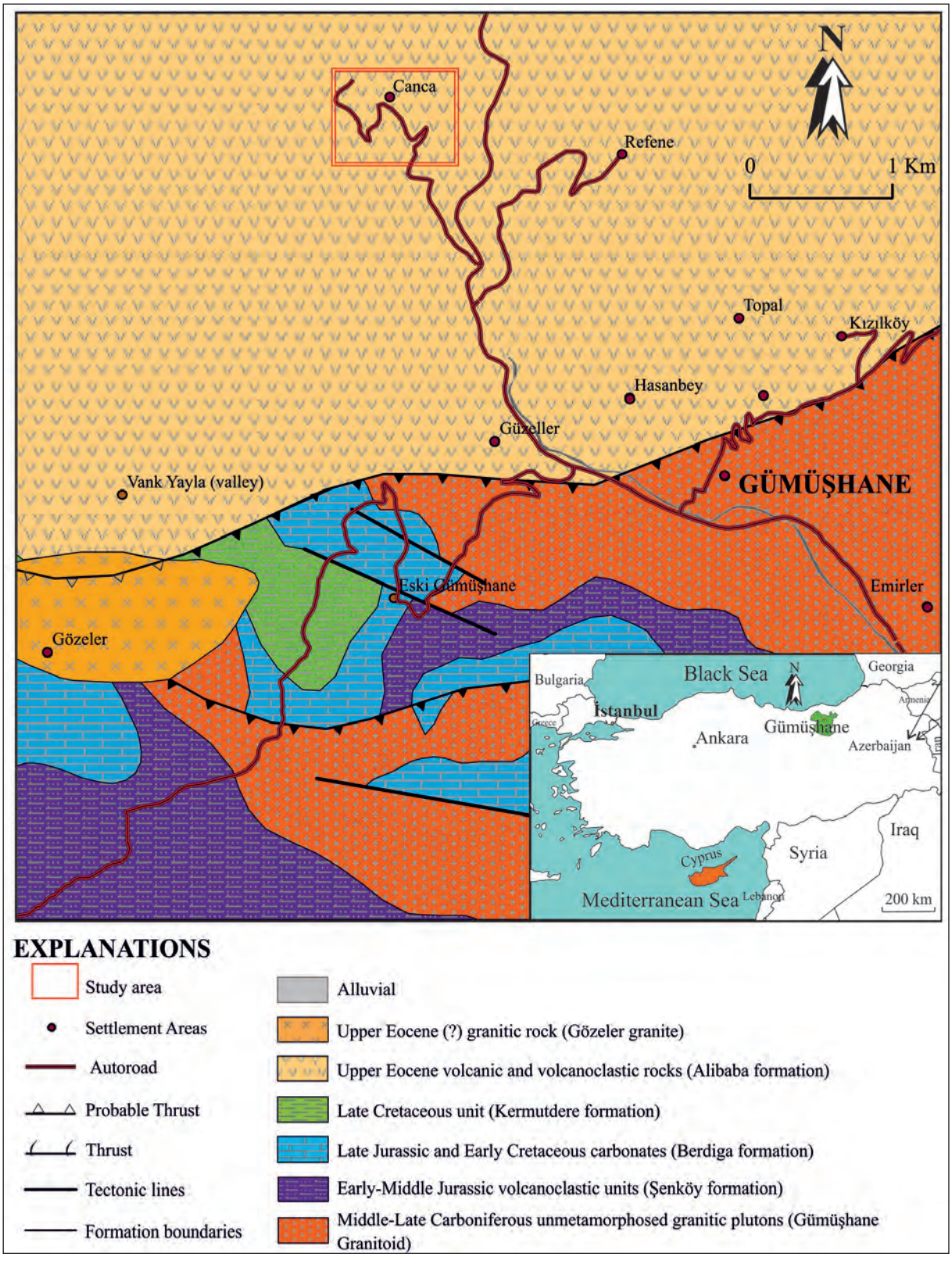

Figure 1- Geological map of Gümüşhane and its close vicinity (modified from Güven, 1993).

Therefore, the alteration-mineralization in the field is tectonical and caused the alteration of the final product fluids of buried granitoidic rocks in the area in surrounding rocks. The fluids along tectonic lines, which are dominantly in E-W, slightly NW-SE directions in accordance with the development of the neotectonic roof of the region, have altered the field along these lines (Figure 2).

Silicifications (phyllic alteration) important for the mineralization have developed along tectonic lines in E-W and NW-SE directions. In particular, the intense hydrothermal alteration (silicification, argillization, hematitization, limonitization and pyritization) is observed along fracture lines. The silicification covers a wider area especially in the western part of the landscape. Kaolinite, smectite and illite have gained importance in the remaining altered section where alunite, chalcedony, gypsum vein and veinlets are seen.

2. Material and Method

In context of soil geochemistry studies, the total of 288 soil samples were collected along NE/SW and NW/SE profiles in the Canca alteration site (Figure 2). Samples were collected, numbered and placed into nylon bags using plastic shovels from a depth of 0-25 cm (zone B of the soil profile) in such a way as not to cause any geochemical contamination and in accordance with the sampling standards for clean nylon bags. Soil specimens were prepared by routine analyze preparing works in the Geological Engineering Laboratory of the Faculty of Engineering and Natural Sciences at the Gümüşhane University. In this context, it was ensured that the samples were dried under natural conditions in a non-humidity environment, then the product was dried at 60°C for 2 days and the natural moisture was removed. Then, the samples were sieved under 2 mm polyethylene sieve and the samples passing through the sieve were milled with a ring mill. They then passed through 80-mesh sieve to obtain 10-15 g packages from soil samples in ideal sizes suggested by Rose et al. (1991). The soil pH measurements were also made at the Geochemistry Laboratory in the Geological Engineering Department at the Gümüşhane University. Soil samples for soil pH measurements were sieved under 100 mesh size and the samples, of which their natural humidities were removed by leaving them in an oven for 2 days under 60°C, were mixed by sample/distilled water mixture in 2/2,5 mass(gr)/volume(mL) ratio then placed into 50 mL flacon tubes. Samples were then rinsed 60 minutes on the shaking table and left 10 hours for suspended materials to settle down. Finally, their pH measurements were made using the Hanna brand desktop pH meter. It was determined that the pH of the soil changed between 3.90 and 7.02 and therefore it was detected that the acidity of the Canca field was higher.

The soil samples were analyzed by ICP-MS (Inductively Coupled Plasma–Mass Spectrometer) in the Central Laboratory of the Gümüşhane University

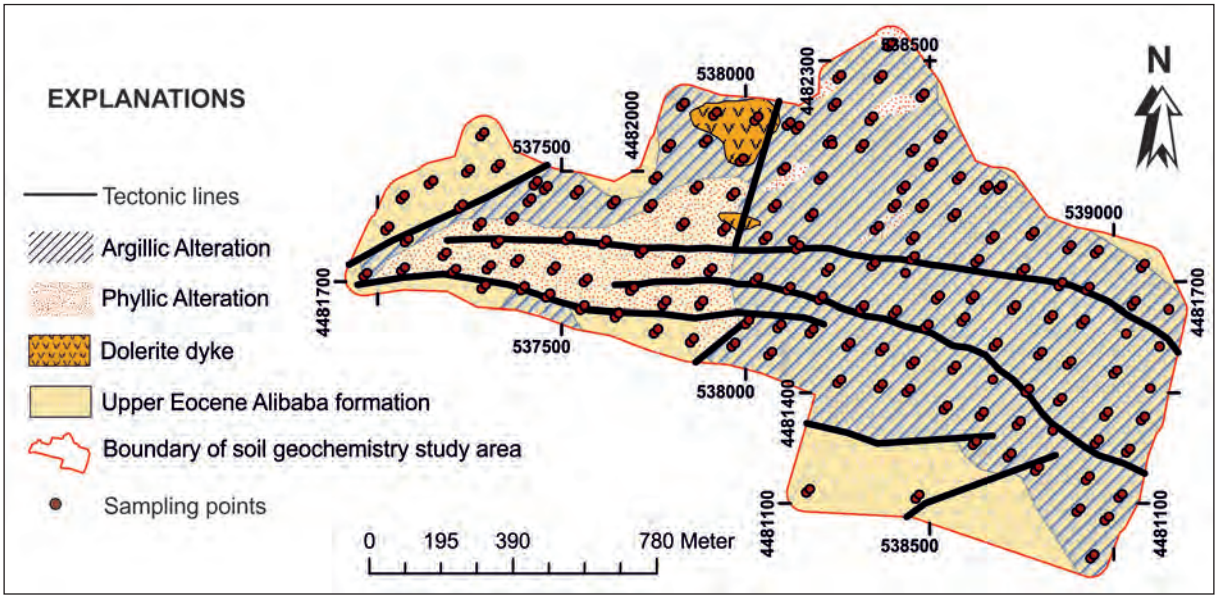

Figure 2- Geology and alteration map of the study area (modified from Güner and Yazıcı, 2008).

after dissolution in the closed circuit microwave dissolution system. From soil samples powdered during analysis, the measurements around 0,20 g (in 0,1 mg sensitivity) were taken and placed in the Teflon beaker of the microwave oven (AGILENT MDS-8G). By adding 4 mL of NHO_3 and 2 mL of HF, they were subjected to the fragmentation under conditions given in table 1 (1st stage), then they again were subjected to the fragmentation under conditions given in table 1 (2nd stage) by adding this time 5 mL of B_3OH_3 to the resulting solution. After the treatment, clear solutions obtained by which the beaker contents were obtained after filtering through glass wool, were quantitatively completed to 50 mL by adding distilled water and analyzed. In order to control the reliability of results; each sample was re-analyzed at least 3 times, the mean and standard deviations of the results were calculated to determine the accuracy and the results were given at a certain reliability interval and level. In addition to using the standard calibration graph, the standard addition to samples and internal standard methods were applied. Besides, the accuracy tests have also been completed by applying the Standard Reference Material (SRM) to the sample solutions by applying spiked/recovery tests. The performance and accuracy of the method applied are; as the soil SRM; sandy soil standard "Sandy Soil C (CRM-SA C)" were used and the quality control/quality assurance (QC/QA) parameters obtained were given in table 2.

3. Results and Discussion

The major and trace element analyzes of soil samples collected from the Canca area were carried out in the Central Laboratory of the Gümüşhane University using ICP-MS instrument and the descriptive statistical parameters of the gold and geochemically related elements were given in table 3. When the results obtained are evaluated, it is seen that the elements exceed the upper crustal values suggested by Rudnick and Gao (2010) at some sampling points. Therefore, there is an enrichment by the elements in the area.

Elements were subjected to Kolmogorov-Smirnov and Shapiro-Wilk normality tests and checked for their normal distribution. Since the significance level was found to be less than 5% for both tests it was seen that data of which their Ho hypothesis (the data showing

Table 1- Partition program in microwave oven.

1st Stage				2nd Stage			
Level	Temperature (°C)	Time (min.)	Power (Watt)	Level	Temperature (°C)	Time (min.)	Power (Watt)
1	120	5	800	1	120	6	800
2	130	5	800	2	130	6	800
3	150	5	800	3	150	6	800
4	210	7	800	4	210	10	800

Table 2- Accuracy tests of analyses.

	Na	Mg	Al	S	K	Ca	V	Cr	Mn	Fe	Co	Ni	Cu
Lower limit, LOD, µg/L	2,3	1,0	1,4	3,4	3,4	3,8	0,12	0,05	0,11	2,0	0,02	0,17	0,09
Lower limit, LOD, µg/kg	575	250	350	850	850	950	30	12,5	27,5	500	5	42,5	22,5
Upper limit, mg/L	100	100	100	100	100	100	10	10	10	100	10	10	10
Upper limit, mg/kg	25000	25000	25000	25000	25000	25000	2500	2500	2500	25000	2500	2500	2500
RSD, %	1,2	3,4	4,9	4,8	2,2	3,1	2,5	1,7	1,1	2,6	2,5	1,9	0,7
	Zn	**As**	**Se**	**Sr**	**Mo**	**Ag**	**Cd**	**Sn**	**Sb**	**Ba**	**Au**	**Hg**	**Pb**
Lower limit, LOD, µg/L	0,52	0,07	0,06	0,12	0,05	0,01	0,02	0,12	0,25	0,00015	0,01	0,01	0,12
Lower limit, LOD, µg/kg	130	17,5	15	30	12,5	2,5	5	30	62,5	0,0375	2,5	2,5	30
Upper limit, mg/L	10	10	10	10	10	10	10	10	10	10	10	10	10
Upper limit, mg/kg	2500	2500	2500	2500	2500	2500	2500	2500	2500	2500	2500	2500	2500
RSD, %	3,3	1,9	2,2	1,6	2,1	1,5	0,6	3,3	2,9	1,9	0,6	1,1	2,1

LOD, Limit of Detection,
RSD, Relative Standard Deviation,

Table 3- Descriptive statistical values of the elements and calculated threshold values with respect to different statistical parameters.

	Au µg/kg	Ag mg/kg	Cu mg/kg	Pb mg/kg	Zn mg/kg	As mg/kg	Sb mg/kg	Bi mg/kg	Mo mg/kg	Sn mg/kg	Hg µg/kg
Amount	39	89	285	269	285	287	142	40	75	124	69
Minimum	0,68	0,02	2,00	7,00	2,10	4,00	0,59	5,00	0,04	0,52	1,25
Maximum	19,20	28,95	314,00	857,57	394,00	199,95	49,29	89,00	37,00	16,30	91,90
Mean	6,97	2,44	69,42	80,61	74,45	37,98	8,00	18,28	5,30	1,53	23,65
Geo. Mean.	5,36	0,69	55,01	55,84	63,29	28,92	4,55	13,36	2,35	1,31	19,60
Median	5,40	0,54	68,00	52,72	70,00	29,06	4,27	12,00	2,63	1,25	21,20
SD	4,83	4,75	42,93	103,76	39,96	31,10	9,65	17,72	7,53	1,52	15,08
Skewness	0,88	3,40	1,61	4,64	2,40	2,20	2,40	2,39	2,62	7,78	2,43
Kurtosity	-0,11	13,20	6,71	26,86	15,10	6,23	6,25	6,43	6,73	73,66	8,55
Mean+2SD	16,62	11,93	155,29	288,14	154,36	100,19	27,30	53,72	20,36	4,57	53,81
Geo.M+2SD	15,01	10,18	140,88	263,37	143,20	91,13	23,85	48,81	17,41	4,34	49,76
Median+2MAD	11,60	1,42	120,00	98,16	91,00	57,34	10,20	24,00	6,77	1,50	32,00
Background values*	1,5	0,053	28	17	67	4,8	0,4	0,16	1,1	2,1	50

Geo.M.: Geometric Mean, SD: Standard deviation, MAD: Median Absolute Deviation
*from Rudnick and Gao (2010).

the normal distribution of the data) had been rejected was found to be non-normal distribution (Table 4). Histograms were created for visual evaluation of dataset distributions (Figure 3). When histograms and descriptive statistical parameters of the elements are considered, it is seen that the element sample groups are skewed rightward. Logarithmic values of the data for all elements were taken and histograms were regenerated (Figure 3). When histograms generated from logarithmic data were examined, it was seen that the distorted data did not form an ideal Gaussian population, although they were converted to some normal distribution. Performing Box-Cox and Arcsin transformations it was tested whether the distribution approached the Gaussian distribution or not. However, it was seen that the most ideal transformation was sub-sampling assemblage obtained only from logarithmic transformations.

Since elements did not show a normal distribution, the correlation of the elements with each other was examined by calculating the Spearman's rho correlation coefficients (Table 5). Spearman's rho correlation coefficients are between -1 and +1. If the correlation coefficient is +1, it can be said that there is an excellent positive linear relationship between the variables, if it is -1 then there is an excellent negative linear relationship between the variables. If the coefficient is 0 then it is understood that there is no linear relationship between the variables. Also according to the correlation coefficient intervals there is a classification as; very weak (0,00-0,25), weak (0,26-0,49), moderate (0,50-0,69), high (0,70-0,89), very high (0, 90-100), and the direction of relationship is stated according to the negative or positive value of the coefficients. Although it is not so strong according to the Spearman's rho correlation coefficients, the

Table 4- Normality tests for elements.

	Kolmogorov-Smirnov[a]			Shapiro-Wilk		
	Statistics	df	Sig.	Statistics	df	Sig.
Au (µg/kg)	0,183	39	0,002	0,908	39	0,004
Ag (mg/kg)	0,305	89	0,000	0,532	89	0,000
Cu (mg/kg)	0,062	285	0,009	0,900	285	0,000
Pb (mg/kg)	0,252	269	0,000	0,518	269	0,000
Zn (mg/kg)	0,094	285	0,000	0,859	285	0,000
As (mg/kg)	0,145	287	0,000	0,791	287	0,000
Sb (mg/kg)	0,221	142	0,000	0,704	142	0,000
Bi (mg/kg)	0,245	40	0,000	0,711	40	0,000
Mo (mg/kg)	0,263	75	0,000	0,637	75	0,000
Sn (mg/kg)	0,265	124	0,000	0,385	124	0,000
Hg (µg/kg)	0,184	69	0,000	0,781	69	0,000

a. Lilliefors (Sig.) correction, df:degree of freedom

Table 5- Spearson's rho correlation coefficients among elements.

Spearman's rho	Au	Ag	Cu	Pb	Zn	As	Sb	Bi	Mo	Sn	Hg
Au	1,00										
Ag	0,14	1,00									
Cu	0,52**	0,31**	1,00								
Pb	-0,16	0,10	-0,21**	1,00							
Zn	0,26	0,38**	0,55**	-0,24**	1,00						
As	-0,31	0,25*	0,11	0,43**	-0,04	1,00					
Sb	-0,36*	0,06	0,08	0,47**	-0,03	0,74**	1,00				
Bi			-0,10	0,31	-0,25	0,23	0,42	1,00			
Mo	-0,07	0,41**	0,02	0,47**	-0,11	0,65**	0,51**	0,43	1,00		
Sn	-0,17	0,33**	0,01	0,37**	0,23*	0,58**	0,56**		0,46**	1,00	
Hg	-0,18	0,11	-0,16	0,11	-0,01	0,11	0,34**		0,05	0,19	1,00

*. Correlation weightiness value around 0,05 and two-tailed.
**. Correlation weightiness value around 0,01 and two-tailed.

presence of a correlation between Cu-Au; Zn-Cu; Sb-Pb-As; and between Mo-Pb, As-Sb; Sn-As, Sb-Mo were determined.

One of the most common problems for geochemical data is that although many methods have been tried for transformations, the ideal distribution cannot always be reached. In these cases, one of the methods especially used in the threshold calculation to reduce the effect of extreme end values is to determine the MAD value and calculate the threshold value (TV) (median +2MAD, (M +2MAD)) similar to the TV calculation preferred in classical methods (average +2standard deviations, geometric mean +2standard deviations and etc.). The reason why median (M) and MAD are used in TV calculation is that it shows less affection against excessive values and deviations (Tum et al., 2011). There are also other methods in TV calculation. Among them, the multifractal modellings are most common (Almasi et al., 2015, Anderson, 2008, Carranza, 2009, Carranza et al., 2009, Carranza and Sadeghi, 2010, Jena, 1996, Zuo et al., 2009). A more detailed evaluation of the field using the aforementioned methods and comparing the methods applied with each other will be carried out in another study.

The M+MAD method is a very useful and practical method for evaluating the initial findings and giving an idea about the site. The MAD method has been rediscovered by Hampel (1974), inspired by the ideas of Carl Friedrich Gauss (1777-1855), and widely recognized in the scientific literature. The MAD is calculated as follows:

$$MMS = M_i(|x_i - m_j(x_j)|) \quad 1$$

where; xi is the number of each element in the sample, xj corresponds to the number of original observations, and Mi is the median of series.

The element distribution/anomaly maps generated by using threshold values obtained from M and MAD data give more realistic and satisfactory results (Reiman and Filzmoser, 2000).

Threshold values obtained by classical methods and by the M +2MAD method in this study are given in Table 3 for comparison. The calculated TVs are as follows: (M +2SD)> (Geo.M +2SD)> (M +2MAD).

3.1. Generation of Element Distribution Maps

Element distribution maps are the most common and ultimately used data evaluation stage in assessing the data in soil geochemistry studies for mineral exploration. The basic models used to generate the element distribution maps can be grouped under two main headings: Deterministic models and Probabilistic (linear statistic) models. The Inverse Distance Weighting (IDW) interpolation and Kriging methods are the best known methods for deterministic and probabilistic methods, respectively.

The IDW interpolation model is the oldest spatial prediction method (Shepard, 1968) and the easiest deterministic interpolation method. There are several decision-making methods to implement the model parameters and provide quick and easy information on the interpolated surfaces. It is preferred because it is easy and fast to use. To estimate the value at any unmeasured point, the IDW uses the measured values near the desired point to be estimated.

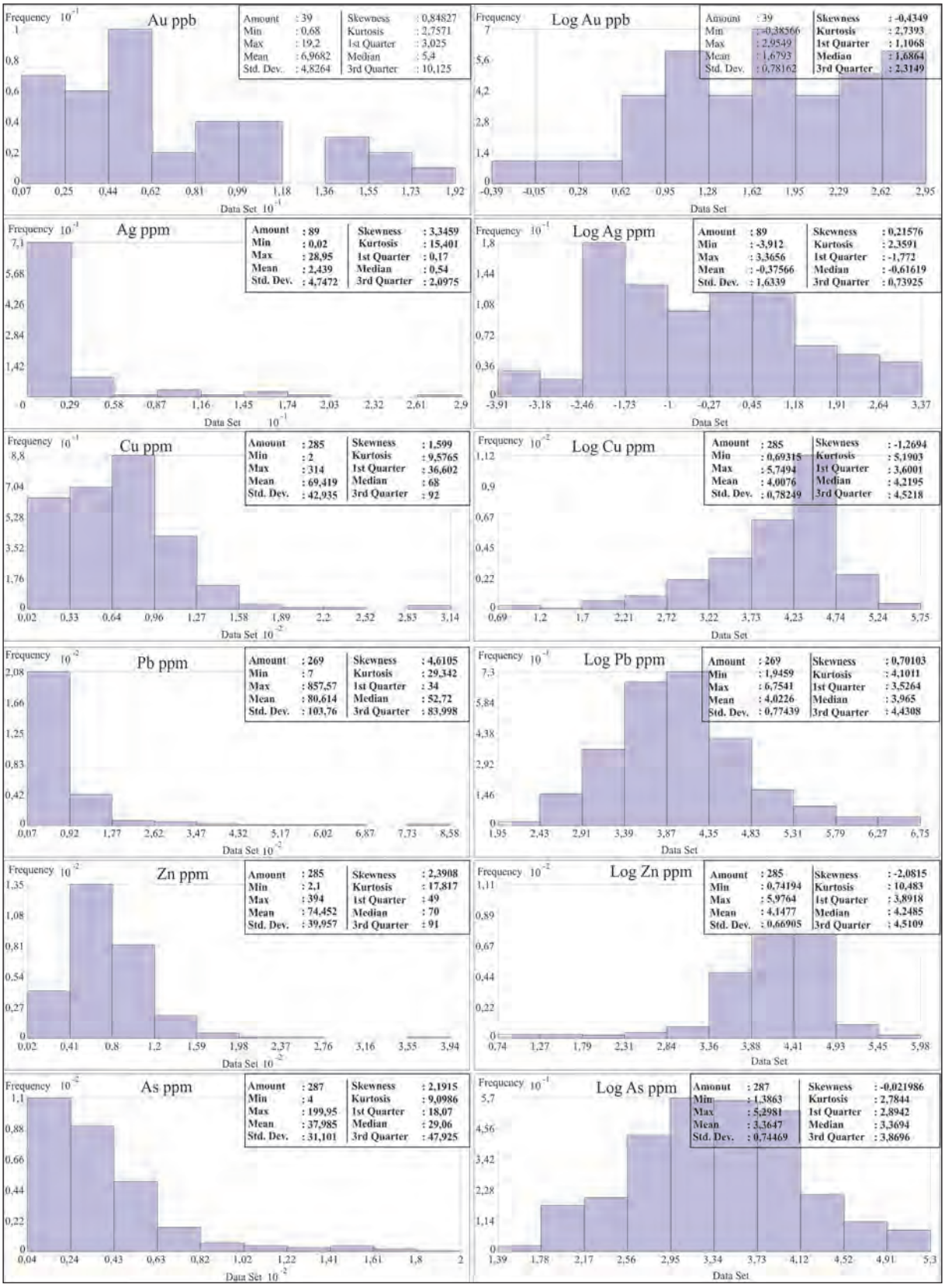

Figure 3- Histograms of raw and logarithmically transformed data.

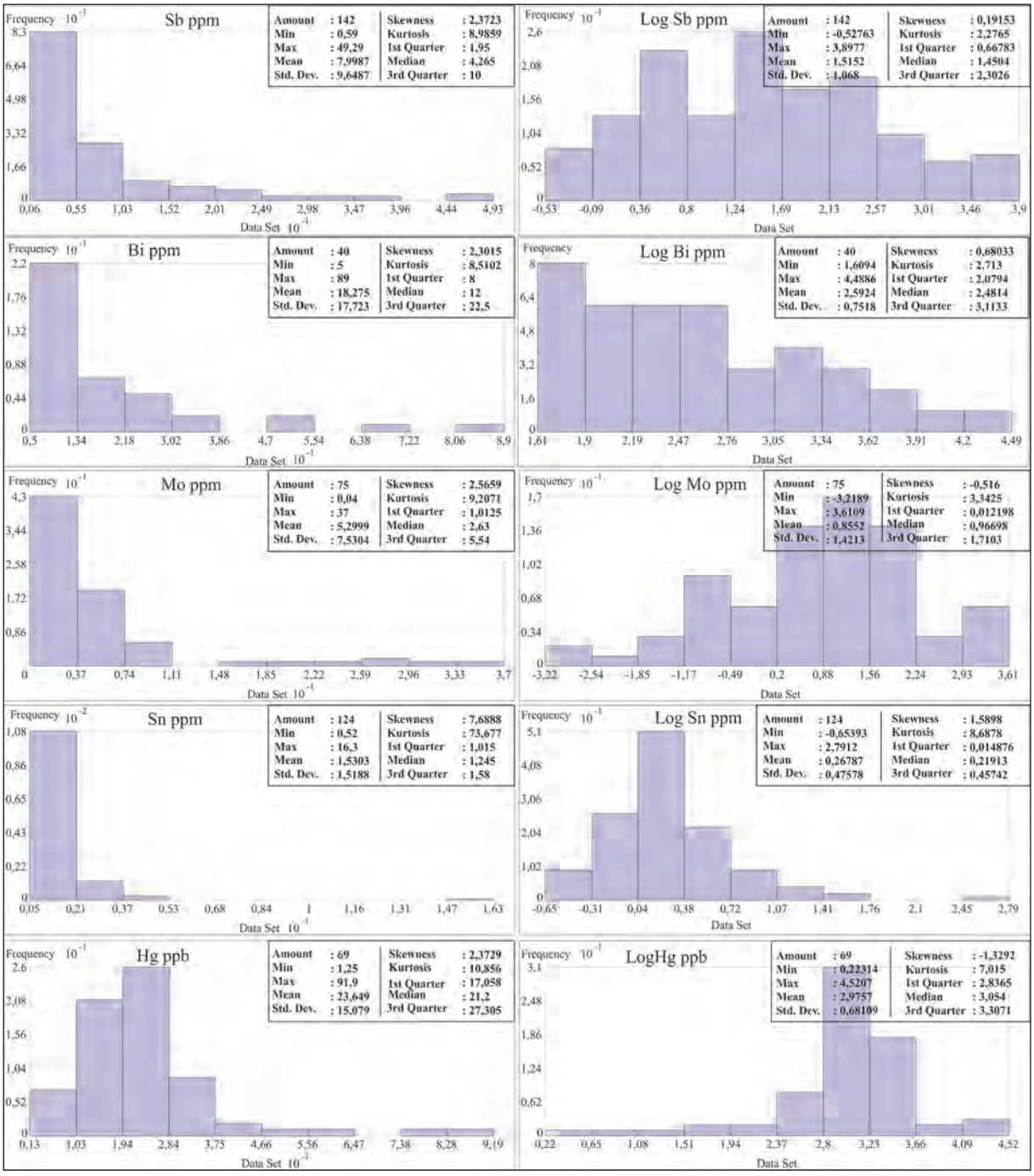

Figure 3- Continue.

The effect of the measured values closest to the desired point is more influential than the distances farthest to the investigated point. The fundamental of IDW was inspired by the principle of Waldo Tobler (Tobler, 1970) "*Everything is related to everything else, but the near ones are more related than the far ones*", the first law of Waldo Tobler in geography. Therefore, large weights are obtained from the points close to each other and small weights are obtained from distant points. Although there are several IDW methods, "Shaperd's Method" is the best known. Since the objective of the article is to evaluate the data belonging to the study area at first hand, it was avoided to give details of the method in the article (formulations and etc.). In the calculation of the IDW method the exponential p takes place. As the exponential values increases in IDW the effect becomes less in farther points. Although IDW has

good results in terms of sampling points at frequent and equal weights, the results obtained may not always be accurate in the case of complex relationships with the environment studied. Also taking into account the fact that the sample collection points are frequent and equal, the p-exponent value was taken as 2. In this study, the principles and details of the method were not mentioned as it is not the part of this study. The element distribution maps were created using the ArcGIS 10.5 package program (Figure 4-14), which is a good method used for less than 1000 data.

The method of Kriging on the other hand has long been used synonymously with geostatistical interpolation. The fundamental of the method originates from the studies of mining engineer D.G. Krige and statistician H.S. Sichel (Krige, 1951). The technique has then become widespread thanks to the formulae derived by the French mathematician G. Matheron, and the method was named as the Kriging referring to D.G. Krige by G. Matheron (Cressie, 1993). In time, the technique has been further developed.

Kriging is an adjustable to many situations and flexible method considering many parameters. The Kriging can produce values for sampled points using the information beneath the spatial automatic correlation provided by semi-variograms in order to determine suitable weighting sets and to predict points and surfaces at non-sampled points. Since the semi-variogram is a function of distance, the weights vary according to the geographic arrangements of the samples. Low weights are assigned to distant patterns and high weights are assigned to nearby patterns. The Kriging also considers the relative positions of the samples with respect to each other. Ordinary Kriging is the most reliable method and can be used for many data sets. Although Simple Kriging forms more aesthetic contours it is less reliable. Using Universal Kriging is relatively difficult compared to others. As can be seen in figure 3, the majority of data belonging to the study area is skewed to the rightmost. As mentioned earlier, many transformation methods have been tried to normalize the data in order to transform it into normal distribution. The log transformation method among these methods yielded satisfactory results compared to the others in converting the given data. However, the data did not become an ideal normal distribution. Some of the data are skewed a little rightward while of some are skewed leftward. Therefore, the data to be used in the Kriging could not be transformed into an ideal normal distribution. However, the Kriging method was used considering that sampling points are frequent and regular. As mentioned above, although the common used method is the Ordinary Kriging method, the method was applied using Simple, Universal, and Log methods according to the characteristics of the data. Cross-validation is used is studying the accuracy of Kriging methods and in the performance assessment of the models used on Kriging surface. The cross-validation performed does not give a definitive answer on the validation of model whether it is correct or false. When the data show normal distributions, the Kriging gives good results. Otherwise, the transformations into normal distribution for data are made to use the method. Although data transformations contribute to elimination of skewness they may not always correct extreme roughness. However, in the study carried out by Chaplot et al. (2006) it was shown that although most of the interpolation techniques (natural neighborhood interpolation, spline interpolation and etc.) showed a similar performance when there is a frequent sampling, the IDW and Kriging methods gave better results where the number of points were not frequent and the distributions were irregular. In this study, sampling points are both frequent and regular. Nevertheless, the detailed evaluation, preliminary studies and cross-validation tests were conducted for the method of Kriging, but these studies were not included in the article because they are not part of the original purpose of the article and are preparatory studies. Given the fact that data obtained by the IDW method and maps produced by the Kriging method give closer results are taken into consideration, a cross validation of the method has been made in this way. The application summaries of the IDW and Kriging methods are given in Table 6. There are a lot of national and international studies both including the comparison of these methods and independent studies including IDW and Kriging methods (Akçay, 1998; Ağca, 2015; Patinha et al., 2008; Buttafuoco et al., 2010; Başaran et al., 2011; Zuo, 2011; Shuguang et al., 2015).

More detailed information on both techniques used in this article can be obtained especially in spatial statistics books (Cressie, 1990, 1993; Chiles and Delfiner, 1999; Ripley, 2004; Webster and Oliver, 2007; Hengl, 2009).

As it was aimed at presenting preliminary findings obtained in this study, the element distribution maps were produced by means of IDW and Kriging methods using the ArcGIS 10.5 package software in order to get first hand and fast information (Figure 4-14). Table

6 summarizes the operational processes of the subject methods.

Although there is not observed any strong correlation between the element concentrations obtained in the soil geochemistry study, there are some correlations between the elements in minor amounts. The single element distribution maps of the elements selected both in accordance with this correlation and the general geochemical principles were produced

Table 6- Process summary table of the Kriging and Inverse Distance Weighting Methods.

Kriging	**Inverse Distance Weighting (IDW)**
Semi-variogram **Considering neighboring points: Standard; Number of points considered: 5, at least 2 points were considered. Area type 4, 45º; Lag number: 12**	**Upper value: 2,** **Neighboring points studied: Standard,** **Neighboring point numbers studied:15 points, at least 10 points** **Field type: All**
Hg (69 samples) **Type:** Simple; **Output Type:** Predictive, **Conversion:** Normal Value Conversion; **Basic Distribution**: Gamma; **Main and Secondary semi axes:** 395,61; **Lag size:** 37,95; **Nugget:** 0.35; **Model Type:** Spherical; **Limit:** 395,1; **Partial threshold:** 0,82	**Hg (69 samples)** **Main and Secondary semi axes:** 543,71
Sb (142 samples) **Type:** Simple; **Output Type:** Prediction; **Conversion:** Normal Value Conversion; **Approach:** Density slope; **Basic distribution:** Log-normal; **Main and secondary axes:** 392,91; **Lag size:** 53,39; **Nugget :** 0,72; **Model Type:** Spherical; **Limit:** 392,9; **Partial threshold:** 0,37	**Sb (142 samples)** **Main and Secondary semi axes:** 575,71
As (287 samples) **Type:** Universal; **Output Type:** Predictive; **Orientation Type:** Stable; **Orientation Removal:** Local Polynomial Interpolation; **Upper value:** 0; **Main and secondary axes:**1834,87; **Lag size:** 212,88; **Nugget:** 854,09; **Model Type:** Spherical; **Limit:** 1834,86; **Partial threshold:** 202,87	**As (287 samples)** **Main and Secondary semi axes:** 648,99
Zn 285 (samples) **Type:** Universal; **Output Type:** Predictive; **Orientation Type:** Stable; **Orientation Removal:** Local Polynomial Interpolation; **Upper value:** 0; **Main and secondary axes:** 70,69; **Lag size:** 7,59; **Nugget:** 1786,69; **Model Type:** Spherical; **Limit:** 70,69; **Partial threshold:** 112,68	**Zn (285 samples)** **Main and Secondary semi axes:** 648,99
Pb (269 samples) **Type:** Universal; **Output Type:** Predictive; **Orientation Type:** Stable; **Orientation Removal:** Local Polynomial Interpolation; **Upper value:** 0; **Main and secondary axes:** 66,87; **Lag size:** 7.61; **Nugget:** 12319,26; **Model Type:** Stable; **Parameter:** 2; **Limit:** 66,87; **Partial threshold:** 3914,42	**Pb (269 samples)** **Main and Secondary semi axes:** 633,98
Mo (75 samples) **Type:** Simple; **Output Type:** Predictive; **Average:** 5,30; **Main and secondary axes:** 361,87; **Lag size:** 78,85; **Nugget:** 45,26; **Model Type:** Spherical; **Limit:** 361,87; **Partial threshold:** 11,48	**Mo (75 samples)** **Main and Secondary semi axes:** 556,43
Bi (40 samples) **Type:** Simple; **Output Type:** Predictive; **Orientation Type:** None; **Conversion:** Normal value conversion; **Approach:** Density slope; **Basic distribution:** Log-normal; **Main and secondary axes:** 1731,95; **Lag size:** 144,33; **Nugget:** 0,60; **Model Type:** Spherical; **Limit:** 1731,95; **Partial threshold:** 0,89	**Bi (40 samples)** **Main and Secondary semi axes:** 569,57
Cu (285 samples) **Type:** Simple; **Output Type:** Predictive; **Average:** 4,01; **Orientation Type:** None; **Conversion:** Log; **Main and secondary axes:** 483,89; **Lag size:** 46,25; **Nugget:** 0.50; **Model Type:** Spherical; **Limit:** 483,89; **Partial threshold:** 0,13	**Cu (285 samples)** **Main and Secondary semi axes:** 648,99
Ag (89 samples) **Type:** Simple; **Output Type:** Predictive; **Orientation Type:** None; **Conversion:** Normal value conversion; **Approach:** Density slope; **Basic distribution:** Log-normal; **Main and secondary axes:** 467,55; **Lag size:** 38,96; **Nugget:** 0,90; **Model Type:** Spherical; **Limit:** 467,55	**Ag (89 samples)** **Main and Secondary semi axes:** 647,66
Au (39 samples) **Type:** Simple; **Output Type:** Predictive; **Average:** 1,68; **Orientation Type:** None; **Conversion:** Log; **Main and secondary axes:** 936,24; **Lag size:** 119,14; **Nugget:** 0,16; **Model Type:** Spherical; **Limit:** 936,24; **Partial threshold:** 0,65	**Au (39 samples)** **Main and Secondary semi axes:** 546,.50
Sn (124 samples) **Type:** Simple; **Output Type:** Predictive; **Orientation Type:** None; **Conversion:** Normal value conversion; **Approach:** Density slope; **Basic distribution:** Log-empirical; **Main and secondary axes:** 563,15; **Lag size:** 49,38; **Nugget:** 0,59; **Model Type:** Spherical; **Limit:** 563,15; **Partial threshold:** 0,61	**Sn (124 samples)** **Main and Secondary semi axes:** 575,71

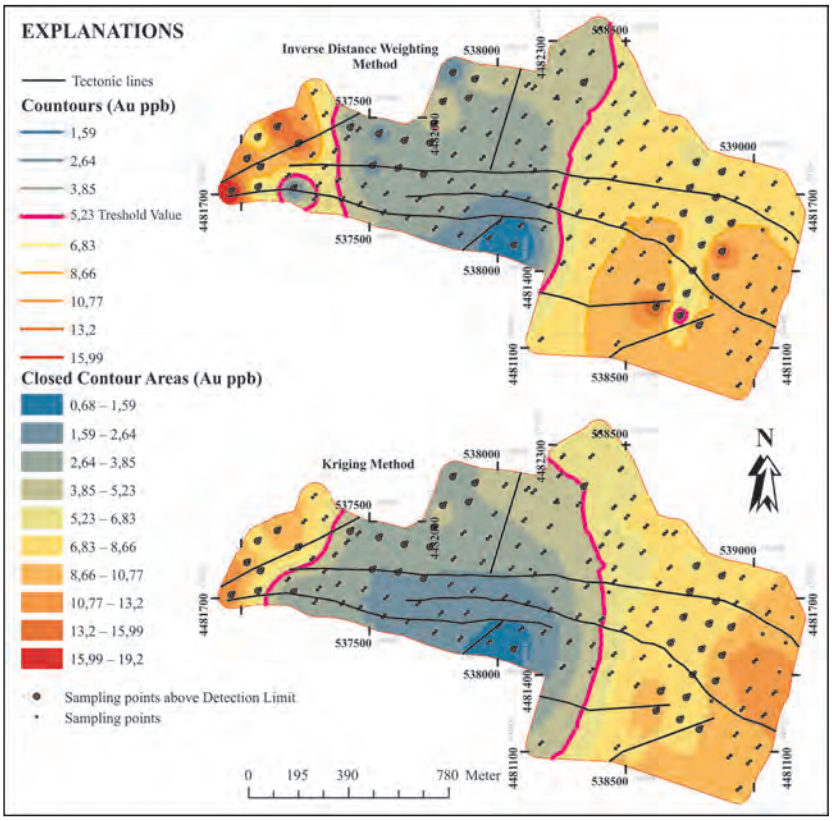

Figure 4- Distribution map generated by IDW and Kriging methods for Au element.

(Au, Ag, Cu, Pb, Zn, As, Sb, Bi, Mo, Sn and Hg) (Figures 4-14). For each element, the TV is obtained by adding M and 2MAD which are not affected much by end values as mentioned above. For each element, the element distribution maps, which had been drawn using IDW interpolation and Kriging methods, were shown together for easier interpretation.

Concentrations were found only in 39 sampling points for the gold element above the limit of detection and slightly above the mean shell values suggested by Rudnick and Gao (2010). It was seen that the TV of the gold concentrations for the area was above 5.23 µm/kg in W and in the E-SW directing sections where the argillic alteration had especially been developed (Figure 4). Although there was not detected any big difference between the map produced by the IDW interpolation and Kriging methods for Au distribution maps, it was seen that the sensitivity in the IDW method had been slightly higher (western and southeastern ends of the figure 4). The effect of tectonic elements in Au enrichment in the area is also observed on the map.

Ag element was detected above the detection limit at 89 sampling locations. It ranges between 0.02 and 28.95 mg/kg, and the calculated TV value for silver is 1.45 mg/kg (Figure 5). The silver values in the area occasionally exceed the upper crustal values suggested by Rudnick and Gao (2010). When element distribution maps generated by two different methods for silver element are examined, it is observed in the map generated by IDW method that Ag values are above TV (1.45 ppm) in the central part of the study area (Figure 5). Silver enrichments concentrates more heavily on areas where argillic and phyllic alterations develop. However, in the map generated by the Kriging method, the silver enrichment area is restricted into a smaller area. It would not be wrong to make an association with technological lines for silver element enrichments.

Cu element was detected above detection limits almost at all sampling points in the study area and TV for Cu was determined as 120 mg/kg by M + 2MAD method. When Cu element distribution maps were examined, there was not observed any remarkable Cu enrichment in the map produced by the Kriging method. Besides, Cu enrichments were noted especially in sections where phyllic alteration

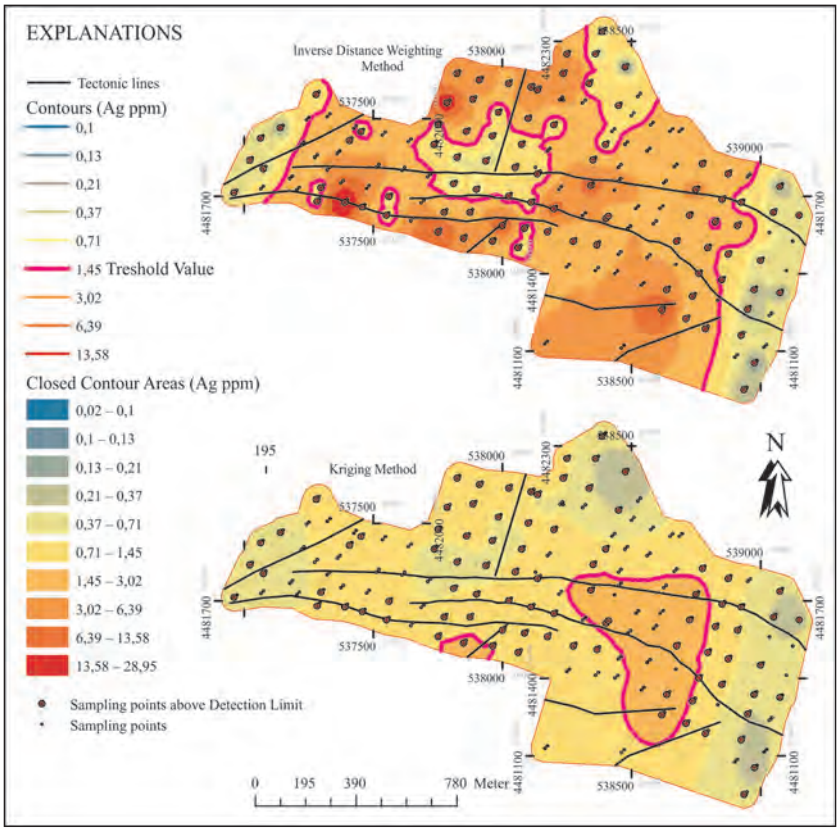

Figure 5- Distribution map generated by IDW and Kriging methods for Ag element

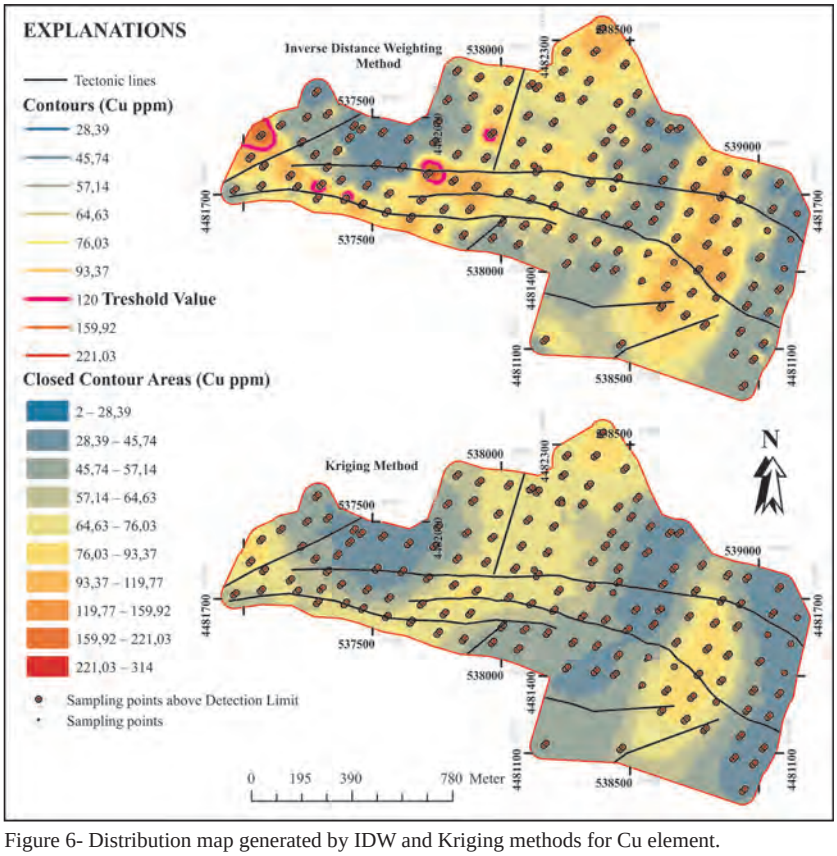

Figure 6- Distribution map generated by IDW and Kriging methods for Cu element.

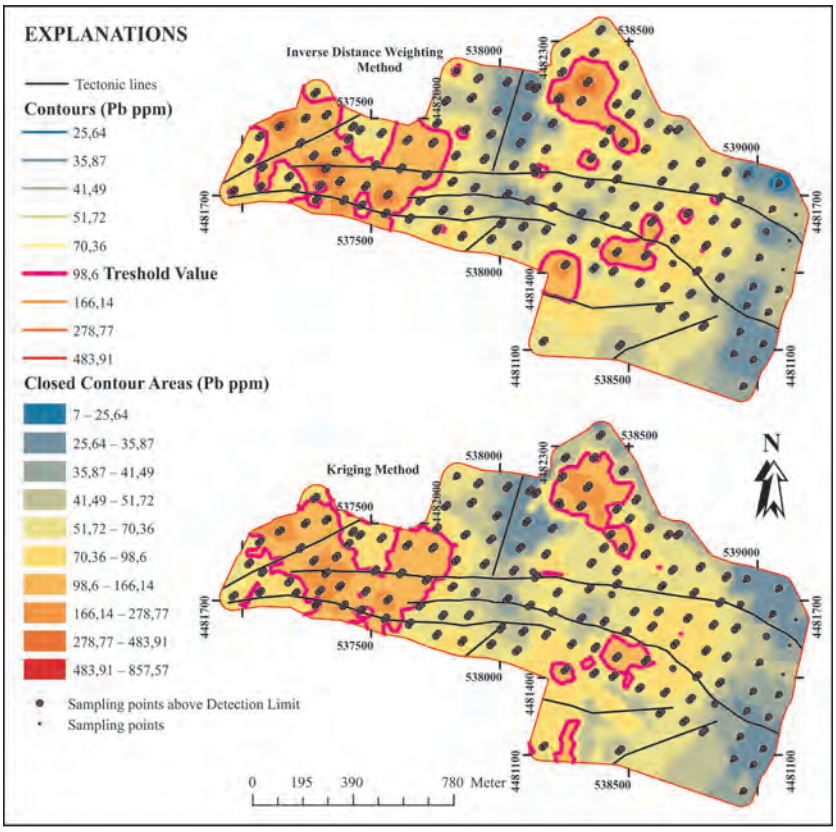

Figure 7- Distribution map generated by IDW and Kriging methods for Pb element.

had been observed, the western part of the study area (though in a limited area), in the map produced by IDW interpolation method (Figure 6). As Au element shows a correlation with Cu element though in weak amounts, this correlation should not be overlooked in detailed research studies that will be done in the field.

Pb element was detected at 269 sampling points above the detection limit in the study area. TV for lead was detected as 98.6 ppm by M+ 2MAD method and there are observed lead enrichments in west of the study area according to the element distribution maps (Figure 7) generated by IDW and Kriging methods. In the element distribution maps generated by both methods, the enriched areas coincide with each other.

Zn element was detected above the detection limit at 285 sampling points in the study area. The TV for Zn element was determined as 91 ppm by M + 2MAD method. Along with some differences in the Zn element distribution maps formed by IDW and Kriging methods, the areas of enrichment fall in the same zones, towards the central sections of the study area.

In the map generated by the IDW method, a small amount of enrichment is observed in a small area in the western part of the study area (Figure 8).

As element was determined above the detection limit at 287 sampling points in the study area. When the element distribution maps generated for the As element were examined, it was seen that As values were enriched in the western part, and these enrichments overlapped with the phyllic alteration areas (Figure 9). Although there was not observed any close relationship between Au and As elements in the correlation analysis, it was seen that the element distribution maps covered the As enrichment area coinciding with Au enrichment area. The fact that the correlation in the distribution map is not captured in the correlation analysis is due to the fact that the Au values are above the detection limit in the study area (Vural and Erdoğan, 2014).

Sb element in the Canca alteration area was found in concentrations above the detection limit at 142 sampling points. It shows a positive relationship with As element though not strong. There is observed Sb

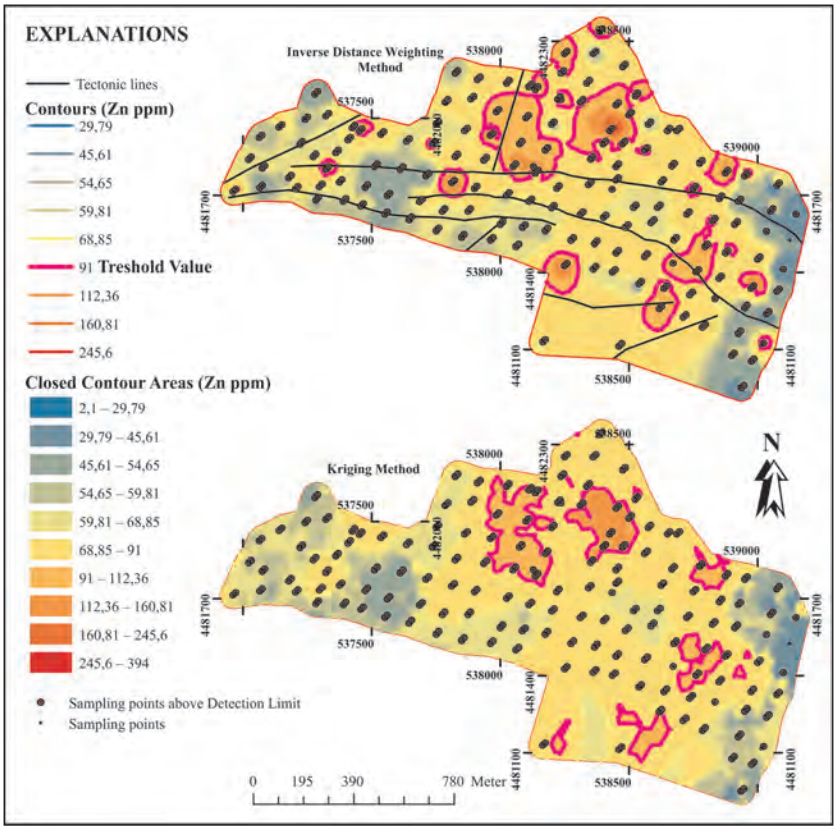

Figure 8- Distribution map generated by IDW and Kriging methods for Zn element.

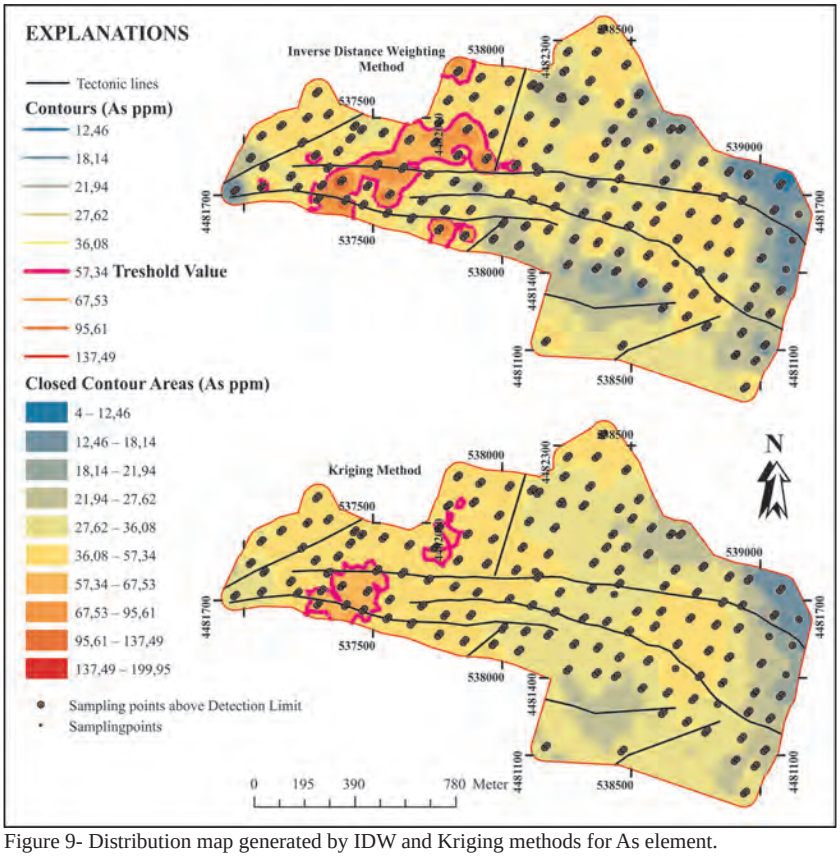

Figure 9- Distribution map generated by IDW and Kriging methods for As element.

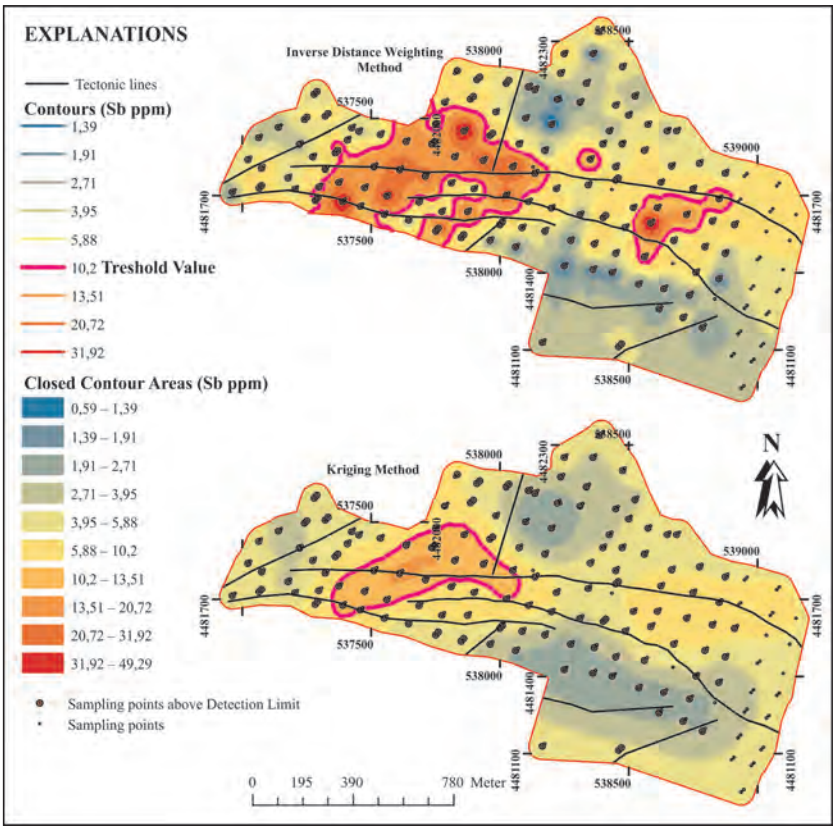

Figure 10- Distribution map generated by IDW and Kriging methods for Sb element.

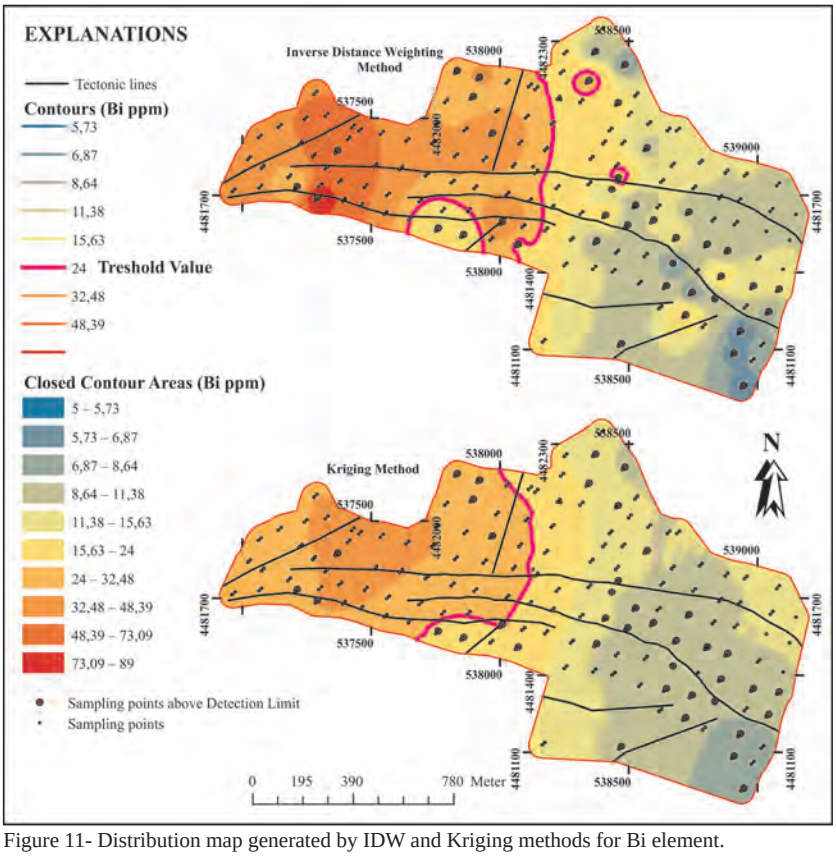

Figure 11- Distribution map generated by IDW and Kriging methods for Bi element.

enrichment in western part of the study area as a result of reflection of this relation in the element distribution maps prepared for Sb and in a limited area in the eastern part of the site in the distribution map generated by the IDW (Figure 10). The Sb enrichments have developed more in the phyllic alteration zone.

Bi element was detected above the detection limit at 40 sampling points and the enrichments in Sb were determined as it was in the western part of the study area (Figure 11). Tectonic lines become intense and get closer to each other in western part of the area and this shows that these tectonic activities are effective in element enrichment. It is seen that the element distribution map generated by the IDW method for Bi element gives more detail in the element distribution as well as in many elements.

Mo element has a concentration above the detection limit at 75 sampling points. In the calculation made by M + 2MAD method, the TV for Mo was found to be 6.77 ppm and it was seen that Mo enrichments in the study area were located in west of the study area where tectonic lines had become intense (Figure 12). Mo enrichments show close similarities with the enrichment areas of other elements. As in other elements, the element enrichment was more precisely detected in the element distribution map generated by the IDW method for Mo element (Figure 12).

Sn element was detected above the detection limit at 124 sampling points. When the element distribution maps prepared for Sn (IDW and Kriging Method) were examined, it was seen that tin enrichment was observed in the section where the argillic alteration occurred mainly in east of the study area (Figure 13). Minor enrichment is seen in the phyllic alteration zone to the west of the area.

Hg element occurred above the detection limit at only 69 sampling points. It was observed that Hg enrichments in the element distribution maps prepared by IDW and Kriging methods were in the eastern/ central parts of the field. According to the distribution map generated by IDW method, some enrichments are also available in west of the study area (Figure 14). This element is seen to have spread to more detailed and wider areas looking at the element distribution map generated by the IDW method.

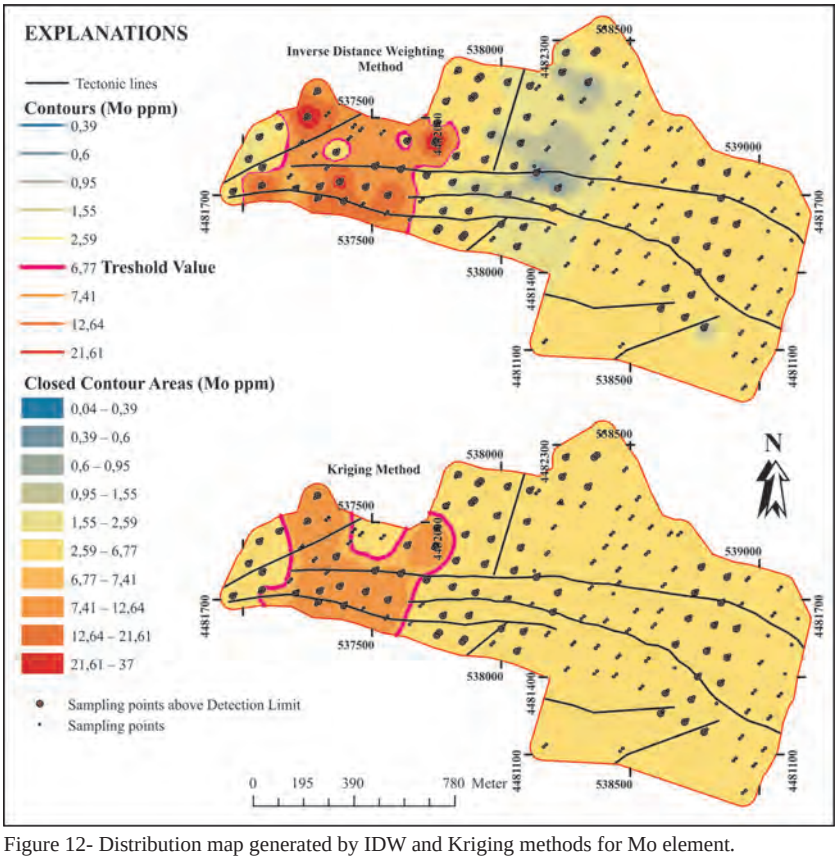

Figure 12- Distribution map generated by IDW and Kriging methods for Mo element.

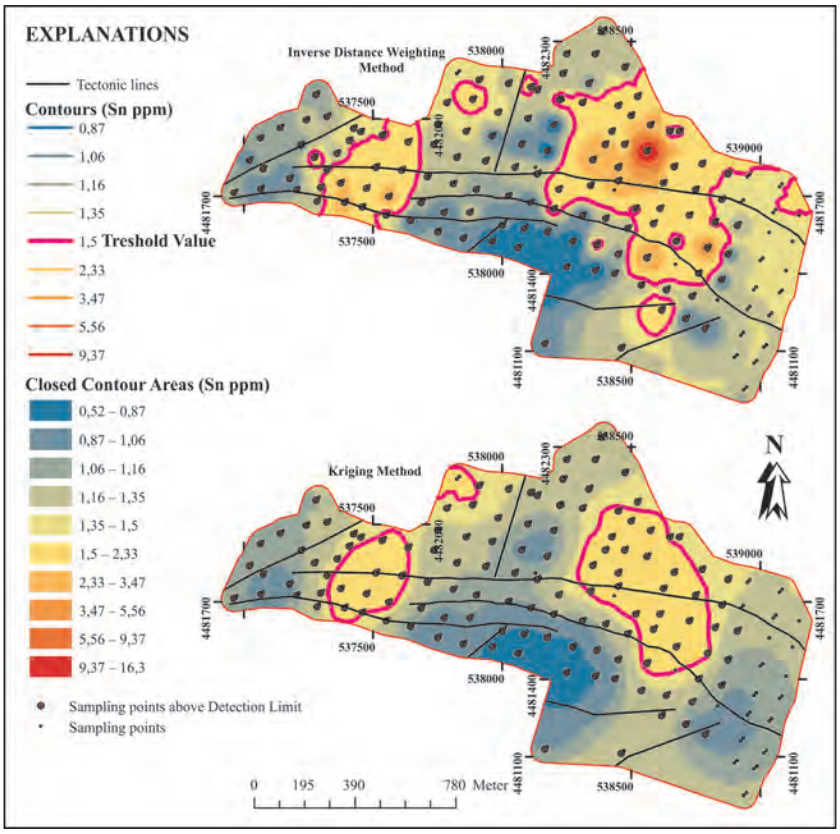

Figure 13- Distribution map generated by IDW and Kriging methods for Sn element.

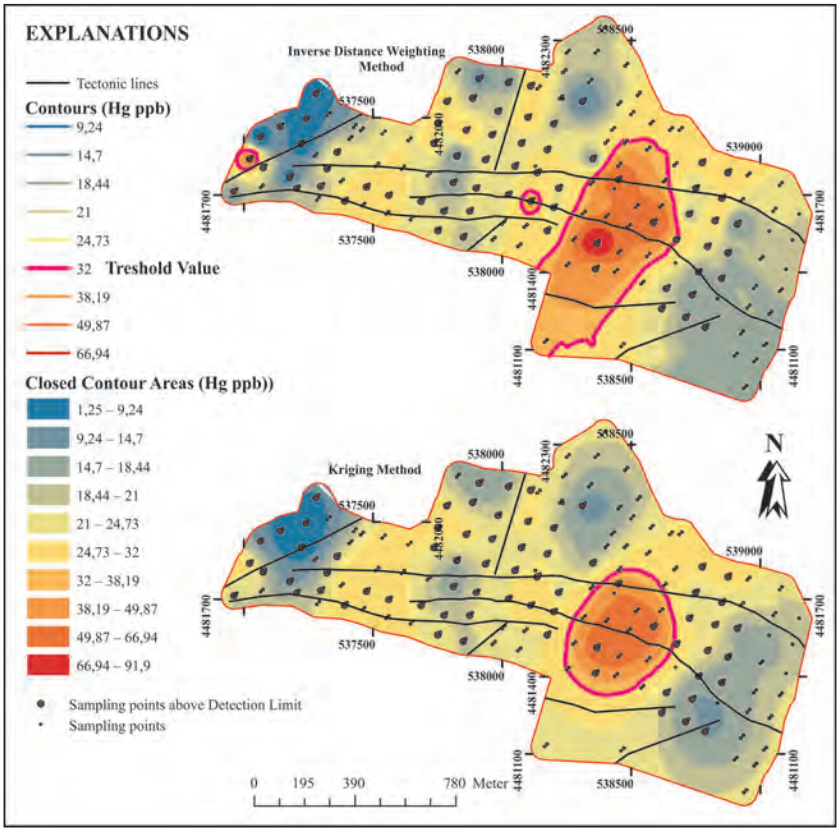

Figure 14- Distribution map generated by IDW and Kriging methods for Hg element.

4. Conclusions

In this study, the presence of soil geochemistry and possibly buried gold mineralization in the Canca (Gümüşhane) alteration area, where intensive alteration had been developed, were investigated. For this purpose, the total of 287 soil samples collected from the area were analyzed in terms of trace elements such as Cu, Pb, Zn, As, Sb, Bi, Mo, SN and Hg, which are pathfinder for gold and silver elements. The data obtained were evaluated by various statistical methods, threshold values belonging to the elements were determined by M+ 2MAD method and the distribution map of elements was generated by IDW and Kriging interpolation methods. IDW method is a well-known and widely used method ever since and it is also known that the later suggested Kriging method gives satisfactory results. These methods are also improved interpolation methods for estimating unknown points around any known sample point of interest (Matheron, 1971, 1963). When the element distribution maps generated by two mentioned methods were examined, it was seen that especially in the western part of the field, remarkable zoning/enrichment had been developed. The enrichment is predominantly in sections where tectonic lines become closer and the phyllic alteration develops, and this shows that alteration and tectonic activities are related to the enrichment. The Canca alteration area has been reported by MTA staffs in 1980s, and intensive alteration has been developed in the area. There have been carried out mapping studies at different scales at different times by MTA. Studies carried out on the area are mostly rock geochemistry studies. In the meantime, the exploratory drillings have been initiated in the area by the organization.

It is hoped that this and earlier geochemical studies carried out at different times in the Canca area will make an important contribution to drilling works currently being carried out by MTA. Therefore, it is suggested to make plan considering the element enrichment and zonations which are detected by the soil geochemistry in exploration and drilling works to be carried out in the area. When the area is investigated in detail, the presence of landslides developed in the eastern part at low altitudes should be considered in plans to be made and the element enrichment/anomaly areas observed in this section should be considered cautiously.

When IDW and Kriging methods used to generate the element distribution maps and data sets for the area were compared, it was seen that the element distribution maps made by the IDW interpolation method gave better results. In other words, the anomaly contrast resolution is higher in the element distribution maps generated by the IDW interpolation method. When all these data obtained in the soil geochemistry study are evaluated together, it was concluded that the detailed drilling and geophysical studies to be carried out for gold mineralization on the area had importance and it would be more appropriate to perform these studies in the western part of the study area.

Acknowledgements

This study was supported by the TUBITAK Project number 113Y569. Some analyzes were repeated in laboratories of the General Directorate of Mineral Research and Exploration for comparison. The author would like to thank to the MTA General Directorate and its employees for their contributions to the analysis. The author also thanks to Mr. Sebahattin Güner (Retired MTA General Directorate Personel) for sharing their experience of almost 30 years in the field of Canca and to trainee students Şükrü Bulut, Mert Karaaslan and Emre Topçu for their assistance on the field and in the laboratory work.

References

Ağca, N. 2015. Spatial distribution of heavy metal content in soils around an industrial area in Southern Turkey. Arab J Geosci. 8(2):1111-1123.

Akçay, M. 1998. Lâdik-Sızma (Konya) civa yatakları çevresinde element dağılım profilleri ve altın-gümüş ve baz metal potansiyeli: Jeokimyasal ve istatistiksel bir yaklaşım. Türkiye Jeoloji Bülteni, 41(1):37-47.

Almasi, A., Jararirad, A., Afzal, P., Rahimi, M. 2015. Orogenic Gold Prospectivity Mapping Using Geospatial Data Integration, Region of Saqez, NW Of Iran (Jeospatial Veri Entegrasyonu ile Orojenik Altın Prospeksiyon Haritasının Oluşturulması, Saqez Bölgesi, Kb İran). Bull. Miner. Res. Explor. 150, 67–78.

Anderson, D.A.J.S. 2008. Quantitative Analysis of Tin- and Tungsten-Bearing Sheeted Vein Systems. Economic Geology, 103 (5): 1043-1056.

Arslan, M., Aliyazıcıoğlu, I. 2001. Geochemical and petrological characteristics of the Kale (Gümüşhane) volcanic rocks: Implications for the Eocene evolution of eastern Pontide arc volcanism, northeast Turkey. Int. Geol. Rev. 43, 595–610. doi:10.1080/00206810109465035

Başaran, M., Erpul, G., Özcan, A.U., Saygın, D.S., Kibar, M., Bayramın, I., Yılman, F.E. 2011. Spatial information of soil hydraulic conductivity and performance of cokriging over kriging in a semi-arid basin scale. Environ Earth Sci, 63:827–838. Doi: 10.1007/s12665-010-0753-6.

Buttafuoco, G., Tallarico, A., Falcone, G., Guagliardi, I. 2010. A geostatistical approach for mapping and uncertainty assessment of geogenic radon gas in soil in an area of southern Italy. Environ Earth Sci, 61:491–505. Doi: 10.1007/s12665-009-0360-6.

Carranza, E.J.M. 2009. Controls on mineral deposit occurrence inferred from analysis of their spatial pattern and spatial association with geological features. Ore Geol. Rev. 35, 383–400. doi:10.1016/j.oregeorev.2009.01.001

Carranza, E.J.M., Sadeghi, M. 2010. Predictive mapping of prospectivity and quantitative estimation of undiscovered VMS deposits in Skellefte district (Sweden). Ore Geol. Rev. 38, 219–241. doi:10.1016/j.oregeorev.2010.02.003

Carranza, E.J.M., Owusu, E.A., Hale, M. 2009. Mapping of prospectivity and estimation of number of undiscovered prospects for lode gold, southwestern Ashanti Belt, Ghana. Miner. Depos. 44, 915–938. doi:10.1007/s00126-009-0250-6

Chaplot, V., Darboux, F., Bourennane, H., Leguedois, S., Silvera, N., Phachomphon, K. 2006. Accuracy of interpolation techniques for the derivation of digital elevation models in relation to landform types and data density. Geomorphology 77, 126–141.

Cheng, Q. 2008. Modeling local scaling properties for multiscale mapping. Vadose Zone Journal 7, 525–532.

Chiles, J. P., Delfiner, P. 1999. Geostatistics: modeling spatial uncertainty. John Wiley and Sons, New York, s. 720.

Cressie, N. A. C. 1990. The origins of kriging. Mathematical Geology 22 (3): 239–252.

Cressie, N.A.C. 1993. Statistics for Spatial Data, revised ed. ed. John Wiley and Sons, New York.

Çınar, S., Türk, O., Er, M., Güç, A.R., Musaoğlu, A., Gümüşel, A., Özdemir, M., Kurtoğulu, T. 1982. Gümüşhane İli ve Güneybatısının Jeolojisi Raporu. Maden Tetkik ve Arama Genel Müdürlüğü Rapor No: 7696, Ankara-Türkiye (unpublished).

Dokuz, A. 2011. A slab detachment and delamination model for the generation of Carboniferous high-potassium I-type magmatism in the Eastern Pontides, NE Turkey: The Köse composite pluton. Gondwana Res. 19, 926–944. doi:10.1016/j.gr.2010.09.006

Eyüboğlu, Y., Santosh, M., Dudas, F.O., Chung, S.L., Akaryalı, E. 2011. Migrating magmatism in a continental arc: Geodynamics of the Eastern Mediterranean revisited. J. Geodyn. 52, 2–15. doi:10.1016/j.jog.2010.11.006

Güner, S., Er, M., Gümüşel, A., Boğuşlu, M. 1985. Gümüşhane-Eski Gümüşhane yöresindeki cevherleşmelere ait jeoloji raporu. Rapor No: 8029. General Directorate of Mineral Research and Exploration, Ankara-Turkey (unpublished).

Güner, S., Yazıcı, E.N. 2008. Gümüşhane Bayburt Yörelerine Ait Epitermal Altın Aramaları Raporu. Rapor No: 11075. General Directorate of Mineral Research and Exploration, Ankara-Turkey (unpublished).

Güven, İ. 1993. Doğu Pontidlerin 1/25000 Ölçekli Kompilasyonu. General Directorate of Mineral Research and Exploration, Ankara-Turkey.

Hampel, F.R. 1974. The influence curve and its role in robust estimation. J. Am. Stat. Assoc. 69, 383–393.

Hengl, T. 2009. A practical Guide to Geostastical Mapping. 2nd editon. Office for Official Publications of the European Communities, Luxembourg (ISBN: 978-92-79-06904-8).

Jena, D.O. 1996. Interesting Papers in Other Journals. Geology 91, 228–237.

Kandemir, R. 2004. Gümüşhane ve Yakın Yörelerindeki Erken-Orta Jura Yaşlı Şenköy formasyonunun Çökel Özellikleri ve Birikim Koşulları. Trabzon.

Kansız, H., Akıncı, S., Kurtoğulu, T., Türkmen, S., Yılmaz, Z., Ağan, A. 1994. Doğu Pontid Güney Zonu Epitermal Altın Aramaları. General Directorate of Mineral Research and Exploration, Ankara-Turkey.

Karslı, O., Uysal, I., Dilek, Y., Aydın, F., Kandemir, R. 2013. Geochemical modelling of early Eocene adakitic magmatism in the Eastern Pontides, NE Anatolia: continental crust or subducted oceanic slab origin? Int. Geol. Rev. 55, 2083–2095. doi:Doi 10.1080/01431161.2013.819958

Kaygusuz, A., Siebel, W., Şen, C., Satır, M. 2008. Petrochemistry and petrology of I-type granitoids in an arc setting: The composite Torul pluton, Eastern Pontides, NE Turkey. Int. J. Earth Sci. 97, 739–764. doi:10.1007/s00531-007-0188-9

Ketin, I. 1966. Tectonic units of Anatolia (Asia Minor). Maden Tetkik ve Arama Genel Müdürlüğü Dergisi 66, 23–34.

Krige, D.G. 1951. A statistical approach to some basic mine valudation problems on the Witwatersrand. J. Chem. Metall. Min. Soc. 52, 119–139.

Matheron, G. 1963. Principals of geostatistics. Economic. Econ. Geol. 58, 1246–1266.

Matheron, G. 1971. The theory of regionalized variables and its application. Cent. Morphol. Math. Fontainebleau, Cah. 5, 211.

MTA, 1986. The Republic of Turkey report on the cooperative mineral exploration of Gümüşhane area, consolidated report. General Directorate of Mineral Research and Exploration, Ankara-Turkey.

Patinha, C., Correia, E., Ferreira da Silva, E., Simões, A., Reis, P., Morgado, F., Cardoso Fonseca, E. 2008. Definition of geochemical patterns on the soil of Paul de Arzila using correspondence analysis. Journal of Geochemical Exploration 98: 34–42.

Pelin, S. 1977. Alucra (Giresun) Güneydoğu yöresinin petrol olanaklan bakımından jeolojik incelemesi. Karadeniz Teknik Üniversitesi Yayını, Yayın No. 87, Trabzon.

Reiman, C., Filzmoser, P. 2000. Normal and lognormal data distribution in geochemistry: death of a myth. Consequences for the statistical treatment of geochemical and environmental data. Environ. Geol. 39, 1001–1014.

Reis, A.P., Sousa, A.J., Cardoso Fonseca, E. 2001. Soil geochemical prospecting for gold at Marrancos (Northern Portugual). J. Geochemical Explor. doi:10.1016/S0375-6742(01)00169-8

Ripley, B. D. 2004. Spatial statistics, 4th Edition. Wiley-IEEE, London, s. 252.

Rose, A.W., Hawkes, H., Webs, J. 1991. Geochemistry in Mineral Exploration, 2nd ed. Academic Press, Londan, England.

Rudnick, R., Gao, S. 2010. Composition of the Continental Crust, in: Holland, H., Turekian, K. (Eds.), Readings of Treatise on Geochemistry. Elsevier, Londan, England.

Shepard, D. 1968. A two-dimensional interpolation function for 52 irregularly-spaced data, in: Blue, R.B.S., Rosenberg, A.M. (Eds.), Proceedings of the 1968 ACM National Conference. ACM 54 Press, New York, pp. 517–524.

Shuguang, Z., Kefa, Z., Yao, C., Jinlin, W., Jianli, D. 2015. Exploratory data analysis and singularity mapping in geochemical anomaly identification in Karamay, Xinjiang, China. Journal of Geochemical Exploration 154:171–179. doi. org/10.1016/j.gexplo.2014.12.007.

Tobler, W. R. 1970. A computer model simulation of urban growth in the detroit region. Economic Geography 46 (2): 234–240.

Tokel, S. 1972. Stratigraphical and volcanic history of Gümüşhane region.

Topuz, G., Altherr, R., Schwarz, W.H., Dokuz, A., Meyer, H.P. 2007. Variscan amphibolite-facies rocks from the Kurtoğlu metamorphic complex (Gümüşhane area, Eastern Pontides, Turkey). Int. J. Earth Sci. 96, 861–873. doi:10.1007/s00531-006-0138-y

Tume, P., Bech, J., Reverter, F., Bech, J., Longan, L., Tume, L., Sepulveda, B. 2011. Concentration and distribution of twelve metals in Central Catalonia surface soils. J. Geochemical Explor. 109, 92–103. doi:10.1016/j.gexplo.2010.10.013.

Vural, A. 2006. Bayramiç (Çanakkale) ve Çevresindeki Altın Zenginleşmelerinin Araştırılması. Ankara Üniversitesi, Ankara Türkiye.

Vural, A. 2014. Trace/heavy metal accumulation in soil and in the shoots of acacia tree, Gümüşhane-Turkey. Bulletin of the Mineral Research and Exploration, 148, 85–106.

Vural, A. 2017. K-Ar Dating for Determining the Age of Mineralization as Alteration Product : A Case Study of Antimony Mineralization Vein Type in Granitic Rocks of Gümüşhane Area , Turkey 132, 792–795. doi:10.12693/APhysPolA.132.792

Vural, A., Erdoğan, M. 2014. Eski Gümüşhane Kırkpavli Alterasyon Sahasında Toprak Jeokimyası. Gümüşhane Üniversitesi Fen Bilim. Enstitüsü Derg. 4, 1–15.

Webster, R., Oliver, M.A. 2007. Geostatistics for Environmental Scientist. 2nd editon, John Wiley and Sons, Ltd. İngiltere. s. 315

Yaylalı-Abanuz, G., Tüysüz, N., Akaryalı, E. 2012. Soil geochemical prospection for gold deposit in the Arzular area (NE Turkey). J. Geochemical Explor. 112, 107–117. doi:10.1016/j.gexplo.2011.08.004

Yazıcı, E.N., Dursun, Ö., Güner, S. 2014. Gümüşhane-Bayburt-Artvin Epitermal Altın Aramaları Raporu. General Directorate of Mineral Research and Exploration, Ankara-Turkey.

Yılmaz, Y. 1972. Petrology ancj structure of the Gümüşhane granite and surrounding rocks, NE Anatolia.

Zuo, R. 2011. Identifying geochemical anomalies associated with Cu and Pb–Zn skarn mineralization using principal component analysis and spectrum–area fractal modeling in the Gangdese Belt, Tibet (China J. Geochemical Explor. 111:13–22.

Zuo, R., Cheng, Q., Agterberg, F.P., Xia, Q. 2009. Evaluation of the uncertainty in estimation of metal resources of skarn tin in Southern China. Ore Geol. Rev. 35, 415–422. doi:10.1016/j.oregeorev.2008.12.001.

Bulletin of the Mineral Research and Exploration

http://bulletin.mta.gov.tr

Geochemical characteristics of Sabalan volcanic rocks in Northwestern Iran

Reza FAHIM GUILANY[a], Ali DARVISHZADEH[a], Seyed Jamal SHEIKHZAKARIAEE[a*] and Mansour VOSOUGHI ABEDINI[a]

[a] *Department of Geology, Science and Research Branch, Islamic Azad University, Tehran, Iran*

Research Article

Keywords:
Sabalan volcano, calc-alkaline, subduction, geochemistry.

ABSTRACT

Sabalan is a voluminous stratovolcano situated in the northwestern part of Alborz-Azerbaijan zone, 25 km from Meshkinshahr. It is separated by a fault creating a tectonic boundary from Sarab plain and Meshkinshahr. The composition of Sabalan volcanic rocks ranges from andesite, trachyandesite to dacite. The rocks have hypocrystalline porphyritic texture with a glassy matrix and microlite . Plagioclase, amphibole, pyroxene, biotite, and oxides are the main phenocryst phase of the rocks. Some plagioclases show disequilibrium textures (sieve texture and oscillatory zoning). The sieve texture and oscillatory zoning in the plagioclases may be indicative of magma mixing processes in the genesis of the Sabalan volcanic rocks. Geochemical data reveal that the Sabalan lavas exhibit calk-alkaline major-oxide trends with a sodic character and they range in composition from andesite to dacite. Pre-caldera and post-caldera volcanic rocks have similar geochemical features with enrichments in LILE and LREE relative to HFSE and HREE, respectively, and have negative Ti, Nb, and Ta anomalies. Ba/Ta ratios higher than 450 and La/Nb ratios ranging between 2 and 3 indicate a volcanic arc setting for the studied rocks. Based on field and geochemical studies, Sabalan is a subduction-related volcano, occurred as a result of subduction of Neo-Tethyan oceanic crust beneath the Iranian microplate.

Received Date: 26.08.2017
Accepted Date: 24.04.2018

1. Introduction

The Sabalan volcanic field that overlies the northwestern Iran is situated in a continental collision zone between the African-Arabian and Eurasian plates (Ghalamghash et al., 2016) (Figure 1). From early Mesozoic to Quaternary, this collision zone underwent a compressional tectonic regime where compression has stemmed from subduction of Neo-Tethyan oceanic crust underneath the Iranian Central Block, and the subsequent collision between the Arabian and Eurasian plates along the Zagros suture zone (Şengör and Kidd, 1979; Dewey et al., 1986; Dilek et al., 2009; Ghalamghash et al., 2016). Sabalan volcano mountain lies in Qaresou valley in northwest of Ardabil city and extends to the east-west direction, with an approximate length of 60 km and 48 km in latitude to the Fushedagh mountain in the south of Ahar city. It has three peaks along the rough east-west direction. The highest peak is called Soltan Sabalan with a height of 4811 m, and the two other peaks are called Heram or Sabalan-e Kuchak (4740 meters) and Aghan Dagh or Kasra (4600 meters) (Figure 2).

On the northwest and southeast, Sabalan volcano complex is surrounded by NE-SW trending two main faults. Almost half of the linear structures are NW-SE trends, which created the Mou'eel valley on the basis of this trend (Haftani et al., 2008). In addition to the above faults, local faults also divided Sabalan horst into smaller pieces and have contributed to the formation of calderas in this volcano and faulty valleys.

* *Corresponding author: Seyed Jamal SHEIKHZAKARIAEE, j.sheikhzakaria@gmail.com*
https://dx.doi.org/10.19111/bulletinofmre.451565.

Figure 1- Iran and Sabalan's geographical position on the map.

Figure 2- Three peaks of Sabalan volcano.

This volcano has experienced more than 7 explosive eruptions during its activity (Fahim Guilany, 2016*a*). Sabalan volcanic rocks with calc-alkaline nature are made up of alternation of andesitic and young trachyandesitic to dacitic lavas as the age of Pliocene-Quaternary (Didon and Gemain, 1976; Mousavi, 2013; Shahbazi Shiran and Shafaii Moghadam, 2014; Fahim Guilany, 2016*b*; Ghalamghash et al., 2016). K-Ar absolute dating of Sabalan lavas revealed that Sabalan volcanic activity started at late Miocene (10.4 ± 0.5 Ma) (Alberti et al., 1976; Mousavi, 2013) and continued up to the 110k years ago (Ghalamghash et al., 2016).

One of the most important issues in Sabalan volcanic activity is the presence of pyroclastic air-fall

and base surge deposits, nuée ardentes, and ignimbrites that formed a volume more than 14 km^3 in area (Fahim Guilany et al., 2016) (Figure 3). Because of its potential volcanic hazards and geothermal potential, Sabalan volcano is an imperative object of study.

In this study, petrographical features of the studied rocks are briefly given and the geochemical features of these rocks are discussed in detail. Considering previous studies, the aim of this study is to reveal the nature of chemical variations between andesite and dacite over time (from 10.5 million years ago to 110,000 years ago) as well as discuss the sodic nature of these rocks, which has been previously accepted as potassic.

2. Geology

Sabalan is a voluminous stratovolcano located in the northwestern part of Alborz-Azerbaijan zone and northern part of Bitlis-Zagros suture zone. In the geological map of Meshkinshahr (1:100.000), the volcanic rocks of the area were described as andesite, trachyandesite, and dacite. Sabalan has a collapsed caldera about 12 km in diameter and a depression of about 400 m. The formation of caldera in Sabalan volcano has been considered as the basis for categorization of its important events by the researchers, and its volcanic activities have been divided into two stages: pre-caldera and post-caldera; in terms of the age of its activity, it can be divided into four or even five periods of volcanic activity (Figure 4) as follows:

The first stage (the old series or pre-caldera activity): The volcanic activity of Sabalan was initiated by andesitic eruptions (Figure 5a) during the middle to upper Miocene time (Alberti et al., 1976; Mousavi et al., 2014). According to Mousavi (2013), this age is computed based on andesitic rocks at an altitude of 2200 meters above sea level. During this phase, pyroclastic air-fall deposits with 5 m thickness near Saeen, (around Nir) and the andesitic lavas accumulate into massive thickness with layers of pumice and ash.

The second stage: The most intense volcanic activity of Sabalan dates back to the early Pliocene with trachyandesite lava eruptions (Figure 5b). Radiometric age of these rocks is 5.2 Ma (Mousavi, 2013). During this stage, thick, extensive ash flows

Figure 3- Sabalan pyroclastic deposits; a) Saeen air-fall deposits, b) Sareyn pyroclastic surges, c) Shirvandareh nuée ardentes, d) Chapaqan ignimbrite.

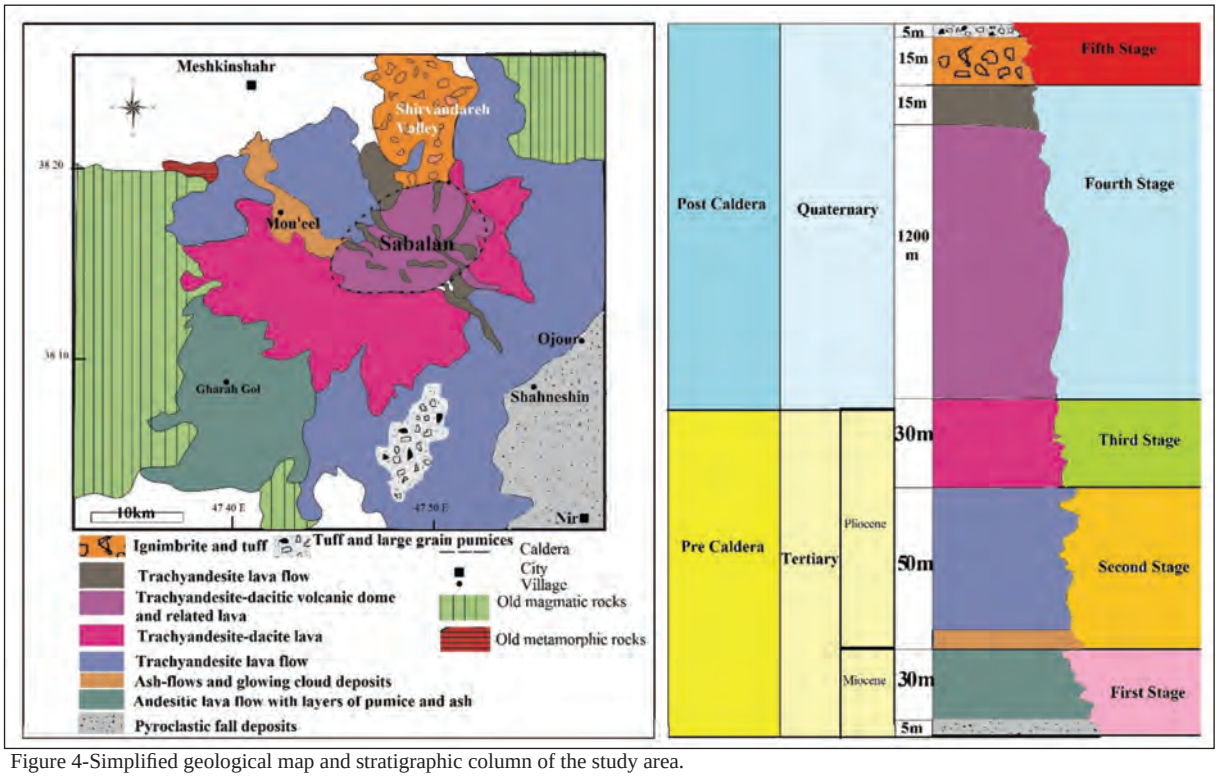

Figure 4-Simplified geological map and stratigraphic column of the study area.

and glowing cloud deposits (Fahim Guilany et al., 2016) as well as lava flows mainly of trachyandesitic composition, erupted possibly from several centers and brought a large volcanic complex reaching a great thickness (Alberti et al., 1976). The above mentioned lavas are more than 50 m thick and spread over 10 km.

The third stage: The evolution of the pre-caldera volcanic sequence with the eruption of a lava flow with the composition of trachyandesite to dacite ends in Sabalan. This lava flow has a fragmental and scrappy morphology with 100 m thickness and a length close to 6 km. The age of these rocks is about 2.8 Ma (Mousavi, 2013).

After pre-caldera eruption, the chamber of magma is discharged and due to the heavy burden of the piled up thick successions of volcanic rocks, the central area collapses and a large caldera develops (Figure 5c). The collapse occurs in two stages in which the second stage, took place with high explosive activity.

The fourth stage or post-caldera activity: This stage, which should be called new series or the post-caldera lavas, actually dates back to the early Quaternary (Alberti, et al., 1976). During this period, immediately after development of the caldera and explosive activities, the volcanic domes, some of which are well preserved and be mostly made up of andesitic to dacitic lava are suspended in the caldera rim (Figure 5d).

The fifth stage: The youngest eruptions of pyroclastic air-fall deposits and ignimbrites occur mainly within the caldera boundaries, and based on Ghalamghash et al. (2016), these tuffs and large grain pumices seen in Sareyn dates back to ca. 110 ka.

3. Methodology

After collecting and providing basic information and records of works done in the study area using aerial photographs and geological maps, all outcrops related to these rocks were identified. These rocks were then systematically sampled in the field during field studies. Eighty-five fresh samples were studied for petrographic investigations. Afterwards, 8 samples were chosen for geochemical analyses at Zarazma lab, Iran. The rock pulps were prepared by using lithium borate fusion for major oxides and ICP-MS (Agilent 4500) for trace and rare earth elements (REE). The results of chemical analyses along with detection limits (DL) are listed in tables 1 and 2. Detection limits were 0.05% for major oxides and 0.02-1 ppm

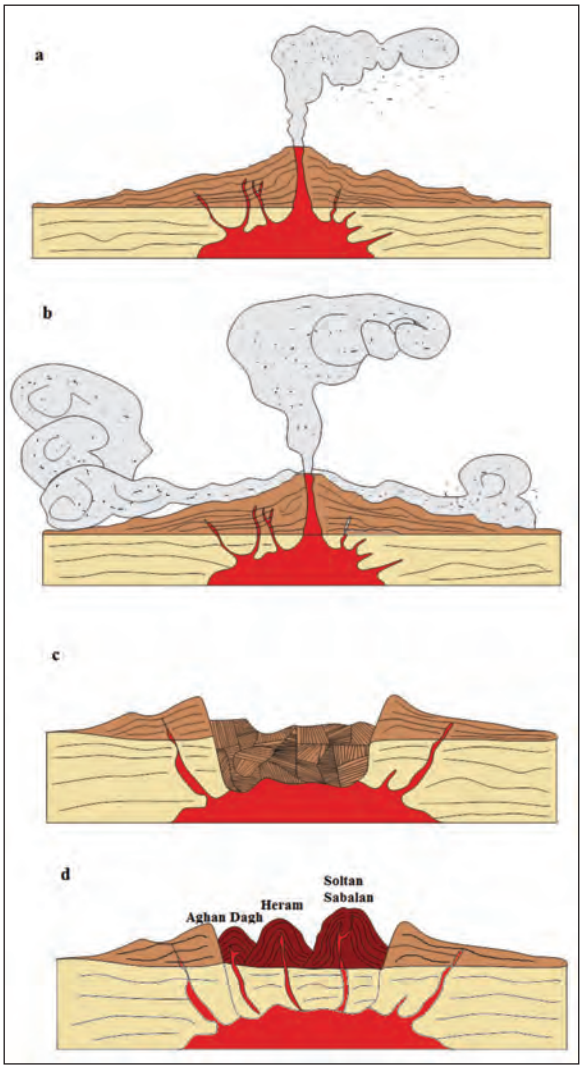

Figure 5- Illustration showing the formation of Sabalan's caldera and pre-caldera and post-caldera volcanic activities; a) pre-caldera explosive eruptions around Nir, b) the most intense pre-caldera volcanic activity of Sabalan, c) caldera subsidence, d) post-caldera series and domes rose in the caldera rim.

for trace elements. The results were compiled using the previously obtained data, and were assessed using software packages such as Igpet 2007 and GCD kit, version 4.1.

4. Results

4.1. Petrography

The lithological differences between the pre-caldera and post-caldera rocks of Sabalan are minor. The pre-caldera series are composed of andesitic to trachyandesitic lavas and the post-caldera series are composed of trachyandesitic to dacitic lavas with minor amount of rhyodacite. The texture of these rocks is porphyritic with glassy to microlitic matrix. Phenocryst phases are plagioclase, amphibole, pyroxene and biotite.

Plagioclase: In some plagioclases, disequilibrium textures such as sieve, dusty, resorbed and oscillatory zoning is observed. Some of the plagioclases have been affected by dissolution and corroded from the margins. The corrosion around plagioclase (Figure 6a) shows physicochemical disequilibrium over magma, and could probably be the result of magma mixing. As mentioned previously, most plagioclases have sieve textures (Figure 6b). There are three theories about the formation of this texture, which are: (a) fast skeletal growth, (b) magma mixing, and (c) rapid drop in pressure or magma decompression. The details related to each of them have been thoroughly discussed by Amini and Jalali (2002). Among these theories, fast skeletal growth does not have many advocates, but in recent studies, two other factors have been introduced and considered the most significant elements in the formation of sieve texture (Mohammadi et al., 2006).

Amphiboles: Amphiboles are observed as euhedral to anhedral crystals, and they are of hornblende type crystals. The most important evidence of disequilibrium in these amphiboles is burned margin texture (Figure 6c). Although Sakoyama (1983) considered this phenomenon to be precipitated by magma mixing, Sigurdsson et al. (2000) related it to resorption of mineral, and magma's rapid rise as well as decrease in steam pressure. Generally, opacitization in amphibole occurs due to a decrease in water pressure (Rutherford and Hill, 1993) or as a result of increase in temperature (Kawabata and Shoutu, 2005; Gill, 2010). The first situation could be associated with magma rise and the second, with magma mixing.

Pyroxene: Augite pyroxene is euhedral to subhedral crystals as both phenocrysts, microphenocrysts and microlites. (Figure 6d).

Biotite: Biotite can be observed as flakes to anhedral in shape with a pleochroism of brown to red and dark brown. On the margin of the biotite, evidences of dissolution border texture can be observed (Figure 6c). Plagioclase and apatite can also be found in these minerals.

Table 1- Results of major-oxide and trace element analysis of the pre-caldera volcanic rocks.

Sample	DL	P1	P2	P3	P4	P5	P6	P7	P8	P9	P10	P11	P12	P13	P14	P15	P16	P17	P18
Wt.%		*				**		***											
SiO_2	0.05	61.34	57.73	57.3	57.2	62.3	61.2	59.2	58.6	60.6	59.8	62.4	52.9	56.7	59.8	62.2	61.5	62.3	62.6
Al_2O_3	0.05	16.59	16.21	16.61	15.6	15.7	14.6	16	16	16.1	15	16.1	17.3	17.3	16.9	17.0	16.8	17.0	16.3
Fe_2O_3[1*]	0.05	4.26	5.58	5.07	5.17	3.78	3.19	4.78	5.54	4.46	3.71	3.26	5.8	5.5	5.05	4.5	3.8	3.8	3.95
CaO	0.05	5.86	6.05	5.15	6.68	4.6	3.42	4.85	4.65	4.3	4.75	4.02	8.2	6.3	5.75	4.65	5.66	5.85	5.2
MgO	0.05	1.97	2.74	2.36	2.58	1.77	1.42	1.98	1.94	1.21	1.78	1.71	3.05	2.5	2.75	2.5	3.3	2.35	2.65
Na_2O	0.05	4.49	5.01	4.7	4.5	4.9	4.3	4.5	4.6	4.6	4.4	4.9	5.1	5.3	4.9	4.1	4.7	5.1	4.75
K_2O	0.05	2.73	2.96	2.46	2.95	2.54	3.14	2.79	3.45	2.96	3.05	2.4	2.3	2.65	2.4	2.15	2.7	2.55	2.4
TiO_2	0.05	0.7	1.35	1.01	0.88	0.61	0.53	0.81	0.9	0.74	0.65	0.63	1.35	1.45	1.05	0.8	1	1.05	0.85
MnO	0.05	0.08	0.05	0.08	0.08	0.06	0.06	0.06	0.08	0.07	0.07	0.06	0.05	0.05	0.1	0.4	0.1	0.1	0.1
P_2O_5	0.05	0.4	0.1	0.72	0.65	0.4	0.34	0.44	0.64	0.38	0.44	0.34	0.1	0.1	0.65	0.1	0.25	0.1	0.5
LOI	0.05	1.4	0.3	1.03	1.99	0.23	4.15	0.87	1.11	0.71	2.4	0.73	1	0.4	0.05	0.8	1.2	0.4	0.35
Ppm																			
Ba	1	715	760	690	730	640	660												
Co	1	11.8	17.1	16.6	16.3	10.8	8.9												
Cs	0.5	2.2	1.4	0.4	2.2	1.4	2.5												
Cu	1	36	56	59	57	36	36												
Dy	0.02	2.39	2.83	2.56	2.73	1.81	1.62												
Er	0.05	1.22	1.35	1.21	1.3	0.83	0.75												
Eu	0.1	1.15	1.87	1.45	1.49	1.1	1.01												
Ga	0.05	19	19	21	19	19	18												
Gd	0.05	3.02	4.48	3.76	4.03	2.73	2.49												
Hf	0.5	2.01	4	4	4	5	3												
Ho	0.05	0.47	0.51	0.48	0.48	0.31	0.29												
Lu	0.1	0.16	0.17	0.2	0.16	0.11	0.12												
Ni	1	22	39	46	41	25	17												
Pr	0.05	6.62	12.4	9.95	10.4	7.6	7.59												
Rb	1	47	57.6	40.8	61.6	53	75.5												
Sn	0.1	0.7	1	1	<1	<1	<1												
Sr	1	927.5	899.2	903	919.5	914.4	911.3												
Tb	0.1	0.46	0.57	0.5	0.51	0.34	0.33												
Th	0.1	13.39	13.6	14.2	14.9	10.8	14.2												
Tm	0.1	0.17	0.19	0.16	0.17	0.12	0.1												
U	0.1	4.12	3.78	3.69	3.43	2.85	4.45												
V	1	75	120	81	92	64	57												
W	1	1.6	2	3	1	1	2												
Y	0.5	11.3	11.3	11.6	12.3	8.3	7.9												
Yb	0.05	1	1.2	1.1	1.1	0.8	0.8												
Zn	1	63	81	82	73	58	56												
Zr	5	87	160	170	160	200	140												
Ag	0.1	0.6	1	1	2	<1	1												
Ce	0.5	73	112	94.3	94.2	73	75.4												
Mo	0.1	3.5	<2	<2	3	<2	3												
Nb	1	15.7	25	25	24	16	19												
Nd	0.5	24.4	44.6	34.6	37.1	26	25.9												
Sm	0.02	4.22	6.6	5.4	5.6	4	3.9												
Tl	0.1	0.2	<0.5	<0.5	<0.5	<0.5	<0.5												
La	1	42	59.9	51.2	51.05	43.02	44.9												
Ta	0.1	1.13	1.6	1.5	1.6	1	1.3												
La/Nb		2.67	2.39	2.04	2.14	2.68	2.36												
Ba/Ta		632	468.7	460	450	640	507.												
La/Yb		42	49.9	46.5	48.8	53.7	56.1												

* Chemical analysis performed by the authors of this study

** Chemical analysis adapted from Mousavi (2013)

** Chemical analysis adapted from Didon and Gemain (1976)

Fe_2O_3-FeO_{total} total

Table 2- Results of major-oxide and trace element analysis of the post-caldera volcanic rocks.

sample	DL	K1	k2	k3	k4	k5	k6	k7	k8	k9	k10	k11	k12	k13	k14	k15
Wt.%		*				**				***					****	
SiO_2	0.05	61.85	60.87	63.02	60.98	61.2	65.4	63.5	65.2	64.6	62.8	64.8	64.4	64.7	62.35	62.89
Al_2O_3	0.05	16.72	16.61	16.87	16.62	16.8	15	14.6	15	15.1	16.2	15.3	16.1	14.3	16.75	16.83
$Fe_2O_3^{2*}$	0.05	3.88	4.96	3.77	3.61	5.09	3.69	3.62	3.75	2.76	3.77	2.99	4.08	2.91	3.38	3.34
CaO	0.05	5.36	6.28	5.04	6.32	5.01	2.62	2.61	2.65	3.12	4.17	3.16	3.99	2.9	4.36	4.2
MgO	0.05	1.96	1.9	1.75	1.81	2.4	1.09	1.08	1.06	1.13	1.81	1.18	1.9	1.18	1.86	1.99
Na_2O	0.05	4.8	4.63	4.9	4.94	3.57	4.11	4.08	4.02	4.6	4.8	4.7	5.3	4.4	5.2	4.98
K_2O	0.05	2.86	2.68	3.	2.81	2.86	4.68	4.17	4.78	3.26	2.7	3.24	3.23	3.5	2.75	2.62
TiO_2	0.05	0.66	0.78	0.63	0.62	0.7	0.7	0.68	0.7	0.46	0.61	0.49	0.68	0.5	0.57	0.55
MnO	0.05	0.07	0.07	0.07	0.07	0.1	0.09	0.09	0.08	0.05	0.06	0.05	0.06	0.05	0.06	0.06
P_2O_5	0.05	0.44	0.31	0.42	0.45	0.27	0.25	0.25	0.25	0.28	0.39	0.3	0.55	0.29	0.4	0.45
LOI	0.05	1.16	0.69	0.27	1.53	1.54	1.32	1.36	1.45	1.7	0.42	1.3	1.08	2.38	1.27	1.2
ppm																
Ba	1	813	638	775	837	844	829	1015	775	630	670	730	810	660		
Co	1	10.5	13.	9.8	11.1					7.1	10.6	7.7	10.6	7.1		
Cs	0.5	1.7	1.6	2.	1.6	2.07	5.07	4.92	4.89	2.6	1.2	2.4	1.9	3.		
Cu	1	31	46	37	36					13.	30	57	17	12.		
Dy	0.02	2.36	2.66	2.23	2.31	3.15	4.06	4.04	4.06	1.39	1.85	1.47	1.8	1.63		
Er	0.05	1.16	1.23	1.03	1.13	1.88	2.48	2.47	2.56	0.78	0.87	0.73	0.86	0.74		
Eu	0.1	1.27	1.24	1.07	1.26	1.29	1.36	1.33	1.35	0.88	1.09	0.95	1.17	0.88		
Ga	0.05									18	19	18	20	17		
Gd	0.05	3.23	3.64	2.96	3.23	4.62	6.27	6.14	6.18	2.28	2.75	2.36	2.85	2.21		
Hf	0.5	2.3	2.76	2.41	2.31	4.9	8.7	8.5	8.7	3.	3.	4.	4.	3.		
Ho	0.05					0.64	0.82	0.84	0.83	0.24	0.33	0.27	0.34	0.29		
Lu	0.1	0.14	0.16	0.13	0.15	0.27	0.41	0.39	0.4	0.09	0.13	0.14	0.09	0.16		
Ni	1	24	23	22	26	28	8.	6.	7.	12.	31	84	24	13.		
Pr	0.05	8.22	7.39	7.16	7.92	7.9	12.45	12.4	12.3	6.57	8.07	7.14	8.47	7.29		
Rb	1	46	53	50	45	72	180.5	173.5	179	77.1	57.1	76.1	65.1	83.9		
Sn	0.1	0.6	0.7	0.7	0.7					<1	<1	<1	<1	<1		
Sr	1	1159.8	899.3	995.4	1164.6	626	401	448	415							
Tb	0.1	0.45	0.51	0.44	0.46	0.61	0.79	0.78	0.78	0.29	0.37	0.33	0.38	0.31		
Th	0.1	10.62	13.82	10.71	10.17	9.28	26.3	25.7	25.8	14.5	11.2	13.4	13.1	17.5		
Tm	0.1	0.16	0.19	0.16	0.15	0.26	0.38	0.36	0.37	0.09	0.12	0.11	0.11	0.11		
U	0.1	3.6	3.3	3.5	3.4	2.75	7.11	6.87	6.98	4.69	3.37	4.22	3.71	5.59		
V	1	68	71	62	71	100	59	58	57	49	85	51	69	42		
W	1	1.2	1.6	1.3	1.3					2.	2.	2.	1.	2.		
Y	0.5	10.3	12.3	9.9	10.6	17.7	23.7	23.5	23.6	7.	8.5	7.4	8.3	7.5		
Yb	0.05	0.9	1.1	0.8	0.8	1.78	2.61	2.58	2.56	0.7	0.8	0.8	0.8	0.8		
Zn	1	62	65	57	63	72	102	72	92	48	62	50	62	50		
Zr	5	98	104	96	102	210	368	356	357	120	140	170	210	130		
Ag	0.1	<0.1	<0.1	<0.1	<0.1					<1	1.	<1	1.	<1		
Ce	0.5	90	81	79	94	78.5	127.5	124.5	125	67.1	77.8	70.3	82.8	73.6		
Mo	0.1	2.8	0.9	2.8	3.1					4.	<2	4.	4.	4.		
Nb	1	17.2	20.4	16.8	17.9	20.9	48.8	47.1	47.5	18	18	17	19	19		
Nd	0.5	29.8	27.2	25.6	28.2	27.6	41.4	41	40.4	21.9	27.2	24.3	28.6	24.2		
Sm	0.02	4.55	4.64	3.98	4.52	4.79	6.61	6.52	6.44	3.1	4.1	3.5	4.3	3.3		
Tl	0.1	0.6	<0.1	0.13	0.39					<0.5	<0.5	<0.5	<0.5	<0.5		
La	1	52	46	47	54	46.6	73.4	71.9	72	40.9	45.4	41.4	48.1	44.5		
Ta	0.1	1.14	1.38	0.94	0.98	1.4	2.4	2.3	1.4	1.3	1.1	1.1	1.1	1.4		
La/Nb		3.02	2.25	2.79	3.01	2.22	1.5	1.5	1.51	2.72	2.52	2.43	2.53	2.34		
Ba/Ta		580.7	462	824.4	854.1	568.1	345.41	441.3	553.5	484.6	609.1	663.6	736.3	471.4		
La/Yb		57.7	41.81	58.7	57.5	26.17	28.12	27.86	28.12	58.4	56.7	51.7	60.1	55.6		

* Chemical analysis performed by the authors of this study

** Chemical analysis adapted from Shahbazi Shiran and Shafaii Moghadam (2014)

*** Chemical analysis adapted from Mousavi (2013)

**** Chemical analysis adapted from Didon and Gemain (1976)

Fe_2O_3-FeO_{total} total

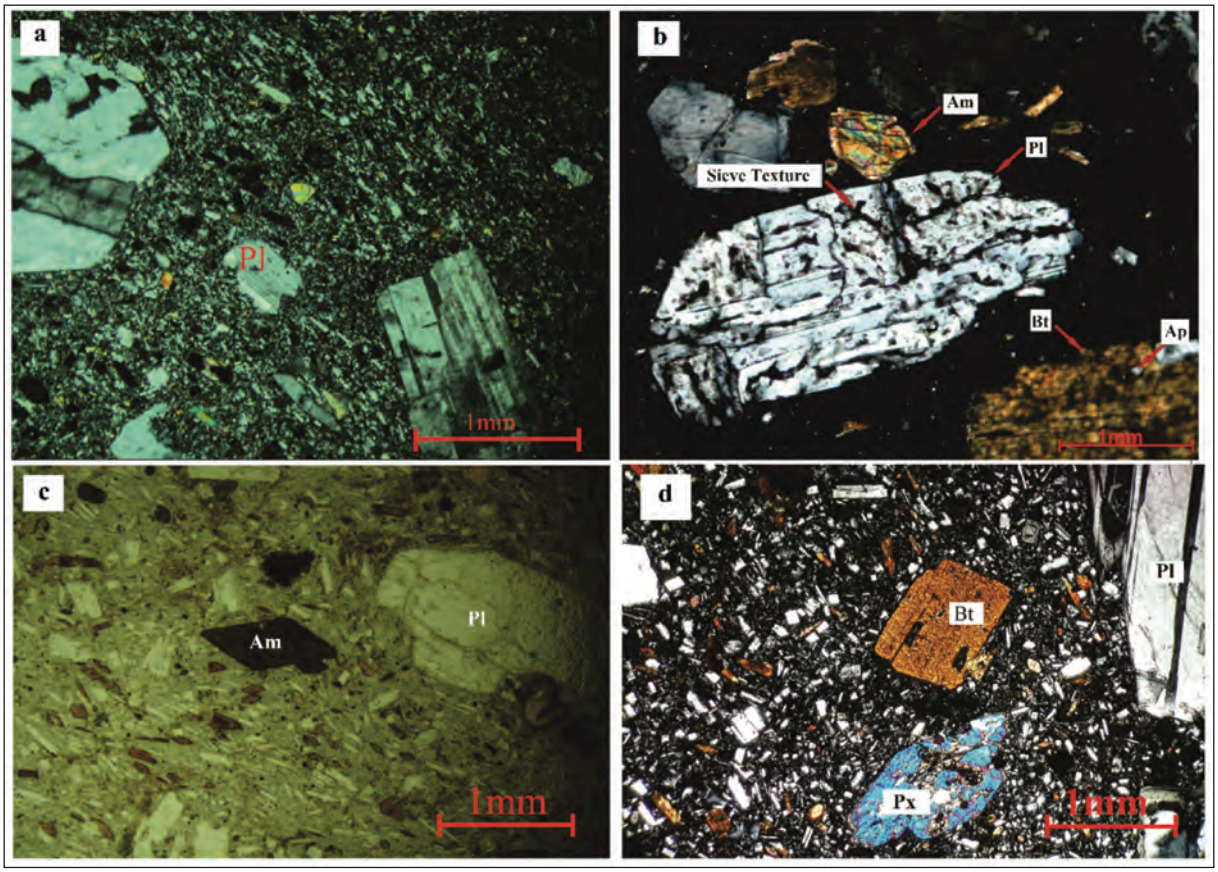

Figure 6- Photomicrographs of; a) Resorbed plagioclase in cross polarised light (XPL), b) Plagioclase with sieve texture in cross polarised light (XPL), c) biotite and opacitized amphibole in plane polarised light (PPL), d) pyroxene and automorph biotite with iron oxides inclusion in cross polarised light (XPL).

4.2. Geochemistry

This study used 33 analyses on pre-caldera and post-caldera rocks series. In addition to the chemical analyses performed by the authors (P1-P4 and K1-K4), chemical analyses conducted by Shahbazi Shiran and Shafaii Moghadam (2014) (K5-K8), Mousavi (2013) (P5-P6 and K9-K13), Didon and Gemain (1976) (P7-P18 and K14-K15) (Tables 1 and 2) were used to make clear assessment by GCDkit software, version 4.1. The samples without trace elements are from Didon and Gemain (1976).

In SiO_2 versus Na_2O+K_2O nomenclature diagram of Le Bas et al. (1986), Sabalan volcanic rocks plot in the field of andesite, trachyandesite, trachydacite and dacite (Figure 7a). In this figure, except for the two samples having alkaline characteristics, the rest are sub-alkaline (Figure 7a). In order to determine the tholeiitic and/or calc-alkaline characteristics of this sub-alkaline series, the AFM diagram (Irvine and Baragar, 1971) has been plotted. It is clear from the figure that the sub-alkaline samples plot on the fractionated calc-alkaline field (Figure 7b).

Calc-alkaline rocks included basalts and andesites that have more alumina (wt% 20-16 = Al_2O_3) and are found in the orogenic belts and rocks related to the island arc. This group of rocks has a clear association with subduction zones and are originally generated in compressional tectonic type (Philpotts, 1990).

The major element variations against SiO_2 for Sabalan volcanic rocks are presented in the form of Harker's (1909) diagram (Figure 8). Similar geochemical behaviours observed in figure 8 indicate that the pre-caldera and post-caldera rocks have a same parental magma and have been fed from one magma chamber. Furthermore, based on the trends of increasing K_2O and SiO_2 and decreasing TiO_2, MgO, FeO, CaO in Harker's diagrams, post-caldera rocks are more differentiated than pre-caldera types. Since MgO contents of all the samples is very low, the volcanic rocks region cannot be suggested to have induced the

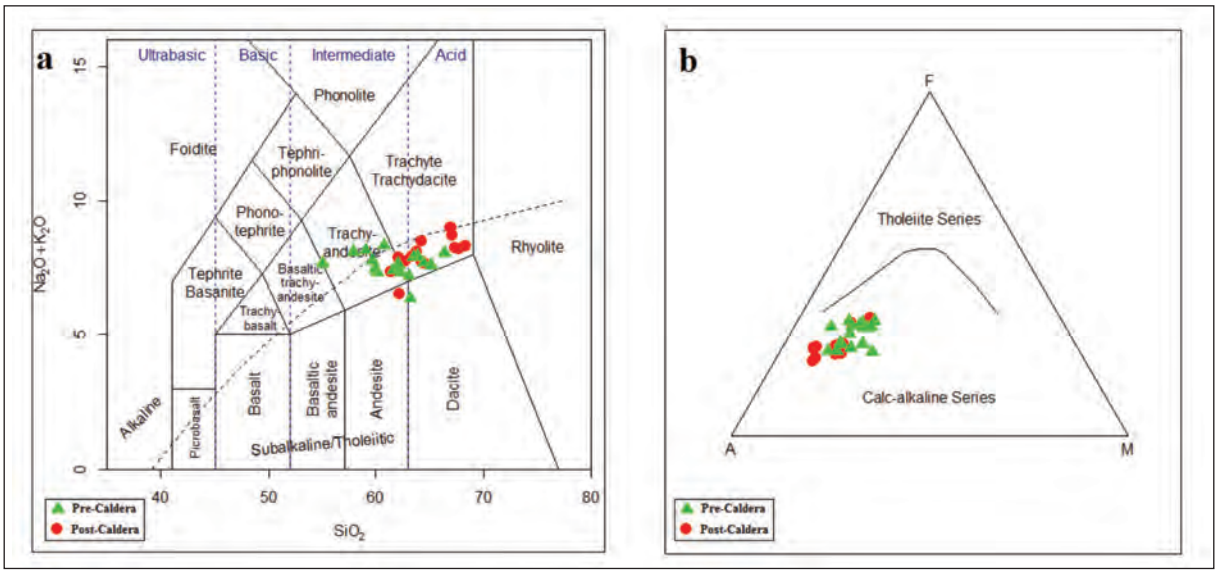

Figure 7- a) Total alkali versus SiO_2 plot for Sabalan volcanic rocks, all values as weight % (Le Bas et al., 1986), b) AFM diagram (Irvine and Baragar, 1971) for Sabalan sub-alkaline samples.

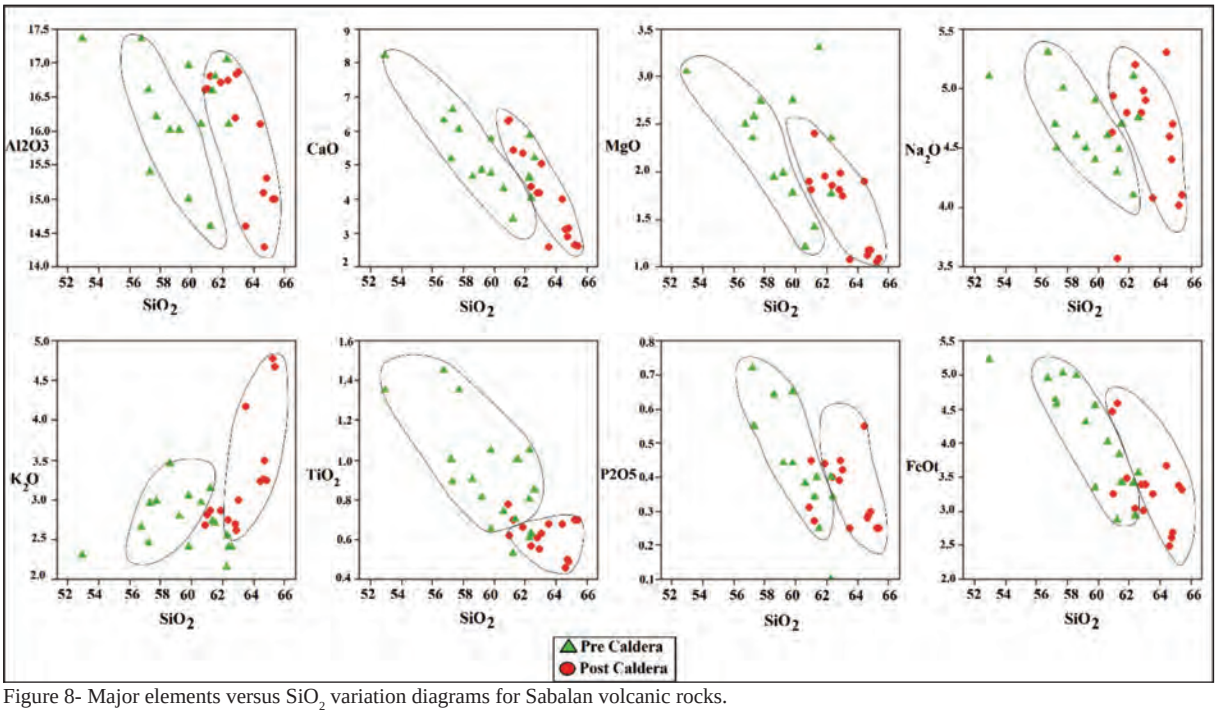

Figure 8- Major elements versus SiO_2 variation diagrams for Sabalan volcanic rocks.

partial melting of peridotite mantle parental magma (Rollinson, 1993). Descending trend of P_2O_5, CaO, FeO, MgO and TiO_2 oxides in post-caldera rocks in comparison with pre-caldera rocks can to some extent be associated with differentiation and crystallization of plagioclase, ferromagnesian minerals (such as olivine and pyroxene), and oxide minerals (such as ilmenite and titano-magnetite) as well as apatite in the location of magma settlement of these rocks. The Al_2O_3 variations in pre-caldera rocks is regular and relatively fixed, but in post-caldera rocks with higher proportion of silica, a slight decrease in trend is visible. The variations in Al_2O_3 can be reflect the removal of Ca-plagioclase during fractional crystallization.

4.3. The Origin

Determination of the tectonic setting of rocks is highly essential in the interpretation of their petrogenesis. To determine and identify the tectonic setting of igneous rocks, the tectonic discrimination diagrams have been used. The diagrams are mostly based on rare earth elements, and immobile elements or elements with low mobility are usually used. Since the high field strength elements (HFSE) such as Zr, Nb, Y, P, and Ti are relatively immobile in aqueous fluids and are stable during weathering, these elements are highly applicable.

Chondrite-normalized (Thompson, 1982) trace element spider diagram of Sabalan volcanic rocks is presented in figure 9a. As can be observed in this figure, the interesting patterns indicate negative anomalies in Nb and Ti and positive peaks in K, Rb, Th, and U, which are characteristic of arc magmas in subduction zones. Enrichment in U and Th in the spider diagrams may be due to the addition of pelagic sediments and/or altered oceanic crust to the source of magma (Fan et al., 2003).

Chondrite-normalized (Nakamura, 1974) rare earth element patterns of the Sabalan volcanic rocks can be seen in figure 9b. Sabalan volcanic rocks are enriched in light rare elements (LREE) (from La to Sm) relative to heavy rare earth elements (HREE), and they also show flat patterns from Dy to Lu. Enrichment in LREE relative to HREE and the low TiO_2, Zr and Nb contents demonstrate the dependency of these rocks on calc-alkaline series (Machado et al., 2005). Eu element showed slight negative anomalies, which was probably related to the existence of plagioclases as the main phenocryst found in the rocks of the region.

Based on tectonic discrimination diagrams (Muller and Groves, 1997), volcanic rocks of the study area are placed within the range of the subduction related magmatic arcs (Figure 10a and b). Additionally, in the Th/Hf versus Ta/Hf diagram (Schandl and Gorton, 2000) (Figure 10c), the studied samples are in the range of active continental margin, and in the (Zr*3)-(Nb*50)-(Ce/P_2O_5) triangular diagram (Muller and Groves, 1997), all samples plot in the field of post-collisional arc zone (Figure 10d). Considering the geochemical characteristics, and taking into account the spatial and temporal position of Sabalan volcano, it seems that these rocks were formed from subduction of Neo-Tethyan oceanic crust under the Iranian microplate and are formed in an arc magmatic zone.

5. Discussion

Three main geodynamic models have been proposed to clarify the melting process of the lithospheric mantle in NW Iran and SE Turkey. They include mantle plume (Ershov and Nikishin, 2004), lower crust delamination (Pearce et al., 1990) and slab break off (Keskin, 2003; Şengör et al., 2003, Ghalamghash et al., 2016). There is no evidence of a mantle plume originating in NW Iran; thus, the melting of mantle lithosphere by heat from a mantle plume is improbable (Dabiri et al., 2011). Although the study of Pearce et al. (1990) in young volcanoes in SE Turkey and the study of Liotard et al. (2008) in the genesis of Quaternary alkaline volcanic rocks in Damavand volcano, proposed lower crust delamination for upper

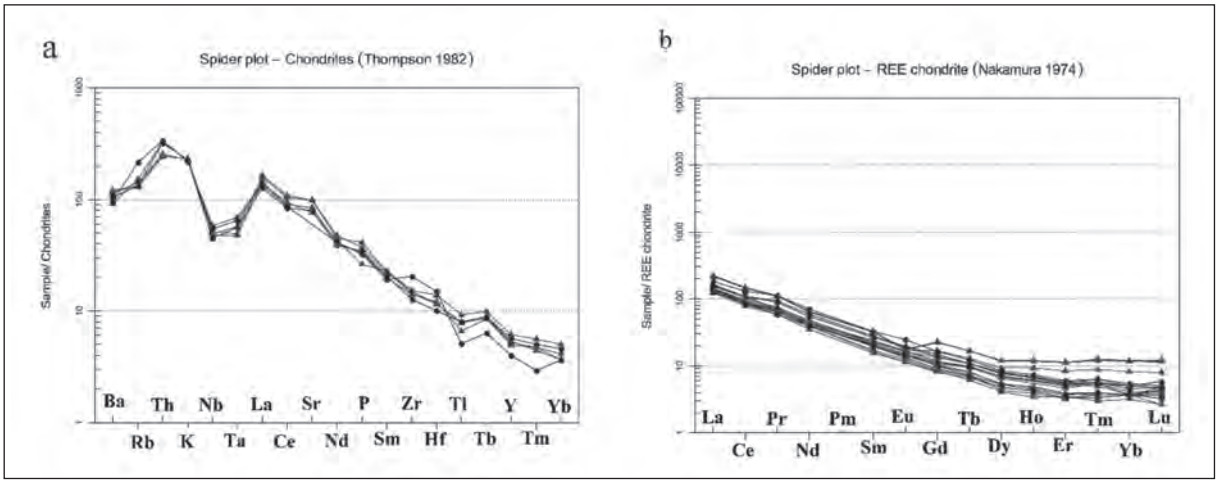

Figure 9- a) Chondrite-normalized (Thompson, 1982) spider diagram, b) Chondrite-normalized (Nakamura, 1974) REE diagram for studied samples.

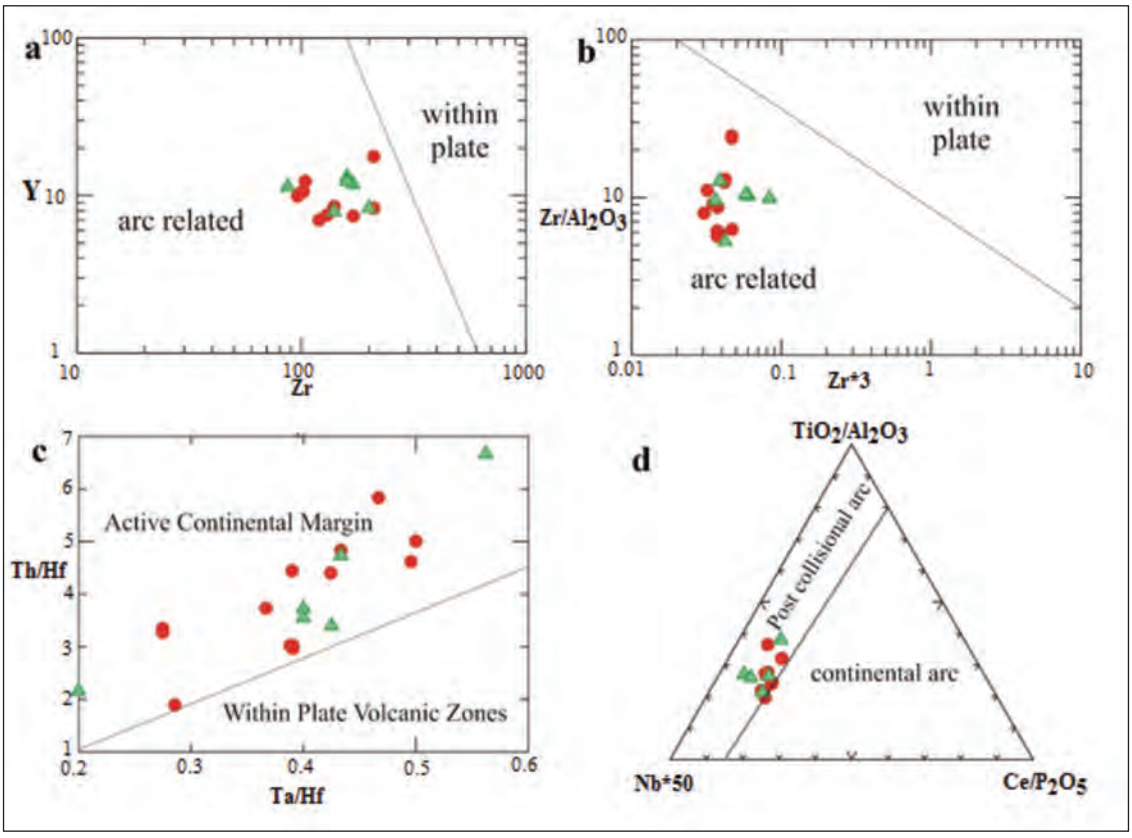

Figure 10- a) Zr-Y diagram (Muller and Groves, 1977); b) Zr/Al_2O_3 – Zr*3 diagram (Muller ve Groves, 1997); c) Th/Hf against Ta/Hf diagram (Schandl and Gorton, 2000) and d) (Zr*3)-(Nb*50)-(Ce/P_2O_5) triangular diagram (Muller and Groves, 1997) of Sabalan volcanic rocks.

Cenozoic magmatism in eastern Turkey and NW Iran. Keskin et al. (2006) and Şengör et al. (2003) suggested that Neo-Tethyan oceanic slab break off under the Eurasia plate was the trigger the Quaternary magmatism in this area (Ghalamghash et al., 2016). Also Neil et al. (2013) proposed that slab break off and perhaps some lithospheric delamination is applicable to Armenia, Eastern Anatolia and NW Iran. Since the slab remnant has been tomographically detected in seismic studies (Gök et al., 2003; Zor et al., 2003; Lee and Zaho, 2007), we tentatively support the model of oceanic crust break off.

Both pre-caldera and post-caldera volcanic rocks share the same geochemical features, indicating that they are probably derived from a long-lived and homogeneous source which produce similar parental magmas. All Sabalan rocks have low MgO (<1.35 wt.%), and direct derivation via partial melting of peridotite mantle parental magma is impossible. High amount of Al_2O_3 in chemical analysis seems logical considering the high amount of plagioclase in the samples. In addition, in intermediate calc-alkaline series, the amount of Al_2O_3 is almost 13 to 16 wt %, which is consistent with the samples' analyses. Except for three samples, in all the samples the amount of Na_2O is more than K_2O (Na_2O/K_2O>1) (Figure 11). This is due to the higher amount of sodic plagioclases in contrast to potassium minerals such as biotite, hornblende and sanidine.

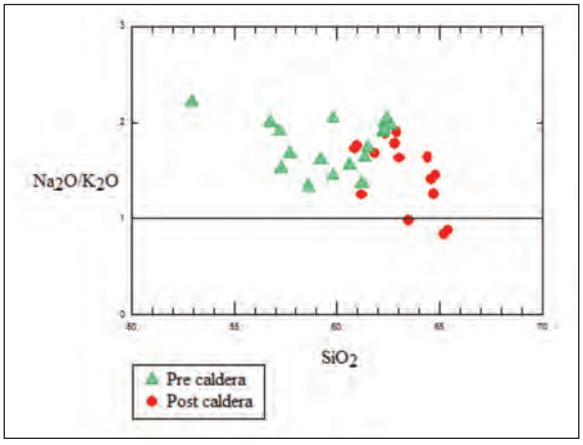

Figure 11- Na_2O/K_2O – SiO_2 diagram of the pre-caldera and post-caldera rock series.

Based on systematic variations in the major elements with increasing SiO_2, fractional crystallization (FC) is identified as a major factor controlling the compositional diversity, but the interaction with crustal rocks along with derivation from a subduction contaminated source for the Sabalan volcanic rocks is also clear from Th/Yb vs. Ta/Yb diagrams (after Pearce, 1983) (Figure 12a). As shown in figure 12a, the volcanic rocks of Sabalan plot in the field of active continental margins and a higher Th content could also result from interaction of ascending lavas with crustal rocks through the process of assimilation fractional crystallization (AFC). In addition, over the compositional range from andesite to dacite, AFC modeling (Figure 12b) suggests that crustal assimilation is negligible due to the very low r values ($r < 0.1$; r = rate of assimilation to rate of fractional crystallization). The results of AFC modeling for volcanic rocks of Sabalan also showed that the degree of magma crust interaction is larger in post-caldera samples (more evolved lavas) than the pre-caldera samples.

Phenocryst assemblages in Sabalan volcanic rocks (plagioclase + amphibole + pyroxene + biotite for pre-caldera series and plagioclase + amphibole ± alkali-feldspar ± quartz for post-caldera series) suggest that amphibole and plagioclase could have been important fractionating phases. Also Geochemical data are also consistent with these petrographic observations: Pre-caldera rocks show a positive correlation in the Rb vs. Y diagram which is consistent with fractionation of plagioclase + clinopyroxene (Pl + Cpx) or plagioclase + amphibole (Pl + Amp) whereas the horizontal or slightly negative trend shown by the post-caldera rocks suggests that the lavas containing hydrous minerals (e.g., amphiboles) display distinct depletion with increasing Rb (Figure 13).

In figure 14, MORB (mid-ocean ridge basalts)-normalized trace element spider diagram of the Sabalan volcanic rocks in northwest Iran is compared with the spider diagram of the Erzurum-Kars plateau volcanic rocks in the east of Turkey (Keskin et al., 1998). The Erzurum-Kars plateau volcanoes in eastern Turkey were described as volcanoes of the type formed after collision (Keskin et al., 1998). The enrichment with LREE and LILE relative to HSFE, and the negative anomalies in Nb and Ta and low values of Y, Ti and Yb are the geochemical characteristics of these two regions.

Ba/Ta ratio greater than 450 and La/Nb ratios of 2-7 are also indicative of the magmas generated in a volcanic arc setting (Gill, 1981; Macdonald et al., 2001). Ba/Ta and La/Nb ratios in Sabalan volcanic rocks are 450-854.1 and 2.04-3.02, respectively. Zr/Y ratio can also be used in determining the tectonic setting (Pearce and Norry, 1979). Accordingly, Zr/Y ratio of continental volcanic arc rocks is generally greater than 3, whereas this ratio is less than 3 in oceanic volcanic arcs. The volcanic rocks of the study area have a Zr/Y ratio more than 3, typical of continental volcanic arc rocks. This ratio for Sahand (another volcano of this region) volcanic rocks is about 19 (Pirmohammadi Alishah et al., 2012). The high La/Yb ratio (from 26 to 60) and the relatively high $(La)_N$ (from 42 to 73) and

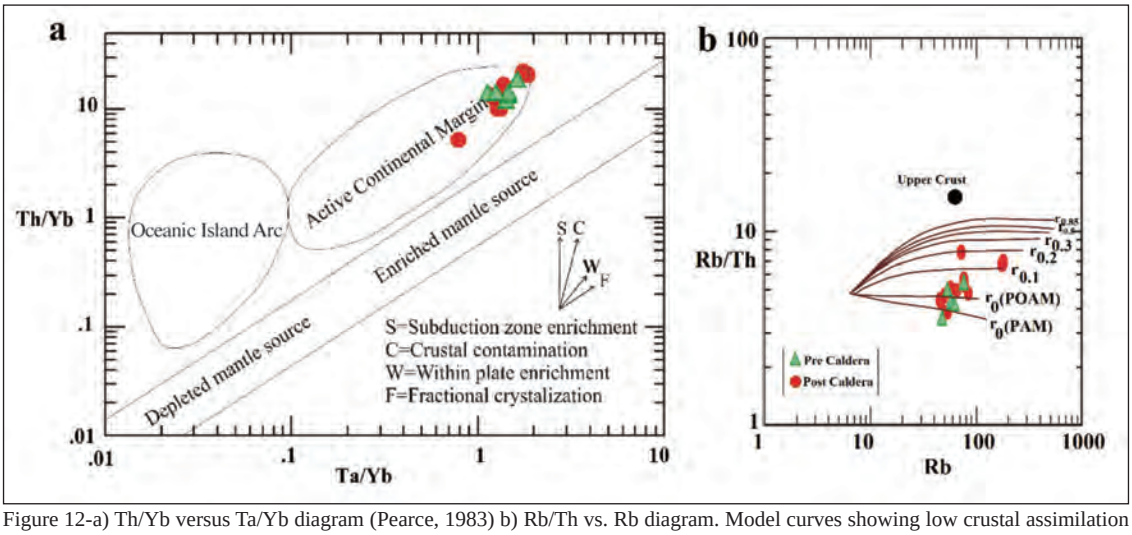

Figure 12-a) Th/Yb versus Ta/Yb diagram (Pearce, 1983) b) Rb/Th vs. Rb diagram. Model curves showing low crustal assimilation in Sabalan volcanic rocks.

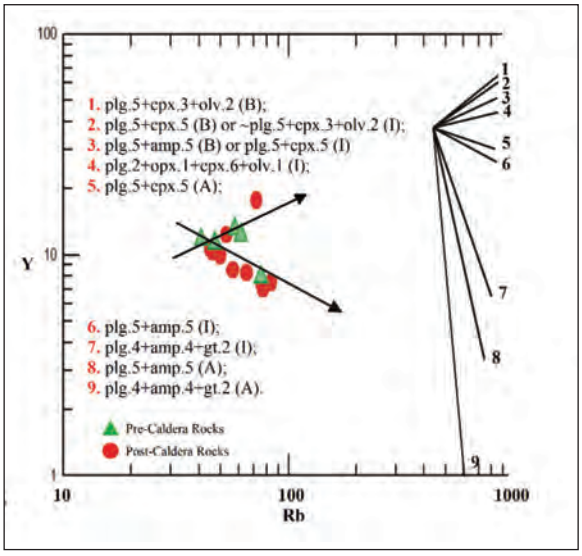

Figure 13- Rb vs. Y model diagram for hydrous (amphibole) vs. anhydrous (clinopyroxene) fractional crystallization. plg: plagioclase, cpx: clinopyroxene, opx: orthopyroxene, olv: olivine, amp: amphibole, gt: garnet. B: basic, I: intermediate, and A: acid magma compositions.

and low magnesium number of the region's rocks substantiate the relevance of these lavas to active continental margins. Since andesites and dacites often belong to mature arcs of continental margin, the existence of ignimbrite deposits with a composition of ryholitic-ryhodacitic in Sabalan's volcano (Fahim Guilany, 2016*a*) shows its relevance to a mature magmatic arc. Accordingly, the tectono-magmatic setting of the study area can be considered as an active continental margin. The Turkish-Iranian high plateau is bounded on the north by the eastern Pontide arc and the lesser Caucasus magmatic belt and is bordered on the south by continental blocks including Bitlis-Pütürge- Sanandaj-Sirjan blocks (Shahbazi Shiran and Shafaii Moghadam, 2014). Such Pliocene-Quaternary volcanic cones and flows as Nemrut, Ararat, Sabalan and Sahand are prevalent in this plateau, and most of them indicate post-collisional affinities (Riou et al., 1981; Özdemir et al., 2006) which substantiates the above results.

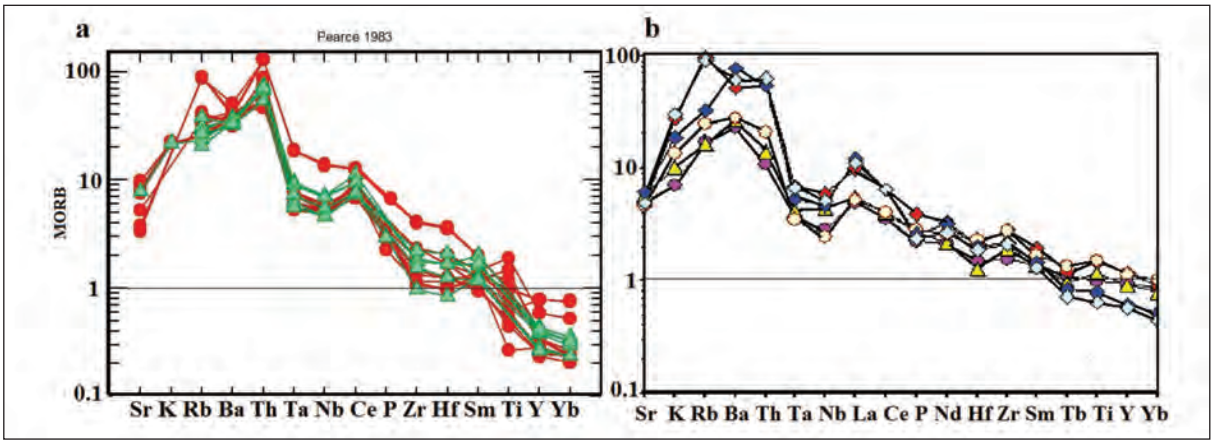

Figure 14- Comparison of MORB (mid-ocean ridge basalts)-normalized trace element spider diagram of the Sabalan volcanic rocks; a) with the Erzurum-Kars Plateau in the east of Turkey, b) (Keskin et al., 1998).

low $(Yb)_N$ (from 0.7 to 2.6) in Sabalan volcanic rocks indicate that they were originated from low degrees of partial melting of enriched mantle. This enrichment is due to the addition of aqueous fluids derived from dehydration of the subducted oceanic crust to lithospheric mantle under Sabalan. The Sm/Yb vs. La/Sm diagram (Figure, 15) (Bezard et al., 2011) has been used to determine the partial melting degrees of the mantle source from which the Sabalan lavas were originated. It is assumed that these rocks are generated from low degree of partial melting (<0.1) similar to Quaternary lavas reported in western Iran (Allen et al., 2013) from lithospheric mantle source, with a composition that supposedly correspond to clinopyroxene-garnet lherzolite. Also Neil et al. (2013) in their study of Turkish-Armenian-Iranian plateau, proposed that magmas in this region are derived from low-degree melting of a shallow, subduction-modified lithospheric mantle source.

The Ba/Nb ratios of the samples range between 31.27 and 47.26. Ba/Nb ratio of the active continental margin magmatism is generally greater than 28 (Gill, 1981; Fitton et al., 1988). Thus, these high Ba/Nb ratios are characteristics of magmatism in active continental margins. Evidence such as the explosive nature of volcanoes in the region, volcanic breccia deposits, agglomerate, acidic tuffs, ignimbrites

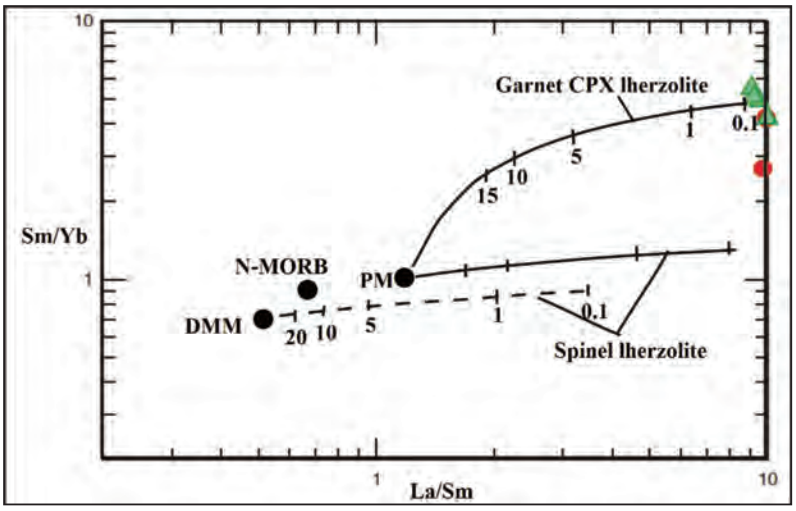

Figure 15-The Sm/Yb vs. La/Sm diagram (Bezard et al., 2011) for Sabalan volcanic rocks. The melting curves were obtained using the non-modal batch melting equations of Shaw (1970), DMM (Depleted MORB Mantle) is from Salters and Stracke (2004), PM (Primitive mantle) is from Sun and McDonough (1989). Spinle lherzolite (with mode and melt mode of olivine (53.3%) + orthopyroxene (27%) + clinopyrocene (17%) + spinel (3%) (Kinzler, (1997)), and garnet-clinopyroxene peridotite (with mode and melting mode of olivine (53.3%) + Clinopyroxene (35.7%) +garnet (11%) (Walter, 1998)) are the source of the melting. Partition coefficients are from McKenzie and O'Nions (1991) (see table 3). Tick marks show the degree of partial melting (%) of the different sources.

Table 3- Partition coefficient values used in the melting models.

	Olivine	Orthopyroxene	Clinopyroxene	Spinel	Garnet
Sm	0.0013	0.01	0.26	0.01	0.217
Yb	0.0015	0.049	0.28	0.01	4.03
La	0.0004	0.002	0.054	0.01	0.01

6. Conclusion

With regard to the long-term activity of Sabalan, it must be accepted that its magma was differentiated in magma chamber. As a result, the initial alkaline andesite under the influence of fractional crystallization turned into intermediate compositions of trachyandesite, trachydacite and dacite. Based on higher SiO_2 in post-caldera rocks compared to pre-caldera rocks, the post-caldera phase generally produced more magma constituents. On the basis of the geochemical data of major and rare elements, Sabalan volcanic rocks are considered to be calc-alkaline. The Zr/Y ratio shows that the studied rocks are related to continental volcanic arcs. In spider plots, Rb, Ba, and K showed enrichment and Nb and Ti showed depletion, which are indicative of magmatic arcs in subduction zones. Therefore, taking into account the spatial and temporal position of volcanic rocks of the area, it seems that these rocks were formed from subduction of Neo-Tethyan oceanic crust under the Iranian microplate and are formed in an arc magmatic zone in the Quaternary.

References

Alberti, A.A., Comin-Chiaramonti, P., Dibattistini, G., Nicoletti, M., Petrucciani, C., Siniqoi, S. 1976. Geochronology of the eastern Azarbaijan volcanic plateau (north-west Iran). Rendiconti della Societa Italiana di Mineralogia e Petrologia 32, 579-589.

Allen, M.B., Kheirkhah, M., Neill, I., Emami, M.H., McLeod, C.L. 2013. Generation of arc and within-plate chemical signatures in collision zone magmatism: Quaternary lavas from Iran. Journal of Petrology 54, 887-911.

Amini, S., Jalali, M. 2002. Sieve texture in plagioclase and its importance in the interpretation of petrological evidence of volcanic rocks in the North East Qorveh. Journal of Sciences Islamic Azad University (JSIAU) 12, 44, 3521-3535.

Bezard R., Hebert R., Wang C., Dostal J., Dai J., Zhong H. 2011. Petrology and geochemistry of the Xiugugabu ophiolitic massif, western Yarlung Zangbo suture zone, Tibet. Lithos 125, 347-367.

Dabiri, R., Emami, M.H., Mollaei, H., Chen, B., Abedini, M.V., Omran, N.R., Ghaffari, M. 2011. Quaternary post-collision alkaline volcanism NW of Ahar (NW Iran): Geochemical Constraints of Fractional Crystallization Process. Geologica Carpathica 62, 547-562. Doi: org/10.2478/v10096-011-0039-2

Dewey, J.F., Hempton, M.R., Kidd, W.S.F., Şaroğlu, F., Şengör, A.M.C. 1986. Shortening of continental lithosphere: The neotectonics of Eastern Anatolia — a young collision zone. Coward, M., Ries, A. (Ed.). Collision Tectonics. Special Publication of the Geological Society. London, 19, 3-36.

Didon, J., Gemain, Y.M. 1976. Le Sabalan, Volcan Plio-quaternair de l'Azerbaidjan oriental (Iran); etude geologique et petrographique de l'edifice et de son environnement regional, These de 3eme Cycle, University, 304 p. Grenoble (unpublished).

Dilek, Y., Imamverdiyev, N.A., Altunkaynak, S. 2009. Geochemistry and tectonics of Cenozoic volcanism in the Lesser Caucasus (Azerbaijan) and the peri-Arabian region: Collision induced mantle dynamics and its magmatic fingerprint. International Geology Review 143, 536-578. Doi: 10.1080/00206810903360422.

Ershov, A.V., Nikishin, A.M. 2004. Recent geodynamics of the Caucasus Arabia, East Africa Region. Geotectonics 38, 2, 123-136.

Fahim Guilany, R. 2016*a*. Sabalan: The most complex volcano in Iran. Third International Conference of Geographical Sciences, Al-Khwarizmi Higher Institute of Science and Technology, Shiraz, Iran.

Fahim Guilany, R. 2016*b*. The pyroclastic deposits of Sabalan volcano. Ph.D. Dissertation, Geology Department, Research and Science Branch, Islamic Azad University, 223 p. Tehran (unpublished).

Fahim Guilany, R., Darvishzadeh, A., Sheikhzakariaee, S.J. 2016. The Nuee Ardentes of Sabalan volcano in Iran. Open Journal of Geology 6, 1553-1566. Doi: org/10.4236/ojg.2016.612110_

Fan, W.M., Guo, F., Wang, Y.J., Lin, G. 2003. Late Mesozoic calc-alkaline volcanism of post-orogenic extension in the northern Da Hinggan Mountains, northeastern China. Journal of Volcanology and Geothermal Research 121, 115-135.

Fitton, J. G., James, D., Kempton, P.D., Ormerod, D.S., Leeman, W.P. 1988. The role of lithospheric mantle in the generation of late Cenozoic basic magmas in the Western United States. J. Petrol., Special Lithosphere Issue, 331-349.

Ghalamghash, J., Mousavi, S.Z., Hassanzadeh, J., Schmitt, A.K. 2016. Geology, zircon geochronology, and petrogenesis of Sabalan volcano (northwestern Iran). Journal of Volcanology and Geothermal Research 327, 192-207. Doi: 10.1016/j. jvolgeores.2016.05.001.

Gill, J.B. 1981. Orogenic andesites and plate tectonics. Springer - Verlag, New York.

Gill, R. 2010. Igneous Rocks and Processes: A Practical Guide. Wiley-Blackwell, Chichester, 428 p.

Gök, R., Sandvol, E., Turkelli, N., Seber, D., Barazangi, M. 2003. Sn attenuation in the Anatolian and Iranian plateau and surrounding regions. Geophysical Research Letters 30, 24, 8043. Doi: 10.1029/2003GL018020

Haftani, M., Bohloli, B., Ellassi, M., Talebi, B. 2008. In-situ stress determination in Sabalan geothermal reservoir. 2nd IASME/ WSEAS International Conference on Geology and Seismology, World Scientific and Engineering Academy and Society, Cambridge, U.K., 88-93.

Harker, A. 1909. The Natural History of Igneous Rocks. Methneu, London, 344 p.

Irvine, T.N., Baragar, W.R.A. 1971. A guide to the chemical classification of the common volcanic rocks. Canadian Journal of Earth Sciences 8, 523-548.

Kawabata, H., Shuto, K. 2005. Magma mixing recorded in intermediate rocks associated with high-Mg andesites from the Setouchi volcanic belt, Japan: Implications for Achenn TTG Formation. Journal of Volcanology and Geothermal Researches 140, 241-271.

Keskin, M. 2003. Magma generation by slab steepening and breakoff beneath a subduction-accretion complex: An alternative model for collision-related volcanism in eastern Anatolia. Geophysical Research Letters 30, 24, 1-9. Doi: 10.1029/2003GL018019.

Keskin, M., Pearce, J.A., Mitehell, J.G. 1998. Volcano stratigraphy and geochemistry of collision-related volcanism on the Erzurum-Kars plateau, northeastern Tuerkey. Journal of Volcanology and Geothermal Research 85, 355-404.

Keskin, M., Pearce, J.A., Kempton, P.D., Greenwood, P. 2006. Magma-crust interactions and magma plumbing in a post-collisional setting: Geochemical evidence from the Erzurum-Kars volcanic plateau, eastern Turkey. Dilek, Y., Pavlides, S. (Ed.). Post-collisional Tectonics and Magmatism in the Mediterranean Region and Asia. Special Papers -- Geological Society of America, 409, 475-505.

Kinzler, R.J., 1997. Melting of mantle peridotite at pressures approaching the spinel to garnet transition: application to midocean ridge basalt petrogenesis. Journal of Geophysical Research 102, 853–874.

Le Bas, M.J., Le Maitre, R.W., Streckeisen, A., Zannetin, B.A. 1986. Chemical classification of volcanic rocks based on the total alkali-silica diagram. Journal of Petrology 27, 745-750.

Lee, J.S., Zhao, D.P. 2007. Teleseismic evidence for a break-off subducting slab under Eastern Turkey. Earth and Planetary Science Letters 257, 14-28.

Liotard, J.M., Dautria, J.M., Bosch, D., Condomines, M., Mehdizadeh, H., Ritz, J.F. 2008. Origin of the absarokite-banakite association of the Damavand volcano (Iran): Trace elements and Sr, Nd, Pb isotope constraints. International Journal of Earth Sciences 97, 89-102.

Macdonald, R., Hawkesworth, C.J., Heath, E. 2001. The lesser Antilles volcanic chain: A study in arc magmatism. Earth Science Reviews 49, 1-76.

Machado, A., Lima, E.F., Chemale, J.F., Morta, D., Oteiza, O., Almeida, D.P.M., Figueiredo, A.M.G., Alexandre, F.M., Urrutia J.L. 2005. Geochemistry constraints of Mesozoic-Cenozoic calc-alkaline magmatism in the South Shetland arc, Antarctica. Journal of South America Earth Sciences 18, 407-425.

McKenzie, D., O'Nions, R.K. 1991. Partial melt distributions from inversion of rare earth element concentrations. Journal of Petrology 32, 1021–1091.

Mohammadi, R., Emami, M.H., Vosoughi Abedini, M. 2006. Petrography and petrology of oligo-miocene lavas of Hamedan Razn Region. Journal of Fundamental Sciences of Islamic Azad University 61, 1-18.

Mousavi, G. 2013. The volcanology and petrology of Sabalan volcano, North West of Iran. Ph.D. Dissertation, Geology Department, Research and Science Branch, Islamic Azad University, 195 p. Tehran (unpublished).

Mousavi, S.Z., Darvishzadeh, A., Ghalamghash, J., Vosoughi Abedini, M. 2014. Volcanology and geochronology of Sabalan volcano, the highest stratovolcano in Azerbaijan region, NW Iran. Nautilus 128, 3-1, 85-98.

Muller, D., Groves, D.L. 1997. Potassic igneous rock and associated gold-copper mineralization. Bhattacharji, S., Friedman, G.M., Neugebauerand, H.J., Seilacher, A. (Ed.). Lecture Notes in Earth Sciences 56, 238 p.

Nakamura, N. 1974. Determination of REE, Ba, Fe, Mg, Na and K in carbonaceous and ordinary chondrites. Geochimica et Cosmochimica Acta 38, 757-775.

Nakamura, N. 1977. Determination of REE, Ba, Mg, Na and K in carbonaceous and ordinary chondrites. Geochemica et Cosmochimica Acta 38, 757-775.

Özdemir, Y., Karaoğlu, Ö., Tolluoğlu, A.U., Güleç, N. 2006. Volcanostratigraphy and petrogenesis of the Nemrut stratovolcano, East Anatolian High Plateau: the most recent post-collisional volcanism in Turkey. Chemical. Geology. 226, 189-211.

Pearce, J.A. 1983. Role of sub-continental lithosphere in magma genesis at active continental margins. In: Hawkesworth, C.J. and Norry, M.J. (eds) Continental basalts and mantle xenoliths, Shiva, Nantwich, pp 230-249.

Pearce, J.A., Norry, M.J. 1979. Petrogenetic implications of Ti, Zr, Y and Nb variations in volcanic rocks. Contributions to Mineralogy and Petrology 69, 33-47.

Pearce, J.A., Bender, J.F., De Long, S.E., Kidd, W.S.F., Low, P.J., Güner, Y., Şaroğlu, F., Yılmaz, Y., Moorbath, S., Mitchell, J.G. 1990. Genesis of collision volcanism in Eastern Anatolia, Turkey. Journal of Volcanology Geothermal Research 44, 189-229.

Philpotts, A.R. 1990. Principles of Igneous and Metamorphic Petrology. Prentice Hall, New Jersey, 498 p.

Pirmohammadi Alishah, F., Ameri, A., Jahangiri, A., Mojtahedi, A., Keskin, M. 2012. Petrology andgeochemistry of volcanic rocks from the south of Tabriz (Sahand volcano). Petrology 9, 1, 37-56.

Riou, R., Dupuy, C., Dostal, J. 1981. Geochemistry of coexisting alkaline and calc-alkaline volcanic rocks from northern Azarbaijan (N.W. Iran). Journal of Volcanology and Geothermal Research 11, 253-275.

Rollinson, H. 1993. Using Geochemical Data: Evolution, Presentation, Interpretation. Longman Scientific and Technical, London, 352 p.

Rutherford, M., Hill, P. 1993. Magma ascent rates from amphibole breakdown: An experimental study applied to the 1980-1986 Mount St. Helens eruptions. Journal of Geophysical Research 98, B11, 19667-19685.

Sakoyama, M. 1983. Petrology of arc volcanic-rocks and their origin by mantle diapirs. Journal of Volcanology and Geothermal Research 18, 297-320.

Salters, V.J.M., Stracke, A. 2004. Composition of the depleted mantle. Geochemistry, Geophysics, Geosystems 5, Q05B07.

Schandl, E.S., Gorton, M.P. 2000. Form continents to island arcs: A geochemical index of tectonic setting for arc-related and within-plate felsic to intermediate volcanic rocks. The Canadian Mineralogist 38, 1065-1073.

Şengör, A.M.C., Kidd, W.S.F. 1979. Post-collision tectonics of the Turkish and Iranian plateau and companions with Tibet. Tectonophysics 55, 3, 261-376.

Şengör, A.M.C., Özeren, S., Zor, E., Genç, T. 2003. East Anatolian high plateau as a mantle-supported, N-S shortened domal structure. Geophysical Research Letters 30, 24, 8045. Doi: 10.1029/2003GL017858

Shahbazi Shiran, H., Shafaii Moghadam, H. 2014. Geochemistry and petrogenesis of the Sabalan Plio-Quaternary volcanic rocks: Implication for post-collisional magmatism. Iranian Journal of Crystallography and Mineralogy 22, 2, 27-68.

Shaw, D.M. 1970. Trace element fractionation during anatexis. Geochimica et Cosmochimica Acta 34, 237–243

Sigurdsson, H., Houghton, B., McNutt, S.R., Rymer, H., Stix, J. 2000. Encyclopedia of Volcanoes. San Diego Academic Press, 1000 p.

Sun, S.-S., McDonough, W.F. 1989. Chemical and isotopic systematics of oceanic basalts: implications for mantle compositions and processes. In: Saunders, A.D., Norry, M.J. (Eds.), Magmatism in the Ocean Basins: Special Publication, 42. The Geological Society of London, pp. 313–345.

Thompson, R.N. 1982. Magmatism of the British tertiary volcanic province. Scotland Geological Journal 18, 49-107.

Walter, M.J. 1998. Melting of garnet peridotite and the origin of komatiite and depleted lithosphere. Journal of Petrology 39, 29–60.

Zor, E., Sandvol, E., Gürbüz, C., Türkelli, N., Seber, D. Barazangi, M. 2003. The crustal structure of the East Anatolian plateau (Turkey) from receiver functions. Geophysical Research Letters 30, 24, 8043. Doi: 10.1029/2003GL018192.

Bull. Min. Res. Exp. (2019) 158: 235-250

Bulletin of the Mineral Research and Exploration

http://bulletin.mta.gov.tr

Porphyry copper prospectivity mapping using fuzzy and fractal modeling in Sonajeel area, NW Iran

Zahra YAZDI[a], Alireza JAFARI RAD[a*], Mehraj AGHAZADEH[b] and Peyman AFZAL[c]

[a] *Department of Geology, Science and Research Branch, Islamic Azad University (IAU), Tehran, Iran*
[b] *Department of Geology, Payame Noor University, Tabriz, Iran*
[c] *Department of Mining Engineering, South Tehran Branch, Islamic Azad University (IAU), Tehran, Iran*

Research Article

Keywords:
Fuzzy logic, fractal, GIS, prospectivity map, porphyry copper, sonajeel.

ABSTRACT

Main purpose of this research is to present a local scale GIS-based mineral prospectivity model for prospecting Cu porphyry mineralization, and to validate the produced model by field observation, surface sampling and drilling data. Sonajeel area which is the subject of this study is a part of Arasbaran mineralization belt, NW of Iran. Constructing a mathematical exploratory algorithm based on a mineralization type is a complicated and interdisciplinary task. For this purpose, results from processing and interpreting different data sets including geology, geochemistry and remote sensing were considered. A comprehensive exploratory integration model was built up considering the exploration stage and the descriptive porphyry mineralization model suggested by Sillitoe (2010). In order to prepare inputs for GIS-based exploration model, value assigned grids or evidence layers were produced using fuzzy membership curves and then integrated via gamma fuzzy function. In addition, for defuzzification and prioritizing the mineral prospectivity map, a Concentration-Area (C-A) fractal model was applied on the pixel values of the prospectivity map. Finally, the results were confirmed via field observation, surface sampling and drilling. Borehole logs at the first priority displayed a Cu mineralization zone with an average grade of 0.5%.

Received Date: 29.08.2017
Accepted Date: 04.01.2018

1. Introduction

Mineral prospectivity mapping (MPM) is carried out based on integration of evidence layers especially at reconnaissance and prospecting scales in mineral exploration (Carranza, 2009 *a*,*b*; Jafarirad, 2009; Porwal and Carranza, 2015; Yousefi and Carranza, 2014, 2015a,b). Each scale is characterized based on the accuracy of evidence maps, where level of accuracy increases with the acceleration of exploration scale. An MPM is drawn in a Geospatial Information System (GIS) environment by different methods (Agterberg et al., 1990; Almasi et al., 2015*a*,*b*; Bonham-Carter et al., 1989; Bonham-Carter, 1994; Carranza et al., 2008; Carranza, 2014; Chung and Agterberg, 1980; Chung and Moon, 1990; Jafarirad and Busch, 2011; Lusty et al., 2012; Magalhaes and Souza Filho, 2012; Nykanen et al., 2008; Parsa et al., 2016; Parsa et al., 2017; Yousefi, 2017). In every scale, data layers are collected, processed and integrated using a variety of available functions (Abedi et al., 2017; Almasi et al., 2015*a*,*b*; Yazdi et al., 2014). In this research, evidence layers including geology, geochemistry, structure and alteration have been produced individually and then checked using field observation. Subsequently, evidence maps were integrated in order to find high potential locations of porphyry copper mineralization in the Sonajeel system, NW Iran. Finally, the MPM has been evaluated and validated by field observation and drilling data.

A wide variety of volcanic, sedimentary and metamorphic units host porphyry copper deposits worldwide, which displays the almost ineffectiveness of the host rock in their mineralization (Sillitoe, 2010). Cross-cutting faults play a major role in the size,

* *Corresponding author: Alireza JAFARI RAD, alirad@yahoo.com*
https://dx.doi.org/10.19111/bulletinofmre.391835.

geometry and setting of the deposits. All the porphyry copper deposit models that has been suggested so far place the potassic alteration at the core of the porphyry system. Moreover, geochemical halo of Zn usually engulfs porphyry mineralization systems.

Iran inherited its mineral endowment from the processes involved in its lithospheric evolution and plate tectonics (Berberian and Kings, 1981; Stocklin 1974). Subduction zones which host porphyry copper mineralization (PCM) constitutes a major part of Iran (Afzal et al., 2012; Aghazadeh et al., 2015; Hassanpour and Afzal, 2013; Jamali and Mehrabi, 2015; Richards and Sholeh, 2016). Post collisional Neo-Tethys oceanic closure process caused the vast and huge magmatism along South to North West of Iran (Aghazadeh et al., 2015; Babaie et al., 2001; Karimzadeh Somarin, 2005; Pazand et al., 2012). This Oligo-Miocene magmatic domain has been suggested to be divided in to two main belts (Moritz et al., 2015). NW-SE trending Urumieh-Dokhtar magmatic arc hosts some well-known deposits namely Sarcheshmeh, Meiduk and Kahang (Afzal et al., 2010; Aghazadeh et al., 2015; Jafarirad, 2009; McInnes et al., 2003; Shahabpour and Keramers, 1987; Yazdi et al., 2014). Arasbaran belt, with a WNW-ESE trending located in NW of Iran, hosts Iran's giant Cu porphyry mine Sungun, and is considered as a top priority potential for finding new deposits (Aghazadeh et al., 2015; Jamali and Mehrabi, 2015). Sonajeel system, the area subjected to this study, is located in the east of the Arasbaran belt (Figure 1).

Several exploration and geological surveys have been done on the Sonajeel mineralization (Hezarkhani, 2008; Hosseinzadeh et al., 2009; 2017; Karimi et al., 2009; Pazand et al., 2013).

Sonajeel system comprises Oligo-Miocene quartz monzodiorite and granodiorite intrusives, and is similar to Sungun and other PCM prospects of Arasbaran belt. Rock exposures in this prospect consist of Eocene volcano-sedimentary units, Oligo-Miocene intrusives and Quaternary volcanic rocks (Figure 1). Eocene volcano-sedimentary units which were deposited in the marine and continental areas, include andesitic to basaltic lava, basaltic to andesitic volcanic rocks, ignimbrite and tuff. Eocene volcano-sedimentary units were intruded by various Oligo-Miocene intrusions including Sonajeel porphyry stock. This stock caused the percolation of hydrothermal fluids and has been suggested as the main factor in

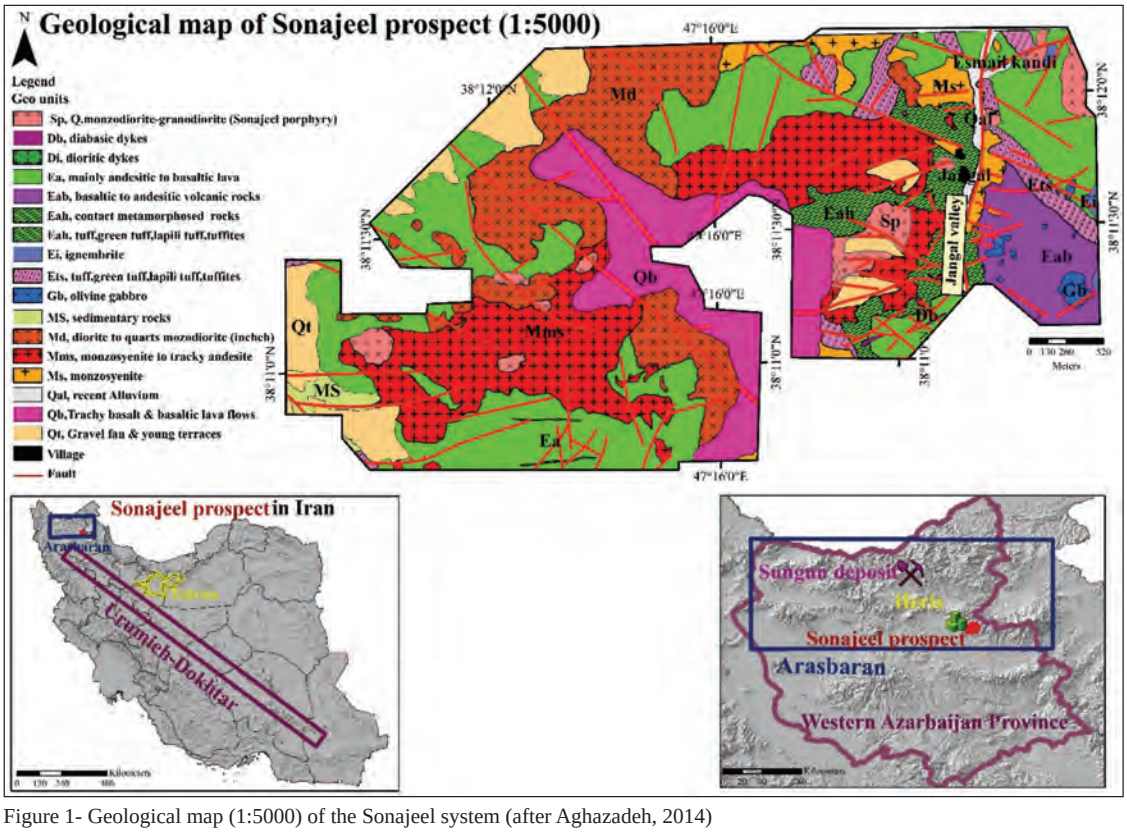

Figure 1- Geological map (1:5000) of the Sonajeel system (after Aghazadeh, 2014)

Sonajeel mineralization (Aghazadeh et al., 2015). Intrusive units are distributed in the forms of stock, sill, dyke and vein in the study area. Quaternary units including tracky basalt and basaltic lava flows, gravel fans and recent alluvium and Eocene volcanic rocks with different thicknesses, cover the older units.

Fault systems in this area have been divided into two main groups as follows (Aghazadeh, 2014):

1- Old deep first order NW-SE system that is related to the Tabriz and Goshadagh faults and has been suggested as the controlling factor of the emplacement of intrusive units.

2- NE-SW system that influenced dykes and quaternary volcanism.

Therefore, fault systems have influenced intrusions and alterations which are major factors for this mineralization.

2. Materials and Methods

Porphyritic igneous bodies are mostly I-type metalliferous intrusions. These bodies are typically calc-alkaline with medium potassium content or rarely alkaline with high potassium content. Their composition range from calc-alkaline diorite and quartz-diorite, to alkaline granodiorite, quartz-monzonite and diorite, to monzonite and syenite (Seedorf et al., 2005). In Sonajeel area, from the alteration and geochemistry perspective, mineralization signatures totally obey global porphyry genetic models.

Geological and structural map of the study area were produced at 1:5000 scale by Coome Madan Company in 2014. Furthermore, alteration zones were detected using remote sensing techniques from ASTER and QuickBird images. Geochemical data used in this paper were obtained by lithogeochemical samples which were collected by Kavoshgaran Company in 2006 (Table 1).

In this study, SPSS 24, Microsoft office excel 7, ENVI 5.1 and ArcGIS 10.2.1 software were employed for statistical analyzes, image processing, producing and integrating evidence maps respectively. In this paper, firstly data layers were processed separately, then controlled via field confirmations. Moreover, evidence maps were generated using fuzzy membership functions, then were integrated via fuzzy logic method. Finally, the integrated map was classified by Concentration-Area (C-A) fractal model and results evaluated by field checking. The first two priorities were suggested for further exploration at 1:1000 scale and drilling. These steps are introduced briefly in the form of a flow chart in figure 2.

Table 1- Lithogeochemical samples.

Laboratory name	Total samples	Method	Date	Number of elements	Elements
AMDEL (Australia)	1248	For all samples except Gold: ICP Mass Gold: F.A.	2006	44	Ag, Al, As, Au, Ba, Be, Bi, Ca, Cd, Ce, Co, Cr, Cs, Cu, Fe, Hg, K, La, Li, Mg, Mn, Mo, Na, Nb, Ni, P, Pb, Rb,Re, S, Sb, Sc, Sn, Sr, Te, Th, Ti, Tl, U, V, W, Y, Zn, Zr

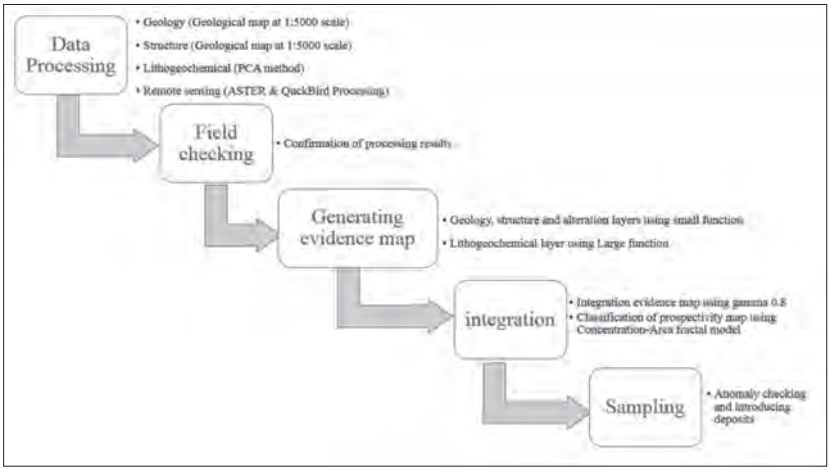

Figure 2- Processing Flowchart.

Used fuzzy membership functions, and the fuzzy operator which was employed for integration, are explained in a summarized format below.

2.1. Small Fuzzy Membership Function

The small fuzzification function has been defined as following equation:

$$\mu_x = \frac{1}{1 + (\frac{x}{f_2})^{f_1}} \quad (1)$$

Where f1 is the spread of the transition from a membership value of 1 to 0 and f2 is the midpoint (Tsoukalas and Uhrig, 1997).

2.2. Logistic Fuzzy Membership Function

Logistic function could be generator of fuzzy membership for spatially continuous weights (Bishop, 2006; Nykänen et al., 2008; Yousefi et al., 2012; 2013; 2014; Yousefi and Carranza, 2015*a*, *b*; Yousefi and Nykänen, 2016). This function has been detected as following equation (Yousefi and Carranza, 2015*a*):

$$\mu_x = \frac{1}{1 + e^{-s(x-i)}} \quad (2)$$

Where i and s are inflexion point and slope of the logistic function, which determined as following equations (Yousefi and Nykänen, 2016):

$$s = \frac{9.2}{X_{MAX} - X_{MIN}} \quad (3)$$

$$i = \frac{X_{MAX} + X_{MIN}}{2} \quad (4)$$

Where Xmin and Xmax are the minimum and maximum evidential values respectively.

2.3. Gamma Fuzzy Operator

The gamma operator is the general form of fuzzy Sum (An increaser function, used when the combination of multiple evidences is more important or larger than any of the inputs alone) and fuzzy Product (A reducer function, used when the combination of multiple evidence is less important or smaller than any of the inputs alone). This operator has been shown in equation 5 (Tsoukalas and Uhrig, 1997):

$$\mu_{Combination} = \left(\prod_{i=1}^{n} \mu_i\right)^{\delta} \left(1 - \left(\prod_{i=1}^{n} (1 - \mu_i)\right)\right)^{1-\delta} \quad (5)$$

Where μCombination = each unit value in output map

μi= the weight of ith factor map

2.4. Concentration-Area (C-A) Fractal Model

Cheng et al. (1994) proposed an element concentration–area (C–A) model, which may be used to define the geochemical background and anomalies. The model has the general form:

$$A(\rho \leq \upsilon) \propto \rho^{-a1} ; A(\rho \geq \upsilon) \propto \rho^{-a2} \quad (6)$$

Where A(ρ) denotes the area with concentration values greater than the contour value ρ; υ represents the threshold; and a1 and a2 are characteristic exponents. Using fractal theory, Cheng et al. (1994) derived similar power-law relationships and equations in extended form (Afzal et al., 2010; 2012; Almasi et al., 2015*a*,*b*).

2.5. Principal Component Analysis (PCA)

Principal component analysis (PCA) is a multivariate technique that reduced variables by several inter-correlated quantitative dependent variables (Abdi &Williams, 2010). Among the advantages of PCA can cite that it's possible to determine the correlation of each PC with each of the original variables, it enables us to find outliers and groups of variables and allows us to reduce the dimensionality of the problem by the elimination of some variables in the next steps of the mineral exploration, if we consider that they are not helping to explain the processes interpreted via PCs.

3. Evidence Maps

3.1. Geological Layer

Sonajeel porphyry intrusive units composed of quartz-monzodiortic to granodioritic rocks, which were suggested as the key mineralization factor are similarly comparable to other porphyry copper deposits and prospects in Arasbaran belt (Aghazadeh et al., 2015). These intrusive units are in the form of stock and apophyse have outcrops around Jangal and Esmailkandi villages in the east of the study area (Figure 1). Sonajeel porphyry intrusive units has been intruded into the Eocene rocks and micromonzosyenite rocks (Figure 3a) which indicated Oligo-Miocene age. These intrusive rocks contain potassic and phyllic alteration in the surroundings of Jangal village and

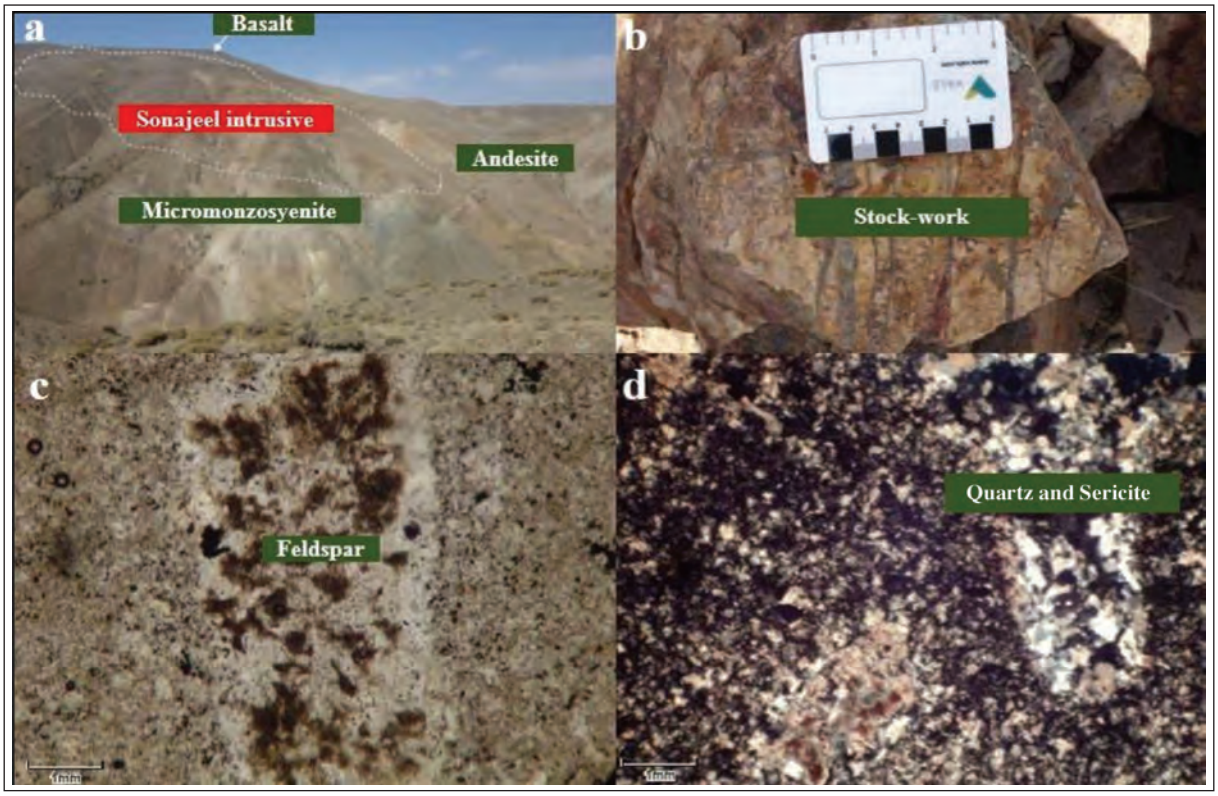

Figure 3- (a) Sonajeel porphyry intrusive (b) distribution of Stock-work in the Sonajeel porphyry intrusive (c) porphyritic texture with feldspar phenocyrist in the sample of Sonajeel porphyry intrusive, PPL (d) spreading Quartz and Sericite due to affecting of phyllic alteration, XPL.

have stockwork mineralization indications (Figure 3b). The texture of this intrusive is porphyrytic with feldspar and phenocrysts of mafic minerals.

Ten thin sections have been studied from these lithologies (Figure 3 c and d). The sample presented here has porphyritic texture with feldspar phenocrysts which has been affected by sericitic alteration. These phenocrystals are distributed in quartz, sericite and secondary biotite background. Sericitic alteration has covered the primary potassic alteration meanwhile some of its biotite has remained intact.

In order to produce the source rock evidence layer, firstly, Euclidian distance map of Sonajeel porphyry intrusives was built due to importance of proximity to these intrusive units in the porphyry models. Afterwards, fuzzy membership of this distance map has been generated using small function with midpoint 400 and spread 5 (Figure 4). This evidence map has been classified using C-A fractal model which is presented in figure 5.

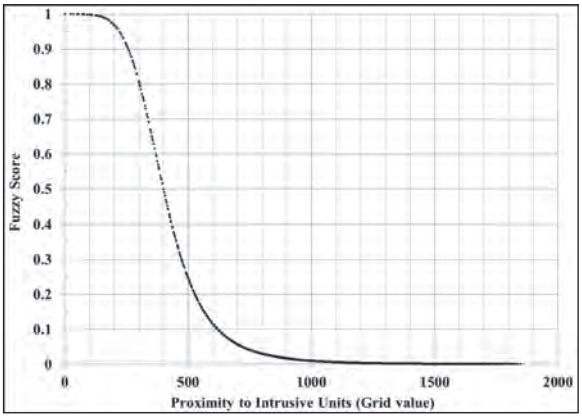

Figure 4- Fuzzy membership of intrusive .

3.2. Structural Layer

Structures play a significant role in porphyry mineralization (Byron and Berger 2008; Richards, 2015). In the study area, structural mapping have been done at 1:5000 scale which mostly of indicated faults is strike-slip and have NW-SE trends (Figure 6). Fuzzification algorithm used in this layer is small with midpoint and spread 200 and 7 respectively (Figure 7).

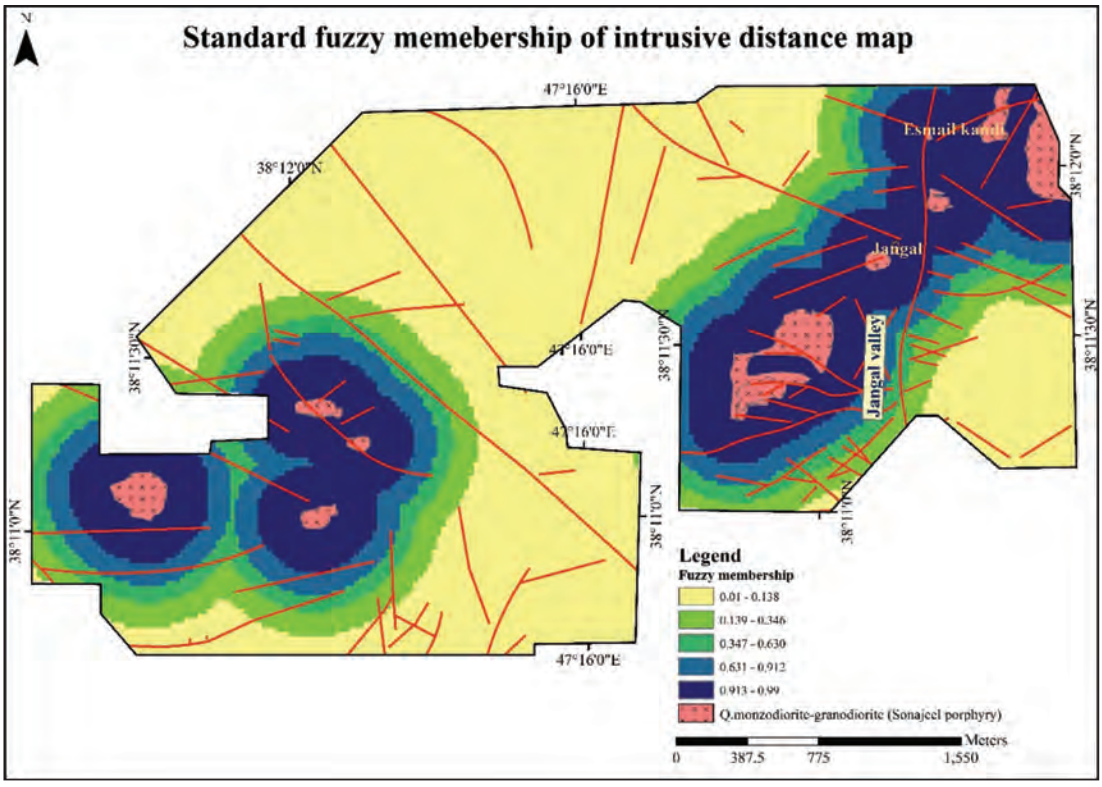

Figure 5- Evidence map of intrusive rocks as the mineralization producer.

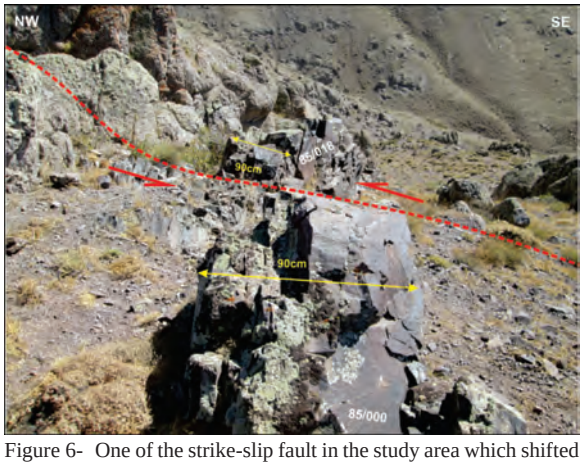

Figure 6- One of the strike-slip fault in the study area which shifted dyke.

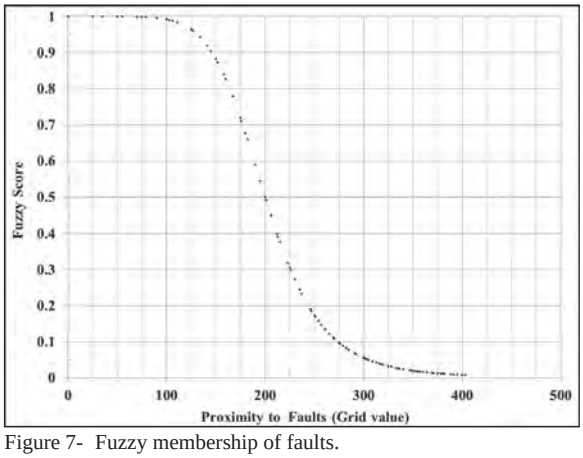

Figure 7- Fuzzy membership of faults.

Moreover, thresholds for classification of this evidence map have been calculated using Concentration-Area fractal method (Figure 8).

Fault concentrations are vastly dispersed in Sonajeel porphyry intrusive units (east of Jangal valley) which is a basic factor in rising hydrothermal fluids and mineralization. This fact has been confirmed by field evidences in the Sonajeel porphyry system.

3.3. Alteration Layer

Hydrothermal fluids broadly effect rocks and produce specific alteration zones including potassic, phyllic, argillic and propyllitic in porphyry copper systems (Alimohammadi et al., 2015; Beane, 1982; Berger et al., 2008; Byron and Berger, 2008; Lowell and Guilbert, 1970; Meyer and Hemley, 1967; Silitoe, 2010; Sillitoe, 2010). Mineralization is related to potassic and phyllic alteration in the Sonajeel

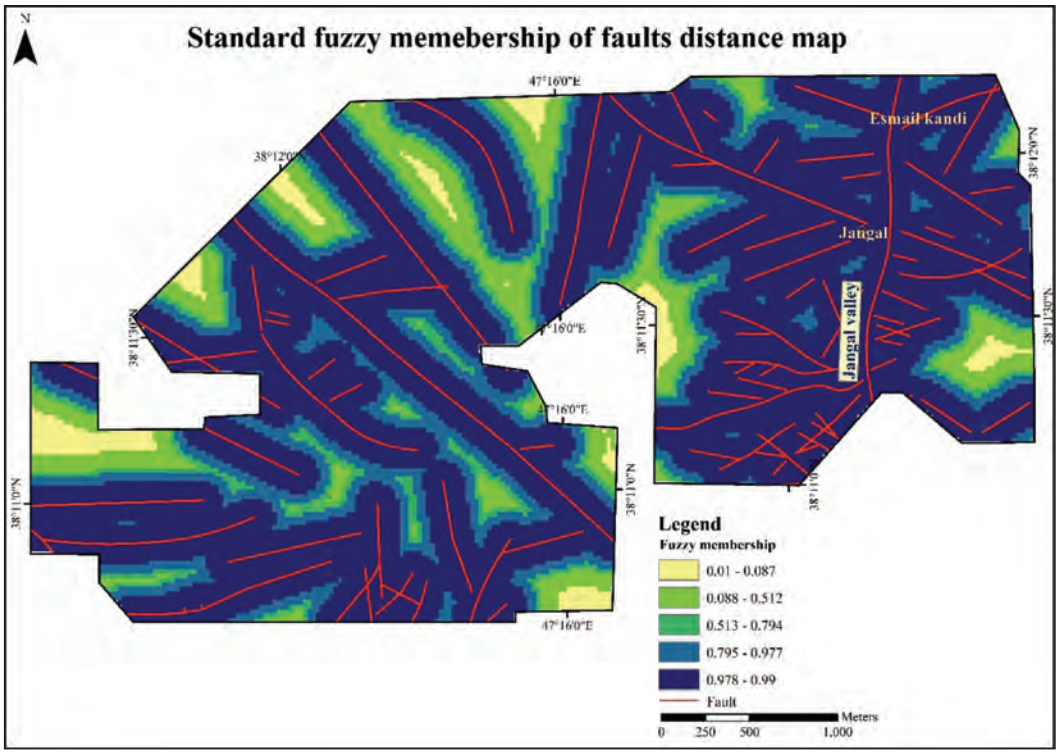

Figure 8- Evidence map of faults.

system which was outlined using remote sensing. For this purpose, Thermal Emission and Reflection Radiometer (ASTER) multispectral image has been geometrically corrected using QuickBird image with pixel width of about 0.5 m as a reference image in order to improve the rectification process. Alteration zones have then been detected using Relative Absorption Band-Depth grids (RBD) method. Afterwards, the image processing results have been evaluated by field evidences (Figure 9). Finally, distance map of potassic

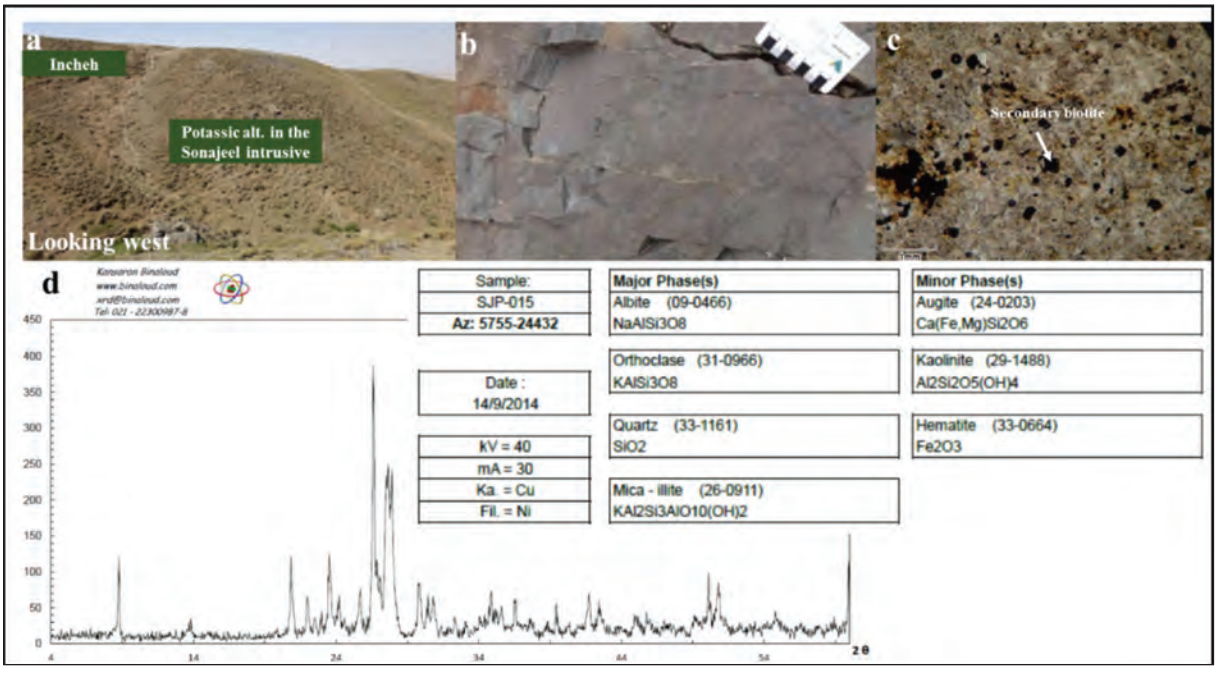

Figure 9- a) potassic alteration in Sonajeel porphyry intrusives (b) gray sample of potassic alteration (c) Thin section of potassic alteration which contains secondary biotite and feldspar in the microgranoular background (d) XRD report of one of the potassic sample.

and phyllic alterations have been produced and fuzzy memberships have been individually created using small fuzzy function with midpoint of 300 and spread of 5 (Figure 10, 11 and 12). Potassic and phyllic alterations were directly observed and are distributed in the east of Jangal velley similar to the faults and intrusive units.

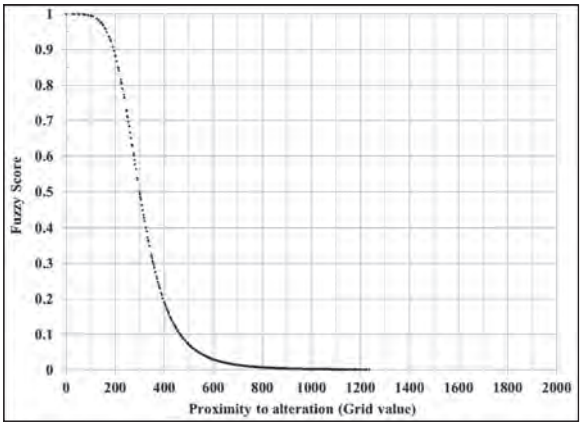

Figure 10- Fuzzy membership of alteration.

3.4. Lithogeochemical Layer

Multivariate principal component analysis method is used for determining elemental correlations and elemental paragenesis (Afzal et al., 2010; Davis, 2002; Deng et al., 2007, 2008). PCA method has reduced dimensions and is commonly used in the geochemical studies (Carranza and Hale, 2002; Carranza, 2010; Wang et al., 2011, 2012, 2013, 2014). In this paper, lithogeochemical samples (with 100 m*100m cells) have been processed using PCA method and resulted in 2 factors including Cu- Zn and Mo- As- Pb. Afterwards, fuzzification was on Cu- Zn performed using Logistic method in order to produce geochemical evidence layer. Inverse Distance Weighted (IDW) technique was used for interpolation and gridding. As mentioned in the methodology part, copper and zinc have a high correlation coefficient. An observable evidence of that is their overlapping anomalies in the east of Jangal valley (Figure 13).

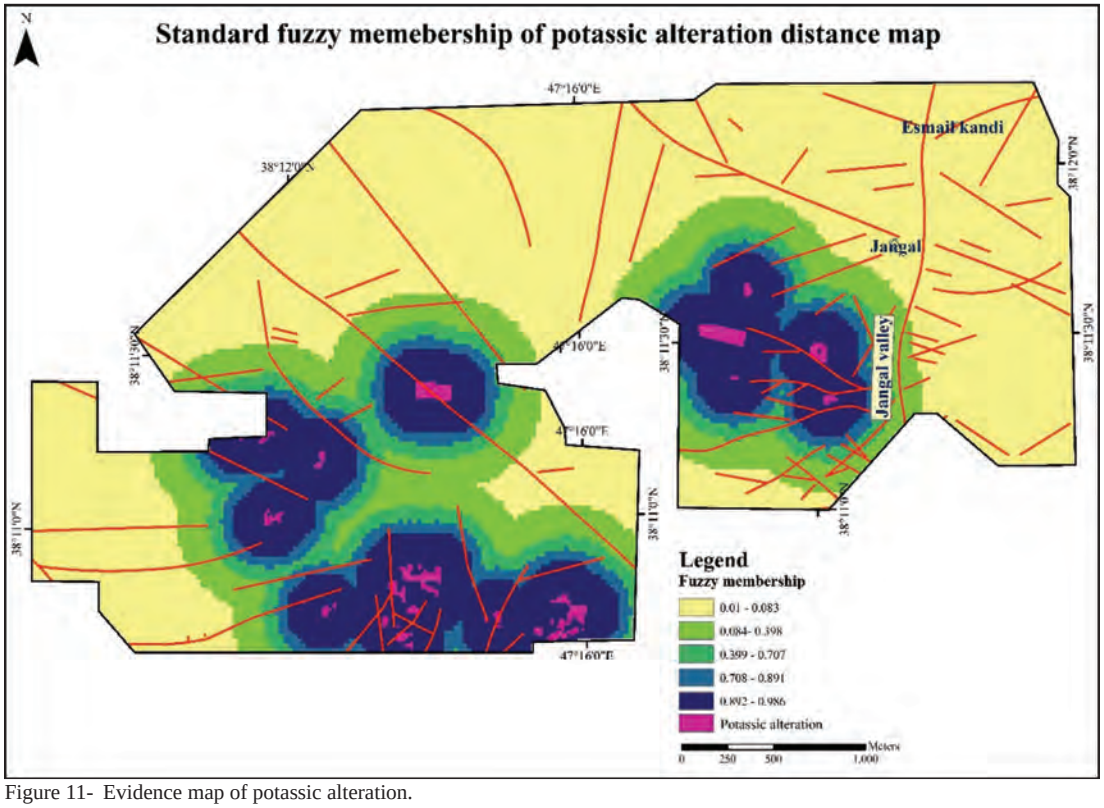

Figure 11- Evidence map of potassic alteration.

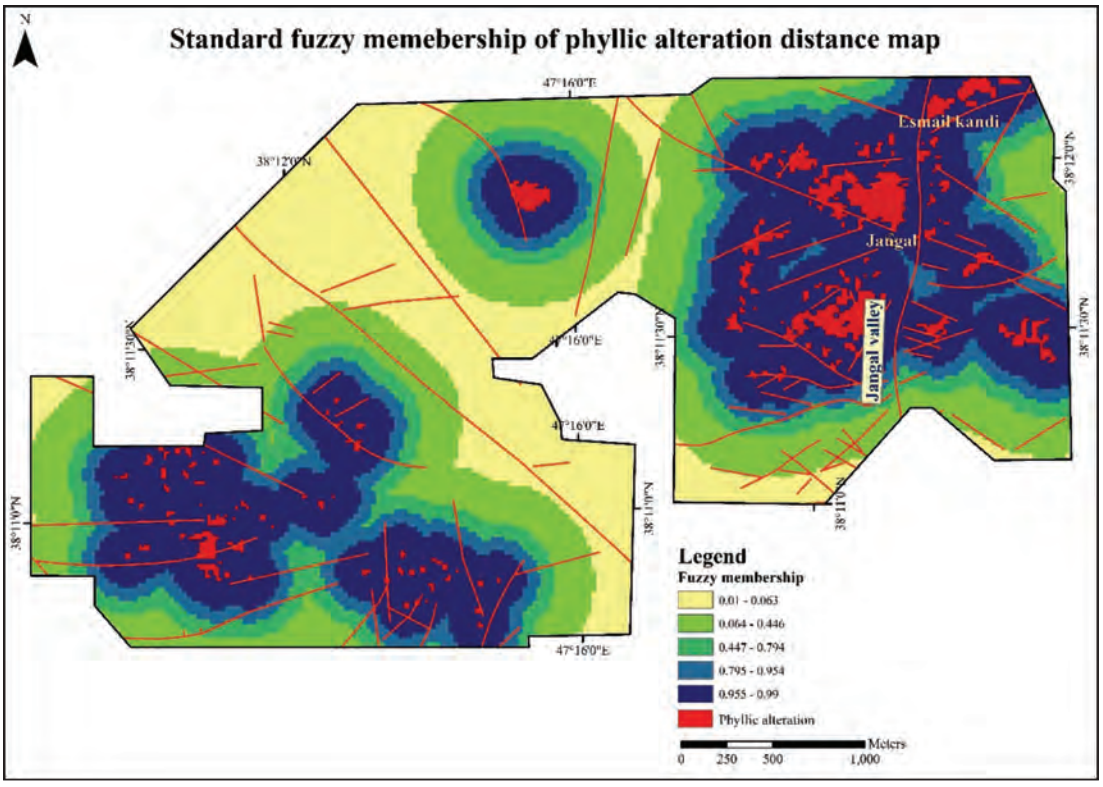

Figure 12- Evidence map of phyllic alteration.

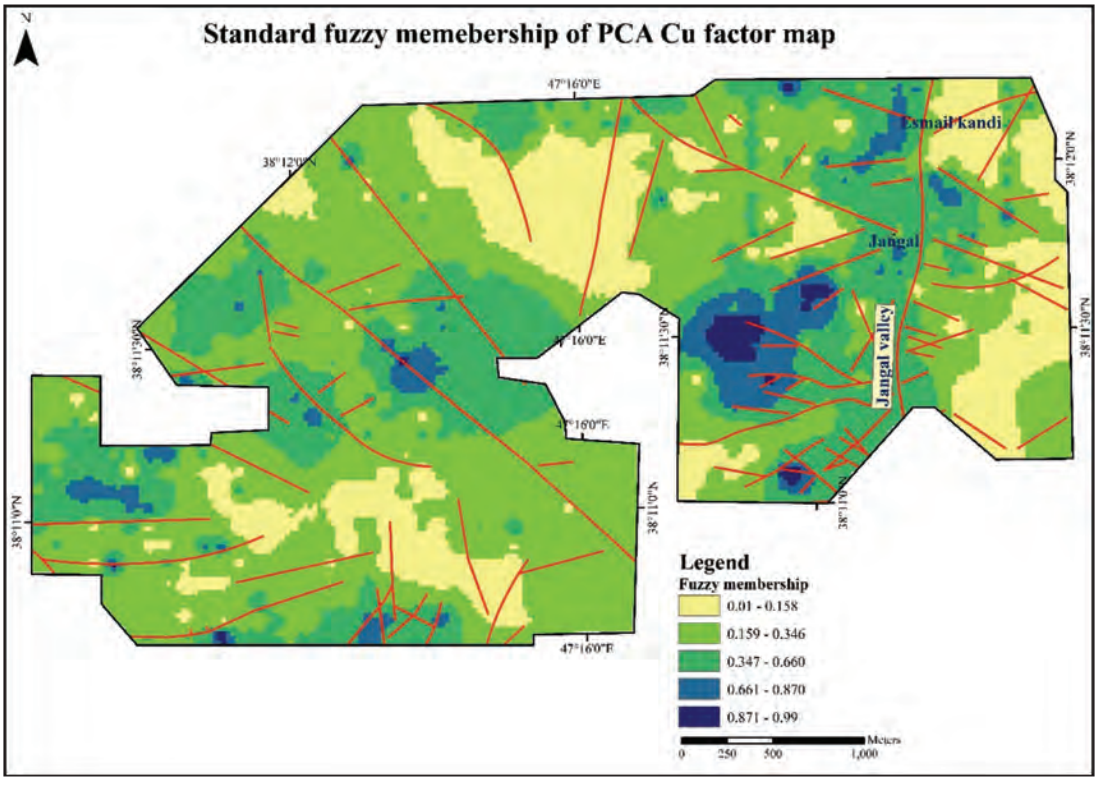

Figure 13- Evidence map of geochemistry.

4. Integration

In knowledge-driven methods, experts (with different fields and levels of expertise) integrate different pieces of information for mineral prospectivity mapping. Assigning integers to different geological features or to several intervals of a grid (e.g. geophysical or geochemical), is a procedure that has been practiced in a voluminous studies of this kind. In this method, a major issue is the controversies which arouse over assigning discrete values to the intervals. To overcome this issue, more recent studies focused on applying functions and curves for preparing integration input grids or evidence layers. These functions commonly situate in the paradigm of the fuzzy theory and convert a set of data into a grid ranging from ~0.01 to ~0.99. Fuzzy operators such as fuzzy and, fuzzy or and fuzzy gamma are among the techniques used for integrating evidence maps.

The fuzzy logic method as one of the knowledge-driven methods is widely accepted for producing MPM. It was firstly used by An et al. (1991) and is still employed in mineral exploration (Ford et al., 2015; Joly et al., 2012; Porwal and Kreuzer, 2010; Lisitsin et al., 2013; Lusty et al., 2012; Nykänen et al., 2008; Parsa et al., 2016; Parsa et al, 2017). In this paper gamma (0.8) operator has been used for combining evidence maps. It is a combination of both sum and product algorithms. Subsequently, the created fuzzy logic MPM has been prioritized using Concentration-Area (C-A) fractal model (Figure 14: Almasi et al., 2015*a*,*b*, 2017).

5. Results and Discussion

Data analysis proves that Sonajeel porphyry system has the adequate potential for becoming a PCM. Its surface indications are: potassic alteration zone, wide stock-work system, and Sonajeel porphyry intrusive units. The produced MPM has been validated via field observations and sampling (Figure 15). Samples were mainly studied using two techniques 1) ICPMS and 2) polished sections. The average Cu grade received from ICPMS analysis was 0.4 percent, a satisfactory grade for surface samples in this scale of exploration. Maximum grade was 2 and Minimum grade of the samples was 0.1 percent.

Several polished section samples have been studied from the identified priorities. SJP011PS sample which represent the supergene zone contains chalcocite (Cu2S) and covellite (CuS). These minerals display the replacement of the primary sulfide minerals such as bornite (Figure 16). SJP06PS sample contains bornite and chalcopyrite primary and secondary sulfide minerals which had been altering to chalcocite and covellite iron hydroxide. Iron oxide (magnetite) has

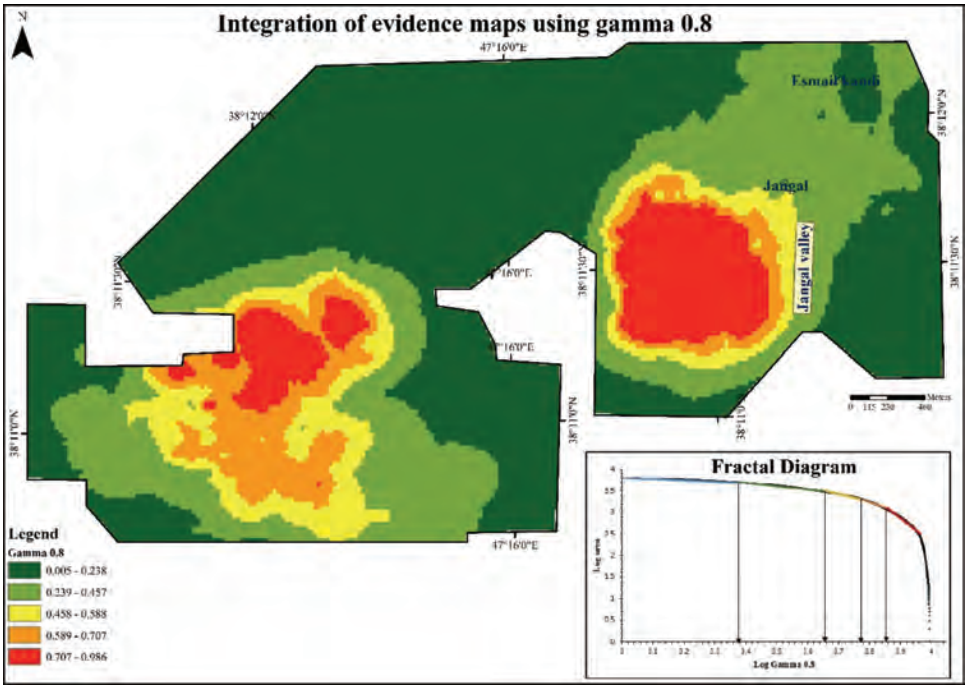

Figure 14- Ranking MPM using C-A fractal method.

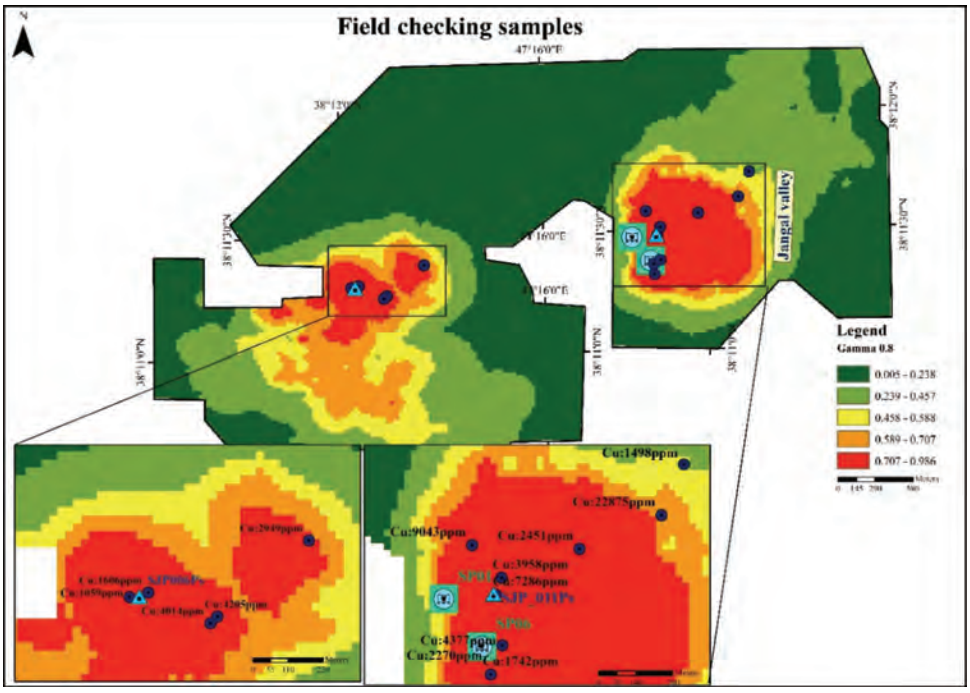

Figure 15- Location of sampling in the field checking.

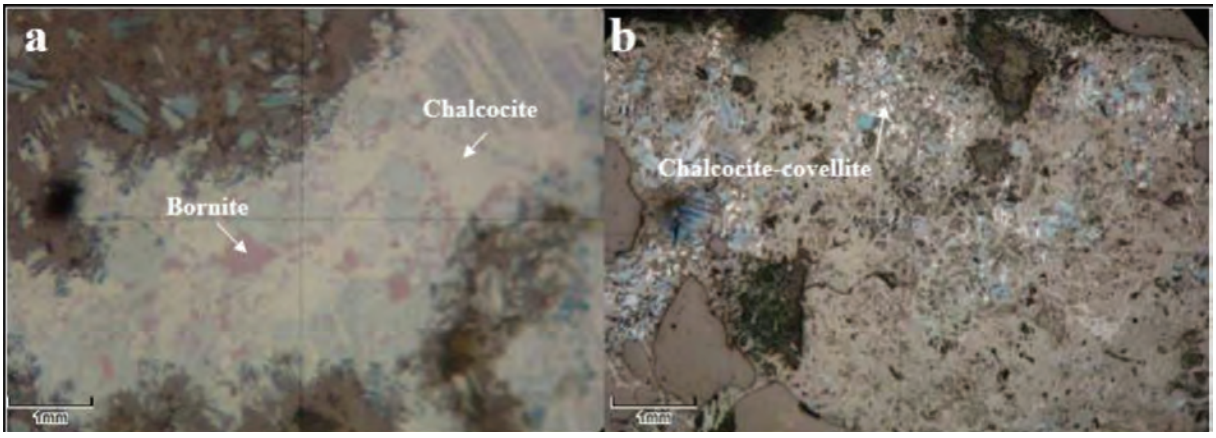

Figure 16- SJP011PS sample (a) replacement of bornite by chalcocite, PPL (b) spread of chalcocite and covellite.

primary occurrence in the background of this sample. This sample displays the boundary of the hypogene and supergene zones (Figure 17).

After positive results from the samples' analysis, two boreholes were drilled in the first identified priority, east of the study area (Jangal valley). Core sample analysis of the boreholes SP01 and SP06 contain average Cu concentrations of 2267 and 2959 ppm respectively. Lithological, alteration and Cu concentration logs are presented in figure 18. Borehole SP01 with the depth of the 400 meters, contain lithological units from quartzdiorite, granodiorite to andesite and andesite-basalt with mainly potassic

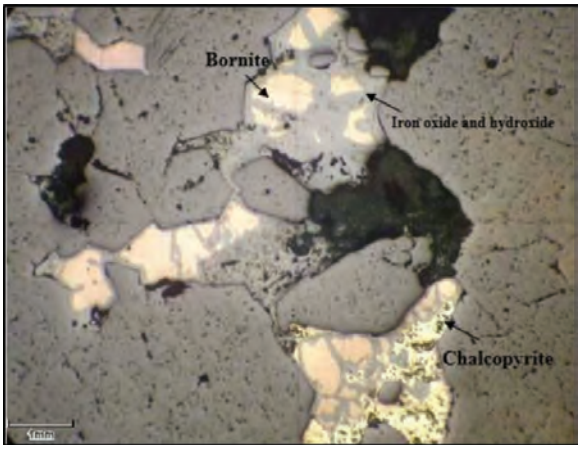

Figure 17- SJP06PS replacement of chalcopyrite and bornite by iron oxide and hydroxide.

and phyllic alterations. A direct relation between Cu concentrations and alterations are displayed. Borehole SP06 with the depth of 200 meters, shows alternation of potassic and phyllic quartzmonzonite. High grades of Cu are recorded at phyllic and especially potassic alteration zones (Figure 18).

6. Conclusion

In this research, the results from the analysis of the datasets (remote sensing and geochemical sampling) and the outcomes of the MPM were validated via field observation. Outlined prospects overlap with all the other anomalies in Jangal valley where the porphyry intrusive unit is exposed to the surface. Statistical analysis of the geochemical dataset displays a high elemental correlation between Cu and Zn which is compatible with global and regional porphyry deposit models.

Two exploratory boreholes which were drilled in the prospects (with the depth of 200 and 400 meters) explicitly displayed 200 to 300 meter porphyry mineralization with average copper concentration of 0.5 percent. A thorough drilling project with the purpose of reserve estimation is now active in the area.

Sonajeel porphyry intrusive units, which are suggested to be the main mineralization factor in the area, are comprised of quartz monzodiorite to granodiorite from Oligo-Miocene age. The outcomes of this paper displayed that, integration of the evidence layers is a valuable technique for determining and prioritizing surface priorities at every scale of mineral exploration. Moreover, validating the outcomes via field observations, sampling and sample analyzing is a necessity. It is a useful method for determining parameters the fuzzy function's midpoint and spread. Remote sensing results showed that one of the most important data layers in porphyry copper exploration is delineated alterations. They can be determined using ASTER multispectral image. In addition, correcting the ASTER image via QuickBird image helped raising the geometrical accuracy. In processing geochemical data exploration, PCA method is suitable for decreasing the elemental variety and is very effective for finding elemental correlations.

Also, Concentration-Area (C-A) fractal method is suggested to be very effective for classification of the created MPM in different types of mineralization in any scale

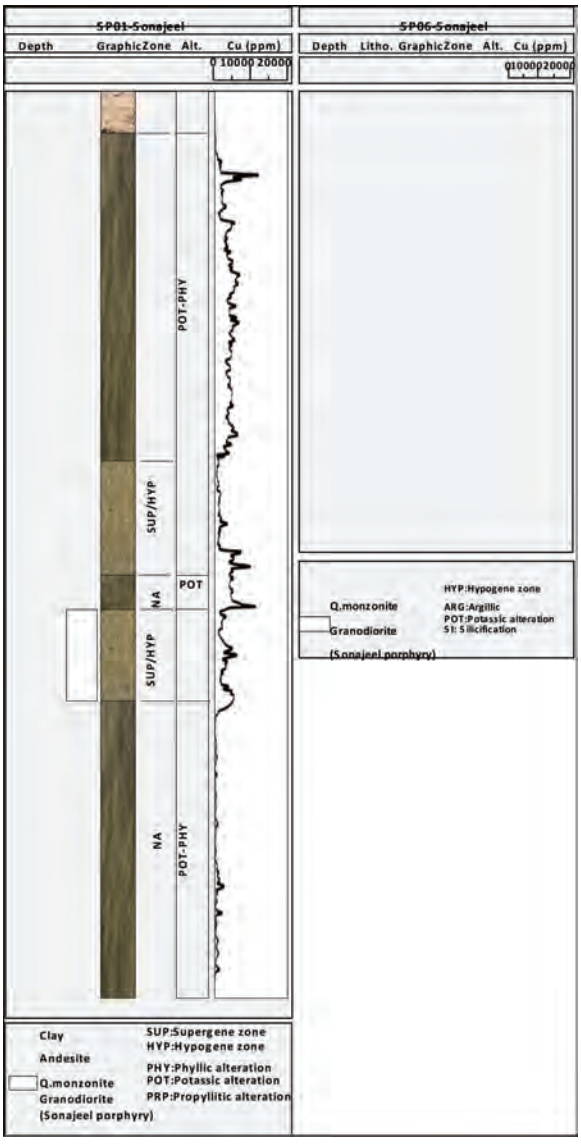

Figure 18- (a) SP01 log (b) SP06 log.

The two boreholes (with about 300 m depth) which was drilled on the first priority displayed 25 m copper mineralization with more than 0.5 percent Cu (BH013 & BH014).

Acknowledgements

We would like to acknowledge thorough reviews of Mr. Almasi and his comments. Also, we would like to express our gratitude to the Coome Madan Pars Company and the Speer Company for their supports.

References

Abdi H., Williams, L.J. 2010. Principal Component Analysis. Wiley Interdisciplinary Reviews: Computational Statistics 2, 433-459.

Abedi M., Mostafavi Kashani, S. B., Norouzi, G. H., Yousefi, M. 2017. A deposit scale mineral prospectivity analysis: A comparison of various knowledge-driven approaches for porphyry copper targeting in Seridune, Iran. Journal of African Earth Sciences 128, 127-146.

Afzal, P., Khakzad, A., Moarefvand, P., Rashidnejad Omran, N., Esfandiari, B., Fadakar Alghalandis, Y. 2010. Geochemical anomaly separation by multifractal modeling in Kahang (Gor Gor) porphyry system, Central Iran. Journal of Geochemical Exploration 104, 34-46.

Afzal, P., Zarifi, A.Z., Khankandi, S.F., Wetherelt, A., Yasrebi, A.B. 2012. Separation of uranium anomalies based on geophysical airborne analysis by using Concentration-Area (C-A) Fractal Model, Mahneshan 1:50000 Sheet, NW IRAN. Journal of Mining and Metallurgy 48A(1), 1-11.

Aghazadeh, M. 2014. Geological report of Sonajeel (1:5000), Koome Madan Company.

Aghazadeh, M., Hou, Z., Badrzadeh, Z., Zhou, L. 2015. Temporal-spatial distribution and tectonic setting of porphyry copper deposits in Iran: Constraints from zircon U-Pb and molybdenite Re-Os geochronology. Ore Geology Reviews 70, 385-406.

Agterberg, F.P., Bonham-Carter, G.F., Wright, D.F. 1990. Statistical pattern integration for mineral exploration. In: Gaal G., Merriam D.F. (Eds.), Computer Applications in Resource Estimation Prediction and Assessment for Metals and Petroleum. Pergamon Press, Oxford New York, 1-21.

Alimohammadi, M., Alirezaei, S., Kontak, D.J. 2015. Application of ASTER data for exploration of porphyry copper deposits: A case study of Daraloo-Sarmeshk area, southern part of the Kerman copper belt, Iran, Ore Geology Reviews 70, 290-304.

Almasi, A., Jafarirad, A., Afzal, P., Rahimi, M. 2015*a*. Prospecting of gold mineralization in Saqez area (NW Iran) using geochemical, geophysical and geological studies based on multifractal modelling and principal component analysis. Arabian Journal of Geosciences 8(8), 5935-5947.

Almasi, A., Jafarirad, A., Kheirollahi, H., Rahimi, M., Afzal, P. 2015*b*. Orogenic Gold Prospectivity Mapping of Region Saqez, Bulletin of the Mineral Research and Exploration 150, 65-76.

Almasi, A., Yousefi, M., Carranza, E.J.M. 2017. Prospectivity analysis of orogenic gold deposits in Saqez-Sardasht Goldfield, Zagros Orogen, Iran. Ore Geology Reviews 91, 1066-1080.

An, P., Moon, W.M., Rencz, A. 1991. Application of fuzzy set theory to integrated mineral exploration. Canadian Journal of Exploration Geophysics, 27(1), 1-11.

Babaie, H.A., Ghazi, A.M., Babaei, A., La Tour, T.E., Hassanipak, A.A. 2001. Geochemistry of arc volcanic rocks of the Zagros crush zone, Neyriz, Iran. Journal of Asian Earth Sciences 19, 61-76.

Beane, R. E. 1982. Hydrothermal alteration in silicate rocks, in Titley S. R., ed., Advances in geology of the porphyry copper deposits, southwestern North America: Tucson. The University of Arizona Press, pp. 117-137.

Berberian, M., King, G.C. 1981. Towards a paleogeography and tectonic evolution of Iran. Canadian Journal of Earth Sciences 18, 210-265.

Berger, B.R., Ayuso, R. A., Wynn, J.C., Seal, R.R. 2008. Preliminary Model of Porphyry Copper Deposits. USGS, Open-File Report, 1321 pp.

Bishop, C.M. 2006. Pattern Recognition and Machine Learning. Springer: New York, NY, USA, 738 pp.

Bonham-Carter, G.F. 1994. Geographic Information Systems for Geoscientists: Modeling with GIS. Pergamon Press, Ontario, Canada, 398 pp.

Bonham-Carter, G.F., Agterberg, F.P., Wright, D.F. 1989. Weights of evidence modelling: new approach to mapping mineral potential In: Agterberg F. P., Bonham-Carter G. F. (Eds.), Statistical Applications in the Earth Sciences Geological Survey of Canada, 171-183.

Byron, R., Berger Robert, A. 2008. Preliminary model of porphyry copper deposits, U.S. Geological survey 3.

Carranza, E.J.M. 2008. Geochemical anomaly and mineral prospectivity mapping in GIS. Handbook of Exploration and Environmental Geochemistry, Vol. 11. Elsevier, Amsterdam.

Carranza, E.J.M. 2009*a*. Mapping of anomalies in continuous and discrete fields of stream sediment geochemical landscapes. Geochemistry: Exploration, Environment, Analysis 10, 171-187.

Carranza, E.J.M. 2009*b*. Controls on mineral deposit occurrence inferred from analysis of their spatial pattern and spatial association with geological features. Ore Geology Reviews 35, 383-400.

Carranza, E.J.M. 2010. Improved Wildcat Modelling of Mineral Prospectivity. Resource Geology 60(2), 129-149.

Carranza, E.J.M. 2014. Data-driven evidential belief modeling of mineral potential using few prospects and evidence with missing values. Natural Resources 24(3), 291-304.

Carranza, E.J.M., Hall, M. 2002. Mineral mapping with Landsat thematic mapper data for hydrothermal alteration mapping in heavily vegetated terrane. International Journal of Remote Sensing 23(22), 4827-4852.

Cheng, Q., Agterberg, F.P., Ballantyne, S.B. 1994. The separation of geochemical anomalies from background by fractal methods. Journal of Geochemical Exploration 51(2), 109-130.

Chung, C.F., Agterberg, F.P. 1980. Regression models for estimating mineral resources from geological map data. Mathematical Geology 12(5), 472-488.

Chung, C.F., Moon, W.M. 1990. Combination rules of spatial geoscience data for mineral exploration. Geoinformatics 2, 159-169.

Davis, J.C. 2002. Statistics and Data Analysis in Geology, 3rd edn. John Wiley & Sons Inc, New York, pp. 342-353.

Deng, J., Wang Q.F., Wan L., Yang L.Q., Liu X.F. 2007. Singularity of Au distribution in alteration rock type deposit, an example from Dayingezhuang gold ore deposit. In: Zhao P.D., Agterberg F., Cheng Q.M. (Eds.), The 12th Conference of the International Association for Mathematical Geology, China University of Geosciences Press, Wuhan, pp. 44-47.

Deng, J., Wang, Q. F., Wan, L., Yang, L.Q., Zhou, L., Zhao, J. 2008. The random difference of the trace element distribution in skarn and marbles from Shizishan ore field, Anhui Province, China. Journal of China University of Geosciences 19(4), 123-137.

Ford, A., Miller, J.M., Mol, A.G. 2015. A comparative analysis of weights of evidence, evidential belief functions, and fuzzy logic for mineral potential mapping using incomplete data at the scale of investigation. Natural Resources Research 25(1_, 19-33.

Hassanpour, Sh., Afzal, P. 2013. Application of concentration-number (C-N) multifractal modelling for geochemical anomaly separation in Haftcheshmeh porphyry system, NW Iran. Arabian Journal of Geosciences 6(3), 957-970.

Hezarkhani ,A. 2008. Hydrothermal Evolution of the Sonajil Porphyry Copper System, East Azarbaijan Province, Iran: The History of an Uneconomic Deposit. International Geology Review 50(5), 483-501.

Hosseinzadeh, G. H., Mouayed, M., Esfehanipour, R. 2009. Supergene Processes in Sonajil Porphyry Copper Deposit With Respect To Using Of Leached Capping For Estimation of Supergene Enrichment in Porphyry Copper Deposits. Iranian Journal Of Geology Summer, Volume 3, Number 10; Page(s) 85 To 96.

Hosseinzadeh, M.R., Maghfouri,, S., Ghorbani, M., Moayyed, M. 2017. Different types of vein-veinlets related to mineralization and fluid inclusion studies in the Sonajil porphyry Cu- Mo deposit, Arasbaran magmatic zone. Scientific Quarterly Journal geosciences 26(101), 219-230.

Jafarirad, A. 2009. Modeling of conceptual and empirical geospatial datasets for mineral prospecting mapping. PhD thesis, TUC, Germany, 190 pp.

Jafarirad, A., Busch, W. 2011. Porphyry copper prospectivity mapping using interval valued fuzzy sets TOPSIS method in Central Iran. International Journal of Geographical Information Science 3, 312–317.

Jamali, H., Mehrabi, B. 2015. Relationships between arc maturity and Cu-Mo-Au porphyry and related epithermal mineralization at the Cenozoic Arasbaran Magmatic Belt. Ore Geology Reviews 65(2), 487-501.

Joly A., Porwal, A., McCuaig, T. C. 2012. Exploration targeting for orogenic gold deposits in the Granites-Tanami Orogen: Mineral system analysis, targeting model and prospectivity analysis. Ore Geology Reviews 48, 349-383.

Karimi, M., Valadan Zoj, M.J. 2009. Mineral Potential Modeling of Sonajil Copper Prospect Using Fuzzy logic and GIS. Materials and Energy. Quarterly Journal of Science Kharazmi University 8(3), 265-282.

Karimzadeh Somarin, A. 2005. Petrology and geochemistry of early tertiary volcanism of the Mendejin area, Iran, and implications for magma genesis and tectonomagmatic setting. Geodinamica Acta 18(5), 343-362.

Lisitsin, V.A., González-Álvarez, I., Porwal, A. 2013. Regional prospectivity analysis for hydrothermal-remobilized nickel mineral systems in western Victoria, Australia. Ore Geology Reviews 52,100-112.

Lowell, J.D., Guilbert, J.M. 1970. Lateral and vertical alteration-mineralization zoning in porphyry ore deposits. Economic Geology 65(4), 373-408.

Lusty, P.A.J., Scheib, C., Gunn, A.G., Walker, A. S. D. 2012. Reconnaissance-scale prospectivity analysis for gold mineralization in the Southern Uplands-Down-Longford Terrane, Northern Ireland. Natural Resources Research 21(3), 359-382.

Magalhaes, L.A., Souza Filho, C.R. 2012. Targeting of gold deposits in Amazonian exploration frontiers using knowledge- and data-driven spatial modeling of geophysical, geochemical and geological data. Surveys in Geophysics 33(2), 211-214.

McInnes, B.I.A., Evans, N.J., Belousova, E., Griffin, W. T., Andrew R. L. 2003. Timing of mineralization and exhumation processes at the Sar Cheshmeh and Meiduk porphyry Cu deposits, Kerman belt, Iran. In: Eliopoulos, et al. (Eds.), Mineral Exploration and Sustainable Development (7th Biennial SGA Meeting, Athens (August 24–28). Millpress, Rotterdam, pp. 1197-1200

Meyer, C., Hemley, J.J. 1967. Wall rock alteration, in Barnes H. L. ed., Geochemistry of hydrothermal ore deposits: New York, Holt, Rinehart and Winston, p. 166-235.

Moritz, R., Rezeau, H., Ovtcharova, M., Tayan, R., Melkonyan, R., Hovakimyan, S., Ramazanov, V., Selby, D., Ulianov, A., Chiaradia, M., Pulitz, B. 2015. Long-lived, stationary magmatism and pulsed porphyry systems during Tethyan subduction to post-collision evolution in the southernmost Lesser Caucasus, Armenia and Nakhitchevan. Durham Research Online, http://dx.doi.org/10.1016/j.gr.2015.10.009.

Nykanen, V., Groves, D.L., Ojala, V.J., Eilo, P., Gardoll, S.J. 2008. Reconnaissance scale conceptual fuzzy-logic prospectivity modelling for iron oxide copper-gold deposits in the northern Fennoscandian Shield, Finland. Australian Journal of Earth Sciences 55(1), 25-38.

Parsa, M., Maghsoudi, A., Yousefi, M., Sadeghi, M. 2016. Prospectivity modeling of porphyry-Cu deposits by identification and integration of efficient mono-elemental geochemical signatures. Journal of African Earth Sciences 114, 228-241.

Parsa, M., Maghsoudi, A., Yousefi, M. 2017. An improved data-driven fuzzy mineral prospectivity mapping procedure; cosine amplitude-based similarity approach to delineate exploration targets. International Journal of Applied Earth Observation and Geoinformation 58, 157-167.

Pazand, K., Hezarkhani, A., Ataei, M. 2012. Using TOPSIS approaches for predictive porphyry Cu potential mapping: A case study in Ahar-Arasbaran area (NW, Iran), Computers and Geosciences 49 (2012) 62–71.

Pazand, K., Hezarkhani, A., Ataei, M. 2013. The application of lithogeochemical and alteration index for copper mineralization in the Sonajil area, NW Iran. Arabian Journal of Geosciences 6(5), 1447-1456.

Porwal, A., Kreuzer, O.P. 2010. Introduction to the Special Issue: Mineral prospectivity analysis and quantitative resource estimation. Ore Geology Reviews 38(3), 121-127.

Porwal, A., Carranza, E.J.M. 2015. Introduction to the Special Issue: GIS-based mineral potential modelling and geological data analyses for mineral exploration. Ore Geology Reviews 71, 477-483.

Richards, J.P. 2015. Tectonic, magmatic, and metallogenic evolution of the Tethyan orogen: From subduction to collision. Ore Geology Reviews 70, 323-345.

Richards, J.P., Sholeh, A. 2016. Chapter 7- The Tethyan Tectonic History and Cu-Au Metallogeny of Iran. Economic Geologists, Inc. Special Publication 19, 193-212.

Seedorff, E., Dilles, J.H., Phoffett, Jr., J.M., Einaudi, M.T., Zurcher, L., Stavast, W.J.A., Johnson, D.A., Barton, M.D. 2005. Porphyry deposits: Characteristics and origin of hypogene features. Littleton. Economic Geology One Hundredth Anniversary Volume, 251-298.

Sillitoe, R.H. 2010. Porphyry copper systems. Economic Geology 105, 3-41.

Shahabpour, J., Kramers, J.D. 1987. Lead isotope data from the Sar Cheshmeh porphyry copper deposit, Kerman. Iran. Mineralium Deposita 22, 278-281.

Stocklin, J. 1974. Possible ancient continental margins in Iran. In: Burk, C.A., Drake, C.L. (Eds.), The Geology of Continental Margins. Springer, Berlin, pp. 873-887.

Tsoukalas, L.H., Uhrig, R.E. 1997. Fuzzy and neural approaches in engineering. Wiley, New York, p 587.

Wang, Y.M., Chin, K.S. 2011. Fuzzy data envelopment analysis: A fuzzy expected value approach. Expert Systems with Applications 38(9), 11678-11685.

Wang, G., Zhu, Y., Zhang, S., Yan, C., Song ,Y., Ma, Z., Hong, D., Chen, T. 2012. 3D geological modeling based on gravitational and magnetic data inversion in the Luanchuan ore region, Henan Province, China. Journal of Applied Geophysics 80, 1-11.

Wang, G., Pang, Z., Boisvert, J.B., Hao, Y., Cao, Y., Qu, J. 2013. Quantitative assessment of mineral resources by combining geostatistics and fractal methods in the Tongshan porphyry Cu deposit (China). Journal of Geochemical Exploration 134, 85-98.

Wang, W., Zhao, J., Cheng, Q., Carranza, E.J.M. 2014. GIS-based mineral potential modeling by advanced spatial analytical methods in the southeastern Yunnan mineral district, China. Ore Geology Reviews 71, 735-748.

Yazdi, Z., Jafarirad, A.R., Ajayebi, K.S. 2014. Analysis and modeling of geospatial datasets for porphyry copper prospectivity mapping in Chahargonbad area, Central Iran. Arabian Journal of Geosciences 8(10), 8237-8248.

Yousefi, M. 2017. Recognition of an enhanced multi-element geochemical signature of porphyry copper deposits for vectoring into mineralized zones and delimiting exploration targets in Jiroft area, SE Iran. Ore Geology Reviews 83, 200-214.

Yousefi, M., Kamkar-Rouhani, A., Carranza, E.J.M. 2012. Geochemical mineralization probability index (GMPI): a new approach to generate enhanced stream sediment geochemical evidential map for increasing probability of success in mineral potential mapping. Journal of Geochemical Exploration 115, 24-35.

Yousefi, M., Carranza, E.J.M., Kamkar-Rouhani, A. 2013. Weighted drainage catchment basin mapping of stream sediment geochemical anomalies for mineral potential mapping. Journal of Geochemical Exploration 128, 88-96.

Yousefi, M., Carranza, E.J.M. 2014. Data-driven index overlay and Boolean logic mineral prospectivity modeling in greenfields exploration. Natural Resources Research 25(1), 3-18.

Yousefi, M., Carranza, E.J.M. 2015*a*. Fuzzification of continuous-value spatial evidence for mineral prospectivity mapping. Computers and Geosciences 74, 97-109.

Yousefi, M., Carranza, E.J.M. 2015*b*. Prediction-area (P-A) plotand C-A fractal analysis to classify and evaluate evidential maps for mineral prospectivity modeling. Computers and Geosciences 79, 69–81.

Yousefi, M., Nykanen, V. 2016. Data-driven logistic-based weighting of geochemical and geological evidence layers in mineral prospectivity mapping. Journal of Geochemical Exploration 164, 94-106.

Bull. Min. Res. Exp. (2019) 158: 251-263

Bulletin of the Mineral Research and Exploration

http://bulletin.mta.gov.tr

Factors controlling the paleo-sedimentary conditions of Çeltek oil shale, Sorgun-Yozgat/Turkey

Berna YAVUZ PEHLİVANLI[a*]

[a] *Bozok University, Department of Geological Engineering, 66900, Atatürk Road, Yozgat, Turkey. orcid.org/0000-0003-0127-8525*

Research Article

Keywords:
Paleo-environment, paleo-salinity, paleo-climate, chemical alteration index (CIA), Çeltek formation oil shales (ÇFOS), total organic carbon (TOC).

ABSTRACT

The study field covering an area of about 1000 km^2 is located in Sorgun town of the city of Yozgat. In the region Paleozoic, Campanian-Maastrichtian, Eocene, Miocene and Quaternary units are exposed. Among these units, the lower Eocene Çeltek formation hosts coal beds and oil shale. The Eocene epoch is important for organic matter deposition regarding oil and gas productivity and anoxic depositional conditions. In order to examine the paleo-sedimentary conditions of oil shales in the study area and their relation to Total Organic Carbon (TOC) contents and major-trace element contents, a total of 29 samples were collected from two boreholes and one Measured Stratigraphic Section (MSS). Samples have TOC contents varying from 1.97 to 16.17 wt% (average 6.30 wt%). The V/Cr, V/(V+Ni), U/Th, δU and Authigenic Uranium (AU) values of the Çeltek formation oil shales (ÇFOS) reveal that the oil shales have been deposited under variable paleo-environmental conditions. For paleo-salinity the Sr/Ba ratios indicate mostly deposition in a freshwater environment. Chemical Alteration Index (CIA) values and Sr/Cu ratios indicate that paleo-climate conditions of ÇFOS were dry, hot and occasionally humid. The Fe/Ti and (Fe+Mn)/Ti ratios reveal hydrothermal activity during sedimentation of oil shales. Zr/Rb ratios of samples are indicative of very weak paleo-hydrodynamics during the deposition of oil shales. Such variable geochemical conditions in the basin resulted in variable paleo-environmental conditions.

Received Date: 28.02.2018
Accepted Date: 25.09.2018

1. Introduction

Some trace elements behave in a sensitive manner under variable redox conditions; thus, they are very useful for the determination of the paleo-redox conditions in depositional environments (Calvert and Pedersen, 1993; Jones and Manning, 1994; Wignall, 1994; Crusius et al., 1996; Dean, 1993, 1997; Yarincik et al., 2000; Morford et al., 2001; Pailler et al., 2002). These trace elements are significantly accumulated in laminated organic-rich facies deposited under euxinic conditions. However, they are hardly ever found in bio-turbation and organic-poor facies.

There are several studies regarding the redox conditions during oil shale deposition and the relation between TOC content and redox-sensitive trace elements (Vine and Tourtelot, 1970; Holland, 1984; Robl and Barron, 1987; Özlük, 2010; Koca et al., 2010; Sarı et al., 2010; Koca, 2011; Yavuz Pehlivanlı, 2011; Sarı and Koca, 2012; Yavuz Pehlivanlı et al., 2013; Koralay and Sarı, 2013; Sarı et al., 2016).

For example, uranium exists as U^{6+}soluble under oxic-suboxic conditions and its enrichment is restricted to oxic environments (Calvert and Pedersen, 1993). Under anoxic conditions uranium is reduced to U^{4+}form. Under reducing conditions, uranium within the sediments forms ligands in the presence of humic acids and is enriched as uraninite (UO_2) at sediment-water interface (Klinkhammer and Palmer, 1991). Although reducing of $U^{6+}$is believed to be controlled by Fe redox reactions, the presence of H_2S may also give rise to sulfate reduction (Langmuir, 1978; Klinkhammer and Palmer, 1991; Zheng et al., 2002).

* *Corresponding author: Berna YAVUZ PEHLİVANLI, bernayavuz80@gmail.com*
http://dx.doi.org/10.19111/bulletinofmre.494703.

Vanadium, nickel and cobalt are very important for determining the redox conditions of depositional environments. Under oxic conditions vanadium exists as V^{+5} in vanadate ions (Wehrli and Stumm, 1989). Humic and fulvic acids catalyze the reduction from vanadate to vanadyl (Templeton and Chasteen, 1980). Vanadium can be adsorbed as V^{4+} or transferred to the sediment as organometallic ligands (Morford and Emerson, 1999). Under extremely reducing conditions, e.g. in the presence of free H_2S, V is reduced to V^{3+}. Vanadium enters the medium in form of geo-porphyrine, solid oxide (V_2O_3) or hydroxide ($V(OH)_3$) (Breit and Wanty, 1991). Vanadium is reduced through a two-stage process which results in the formation of different V phases with different solubility under non-sulfidic anoxic versus euxinic conditions (Calvert and Pedersen, 1993).

Nickel generally occurs as Ni-carbonate ($NiCO_3$) or dissolved species accompanied by humic and fulvic acids (Achterberg et al., 1997). Under oxic conditions it occurs as Ni^{+2} or $NiCl^{+}$ ions (Calvert and Pedersen, 1993).The presence of organic compounds accelerates the transfer of Ni to the sedimentary environment and Ni is free in pore water at the sediment-water interface. Under anoxic conditions it may also be hold in pyrite as solid solution (Huerta-Diaz and Morse, 1992; Morse and Luther, 1999).

At oxic conditions cobalt may form compounds of dissolved cations (Co^{+2}) or humic and fulvic acids (Achterberg et al., 1997) and may exist as insoluble sulfide (CoS) at anoxic conditions (Huerta-Diaz and Morse, 1992). Moreover, since Co is slowly absorbed due to kinetic reasons, it is rarely found in authigenic sulfides (Morse and Luther, 1999).

Based on Ni/Co, V/Cr and V/(V+Ni) ratios the paleo-environmental conditions of organic-rich sedimentary rocks can be assessed (Hatch and Leventhal, 1992; Jones and Manning, 1994; Rimmer, 2004). Li et al. (2018) reconstructed the paleo-environmental conditions through the V/Cr, V/(V+Ni), U/Th, δU and Authigenic Uranium (AU) values; the Sr/Ba ratio was used for paleo-salinity; paleo-climate data was used for Chemical Index of Alteration (CIA); and Sr/Cu ratios, Fe/Ti and (Fe+Mn)/Ti ratios for hydrothermal activity during sedimentation of oil shales, and Zr/Rb ratios for paleo-hydrodynamics.

The aim of this study is to examine the organic material abundance, the paleo-salinity, the paleo-climate, the hydrothermal conditions during deposition and the factors affecting the paleo-environmental characteristics (e.g. paleo-hydrodynamics) of oil shale samples obtained from Çeltek formation in the vicinity of Sorgun, Yozgat area, Central Turkey (Figure 1).

2. Geological Setting

The study area covering an area of about 1000 km^2 is located close to Sorgun town of the city of Yozgat (Figure 1). In the region Paleozoic, Campanian-Maastrichtian, Eocene, Miocene and Quaternary units crop out. The central Anatolian granitoids (Erler and Bayhan, 1993; Dönmez et al., 2005) are

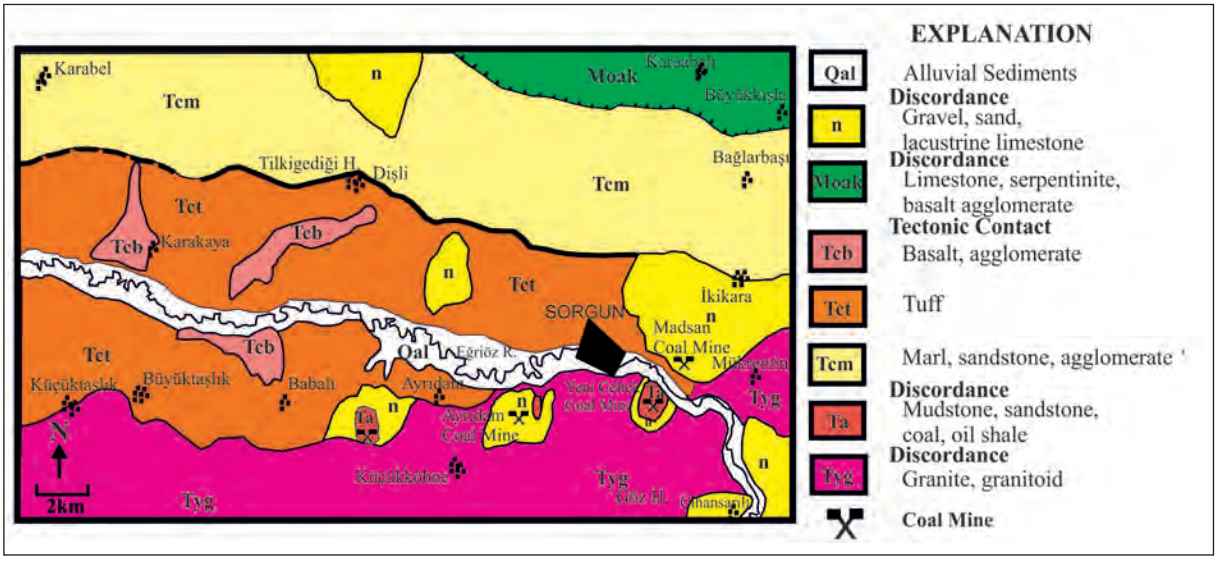

Figure 1- Geological map of the study area (Cicioğlu, 1995).

the oldest rock units around the study area which are unconformably overlain by the lower Eocene Çeltek formation composed of sandstone, coal, oil shale, lenticular sandstone and mudstone alternations (Cicioğlu, 1995). This formation is unconformably covered by the lower-middle Eocene Boğazköy formation starting with a basal conglomerate and continuing to the top with volcanic-interbedded sandstone, fossiliferous limestone, clay stone, clayey limestone, marl and various volcanic rocks including rhyolite, rhyolitic tuff, agglomerate, dacite, andesite and basalt. At the end of Lutetian ophiolitic rocks of the İzmir-Ankara-Erzincan suture zone were thrusted over the Boğazköy formation. All these units are overlain by Neogene deposits (Figures 1 and 2) (Cicioğlu, 1995; Beyazpirinç et al., 2014). The Kızılırmak formation, from bottom to the top consists of terrestrial conglomerate, sandstone, siltstone, claystone, mudstone and limestone (Beyazpirinç et al., 2014). It is covered by Anatolian granitoids and Plio-Quaternary units.

3. Material and Methods

Nineteen Çeltek formation oil-shale (ÇFOS) samples were collected from three different locations in the coal field of the Yeni Çeltek Coal Management in Sorgun: nine surface samples from a Measured Stratigraphic Section (MSS) (YÇ) and 10 samples from two cores (SJ and Ç). The samples from the MSS were taken systematically and the core samples were collected at 10 cm intervals per meter (Figure 3). Major and trace element contents were determined at the laboratories of the Bozok University. About 30 g of each sample was grinded to pass the 90 μm mesh. For trace and rare earth element contents 0.5 g sample was analyzed through ICP-ES (ICP emission spectrometry) and ICP-MS (ICP mass spectrometry) techniques at the Acme Analytical Laboratories Ltd (Canada). Moreover, the samples were analyzed using a Rock-Eval VI pyrolysis device at the Laboratories of the Turkish Petroleum Corporation (TPAO).

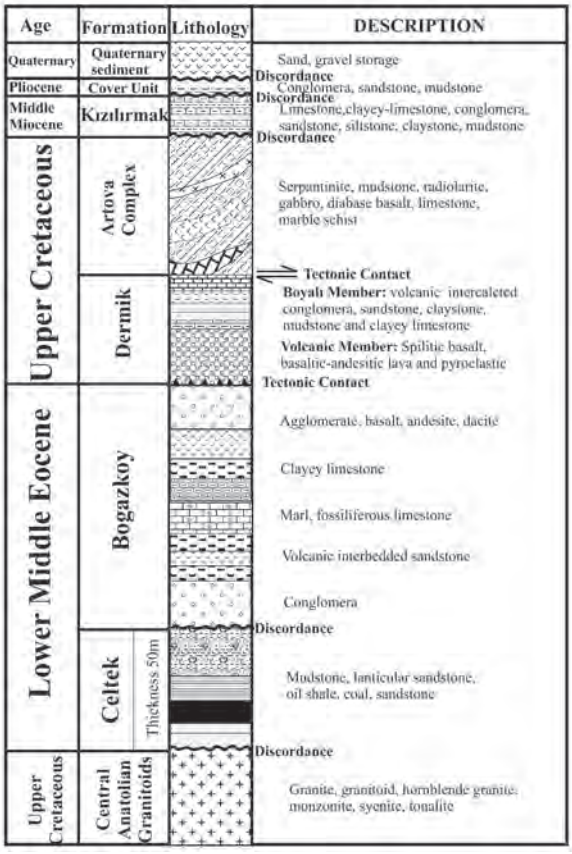

Figure 2- Generalized stratigraphic section of the study area of Sorgun basin (Modified from Beyazpirinç et al., 2014; Cicioğlu, 1995).

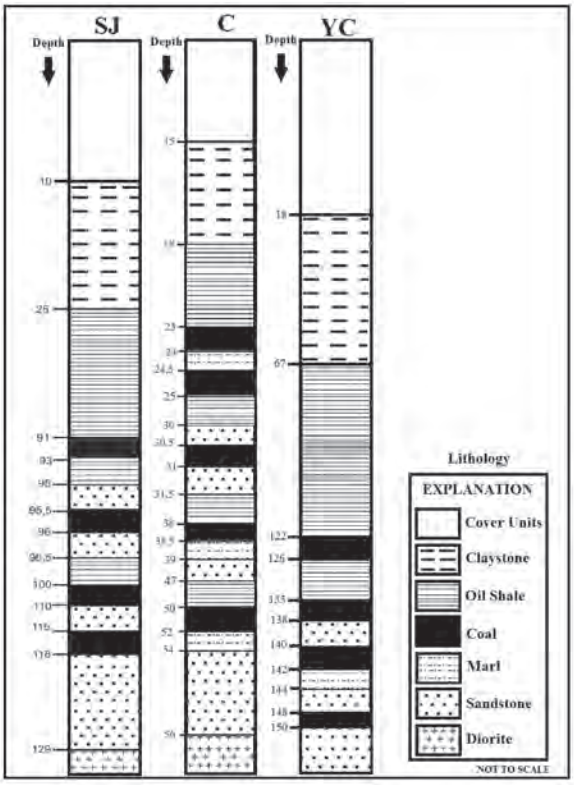

Figure 3- The lithological columns of the SJ and Ç cores and the YC Measured Stratigraphic Section (MSS) (not to scale).

4. Results and Discussion

4.1. Rock Eval Pyrolysis

The TOC (Total Organic Carbon) contents of oil shales range from 1.97 to 16.17 % with average of 6.30 %. The values show very good to prefect source rock character (Table 1).The HI-OI and HI-T_{max} diagrams indicate that the organic material consists of Type-1 and Type-2 kerogen (Figure 4a and b). Considering the T_{max} values (Table 2) and the kerogen types, the samples are generally within the oil window and depth-dependent variations of samples are indicative of immature to early mature stages (Espitalie et al., 1984).

Table 1- Source rock properties of ÇFOS based on Total Organic Carbon (TOC) content.

Peters and Cassa (1994)		Tissot and Welte (1984)		Jarvie (1991)		Sample	TOC (%)	Source Rock Quality
Corg (%)	Oil Potential	TOC (%)	Source Rock Quality	TOC (%)	Source Rock Quality			
0-0.5	Weak	0.1-0.5	Weak	0-0.5	Insufficient			
0.5-1	Middle	0.5-1	Middle	0.5-1	Middle	C	1.97-16.17	Good - Very Good
1-2	Good	1- 2	Good	>1	Enough	YC	2.14-14.85	Very Good
2- 4	Very good	2 - 10	Rich			SJ	2.48-3.13	Very Good

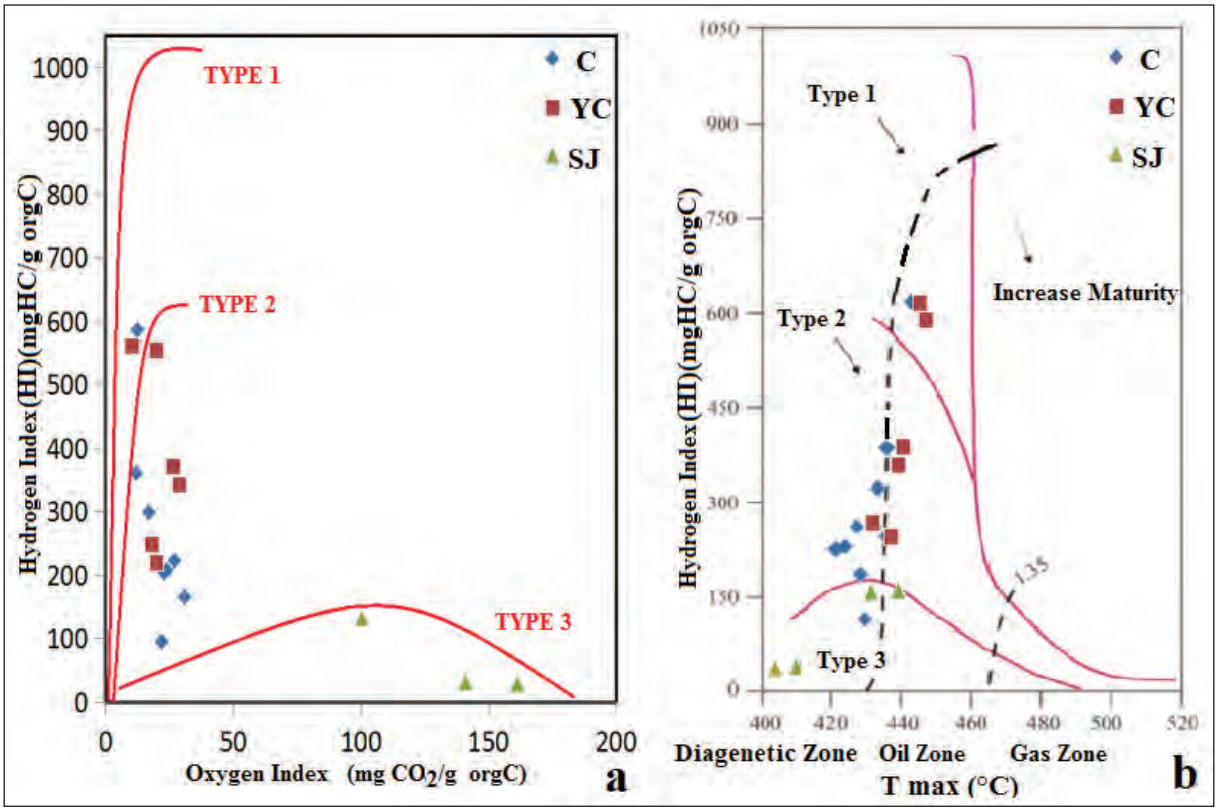

Figure 4 a- Characterization of organic matter in HI vs. OI diagram (Espitalie et al., 1977); b-Plot of Hydrogen Index (HI) vs. T_{max} of the ÇFOS samples (Mukhopadhyay et al., 1995).

Table 2- T_{max} limit values of ÇFOS according to kerogen types (Espitalie et al., 1984).

Type I	Type II	Type III	Degree of Maturation	Sample	TMAX (°C)
	<425 °C	<435 °C	Immature-Early Mature	C	418-436
440-448 °C	425-450 °C	435-465 °C	Oil window	YC	427-439
	>450 °C	>465 °C	Gas window	SJ	404-433

4.2. Elemental Composition

The distribution of major (>0.1 %), minor (between 100 ppm and 0.1%) and trace elements (<100 ppm) reflects the geochemical characteristics of the sediments. Although the use of element abundances is not the sole tool to determine the depositional conditions (Degens et al., 1958), all factors which are adsorbed from the water to organic and inorganic substances, which control the element contribution to the environment, are taken into consideration to figure out the paleo-environmental conditions. The enriched elements are retained within minerals or absorbed in organic material that formed in water at the immediate vicinity and are incorporated into authigenic minerals during or after the sedimentation (Cody, 1971).

In this study, all the samples evaluated are organic-rich oil shales. Major, trace elements and average concentrations of ÇFOS samples were computed (Tables 3 and 4).

4.3. Element Enrichments

Element enrichment of ÇFOS samples were computed on the basis of average shale values (Turekian and Wedepohl, 1961) using the equation:

$[EF_{element}\ X = (X/Al)_{sample} / (X/Al)_{standard}]$ (Brumsack, 2006).

Values >1 represent element enrichment whilst those <1 element depletion (Table 5). Results of calculations reveal that Si, Pb, U and As elements in almost all the samples show enrichment. It is noticeable that uranium appears enriched in all the elements with an enrichment factor varying from 1.19 to 153.7 (Table 5).

4.4. Paleo-environmental Conditions

The paleo-environmental conditions exert a great control on the preservation of organic matter (Li et al., 2018). Some redox-sensitive elements are used for determining the paleo-environmental conditions. In this study, some element ratios such as V/Cr, V/(V+Ni), U/Th, δU[dU=2U/(U+Th/3)] and authigenic uranium (AU=U-Th/3) were used to investigate the paleo-environmental conditions. V/Cr ratios > 4.25 are indicative of strong reducing conditions, those between 2 and 4.25 depict moderate reducing conditions and V/Cr ratios < 2 show oxidative conditions (Teng et al., 2004). V/(V+Ni) ratios > 0.5 are indicative of reducing conditions but ratios lower than this value depict oxidative conditions (Tribovillard et al., 2006). U/Th ratios > 1.25 are indicative of strong reducing conditions, those between 0.75 and 1.25 depict moderate reducing but ratios lower than this value represent oxidation (Ernst, 1970; Jones and Manning, 1994). δU values < 1 indicate oxidation and those > 1 depict reducing conditions (Zhao et al., 2016). AU values > 12 ppm are indicative of strong reducing conditions, those between 5-12 ppm moderate reducing conditions and values < 5 ppm represent oxidation (Deng and Qian, 1993; Teng et al., 2005).

Paleo-environmental assessment for ÇFOS samples based on these parameters are listed in table 6. The average V/Cr, V/(V+ Ni), U/Th, δU and AU values of ÇFOS samples are 3.32, 0.89, 0.61, 1.10 and 34.86, respectively (Table 6). Results of assessments and depth-dependent changes of V/Cr and U/Th reveal variable sedimentation processes and strong reducing to oxidative conditions (Figures 5 and 6).

4.5. Paleo-salinity

The Sr/Ba ratio is used to assess the paleo-salinity in the depositional environment. According to Wang and Wu (1983), Sr/Ba ratio> 1 is indicative of seawater influence, those between 1 and 0.6 depict brackish water and ratios < 0.6 represent freshwater conditions. The Sr/Ba ratios of ÇFOS samples are between 0.05 and 1.27 with a basin average of 0.57. These values indicate that the basin was mostly supplied with freshwater which was occasionally replaced by saline and brackish water (Table 6).

Table 3- Average main element contents (in %) of the ÇFOS samples from Sorgun Basin.

Sample	SiO_2	Al_2O_3	Fe_2O_3	MgO	CaO	Na_2O	K_2O	TiO_2	P_2O_5	MnO	Cr_2O_3
C avr (n=10)	42.06	20.42	4.18	0.46	1.13	0.17	2.02	0.51	0.06	0.06	0.003
YC avr (n=9)	46.38	22.23	6.25	0.93	0.66	0.19	2.42	0.48	0.10	0.12	0.005
SJ avr (n=10)	59.94	13.72	4.63	1.28	4.73	1.14	3.91	0.52	0.10	0.06	0.005
ÇFOS Average	49.46	18.79	5.02	0.89	2.17	0.50	2.78	0.50	0.08	0.08	0.004

Table 4- Average trace element contents (in ppm) of the ÇFOS samples from Sorgun Basin.

Sample	Ba	Sc	Co	Cs	Ga	Hf	Nb	Rb	Sn	Sr	Ta	Th	U	V	W	Zr	Mo	Cu	Pb	Zn	Ni	As	Cd	Sb	Bi
C avr (n=10)	724.1	7.1	10.6	22.5	25.1	5.0	18.2	142.9	4.5	228.8	1.0	63.0	45.6	74.1	34.5	187.0	3.3	18.7	104.1	100.5	7.9	28.6	0.3	0.8	2.7
YC avr (n=9)	370.4	12.0	17.4	20.8	26.9	3.8	13.7	153.3	4.5	185.9	0.8	49.4	13.4	112.6	27.8	132.9	4.0	27.8	72.0	166.0	12.4	34.5	0.4	0.5	2.4
SJ avr (n=10)	732.8	9.3	15.7	37.1	14.8	5.3	13.9	186.1	3.2	409.7	0.9	29.3	81.5	82.5	75.4	214.2	4.5	17.6	41.6	72.1	12.6	39.5	0.2	0.7	0.8
ÇFOS Average	609.1	9.5	14.5	26.8	22.2	4.7	15.3	160.8	4.1	274.8	0.9	47.2	46.9	89.7	45.9	178.0	3.9	21.4	72.6	112.9	11.0	34.2	0.3	0.7	2.0

Table 5- Elemental enrichment factors of ÇFOS samples in comparison to the World Shale Average (Turekian and Wedepohl, 1961).

According to Average Shale EF	Mn	Mg	Fe	Si	K	Ti	Ca	Na	**Pb**	Zr	P	Sr	Rb	**U**	Ba	Cu	Ni	**As**	V	Zn	Sb	Co	Mo	Cd
C5	0.75	0.24	0.42	**2.90**	0.85	0.74	0.62	0.31	**2.53**	**1.66**	0.31	0.73	**1.02**	**3.64**	0.89	0.26	0.08	**1.10**	0.40	0.67	0.17	0.51	0.08	0.28
C8	**2.27**	0.30	**1.33**	**3.24**	0.94	0.59	**2.40**	0.32	**2.97**	**1.47**	0.49	**1.48**	**1.09**	**5.68**	**1.21**	0.44	0.17	**3.82**	0.62	0.84	0.53	0.97	0.30	0.44
C10	0.27	0.23	0.70	**2.07**	0.54	0.52	0.16	0.10	**3.18**	0.76	0.55	0.58	0.81	**4.16**	0.52	0.46	0.18	**2.42**	0.50	**1.43**	0.38	0.64	0.15	0.67
C12	**1.19**	0.17	0.55	**2.15**	0.57	0.52	0.12	0.09	**2.46**	0.77	0.43	0.57	0.79	**2.65**	0.61	0.32	0.11	**1.98**	0.47	**1.41**	0.32	0.50	0.08	0.46
C19	0.37	0.15	0.43	**2.10**	0.57	0.61	0.08	0.07	**3.01**	0.90	0.20	0.52	0.81	**2.35**	0.60	0.29	0.11	**2.12**	0.46	0.57	0.21	0.54	0.06	0.21
C22	0.06	0.13	0.41	**2.89**	0.77	0.83	0.07	0.17	**3.49**	**2.08**	0.19	0.62	0.94	**2.92**	**1.00**	0.28	0.12	**1.71**	0.46	**1.33**	0.36	0.63	0.11	0.39
C28	0.03	0.07	0.14	**1.41**	0.22	0.44	0.06	0.02	**2.84**	0.42	0.15	0.36	0.67	**9.00**	0.21	0.34	0.01	0.28	0.21	0.13	0.34	0.04	0.20	0.07
C29	0.10	0.07	0.95	**1.27**	0.12	0.22	0.17	0.02	**19.69**	0.33	0.72	0.74	0.37	**85.78**	**7.34**	0.32	0.11	**3.99**	0.89	**2.22**	**1.97**	0.52	**1.07**	**2.15**
C32	0.07	0.07	0.41	**1.40**	0.25	0.49	0.09	0.02	**2.28**	0.60	0.05	0.40	0.66	**5.80**	0.22	0.15	0.03	**1.86**	0.32	0.29	0.29	0.23	0.33	0.15
C33b	0.04	0.06	0.16	**1.37**	0.18	0.38	0.07	0.02	**3.10**	0.30	0.10	0.34	0.54	**2.87**	0.18	0.26	0.03	**0.29**	0.33	0.19	0.14	0.15	0.27	0.17
YC2	0.05	0.08	0.46	**1.44**	0.21	0.40	0.07	0.02	**2.92**	0.32	0.17	0.27	0.57	**4.60**	0.20	0.36	0.05	**1.77**	0.44	**2.17**	0.36	0.77	0.70	0.67
YC5	**2.86**	0.32	**1.22**	**2.03**	0.52	0.60	0.32	0.06	**2.77**	0.88	0.51	0.50	0.74	**2.18**	0.55	0.26	0.09	0.97	0.46	0.71	0.20	0.50	0.07	0.25
YC6	0.48	0.16	0.39	**2.10**	0.54	0.56	0.11	0.06	**2.62**	0.82	0.41	0.47	0.79	**2.92**	0.54	0.32	0.13	**1.30**	0.47	0.75	0.26	0.55	0.11	0.32
YC7	0.18	0.19	0.52	**2.28**	0.59	0.55	0.15	0.08	**2.54**	0.87	0.65	0.56	0.82	**3.01**	0.61	0.42	0.11	**1.65**	0.49	**2.14**	0.20	0.99	0.14	0.99
YC10	0.36	0.28	0.52	**1.89**	0.53	0.41	0.14	0.11	**2.34**	0.39	0.58	0.32	0.72	**1.44**	0.36	0.62	0.20	**1.67**	0.73	0.59	0.29	0.77	0.16	0.21
YC12	0.56	0.32	0.74	**2.44**	0.56	0.39	0.17	0.08	**2.17**	0.46	0.43	0.48	0.80	**1.95**	0.47	0.39	0.15	**2.63**	0.69	0.71	0.20	0.56	0.33	0.25
YC13	0.84	0.26	0.63	**1.83**	0.51	0.39	0.12	0.09	**1.91**	0.40	0.32	0.38	0.74	**2.05**	0.37	0.45	0.12	**2.80**	0.68	0.68	0.21	0.42	0.28	0.21
YC14	0.64	0.35	0.56	**2.15**	0.59	0.50	0.12	0.27	**2.37**	0.45	0.28	0.42	0.79	**1.69**	0.42	0.51	0.13	**1.62**	0.73	**1.83**	0.22	0.43	0.18	0.33
YC15	0.17	0.35	0.70	**2.10**	0.59	0.44	0.13	0.13	**2.17**	0.42	0.51	0.43	0.82	**5.67**	0.41	0.59	0.21	**1.52**	0.74	0.51	0.09	**1.23**	0.12	0.56
SJ2	0.61	0.53	0.65	**4.69**	**1.42**	0.84	**3.16**	**1.11**	**1.49**	**1.60**	0.70	**1.67**	**1.37**	**1.78**	**1.94**	0.32	0.33	**1.12**	0.53	0.45	0.33	0.65	0.06	0.21
SJ4	**3.23**	**1.32**	**1.27**	**5.41**	**1.97**	0.70	**7.92**	0.25	**4.73**	**3.24**	0.74	**2.38**	**2.25**	**24.85**	**1.29**	0.42	0.22	**1.21**	0.76	**1.31**	0.45	**1.34**	0.05	0.28
SJ6	0.68	0.82	0.78	**3.92**	**1.35**	0.89	1.82	**1.58**	**2.51**	**1.49**	**1.03**	**1.49**	**1.55**	**23.10**	**1.65**	0.45	0.30	**2.44**	0.84	**1.05**	0.28	0.88	0.01	0.34
SJ8	**1.62**	0.74	0.94	**3.78**	**1.11**	**1.08**	**7.07**	**2.64**	**2.85**	**1.85**	**1.39**	**3.85**	**1.21**	**3.13**	**1.57**	0.23	0.18	**1.93**	0.74	0.61	0.53	**1.00**	0.01	0.44
SJ10	0.15	0.49	**1.09**	**3.02**	0.96	0.73	0.21	0.12	**3.25**	0.98	0.35	0.90	**1.47**	**9.62**	0.69	0.62	0.33	**6.90**	0.73	**1.96**	0.50	**1.12**	0.48	**1.25**
SJ12	0.07	0.37	0.55	**3.18**	0.96	0.72	0.17	0.18	**2.42**	**1.09**	0.28	0.90	**1.18**	**153.7**	0.74	0.66	0.17	**6.88**	0.71	0.82	**1.88**	0.64	**3.22**	0.59
SJ14	0.09	0.31	0.30	**5.97**	**1.54**	0.66	0.12	**1.03**	**1.19**	**1.41**	0.38	**1.36**	**1.49**	**5.32**	**1.67**	0.14	0.07	**4.87**	0.41	0.36	0.33	0.81	0.07	0.18
SJ16	0.18	0.43	**1.05**	**4.80**	**1.27**	0.92	0.13	0.62	**1.16**	**1.83**	0.28	**1.08**	**1.50**	**1.26**	**1.11**	0.30	0.09	**3.37**	0.77	0.54	0.59	0.55	0.04	0.17
SJ19	0.23	0.47	0.59	**3.78**	**1.62**	0.88	0.18	0.88	**1.51**	**1.55**	**1.09**	**1.58**	**1.67**	**2.11**	**2.13**	0.32	0.15	**1.79**	0.62	0.63	0.25	0.63	0.02	0.14
SJ22	0.17	0.54	0.55	**4.88**	**1.55**	0.71	0.17	**1.61**	**1.32**	**1.37**	0.78	**1.57**	**1.36**	**1.19**	**2.04**	0.20	0.07	**1.74**	0.38	0.53	0.28	0.61	0.01	0.16
ÇFOS Average	0.63	0.34	0.66	**2.84**	0.81	0.61	0.90	0.42	**3.10**	**1.06**	0.48	0.93	**1.02**	**12.98**	**1.09**	0.37	0.14	**2.34**	0.57	0.95	0.42	0.66	0.30	0.43
World Average Shale (Element/Al)	96.00	0.19	0.59	0.91	0.33	0.05	0.28	0.12	2.50	20.00	0.01	37.50	17.50	0.46	72.50	5.63	8.50	1.63	16.25	11.8	0.19	2.38	1.38	0.08

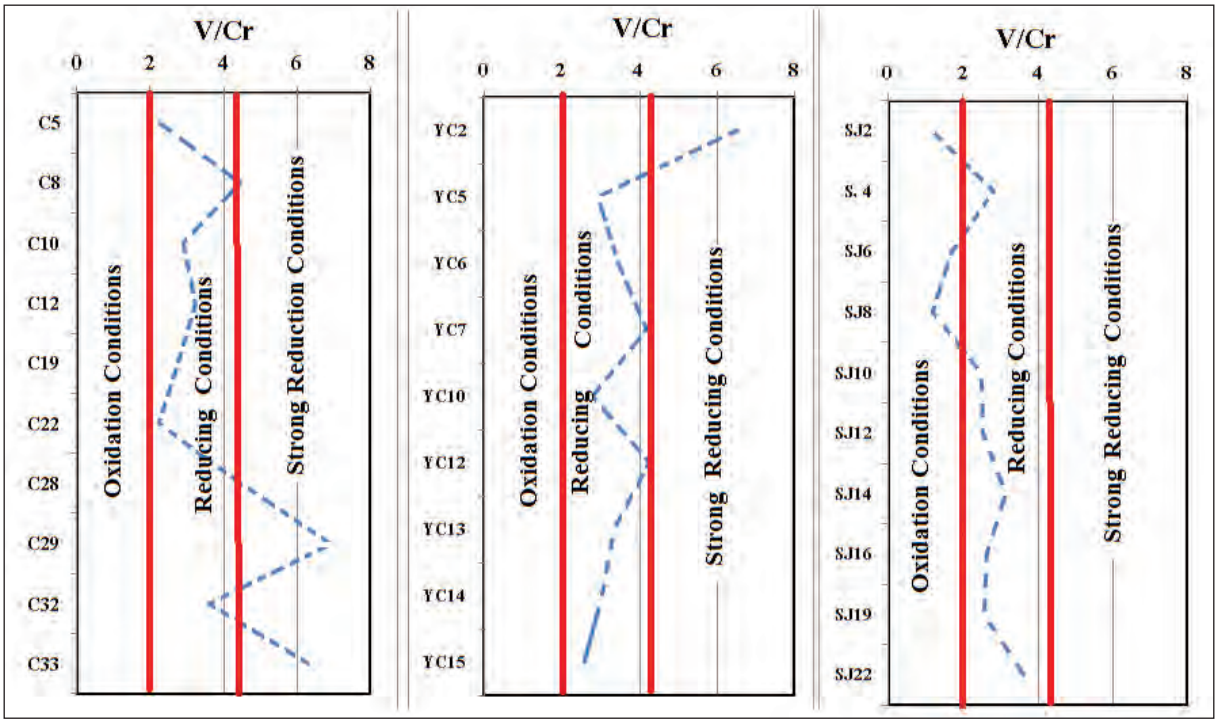

Figure 5- According to V / Cr ratios, Depth-dependent redox changes of ÇFOS.

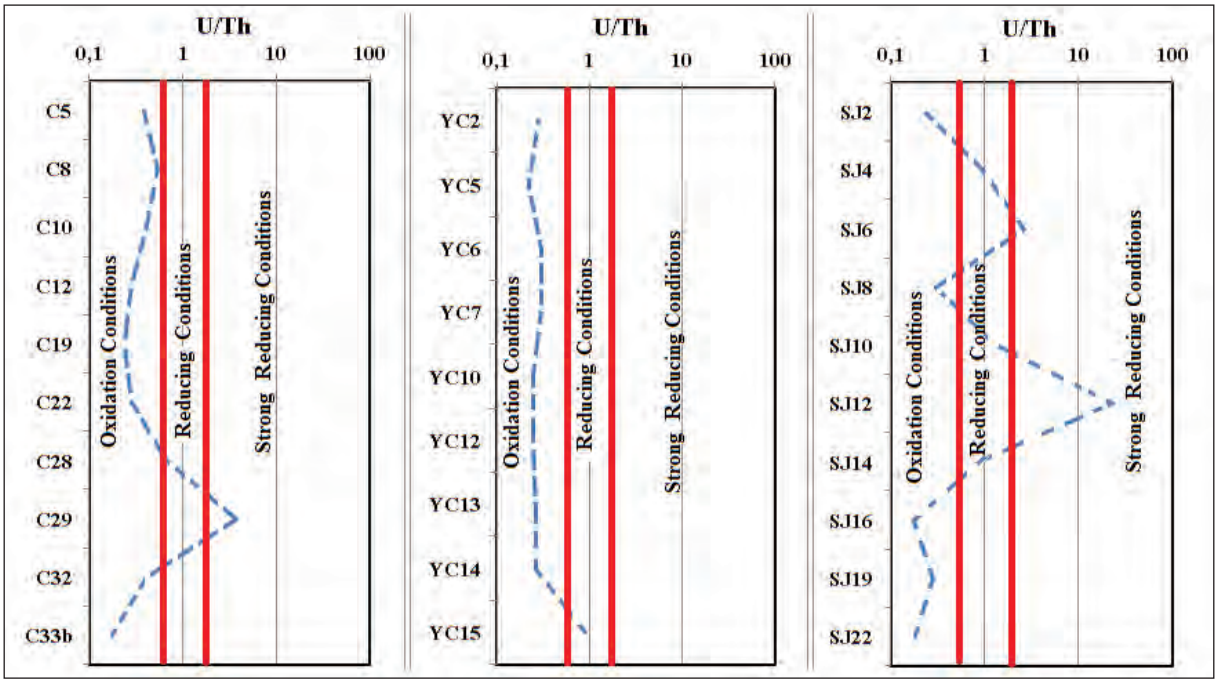

Figure 6- According to U/Th ratios, Depth-dependent redox changes of ÇFPS.

Table 6- The parameters characterizing the paleo-depositional environment of the ÇFOS samples.

Sample	V/Cr	V/(V +Ni)	U/Th	δU	AU	Sr/Ba	CIA	Sr/Cu	Fe/Ti	(Fe+ Mn)/Ti	Zr/Rb
C5	2.30	0.90	0.38	1.07	2.07	0.42	75.66	18.44	6.43	6.65	1.85
C8	4.46	0.87	0.54	1.23	6.07	0.63	58.84	22.34	24.97	25.82	1.54
C10	2.92	0.84	0.41	1.10	3.53	0.59	88.06	8.52	14.94	15.05	1.08
C12	3.25	0.89	0.28	0.91	-2.73	0.48	87.88	11.87	11.58	12.08	1.11
C19	2.75	0.89	0.24	0.83	-5.53	0.45	87.99	11.80	7.96	8.09	1.28
C22	2.25	0.88	0.28	0.92	-2.53	0.32	84.30	14.76	5.52	5.54	2.53
C28	4.46	0.97	0.65	1.32	35.00	0.87	94.70	6.96	3.43	3.45	0.72
C29	6.92	0.94	3.69	1.83	224.23	0.05	96.55	15.45	48.32	48.42	1.00
C32	3.62	0.95	0.41	1.10	4.40	0.97	93.34	18.29	9.36	9.39	1.05
C33b	6.31	0.95	0.18	0.69	-18.47	1.00	95.28	8.81	4.76	4.78	0.63
YC2	6.54	0.95	0.29	0.92	-4.17	0.69	94.88	5.04	12.92	12.94	0.65
YC5	2.96	0.91	0.22	0.80	-5.47	0.47	86.07	12.94	22.84	23.91	1.37
YC6	3.47	0.88	0.31	0.96	-1.47	0.45	88.79	9.83	7.75	7.94	1.18
YC7	4.19	0.89	0.31	0.96	-1.27	0.48	87.73	8.86	10.68	10.75	1.21
YC10	2.80	0.87	0.25	0.86	-2.90	0.46	88.61	3.46	14.00	14.19	0.61
YC12	4.28	0.90	0.25	0.85	-3.27	0.54	87.34	8.30	21.19	21.52	0.65
YC13	3.36	0.91	0.27	0.89	-3.07	0.53	88.46	5.62	18.15	18.63	0.61
YC14	3.05	0.91	0.26	0.88	-2.63	0.52	85.97	5.49	12.53	12.82	0.65
YC15	2.59	0.87	0.91	1.46	19.67	0.54	87.33	4.84	17.73	17.81	0.58
SJ2	1.15	0.76	0.23	0.82	-2.27	0.45	49.55	35.32	8.60	8.77	1.34
SJ4	2.83	0.87	0.97	1.49	35.33	0.96	32.98	37.38	20.16	21.18	1.64
SJ6	1.71	0.84	2.67	1.78	72.30	0.47	56.88	22.33	9.79	9.96	1.10
SJ8	1.19	0.89	0.30	0.95	-0.83	1.27	34.98	114.04	9.68	10.01	1.75
SJ10	2.48	0.81	1.33	1.60	28.57	0.68	80.30	9.71	16.67	16.72	0.76
SJ12	2.53	0.89		1.97	634.80	0.63	80.35	9.10	8.41	8.43	1.06
SJ14	3.14	0.92	0.90	1.46	10.07	0.42	70.16	66.42	4.97	5.00	1.08
SJ16	2.63	0.94	0.18	0.69	-3.70	0.51	74.64	24.02	12.62	12.66	1.40
SJ19	2.57	0.89	0.29	0.93	-1.37	0.38	70.51	33.06	7.38	7.43	1.06
SJ22	3.62	0.92	0.18	0.71	-3.50	0.40	67.92	52.12	8.58	8.63	1.15
ÇFOS Average	3.32	0.89	0.61	1.10	34.86	0.57	78.48	20.87	13.17	13.40	1.13

4.6. Paleo-climate

The climate generally affects mineral alteration, transport and source rock chemistry (Zhang et al., 2011).Thus, the Chemical Index of Alteration (CIA) may be modified by paleo-climate conditions (Bai et al., 2015). The CIA is computed from the equation $CIA=100x[Al_2O_3/(Al_2O_3+CaO^*+Na_2O+K_2O)]$ (Cox et al., 1995).

CIA values between 50 and 65 reflect cold and dry climate conditions during sedimentation. The values between 65 and 85 are indicative of a warm and humid climate regime. If CIA is in the range of 85 to 100, the climate is hot and humid. CIA values of ÇFOS samples vary from 32.98 to 96.55 and the basin average is 78.48 (Table 6). These values show that the paleo-climatic conditions change from cold to dry and hot to humid conditions from time to time, but the environment may have been generally hot and humid.

The Sr/Cu ratios are also informative for paleo-climate conditions. Sr/Cu ratios of 1.3 to 5.0 reflect hot and humid climate regime whilst ratios >5 are indicative of dry and hot conditions (Liang et al., 2015). The Sr/Cu values of ÇFOS samples vary from 3.46 to 114.04 and basin average is 20.87. These findings imply paleo-climate conditions show dry and hot and occasionally hot-humid environment (Table 6).

4.7. Hydrothermal Depositional Conditions

Sediments associated with hydrothermal fluids are called hydrothermal deposits (Zhong et al., 2015). Hydrothermal fluids exert a great control on trace element concentrations and the abundance of organic material accumulated in sedimentary rocks (Chu et al., 2016). The Fe/Ti and (Fe+Mn)/Ti ratios reflect a hydrothermal contribution to the sediments (Li et al., 2018). Fe/Ti ratios >20 and (Fe+Mn)/Ti ratios of 20±5 show hydrothermal interaction with

the sediments (Boström,1983). Fe/Ti and (Fe+Mn)/Ti ratios of ÇFOS samplesreveal that hydrothermal fluids occasionally contributed to element enrichment during sedimentation (Table 6).

4.8. Paleo-hydrodynamics

Zircon is typically deposited in terrestrial and shallow marine environments. Due to its active chemical properties, Rb is likely transported and accumulated in deep water (Teng et al., 2005). Therefore, Zr/Rb can be used for the assessment of changes in water depth. Lower Zr/Rb ratios are a result of deeper sedimentary water circulation and weaker hydrodynamic forces. It is suggested that Zr/Rb ratio of around 0.92 represents weak hydrodynamic forces whilst higher ratios from 1.25 to 4.76 are indicative of an environment with strong paleo-hydrodynamic forces (Teng, 2004; Zhao et al., 2016). The Zr/Rb ratios of ÇFOS samples vary from 0.58 to 2.53 and basin average is 1.13. These values imply that both weak and strong hydrodynamic prevailed from time to time during the sedimentation in the basin (Table 6).

4.9. Factors Controlling the Paleo-environmental Conditions During the Total Organic Carbon (TOC) in Oil Shales

Paleo-environmental data (V/Cr, V/(V+Ni), U/Th, δU, authigenic uranium (AU), Sr/Ba, CIA, Sr/Cu, Fe/Ti, (Fe+Mn)/Ti and Zr/Rb ratios) of the ÇFOS samples were correlated on an individual basis with the total organic carbon (TOC) contents of oil shales (Figure 7a-k). Samples collected from different locations and

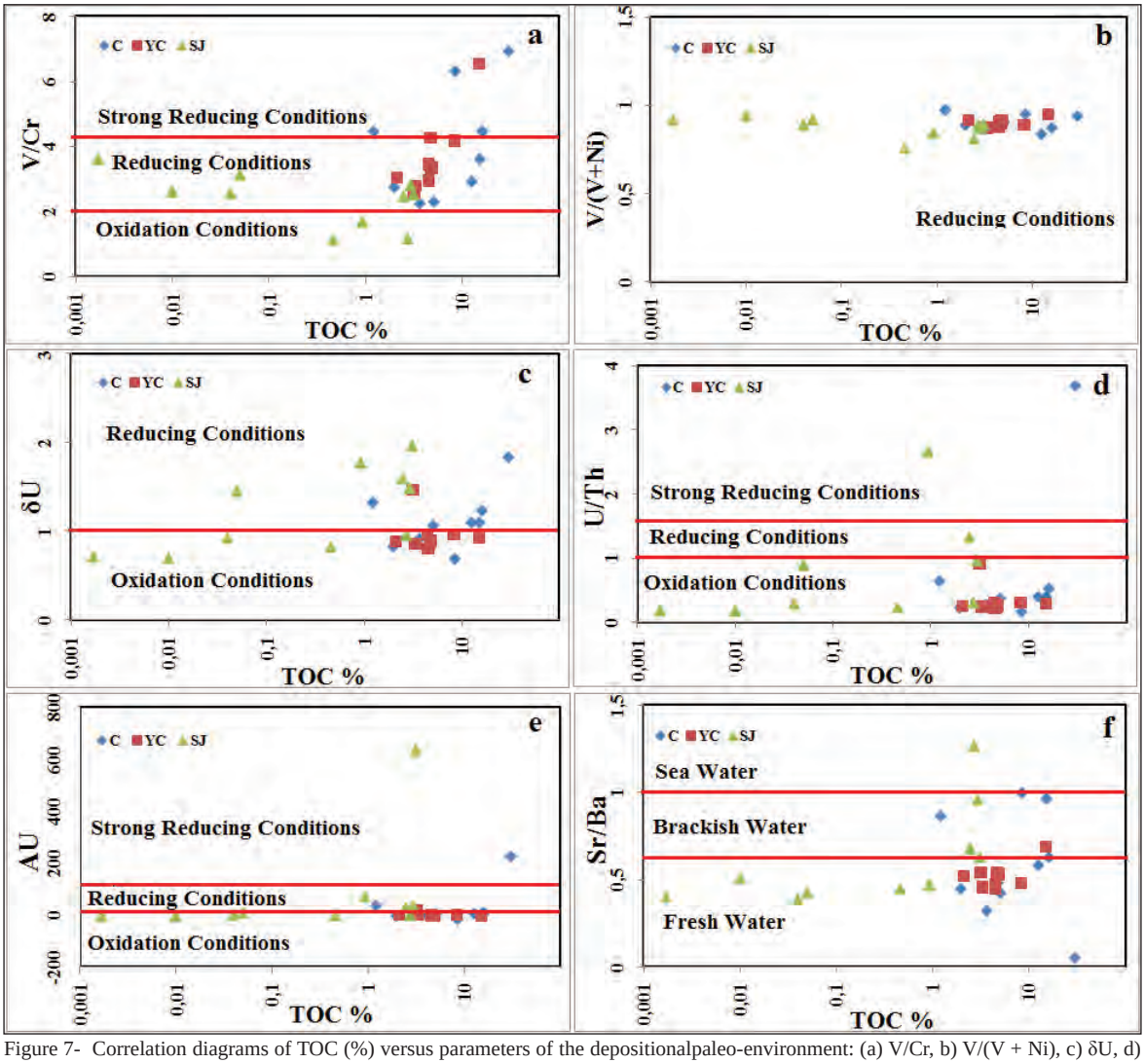

Figure 7- Correlation diagrams of TOC (%) versus parameters of the depositionalpaleo-environment: (a) V/Cr, b) V/(V + Ni), c) δU, d) U/Th, e) Authigenic Uranium (AU), f) Sr/Ba ratios, g) Chemical Index of Alteration (CIA), h) Sr/Cu, i) Fe/Ti, j) (Fe + Mn)/Ti and, k) Zr/Rb of ÇFOS samples (Li et al., 2018).

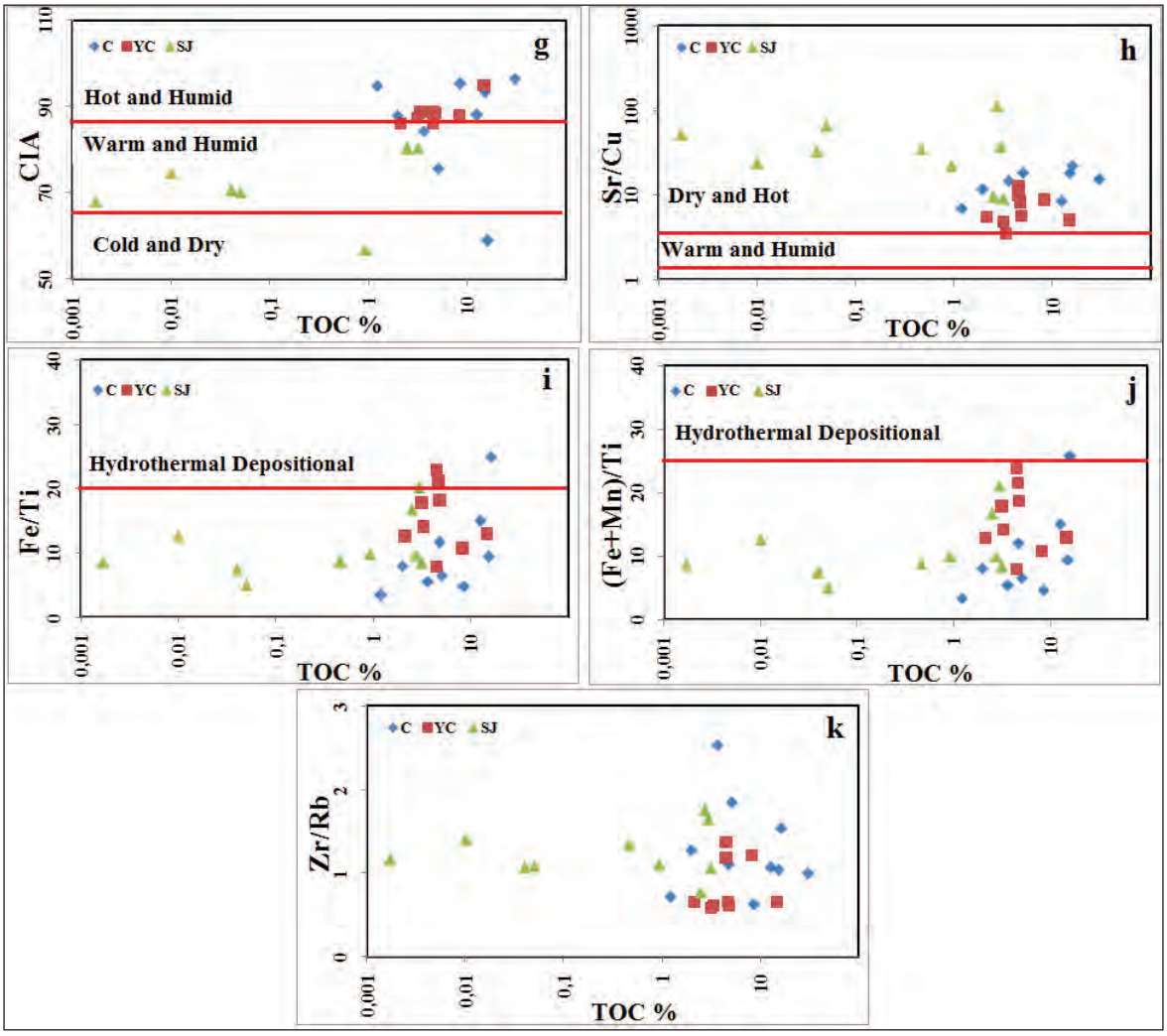

Figure 7- continued.

depths are differently correlated with TOC. Figure 7 reveals that V/Cr (a), CIA (g), Sr/Ba (f), Fe/Ti (i) and (Fe+Mn)/Ti (j) ratios have positive correlation with TOC. The data shows that element characteristics of ÇFOS samples are consistent with the preservation of organic material and high reducing conditions.

5. Conclusions

In this study the conditions dominating during the formation of the oil shales hosted in the Çeltek formation (ÇFOS), are assessed. The samples have TOC values varying from 1.97 to 16.17 wt% (average 6.30 wt%) revealing a very good source rock. The T_{max} values indicate that in respect of the oil window the samples are at immature-early mature stage. Considering the average values of the world shales provided by Turekian and Wedepohl (1961), Si, Pb, U and As reveal enrichment at all sampling locations. Under oxic-suboxic conditions uranium exists as soluble U^{6+} which necessitates the restriction of uranium enrichment to oxic environments. However, as shown from Figure 6, high uranium enrichment is consistent with strong reducing conditions.

Geochemical data of the ÇFOS samples (e.g. V/Cr, V/(V+Ni), U/Th, δU and AU (authigenic uranium)) indicate that the oil shales were deposited under variable paleo-environmental conditions. The Sr/Ba ratios point to deposition in a freshwater environment. The paleo-climatic data of ÇFOS samples show that when the chemical change index (CIA) and Sr / Cu ratios are evaluated, there are sedimentation environments ranging from dry-hot climate to hot-humid climate. Chemical weathering typically increases as temperatures rise and rain falls, which means rocks in hot and wet climates experience faster

rates of chemical weathering than do rocks in cold, dry climates. The Fe/Ti and (Fe+Mn)/Ti ratios reflect hydrothermal contribution during the sedimentation of oil shales. According to the Zr/Rb ratios, weak paleo-hydrodynamics prevailed during deposition. The relations between TOC and redox element ratios indicate that the paleo-environmental conditions exerted a great control on the deposition of organic matter. The studied oil shale samples point to variable redox conditions and therefore, water chemistry, environment-climate conditions and organic productivity on the lake surface must have also varied.

The paleo-climatic data of ÇFOS samples show that when the chemical change index (CIA) and Sr / Cu ratios are evaluated, there is precipitation from dry-hot environments to hot-humid environments.

Acknowledgements

This study was supported by the Scientific Research Projects Committee of the Bozok University under grand no 2015 MMF/180 (Organic geochemistry and rare earth element characteristics of oil shales in the lower Eocene Çeltek formation, Sorgun, Yozgat, Turkey).

References

Achterberg, E. P., Van Den Berg, C. M. G., Boussemart, M., Davison W. 1997. Speciation and Cycling of Trace Metals in Esthwaite Water: A Productive English Lake With Seasonal Deep-Water Anoxia. Geochim. Cosmochim. Acta,Vol. 61, pp. 5233–5253.

Bai, Y., Liu, Z., Sun, P., Liu R., Hu, X., Zhao, H., Xu, Y. 2015. Rare earth and major element geochemistry of Eocene fine-grained sediments in oil shale- and coal-bearing layers of the Meihe Basin, Northeast China. J Asian Earth Sci., 97, Vol., 97, pp. 89–101.

Beyazpirinç, M., Akçay, A.E., Tarhan, N., Sönmez, M.K., Havzoğlu, T., Bilgiç, T., Bademler, F., Ünal, M. 2014. Akdağmadeni masifi nin jeolojisi ve jeodinamik evrimi projesi 2011-2012 yıllarına ait ara rapor. Maden Tetkik ve Arama Genel Müdürlüğü Rapor No: 11763, Ankara (unpublished).

Boström, K. 1983. Genesis of ferromanganese deposits-diagnostic criteria for recent and old deposits. Hydrothermal Processes at Seafloor Spreading Centers, Springer, Berlin, pp 473–489

Breit, G. N., Wanty, R. B. 1991. Vanadium accumulation in carbonaceous rocks: a review of geochemical controls during deposition and diagenesis. Chemical Geology, Vol. 91, pp. 83-97.

Brumsack, H. J. 2006. The trace metal content of recent organic carbon-rich sediments: Implications for Cretaceous black shale formation; Palaeogeography, Palaeoclimatology, Palaeoecology, Vol. 232, pp. 344–361.

Calvert, S. E., Pedersen, T. F. 1993. Geochemistry of Recent oxic and anoxic marine sediments: implications for the geological record. Marine Geology, Vol. 113, pp. 67-88.

Cicioğlu, E. 1995. Sorgun (Yozgat) Kömürlerinin Kimyasal ve Petrografik Özelliklerinin İncelenmesi,Yüksek Lisans Tezi, Hacettepe Üniversitesi, Ankara.

Chu, C. L., Chen, Q. L., Zhang, B., Shi, Z., Jiang, H. J., Yang, X. 2016. Influence on formation of Yuertusi Source Rock by hydrothermal activities at Dongergou section, Tarim Basin. Acta Sedimentol Sin., 34, Vol. 4, pp. 803–810.

Cody, R. D. 1971. Adsorption and the reliability of trace elements as environmental indicators for shales. J. Sediment. Petrol., Vol. 41, pp. 461-471.

Cox, R., Lowe, D. R., Cullers, R. L. 1995. The influence of sediment recycling and Basement Composition of Evolution of Mudrock Chemistry in the Southwestern United States. Geochim Cosmochim Acta, 59, Vol. 14, pp. 2919–2940.

Crusius, J., Calvert, S., Pedersen, T., Sage, D. 1996. Rhenium and molybdenum enrichments in sediments as indicators of oxic, suboxic and sulfidic conditions of deposition. Earth Planet Science Letter, Amsterdam, Vol. 145, pp. 65–78.

Dean, W. E. 1993. Physical properties, mineralogy, and geochemistry of Holocene varved sediments from Elk Lake, Minnesota. In Bradbury J. P., W. E. Dean (eds.), Elk Lake, Minnesota: Evidence for Rapid Climate Change in the North-Central United States. Geol. Soc. America Spec. Paper 276, Boulder (CO), pp. 135–157.

Dean, W. E. 1997. Rates, timing, and cyclicity of Holocene eolian activity in north-central United States: Evidence from varved lake sediments. Geology, Vol. 25, pp. 331–334.

Degens, E. T., Williams, E. G., Keith, M. L. 1958. Environmental studies of carboniferous sediments: part II. Application of geochemical criteria. Bull J Immunol. Vol. 42, pp. 981–997.

Deng, H. W., Qian, K. 1993. Sedimentary geochemistry and environmental analysis. Gansu Science And Technology Press, Gansu (in Chinese).

Dönmez, M., Bilgin, Z. R., Akçay, A. E., Kara, H., Yergök, A. F., Esentürk, K. 2005. Türkiye Jeoloji Haritaları, Kırşehir-İ31 Paftası, No: 46, Maden Tetkik ve Arama Genel Müdürlüğü Yayını, Ankara.

Erler, A., Bayhan, H. 1993. Orta Anadolu Granotoidleri, Hacettepe Üniversitesi, Yer Bilimleri 25. Yıl Sempozyumu, Tebliğ, 20. Sayfa, Ankara.

Ernst, T. 1970. Geochemical Facieses Analysis, Elsevier, Amsterdam, pp. 152.

Espitalie, J., Madec, M., Tissot, B., Mennig, J.J., Leplat, P. 1977. Source rock characterization method for exploration: Proceedings, Ninth Annual Offshore Technology Conference, Vol. 3, p. 439-444.

Espitalie, J., Marquis, F., Borsony, I. 1984. Geochemical logging, in Voorhees, K. J., ed., Analytical pyrolysis: London, Butterworth and Co., Ltd., p. 276-304.

Hatch, J. R., Leventhal, J. S. 1992. Relationship between inferred redox potential of the depositional environment and geochemistry of the Upper Pennsylvanian (Missourian) Stark Shale Member of the Dennis Limestone, Wabaunsee County, Kansas, U.S.A. Chemical Geology, Vol. 99, pp. 65–82.

Holland, H. D. 1984. The Chemical Evolution of the Atmosphere and the Oceans. Princeton University Press, 598 pp.

Huerta-Diaz, M. A., Morse, J. W. 1992. Pyritization of trace metals in anoxic marine sediments. Geochim. Cosmochim. Acta., Vol. 56, pp. 2681-2702.

Jarvie, D. M. 1991. Total Organic Carbon TOC Analysis. Merrill, R. K., ed., Source and Migration Processesand Evaluation Techniques, Tulsa, American Association of Petroleum Geologists, pp. 113-118.

Jones, B., Manning, D.A.C. 1994. Comparison of geochemical indices used for the interpretation of depositional environments in ancient mudstones. Chem Geol. 111, Vol. 1–4, pp. 112–129.

Klinkhammer, G.P., Palmer, M.R. 1991. Uranium in the oceans: Where it goes and why. Geochimica et Cosmochimica Acta, Vol. 55, pp. 1799-1806.

Koca, D. 2011. Nallıhan (Ankara, Türkiye) civarı bitümlü şeyllerinde organik madde ve iz element zenginleşmeleri. Ankara Üniversitesi Fen Bilimleri Enstitüsü Jeoloji Mühendisliği Anabilim Dalı, Doktora tezi, pp.392.

Koca, D., Sarı, A., Engin, H., Koç, Ş., Yavuz, B. 2010. Şeyl türü kayaçların (Tekirler-Nallıhan/Ankara) redoks depolanma koşulları. 35. Yıl Jeoloji Sempozyumu, s. 111-112, 4-7 Ekim 2010, Konya.

Koralay, D. B., Sarı, A. 2013. Redox Conditions and Metal-Organic Carbon Relations of Eocene Bituminous Shales (Veliler/Mengen-Bolu/Turkey). Energy Sources, Part A, Vol., 35, pp.1597-1607.

Langmuir, D. 1978. Uranium solution metal equilibra at low temperatures with applications to sedimentary ore deposits. Geochimica et Cosmochimica Acta, Vol. 42, pp. 547-569.

Li, D., Li, R., Zhu, Z., Xu, F. 2018. Elemental characteristics of lacustrine oil shale and its controlling factors of palaeo-sedimentary environment on oil yield: a case from Chang 7 oil layer of Triassic Yanchang Formation in southern Ordos Basin. Acta Geochim, Vol. 37, 2, pp. 228–243.

Liang, W. J., Xiao, C. T., Xiao, K., Lin, W. 2015. The relationship of Late Jurassic paleoenvironment and paleoclimate with geochemical elements in Amdo Country of northern Tibet. Geol China, 42, Vol. 4, pp.1079–1091 (in Chinese with English abstract)

Morford, J. L., Emerson, S. 1999. The geochemistry of redox sensitive trace metals in sediments. Geochimicaet Cosmochimica Acta, Vol. 63, pp. 1735-1750.

Morford, J. L., Russell, A. D., Emerson, S. 2001. Trace metal evidence for changes in the redox environment associated vvith the transition from terrigenous clay to diatomaceous sediment, Saanich inlet, B. C. Marine Geology, Vol. 174, pp. 355-369.

Morse, J. W., Luther, G.W. 1999. Chemical influences on trace metal-sulfıde interactions in anoxic sediments. Geochimica et Cosmochimica Acta, Vol. 63, pp. 3373-3378.

Mukhopadhyay, P. K., Wade, J. A., Kruge, M. A. 1995. Organic Facies and Maturation of Jurassic/ Cretaceous Rocks and Possible Oil-Source Rock Corelation Based on Pyrolysis of Asphaltenes, Scotion Basin, Canada. Organic Geochemistry, Vol. 221, pp. 85-104.

Özlük, M. 2010. Himmetoğlu Formasyonu (Bolu) Bitümlü Şeyllerinde Organik Karbon ve Cr, Fe, Mo, Mn ve V Elementlerinin İlişkilerinin İncelenmesi. Ankara Üniversitesi FBE, Jeoloji Mühendisliği ABD. Yüksek Lisans tezi 109s.

Pailler, D., Bard, E., Rostek, F., Zheng, Y., Mortlock, R., Geen, A. 2002. Burial of redox-sensitive metals and organic matter in the equatorial Indian Ocean linked to precession. Geochimica et Cosmochimica Acta, Vol. 66, pp. 849-865.

Peters, K. E., Cassa, M. R. 1994. Applied source rock geochemistry. In: The petroleum system- from source to trap, L. B. Magoon and W. G. Dows eds., AAPG, Vol. 60, pp. 93-117.

Rimmer, S. M. 2004. Geochemical paleoredox indicators in the Devonian Mississippian black shales, Central Appalachian Basin USA. Chemical Geology, Vol. 206, pp. 373-391.

Robl,T. L., Barron, L. S. 1987. The geochemistry of black shales in central Kentucky and its relationship

to inter-basinal correlation and depositional environment. In: McMillan ,A. F., Embry, A. F., Glass, D. G.(Eds.), Devonian of the World, Vol.II: Sedimentation. Mem. Can. Soc. Pet.Geol., Vol.14, pp.377-396.

Sarı, A., Koca, D. 2012. Jura - Kretase yaşlı Akkuyu Formasyonunun (Orta Toroslar/ Türkiye) provenans, tektonik ve redoks koşullarına bir yaklaşım. Maden Tetkik ve Arama Dergisi, Sayı 144, S.51-73.

Sarı, A., Yavuz Pehlivanlı, B., Koca, D., Koç, Ş. 2010. During Triassic Paleoredox and Provenance Investigation of Rich Organic Matter Tarasçı Formation (Middle Taurus/Turkey), Elec Lett Sci Eng, Vol. 6, pp. 9-24.

Sarı, A., Akkaya, P., Özakar, E. 2016. Kürnüç/Göynük-Bolu Alt Eosen Bitümlü Kayaçlarının Depolanma Ortamı ve Organik Jeokimyasal Karakteristikleri. Maden Tetkik ve Arama Dergisi, Sayı 152, S. 1-17.

Templeton, G. D., Chasteen, N. D. 1980. Vanadium–fulvic acid chemistry conformational and binding studies by electron spin probe techniques. Geochim. Cosmochim. Acta, Vol. 44, pp. 741.

Teng, G. E, 2004. The Distribution of elements, carbon and oxygen isotopes on Marine Strata and environmental correlation between they and hydrocarbon source rocks formation an example from Ordovician Basin, China. Graduate School of Chinese Academy of Sciences (Lanzhou Institute of Geology), Lanzhou.

Teng, G. E., Liu, W. H., Xu, Y. C., Chen, J. F. 2004. Identification of effective source rocks of Ordovician marine sediments in Ordos Basin. Prog Nat Sci., 14, Vol. 11, pp. 1249–1252 (in Chinese).

Teng, G. E., Hui, L. W., Xu, Y. C., Chen, J. F. 2005. Correlative study on parameters of inorganic geochemistry and hydrocarbon source rocks formative environment. Adv Earth Sci., 20, Vol. 2, pp.193-200

Tissot, B., Welte, D. H. 1984. Petroleum formation and occurrence: 2. edition Springer-Verlag, Berlin, pp. 699.

Tribovillard, N., Algeo, T. J., Lyons, T., Riboulleau, A. 2006. Trace metals as paleoredox and paleoproductivity proxies an update. Chem Geol, 232, Vol. 1–2, pp.12–32.

Turekian, K. K., Wedepohl, K. H. 1961. Distribution of the elements in some major units of the Earth's crust. Bull. Geol. Soc. America, 72, Vol. 2, pp. 175-192

Vine, J., Tourtelot, E. 1970. Geochemistry of black shale deposits a summary report. Econ. Geo., Vol. 65, pp. 253-272.

Wang, Y. Y., Wu, P. 1983. Geochemical criteria of sediments in the coastal area of Jiangsu and Zhejiang Provinces. J Tongji Univ (Nat Sci), Vol. 4, pp.82–90 (in Chinese with English abstract)

Wehrli, B., Stumm, W. 1989. Vanadyl in natural waters: Adsorption and hydrolysis promote oxygenation. Geochim. Cosmochim. Acta, Vol. 53, pp. 69–77.

Wignall, P. B. 1994. Black Shales. Oxford Monographs on Geology and Geophysics No. 30, Oxford Scientific Publications, Oxford, U.K., pp.127.

Yarincik, K. M., Murray, R. W., Lyons, T. W., Peterson, L.C., Haug, G.H. 2000. Oxygenation history of bottom waters in the Cariaco Basin, Venezuela, over the past 578,000 years: results from redox-sensitive metals (Mo, V, Mn, and Fe) Paleoceanography, 15, Vol. 6, pp.593–604. doi:10.1029/1999PA000401.

Yavuz Pehlivanlı, B. 2011. Hırka Formasyonu (Beypazarı, Ankara, Türkiye) Bitümlü şeyllerinin İnorganik element depolanmaları ve organik-inorganik elementler arasındaki kökensel ilişkiler. Ankara Üniversitesi Fen Bilimleri Enstitüsü Jeoloji Mühendisliği Anabilim Dalı, Doktora tezi, pp. 550.

Yavuz Pehlivanlı, B., Koç, Ş., Sarı, A. 2013. Geochemical Paleoredox Variations Dependent upon Depth of Samples Contain Rich Organic Matter in Hırka Formation, Beypazarı-Ankara, Turkey", 33rd Oil Shale Symposium, October 14-18 2013. Colorado School of Mines Golden Colorado, USA. 49. p.

Zhang, C. L., Gao, A. L., Liu, Z., Huang, J., Yang, Y. J., Zhang, Y. 2011. Study of character on sedimentary water and Palaeoclimate for Chang 7 oil layer in Ordos Basin. Nat Gas Geosci, 22, Vol. 4, 582–587 (in Chinese with English abstract).

Zhao, B. S., Li, R. X., Wang, X. Z., Wu, X. Y., Wang, N., Qin, X. L., Cheng, J. H., Li, J. J. 2016. Sedimentary environment and preservation conditions of organic matter analysis of Shanxi formation mud shale in Yanchang exporation area, Ordos Basin. Geol Sci Technol Inf 35, Vol. 6, pp.103–111 (in Chinese with English abstract).

Zheng, Y., Anderson, R. F., Van Geen, A., Fleischer, M. Q. 2002. Remobilization of authigenic uranium in marinesediments by bioturbation. Geochimica et Cosmochimica Acta, Vol. 66, pp. 1759-1772.

Zhong, D. K., Jiang, Z. K., Guo, Q., Sun, H. T. 2015. A review about research history, situation and prospects of hydrothermal sedimentation. Palaeogeogr 17, Vol. 3, 285–296 (in Chinese with English abstract).

Bull. Min. Res. Exp. (2019) 158: 265-289

Bulletin of the Mineral Research and Exploration

http://bulletin.mta.gov.tr

Investigation of feldspar raw material potential of alkali feldspar granites and alkali feldspar syenites within Central Anatolia

Kıymet DENİZ[a*] and Yusuf Kağan KADIOĞLU[b]

[a] *Ankara University, Faculty of Engineering, Dept. Of Geological Engineering, 06830 Gölbaşı, Ankara, Turkey*
orcid.org. 0000-0003-3208-1354
[b] *Earth Sciences Application and Research Center (YEBİM) of Ankara University, 06830 Gölbaşı, Ankara, Turkey*
orcid.org/0000-0002-7894-2220

Research Article

Keywords:
Alkali feldspar granite, syenite, orthoclase, albite, raw material, glass, ceramic, Central Anatolia.

ABSTRACT

Alkali feldspar granites represent one of the major sources that provide raw materials for glass and ceramics industry because of their high feldspar and quartz contents. In addition, also alkali feldspar syenites have potential to become raw material due to their high feldspar and feldspathoid contents. For this reason, alkali feldspar granites within Ağaçören Intrusive Suite (AIS) (Kalebalta, Yıldırımlı, Çerkezuşağı, Çatalçeşme, İbrahimbeyli, Deliler, Ekecik, Sipahiler, Camili, Yaylak, Namlıkışla), Hacılı Suite (Sarıhacılı), Cefalık, Behrekdağ, Terlemez and alkali feldspar syenites within Bayındır, Hamit and İdişdağı Suites are investigated. This study aims to investigate possible potential of alkali feldspar, plagioclase and quartz minerals within these rocks in glass and ceramic industry as raw materials. These rocks have high alkaline element content and relatively high Fe_2O_3 values compared to world granites. Fe_2O_3 values depend on mafic and independent Fe minerals such as magnetite. Feldspars have high K_2O (> %14) and low FeO (< %0.05), thus have high feldspar potential in ceramic industry. Alkali feldspar granites within AIS have promising potential as feldspar raw material, they have low reserve due to their occurrence as dykes. Hacılı, Cefalık, Behrekdağ, Terlemez, Bayındır, Hamit and İdişdağı Suites have both good quality and high reserve for feldspar potential.

Received Date: 22.06.2017
Accepted Date: 05.12.2017

1. Introduction

Alkali feldspar granites represent rocks with the highest content of quartz and alkali feldspar in the granitoid family. In general, alkaline feldspar granites are mainly light-colored plutonic rocks containing quartz (20-60%) and alkali feldspar (40-80%) and plagioclase amount ranging between 0-10%. Although their felsic (light color) mineral contents are high, they have very low mafic (dark color) mineral contents. In terms of their mineralogical composition, they can be divided into two groups as single and double micaceous. The proportion of mafic minerals (biotite, etc.) in alkaline feldspar granites is generally below 5%. Such rocks represent products crystallized from residual silicon (Si) and potassium (K) rich melts in the last stages of the magma. Therefore, mafic minerals are observed in a small proportion in the products formed due to the depletion of iron (Fe) and magnesium (Mg) in these melts. They are generally beige-pink in color and have fine crystalline granular texture and their thickness may range between cm to hundreds of meters. Alkali feldspar granites are geologically formed in two forms. The most common formation is the aplitic dykes consisting of the last residual products of the granitoid magma and located along the articular direction of the main mass. The second formation is mostly the pre-collisional magmatism and partial melting event resulting from thrust faults in the upper crust. In addition, they may also form as lenses in metamorphics in small thicknesses and distributions due to high temperature. They may exhibit sharper and higher topography due to the mineral composition they contain. Besides, they can be in alkaline feldspar

* *Corresponding author: Kıymet DENİZ, kdeniz@eng.ankara.edu.tr*
https://dx.doi.org/10.19111/bulletinofmre.438197.

syenite composition as quartz-free or quartz poor rocks can be crystallized in syenitoid magma-based products. Alkali feldspar syenites are light colored plutonic rocks, which contain high alkaline feldspar (80-100%), plagioclase between 0-10%, and quartz below 20%. Alkali feldspars [(K, Na) $AlSi_3O_8$], which are observed in rocks, are generally in orthoclase and microcline ($KAlSi_3O_8$) composition. These minerals have been used as raw materials in the production of glass and ceramics for many years as they contain 0.80-8.44% Na_2O, 3.29-15.60% K_2O, 19.10-20.23% Al_2O_3, 63.66-65.76% SiO_2 and very small amounts of Fe (0.08-0.40% Fe_2O_3) (Deer et al., 1992; Öbelik, 2011). From the viewpoint of operability, in which the rocks K and Na containing minerals are mostly available, with which Fe-Mg-containing mafic minerals they are present, at what ratios these mafic minerals are contained and where the rocks are located have a great significance. In addition, the grain size of mafic and/or accessory minerals released during enrichment of feldspars is also very important.

There have been carried out several studies related to the determination, enrichment and management of the feldspar deposits in Turkey (Şahin, 1989; Uğur, 1990; Akkoyuncu, 1994; Kalyon, 2003; Erdinç, 2007; Nizamoğulları, 2007; Demirbaş, 2010). On the other hand, there are also other studies related to the development of magnetic separation and flotation methods in the differentiation of such undesirable minerals, which have coloring properties such as amphibole, biotite and muscovite in the form of inclusions within feldspar minerals (Bayraktar et al., 1997; 1999; Şahin Kılavuz, 2000; Demir, 2001; Doğu, 2002; Kalyon, 2003; Kademli, 2004; Gülsoy, 2005; Erdinç, 2007; Özün, 2012). Although the quartz, which is one of the major minerals of the alkali feldspar granite rocks, does not form any problem in terms of color and brightness, it can increase the fragility due to their hardness. Therefore, the quartz ratio is also important in the prescriptions produced. Apart from these, there are also other studies on the effects of feldspar on ceramics or frit (Töre, 1999; Kula, 2003; Daday, 2012). Feldspars are not only used in ceramic bodies as melts but they can also be used in glasses, glass and porcelain enamel (Kadıoğlu, 2001; Özcan, 2002; Yeşilbaş, 2002). The 70% of feldspars are generally used in glass production, while 30% are used in ceramics and other products (Potter, 1996). Feldspars with high sodium (Na) content have lower viscosity and glazing temperature than feldspars with high potassium (K) content (Ryan, 1978; Köprülü, 1997; Tayçu, 2009). Besides, they are more susceptible to shrinkage during the cooking process (Ryan, 1978). As seen, almost all of the feldspar group minerals can be used for different purposes in the production of glass and ceramics. This situation shows that alkali feldspar granites have a high importance in the production of ceramic raw materials and these rocks have a significant place in ceramics produced for different purposes.

The main feldspar producers are Norway, Switzerland, Russia, United States (USA), Canada, Germany, Italy, France, Spain, Japan, Thailand, Finland, Mexico, Romania, South Africa, Czech Republic and Poland (Ryan, 1978; Ariffin, 2003; Lewicka, 2010). Feldspar deposits in Turkey are mainly located in Çanakkale, Balıkesir, Aydın (Akçaova, Çine), Manisa (Demirci, Gördes), Kütahya (Simav), Bilecik (Söğüt), Bitlis (Bölükyazı–Hizan) and Afyon (Geredeli, 1990; Sümer, 1994; Yalçın, 1995; Ermiş, 1996; Oyman, 1996; Bayraktar et al., 1999; Gürsoy, 1999; Akkurt, 2001; Karagüzel, 2001; Güven, 2002; Kaya, 2002; Oyan, 2004; Demirbaş, 2010; Çelik and Denizhan, 2016). Turkey is quite rich in terms of intrusive rocks with high feldspar content (mainly alkali feldspar granite). These rocks were selected as the study area because they have wide spreads in the Central Anatolia Region (Figure 1).

The alkali feldspar granites in the Central Anatolian Crystalline Complex (CACC) (Göncüoğlu et al., 1991, 1992, 1993) are mainly located in the Granite Supersuite and Monzonite Supersuite, and the alkali feldspar syenites are located in the Syenite Supersuite (Kadıoğlu et al., 2006). These rocks are exposed in large masses or in the form of aplitic dykes in all intrusive assemblages in the CACC. However, the masses with high economic reserves are seen in limited areas. Alkali feldspar granites in the Granite Supersuite outcrops in the Ağaçören Intrusive Suite (AİT), Behrekdağı Suite, Sulakyurt-Balışeyh Suite, Hacılı Suite, Akdağmadeni Suite and Karakeban Suite, however the Monzonite Supersuite outcrops in the Cefalık Suite, Baranadağ Suite, Akçakent Suite and Murmano Suite. The alkali feldspar syenites in the Syenite Supersuite are observed in the İdişdağı Suite, Devedamı Suite, Hayriye Suite, Bayındır Suite, İğdişdağı Suite, Akçakent Suite and in the Ömerli Suite. In this study, samples were taken from Sarıhacılı-Hacılı (Hacılı Suite-Yozgat) and from different locations of AIT (Granite Supersuite: Hacılı, Kalebalta, Yıldırımlı, Çerkezuşağı, Çatalçeşme,

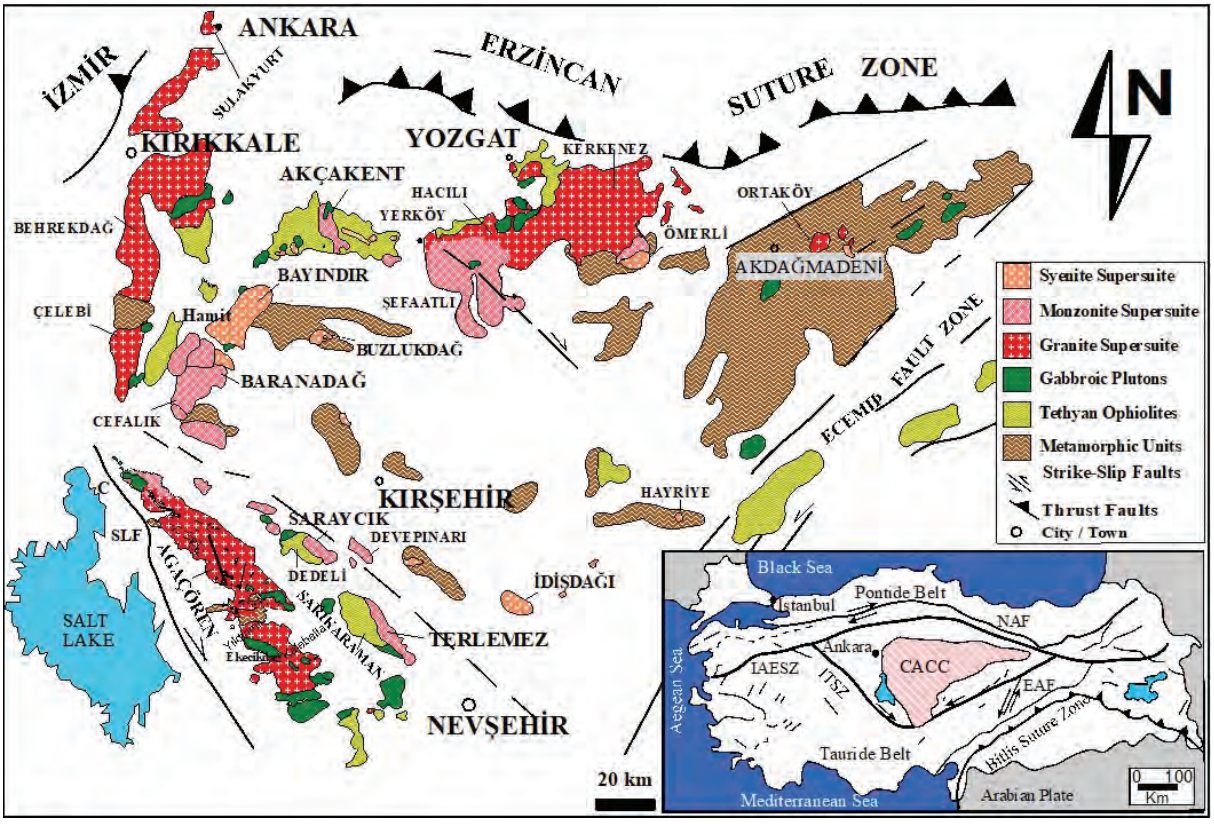

Figure 1- Simplified geology map of CACC (NAF: North Anatolian Fault; EAF: East Anatolian Fault; CACC: Central Anatolian Crystalline Complex; ITSZ: Intra Tauride Suture Zone) (simplified from Kadıoğlu et al., 2006).

İbrahimbeyli, Deliler, Ekecik, Sinandı, Sipahiler, Camili, Yaylak, Namlıkışla Sub-Suits), Monzonite Supersuite (Cefalık, Behrekdağ, Terlemez Sub-Suites) and from the Syenite Supersuite (Bayındır, Hamit and İdişdağı Sub-Suites).

In this study, the potential of being a raw material in terms of Na (albite-$NaAlSi_3O_8$) or K-rich feldspar (orthoclase-$KAlSi_3O_8$) were targeted comparing the geology, mineralogy, petrography and geochemistry of rocks and sampling from different locations where alkali feldspar granites and alkali feldspar syenites in Central Anatolia Region were exposed. In addition, the operability of them in the form of by-product as were also investigated as these rocks have high silica content. While evaluating the results of the assessment, interpretation was made by comparing the chemical compositions of alkali feldspar granite and alkali feldspar syenite rocks in different parts of the world. In the scope of the study, mechanical tests such as the strength, color and firing shrinkage, which should be determined for the raw materials used in the glass and ceramics industries, were not performed and the regional feldspar potential were revealed by using the whole rock and mineral chemistry data. In doing so, the attention was drawn to alternative deposits that could contribute to the economy of the country.

2. Material and Method

As a result of the field study carried out in different places of the CACC alkali feldspar granite and alkali feldspar syenite rock samples were collected and detailed mineralogical and petrographical investigations were carried out in the thin sections. By doing so, their mineralogical compositions, microscopic textural features and the alteration types were studied. The observations were made on the Leica DMLP model polarizing microscope. In order to reveal the normative mineralogical compositions of the alkaline feldspar granite and the alkali feldspar syenite samples, calculations were made based on the norms of Cross, Iddings, Pirsson and Washington (CIPW) (1931) by using chemical composition.

For the major oxide and trace element geochemical analyzes samples were broken in a Retsch Brand jaw crusher and then milled using a Tungsten carbide mill

in a FRITSCH brand mill. The 4 g ground sample was mixed with 0.9 g of binding material (Wachs) and compressed under hydraulic pressure into a press-paste (powder pellet) then major and trace element analyzes were carried out using X-LAB 2000 model of Polarized Energy Dispersive X-Ray Fluorescence Spectrometer (PEDXRF). Analyzes were performed based on the GEO-7220 method and the instrument was calibrated using K02-GSR-09 and G01-GS-N-Granite standards for plutonic rocks (granite, granodiorite etc.) of USGS.

In addition, the chemistry of the feldspar (alkali feldspar) minerals were determined from selected rock samples by using the Electron Probe Micro Analysis (EPMA) method. Thin sections were coated with carbon using Quorum brand Q150T ES device and the major oxide compositions of feldspar minerals were determined on polished thin sections using JEOL brand JXA 8230 device under 20 kV voltage and 15 nA current. Chemical analysis results are given in table 5. During all studies carried out throughout the study, laboratories and equipment of the Earth Sciences Application and Research Center (YEBİM) of Ankara University were used.

All the data obtained from the literature, field and laboratory studies were evaluated, compared with some samples in the world and making interpretations related to the usage of alkali feldspar granites and alkali feldspar syenites in the glass and ceramic industries the potential deposits were revealed in Central Anatolia Region.

3. Regional Geology

The CACC, which is also known as the Kırşehir Massif (Seymen, 1982), Central Anatolian Massif (Ketin, 1955), Kırşehir Block (Görür et al., 1984), Kırşehir Complex (Lünel, 1985) or Kırşehir Microplate (Erler et al., 1991) is restricted by the İzmir-Ankara-Erzincan Suture Zone (IAESZ) in the north, Tuz Lake in the west and Intra Tauride Suture Zone (ITSZ) in the east. The region consists of four rock groups, namely Central Anatolian Metamorphics (CAM), Intra Anatolian Ophiolites (IAO), Central Anatolian Felsic Intrusives (CFI) and mantle-derived mafic rocks (Göncüoğlu et al., 1991, 1992; Kadıoğlu and Güleç, 1996; Özsan, 1997; Kadıoğlu et al., 2003).

AIT mainly consists of granite, monzonite and gabbroic rocks and cutting by alkali feldspar granite in the shape of small dykes (Kadıoğlu, 1991; 1996; Kadıoğlu and Güleç, 1996) (Figure 2).

Intrusive rocks located around Yozgat are mainly composed of granite, monzonite and syenite (Ekici, 1997; Tatar, 1997; Akçe, 2003, 2010; Akçe and Kadıoğlu, 2005; Aydoğdu, 2010; Tiryaki, 2012; Tüvar, 2015). The Hacılı Suite, which is one of the regions with the largest spread in terms of felsic masses, is located in the vicinity of Sarıhacılı village in the east of Yozgat (Figure 3). It is light pink in color and exhibits phaneritic texture as it is leucocratic in character and mainly rich in quartz and alkali feldspar (Akçe, 2010).

Cefalık, Behrekdağ and Terlemez Suites are composed of rocks in the monzonitic composition (Ataman, 1972; Seymen, 1982; Bayhan, 1987; Erler et al., 1991; Geven, 1992; İlbeyli, 1998, 2005; Yalınız et al., 1999; Tatar, 2003; İlbeyli et al., 2004; İlbeyli and Pearce, 2005; İlbeyli and Kibici; 2009, İlbeyli et al., 2009; Kadıoğlu et al., 2006; Köksal et al., 2013). The Cefalık Suite was distinguished as monzodiorite, quartz monzonite and the alkali feldspar granite and reported that they were cut by aplitic, pegmatitic, mafic and leucite phonolitic dykes (Geven, 1992; İlbeyli, 1998; Kadıoğlu et al., 2006). It was defined that Behrekdağ Suite was in quartz monzonite and granite composition (Bayhan 1986, 1989; Yadete, 1990, İlbeyli et al., 2004). The Terlemez Suite is composed of quartz monzonite, medium-coarse crystalline rocks and consists of 3 cm x 10 cm K-feldspar megacrystals (Yalınız et al., 1999).

Bayındır, Hamit and İdişdağı Suites represent the latest products of Late Cretaceous-Early Cenozoic magmatism in CACC and have syenitic composition (Seymen, 1982; Akıman, 1985; Bayhan, 1988; İlbeyli, 1998; Köksal, 1996; Köksal and Göncüoğlu, 1997; Köksal et al., 2001). The Bayındır Suite consists of quartz syenite and feldspathoid syenite (Bayhan, 1988). The Hamit Suite was named as feldspathoid bearing monzosyenite and they are dark gray, medium crystalline, porphyritic textured rocks (İlbeyli, 1998). İdişdağı Suite was defined as the syenite rich in quartz syenite and alkali feldspar (Köksal et al., 2001). Porphyritic texture can be observed locally in the medium-fine crystalline rock.

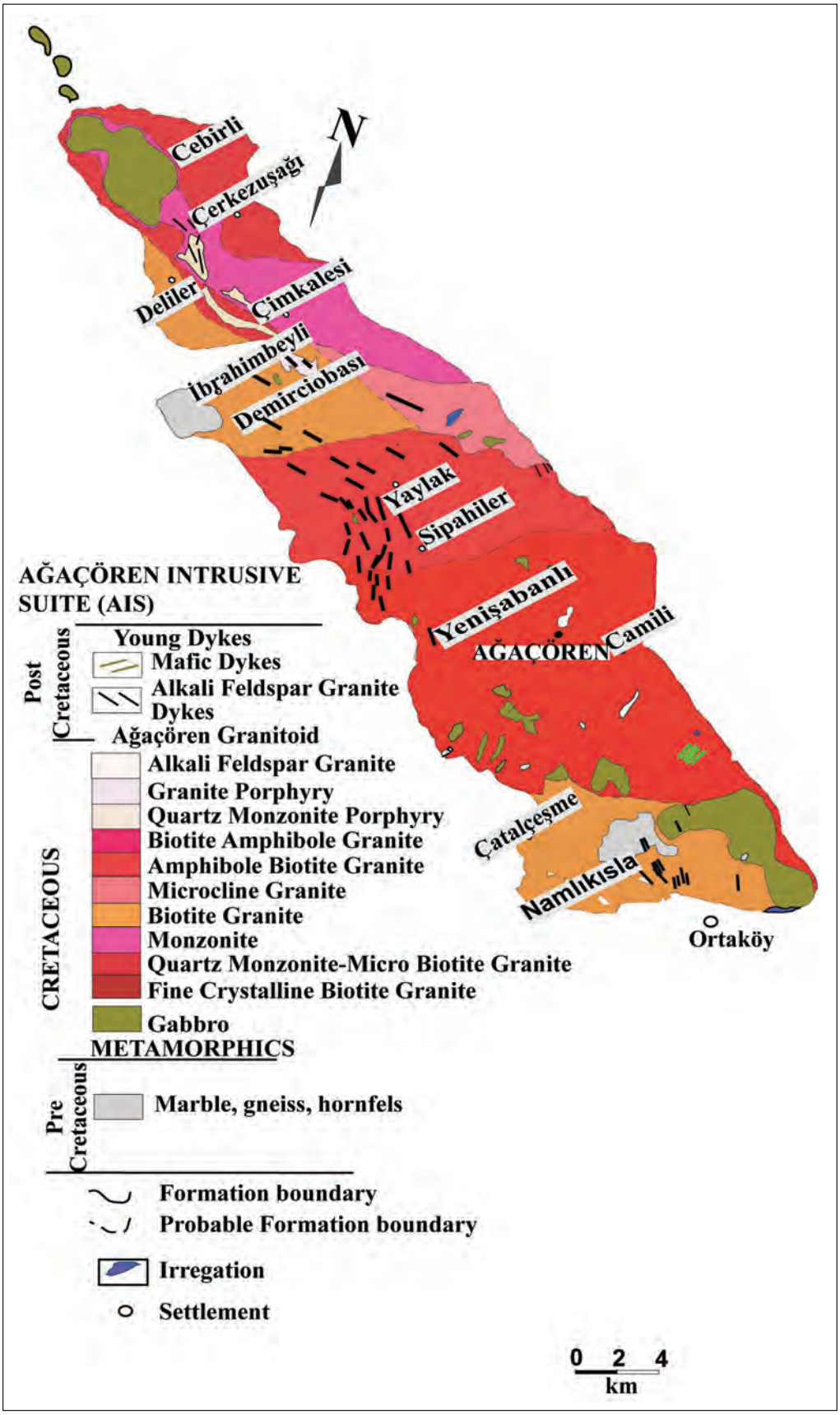

Figure 2- Geology map of the Ağaçören Intrusive Suit (AIT) (simplified from Kadıoğlu et al., 2006).

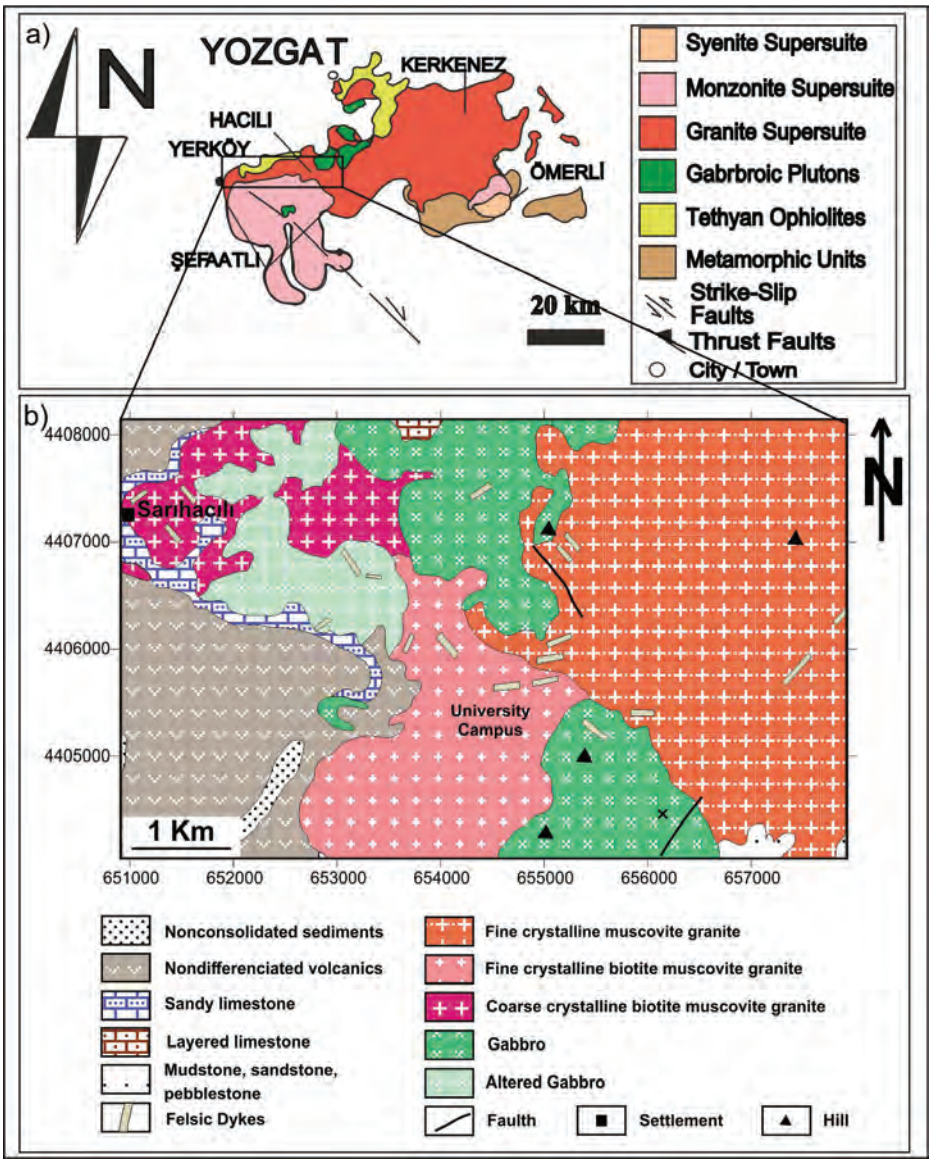

Figure 3- a) Simplified geology map of the Hacılı Suit (simplified from Kadıoğlu et al., 2006), b) Geology map of the Sarıhacılı vicinity (from Akçe and Kadıoğlu, 2005).

4. Mineralogy and Petrography

CACC; alkali feldspar containing rocks are divided into two main groups as; non feldspathoid containing (granitic-silicate-saturated) and feldspathoid-bearing (syenite-silica unsaturated) (Kadıoğlu et al., 2006). The felsic, mafic and accessory mineral contents of the Central Anatolian alkali feldspar granites and alkali feldspar syenites are given in Table 1. Alkali feldspar granites are fine-crystallized, holocrystalline hipidiomorph granular texture, and are composed of plagioclase minerals with equi-dimensional, sub-hedral quartz, alkali feldspar, biotite and muscovite (Figure 4a, 4b). Alkali feldspars have 0.5-5 mm in grain size and mostly orthoclase and microcline in composition, and plagioclases are 0.3-3 mm in size and mainly in oligoclase and locally in albite composition (An_{10-35}%). Mica group minerals consist of wedge and leafy biotite and muscovite with dimensions of 0.1-2 mm (Figure 4). In some alkaline feldspar granites (Hacılı and Kalebalta) garnet minerals are observed as secondary minerals. Within the orthoclase, cuneiform like quartz are observed and exhibit typical graphic and myrmekitic textures. In some of the orthoclases and plagioclases within rocks, argillization and sericitization are observed as a result of surficial effects (Figure 4). Fe bearing magnetite and ilmenite minerals in the form of accessory with dimensions ranging

Table 1- Felsic, mafic and accessory mineral contents of the Central Anatolian alkali feldspar granites and syenites.

Intrusion Name	Supersuite		Felsic Minerals	Mafic Minerals	Isotrope Minerals	Accessory Minerals
Kalebalta	Granite	AİT	Quartz, orthoclase, plagioclase	-	Grossular, andradite	Magnetite, ilmenite
Agaçören			Quartz, orthoclase, plagioclase, muscovite	Chlorite, epidote	-	Magnetite
Yıldırımlı			Quartz, orthoclase, plagioclase	-	-	Magnetite, hematite
Çerkezuşağı			Orthoclase, plagioclase	Amphibole, biotite, chlorite, epidote	-	Magnetite, ilmenite
Çatalçeşme			Quartz, orthoclase, plagioclase	Biotite, Amphibole, chlorite, epidote	-	Magnetite, ilmenite, hematite
İbrahimbeyli			Quartz, orthoclase, plagioclase	Biotite, Amphibole, chlorite, epidote	-	Magnetite
Deliler			Quartz, orthoclase, plagioclase	Biotite, Amphibole, chlorite, epidote	-	Magnetite
Ekecik			Quartz, orthoclase, plagioclase	Biotite, Amphibole, chlorite, epidote	-	Magnetite, ilmenite
Sipahiler			Quartz, orthoclase, plagioclase	Amphibole, biotite, chlorite, epidote	-	Magnetite
Camili			Quartz, orthoclase, plagioclase	Amphibole, biotite, chlorite, epidote	-	Magnetite
Yaylak			Quartz, orthoclase, plagioclase	Amphibole, biotite, chlorite, epidote	-	Magnetite
Cefalık	Monzonite		Orthoclase, plagioclase	Amphibole, biotite, chlorite, epidote	-	Magnetite, ilmenite
Behrekdağ			Orthoclase, plagioclase	Amphibole, biotite, chlorite, epidote	-	Magnetite, ilmenite
Terlemez			Orthoclase, plagioclase	Amphibole, biotite, chlorite, epidote	-	Magnetite, ilmenite
Bayındır	Syenite		Nepheline, orthoclase, plagioclase	Biotite, Amphibole	Melanite, fluorite	Magnetite, ilmenite, hematite
Hamit			Nepheline, orthoclase, plagioclase	Biotite, Amphibole	Melanite, fluorite	Magnetite, ilmenite
İdişdağı			Nepheline, orthoclase, plagioclase, quartz, muscovite	Amphibole, biotite,	Melanite, fluorite	Magnetite, ilmenite
Sarıhacılı	Granite		Quartz, orthoclase, plagioclase, muscovite	Biotite, chlorite, epidote	Grossular, andradit	Magnetite

from 0.1 mm to 0.4 mm are freely and independently located in the rock.

Some of the rocks in alkali feldspar granite cut other rocks in the region in the form of dykes and are largely found in AIT. They are mainly composed of orthoclase, quartz and in few amounts plagioclase and muscovite. Within the alkaline feldspar granite dykes around Yaylak in the AIT, the biotites are located within the rock, forming the magma segregation enclaves (Figure 4i, 5).

Cefalık, Behrekdağ, Terlemez Sub-Suites are monzonitic in composition (Akıman et al., 1993; Yalınız et al., 1999; Tatar, 2003; İlbeyli et al., 2004; İlbeyli, 2005; İlbeyli and Pearce, 2005; İlbeyli and Kibici, 2009; 2009; Kadıoğlu et al., 2006; Köksal et al., 2013). The coarse crystalline monzodioritic rocks in the Cefalık Suite are porphyritic texture as they contain feldspar megacrystals reaching up to 10 cm. The rocks are mainly composed of plagioclase, alkali feldspar, biotite and amphibole minerals and their mafic mineral ratios are higher than other felsic rocks (Kadıoğlu et al., 2006). The rocks in monzonitic composition are gray and coarse crystalline. The mafic mineral composition of these porphyritic rocks is composed of biotite, amphibole and few pyroxenes. Terlemez monzonites are mainly composed of K-feldspar, plagioclase, hornblende, biotite and rarely pyroxene minerals. Epidote minerals up to 3% in Terlemez monzonites are observed as a result of alteration.

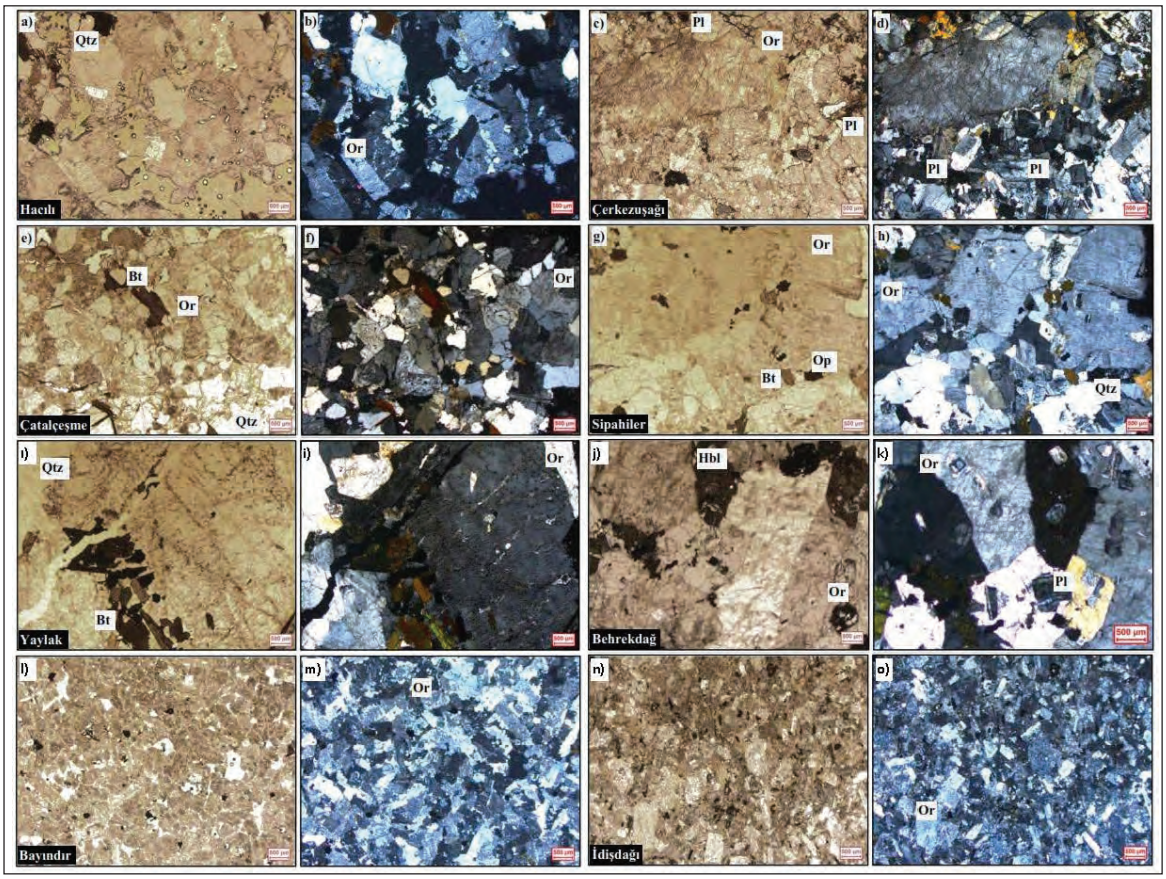

Figure 4- Thin section photos of some alkali feldspar granites and syenites in the study area (a, b) Hacılı, (c, d) Çerkezkuşağı (AIT), (e, f) Çatalçeşme (AIT), (g, h) Sipahiler (AIT), (ı, i) Yaylak (AIT), (j, k) Thin section photo of orthoclase minerals within Behrekdağ alkali feldspar granite, (l, m) photo of İnce crystalline Bayındır alkali feldspar syenite, (n, o) thin section photo of the İdişdağı alkali feldspar syenite.

Bayındır, Hamit and İdişdağı Sub-Suites represent the syenite silica unsaturated rock groups, and the felsic dykes that cut them are also in alkaline feldspar syenite composition (Kadıoğlu et al., 2006). Alkali feldspar syenites are generally have holocrystalline granular textures consisting mainly of alkaline feldspar, nepheline, plagioclase, amphibole, rare biotite and clinopyroxene, as well as secondary minerals such as titanite, zircon, apatite and accessory minerals and secondary minerals such as epidote, chlorite and calcite (Figures 5n, 5o). The most characteristic feature of alkali feldspar syenite is that they contain feldspathoid minerals like nepheline. Therefore, the alkali feldspar (orthoclase, microcline, anorthoclase) minerals of these rocks cause K and Na ratios to be higher than the alkaline feldspar granites due to the presence of nepheline.

CIPW norm values based on the chemical composition of rocks were calculated to determine the type and proportion of felsic minerals and accessory minerals in each locality studied (Table 2). According to this, it was seen that accessory minerals within the rocks were formed by ilmenite, magnetite, hematite and rutile minerals (Table 2). The rocks in AIT (Kalebalta, Yıldırımlı, Çerkezuşağı, Çatalçeşme, İbrahimbeyli, Deliler, Ekecik, Sipahiler, Camili, Yaylak and Namlıkışla) constitute mainly hematite (0.28-1.66%), ilmenite (0.06-0.51%) and rutile (0.02-0.20%). The Hacılı Suite samples on the other hand constitute accessory minerals in ilmenite (0.11-0.13%) and rutile (0.34%) compositions (Table 2). Accessory minerals in Cefalık, Behrekdağ, Terlemez Suites are in combination with ilmenite (0.06-0.15%), hematite (2.83%) and rutile (0.14-0.23%) (Table 2). Bayındır, Hamit and İdişdağı Suites contain ilmenite (0.30-0.39%), magnetite (0.12%) and hematite (0.38-0.43%) (Table 2). As quartz contents in the rocks increase, feldspar (plagioclase and orthoclase) contents decrease whereas mafic mineral contents increase (Table 2).

Table 2- CIPW normative values of the Central Anatolian alkali feldspar granites and syenites.

Sample Number	Location	Quartz	Plagioclase	Orthoclase	Diopside	Corundum	Wollastonite	Hypersthene	Apatite	Sphene	İlmenite	Magnetite	Hematite	Rutile	Nepheline	Akmite
Kaleb-1	Kalebalta	26.02	28.25	40.72	0.54	0.00	0.78	0.00	0.12	0.42	0.51	0.00	1.66	0.00	0.00	0.98
Kaleb-2	Kalebalta	24.56	28.18	40.89	0.32	0.00	0.10	0.00	0.14	0.24	0.73	0.00	0.00	0.00	1.56	3.27
Kaleb-3	Kalebalta	39.29	20.05	34.63	0.00	1.49	0.00	1.44	0.21	0.00	0.85	0.20	1.86	0.00	0.00	0.00
Kaleb-4	Kalebalta	41.14	28.69	23.64	0.00	2.11	0.00	2.22	0.07	0.00	0.23	0.57	1.33	0.00	0.00	0.00
Kaleb-5	Kalebalta	23.32	30.84	41.54	1.65	0.00	0.00	1.03	0.07	0.00	0.36	0.23	0.97	0.00	0.00	0.00
Kaleb-6	Kalebalta	37.04	28.00	28.48	0.00	2.80	0.00	1.67	0.07	0.00	0.62	0.00	0.83	0.47	0.00	0.00
Agac-1	Agaçören	33.16	29.02	33.80	0.00	1.23	0.00	1.74	0.09	0.00	0.28	0.15	0.51	0.00	0.00	0.00
Agac-2	Agaçören	36.05	24.12	33.33	0.00	3.08	0.00	2.32	0.05	0.00	0.19	0.00	0.85	0.03	0.00	0.00
Agac-3	Agaçören	36.53	28.51	29.08	0.00	2.63	0.00	2.39	0.05	0.00	0.25	0.37	0.19	0.00	0.00	0.00
Agac-4	Agaçören	34.78	29.11	29.19	0.00	3.65	0.00	2.34	0.12	0.00	0.21	0.53	0.08	0.00	0.00	0.00
Yıld-1	Yıldırımlı	43.95	24.89	26.06	0.00	3.11	0.00	1.27	0.09	0.00	0.17	0.00	0.36	0.10	0.00	0.00
Yıld-2	Yıldırımlı	36.70	34.68	25.23	0.00	1.27	0.00	1.44	0.12	0.00	0.17	0.00	0.29	0.10	0.00	0.00
Yıld-3	Yıldırımlı	28.79	22.19	44.20	0.21	0.00	1.42	0.00	0.16	0.19	0.21	0.00	0.00	0.00	1.95	0.64
Yıld-4	Yıldırımlı	28.64	24.27	43.49	0.00	0.00	0.00	1.59	0.37	0.61	0.19	0.00	0.65	0.16	0.00	0.00
Cerk-1	Çerkezuşağı	24.23	18.41	46.69	1.85	0.00	0.00	1.58	0.21	0.46	0.19	0.00	0.00	0.00	5.97	0.41
Cerk-2	Çerkezuşağı	33.08	26.65	37.17	0.00	0.50	0.00	1.20	0.42	0.00	0.19	0.00	0.94	0.08	0.00	0.00
Cerk-3	Çerkezuşağı	32.46	27.42	36.64	0.00	1.04	0.00	1.54	0.39	0.00	0.19	0.00	0.28	0.05	0.00	0.00
Nkisla-1	Çatalçeşme	23.55	28.12	41.13	0.74	0.00	0.00	1.37	0.30	0.65	0.06	0.00	0.00	0.00	3.00	1.07
Nkisla-2	Çatalçeşme	26.66	25.34	42.49	2.14	0.00	0.00	1.10	0.32	0.04	0.21	0.00	0.00	0.00	0.88	0.81
İbrah-1	İbrahimbeyli	35.95	19.88	40.78	0.00	1.55	0.00	0.62	0.30	0.00	0.21	0.00	0.78	0.04	0.00	0.00
İbrah-2	İbrahimbeyli	38.42	24.67	31.56	0.00	1.59	0.00	1.97	0.30	0.00	0.15	0.00	0.91	0.44	0.00	0.00
Delil-1	Deliler	48.80	21.83	24.05	0.00	3.02	0.00	1.10	0.28	0.00	0.15	0.00	0.68	0.09	0.00	0.00
Delil-2	Deliler	39.36	29.69	25.53	0.00	2.61	0.00	1.67	0.37	0.00	0.06	0.00	0.56	0.15	0.00	0.00
Delil-3	Deliler	39.42	27.74	26.00	0.00	3.13	0.00	2.14	0.37	0.00	0.17	0.00	0.93	0.09	0.00	0.00
Ekeck-1	Ekecik	40.60	26.31	26.36	0.00	3.18	0.00	1.89	0.42	0.00	0.15	0.00	0.62	0.47	0.00	0.00
Ekeck-2	Ekecik	37.07	34.68	23.93	0.00	2.86	0.00	0.25	0.14	0.00	0.13	0.00	0.73	0.21	0.00	0.00
Ekeck-3	Ekecik	28.16	26.71	41.78	1.15	0.00	0.00	0.36	0.28	0.89	0.15	0.00	0.53	0.00	0.00	0.00
Siph-1	Sipahiler	17.01	39.04	39.42	1.15	0.00	0.00	1.01	0.16	0.25	0.17	0.00	0.00	0.00	1.62	0.17
Siph-2	Sipahiler	27.29	39.32	29.96	0.00	1.45	0.00	1.39	0.21	0.00	0.11	0.00	0.12	0.15	0.00	0.00
Siph-3	Sipahiler	23.23	28.34	45.92	0.83	0.00	0.00	0.91	0.14	0.23	0.13	0.00	0.00	0.00	0.15	0.12
Cefalık-1	Cefalık	22.52	24.04	47.10	1.67	0.00	0.00	0.82	0.23	0.20	0.15	0.00	0.00	0.00	2.98	0.29
Cefalık-2	Cefalık	27.45	31.27	37.35	0.00	0.50	0.00	2.52	0.16	0.00	0.15	0.00	0.36	0.22	0.00	0.00
Cefalık-3	Cefalık	31.90	19.85	43.26	0.00	1.96	0.00	0.67	0.76	0.00	0.11	0.00	1.37	0.12	0.00	0.00
Cefalık-4	Cefalık	37.28	31.53	25.59	0.00	2.82	0.00	0.95	0.12	0.00	0.11	0.00	1.52	0.09	0.00	0.00
Behrek-1	Behrekdag	17.14	30.14	47.40	0.00	0.00	0.00	2.39	0.19	0.00	0.15	0.00	0.00	0.23	1.20	1.27
Behrek-2	Behrekdag	13.51	31.48	46.63	1.25	0.00	0.00	1.88	0.16	0.32	0.13	0.00	0.00	0.00	4.36	0.29
Behrek-3	Behrekdag	15.91	34.12	42.02	2.40	0.00	0.00	1.11	0.19	0.47	0.15	0.00	0.00	0.00	1.20	2.46
Behrek-4	Behrekdag	27.79	37.22	29.37	0.00	2.34	0.00	2.44	0.16	0.00	0.17	0.00	0.46	0.03	0.00	0.00
Behrek-5	Behrekdag	18.07	38.01	40.19	0.00	0.00	0.00	2.57	0.21	0.00	0.19	0.00	0.38	0.19	0.00	0.28

Table 2- continued.

Sample Number	Location	Quartz	Plagioclase	Orthoclase	Diopside	Corundum	Wollastonite	Hypersthene	Apatite	Sphene	İlmenite	Magnetite	Hematite	Rutile	Nepheline	Akmite
Behrek-6	Behrekdag	28.06	38.99	26.77	0.00	2.45	0.00	1.59	0.16	0.00	0.02	0.00	1.75	0.19	0.00	0.00
Terlm1	Terlemez	27.32	31.08	31.79	0.00	2.57	0.00	3.86	0.35	0.00	0.06	0.00	2.83	0.14	0.00	0.00
Terlm2	Terlemez	31.71	30.88	31.97	0.47	0.00	0.60	0.00	0.07	0.00	0.04	0.00	0.00	0.00	1.81	2.46
Cam-1	Camili	29.77	41.68	25.71	0.00	1.79	0.00	0.25	0.25	0.00	0.02	0.00	0.50	0.03	0.00	0.00
Cam-2	Camili	34.88	34.90	28.96	0.00	0.22	0.00	0.20	0.05	0.00	0.04	0.04	0.71	0.00	0.00	0.00
Cam-3	Camili	27.78	29.51	34.63	0.63	0.00	0.00	0.41	0.12	0.00	0.02	0.00	0.00	0.00	4.75	2.17
Yaylak-1	Yaylak	25.63	41.17	30.43	0.00	1.61	0.00	0.32	0.32	0.00	0.21	0.00	0.28	0.02	0.00	0.00
Yaylak-2	Yaylak	43.48	19.72	28.48	0.00	6.73	0.00	0.37	0.28	0.00	0.21	0.00	0.77	0.04	0.00	0.00
Yaylak-3	Yaylak	42.75	24.41	25.35	0.00	5.64	0.00	0.45	0.30	0.00	0.15	0.00	0.90	0.04	0.00	0.00
Yaylak-4	Yaylak	43.05	30.21	23.87	0.00	1.33	0.00	0.35	0.28	0.00	0.15	0.00	0.68	0.09	0.00	0.00
Hacılı-9	Yozgat	28.41	27.77	35.93	1.98	0.00	0.00	0.28	0.30	0.55	0.13	0.00	0.00	0.00	0.25	4.43
Hacılı-10	Yozgat	34.17	26.16	32.56	1.71	0.00	0.00	0.28	0.35	0.59	0.13	0.00	0.41	0.00	0.00	3.64
Hacılı-11	Yozgat	34.38	22.76	34.10	0.00	1.02	0.00	4.36	1.20	0.00	0.15	0.00	1.67	0.39	0.00	0.00
Hacılı-12	Yozgat	32.90	25.79	32.56	0.00	0.31	0.00	4.98	1.00	0.00	0.17	0.00	1.86	0.45	0.00	0.00
Hacılı-13	Yozgat	30.11	23.01	38.41	0.14	0.00	0.00	2.20	0.51	0.72	0.13	0.00	0.00	0.00	0.35	4.43
Hacılı-14	Yozgat	31.44	19.98	39.77	0.45	0.00	0.00	1.98	0.46	0.74	0.17	0.00	0.00	0.00	1.60	3.38
Hacılı-15	Yozgat	29.24	22.56	40.36	1.30	0.00	0.00	1.74	0.51	0.71	0.15	0.00	0.05	0.00	0.00	3.38
Hacılı-16	Yozgat	31.66	28.61	37.70	0.00	0.00	0.00	0.62	0.14	0.10	0.04	0.00	1.07	0.05	0.00	0.00
Hacılı-17	Yozgat	32.23	23.16	38.47	0.00	0.00	0.00	1.84	0.49	0.00	0.11	0.00	0.00	0.34	1.29	2.14
Hacılı-18	Yozgat	40.72	22.93	31.50	0.00	1.88	0.00	0.80	0.95	0.00	0.26	0.00	0.84	0.53	0.00	0.00
Hacılı-19	Yozgat	41.23	22.59	30.67	0.00	2.92	0.00	0.35	1.02	0.00	0.26	0.00	0.84	0.54	0.00	0.00
Hacılı-1	Yozgat	38.65	25.13	31.91	0.00	1.71	0.00	0.45	1.02	0.00	0.26	0.00	0.75	0.54	0.00	0.00
Hacılı-2	Yozgat	39.24	22.09	34.10	0.00	2.45	0.00	0.47	1.07	0.00	0.17	0.00	0.32	0.50	0.00	0.00
Hacılı-3	Yozgat	41.22	21.07	32.68	0.00	3.06	0.00	0.40	1.02	0.00	0.28	0.00	0.23	0.49	0.00	0.00
Hacılı-4	Yozgat	39.97	23.02	32.62	0.00	2.59	0.00	0.45	0.90	0.00	0.24	0.00	0.13	0.50	0.00	0.00
Hacılı-5	Yozgat	32.99	6.35	58.45	0.00	0.00	0.00	0.05	0.07	0.00	0.04	0.00	0.00	0.04	1.23	0.78
Hacılı-6	Yozgat	27.79	28.25	40.66	0.00	0.00	0.00	0.62	0.21	0.21	0.02	0.00	0.00	0.08	1.62	0.52
Hacılı-7	Yozgat	24.26	29.93	40.19	0.00	0.00	0.00	0.40	0.16	0.59	0.04	0.00	0.00	0.05	3.97	0.41
Hacılı-8	Yozgat	39.27	18.02	38.71	0.00	2.82	0.00	0.42	0.37	0.00	0.02	0.00	0.17	0.25	0.00	0.00
Bayınd-1	Bayındır	19.70	50.82	25.65	0.00	1.54	0.00	1.42	0.07	0.00	0.30	0.12	0.38	0.00	0.00	0.00
Bayınd-2	Bayındır	8.57	48.39	32.38	5.27	0.00	0.94	0.00	0.16	0.00	0.08	0.44	0.18	0.00	0.00	3.59
Bayınd-3	Bayındır	4.33	49.50	36.29	0.58	0.00	3.75	0.00	0.07	0.00	0.23	0.00	0.00	0.00	1.65	3.59
Bayınd-4	Bayındır	3.77	46.50	32.92	3.71	0.00	0.62	0.00	0.07	2.32	0.45	0.00	0.00	0.00	2.57	7.09
Hamt-1	Hamit	7.54	51.37	30.26	3.87	0.00	1.19	0.00	0.25	0.17	0.39	0.00	0.43	0.00	0.00	4.54
Hamt-2	Hamit	6.11	49.07	36.11	5.16	0.00	0.58	0.00	0.21	0.29	0.34	0.00	2.14	0.00	0.00	0.00
Hamt-3	Hamit	7.54	55.99	24.76	4.83	0.00	0.85	0.00	0.21	0.00	0.32	0.00	0.00	0.00	0.74	4.77
idis-1	İdişdağı	7.41	50.30	26.53	5.33	0.00	0.00	0.04	0.16	0.00	0.32	0.00	0.00	0.00	0.05	9.84
idis-2	İdişdağı	19.32	41.63	32.03	0.00	0.54	0.00	2.29	0.05	0.00	0.32	0.00	2.85	0.97	0.00	0.00
idis-3	İdişdağı	9.76	32.19	43.14	4.71	0.00	0.00	1.35	0.07	0.00	0.32	0.16	0.45	0.00	0.00	7.87
idis-4	İdişdağı	5.97	59.81	25.18	2.96	0.00	0.66	0.00	0.07	0.44	0.53	0.00	3.93	0.00	0.00	0.46

5. Geochemistry

The major oxide % element contents of alkali feldspar granite and alkali feldspar syenites examined in the study are given in table 3. The results of the geochemical analysis were interpreted by comparing with some of the alkaline feldspar granites in the literature (Junggar-Mongolia, Changyi-China, Alvand-Iran, Katharina-Egypt, Scotland, Klipberg-Africa) (Table 4) (Data were taken from Scheepers and Schoch, 1988; Murphy et al., 1998; Katzir et al., 2007; Geng et al., 2009; Aliani et al., 2011; Lan et al., 2015).

Alkaline feldspar granites outcropping in the form of dykes in the vicinity of Kalebalta, Yıldırımlı, Çerkezuşağı, Çatalçeşme, İbrahimbeyli, Deliler, Ekecik, Sipahiler, Camili, Yaylak and Namlıkışla in the AIT have values of 71.05-78.84% (average 74.64%) SiO_2, 11.56-15.70% (average 13.28%) Al_2O_3, 3.92-7.78% (average 5.58%) K_2O and 2.11-6.22% (average 3.48%) Na_2O (Table 3). It is seen that the rocks have very low amounts of Fe_2O_3 (0.04-1.99%), MgO (0.04-0.98%) and TiO_2 (0.01-0.79%). This situation is due to the low ratios of accessory minerals such as the mafic and magnetite and ilmenite in the rocks.

There are observed slight differences in the contents of some elements in the case of two micaceous alkali feldspar granites and muscovite alkali feldspar granites in the Hacılı Suite (Sarıhacılı) located to the east of Yozgat province (Table 3). The SiO_2 and Al_2O_3 contents of the rocks are almost similar, but there are differences in Na_2O, K_2O, Fe_2O_3, MgO and TiO_2 contents. Na_2O contents of the two micaceous alkali feldspar granites are 2.67-4.02%, the K_2O contents 5.43-6.84%, the Fe_2O_3 contents 1.06-1.83%, the MgO contents 0.25-1.97% and the TiO_2 contents 0.11-0.53%. On the other hand, the contents of these oxides vary between 1.48-5.58%, 5.15-9.90%, 0.13-0.84%, 0.02-0.74% and 0.06-0.68%, respectively. Muscovite alkali feldspar is high in K_2O ratio in granites, because of the high ratio of muscovite. Moreover, the reason for the high Na_2O ratio is due to the fact that some of the feldspar minerals are in albite composition. Similarly; since the two micaceous alkali feldspar granites contain both muscovite and biotite minerals, Fe and Mg values are higher than those of muscovite granites. Moreover, TiO_2 value due to the observation of accessory titanites in free state in two-micaceous granites is found to be higher than TiO_2 content in muscovite granites. (Figure 5).

When the chemical compositions of the alkali feldspar granites located around Cefalık, Behrekdağ and Terlemez are compared with AIT and the Hacılı Suite (Sarıhacılı), it is seen that SiO_2 and TiO_2 contents are low, but Al_2O_3, Fe_2O_3, MgO, Na_2O and K_2O contents are relatively high (Table 3, Figure 5). SiO_2 and TiO_2 contents of these rocks are between 68.80-76.40 (average 72.37%) and 0.02-0.30% (mean 0.19%), respectively (Table 3). Elements and their amounts with average values are as follows; MgO 0.08-1.53% (average 1.00%), Na_2O 2.21-5.90% (average 4.13), K_2O 4.33 to 7.91 (average 6.28%), Al_2O_3 11.86-15.35% (average 14.04%), Fe_2O_3 0.10-2.79% (average 14.09%) (Table 3).

The alkali feldspar syenites outcropping in Bayındır, Hamit and İdişdağı Suites were chemically compared with the alkali feldspar granites, and it was seen that Al_2O_3 (14.07-16.81%, average 15.30%), Fe_2O_3 (0.46-3.99%, average 2.25%), Na_2O (4.19-7.64%, average %6.19) and TiO_2 (0.04-1.16%, average 0.41%) were relatively high, however; SiO_2 (64.11-68.56%, average 66.13%) content was low (Table 3). On the other hand, K_2O (4.16-7.25%, average 5.28%) values are close to each other (Figure 5c-d, Figure 7). There is observed a positive correlation between the amounts of Na_2O and K_2O and the amounts of Fe_2O_3 and TiO_2 in these samples (Figure 5).

Klipberg (Africa) alkali feldspar granites contain 4.47-5.71% (average 4.92%) Na_2O, 4.40-5.27% (average 4.80%) K_2O, 0.35-3.08% (average 1.49%) Fe_2O_3 and 0-0.16% TiO_2 (Table 4). Junggar (Mongolia) alkaline feldspar granites consist of 0.93-3.40% Fe_2O_3 (average 1.96%), 0.08-0.42% TiO_2 (average 0.20%), 3.36-5.14% Na_2O (average 4.21%), 2.56-6.29% K_2O (Table 4). The contents of Fe_2O_3 (1.69-3.67%, 2.99% average) and TiO_2 (0.24-0.29%, 0.26%) are higher in the Changyi (China) alkali feldspar granites while Na_2O (2.86-6.56%, average 3.82%) and K_2O (0.29-5.14%, average 4.10%) contents are partially lower (Table 4). The Na_2O and K_2O contents are not very variable, but differences in Fe_2O_3 and TiO_2 contents are observed. The Katharina (Egypt) alkali feldspar granites have contents of 1.10-1.80% Fe_2O_3 (average 1.42%) and 0.07-0.09% TiO_2 (average 0.08%) (Table 4). The lowest Fe_2O_3 (0.41-1.13%, average 0.78%) and TiO_2 (0.02-0.05%, average 0.03%) contents are observed in Scottish granites. Alvand (Iran) granites have K_2O (6.12%) contents higher than Na_2O (2.41%) and Fe_2O_3 contents are 1.5% (Table 4).

Table 3- Major oxide geochemistry of the Central Anatolian alkali feldspar granites and alkali feldspar syenites.

Sample Number	Location	SiO_2	Al_2O_3	Fe_2O_3	MgO	CaO	Na_2O	K_2O	TiO_2	K_2O/Na_2O	Na_2O/K_2O
Kaleb-1	Kalebalta	72.67	12.86	1.99	0.10	0.70	3.45	6.84	0.44	1.98	0.50
Kaleb-2	Kalebalta	72.61	12.87	1.12	0.06	0.28	4.52	6.87	0.48	1.52	0.66
Kaleb-3	Kalebalta	75.24	11.56	1.97	0.57	0.09	2.33	5.78	0.44	2.48	0.40
Kaleb-4	Kalebalta	75.30	12.22	1.69	0.87	0.56	3.02	3.92	0.12	1.30	0.77
Kaleb-5	Kalebalta	71.64	13.64	1.11	0.71	0.72	3.44	6.93	0.19	2.02	0.50
Kaleb-6	Kalebalta	73.65	13.81	0.82	0.66	0.71	2.86	4.74	0.79	1.66	0.60
Agac-1	Agaçören	73.96	13.69	0.61	0.69	0.98	2.85	5.65	0.15	1.98	0.50
Agac-2	Agaçören	73.54	13.49	0.83	0.90	0.02	2.77	5.49	0.13	1.98	0.51
Agac-3	Agaçören	74.57	13.39	0.44	0.94	0.23	3.18	4.82	0.13	1.51	0.66
Agac-4	Agaçören	72.55	14.45	0.44	0.91	0.33	3.18	4.79	0.11	1.51	0.66
Yıld-1	Yıldırımlı	78.17	12.73	0.36	0.51	0.14	2.87	4.38	0.19	1.53	0.65
Yıld-2	Yıldırımlı	76.62	12.77	0.29	0.57	0.37	3.88	4.23	0.19	1.09	0.92
Yıld-3	Yıldırımlı	73.37	12.16	0.22	0.04	0.87	3.63	7.33	0.19	2.02	0.50
Yıld-4	Yıldırımlı	74.23	12.76	0.65	0.64	0.52	2.78	7.34	0.51	2.64	0.38
Cerk-1	Çerkezuşağı	72.20	12.10	0.14	0.98	0.73	5.25	7.88	0.29	1.50	0.67
Cerk-2	Çerkezuşağı	74.82	12.27	0.92	0.47	0.01	3.09	6.18	0.18	2.00	0.50
Cerk-3	Çerkezuşağı	75.02	12.92	0.28	0.61	0.20	3.20	6.12	0.15	1.91	0.52
Nkisla-1	Çatalçeşme	71.86	12.80	0.36	0.68	0.54	4.91	6.86	0.30	1.40	0.72
Nkisla-2	Çatalçeşme	73.67	12.60	0.28	0.83	0.74	3.52	7.13	0.13	2.03	0.49
İbrah-1	İbrahimbeyli	75.32	12.70	0.77	0.25	0.06	2.32	6.80	0.15	2.93	0.34
İbrah-2	İbrahimbeyli	76.29	12.06	0.90	0.78	0.18	2.88	5.30	0.52	1.84	0.54
Delil-1	Deliler	78.84	12.32	0.68	0.44	0.96	2.11	4.06	0.17	1.93	0.52
Delil-2	Deliler	76.81	13.15	0.56	0.67	0.38	3.40	4.31	0.18	1.27	0.79
Delil-3	Deliler	75.28	13.60	0.92	0.85	0.71	2.95	4.36	0.18	1.48	0.68
k-Ekeck-1	Ekecik	76.31	13.50	0.62	0.76	0.68	2.85	4.46	0.55	1.56	0.64
k-Ekeck-2	Ekecik	75.20	14.21	0.72	0.10	0.51	3.80	4.01	0.28	1.06	0.95
k-Ekeck-3	Ekecik	74.25	13.04	0.53	0.36	0.96	3.00	7.05	0.44	2.35	0.43
Siph-1	Sipahiler	71.05	14.70	0.06	0.62	0.46	5.42	6.62	0.19	1.22	0.82
Siph-2	Sipahiler	73.08	14.80	0.12	0.55	0.58	4.32	5.01	0.21	1.16	0.86
Siph-3	Sipahiler	73.01	13.80	0.04	0.52	0.36	3.41	7.70	0.16	2.26	0.44
Cefalık-1	Cefalık	72.10	13.20	0.10	0.64	0.62	4.36	7.91	0.16	1.81	0.55
Cefalık-2	Cefalık	73.78	14.11	0.36	1.01	0.87	3.25	6.34	0.30	1.95	0.51
Cefalık-3	Cefalık	74.13	14.07	1.38	0.27	0.70	2.21	7.37	0.18	3.33	0.30
Cefalık-4	Cefalık	75.47	14.01	1.52	0.38	0.52	3.46	4.33	0.15	1.25	0.80
Behrek-1	Behrekdağ	69.91	14.27	0.43	0.94	0.01	4.26	7.87	0.30	1.85	0.54
Behrek-2	Behrekdağ	68.80	14.50	0.10	0.98	0.50	5.90	7.80	0.20	1.32	0.76
Behrek-3	Behrekdağ	70.82	14.38	0.85	0.89	0.86	4.99	7.14	0.27	1.43	0.70
Behrek-4	Behrekdağ	72.80	14.87	0.45	0.97	0.21	4.28	4.91	0.12	1.15	0.87
Behrek-5	Behrekdağ	71.21	14.61	0.48	1.02	0.01	4.49	6.74	0.29	1.50	0.67
Behrek-6	Behrekdağ	72.67	15.35	1.75	0.64	0.55	4.35	4.54	0.20	1.04	0.96
Terlm1	Terlemez	69.85	14.75	2.79	1.53	0.79	3.27	5.31	0.17	1.62	0.62
Terlm2	Terlemez	76.40	11.86	0.85	0.08	0.45	4.90	5.41	0.02	1.10	0.91
Cam-1	Camili	75.06	14.99	0.50	0.10	0.53	4.72	4.37	0.04	0.93	1.08
Cam-2	Camili	77.36	12.66	0.74	0.08	0.41	3.90	4.91	0.02	1.26	0.79
Cam-3	Camili	74.86	12.13	0.75	0.28	0.23	6.22	5.88	0.01	0.95	1.06
Yaylak-1	Yaylak	72.83	15.60	0.28	0.13	0.74	4.52	5.13	0.13	1.13	0.88
Yaylak-2	Yaylak	75.32	15.70	0.77	0.15	0.06	2.32	4.80	0.15	2.07	0.48
Yaylak-3	Yaylak	76.29	15.06	0.90	0.18	0.18	2.88	4.30	0.12	1.49	0.67
Yaylak-4	Yaylak	78.84	12.32	0.68	0.14	0.96	3.11	4.06	0.17	1.31	0.77
Hacılı-9	Yozgat	76.08	11.57	0.74	0.74	0.21	3.69	6.52	0.40	1.77	0.57
Hacılı-10	Yozgat	77.06	12.06	0.84	0.32	0.12	2.70	5.31	0.67	1.97	0.51
Hacılı-11	Yozgat	76.28	12.84	0.83	0.14	0.15	2.65	5.15	0.68	1.94	0.51

Table 3- continued.

Sample Number	Location	SiO_2	Al_2O_3	Fe_2O_3	MgO	CaO	Na_2O	K_2O	TiO_2	K_2O/Na_2O	Na_2O/K_2O
Hacılı-12	Yozgat	76.20	12.33	0.74	0.18	0.17	2.94	5.35	0.67	1.82	0.55
Hacılı-13	Yozgat	76.35	12.92	0.32	0.19	0.18	2.60	5.74	0.59	2.21	0.45
Hacılı-14	Yozgat	76.16	12.98	0.23	0.16	0.13	2.46	5.46	0.63	2.22	0.45
Hacılı-15	Yozgat	76.85	12.98	0.13	0.18	0.09	2.71	5.50	0.62	2.03	0.49
Hacılı-16	Yozgat	76.29	11.95	0.27	0.02	0.03	1.48	9.90	0.06	6.69	0.15
Hacılı-17	Yozgat	74.62	12.87	0.18	0.25	0.18	4.21	6.84	0.18	1.62	0.62
Hacılı-18	Yozgat	73.08	13.11	0.14	0.16	0.26	5.58	6.77	0.31	1.21	0.82
Hacılı-19	Yozgat	76.54	13.33	0.17	0.17	0.16	2.12	6.51	0.26	3.07	0.33
Hacılı-1	Yozgat	75.00	12.04	1.54	0.48	0.84	4.02	6.11	0.29	1.52	0.66
Hacılı-2	Yozgat	79.03	11.43	1.73	0.44	0.84	3.70	5.70	0.32	1.54	0.65
Hacılı-3	Yozgat	74.11	11.60	1.66	1.74	0.63	2.67	5.72	0.47	2.14	0.47
Hacılı-4	Yozgat	73.40	11.28	1.83	1.97	0.74	2.90	5.43	0.53	1.87	0.53
Hacılı-5	Yozgat	74.32	11.42	1.52	0.90	0.53	3.46	6.45	0.36	1.86	0.54
Hacılı-6	Yozgat	74.86	11.13	1.17	0.88	0.59	3.62	6.70	0.39	1.85	0.54
Hacılı-7	Yozgat	74.73	11.80	1.22	0.94	0.83	3.12	6.84	0.37	2.19	0.46
Hacılı-8	Yozgat	74.60	12.88	1.06	0.25	0.73	2.98	6.32	0.11	2.12	0.47
Alkali Feldspar Syenite											
Bayınd-1	Bayındır	68.56	16.81	0.46	0.56	1.34	5.08	4.23	0.16	0.83	1.20
Bayınd-2	Bayındır	67.26	15.16	1.70	0.97	1.89	6.13	5.41	0.04	0.88	1.13
Bayınd-3	Bayındır	64.99	15.83	1.21	0.06	1.94	6.98	5.98	0.12	0.86	1.17
Bayınd-4	Bayındır	64.16	14.86	2.42	0.68	1.93	7.64	5.49	1.16	0.72	1.39
Hamt-1	Hamit	65.59	15.06	1.94	0.70	1.72	6.48	4.97	0.26	0.77	1.30
Hamt-2	Hamit	64.89	15.80	2.09	0.94	1.81	5.65	5.96	0.29	1.06	0.95
Hamt-3	Hamit	68.06	15.43	1.65	0.86	1.77	7.64	4.19	0.17	0.55	1.82
idis-1	İdişdağı	65.66	14.29	3.32	0.97	1.43	7.11	4.38	0.17	0.62	1.62
idis-2	İdişdağı	66.77	14.92	2.77	0.89	1.02	4.19	5.26	1.11	1.26	0.80

When the samples of some alkali feldspar granites (Junggar-Mongolia, Changyi-China, Alvand-Iran, Katharina-Egypt, Scotland, Klipberg-Africa) in different places of the world are compared with the chemistry of the studied samples, Fe_2O_3 and partly Na_2O values are high while K_2O values are lower (Tables 3 and 4) (Figure 5). TiO_2 contents have similar values with that of samples in the study area (except Yozgat-Hacılı samples) (Figure 5c-d).

6. Discussion

Although feldspar is a very common mineral, quartz, albite, accessory or iron-bearing minerals, which are in the form of inclusions, affect the feldspar's color, purity and the quality, and most of them cannot be used in the glass and ceramics industries. Therefore, when the accessory and iron bearing minerals in the alkali feldspar granites are removed by using techniques such as the magnetic separator and flotation they can be used as a raw material in ceramics and glass industries. As the reserve of alkaline feldspar granites increases, the proportion of minerals such as mafic minerals, magnetite and ilmenite also increases. The morphological features, mineralogical and petrographic characteristics of the alkali feldspar granite and alkaline feldspar syenites were evaluated together. Since the alkali feldspar granites in the AIT are in the form of dykes, the pertitizations in orthoclase minerals which they contain are not observed and quartz or iron bearing accessory minerals are not found as inclusions. On the other hand, due to the widespread exposure of alkaline feldspar granites in Hacılı and Kalebata, the presence of pertitization and poiklitic texture in alkali feldspar minerals can be partially observed. Similar situations in feldspars are more observed in Cefalık, Behrekdağ, Terlemez, Bayındır, Hamit and İdişdağı Suites.

Feldspar minerals are used for different purposes in the production of glass and ceramics according to their chemical compositions. The melting temperature of the orthoclase mineral in $KAlSi_3O_8$ composition is 1170°C, but it can be used largely in the ceramic sector as the melting temperature can even reach up to

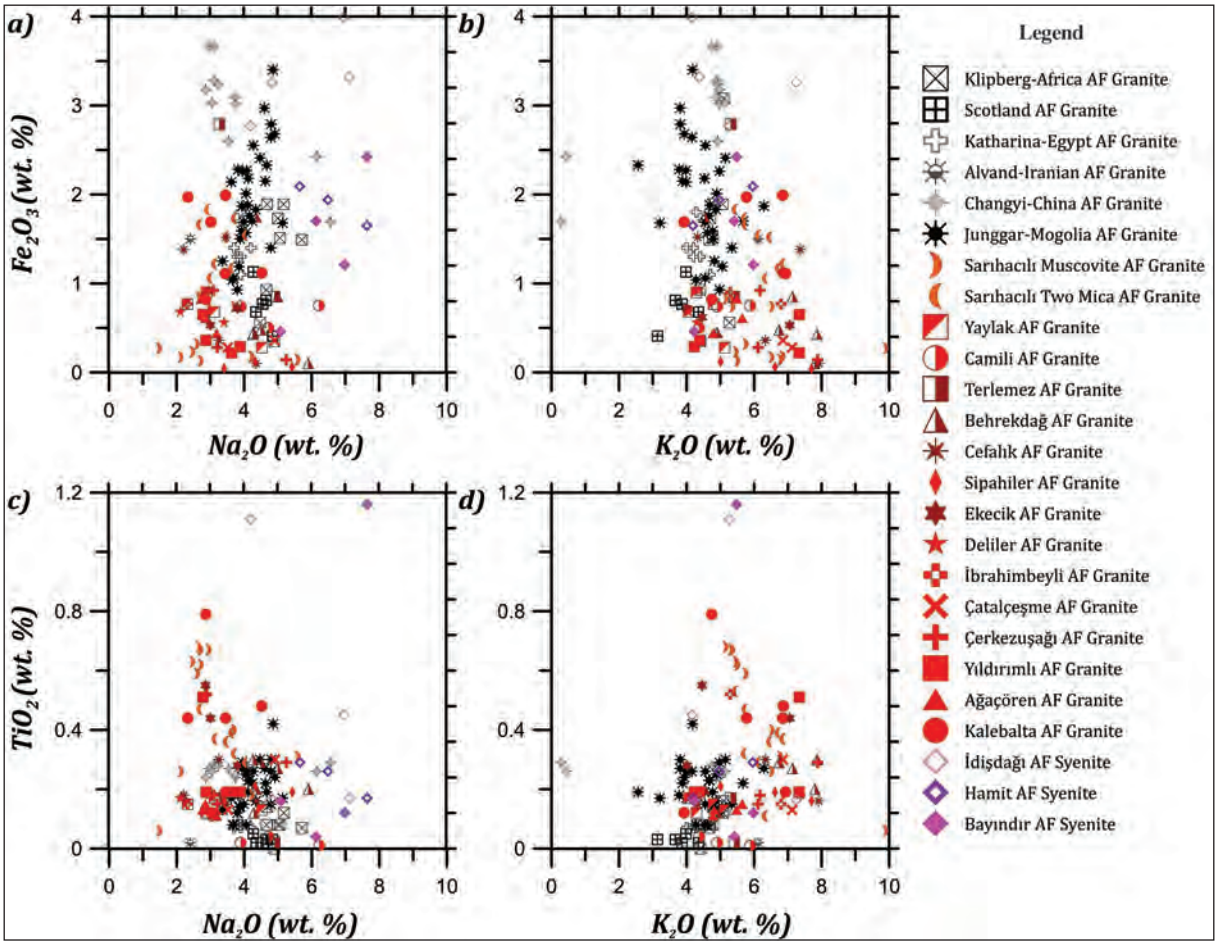

Figure 5- Fe_2O_3 and TiO_2 vs Na_2O and K_2O variation diagram of some alkali feldspar granites and alkali feldspar syenites from the Central Anatolia and the World (AF: Alkali Feldspar).

Table 4- Major oxide geochemistry of some alkali feldspar granites and alkali feldspar syenites from the Central Anatolia and the world.

Sample Number	Location	SiO_2	Al_2O_3	Fe_2O_3	MgO	CaO	Na_2O	K_2O	TiO_2	K_2O/Na_2O	Na_2O/K_2O
idis-3	İdişdağı	66.93	14.07	3.26	1.41	1.25	4.83	7.25	0.17	1.50	0.67
idis-4	İdişdağı	64.11	15.84	3.99	0.54	1.22	6.95	4.16	0.45	0.60	1.67
Junggar-Mongolia Alkali Feldspar Granite (from Geng et al., 2009)											
KM1	Junggar	74.80	12.20	2.28	0.36	1.13	3.82	3.78	0.18	0.99	1.01
KM9802-6	Junggar	74.90	12.60	2.33	0.47	1.51	4.67	2.56	0.19	0.55	1.82
KM2	Junggar	77.90	11.10	1.06	0.02	0.39	3.69	4.55	0.08	1.23	0.81
KM9918-3	Junggar	70.00	13.60	3.40	0.23	1.24	4.86	4.18	0.42	0.86	1.16
MG9951-1	Junggar	78.40	10.70	1.04	0.01	0.46	3.66	4.28	0.08	1.17	0.86
MG136-1	Junggar	73.10	14.40	1.68	0.23	1.70	5.14	3.21	0.17	0.62	1.60
MG9942-1	Junggar	74.30	12.70	2.27	0.38	1.28	4.08	3.98	0.26	0.98	1.03
MG9918-3	Junggar	76.40	11.70	1.69	0.04	0.41	3.99	4.55	0.15	1.14	0.88
MG106-2	Junggar	76.90	11.70	1.25	0.08	0.59	3.36	4.82	0.13	1.43	0.70
MG4*	Junggar	74.40	13.10	2.26	0.19	0.84	3.95	4.97	0.29	1.26	0.79
MG13*	Junggar	71.40	14.80	1.87	0.16	0.70	3.94	6.29	0.27	1.60	0.63
MG16*	Junggar	74.40	12.90	2.01	0.24	0.82	4.06	4.89	0.25	1.20	0.83
MG19*	Junggar	72.50	13.70	2.41	0.13	0.83	4.47	5.15	0.30	1.15	0.87
MG24*	Junggar	73.30	13.60	1.88	0.26	1.71	4.11	4.69	0.23	1.14	0.88
MG26*	Junggar	73.50	14.10	1.59	0.34	1.33	3.92	4.77	0.19	1.22	0.82

Table 4- continued.

Sample Number	Location	SiO_2	Al_2O_3	Fe_2O_3	MgO	CaO	Na_2O	K_2O	TiO_2	K_2O/Na_2O	Na_2O/K_2O
HONG4	Junggar	72.30	12.90	2.97	0.33	0.87	4.60	3.81	0.27	0.83	1.21
HONG5	Junggar	73.50	13.40	2.79	0.26	0.95	4.80	3.82	0.30	0.80	1.26
HONG2	Junggar	74.00	13.80	2.68	0.32	0.92	4.91	3.93	0.24	0.80	1.25
HONG1	Junggar	75.20	12.00	2.15	0.24	0.86	4.63	3.88	0.22	0.84	1.19
HONG3	Junggar	76.40	12.90	1.57	0.03	0.19	4.06	4.62	0.08	1.14	0.88
AK2-1	Junggar	71.50	13.70	2.55	0.45	1.05	4.27	4.56	0.26	1.07	0.94
AK2-2	Junggar	73.00	13.60	2.64	0.44	1.07	4.79	4.16	0.26	0.87	1.15
AK8	Junggar	75.20	12.80	2.18	0.26	0.78	4.12	4.53	0.19	1.10	0.91
AK1-3	Junggar	74.10	12.90	1.83	0.13	0.56	4.34	4.87	0.16	1.12	0.89
AK154-2	Junggar	76.50	11.70	1.50	0.02	0.55	3.88	4.79	0.14	1.23	0.81
AT6*	Junggar	73.00	14.30	1.76	0.29	1.07	4.16	4.66	0.23	1.12	0.89
AT14*	Junggar	76.50	12.60	1.19	0.03	0.38	3.85	5.06	0.14	1.31	0.76
AT19*	Junggar	71.60	14.90	1.70	0.26	0.96	4.24	5.67	0.22	1.34	0.75
AT20*	Junggar	76.80	12.50	0.93	0.01	0.42	3.80	4.98	0.12	1.31	0.76
AT22*	Junggar	72.80	14.40	1.40	0.08	0.61	4.79	5.34	0.15	1.11	0.90
Hatu	Junggar	76.60	11.00	2.14	0.11	0.45	3.62	3.98	0.17	1.10	0.91
KM1	Junggar	74.80	12.20	2.28	0.36	1.13	3.82	3.78	0.18	0.99	1.01
Alvand-Iran Alkali Feldspar Granite (from Aliani et al., 2011)											
AL	Alvand	75.60	12.90	1.50	0.08	0.42	2.41	6.12	0.02	2.54	0.39
Katharina-Egypt Alkali Feldspar Granite (Katzir et al., 2007)											
D97	Katharina	76.60	12.80	1.10	0.05	0.30	3.90	4.70	0.09	1.21	0.83
D54	Katharina	76.90	12.10	1.40	0.01	0.60	3.70	4.20	0.07	1.14	0.88
D59	Katharina	76.90	12.60	1.30	0.01	0.30	3.90	4.40	0.08	1.13	0.89
D93	Katharina	77.00	12.40	1.70	0.05	0.20	3.90	4.50	0.07	1.15	0.87
D100	Katharina	77.60	12.50	1.30	0.05	0.20	3.80	4.20	0.08	1.11	0.90
D43	Katharina	76.80	12.10	1.80	0.01	0.20	3.90	4.30	0.07	1.10	0.91
D40	Katharina	77.20	12.40	1.40	0.01	0.30	4.20	4.00	0.07	0.95	1.05
Scotland Alkali Feldspar Granite (Murphy et al., 1998)											
A1-2	Scotland	77.52	12.32	0.81	-	-	4.65	3.67	0.03	0.79	1.27
A1-4	Scotland	78.07	12.27	0.77	-	-	4.55	3.87	0.02	0.85	1.18
A1-7	Scotland	76.94	12.45	0.68	-	-	4.35	4.35	0.02	1.00	1.00
A1-8	Scotland	78.28	12.19	0.41	-	-	4.84	3.14	0.03	0.65	1.54
A1-10	Scotland	77.18	12.51	1.13	0.13	-	4.27	3.98	0.05	0.93	1.07
A1-15	Scotland	76.12	12.72	0.92	0.03	-	4.94	3.70	0.03	0.75	1.34
Klipberg-Africa Alkali Feldspar Granite (from Scheepers and Schoch, 1988)											
81-05	Africa	70.24	14.12	1.89	0.00	0.74	5.17	5.07	0.12	0.98	1.02
81-12	Africa	75.01	12.79	0.93	0.18	0.01	4.66	4.40	0.08	0.94	1.06
81-22A	Africa	74.24	13.24	0.56	0.18	0.06	4.47	5.27	0.07	1.18	0.85
81-34	Africa	73.66	13.45	1.51	0.14	0.00	5.06	4.78	0.08	0.94	1.06
81-35	Africa	75.97	13.02	0.35	0.13	0.00	4.89	4.41	0.00	0.90	1.11
81-36	Africa	72.88	13.66	1.73	0.15	0.40	5.33	4.70	0.08	0.94	1.06
81-51	Africa	71.77	13.79	3.08	0.00	0.17	4.68	5.09	0.16	0.15	6.48
81-14	Africa	71.49	13.56	1.89	0.12	0.29	4.88	4.78	0.14	1.02	0.98
81-25	Africa	72.52	13.40	1.49	0.14	0.02	5.71	4.67	0.07	0.82	1.22
Changyi–China (from Lan et al., 2015)											
CY2-49	China	76.00	12.00	3.28	0.26	0.73	3.11	4.89	0.28	1.57	0.64
CY2-75	China	76.30	11.90	3.67	0.24	0.64	2.98	4.90	0.27	1.64	0.61
CY2-76	China	76.60	11.60	3.09	0.23	0.58	3.73	4.88	0.24	1.31	0.76
CY2-77	China	76.60	11.70	3.02	0.21	0.62	3.75	4.98	0.25	1.33	0.75
CY2-78	China	76.70	12.00	2.60	0.17	0.57	3.54	4.92	0.27	1.39	0.72
CY2-79	China	76.40	11.80	3.66	0.26	0.75	3.10	4.76	0.28	1.54	0.65
CY2-80	China	76.60	11.90	3.03	0.20	0.53	3.05	5.14	0.26	1.69	0.59
CY2-86	China	76.40	11.80	3.24	0.22	0.69	3.23	4.93	0.28	1.53	0.66
CY2-92	China	77.40	11.60	3.18	0.23	0.39	2.86	4.97	0.24	1.74	0.58
CY2-43	China	78.30	12.30	1.69	0.39	0.57	6.56	0.29	0.29	0.04	22.62
CY2-44	China	77.90	12.00	2.43	0.58	0.70	6.15	0.44	0.26	0.07	13.98

1280°C. On the other hand, as the melting temperature of the albite in $NaAlSi_3O_8$ composition is 1120°C, it has high melting characteristics. For this reason, it is used in glaze phase (Önem, 1997; Gürsoy, 1999). The plagioclase minerals in the rocks can be used for making glazes in ceramics as types of plagioclase minerals are albite and oligoclase, and these minerals are rich in Na. Therefore, it is also important to determine the species of plagioclase minerals.

Because of the high amount of the quartz ratio as well as the feldspar amounts of the studied rocks, the quartz also seems to be a by-product in addition to the feldspar content. In addition to the quartz has also an important role in the production of ceramics. Quartz increases stiffness, prevents deformation, reduces capillary cracking as it reduces heat expansion, and increases the strength when added into glaze. However, secondary silica minerals, such as tridimite in SiO_2 composition formed at low temperatures also become a member of the undesired mineral group as the raw material. The tridimite mineral causes delamination as it easily decomposes, raises the melting temperature and increases water absorption and porosity in baked ceramics (Gürsoy, 1999). For this reason, it is formerly necessary to determine the ratio of the secondary silica minerals at low temperature.

The results of whole rock chemical analyzes are guiding for the feldspar minerals to be raw materials. In addition to this, the mineral chemistry of the feldspar minerals in the rock or the concentrated mineral feldspars obtained after the enrichment are very important in terms of being used in the industry. The chemical properties of feldspars (according to TS 11325) that can be used in the industry and the EPMA results of feldspar minerals taken at different locations from the study area are given in Table 5. According to point chemical analysis results, the alkali feldspars have values of 64.07-66.14% SiO_2, 18.20-19.09% Al_2O_3, 14.44-16% K_2O, 0.64-1.66% Na_2O and 0-0.05% FeO. The alkali feldspars are generally in orthoclase and microcline composition according to the results of point analysis (Figure 6). It was found that there was no significant change between edge and core measurements of alkali feldspar and it showed a more homogeneous composition (Table 5). On the other hand, the fact that the FeO content ratios are very low on the same measurements significantly increases the usability of these minerals in the ceramic industry. According to this, when the point chemical results of alkali feldspar and plagioclase minerals are compared with chemical properties that should be in the Class I, II and III feldspar raw material in the results of EPMA analysis, the K_2O content of alkali feldspar is higher than the minimum values (Tables 5 and 6). Therefore, it is seen that alkali feldspar minerals of rocks in the region can be used as class I alkali feldspar. In addition, the amounts of Fe and Ti, which represent the content of undesirable elements in the feldspar, are well below the desired maximum values (Tables 5 and 6). Although K_2O content of the feldspar to be used in the ceramic industry based on TS11325 standard seems to be the most important parameter, the feldspar minerals in different chemical composition can be used in different purposes at different stages of the production. For this reason, feldspar minerals in different composition in rocks can be used as raw materials for different purposes.

In high quality porcelains, the amount of Fe_2O_3 in the total product should not exceed 0.15% and the amount of TiO_2 should not exceed 0.05%, whereas the content of Fe_2O_3 in glass should be maximum 0.08% (Lewicka, 2010). As Fe contents of alkali feldspar granite and alkali feldspar syenites have low Fe contents, they are suitable raw materials for ceramic and glass making (Table 3, Figure 7). The high Fe contents of Hacılı alkaline feldspar granites with respect to other alkali feldspars can be reduced by appropriate magnetic separation and flotation. When we look at the world examples of alkali feldspar granites, it is seen that the Fe contents are higher than most of the studied granites. Therefore, it was revealed that the usage potential of alkali feldspar granites in the Central Anatolian Region had in the ceramic industry.

In modern fast cooking techniques, Na rich feldspar (K_2O / Na_2O <1) or nepheline syenite (Na_2O / K_2O ~ 2) because of strong melting behaviors is preferred due to strong solvent behavior (Lewicka, 2010). In all alkali feldspar granites, except for the Camili alkali feldspar, the K_2O / Na_2O is higher than 1 (Table 3) (Figures 8 and 9). This situation is related with the feldspars rich in K rather than Na in these rocks and the high orthoclase contents as clearly seen from normative mineral ratios (Table 2). It can be said that these rocks have suitable minerals and chemical compositions to be raw materials, but they are not suitable for rapid cooking techniques due to low Na. On the other hand, the K_2O / Na_2O ratio of alkali feldspar syenites of Bayındır, Hamit (except 1 sample) and İdişdağı (except for the sample 2) is less than 1 (Chart 3) (Figures 8 and 9). In this case, it seems that the fast

Table 5- Results of mineral chemistry of some feldspar minerals of rocks (EPMA).

	A1	A2	A3	A4	A5	A6	A7	A8	A9	A10	A11	A12	A13	A14
	Core	Core	Rim	Rim	Core	Rim	Rim	Rim	Rim	Rim	Core	Rim	Rim	Rim
SiO_2	64.64	65.59	65.34	65.75	65.46	65.54	66.14	64.07	64.57	65.26	64.81	64.79	64.07	65.57
Al_2O_3	18.75	18.61	18.20	18.47	18.23	18.42	18.66	18.30	19.09	18.88	18.33	18.65	18.30	19.09
TiO_2	0.06	0.03	0.02	0.04	0.01	0.01	0.01	0.02	0.02	0.02	0.06	0.03	0.02	0.02
Cr_2O_3	0.01	0.01	0.00	0.04	0.02	0.04	0.04	0.02	0.00	0.03	0.04	0.04	0.03	0.00
FeO	0.01	0.00	0.02	0.05	0.05	0.04	0.03	0.01	0.04	0.00	0.02	0.05	0.01	0.04
MnO	0.01	0.00	0.01	0.01	0.03	0.03	0.02	0.02	0.01	0.01	0.03	0.03	0.02	0.01
MgO	0.00	0.00	0.00	0.00	0.00	0.00	0.00	0.00	0.00	0.00	0.00	0.00	0.00	0.00
CaO	0.06	0.02	0.00	0.04	0.02	0.01	0.02	1.43	0.43	0.23	0.01	0.03	1.43	0.43
Na_2O	1.43	1.28	1.10	1.37	1.35	1.07	1.29	0.86	1.66	1.26	0.64	1.58	0.86	1.66
K_2O	14.93	15.46	15.65	15.05	15.20	15.31	15.03	15.53	14.44	15.20	16.10	14.57	15.53	14.44
Total	99.90	101.00	100.34	100.82	100.37	100.47	101.24	100.26	100.26	100.89	100.02	99.76	100.27	101.26
Ions according to 32O														
Si	11.920	11.975	12.019	12.003	12.019	12.013	12.009	11.861	11.858	11.923	11.982	11.945	11.860	11.905
Al	4.076	4.006	3.947	3.975	3.946	3.980	3.994	3.994	4.133	4.067	3.995	4.054	3.994	4.086
Ti	0.008	0.004	0.003	0.005	0.001	0.001	0.001	0.003	0.003	0.003	0.006	0.003	0.003	0.003
Cr	0.001	0.001	0.000	0.006	0.003	0.006	0.006	0.003	0.000	0.004	0.006	0.006	0.004	0.000
Fe^{+2}	0.002	0.000	0.003	0.008	0.008	0.006	0.005	0.002	0.006	0.000	0.003	0.008	0.002	0.006
Mn	0.002	0.000	0.002	0.002	0.005	0.005	0.003	0.003	0.002	0.002	0.005	0.005	0.003	0.002
Mg	0.000	0.000	0.000	0.000	0.000	0.000	0.000	0.000	0.000	0.000	0.000	0.000	0.000	0.000
Ca	0.012	0.004	0.000	0.008	0.004	0.002	0.004	0.284	0.085	0.045	0.002	0.006	0.284	0.084
Na	0.511	0.453	0.392	0.485	0.481	0.380	0.454	0.309	0.591	0.446	0.229	0.565	0.309	0.584
K	3.512	3.601	3.673	3.505	3.560	3.580	3.482	3.668	3.383	3.543	3.797	3.427	3.668	3.345
Estimated molecular percent values														
An	0	0	0	0	0	0	0	7	2	1	0	0	7	2
Ab	13	11	10	12	12	10	12	7	15	11	6	14	7	15
Or	87	89	90	88	88	90	88	86	83	88	94	86	86	83

frying technique can be applied to alkaline feldspar syenites. The excess Na content in such rocks is due to feldspatoid minerals such as nepheline it contains. The fact that the Na_2O / K_2O ratio of alkaline feldspar granite samples is not around 2 and even below this value indicates that the feldspars in these rocks do not have fast solvent behavior (Figure 3) (Figures 8 and 9). On the other hand, in most of alkaline feldspar syenite samples this ratio is close to desired value and these minerals contain normative nepheline based on CIPW normative which causes them to show solvent behavior (Figures 8 and 9). It is considered that rocks in the area where the ratio of K_2O / Na_2O is more than one are suitable for use by applying traditional cooking techniques (Figure 9).

As the plagioclase ratio increases the orthoclase ratio decreases in the rocks studied. Accordingly; K_2O contents decrease as Na_2O content increases (Tables 2 and 3) (Figure 10a). The total alkali (Na_2O + K_2O) amount decreases with increasing SiO_2 in all samples (Figure 10b). This situation is related to the decrease in the ratio of feldspar minerals with the increase of the quartz ratio in the rock. It is known that the melting temperature of ceramics changes with the content of free silica and alkali oxides. The orthoclase rate decreases as the plagioclase ratio in the rocks to be studied increases. Therefore, as Na_2O content increases, K_2O contents decrease (Tables 2 and 3) (Figure 10a). The total amount of alkali (Na_2O + K_2O) decreases with increasing SiO_2 in all samples (Figure 10b). This is related to the decrease in the ratio of

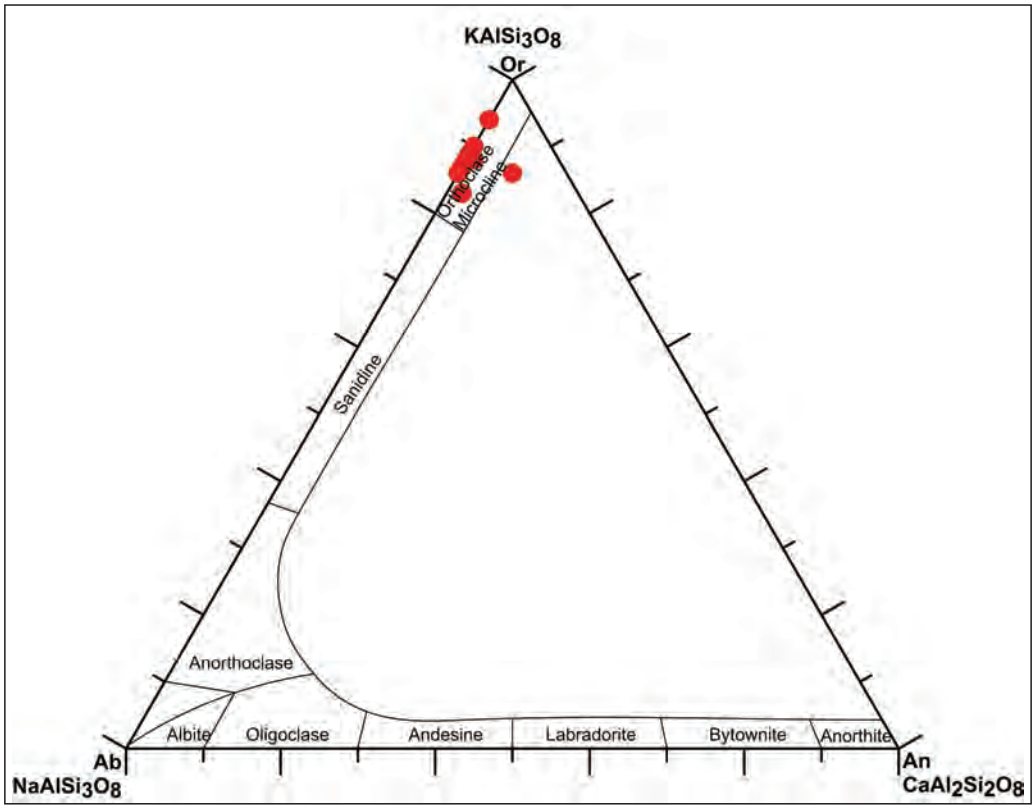

Figure 6- Ternary classification diagram of Ab-Or-An minerals.

Table 6- Required chemical compositions of feldspar classes in the Ceramic sector (TS 11325).

Feldspar Chemistry (%)	I. Class	II. Class	III. Class
Na_2O+K_2O	10.0	9.00	8.00
K_2O	9.00	7.00	-
Na_2O	3.00	3.50	-
Fe_2O_3	0.10	0.20	0.50
TiO_2	0.15	0.30	0.40
CaO+MgO	1.00	1.20	1.60
TiO_2+CaO+MgO	1.15	1.50	2.00

feldspar minerals with the increase of the quartz ratio in the rock. It is known that the melting temperature of ceramics changes with the content of free silica and alkali oxides. The melting temperature of the rocks will also decrease as the silica and quartz content decreases compared to the feldspar contents. It can be said that the melting temperatures of alkali feldspar granites are lower than those of alkaline feldspar syenites (Figure 10b). Besides, it seems impossible to operate the quartz mineral as a byproduct besides the feldspar minerals because of the absence or very little (0-5%) of quartz content in alkali feldspar syenites.

7. Conclusions

The need for quality raw materials, which do not contain particularly undesirable coloring minerals, has increased with the recent introduction of feldspar minerals as raw materials in many areas such as sanitary ware, refractory, cement, special glass, abrasive and superconductor. This requires the determination of new deposits in addition to known deposits with their specification. When geological, petrographical and geochemical data obtained in the study carried out in Central Anatolia Region for this purpose were evaluated together, it was determined that alkali feldspar granites in the AIT had good quality as feldspar raw materials but had relatively low reserves as they were not present in the form of dykes. On the other hand, it is possible to produce good quality feldspar with high reserve as it is not the same in other deposits (Hacılı, Cefalık, Behrekdağ, Terlemez, Bayındır, Hamit and İdişdağı). However, it seems possible to produce feldspar in the desired quality when considering that the coloring elements in the rocks are below the desired values as the availability of high quality feldspar is completely dependent on

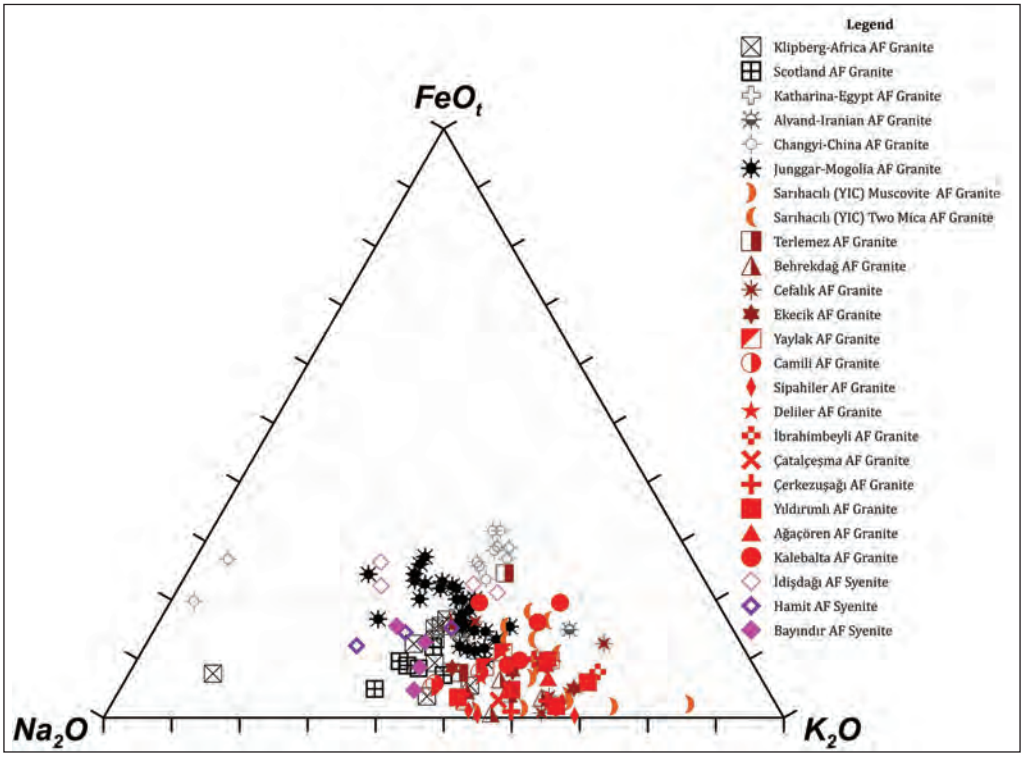

Figure 7- Na_2O–FeOt–K_2O ternary variation diagram of some alkali feldspar granites and alkali feldspar syenites from the Central Anatolia and the World (AF: Alkali Feldspar).

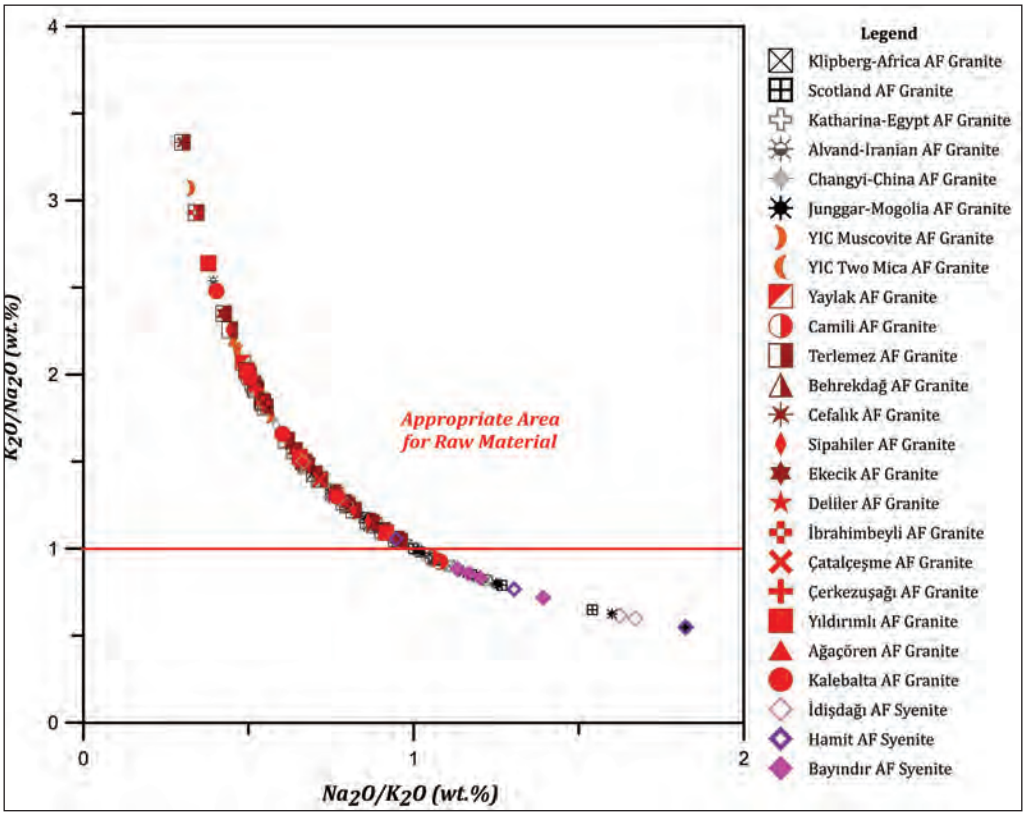

Figure 8- K_2O/Na_2O–FeOt–Na_2O/K_2O ternary variation diagram of some alkali feldspar granites and alkali feldspar syenites from the Central Anatolia and the World (AF: Alkali Feldspar).

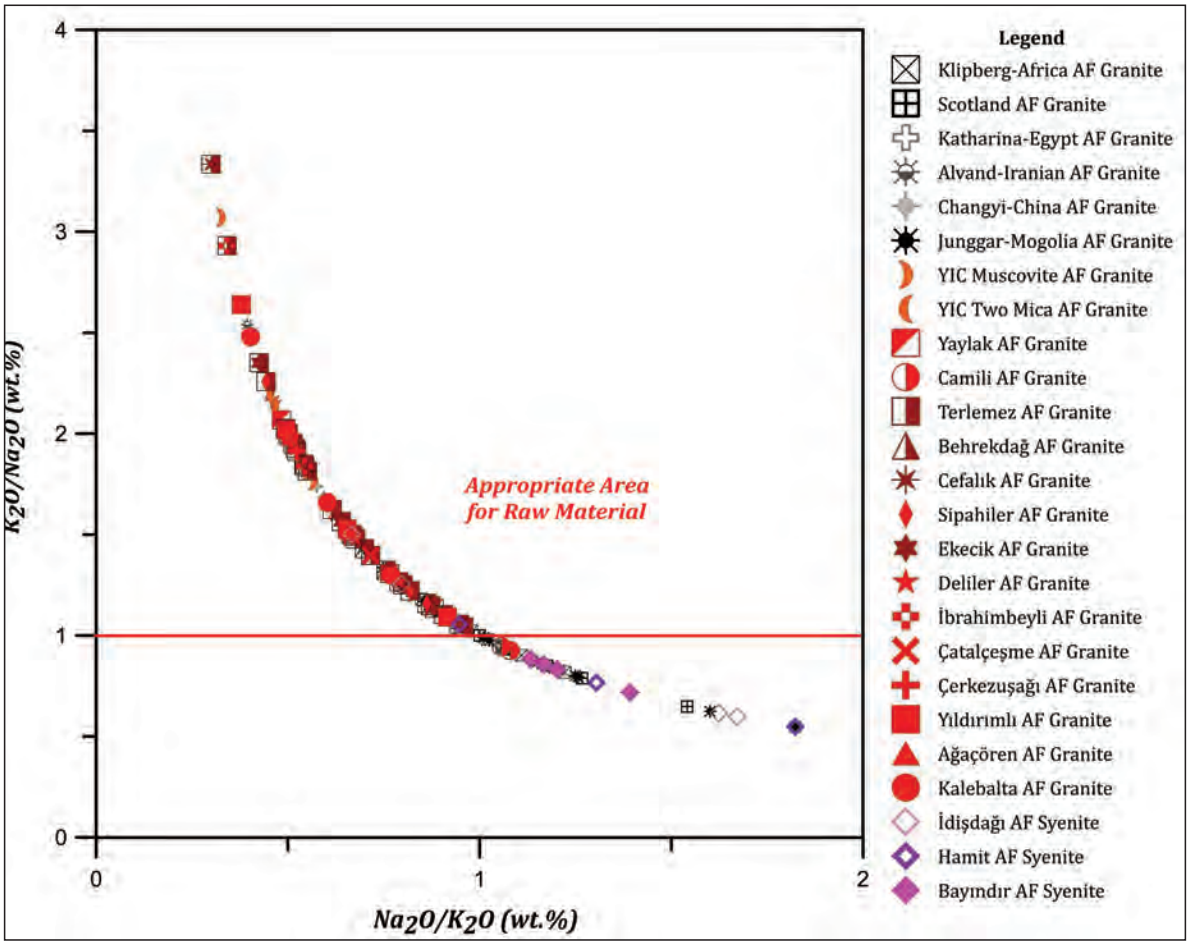

Figure 9- K_2O/Na_2O vs Na_2O/K_2O variation diagram of some alkali feldspar granites and alkali feldspar syenites from the Central Anatolia and the World.

the removal of undesired minerals by means of latest technologies. The lower proportion of color-forming oxides, such as Fe_2O_3, in the mineral and/or rock will lead to a reduction in the magnetic separation phases, thereby resulting in time and labor savings. Feldspar (especially K-feldspar) minerals, which are used as industrial raw materials in ceramic and glass industries in our country, are obtained from pegmatites and nepheline syenites (Çelik and Denizhan, 2016).

In order to meet both the Na-feldspar and K-feldspar requirements, alternative rocks should be determined and their sources must be identified. In this study the feldspar raw material potential of the Central Anatolia alkali feldspar granites and alkali feldspar syenites were revealed by geological, petrographical and chemical data. Thus, it was determined that the feldspar formations in the sector constituted a great potential area for the ceramic industry.

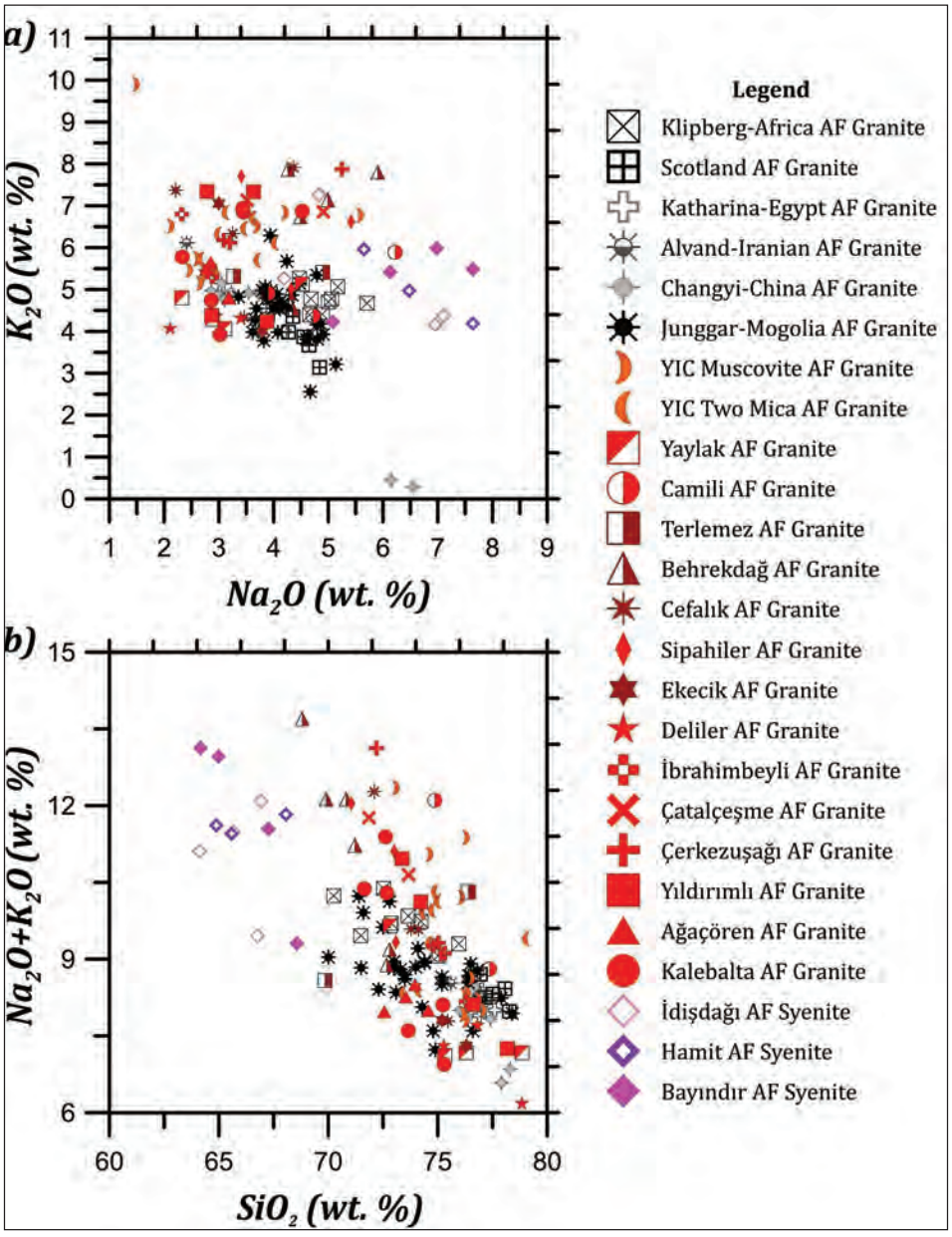

Figure 10- (a) Na_2O vs K_2O and (b) SiO_2 vs Na_2O+K_2O variation diagrams (AF: Alkali Feldspar).

8. Acknowledgements

This study has been partially supported within scope of Ministry of Development (2012K120440) project and Scientific Research Projects, Ankara University (BAP) (17B0443003). The authors thank to Prof. Dr. Osman Candan, Prof. Dr. Özcan Yıldırım Gülsoy and unknown reviewers for their contributions to the manuscript.

References

Aliani, F., Sabouri, Z., Maanijou, M. 2011. Petrography and Geochemistry of Porphyroid Granitoid Rocks in the Alvand Intrusive Complex, Hamedan (Iran). Australian Journal of Basic and Applied Sciences 5, 12, 2192-2199.

Akçe, M.A. 2003. Yozgat batolitinin kuzey bölümünün jeolojisi ve petrolojisi. Yüksek Lisans Tezi, Ankara Üniversitesi Fen Bilimleri Enstitüsü, 118s. Ankara (unpublished).

Akçe, M.A. 2010. Yozgat İntrüzif Kompleksinin Jeolojisi, Petrolojisi ve Orta Anadolu Kristalen Karmaşığındaki Zamansal ve Mekansal Konumu. Doktora Tezi, Ankara Üniversitesi Fen Bilimleri Enstitüsü, 255s. Ankara (unpublished).

Akçe, M.A., Kadıoğlu, Y.K. 2005. Yozgat Batoliti Kuzey Bölümündeki Lökogranitlerin Petrolojisi. Türkiye Jeoloji Bülteni 48, 2, 1-20.

Akıman, O., Erler, A., Göncüoğlu, M.C., Güleç, N., Güven, A., Türeli, T.K., Kadıoğlu, Y.K. 1993. Geochemical Characteristics of Granitoids along the Western Margin of the Central Anatolian Crystalline Complex and Their Tectonic Implications. Geol. J. 28, 371-382.

Akkoyuncu, H. 1994. Porselen hammaddelerinin zenginleştirilmesi. Yüksek Lisans Tezi, Eskişehir Osmangazi Üniversitesi, 52s. Eskişehir (unpublished).

Akkurt, İ. 2001. Çanakkale civarındaki alkalili hammaddelerin seramik yer karosu üretiminde kullanımı. Yüksek Lisans Tezi, Yıldız Teknik Üniversitesi, 107s. İstanbul (unpublished).

Ariffin, K.S. 2003. Feldspathic Minerals. EBS42573 Mineral Perindustrian, 1-16.

Ataman, G. 1972. Ankara'nın güneydoğusundaki granodiyoritik kütlelerden Cefalik Dağının radyometrik yasi hakkında ön çalışma. Hacettepe Fen ve Mühendislik Bilimleri Dergisi 2, 44-49.

Aydoğdu, B. 2010. Yozgat batoliti doğu kenarında (Sorgun Güneyi) yer alan plütonik kayaçların mineralojik-petrografik, jeokimyasal ve petrojenetik özellikleri. Yüksek Lisans Tezi, Cumhuriyet Üniversitesi, 132s. Sivas (unpublished).

Bayhan, H. 1986. Geochemical and genetic interpretation of the Celebi intrusion in the inner Anatolian granitoid belt (in Turkish). Jeoloji Muhendisligi 29, 27–36.

Bayhan, H. 1987. Cefalık ve Baranadağ plütonlarının (Kaman) petrografik ve kimyasal-mineralojik özellikleri. Jeoloji Mühendisliği 30, 3, 11-16.

Bayhan, H. 1988. Bayındır, Akpınar (Kaman) yöresindeki alkali kayaçların jeokimyası ve kökensel yorumu. Türkiye Jeol. Kur. Bült. 31, 59-70.

Bayhan, H. 1989. Petrographical and chemical-mineralogical characteristics of Keskin pluton (in Turkish). Hacettepe Yerbilimleri 15, 29–36.

Bayraktar, I., Ersayın,. S., Gülsoy, Ö.Y. 1997. Upgrading Titanium Bearing Na-Feldspar By Flotation Using Sulphonates, Succinamate And Soaps Of Vegetable Oils. Minerals Engineering I, 12, 1363-1374.

Bayraktar, I., Ersayın,. S., Gülsoy, Ö.Y., Ekmekçi, Z., Can, M. 1999. Temel Seramik ve Cam Hammaddelerimizdeki (Feldispat, Kuvars ve Kaolin) Kalite Sorunlan ve Çözüm Önerileri. Ş. Endüstriyel Hammaddeler Sempozyumu, 14-15 Ekim 1999, İzmir, Türkiye, 22-33.

Bolger, R.B. 1995. Feldspar and nepheline syenite. Industrial Minerals 332, 25-45.

Çelik, M.Y., Denizhan, T. 2016. Kınık-Dinar (Afyonkarahisar) Trakitlerinin K-feldispat Potansiyelinin İncelenmesi. AKÜ FEMÜBİD, 16, 035801, 747-758.

Daday Taykurt, M. 2012. Seramik sağlık gereçlerinde damar hatalarının giderilmesi. Yüksek Lisans Tezi, Anadolu Üniversitesi, 279 s. Eskişehir (unpublished).

Deer, W.A., Howie, R.A., Zussman, J. 1992. An Introduction to the Rock –Forming Minerals. 2nd Etition, Longman, 720 p.

Demir, C. 2001. Na-feldispatın K-feldispattan flotasyonla ayrılmasında inorganik tuzların etki mekanizması. Doktora Tezi, İstanbul Teknik Üniversitesi, 159s. İstanbul (unpublished).

Demirbaş, E. 2010. Kavşit (Çine-Aydın) yöresinin jeolojisi ve feldispat yataklarının incelenmesi. Yüksek Lisans Tezi, Selçuk Üniversitesi, 58s. Konya (unpublished).

Doğu, İ. 2002. Investigation of separation of dark colored minerals from feldspar by selective flocculation. Yüksek Lisans Tezi, Orta Doğu Teknik Üniversitesi, 121s. Ankara (unpublished).

Ehlers, E.G. 1972. The interpretation of geological phase diagrams. W.H. Freeman and Co, San Francisco, 492 p.

Ekici, T. 1997. Yozgat batoliti Yozgat güneyi kesiminin petrolojisi. Yüksek Lisans Tezi, Cumhuriyet Üniversitesi, 90s. Sivas (unpublished).

Erdinç A.Z. 2007. K-feldspar/kuvars ayrımında optimum flotasyon koşullarının belirlenmesi. Yüksek Lisans Tezi, Dokuz Eylül Üniversitesi, 120s. İzmir (unpublished).

Erler, A., Akıman, O., Unan, C., Dalkılıç, B., Geven, A., Önen, P. 1991. Kaman (Kırşehir) ve Yozgat yörelerinde Kırşehir Masifi magmatik kayalarının petrolojisi ve jeokimyası. Doğa-Tr J. Of Engineering and Environmental sciences 15, 76–100.

Ermiş, İ.U. 1996. Determination of the processing parameters of Aydın Çine feldspar and recovering of rutile as a by product. Doktora Tezi, İstanbul Teknik Üniversitesi, 90s. İstanbul (unpublished).

Geng, H., Sun, M., Yuan, C., Xiao, W., Xian, W., Zhao, G., Zhang, L., Wong, K., Wu, F. 2009. Geochemical, Sr–Nd and zircon U–Pb–Hf isotopic studies of Late Carboniferous magmatism in the West Junggar, Xinjiang: Implications for ridge subduction?. Chemical Geology 266, 364–389.

Geredeli, A. 1990. Flotation of feldspar from Balıkesir district. MSc Thesis, Middle East Technical University, 103s. Ankara (unpublished).

Geven, A. 1992. Mineralogy, Petrography and Geochemistry of Cefalikdag Plutonic Rocks (Kaman Region-Central Anatolia). Ph.D. Thesis, Middle East Tehnical University, 165 pp. (unpublished).

Göncüoğlu, M.C., Toprak, V., Kuşcu, İ., Erler, A., Olgun, E. 1991. Orta Anadolu Masifinin Batı Bölümünün Jeolojisi, Bölüm 1-Güney Kesim. TPAO Rapor No. 2909, 140 s.(unpublished).

Göncüoğlu, M.C., Toprak, V., Kuşçu, İ., Erler, A., Olgun, E., Rojay, B. 1992. Orta Anadolu Masifinin Batı Bölümünün Jeolojisi, Bölüm 2: Orta Kesim. T.P.A.O. Rap.No:3155, 76 s.

Göncüoğlu, M.C., Erler, A., Toprak, V., Olgun, E., Yalınız, K., Kuşcu, İ., Köksal, S., Dirik, K. 1993. Orta Anadolu Masifi'nin Orta Bölümü'nün Jeolojisi, Bölüm 3: Orta Kızılırmak Tersiyer Baseni'nin Jeolojik Evrimi. TPAO Rap. No. 3313, 104 s.

Görür, N., Oktay, F.Y., Seymen, İ., Şengör, A.M.C. 1984. Paleotectonic evolution of the Tuzgölü Basin complex. central Anatolia (Turkey): Sedimentary record of Neo-Tethyan closure. Editors: Dixon JE, Robertson AHF. In the geological evolution of the eastern Mediterranean, Geological Society of London, Special publications 17, 467-482.

Gülsoy, Ö.Y. 2005. A Simple Model for the Calculation of Entrainment in Flotation. Korean J. Chem. Eng. 22, 4, 628-634.

Gürsoy, Y.H. 1999. Sarıkaya yöresi altere granitlerinden feldispatın kazanımı. Yüksek Lisans Tezi, Osmangazi Üniversitesi, 112s. Eskişehir (unpublished).

Güven, Z. 2002. Söğüt Çöplük feldispatının duvar karosu üretiminde kullanımı. Yüksek Lisans Tezi, Anadolu Üniversitesi, 58s. Eskişehir (unpublished).

Harben, P.W., Kuzvart, M. 1996. Industrial Minerals A global geology. Industrial Minerals Information Ltd., London, 462 p.

İlbeyli, N. 1998. Petrogenesis of Collision Related Plutonic Rocks, Central Anatolia (Turkey). Doctorate Thesis, University of Durham, 302p. Durham (unpublished).

İlbeyli, N. 2005. Mineralogical-geochemical constraints on intrusives in central Anatolia, Turkey: tectono-magmatic evolution and characteristics of mantle source. Geol. Mag. 142, 187-207.

İlbeyli, N., Pearce, J. 2005. Petrogenesis of igneous enclaves in plutonic rocks of the Central Anatolian Crystalline Complex, Turkey. International Geology Review 47, 78-97.

İlbeyli, N., Kibici, Y. 2009. Collision-related granite magma genesis, potential sources and tectono-magmatic evolution: comparison between central, northwestern and western Anatolia, Turkey. International Geology Review 51, 3, 252-278.

İlbeyli, N., Pearce, J.A., Thirlwall, M.F. and Mitchell, J.G. 2004. Petrogenesis of collision-related plutonics in Central Anatolia, Turkey. Lithos 72, 163-182.

İlbeyli, N., Pearce, J.A., Meighan, I.G., Fallick, A. 2009. Contemporaneous Late Cretaceous Calc-Alkaline and Alkaline Magmatism in Central Anatolia, Turkey: Oxygen Isotope Constraints on Petrogenesis. Turkish Journal of Earth Sciences 18, 529-547.

Kademli, M. 2004. Feldispat cevherinden spiral zenginleştirici ile mikanın uzaklaştırılması. Yüksek Lisans Tezi, Hacettepe Üniversitesi, 100s. Ankara (unpublished).

Kadıoğlu, H. 2001. Sert porselende değişik sır denemelerinin araştırılması. Yüksek Lisans Tezi, Dumlupınar Üniversitesi, 143s. Kütahya (unpublished).

Kadıoğlu, Y.K. 1991. Geology, petrography and geochemistry of Ağaçören (Aksaray) magmatic rocks. MSc Thesis, Middle East Technical University, 141p. Ankara (unpublished).

Kadıoğlu, Y.K. 1996. Genesis of Ağaçören Intrusive Suite and Its Enclaves (Central Anatolia): Constraits From Geological, Petrographic, Geophysical and Geochemical Data. PhD Thesis, Middle East Technical University, 242p. Ankara (unpublished).

Kadıoğlu, Y.K., Güleç, N. 1996. Mafic Microgranular Enclaves and Interaction Between Felsic and Mafic Magmas in the Ağaçören Intrusive Suite: Evidence from Petrographic Features and Mineral Chemistry. International Geology Review 38, 854-867.

Kadıoğlu, Y.K., Özsan, A. 1997. Sulakyurt granitoidindeki ofitik olmayan gabroların konumunun sondajlarla belirlenmesi. 50. Türkiye Jeoloji Kurultayı, Ankara, Türkiye, 14.

Kadıoğlu, Y.K., Dilek, Y., Güleç, N., Foland, K.A. 2003. Tectonomagmatic Evolution of Bimodal Plutons in the Central Anatolian Crystalline Complex, Turkey. The Journal of Geology 111, 671-690.

Kadıoğlu, Y.K., Dilek, Y., Foland, K.A. 2006. Slab break-off and syncollisional origin of the Late Cretaceous magmatism in the Central Anatolian crystalline complexs. Geological Society of America 409, 381-415.

Kalyon, D. 2003. Feldispat kuvars ayırımında kullanılan HF'siz flotasyon yöntemleri. Yüksek Lisans Tezi, Hacettepe Üniversitesi, 117s. Ankara (unpublished).

Karagüzel, C. 2001. Simav yöresi feldispatlarının seramik sanayinde kullanım olanaklarının araştırılması. Doktora Tezi, Dumlupınar Üniversitesi, 136s. Kütahya (unpublished).

Katzir, Y., Eyal, M., Litvinovsky, B.A., Jahn, B.M., Zanvilevich, A.N., Valley, J.W., Beeri, Y., Pelly, I., Shimshilashvili, E. 2007. Petrogenesis of a-Type granites and origin of vertical zoning in the Katharina pluton, Gebel Mussa (Mt. Moses) Area, Sinai, Egypt. Lithos 95,208–228.

Kaya G. 2002. Aydın Çine yöresi albit flotasyon ve triyaj atıklarının seramik bünyelerde kullanımının bünye özelliklerine etkisi. Yüksek Lisans Tezi, Anadolu Üniversitesi, 93s. Eskişehir (unpublished).

Ketin, İ. 1955. Yozgat bölgesinin jeolojisi and Orta Anadolu Masifinin tektonik durumu. TJK Bülteni C, VI, 1, 1-40,

Köksal, S. 1996. The Geological and petrological characteristics of the İdiş Dağı-Avanos area (Nevşehir-central anatolian). MSc Thesis, Middle East Technical University, 140p. Ankara (unpublished).

Köksal, S., Göncüoğlu, M.C. 1997. Geology of İdişdağı-Avanos Area (Nevşehir-Central Anatolia). Mineral Research and Exploration Bulletin 119, 41-58.

Köksal, S., Göncüoğlu, M.C., Floyd, P.A. 2001. Extrusive members of post collisional A-type magmatism in Central Anatolia: Karahıdır Volcanics, İdiş Dağı-Avanos area, Turkey. International Geology Review 43, 8, 683-694.

Köksal, S., Moller, A., Göncüoğlu, C.M., Frei, D., Gerdes, A. 2012. Crustal homogenization revealed by U–Pb zircon ages and Hf isotope evidence from the Late Cretaceous granitoids of the Ağacören intrusive suite (Central Anatolia/Turkey). Contrib Mineral Petrol 163, 725–743.

Köksal, S., Toksoy-Köksal, F., Göncüoğlu, M.C., Möller, A., Gerdes, A., Frei, D. 2013. Crustal source of the Late Cretaceous Satansari monzonite (central Anatolia/Turkey) and its significance for the Alpine geodynamic evolution. Journal of Geodynamics, doi: 10.1016/j.jog.2012.06.003.

Köprülü Tunç, F. 1997. Sintering kinetics of feldspar by the rising temperature technique. Doktora Tezi, Ege Üniversitesi, 46s. İzmir (unpublished).

Kula, S. 2003. Hammaddelerin firit özellikleri üzerine etkisi. Yüksek Lisans Tezi, Anadolu Üniversitesi, 67s. Eskişehir (unpublished).

Lan, T.G., Fan, H.R., Yang, K.F., Cai, Y.C., Wen, B.J., Zhang, W. 2005. Geochronology, mineralogy and geochemistry of alkali-feldspar granite and albite granite association from the Changyi area of Jiao-Liao-Ji Belt: Implications for Paleoproterozoic rifting of eastern North China Craton. Precambrian Research 266, 86–107,

Levin, E.M., Robbins, C.R., McMurdie, H.F. 1974. Phase diagrams for ceramists. The Amer. Cer. Soc., Columbus, Ohio, USA, 626 p.

Lewicka, E. 2010. Conditions of the feldspathic raw materials supply from domestic and foreign sources in Poland. Gospodarka Surowcami Mineralnymi 26, 4, 5–18.

Lünel, A.T. 1985. An approach to the naming. origin and age of Baranadağ monzonite of the Kırşehir intrusive suite. METU Journal of Pure and Applied Sciences 18, 385–404,

Murphy, J.B., Anderson, A.J., Archibald, D.A. 1998. Postorogenic alkali feldspar granite and associated pegmatites in West Avalonia: the petrology of the Neoproterozoic Georgeville Pluton, Antigonish Highlands, Nova Scotia. Can. J. Earth Sci. 35, 110–120.

Nizamoğulları, E. 2007. Kalsiyum içerikli feldispatların porselen bünyelerde kullanılabilirliği. Yüksek Lisans Tezi, Anadolu Üniversitesi, 88s. Eskişehir (unpublished).

Oyan, V. 2004. Bölükyazı-Hizan (Bitlis masifi) çevresindeki Na- feldispat oluşumlarının jeolojik özellikleri ve ekonomik önemi. Yüksek Lisans Tezi, Yüzüncü Yıl Üniversitesi, 126s. Van (unpublished).

Oyman, T. 1996. K-feldspar bearing pegmatities of Çine (Aydın) area, Menderes massif. Yüksek Lisans Tezi, Dokuz Eylül Üniversitesi, 79s. İzmir (unpublished).

Öbelik, Y. 2011. Cam hammaddesi mineralojisi ve cam teknolojisi. Yüksek Lisans Tezi, Niğde Üniversitesi, 84s. Niğde (unpublished).

Önem, Y. 1997. Sanayi Madenleri, Ankara.

Özcan, Ö. 2002. Stoneware bünye ve sır kompozisyonlarında alternatif hammadde kullanımı. Yüksek Lisans Tezi, Anadolu Üniversitesi, 78s. Eskişehir (unpublished).

Özün, S. 2012. Flotation Characteristics of Minerals in Feldspar Ore. PhD Thesis, Middle East Technical University, 276s. Ankara (unpublished).

Potter, M.J. 1996. Feldspar and Nepheline Syenite: Minerals Yearbook, US Dept. Of Interior, US Geological Survey; (//minerals er.usgs.gov/minerals).

Ryan, W. 1978. Properties Of Ceramic Raw Materials. 2nd Edition, Pergamon Press, Londra, 123 p.

Scheepers, R., Schoch, A.E. 1988. Geology and geochemistry of the Klipberg alkali feldspar granite and associated hydrothermally altered rocks in the Darling batholith, southwestern Cape Province. S.-Afr. Tydskr. Geol. 91, 2, 212-225.

Selzer, S. 2000. Keeping the plates spinning—A European tableware focus. Industrial Minerals 397, 77-85.

Seymen, İ. 1982. Kaman dolayında Kırşehir Masifinin jeolojisi. Doçentlik Tezi, İstanbul Teknik Üniversitesi (İTÜ), İstanbul (unpublished).

Sümer, G. 1994. Aydın-Çine feldispatlarının özellikleri ve flotasyon yöntemi ile zenginleştirilmesi. Doktora Tezi, Eskişehir Osmangazi Üniversitesi, 160s. Eskişehir (unpublished).

Şahin, M. 1989. Feldispatların zenginleştirilebilirlik etüdü ve Türkiye feldispat potansiyelinin değerlendirilmesi. Yüksek Lisans Tezi, Dokuz Eylül Üniversitesi, 73s. İzmir (unpublished).

Şahin Kılavuz, F. 2000. Feldispat-Kuvars flotasyonunda metal iyonlarının seçimliliğe etkisinin incelenmesi. Yüksek Lisans Tezi, Hacettepe Üniversitesi, 94s. Ankara (unpublished).

Tatar, S. 1997. Yozgat batoliti Şefaatli kuzey kesiminin (Güney Yozgat) petrolojik incelenmesi. Yüksek Lisans Tezi, Cumhuriyet Üniversitesi, 94s. Sivas (unpublished).

Tatar, S. 2003. Behrekdağ Batoliti'nin Kırıkkale ili-Hirfanlı barajı arasında kuzey-guney yönlü bir jeotravers boyunca petrolojik incelenmesi. Doktora Tezi, Cumhuriyet Üniversitesi, 259s. Sivas (unpublished).

Tayçu, A. 2009. Seramik sağlık gereçleri pişirim koşullarının incelenmesi. Yüksek Lisans Tezi, Anadolu Üniversitesi, 194s. Eskişehir (unpublished).

Tiryaki, C. 2012. Yozgat batolitini oluşturan lökogranitlerin ve yozgat volkanitlerinin petrolojisi. Yüksek Lisans Tezi, Cumhuriyet Üniversitesi, 135s. Sivas (unpublished).

Töre, İ. 1999. Siyenit hammaddesinin seramik bünyelere etkilerinin incelenmesi. Yüksek Lisans Tezi, Anadolu Üniversitesi, 82s. Eskişehir (unpublished).

TS11325, Türk Standartları, 1994, Feldispat Seramik Sanayinde Kullanılan, TSE, Ankara.

Tüvar, O. 2015. Yozgat-Yerköy doğusunun mineralojik, petrografik ve jeokimyasal incelenmesi. Yüksek Lisans Tezi, Cumhuriyet Üniversitesi, 112s. Sivas (unpublished).

Uğur, G. 1990. Feldispatların manyetik yolla zenginleştirilmesi. Yüksek Lisans Tezi, Anadolu Üniversitesi, 67s. Eskişehir (unpublished).

Yadete, H.M. 1990. Rock Geochemical Exploration in Intrusive Rocks of the Behrekdag Area (Celebi-Kirikkale). MSc. Thesis, Middle East Technical University, 120 pp. (unpublished).

Yalçın, A.H. 1995. Çine güneyi (Akçaova) pegmatitlerinin jeolojisi ve petrojenezi. Yüksek Lisans Tezi, İstanbul Üniversitesi, 107s. İstanbul (unpublished).

Yalınız, M.K., Aydın, N.S., Göncüoğlu, M.C., Parlak, O. 1999. Terlemez quartz monzonite of Central Anatolia (Aksaray-Sarıkaraman): age, petrogenesis and geotectonic implications for ophiolite emplacement. Geol. J. 34, 233-242.

Yeşilbaş Günsal, Y. 2002. Sodyum feldispat atıklarının çinko esaslı yumuşak porselen sırlarında değerlendirilmesi. Yüksek Lisans Tezi, Anadolu Üniversitesi, 77s. Eskişehir (unpublished).

Bull. Min. Res. Exp. (2019) 158: 291-297

Bulletin of the Mineral Research and Exploration

http://bulletin.mta.gov.tr

The role of enhanced oil recovery in the upstream petroleum sector, a case study from Turkey

Emre ÖZGÜR[a*]

[a] *General Directorate of Petroleum Affairs, Ankara, TURKEY. orcid.org 0000-0001-5407-9189*

Research Article

Keywords:
Enhanced oil recovery, upstream, crude oil production, Turkey.

ABSTRACT

The upstream petroleum sector issues still keep its popularity worldwide. Enhanced Oil Recovery (EOR) is an essential unconventional method of improving production in the petroleum sector. The EOR is gaining more importance in the sector. 2% of the global crude oil production is performed by EOR operations currently. The crude oil production of Turkey which is now in a decreasing trend is performed from old and mature oil fields. Sharp declines are expected for the oil production in the near future if new discoveries do not take place or enhanced oil production techniques are not performed. The average recovery rate for the crude oil fields in Turkey is about at 20%. An increase in this ratio can provide significant amount of crude oil to Turkish production. The ratio of crude oil production by EOR methods is about 15% currently in Turkey. In this study, the historical background of EOR projects is explained and potential EOR methods have been discussed for Turkish crude oil fields. The aim of the research is to evaluate the crude oil production potential from existing oil fields of Turkey based on EOR methods matching with the characteristics of oil fields with statistical information on world EOR outlook.

Received Date: 15.01.2018
Accepted Date: 08.05.2018

1. Introduction

The energy consumption in the world is increasing every year. The crude oil consists 32% of the world primary energy consumption taking the first place among all fuel types (IEA, 2017). On the other hand, the crude oil reserves and the new crude oil field discoveries are decreasing. The utilization of existing reserves may yield significant amounts of crude oil equivalent production to overcome the need for new oil field discoveries. Crude oil production is separated into three phases: primary, secondary and tertiary which is also known as Enhanced Oil Recovery (EOR). The active usage of EOR projects worldwide started after first oil crisis in 1973 and then showed wavy behavior due to instable crude oil prices. The number of EOR projects increase with increasing price of crude oil. Although EOR operations are said to bring significant economic and technical challenges, the private companies tackle 80% of the EOR operations globally (Koottungal, 2014). This is a fact showing the positive feasibility of the projects.

1.1. Enhanced Oil Recovery (EOR)

The first stage of crude oil production is called primary production which is performed by natural flow or artificial lift (pump). The second stage, called the secondary production is performed by either water or gas injection (by the gas produced from the reservoir). The importance of EOR increases with the decrease of API gravity of oil since the share of crude oil that can be produced by EOR increases as the API gravity of crude oil decreases. In case of heavy crude oil reservoir conditions the EOR ratio can even become some 90% (Sheng, 2013).

The average recovery rate for the crude oil fields is 1/3 of the reservoir volume worldwide presently. The carbonate reservoirs have lower recovery rates

* *Corresponding author: Emre ÖZGÜR, emreozgur@gmail.com*
http://dx.doi.org/10.19111/bulletinofmre.444903.

compared to sandstone reservoirs due to their fractured structure, heterogeneity, oil-wet tendency, lower permeability and porosity (Sheng, 2013). Nearly all crude oil fields of Turkey include carbonate type reservoirs with the average recovery rate 20% (GDPA, 2017). The low recovery rate for oil fields in Turkey is also a result of viscous and low gravity crude oils and poor reservoir pressure support mechanisms.

2. EOR Methods

Three major categories of EOR have been found to be commercially successful in varying degrees: Thermal Methods, Chemical Methods, Gas Injection Methods (Sheng, 2013). The thermal EOR includes the hot water flooding, in-situ combustion, and steam injection. The purpose of thermal EOR is to heat the heavy oil and mobilize it by decreasing the viscosity. The most feasible method is steam injection among thermal EOR methods due to its heat efficiency and better control. The chemical EOR includes surfactant, alkaline, and polymer flooding. The purpose in chemical EOR is to decrease the interfacial tension between crude oil, water, and rock. The viscosity arrangement to prevent viscous fingering effect is also used in polymer flooding. The gas injection EOR methods mostly include CO_2, CH_4, and N_2 injection. They aim to decrease the viscosity of crude oil and mobilize the crude oil by mainly the swelling effect. The choice of the method depends on the reservoir parameters and availability of gas source. Apart from the known EOR methods the microbial flooding and smart water injection are the new EOR methods in the upstream petroleum sector still in the trial stage which may have positive, negative, or no effects on crude oil production. The studies on these methods are mostly focused on laboratory tests and the reported results show no consensus on the usage of these methods. Thermal and chemical methods are suitable in sandstone reservoirs due to technical reasons; however gas injection and other EOR methods can be applied in both carbonate and sandstone reservoirs.

3. EOR Operations Worldwide

There are currently about 280 EOR operations worldwide providing 1.4 million barrel of crude oil per day forming 2% of the global crude oil production (Koottungal, 2014; IEA, 2017). The list of EOR operations by country and method is presented in table 1. The table excludes China, because the data series for China are incomplete; China is estimated to produce about 170 kb/d; 150 kb/d from steam technologies and 20 kb/d with polymer injection (IEA, 2013). 55% of EOR projects are active in Unites States, 15% in Canada and 15% in Venezuela. The rest are operated in other countries. In terms of production amounts, 31% of EOR comes from US based production, 27% from Venezuela, 24% from Canada and the rest from other countries. The role of EOR is becoming more important for the countries possessing heavy oil deposits. To give example to this case, the rate of EOR in crude oil production is 5% for USA, 10% for Canada, and 15% for Venezuela, which is above the world average. The role of thermal EOR is the highest worldwide. Gas injection methods follow the thermal methods. The world EOR production by methods is presented in figure 1

Table 1- EOR Applications by country and method (Koottungal, 2014)

Country	EOR Method	Number of Field
USA	Miscible CO_2 Injection	127
USA	Immiscible CO_2 Injection	9
USA	Miscible Hydrocarbon Gas Injection	12
USA	Immiscible Hydrocarbon Gas Injection	2
USA	Immiscible N_2 Injection	3
USA	Chemical Injection	3
Germany	Steam Injection	8
Brazil	Immiscible CO_2 Injection	1
Brazil	Miscible CO_2 Injection	2
Brazil	Microbial Injection	1
Brazil	Steam Injection	5
Indonesia	Steam Injection	2
Netherlands	Steam Injection	1
Canada	Miscible CO_2 Injection	7
Canada	Miscible Hydrocarbon Gas Injection	20
Canada	Steam Injection	10
Canada	Immiscible N_2 Injection	1
Canada	Polymer Injection	2
Egypt	Steam Injection	1
Trinidad	Steam Injection	9
Trinidad	Immiscible CO_2 Injection	5
Trinidad	Hot Water Injection	2
Turkey	Immiscible CO_2 Injection	1
Venezuela	Steam Injection	43
Venezuela	Combustion Flooding	1
Venezuela	Chemical Injection	1
Venezuela	Miscible Hydrocarbon Gas Injection	4

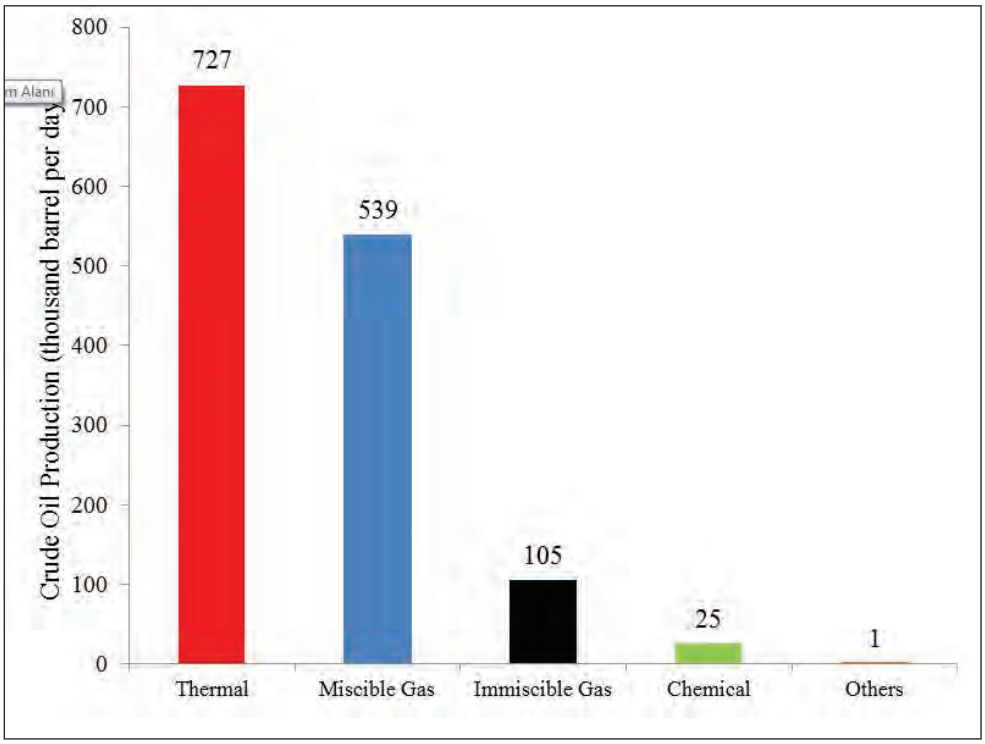

Figure 1- World EOR Productions by Methods (Koottungal, 2014)

4. EOR Background and Assessment in Turkish Upstream Petroleum Sector

There have been six enhanced oil recovery operations at four crude oil fields in Turkey until now (Şahin et al., 2014). The general overview of the EOR projects is presented in table 2. There is only one on-going EOR project since 1986 which is an immiscible CO_2 injection, in Batı Raman oil field in Turkey presently. The first EOR project started in Turkey is the steam injection performed in Batı Raman oil field. The steam injection and immiscible CO_2 injection have been performed at İkiztepe oil field. The immiscible CO_2 injection has also been performed in Çamurlu and Batı Kozluca oil fields. The results are promising for CO_2 injection projects. However, EOR project on Batı Kozluca was stopped until the construction of recycling unit at the field to prevent the depletion of CO_2 reserve. The CO_2 projects on Çamurlu and İkiztepe oil fields have been stopped because of technical and economical reasons (Şahin et al., 2012). Apart from on-going immiscible CO_2 project in Batı Raman field, the other EOR operations were rather research projects in Turkey.

Table 2- The list of EOR performed crude oil fields in Turkey (GDPA, 2017).

City	Field	EOR Method	Operator	Years
Batman	Batı Raman	Immiscible CO_2 Steam	TPAO	1986-cont. (CO_2) 1967-1969 (steam) 2012-2013 (steam)
Şırnak	Batı Kozluca	Immiscible CO_2	TPAO	2003-2007
Mardin	Çamurlu	Immiscible CO_2	TPAO	1984-1986
Mardin	İkiztepe	Immiscible CO_2 Steam	TPAO-JNOC	1993-1995

(JNOC: Japan National Oil Company, TPAO: Turkish National Oil Company)

Based on the Hubbert curve approach for the Turkish crude oil production life, the production will likely come to the end between the years 2040 - 2045 (Özgür, 2016). The recoverable reserve amount can be increased and the life of the production can be extended if EOR projects are performed on the noticeable oil fields of Turkey.

CO_2 injection operation in Batı Raman field is currently underway. The implementation of this method in other fields can significantly increase the oil production in Turkey. There are 10 remarkable crude oil fields with recoverable reserves over 25 million barrels based on Ivanhoe and Leckie's technique (Ivanhoe and Leckie, 1993) located at southeastern part in Turkey which are candidates for enhanced oil recovery in terms of technical and economical aspects. The optimum enhanced oil recovery methods are selected for the fields considering reservoir characteristics and enhanced oil recovery criteria.

The methods which are steam injection, in-situ combustion, hot water flooding, alkaline flooding, polymer flooding, surfactant flooding, microbial flooding, miscible/immiscible gas flooding, smart-water injection and other methods are also investigated.

Because of the suitable characteristics of oil fields and carbon source potential of thermal power plants, steel factories, cement factories, refineries, sugar factories in the region, the CO_2 injection method is the optimum enhanced oil recovery method for Turkey. Construction of a pipeline network between the sources and the fields can extend the scope of CO_2 injection, and as a result, lead to environmental, economical, and strategic benefits. It is expected that the additional produced crude oil may be equal to the amount of almost two large oil field discoveries.

4.1. Evaluation and Predictions on EOR in Turkey

The crude oil fields in Turkey are carbonate types. It is a fact that the EOR operations have limited application in carbonate reservoirs. 80% of the EOR crude oil production comes from sandstone reservoirs worldwide (Koottungal, 2014). However, the good carbonate field examples are also present. The reservoir properties of remarkable crude oil fields in Turkey are given in table 3. The evaluations are based on the reservoir parameters of the fields.

The chemical EOR methods are feasible in sandstone formations. Therefore the chemical EOR are not considered for Turkey as an option due to the carbonate type reservoirs. The thermal methods are also more practical for sandstones however they may be applied in also carbonates at certain circumstances. Although the thermal methods are not advised for Turkey in this study, steam injection is also evaluated in case of a test operation. 1,500 meter depth is accepted as economic limit for steam injection in the literature. In deeper reservoirs, the heat loss problem would affect the operation economically and technically in negative manner (Sheng, 2013). Raman, Batı Raman and Garzan fields fit the criteria of the feasible steam injection operation.

Other EOR methods like microbial flooding and smart water injection were also analyzed from a research point of view for pilot field studies and applications. In microbial flooding, the temperature and salinity of the reservoir are important. Generally speaking, the temperature should be lower than 70 ^oC and salinity should be lower than 50,000 ppm for the increase of microorganism activities. Besides, the higher permeability is better for the distribution of microorganisms in reservoir. Raman field seems the ideal oil field for the pilot application of microbial flooding. For smart water injection, the high temperature reservoir is the good option. Karakuş and Kuzey Karakuş fields meet the criteria and they are

Table 3- Reservoir Properties of Remarkable Crude Oil Fields of Turkey (GDPA, 2017).

Field	Formation	Ø	k, md	Depth, m	Salinity (1000 ppm)	T,^oC	API	μ, cp
Raman	limestone	14	50	1360	40	60	18	60
B. Raman	limestone	18	58	1300	120	65	13	600
Kurkan	limestone	15	9	1600	20	55	31	9
B. Kayaköy	limestone	17	4	1890	5	58	35	5
Beykan	limestone	12	1	1900	25	58	33	4
Şelmo	dolomitic limestone	7	100	1890	12	77	34	3
Karakuş	dolomitic limestone	6	100	2700	30	118	30	3
Garzan	limestone	11	15	1450	45	70	24	7
Kayaköy	limestone	15	2	2100	10	60	38	3
K. Karakuş	dolomitic limestone	6	100	2590	25	110	30	3

also close to the low salinity water sources (lakes and rivers).

Among all EOR methods CO_2 gas injection method is the most suitable method for Turkish oil fields. The good example of "Batı Raman" oil fields and good reservoir parameters make the gas injection best choice for Turkey. It is expected that the miscible CO_2 gas injection will increase recovery factor by 15% and the immiscible CO_2 gas injection by 10% (Sheng, 2013; Perera et al., 2016). The API gravity of crude oil is one of the most important things to determine the type of injection whether it would be miscible or immiscible along with the reservoir temperature, reservoir pressure and injected gas composition (Meyer, 2007). After a certain lower API value, the injection process cannot be performed as immiscible regardless of the injection pressure. The oil fields with the gravity over 25 API are good candidates for miscible gas injection practically (Perera et al, 2016). Raman, Batı Raman and Garzan fields which have lower API gravities than 25 are suitable for immiscible gas injection. On the other hand Kurkan, Batı Kayaköy, Beykan, Şelmo, Karakuş, Kayaköy, and Kuzey Karakuş are suitable for miscible gas injection.

Extra 385 million barrels of crude oil can be produced from existing production fields in Turkey considering the characteristics of fields and EOR methods. The amount of necessary CO_2 to produce 385 million barrel of oils is 85,42 million tones based on the Batı Raman case in Turkey; 4.5 ton CO_2 is required for the production of one barrel oil (GDPA, 2017). The EOR project is planned for 35 year duration. The yearly necessity for CO_2 will be about 2,5 million tones. The required CO_2 amount can be provided from the cement factories through the construction of pipelines in the region. The annual CO_2 emission of cement factories is about 15 million tons and the factories in the southeastern part of Turkey can provide enough CO_2 for the EOR operations in the region (Okandan et al., 2011). The EOR analysis of Turkish oil fields is presented in table 4, table 5, and figure 2. The reserve information about the crude oil fields is provided in table 5 (GDPA, 2015).

Table 4- EOR Analysis of Remarkable Crude Oil Fields of Turkey (GDPA, 2017).

Technical Information of 10 Remarkable Crude Oil Fields	
Original Oil in Place, million barrel	4536,6
Recoverable Reserve, million barrel	841,1
Recovery Factor, %	18,5
Suggested EOR Method	**Miscible/Immiscible CO_2 Injection**
New Recovery Factor After EOR, %	27,0
Extra Crude Oil Production After EOR, million barrel	384,4
Necessary CO_2 Amount (million tons)	85,42

Table 5- Prediction on EOR Potential of Remarkable Turkish Crude Oil Fields (GDPA, 2017).

Field	**Original Oil in Place**	**Recoverable Oil Reserve**	**Recovery Factor**	**Suggested EOR Method**	**New Recovery Factor**	**Extra Oil Production**
Raman	615,3	146,9	23,9	Immiscible CO_2	33,9	61,7
Batı Raman	1841,0	192,9	10,5	Immiscible CO_2	12,0	28,0
Kurkan	287,0	67,3	23,4	Miscible CO_2	38,4	42,9
Batı Kayaköy	225,6	63,4	28,1	Miscible CO_2	43,1	33,8
Beykan	432,8	89,8	20,7	Miscible CO_2	35,7	64,7
Şelmo	539,0	99,3	18,4	Miscible CO_2	33,4	80,7
Karakuş	209,1	61,6	29,5	Miscible CO_2	44,5	31,4
Garzan	199,1	46,5	23,4	Immiscible CO_2	33,4	20,0
Kayaköy	99,9	31,2	31,2	Miscible CO_2	46,2	15,0
Kuzey Karakuş	87,8	42,2	48,1	Miscible CO_2	55,0	6,1
Total	4536,6	841,1	18,5 (avg.)	-	27,0 (avg.)	384,4

(Reserves and production amounts are presented in "million barrel")

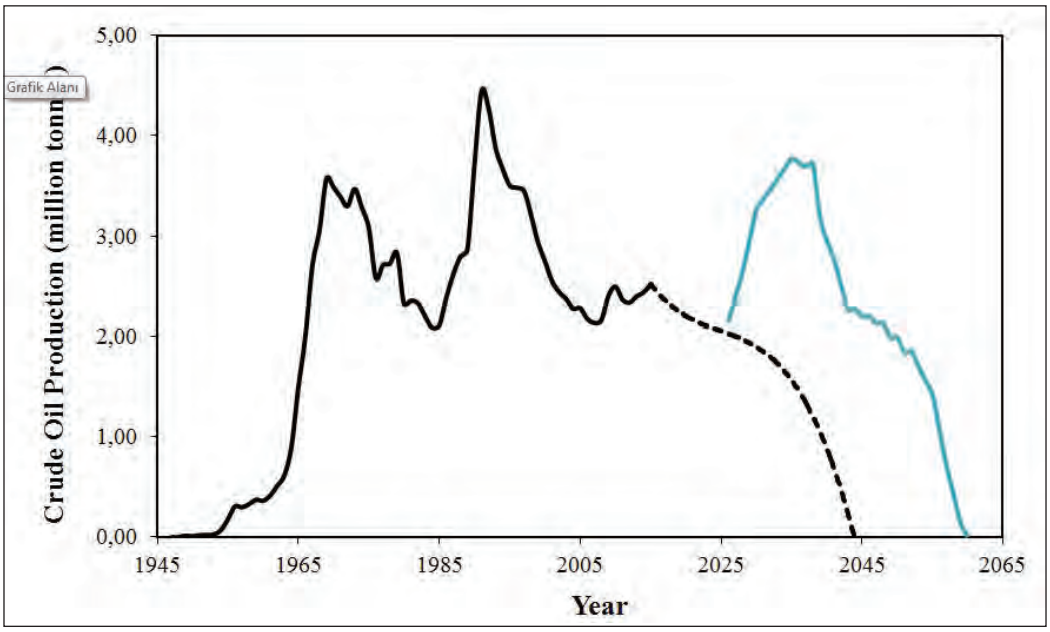

Figure 2- Turkey's Historical Crude Oil Production and Forecast (Black line: historical production, dashed line: oil production forecast, blue line: oil production forecast with EOR production)

5. Conclusions

Although EOR projects are expensive operations and require skilled staff, the existing infrastructure and pipelines in the fields provide advantage and easy access of produced oil to markets with no additional exploration costs. 20% of the EOR based crude oil production worldwide is performed by national oil companies (Koottungal, 2014). The rest is produced by private oil companies showing the positive feasibility of the EOR projects worldwide. The current ratio of crude oil production by EOR methods is about 2% (1.4 million barrel per day) of global production; however according to the International Energy Agency report (IEA, 2017) this ratio will increase to 4.25% (4.3 million barrel per day) by 2040.

There are currently 132 crude oil fields Turkey and 10 of them (Batı Raman, Raman, Kurkan, Batı Kayaköy, Beykan, Şelmo, Karakuş, Garzan, Kayaköy, and Kuzey Karakuş) are remarkable whose recoverable reserves over 25 million barrels. There is currently one active immiscible CO_2 EOR project performed for 30 years on the biggest crude oil field, Batı Raman, of Turkey forming 15% of the Turkish crude oil production. The application of immiscible / miscible CO_2 injection EOR methods on other fields together with the current one can provide about 385 million barrels of extra crude oil increasing the average recovery ratio of those 10 fields from 18.5% to 27%. This may extend the depletion of crude oil to the years 2060-2065 from the presently expected 2040-2045. One word for the pilot application of other EOR methods for research purpose: Raman oil field seems ideal for microbial flooding. Karakuş and Kuzey Karakuş fields seem ideal for smart water injection.

Some comments may also be made regarding the regulations in Turkey. The reduction in the royalty tax for the crude oil production by EOR would be a good motivation for oil companies. Considering lower crude oil prices, decreasing crude oil production trend and difficult geological conditions for petroleum exploration in Turkey, the introduction of such a regulation may lead to positive results in the long term.

References

General Directorate of Petroleum Affairs (GDPA). 2017. www.pigm.gov.tr

International Energy Agency (IEA). 2013.World Energy Report.

International Energy Agency (IEA). 2017.World Energy Report.

Ivanhoe, L.F., Leckie, G.G. 1993. Global oil, gas fields, sizes tallied, analyzed. Oil Gas. J. 91 (7), 8–91.

Koottungal, L. 2014. Worldwide EOR survey, Oil and Gas Journal.

Meyer, J.P. 2007. Summary of carbon dioxide enhanced oil recovery (CO_2 EOR) injection well technology. American Petroleum Institute - Background Report.

Okandan, E., Karakece,Y., Çetin, Ç., Topkaya, I., Parlaktuna, M., Akın, S., Bulbul, S., Dalha , C., Anbar, S., Cetinkaya, C., Ermis, I.,Yılmaz, M., Ustun, V., Yapan, K., Erten, A.T., Demiralın, Y., Akalan, E. 2011. Assessment of CO_2 emissions from industrial sites, potential for underground storage in Turkey and modelling of storage in an oil field, Energy Procedia 4, 4849-4856.

Özgür, E. 2016.Upstream petroleum law and activities in Turkey. Energy Policy 88, 131-137.

Perera, M.S.A., Gamage, R.P., Rathnaweera, T.D., Ranathunga, A.S., Koay, A., Choi, X. 2016. A review of CO_2-enhanced oil recovery with a simulated sensitivity analysis. Energies 9 (7), 481.

Sheng, James J. 2013. Enhanced Oil Recovery Field Case Studies, Gulf Professional Publishing.

Şahin, S., Kalfa, Ü., Çelebioğlu D., Duygu, E., Lahna, H. 2012. A quarter century of progress in the application of CO_2 immiscible EOR project in Batı Raman heavy oil field in Turkey, SPE (Society of Petroleum Engineers) 157865.

Şahin, S., Kalfa, Ü., Uysal, S., Kılıç, H., Lahna, H. 2014. Design, implementation and early operating results of steam injection pilot in already CO_2 flooded deep-heavy oil fractured carbonate reservoir of Batı Raman field – Turkey, SPE (Society of Petroleum Engineers) 169035-MS.

Bull. Min. Res. Exp. (2019) 158: 299-310

Bulletin of the Mineral Research and Exploration

http://bulletin.mta.gov.tr

The prediction of the expandability of clays using a ternary diagram

Ahmet ÖZGÜVEN[a*]

[a] *General Directorate of Mineral Research and Exploration, Ankara, Turkey orcid.org 0000-0002-3807-2267*

Research Article

Keywords:
Expanded clay, ternary diagram, prediction of expandibility.

ABSTRACT

The aim of this study is to put forward a prediction scheme for the expandability of clays by use of inexpensive and rapid chemical analysis. Seventy clay ores from fourteen locations throughout central and west Turkey were characterized mineralogically, chemically, and for expansion testing. Using the ternary plotting scheme of SiO_2-Al_2O_3-fluxing samples exceeding 50% expansion plotted within and slightly beyond the region proposed by Riley (1951). This study newly extends the region in ternary space for samples suitable for expansion and use in light weight aggregate. Non-expanding samples are associated with mineral assemblages dominated by quartz. In this study, it was determined that the samples without the expandability property were lacking the required chemical aspect of SiO_2-Al_2O_3-fluxing ratios, mineralogical clay structures, proportions and gas agents. In addition, the effect of having a too low or high position on the triangle diagram was found to have a negative impact on the expandability. When mineralogical analyses, mineral associations, chemical compositions and expandability results were evaluated together, it was observed that Mica GM-Chloride GM; Montmorillonite-Zeolite-Amorphous matter and Clay GM-Amorh Silica-Cristobalite are the samples showing expandability properties for the extent of this study. Also, it was noted that almost all samples with graphite content did expand. The extension of the suitability field on the ternary diagram for prediction of expansion properties, combined with low cost and rapid chemical analysis demonstrate benefits for the clay production industry in Turkey, particularly for saving energy and financial resources needed during exploration and early stages of production clay ores.

Received Date: 18.02.2018
Accepted Date: 23.04.2018

1. Introduction

Since the discovery of the expansion of some clays approximately one hundred years ago, expanded clay aggregates have been used extensively in several sectors, especially in developed countries. In Turkey, production methods and other features have begun to be determined by studies performed in recent years. Expanded clay aggregate has better features than other light aggregates, and it is used in several industrial sectors, especially in the construction industry (Özgüven, 2009).

Expanded clay aggregates are used in many different industries for their high technical features and numerous advantages when compared to many other industrial raw materials. One of the materials with the greatest compressive strength among lightweight aggregates is expanded clay aggregates. This gives it a significant position in the construction industry. 20% may be saved in reinforcing steel while up to 50% may be saved in heating–cooling expenses in buildings containing expanded clay aggregate in Turkey (Doğan and Şener, 2004; Özgüven, 2009).

Expanded clay aggregates are a new topic for Turkey and detailed studies on their production have begun to be conducted recently. Considering that there is no factory manufacturing expanded clay aggregate in Turkey, this study is an original study, especially for Turkey. It is also very important to note that Turkish clays are spread over a large area and the reserves are high. Therefore, it is very important that studies on the use and production of expanded clay aggregate

* *Corresponding author: Ahmet ÖZGÜVEN, ahmet.ozguven@mta.gov.tr*
https://dx.doi.org/10.19111/bulletinofmre.417966.

should be conducted rapidly and the use of it should be made more popular in Turkey considering its superior advantages to current alternatives (Özgüven and Gündüz, 2012).

The natural materials most used for the production of lightweight aggregates are sedimentary or very low-grade metamorphic rocks such as clays or shales (Purbrick, 1991). The main constituents of these rocks are: mica-illite, kaolinite, smectite, and chlorite with variable amount of quartz, feldspars, carbonates, iron oxi-hydroxides, and small amount of sulfides and organic matter. Since some of these components (e.g. iron or calcium compounds) contain the chemical elements considered to be in the so-called fluxing parameter [fluxing=CaO+MgO+Na_2O+K_2O+Fe_2O_3] (Riley, 1951), their presence may also influence the softening and melting temperatures as well as the bloating of the aggregates (de'Gennaro et al., 2004).

General statements regarding the chemical/mineral composition and other characteristics of materials with proven expandability are as follows (EIPPCB, 2005):

- relatively high plasticity, large fines content (less than 2 μm, 35 % min.); for lumpy shale, the primary grain size is the crucial factor
- relatively high content of layered silicates, particularly from the illite or mica group; more than 40 % is advantageous, and the kaolinite content is usually low
- calcite or dolomite content reduces expansion time; lumpy lime is harmful, because it may subsequently lead to spalling
- chemical composition:
- Al_2O_3: 12 – 25 %
- SiO_2: 50 – 78 %
- Flux (Na_2O, K_2O, CaO, MgO, Fe_2O_3, FeO): 8 – 25 %
- $C_{organic}$: 0.6 – 2.5 %
- FeS_2: should be fine-grained (residue in the finished product ≤ 1.0 or 1.5 % SO_3)
- expansion characteristics improve with higher Fe_2O_3 content of the ceramic raw materials (usually 5 to 10 %, perhaps higher)
- the sinter and melting point temperatures should be relatively close to each other, preferably up to and less than about 1200 ºC
- pyroplastic softening of the mass or the granules should occur during the most favourable stage of the gas formation process; this offers the most advantageous expansion range of at least 50 to 100 K

An expanded aggregate is formed by quick heating the materials which are able to bloat at high temperature. Three conditions are necessary to get a suitable expanded material (Riley, 1951):

1. It must contain substances that develop gases at high temperature (T1);
2. It must produce a highly viscous liquid phase at the temperature T1 that could entrap the gases;
3. It must develop an external glassy film during cooling, making the outer surface impervious to water, homogeneous, and mechanically resistant.

The gases causing expansion come from thermally instable materials, such as the following (Heller-Kallai et al., 1988; Kazantseva et al., 1996):

1. Water vapor from the volatilization of interlayer water molecules or crystallization water of clay minerals or other silicates,
2. CO and CO_2 from the combustion of organic matter,
3. CO_2 from the dissociation of carbonates,
4. O_2 and CO_2 formed from the reduction of ferric iron,
5. SO_X from sulfide oxidation,
6. F and Cl from clay minerals,
7. O_2 and CO_2 generated by adding extra gas-releasing materials, such as coal, waxes, and hydrocarbons.

Some limits must exist in the proportions of silica, alumina, and total fluxing agents beyond which the mass of the clay either will not fuse at a low enough temperature or will fuse to a melt not viscous enough to trap gas. In order to establish these limits, the analyses made by Conley et al. (1948) plus those of the present author were plotted on a composition diagram with silica, alumina, and total fluxing constituents as the corners. Minor constituents and volatile material were excluded, and the analyses were then recalculated to 100% before being plotted on the diagram (Figure 1). A dashed line was drawn

around the points representing bloating clays. and this is considered the approximate limit beyond which a clay will not bloat. It must be remembered, however, that this "area of bloating" defines only one of the two necessary conditions for a bloating clay, i.e., it indicates the correct chemical composition to produce a mass of the proper viscosity at the bloating temperature. If these approximated limits are correct, all bloating clays should fall in between them. It can be assumed, then, that any nonbloating clay which lies within this area satisfies the condition of viscosity but does not have a constituent which will produce a gas at the proper temperature and thus fails in terms of the other necessary conditions for bloating. Several such clays are plotted in figure 1. Other nonbloating clays, shown to the left of the area of bloating, are deficient in fluxing constituents and may lack a gas-producing agent as well (Riley, 1951).

There are important studies performed using the triangle diagram, which was proposed by Riley (1951). In their study on Italian zeolitic rocks light weight aggregates, de Gennaro et al. (2004) investigated whether the chemical composition of the samples take place in the areas shown in figure 1. According to the expansion results of the 15 samples, they came to the conclusion that chemical composition has a large impact on expansion. With results similar to those of this study, researchers like Salakhov et al. (2005), Tsai et al. (2006), Al-Bahar and Bogahawatta (2006), de Gennaro et al. (2008), Chen et al. (2010), and Kavas et al. (2011) conducted studies by performing expansion tests mainly using the Riley diagram (1951). All these researchers came to the conclusion that samples in the expansion area had expanded and, therefore, this diagram would be important for prediction of the expandability of raw materials.

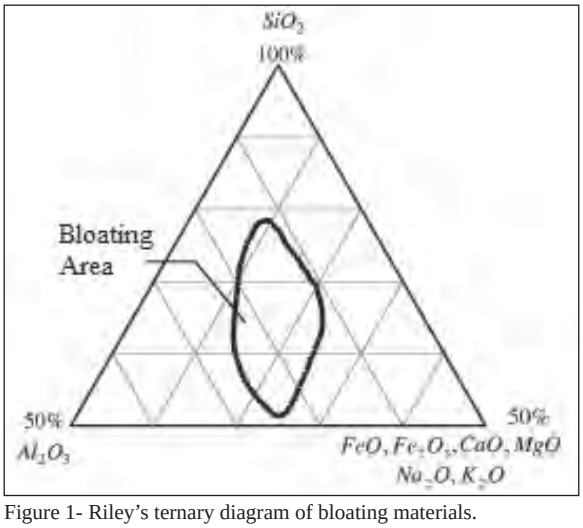

Figure 1- Riley's ternary diagram of bloating materials.

Therefore, in this study, It was aimed to put forward a prediction scheme for expandability by the use of a cheap, quick chemical analysis of samples from various regions of Turkey instead of time consuming and costly expansion tests. SiO_2, Al_2O_3 and Fluxing triangle diagrams which were proposed by Riley (1951) and used by the several researchers have been evaluated once more by considering the tests of the 70 samples used in this study.

2. Materials and Methods

For this study, samples that might present expandability features were taken from 70 different clay fields in Turkey. Locations of the samples are given on the map in figure 2 and table 1. To determine the chemical composition of the samples, the XRF Spectrometric method was used. By evaluating the analysis results in the UQ program of the ARL XRF device, numerical values were obtained. Loss on ignition values were obtained at the temperature of 1050° C. Results of the chemical analysis are shown in table 2. To determine the basic mineralogical features of the samples, XRD analysis was performed at 2^0 and 70^0 ranges using the Bruker D8 with Cu X-ray Advance XRD analysis device. Results are given in table 3.

All samples taken from the study areas were crushed and then milled below 200 μm size. Ground clay was mixed with water only without any additives to produce clay dough. Dough preparations were left to mature for one day and shaped through an extruder. Pellets of 15 mm were prepared by using caps. The pellets were then dried in the ovens and then expanded in a furnace. When the sample preparation and shaping operations are well performed, greater expansion of the clay can be obtained. Only optimum furnace conditions produce the desired expanded clay aggregate. In this study, a high volume stationary furnace, which is resistant to sudden thermal shocks, allowing the temperature to be raised rapidly, was employed. Studies were conducted at different furnace temperatures to determine at which temperature expansion was effective, at which temperature raw pellets began to expand, and which temperature yielded optimum expansion. The firing processes took place at different temperatures ranging between 1000 °C and 1300 °C. Raw pellets were kept inside

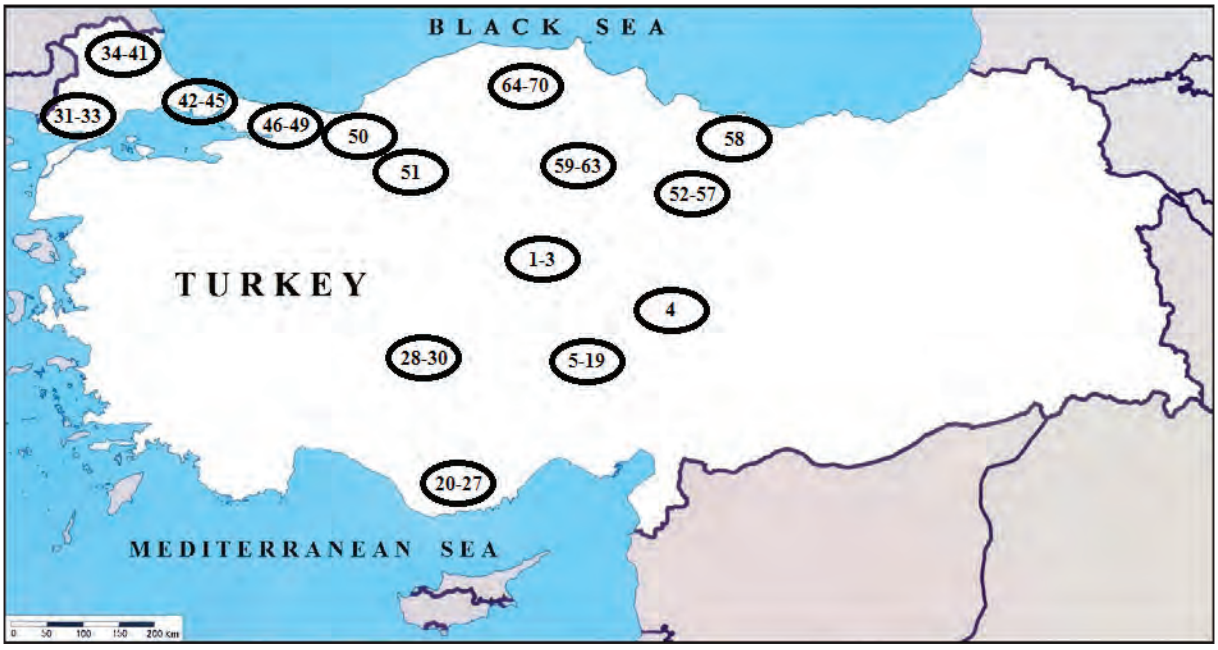

Figure 2- Locations of the samples used in this study.

the furnace for various durations (i.e. 5, 10, 15 and 20 minutes) at the same temperature in order to determine optimum time. Then the fired pellets were removed from the furnace and cooled rapidly.

The mass of a unit volume of the produced aggregates was measured by using the ASTM C493-98 standard to determine which manufacturing conditions yielded reasonable results. Because the unit volume of the aggregates is very small and it is impossible to weigh them in water, the mass of a unit volume was found by using the mercury method. Submerges the test object in a pool of mercury and measures the displaced mercury volume. Mercury is a non-wetting fluid that bridges the pore entrances and does not penetrate small cracks, holes, or pores. The volume of the medium displaced by the sample is measured. If the sample material is porous, fine particles will not penetrate into the smaller pores that liquids or gases can enter. Mercury, being a non-wetting liquid to most solids, also will not penetrate pores under ambient pressure. The unit volume masses of the expanded clay aggregates were compared with the Unit Volume Masses (UW) of the raw pellets to calculate the expansion ratio. The expansion ratio was calculated as (UVMorj/UVMexp) x 100. The results are given in table 2 and 3 with chemical and mineralogical analysis results.

Table 1- Region where the sample taken.

No	Samples	Region
1	1-3	Kırşehir
2	4	Kayseri
3	5-19	Adana
4	20-27	Mersin
5	28-30	Niğde
6	31-33	Edirne
7	34-41	Kırklareli
8	42-45	İstanbul
9	46-49	Kocaeli
10	50	Sakarya
11	51	Bolu
12	52-57	Tokat
13	58	Ordu
14	59-63	Çorum
15	64-70	Kastamonu

Table 2- Chemical compositions of the samples.

No	Na_2O	MgO	Al_2O_3	SiO_2	P_2O_5	K_2O	CaO	TiO_2	MnO	Fe_2O_3	Fluxing	LOI	UW (g/cm^3)	ER (%)
1	1,18	2,94	16,94	58,76	0,13	5,01	4,22	0,54	0,06	5,63	18,98	4,35	1,32	124
2	1,45	2,38	15,04	57,94	0,14	2,79	7,16	0,68	0,08	5,03	18,81	7,15	-	-
3	0,62	1,73	16,08	67,83	0,12	2,80	1,21	0,73	0,06	5,33	11,69	3,35	-	-
4	0,87	2,78	10,36	38,93	0,12	1,36	33,40	0,59	0,19	7,39	45,8	22,75	-	-
5	1,15	2,39	20,55	57,18	0,13	2,47	1,21	0,75	0,09	7,79	15,01	5,55	0,96	197
6	1,25	2,37	21,46	55,95	0,14	2,36	1,02	0,75	0,06	8,55	15,55	5,20	0,81	235
7	1,51	2,35	24,02	53,15	0,11	2,52	0,32	0,83	0,02	9,40	16,1	5,10	0,92	207
8	1,11	2,56	22,21	56,06	0,13	3,07	0,83	0,80	0,05	7,41	14,98	5,25	0,78	248
9	0,77	1,67	14,74	35,24	0,48	2,68	12,00	0,73	0,05	6,11	23,23	20,95	-	-
10	0,61	2,02	12,84	53,67	0,16	2,00	8,88	0,56	0,20	4,72	18,23	12,75	1,14	166
11	0,51	0,20	5,14	84,53	0,02	0,95	0,07	0,18	0,01	1,36	3,09	4,80	-	-
12	1,73	2,68	21,50	56,64	0,20	3,27	0,37	0,93	0,04	8,02	16,07	4,10	0,64	293
13	0,93	0,35	5,47	82,56	0,03	0,96	0,10	0,20	0,02	2,08	4,42	5,70	-	-
14	1,11	2,32	22,54	56,56	0,14	3,54	0,49	0,80	0,03	7,06	14,52	4,45	1,00	191
15	1,31	2,91	22,56	53,31	0,22	3,32	0,75	0,92	0,07	8,79	17,08	5,20	0,69	288
16	0,54	2,02	16,55	39,85	0,52	2,60	10,70	0,91	0,08	10,30	26,16	13,90	1,18	167
17	0,77	11,90	11,93	43,18	0,05	0,26	10,50	0,35	0,13	8,93	32,36	11,80	-	-
18	0,26	7,18	6,39	23,88	0,04	0,21	28,10	0,18	0,13	5,55	41,3	27,35	-	-
19	0,42	14,90	10,00	42,74	0,03	0,24	9,20	0,34	0,12	8,85	33,61	12,90	-	-
20	1,59	2,04	21,24	57,57	0,12	2,63	1,24	0,76	0,08	6,94	14,44	5,00	1,30	144
21	0,36	1,84	16,63	45,91	0,16	3,86	11,30	0,67	0,28	6,24	23,6	11,85	0,95	198
22	0,86	3,87	7,62	27,28	0,13	1,49	29,40	0,37	0,22	4,15	39,77	24,30	-	-
23	0,15	2,95	6,17	26,52	0,06	1,37	32,40	0,36	0,08	2,84	39,71	26,75	-	-
24	1,40	2,10	20,40	54,29	0,20	3,10	3,21	0,85	0,09	6,58	16,39	7,15	0,94	196
25	0,82	2,52	24,39	53,18	0,09	3,19	0,41	0,82	0,02	8,42	15,36	5,60	1,03	185
26	0,96	2,53	22,82	54,71	0,14	2,88	0,71	0,85	0,05	7,72	14,8	5,55	0,86	225
27	1,47	1,24	27,07	51,85	0,13	3,24	0,83	0,94	0,01	6,68	13,46	6,35	0,97	191
28	1,46	8,22	15,02	47,94	0,12	2,28	5,75	0,85	0,16	8,70	26,41	9,10	0,77	241
29	1,08	5,24	14,55	43,95	0,05	2,22	10,70	0,58	0,22	7,55	26,79	13,00	1,21	163
30	1,40	2,10	20,04	54,29	0,20	3,10	3,21	0,85	0,09	6,58	16,39	8,10	1,03	186
31	1,13	2,40	18,52	60,34	0,35	1,71	2,62	0,58	0,10	5,16	13,02	6,85	0,56	341
32	0,54	2,31	18,84	62,11	0,22	1,84	2,28	0,54	0,04	3,92	10,89	7,10	0,82	215
33	0,75	4,99	14,35	43,99	0,15	1,83	11,60	0,58	0,09	6,47	25,64	14,90	-	-
34	0,68	2,53	20,37	55,27	0,35	2,61	0,54	0,76	0,57	10,80	17,16	5,30	1,04	159
35	0,98	1,51	26,47	50,80	0,21	3,97	0,59	0,99	0,18	6,86	13,91	7,25	1,26	129
36	1,73	1,92	21,80	58,48	0,19	2,28	0,25	0,76	0,25	7,58	13,76	4,40	0,78	241
37	1,72	1,23	21,82	60,10	0,13	2,57	0,05	0,78	0,05	6,36	11,93	4,80	0,99	183
38	1,08	1,94	22,30	58,71	0,11	2,93	0,12	0,81	0,11	7,26	13,33	4,45	0,84	212
39	0,85	1,55	23,08	56,66	0,20	3,06	0,21	0,79	0,15	7,66	13,33	5,60	0,76	240
40	0,48	0,79	21,30	58,97	0,22	3,60	0,10	0,78	0,02	8,01	12,98	5,40	1,15	159
41	1,36	1,60	20,43	61,72	0,13	2,58	0,14	0,71	0,07	6,78	12,46	4,30	1,16	150
42	2,39	3,98	18,43	56,30	0,15	2,25	1,82	0,87	0,10	8,06	18,5	4,95	0,68	274
43	2,11	4,04	19,53	55,19	0,16	2,56	1,76	0,86	0,13	8,78	19,25	4,55	0,55	346
44	0,42	1,77	21,91	50,66	0,09	3,65	3,62	0,69	0,11	6,31	15,77	10,35	0,88	194
45	0,79	3,53	16,98	59,12	0,16	2,09	1,58	0,70	0,22	7,62	15,61	7,00	0,91	216
46	1,52	1,58	20,89	62,49	0,17	3,46	0,11	0,58	0,03	4,90	11,57	4,15	1,00	175
47	1,18	1,63	22,17	59,28	0,11	4,31	0,10	0,69	0,02	4,83	12,05	5,50	1,23	131
48	1,75	2,26	19,34	62,81	0,11	3,15	0,56	0,55	0,07	5,40	13,12	3,85	0,89	167
49	1,28	1,78	20,85	61,70	0,13	3,66	0,22	0,59	0,06	5,43	12,37	4,15	0,86	192
50	1,37	4,30	13,12	43,59	0,16	1,78	12,60	1,00	0,09	7,51	27,56	13,50	-	-
51	0,80	3,07	9,22	28,31	0,09	1,50	27,10	0,69	0,14	5,74	38,21	22,85	-	-
52	0,66	2,18	16,62	56,04	0,14	3,42	1,14	0,79	0,26	8,40	15,8	10,10	0,85	223
53	0,37	2,36	15,34	63,90	0,12	0,87	3,29	0,34	0,06	3,92	10,81	9,10	-	-
54	2,81	2,41	15,05	62,28	0,13	0,65	3,62	0,32	0,12	3,87	13,36	8,50	0,52	302
55	2,71	2,19	14,13	58,60	0,15	1,10	6,15	0,31	0,16	4,06	16,21	10,15	0,65	218

Table 2- continued.

No	Na_2O	MgO	Al_2O_3	SiO_2	P_2O_5	K_2O	CaO	TiO_2	MnO	Fe_2O_3	Fluxing	LOI	UW (g/cm^3)	ER (%)
56	0,31	1,73	17,04	55,97	0,16	2,08	1,50	0,78	0,07	7,35	12,97	12,75	0,43	455
57	1,47	3,21	18,10	52,17	0,23	3,74	1,77	2,07	0,12	11,69	21,88	4,95	1,04	177
58	0,46	3,35	13,83	66,48	0,02	1,59	1,98	0,16	0,02	2,28	9,66	9,60	1,17	150
59	1,02	2,20	16,62	61,73	0,19	3,12	1,07	0,74	0,09	7,67	15,08	5,25	0,89	201
60	1,44	2,51	17,51	59,51	0,20	3,82	1,00	0,79	0,12	7,69	16,46	5,15	0,55	333
61	1,16	3,26	15,38	58,21	0,16	3,24	3,97	0,75	0,13	7,11	18,74	6,15	0,74	235
62	1,66	2,82	16,85	60,63	0,18	3,42	0,58	0,87	0,09	8,32	16,8	4,30	0,60	323
63	1,75	3,90	13,85	51,23	0,19	1,98	7,75	0,97	0,15	8,73	24,11	9,10	0,91	204
64	1,28	2,65	13,77	60,11	0,14	2,51	4,03	0,68	0,12	6,63	17,1	7,40	0,89	204
65	1,45	1,50	16,62	59,07	0,17	3,48	3,15	0,78	0,10	7,50	17,08	5,90	1,35	121
66	1,13	1,66	19,56	59,67	0,17	3,47	0,23	0,88	0,11	7,66	14,15	5,15	1,29	145
67	1,21	1,83	19,13	59,82	0,20	3,34	0,22	0,88	0,13	8,21	14,81	4,75	0,93	205
68	1,06	1,81	19,14	60,39	0,16	3,25	0,23	0,88	0,09	7,69	14,04	5,05	1,16	161
69	1,01	1,53	17,67	62,60	0,20	2,84	0,69	0,80	0,09	7,48	13,55	4,75	1,10	174
70	1,19	2,04	18,98	59,74	0,15	3,00	0,22	0,87	0,25	8,82	15,27	4,45	0,95	187

Fluxing: $CaO+MgO+Na_2O+K_2O+Fe_2O_3$; LOI: Loss on Ignition; UW: Unit weight of expanded clay agregate; ER: Expansion ratio;

3. Results

The chemical data of the ground mixtures (recalculated to 100%) were plotted on the SiO_2-Al_2O_3-Fluxing elements ($CaO+MgO+K_2O+Na_2O+FeO+Fe_2O_3$) diagram (Riley, 1951). The raw materials with a chemical composition located within the ''bloating area'' are shown on the SiO_2-Al_2O_3-Fluxing Triangle diagram which is drawn according to the results of the chemical analysis, and the expansion tests of the samples is shown in figure 3. In figure 3, it can be seen that 60 of the 70 total samples presented within the expansion area, which had been proposed by Riley (1951) and it is determined that this constituted 85.7 % of the total test samples.

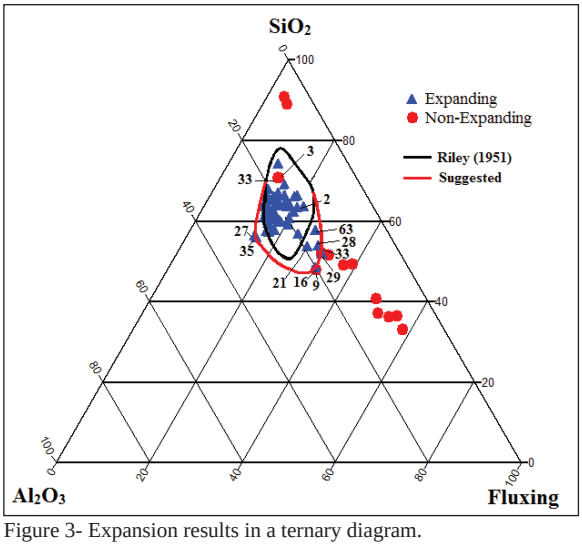

Figure 3- Expansion results in a ternary diagram.

Seven samples of the total 55 that exhibited expandability features were out of the expansion area. Only approximately 12.7 % of the total expanded samples were out of the area, which was proposed by Riley (1951). Samples having the expandability features but out of the area were the samples numbered 16, 21, 27, 28, 29, 35, and 63. These seven samples circumscribed the expansion area.

Three of the total 15 and 20 % of the total unexpanded samples that did not exhibit expandability features did not expand although they were in the expansion area with respect to their chemical compositions. Samples that did not expand in spite of being in the expansion area were the samples 2, 3 and 53.

The samples no 2 and no 3 were observed not to expand although they were in the expandability area. The reasons behind these conditions are thought to be not having enough clay in its mineralogical content for the sample no 2, and not having enough content to form gaseous structure for the sample no 3. It is considered possible for the sample no 3 to gain expandability properties with additive materials. In addition, the sample no 53 is thought to have low clay and melting contents, therefore it was not able to expand.

In figure 3, a new expansion area was proposed with the samples that expanded outside of the expandability area although expansion area proposed by the Riley (1951) represents the majority of the expanded samples. This area is in figure 3. By extending the expansion area, all the expanded

Table 3. XRD analysis results.

No	UW (g/cm³)	ER (%)	Mica GM	Chloride GM	Feld.	Quartz	Dol.	Cal.	Graphite	Hem.	Apa.	AS	Cris.	Clay GM	T	S	Am	Gy	O	P	Z	Mont.	A
1	1,32	124	xxx		x	xx	x																
2	-	-	x	x	x	xxx		xx															
3	-	-	xxx	xxx	x	xxx																	
4	-	-	x	x	xx	xxx	xx	xx															
5	0,96	197	xx	xx	x	xxx			x														
6	0,81	235	xx	xxx	x	xxx	x		x		x												
7	0,92	207	xxx	xxx	x	xxx		x		x													
8	0,78	248	x	xx	x	xxx	x																
9	-	-	xx	xx	xx	xxx	xxx	xxx		xx		xx											
10	1,14	166	x	x	x	xxx	xx	xx	xxx														
11	-	-	x		x	xxx			xxx														
12	0,64	293	xx	xx	xx	xxx			x														
13	-	-			x	xxx			xxx				x										
14	1,00	191	xx	xxx	x	xxx																	
15	0,69	288	xx	xxx	xx	xxx			xxx														
16	1,18	167	xx	xx	x	xxx	x	xx	xx	x													
17	-	-	xx	xxx	xx	xxx		xxx		x			xx	xxx	xxx	xxx	xxx						
18	-	-	x	x	x	xx		xxx		x			x	xx	x	x							
19	-	-	xx	xx	x	xx	x	xx		x				xxx	xx	xx	xx						
20	1,30	144	x	xxx	x	xxx	x																
21	0,95	198	xx	xx	x	xxx		xx	xxx									x					
22	-	-	xx	xx	x	xxx	x	xxx	xxx														
23	-	-	xxx	xxx	x	xxx	x	xxx	xxx										x				
24	0,94	196	x	x	x	xxx	x	x	x	x													
25	1,03	185	x	xx	x	xxx			x					x			x						
26	0,86	225	xx	xxx	x	xxx	x																
27	0,97	191	xx	x	x	xxx		x				x		xx				x	x				
28	0,77	241	x	xx	xx	xxx	x	xx					x			x	x						
29	1,21	163	xx	xx	x	xxx		xx					x										
30	1,03	186	x	xx	xx	xxx		xx		x						x							
31	0,56	341		x	xxx	xx	x	xx				xxx	xxx	xxx			x			xx	x		
32	0,82	215	x		xxx	xx	x					xxx	xxx	xxx						x			
33	-	-	xx	xx	x	xxx	x	xx													x		
34	1,04	159	xxx	xxx	x	xx			xx		x												
35	1,26	129	xxx	xx	xx	xxx			xx		x												
36	0,78	241	x	xx	x	xxx			x														

Table 3- continue.

No	UW (g/cm³)	ER (%)	Mica GM	Chloride GM	Feld.	Quartz	Dol.	Cal.	Graphite	Hem.	Apa.	AS	Cris.	Clay GM	T	S	Am	Gy	O	P	Z	Mont.	A
37	0,99	183	x	x	x	xxx			x														
38	0,84	212	xx	xxx	x	xxx			x														
39	0,76	240	xxx	xxx	x	xxx			x		x												
40	1,15	159	xxx	x	x	xxx			x		x												
41	1,16	150	xx	xxx	x	xxx			x		x												
42	0,68	274	x	xx	xx	xxx							x							x			
43	0,55	346	xx	xxx	xx	xxx							x							x			
44	0,88	194	xx		x	xxx	x		x														
45	0,91	216	x	x	x	xxx	x													x			
46	1,00	175	xxx	xx	x	xxx			xx		x												
47	1,23	131	xxx	xx	x	xxx			xx		x												
48	0,89	167	x	x	xx	xxx			xxx		x		x										
49	0,86	192	xxx		x	xxx			xx		x												
50	-	-	x	x	x	xxx		xx															
51	-	-	x	x	x	xx		xxx		x				xxx									
52	0,85	223	xxx	xx	x	xxx																	
53	-	-		x	x		xx	x						xxx			x				x		
54	0,52	302			xxx			xxx											xxx		xxx	xxx	xxx
55	0,65	218			xxx			xxx											xxx		xxx	xxx	xxx
56	0,43	455	x		x	xxx	x		x					xxx									
57	1,04	177	xx	xx	x	xxx		xx		x													
58	1,17	150	x	x	x		x					xxx	xxx	xxx						x	x		
59	0,89	201	xx	xxx	x	xxx			xx														
60	0,55	333	xx	xxx	x	xxx			xx														
61	0,74	235	xx	xxx	x	xxx			xx														
62	0,60	323	xx	xxx	x	xxx			xx														
63	0,91	204	x	xx	x	xxx		xx		x			x										
64	0,89	204	xx	xx	x	xxx		xx	xx														
65	1,35	121	xxx	xx	xx	xxx		x	xx														
66	1,29	145	xx	xx	x	xxx		x	xxx														
67	0,93	205	x	xx	x	xxx				x													
68	1,16	161	x	x	x	xxx			xxx														
69	1,10	174	x	xx	x	xxx			xx														
70	0,95	187	xx	xxx	x	xxx			xx														

UW: Unit weight of expanded clay agregate; ER: Expansion ratio; GM: Groups Minerals; Feld:Feldspar; Dol: Dolomite; Cal: Calcite, Hem: Hematite, Apa: Apatite; AS: Amorphous Silica; Cris: Cristobalite; T:Talc; S: Serpentine; Am: Amphiboles GM; Gy: Gypsium; O: Opal-CT; P: Pyroxen GM; Z: Zeolite; Mont: Montmorillonite; A: Amorphous Matter

samples were included in this area. Despite the three unexpanded samples that were in the area proposed by Riley (1951), there were five unexpanded samples in the new area. However, the location of the additional two unexpanded samples was at the edge of the newly proposed area, and this should not be neglected. It was observed that the expansion area will be very useful for prediction beforehand of the expandability of the clays because, excluding a few exceptional ones, this area was applicable for all the investigated samples. Besides the location of the samples within this area, another feature was their appropriate SiO_2-Al_2O_3-Fluxing content. De Gennaro et al. (2004 and 2008) has stated that the quantity of the silica and the dissolver elements were factors in the expansion mechanism, and they played an important part in the determination of the liquid phase viscosity.

When the chemical analyses results (Table 2) are examined, the chemical content intervals for the samples that were able to expand are noted as 39.85 – 66.48 % SiO_2 (samples no 16 - 58), 12.84 – 27.07 % Al_2O_3 (samples no 10 - 27) 9.66 – 26.79 % Fluxing (samples no 58 - 29).

It is not surprising to observe that the samples (no 2, 4, 9, 11, 13, 22, 23, 33, 50 and 51) with low clay content were not able expand when the mineralogical analyses results (Table 3) are examined. From the results, it can be deducted that the fundamental condition for the expandability is to have an expandable structure like clay, along with other supporting conditions.

High SiO_2 content is expected to affect the expansion negatively. This event requires more dissolver quantity that would be adequate for softening the SiO_2 which would form the cage structure. For content that provides sufficient viscosity for expansion, one of the components that constitute the structure should be extremely high. This factor is very important for prediction. It can also be understood from the fact that the samples no 11 and 13 with very high SiO_2 proportions did not expand.

When table 2 is examined, the sample with the lowest Al_2O_3 proportion to expand is found to be the sample no 10 (12.84%), and the 9 samples with lower Al_2O_3 content (samples no 4, 11, 13, 17, 18, 19, 22, 23 and 51) were noted as not expanding. Only 6 samples (2, 3, 9, 33, 50 ve 53) with slightly higher Al_2O_3 contents were found not to be expanding due to their low clay content or high melting proportions.

It was observed that the samples with more than 25% melting content were also not able to expand. Additionally, the samples no 11 and 13 were not able to expand, with melting contents 3% and 4%, respectively. Very high flux content also negatively affects expansion. The important thing is to sustain the minimum level of dissolvers to maintain a viscosity adequate to form a pyroclastic structure along with a gas exit within the cage structure. If there is too much flux, viscosity will decrease, and gas will not stay in the system. With the help of additions that decrease the dissolver level, expandability can be increased. Having low melting content also would not be helpful for expandability, as it would not create any significant melting effect. Optimal proportion should be provided for this condition.

When figure 3 is examined, it is understood that expanded samples are gathered inside an "expandability area", and clay samples should have a chemical equilibrium in order to expand, also having too high contents of SiO_2 and Fluxing or too low Al_2O_3 content would affect the expandability adversely. In the light of these results, expandability area is considered to be promising.

Mineralogical contents in reference to fields were investigated and the results below were obtained;

- Samples 1-3 (Kırşehir Region) contain both Mica GM-Chloride GM with Quartz.
- Sample 4 (Kayseri Region) contains calcite-dolomite and mica GM-Chloride GM alongside its main content of Quartz.
- Samples 5-19 (Adana Region) contains mostly Quartz, alongside Mica GM-Chloride GM, calcite-dolomite, feldspar and graphite. Non-expanding samples were noted to have low levels of these associations or none at all.
- Samples 20-27 (Mersin Region) contain mostly Quartz, also Mica GM-Chloride GM, calcite-dolomite associations with graphite and feldspar content. Clay samples with this structure have a high expandability property. The reason for samples no 22 and 23 not having the same property is thought to be related to their high melting proportions (38.77-39.71%).
- Samples 28-30 (Niğde Region) also contain mostly Quartz, and Mica GM-Chloride GM associations with minor abundance of calcite

and feldspar. High expandability features were observed with all of these samples.

- Out of Samples 31-33 (Edirne Region), samples no 31 and 32 were noted to show similar expandability properties. It was possible to produce a clay aggregate with specific weights of 0,56-0,82 g/cm^3 with Clay GM-Amorh Silica-Feldspar-Cristobalite associations. Sample no 33 was obserbed to have a low level of clay content with a high amount melting content of 25.64%, and these are the reasons thought to be the main factors in its failing to expand.
- Almost all of the Samples 34-41 (Kırklareli Region) show the same mineral association and all of them were observed to expand. In addition to Quartz, Mica GM-Chloride GM combination and graphite, apatite and feldspar contents provide good expansion results (0.76-1.26 g/cm^3).
- Samples 42-45 (Istanbul Region) have Mica GM-Chloride GM association and Feldspar contents besides Quartz. Apart from these, very few pyroxene, dolomite and cristobalite are contained. It is observed that all the samples in this region were able to expand.
- Samples 46-49 (Kocaeli Region) are similar in mineral content. In addition to Quartz, Mica GM-Chloride GM association and graphite are the main components. Feldspar and Apatite are also found in all samples. Good expansion results were obtained with the samples from this region.
- Sample 50 (Sakarya Region) did not demonstrate any expansion characteristics. The reason behind this is thought to be the lacking content (clays and fluxing). Quartz and calcite are observed in the results of mineralogical analyses.
- Sample 51 (Bolu Region) sample also did not demonstrate any expansion characteristics. Despite the fact that main structure is formed by Clay GM, due to its Calcite content and its high melting proportion of 38.21% the sample was not able to expand.
- Among the Samples 52-57 (Tokat Region), three different groups of samples were investigated and all of them were able to expand. Only the sample no 53 was not able to show any expandability characteristics due to lacking content (fluxing). The associations observed in the expanding samples can be listed as; a) Mica GM-Chloride GM-Quartz; b) Montmorillonite-Zeolite-Amorph Matter; c) Clay GM-Quartz. All samples contain feldspar.
- Sample 58 (Ordu Region) shows mainly Clay GM-Amorph Silica-Cristobalite association. With this expandable sample, expanded clay aggregates weighing 1.17 g/cm^3 were able to be produced.
- Samples 59-63 (Çorum Region) contain Mica GM-Chloride GM association, Graphite and Feldspar besides their Quartz content. All samples were able to produce expanded clay aggregates with low unit weights such as 0.55-0.91 g/cm^3.
- Samples 64-70 (Kastamonu Region) have similar mineral associations with Çorum Region and high expansion rates. Graphite, Mica GM-Chloride GM association, feldspar and calcite contents are observed beside Quartz in the examined samples.

Considering the mineralogical analyses, mineral associations, chemical contents and expandability results according to regions stated above, the mineral groups with expandability characteristics are noted as; a) Mica GM-Chloride GM; b) Montmorillonite-Zeolite-Amorph Madde; c) Clay GM-Amorh Silica-Cristobalite. It was also noted that almost all the samples with graphite content demonstrated expandability features. Out of 37 samples with graphite content, 33 were able to observed to be expanding. Samples no 11 and 13 were not able expand due to their high content of SiO_2 contents, 84.53 and 82.5% respectively. As for the samples no 22 and 23, it was found to be the high melting contents preventing the expansion, 38.77 and 39.71% respectively.

Unit weights of the expanded and investigated samples range between 0.43 and 1.35 g/cm^3. Expansion rates range between 121 % and 455 %. The location of the samples with the best expanding features on the triangle diagram were investigated, and results are shown in figure 4(a). As can be seen here, the unit weights of the best expanded samples range between the 0.43 and 0.69 g/cm^3. Since they located at almost the same places in the triangle area, this event shows the importance of the chemical composition. 10 samples that had minimum expandability features were investigated separately. When their unit weights were investigated, the locations of the samples with

unit weights between 1.16 and 1.35 g/cm^3 are shown in the triangle diagram in figure 4(b). Here, it can be seen that the chemical compositions of the samples that have low expandability features are quite different from each other. All three of these samples were out of the expansion area which was proposed by the Riley (1951). Prediction of the expansion shows the importance of results that can be obtained from chemical analysis as shown in figure 4.

4. Conclusions

Following results were obtained when the results received from the chemical analysis and expansion tests were evaluated by the SiO_2-Al_2O_3 – Fluxing triangle diagram:

- Expansion area in the SiO_2, - Al_2O_3 – Fluxing triangle diagram which was proposed by Riley (1951) gives an idea of the expansion before the expansion tests. However, chemical analysis or the mineralogical structure alone is not sufficient. Expansion can be sustained by the combination of an optimal temperature and the duration with adequate content and mineralogical structure.
- Although most of the expansion results are within the expansion area, the samples of chemical compositions which are outside the area can be expanded.
- Although most of the samples not having expandability features lie outside the area, it was understood that, among the samples within the expansion area, not all the samples could exhibit expandability features.
- Being out of the expansion area but exhibiting expandability features and being within the expansion area but not having expandability features shows us that mineralogical structure is very important.
- Clays, shales, slates, etc., which are appropriate for the production of the expanded clay aggregate, will be useful for predicting the expansion if the chemical analysis and mineralogical analysis are performed before the expansion tests.
- It was seen that the raw material should exhibit adequate chemical content for the occurrence of the expansion. It was also seen that all the elements that constitute the triangle diagram have importance separately. Any deficiency in one of the elements, negatively affects the expansion. In this study, it was observed that clays with high SiO_2 and fluxing contents were not able to expand. It is obvious that there is a certain balance when considering the place in the triangular diagram.
- In this study, if the clays in Turkey, mineralogical analyses, mineral associations, chemical contents and expansion results are evaluated together, the mineral groups with expandability characteristics were noted as; a) Mica GM-Chloride GM; b) Montmorillonite-

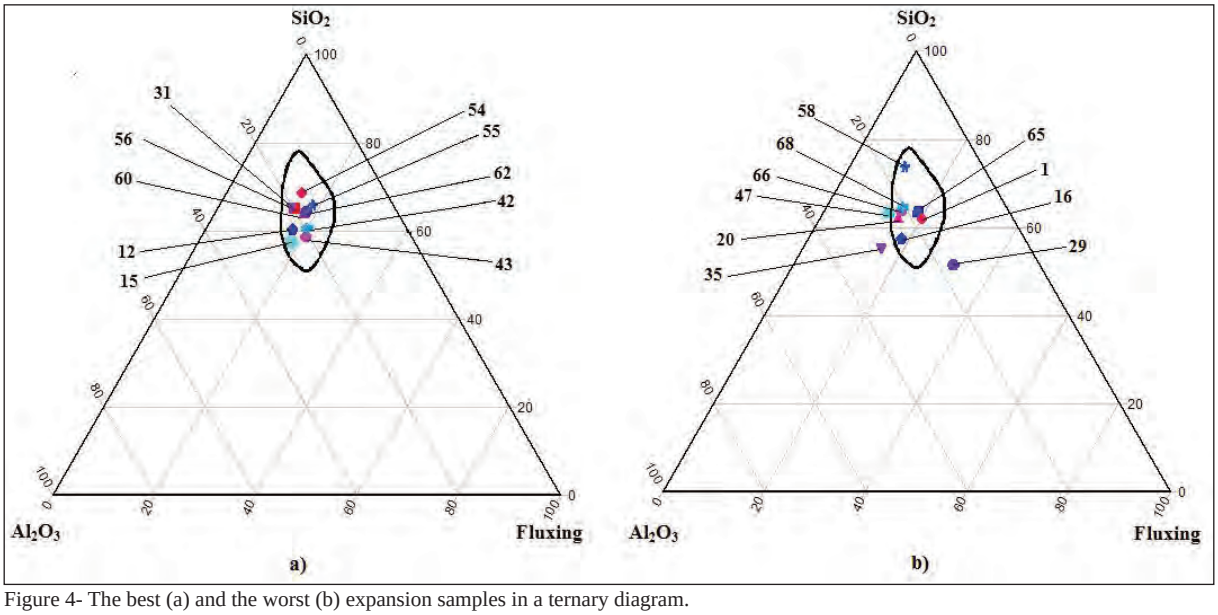

Figure 4- The best (a) and the worst (b) expansion samples in a ternary diagram.

Zeolite-Amorph Madde; c) Clay GM-Amorh Silica-Cristobalite. Different associations can be identified by increasing the number of samples.

- This study shows the prominence of graphite content in the production of expanded clay aggregate. Almost all of the samples with graphite content were found to exhibit expansion.
- The expansion area proposed previously was tested once more by investigating the various samples. After considering the test results, a new expansion area was proposed. It was also determined that this area is appropriate for the clays of Turkey.

As a result, SiO_2-Al_2O_3-Fluxing triangle diagram is very important for the raw materials that exhibit expandability features. It was determined that most of the raw materials exhibiting expandability features are within this area. Using this diagram before the expansion tests will be useful in predicting of the expansion.

Acknowledgements

Author is thankful to Dr. Mustafa Albayrak and Dr. Sezin Özaksoy for XRD analyses of the samples and to Yasemin Güneş Dulkadir for XRF analyses of the samples.

References

Al-Bahar, S., Bogahawatta, V.T.I. 2006. Development of lightweight aggregates in Kuwait. Arab J Sci Eng:31:231-239.

ASTM C493–98. 1998. Standard test method for bulk density and porosity of granular refractory materials by mercury displacement.

Chen, H.J., Wang S.Y., Tang, C.W. 2010. Reuse of incineration fly ashes and reaction ashes for manufacturing lightweight aggregate. Constr Build Mater. 24,46-55.

Conley, J.R., Wilson, H., Klinefelter, T.A. 1948. Production of lightweight concrete aggregates from clays, shales, slates, and other materials, US Bur Mines Repts Invest, 4401, 121 pp.

de'Gennaro, R., Cappelletti, P., Cerri , G., de'Gennaro, M., Dondi, M., Langella, A. 2004. Zeolitic tuffs as raw materials for lightweight aggregates, Appl Clay Sci, 25, 71-81.

de'Gennaro, R., Langella, A., D'Amore, M., Dondi, M., Colella, A., Cappelletti, P., de'Gennaro, M. 2008. Use of zeolite-rich rocks and waste materials for the production of structural lightweight concretes, Appl Clay Sci, 41, 61-72.

Doğan, H., Şener, F. 2004. Hafif yapı malzemeleri (pomza-perlit-ytong-gazbeton) kullanımının yaygınlaştırılmasına yönelik sonuç ve öneriler. TMMOB. The Newsletter of the Chamber of Geology Engineers, vol. 1, p. 51–3 (in Turkish).

EIPPCB, 2005. Best Available Techniques in the Ceramic Manufacturing Industry, European Comission Directorate General Joint Research Center, Draft Reference Document, 253 p.

Heller-Kallai, L., Miloslavski, I., Aizenshtat, Z., Halicz, L. 1988. Chemical and mass spectrometric analysis of volatiles derived from clays. Am Miner.73:376–82.

Kavas, T., Christogerou, A., Pontikes, Y., Angelopoulos, G.N. 2011. Valorisation of different types of boron-containing wastes for the production of lightweight aggregates. J Hazard Mater. 185:1381-1389.

Kazantseva, L.K., Belitsky, I.A., Fursenko, B.A. 1995. Zeolite containing rocks as raw material for siberfoam production. In: Kirov G, Filizova L, Petrov O, editors. Natural Zeolites, Sofia'95., Sofia, Bulgaria: Pensoft Publishers. p. 33–42.

Kazantseva, L.K., Belitsky, I.A., Fursenko, B.A, Dement'ev, S. N. 1996. Physicomechanical properties of sibirfom, a porous building material zeolite-containing rock. Glass Ceram52:257–60.

Özgüven, A. 2009. Genleşen kil agrega üretimi ve endüstriyel olarak değerlendirilmesi. PhD thesis. Isparta: University Süleyman Demirel; (in Turkish).

Özgüven, A, Gündüz, L., 2012. Examination of effective parameters for the production of expanded clay aggregate, Cement & Concrete Composites, v. 34 pp. 781-787.

Purbrick, J. 1991. Lightweight aggregates-manufacture and applications. Exploration, Mining and Uses of Ceramic Raw Materials, Proc. 23rd Ann. Symp. African Ceram. Soc., pp.45-49.

Riley, C.M., 1951. Relation of chemical properties to the bloating of clays, J Am Ceramic Soc, 34(4), 121-128.

Salakhov, A.M., Morozov, V.P., Tuktarova, G.R. 2005. Upgrade of production technology of building ceramics and expansion of product range. Glass Ceram. 62:80-83.

Tsai, C.C., Wang, K.S., Chiou, I.J. 2006. Effect of SiO_2-Al_2O_3-flux ratio change on the bloating characteristics of lightweight aggregate material produced from recycled sewage sludge. J Hazard Mater. B134:87-93.

Bulletin of the Mineral Research and Exploration

http://bulletin.mta.gov.tr

Hydro-chemical and isotopic investigation of the Ispendere mineral and thermal water springs, Malatya, Turkey

Murat ÇELIKER[a*] O. Faruk DURSUN[b] and Mahmut FIRAT[c]

[a] *General Directory of State Hydraulics Works, 9th Regional Directory, Elazig, Turkey orcid.org/0000-0003-1211-5561*
[b] *Department of Civil Engineering, Faculty of Engineering, Inonu University, Malatya, Turkey orcid.org/ 0000-0003-3923-5205*
[c] *Department of Civil Engineering, Faculty of Engineering, Inonu University, Malatya, Turkey orcid.org/0000-0002-8010-9289*

Research Article

Keywords:
Environmental isotopes, İspendere, mineral and thermal waters, geochemistry.

ABSTRACT

The objective of this study is to determine the source, chemical characteristics and isotopic components of the İspendere mineral and thermal waters, Malatya, Turkey. There are many mineral and thermal water springs in the area with flow rates ranging between 0.01 – 0.4 l/s. Geochemical and isotope chemistry studies were carried out at three different thermal springs in the region as well as three different cold water springs during May-October 2011. The temperature of mineral and thermal waters were measured as between 21.1°C – 23.6°C in May 2011 and as 20.8°C in October 2011. The region was determined as a low geothermal area and the reason for this is thought to be cold water mixing. The pH values of mineral and thermal spring waters were measured to be between 6.19 –6.69, EC values were measured to be between 1420 µS/cm and 2720 µS/cm, pH values of shallow and deep wells ranged between 6.04 and 7.82, whereas EC values were measured approximately between 275 µS/cm and 3300 µS/cm. The $MgHCO_3$ water type dominates the chemistry of mineral and thermal water in study area. The results of ^{18}O and ^{2}H isotope analysis yield that the springs of mineral and thermal waters as well as cold waters are fed by meteoric rains. It was determined that the İspendere mineral and thermal waters have low tritium (^{3}H), low Cl and high EC values. Reservoir rock temperatures have been estimated to be between 95 -132° C as a result of the quartz geo-thermometer calculations.

Received Date: 04.04.2018
Accepted Date: 08.10.2018

1. Introduction

Thermal springs are benefited for a variety of purposes, such as the generation of power, direct space heating, industrial processes, agriculture, aquaculture, bottled water and the extraction of rare elements (Hellman and Ramsey, 2004; Petraccia et al., 2005). With the increasing demand of spas and the growing importance attached to the 'natural' health sector, mineral and thermal springs are becoming centers of hydrotherapy (Bojadgieva et al., 2002; Harvey, 2007; Olivier et. al. 2008). The optimal use of a mineral and thermal spring is largely dependent upon its physical and chemical contents.

The aims of geochemical studies in geothermal systems are to estimate the subsurface temperatures, to understand the circulation of the thermal fluids and to have information on their origin (Battistel et al. 2014). Hydrogeochemistry, including isotope geochemistry, has significantly contributed to the understanding of geothermal systems (Chenaker et al. 2017). The chemical and isotopic composition of the geothermal water provides information about their origin, recharge areas and flow paths. Also, the major ion chemistry was used in the estimation of the sub-surface reservoir temperatures of thermal waters (Anees et al., 2015).

* *Corresponding author: Murat ÇELİKER, mceliker23@gmail.com*
https://dx.doi.org/10.19111/bulletinofmre.494681.

Oxygen is the most abundant element in the earth's crust. Contrary to ^{18}O, ^{2}H is generally found in waters more than mineral and rocks. This contradictory structure of these two isotopes is very important for the isotopic evaluation of water in high temperature systems (Clark and Fritz, 1997). The $\delta^{18}O$ contents of magmatic waters vary between ‰ +5.5 and +13, whereas the $\delta^{18}O$ contents of metamorphic waters vary between ‰ +3 and +25 (Hugh and Taylor, 1974; Sheppard, 1981). No significant change is observed in the ^{2}H content of mineral and thermal waters as a result of water-rock interaction, because ^{2}H is not commonly observed in rock forming minerals. In addition, it has been put forth that the value of ^{2}H can be enriched and that it increases in direct proportion with ^{18}O in many geothermal and volcanic systems that are located at convergent plate boundaries (Arnorsson et. al., 2000). The radioactive isotope that is most commonly used in hydrogeology is tritium (^{3}H).Tritium is generally used in geothermal systems to estimate the mixing ratio of water and underground residence times (Panichi and Gonfiantini, 1978). Although prior to 1952, the tritium amount in groundwater was zero (<0.5 TU in practice), it has reached significant amounts after 1952 (>10TU in practice). For some regions, measurable tritium (0.5–10 TU) represents to be a mixture of pre-1952 and post-1952 water (Mazor, 2004). Many studies have been carried out until today to determine the chemical and isotopic properties of low, moderate and high temperature mineral waters. Pasvanoğlu and Chandrasekharam (2011) carried out the hydrochemical and isotopic analyses of mineral and thermal waters at the Kozaklı district of Nevşehir (Turkey). Hydrochemical and isotopic analyses of natural spring waters of the same area were investigated and evaluated by Afşin and Canik (2013). Pasvanoğlu (2013) constructed a hydro-geochemical model for the mineral and thermal water springs in the Diyadin district located 70 km east of Ağrı (Turkey). Chandrajith et al. (2013) investigated the geochemical and isotope characterization of geothermal spring waters in Sri Lanka. Ersoy and Sonmez (2014) examined the hydrochemical and isotopic characteristics of geothermal springs in Ilıca (Erzurum, Turkey) and they determined that these geothermal springs located along the main fault zone are fed by groundwater with varying chemical and isotopic structures. Baba and Şanlıyüksel (2011) examined the hydrochemical and isotopic properties of the low temperature geothermal springs in Kırkgeçit (Northwest Turkey).

The objective of this study is to determine the source and underground transportation process of the İspendere mineral and thermal waters (Malatya, Turkey) by using physical-chemical parameters and environmental isotopes. For this purpose, analyses were carried out on samples collected from three different thermal springs that discharge in the same area as well as three different cold water springs that discharge close to the study area.

2. Study Area

The study area is located in the Eastern Anatolia region of Turkey between the cities of Elazığ – Malatya and about 20 km southeastof the Malatya city (Figure 1). This region was studied by various researchers

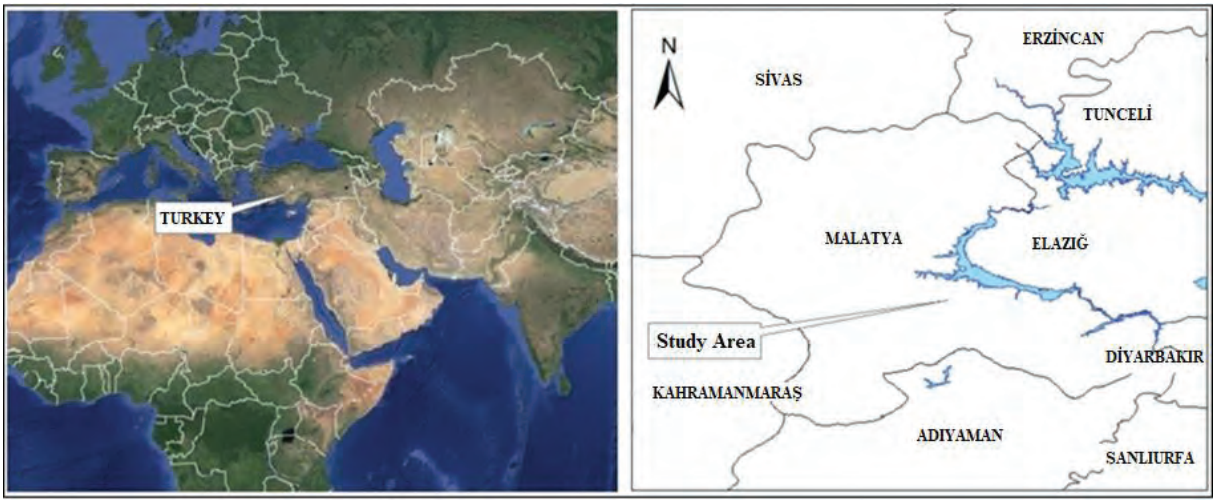

Figure 1- Study area.

in terms of geological, tectonic, petrographical, petrological and hydrogeochemical aspects (Yazgan et al., 1987; Beyarslan, 1991; Dumanlılar, 1993; Çetindağ et al., 1993; Dumanlılar et al., 1999; Gürocak and Alemdağ, 2002, Beyarslan and Bingöl, 2010; Parlak et al., 2010). The İspendere mineral and thermal springs discharge along the fault line in the N-S direction at the contact of İspendere ophiolite and Elazığ magmatics (Figure 2). They have outlet temperatures between 20.8°–23.9°C and their discharges are between 0.01-0.04 l/s. These springs are used for medical purposes and a geothermal well (well/521) with a depth of 292 m was drilled by the local administration in order to use the thermal properties of the waters in the region. However, desired temperature has not been obtained in geothermal well (well/521).

2.1. Climate

The İspendere, Malatya region has a continental climate with an average annual precipitation of 378.1 mm (1929 – 2010). The highest amount of monthly rainfalls were received in March, April and May and the averages are reported as 49.71, 56.33, and 46.2 mm, respectively. The maximum monthly air temperature (42.2°C) occurs in July, and the minimum monthly air temperature (–14.6°C) in January (DMI, 2010).

2.2. Regional Geology

The geological map of the study was prepared by Beyarslan and Bingöl (2010) (Figure 2). Geological units in the study area have tectonic and intrusive relations. These units are İspendere ophiolites, Elazığ Magmatics, Maden complex and Kırkgeçit formation (Beyarslan and Bingöl, 2010). İspendere ophiolite thrusts over the Mid Eocene aged volcano-sedimentary Maden group towards the south and is overlain by the Mid Eocene-Oligocene aged Kırkgeçit formation

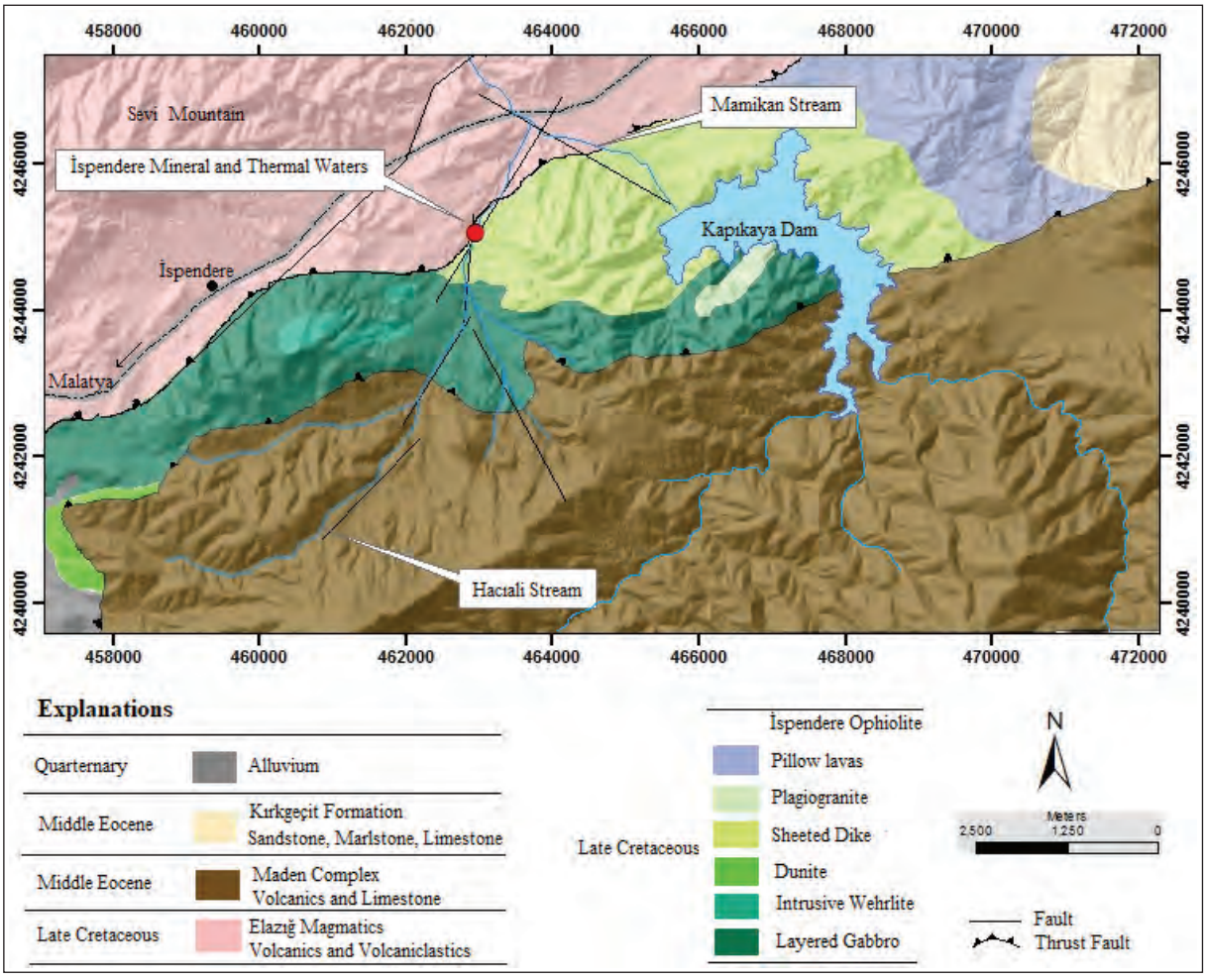

Figure 2- The Geological map of study area from Beyarslan and Bingöl (2010).

(Parlak et al., 2010). Upper Cretaceous aged İspendere ophiolites put forth a complete oceanic lithosphere crosssection and are parts of the Southeastern Anatolia ophiolite band between the Arabian and Taurus (Anatolia) Platforms. İspendere ophiolites are made up of dunite, layered and isotrope gabbro, plagiogranite, plate dyke complex, pillow and massive basaltic and andesitic lava and volcano-sedimentary rocks. Mantle rocks are harzburgitic. Ultramafic-mafic cumulate rocks are represented by verlite, dunite, troctolite, olivine gabbro and gabbro. Whereas dyke complex forms the thickest unit of the Ispendere ophiolite at the top regions of which radiolarites, micritic limestone and tuffites are observed (Beyarslan, 1991; Çetindağ et al., 1993; Dumanlılar et al., 1999; Beyarslan and Bingöl, 2010; Parlak et al., 2010). Elazığ magmatics in contact with İspendere ophiolites contain andesite and dacite dykes, agglomerate, pillow lava and tuff units (Yazgan et al., 1987; Çetindağ et al., 1993).

2.3. Hydrogeology

The main drainages of the study area are the Mamikan Stream and the Hacıali Creek and they discharge to the Karakaya Dam lake. Kapıkaya Dam has been built over the Mamikan Stream by DSI (State Hydraulic Works). İspendere mineral and thermal water springs emerge from the bed of the Hacıali Creek. The fault systems formed between Elazığ Magmatics and İspendere Ophiolites are primary cause of discharge of the mineral and thermal water springs. Secondary porosity was also developed in the Elazığ magmatics and İspendere ophiolites due to tectonic activity (Çetindağ et al., 1993). The marln and clayey levels that surface around the mineral and thermal water springs are impermeable whereas the sandstone, limestone and alluvial levels are permeable. The impermeable ophiolites act as cap rock of the geothermal reservoirs. The heat source of the geothermal system is likely the combination effect of the volcanic and tectonic activities. Limestones, sandstones, alluvial levels and structural features in magmatic rocks (faults, fractures and contacts) act as reservoir rocks in region. Many mineral and thermal water springs were determined in the study area with flow rates varying between 0.01 – 0.4 l/s. A 292 m deep geothermal well (well/541) was drilled by the local administration for benefit from the mineral and thermal waters. The flow rate of the water acquired at the end of the well was measured as 40 l/s whereas the well base temperature was measured as 25°C. The units belonging to alluvial, sandstone, limestone, marln, dacite, agglomerate, tuff, basalt, serpentine, diabase, gabbro, diabase sheets were cut through during drilling. The static level of the geothermal well was water determined as 13 m, whereas the dynamic level was determined as 33 m. Intensive water leakage was observed at 64 m and partial water leakage was observed at 176 m during drilling (Geothermal management report, 2010). It was observed as a result of the examination of the basic borehole logs of the Kapıkaya Dam built over the ophiolites about 3 km east of the İspendere mineral and thermal waters that the ophiolite unit has cracked and fractured structure due to tectonic movements and that these cracks and fractures have been covered with clay and calcite filling (DSİ. 1991). Browne (1991) has explained the calcite filling formation by stating that calcite is the main substance precipitated by geothermal fluids containing high amounts of bicarbonate and dissolved CO_2 because they are at very low temperatures below their boiling points at regions near the surface where they mix with cold water at high elevations near high temperature geothermal areas or during the rising of these systems.

3. Sampling and Analytical Methods

The groundwater level and chemistry are governed by various factors. Parallel to global climate change, climate change in study area, as reflected in precipitation and evaporation rates, influences the groundwater level fluctuation and chemistry. For this reason, sampling studies have been carried out in rainy and dry seasons. Two water samples were collected from 6 different locations in May and October 2011 in the study area in order to determine the major and minor ion chemistry of the mineral and thermal waters as well as cold waters and their oxygen-18, deuterium and tritium contents (Figure 3). The samples, which had been taken for isotope analyses as well as physicochemical analyses, were put in 1000 ml closed bottles without filtration. The water temperature, pH and electrical conductivity were measured during sample collection by using a WTW Cond 720 measuring instrument. The analyses of the major and minor elements in the waters were carried out at the Malatya Provincial Administration laboratories whereas isotopic analyses were carried out at the General Directorate of State Hydraulic Works (Ankara) laboratories.

Water samples have been analyzed for chemical constituents such as major ions in the laboratory using

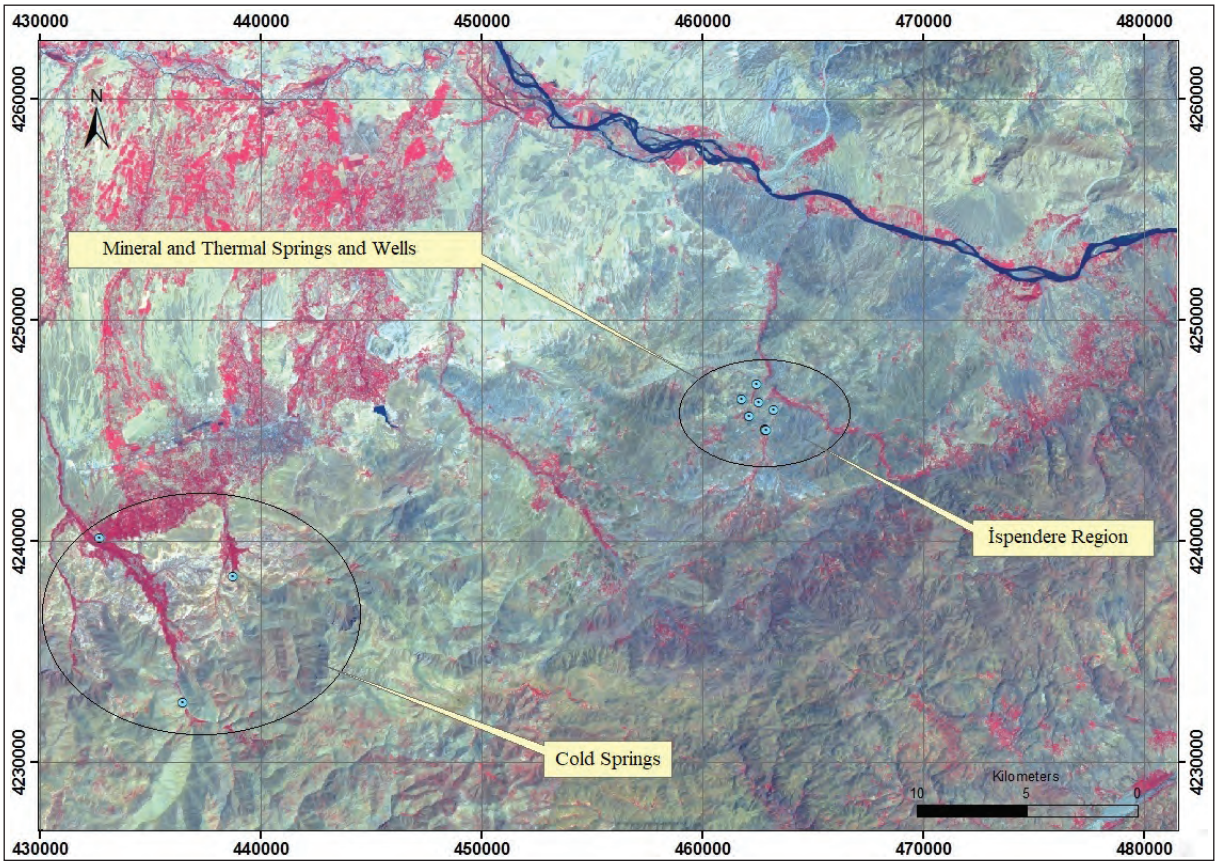

Figure 3- Sampling location (Lansat 4: 3: 1 satellite image).

the standard methods as recommended by the APHA (2005). The major cations (Ca^{2+}, Mg^{2+}, Na^{+}, K^{+}) of water samples were analyzed by ICP-OES (inductively coupled plasma optical emission spectrometry). Bicarbonate (HCO_3^-), were measured by acidimetric titration method while chloride (Cl^-) was measured by argent metric titration method. Spectrophotometer was used for determination of sulfate (SO_4^{2-}). The oxygen-18 and deuterium isotope ratios were analyzed via mass spectrometric methods by an IsoPrime dual inlet isotope-ratio mass spectrometer. Tritium values were determined by counting its radioactive decay, using liquid scintillation spectrometers (IAEA, 2010). In addition, to the data obtained in this study, chemical analyses results obtained in previous studies (Çetindağ et al., 1993) have also been used.

4. Results and Discussion

4.1. Hydrogeochemistry

The main elements of mineral and thermal waters are silica (SiO_2), sodium (Na^{+}), potassium (K^{+}), calcium (Ca^{2+}), magnesium (Mg^{2+}), carbonate (CO_3^{2-} and HCO_3^-), hydrogensulphide (H_2S), sulphate (SO_4^{2-}), chlorid(Cl^-) and fluoride (F^-). Cold water components are important for the calculation of mixing during operation. These elements provide valuable information for the chemical monitoring of the operated geothermal area (Gunnlaugsson, 2008). In general, mineral and geothermal waters contain dissolved minerals such as sodium, calcium, sulphate, chloride, silica at concentrations that are greater than those of local cold waters (Kipng'ok and Kanda, 2011).

Analysis results of the groundwater samples obtained from different locations at the study area as well as the analysis results of previous studies were given in table 1.

The temperatures of mineral and thermal waters were measured to be between 21.1°C – 23.6°C in May 2011 and as 20.8°C in October 2011. The temperatures of cold waters were measured in the interval of 10.5°C - 17°C. The maximum temperature at well base was

Table 1- Physical,chemical and isotope analyses results of water samples.

Sample Date	Location Type	T°C	pH	EC µS/cm	Ca (mg/l)	Mg (mg/l)	Na (mg/l)	K (mg/l)	Cl (mg/l)	SO_4 (mg/l)	HCO_3 (mg/l)	SiO_2 (mg/l)	$\delta^{18}O$ (‰)	δD (‰)	T (TU)	Water Type (IAH, 1979)
05.05.2011	Hot Spring 1	23.6	6.47	2710	209.4±3.44	243.5±3.98	60.21±3.44	0.018±0.002	7.26±1.44	41.3±2.44	1994.7±15.54		-9.23±0.32	-64.8±1.70	0.15±0.70	Mg-Ca-HCO_3
05.05.2011	Hot Spring 2	21.1	6.61	1460	174.7±3.42	196.5±4.01	50.85±3.09	0.001±0.001	7.96±1.41	43.9±2.45	1555.5±11.44		-8.09±0.44	-60.5±1.60	1.1±0.90	Mg-Ca-HCO_3
05.05.2011	Hot Spring 3	21.9	6.32	2015	165.3±.3.48	177.9±4.43	41.25±2.98	0.001±0.001	5.93±1.34	13.4±1.35	1464±10.54		-8.72±0.44	-61.9±1.70	0	Mg-Ca-HCO3
04.05.2011	Cold Spring 1	11.5	7.85	278	46.98±2.28	5.00±2.44	0.62±0.02	0.16±0.11	3.59±1.29	0.001±0.001	158.6±11.49		-8.73±0.43	-53.2±1.40	4.45±2.30	Ca- HCO_3
04.05.2011	Cold Spring 7	14.6	7.67	420	69.72±2.29	6.96±2.02	3.36±0.80	0.92±0.23	5.57±1.36	6.79±0.94	213.5±11.48		-9.34±0.36	-58.8±1.70	5.8±1.15	Ca- HCO_3
04.05.2011	ColdSpring 8	10.5	8.01	228	38.57±2.28	3.39±2.23	0.32±0.10	0.19±0.09	1.53±0.44	0.001±0.001	125.05±9.44		-10.4±0.35	-64.4±1.60	5.95±1.15	Ca- HCO_3
27.10.2011	Hot Spring 1	20.8	6.38	2720	216.5±3.56	282.9±3.48	64.11±3.49	3.27±1.47	8.59±1.74	44.5±2.38	1958±16.47		-8.99±0.21	-68.3±0.90	0.41±0.70	Mg-Ca-HCO_3
27.10.2011	Hot Spring 2	20.9	6.69	1420	108.3±3.04	125.5±4.08	29.74±2.28	3.35±1.54	6.1±1.32	12.7±2.44	969.9±9.08		-9.12±0.21	-61.2±0.90	0.21±0.68	Mg-Ca-HCO_3
27.10.2011	Hot Spring 3	20.9	6.19	2015	158.7±3.34	191.8±4.45	38.68±2.36	3.6±1.61	7.41±1.47	19.3±2.44	1421±10.49		-9.2±0.19	-65.4±0.90	0	Mg-Ca-HCO_3
14.10.2011	Cold Spring 1	12.1	7.69	275	47.26±2.20	6.63±1.77	0.51±0.12	0.53±0.12	2.83±0.89	0.001±0.001	170.8±9.48		-9.07±0.28	-54.2±0.80	5.11±0.81	Ca- HCO_3
14.10.2011	Cold Spring 7	16.3	7.43	435	76.90±2.21	10.03±2.03	3.60±0.34	1.98±0.23	7.14±1.39	0.01±0.01	256.2±10.14		-9.03±0.21	-53.4±0.90	5.59±0.84	Ca- HCO_3
14.10.2011	Cold Spring 8	13.5	7.89	251	41.07±2.19	6.32±1.98	0.42±0.11	1.98±0.22	3.42±1.18	0.01±0.01	152.5±9.64		-10.8±0.21	-68.6±0.90	6.19±0.86	Ca-Mg-HCO_3
02.06.2010	Well / 521*	25	6.04	3300	243.9±3.44	316.5±5.06	86.46±4.24	5.11±0.86	9.23±1.89	92.8±2.84	2724.9±19..98	146,9±2.33				Mg-Ca-HCO_3
21.10.2011	Well /1901**	12.1	7.5	293	47.26±2.14	6.63±1.23	0.52±0.18	0.53±0.12	2.83±0.43	0.001±0.001	170.8±9.44					Ca- HCO_3
21.10.2011	Well / 1903**	16.2	7.27	577	95.83±2.67	15.50±2.33	0.69±0.20	1.72±0.36	4.82±1.46	4.2±0.49	335.5±10.12					Ca- HCO_3
21.10.2011	Well / 1905**	15.9	7.82	333	60.09±2.23	4.95±1.17	0.29±0.08	1.42±0.32	3.29±1.40	0.01±0.01	219.6±3.44					Ca- HCO_3
21.10.2011	Well / 1909**	14.6	7.38	469	76,90±2.63	10.03±2.03	3.61±0.44	1.98±0.37	7.14±1.34	0.01±0.01	256.2±10.17					Ca- HCO_3
21.10.2011	Well / 1910**	14.8	7.55	275	41.07±2.14	6.32±1.97	0.42±0.11	1.98±0.36	3.42±1.45	0.01±0.01	152.5±9.78					Ca-Mg-HCO_3
10.12.2010	Well / 2244**	16.2	6.74	256	28.00±2.01	9.60±1.96	14.95±1.44	0.39±0.11	3.76±1.45	3.01±0.97	146.4±9.55					Ca-Mg-HCO_3
Çetindağ. (1992)	Hot Spring 1	19 - 22	6.4	2900	216	331	65	0.2	11.10	28	2410	78				Mg-Ca-HCO_3

* Physical-chemical analysis results of the geothermal drilled by local administration,

** Physical-chemical analysis of the personal wells were analyzed by Public health organization.

measured as 25°C during the geothermal water drilling (well/541; 292 m). The change in the temperature of the drill sludge during drilling was given in figure 4. It showed a slight increase due to the geothermal gradient and significant changes were observed after 104 meters (Geothermal Prossesing Report, 2010). The pH values of mineral and thermal springs are close to neutral. The lowest pH value was measured in the spring numbered 3 in October 2011 (6.19) whereas the pH value of the same spring was measured as 6.32 in November 2011. Carbon dioxide is the major cause of acidity and low pH values in mineral and thermal spring waters. The EC values of thermal springs vary seasonally and between 1420 µS/cm and 2720 µS/cm. These values do not show significant changes in both seasons. The EC values of wells drilled in the region have been determined between 275 µS/cm and 3300 µS/cm. Groundwater conductance is an indirect measurement of present ions and of dissolved constituents, and it is temperature dependent (Boyed, 2000; Hem, 1985). A number of studies on EC-temperature relations important in terms of the water chemistry are presented in the literature. Sorensen et al. (1987) have reported that the relationship between EC and temperature for natural waters is generally nonlinear. However, they stated that the degree of nonlinearity is relatively small between 0˚C - 30˚C. In 2004, Hayashi published another study of the EC and temperature relation of natural waters. In this study, it is nonlinear in a temperature range 0–30°C, but the linear equation approximated the relation reasonably well. In our study similar results also were obtained.

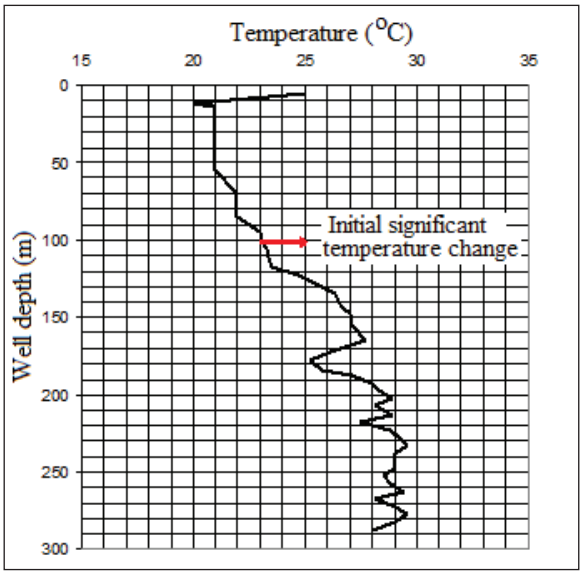

Figure 4- Well depth-temperature variation of geothermal well.

As the temperature increases, the concentrations of dissolved ions increase as shown by the upward trend in the graph (Figure 5).

Cold waters signify low ion concentration groundwater that circulates fast at shallow zone. The high bicarbonate concentration of mineral and thermal waters (969.9–2724.87 mg/l) is due to the reaction of CO_2 rich groundwaters with carbonated rocks (Giggenbach and Glover, 1992). The Mg^{2+} concentration of İspendere mineral and thermal waters have been measured between 125.5–316.5 mg/l, Ca^{2+} concentration is between 108 – 243 mg/l and Na^{+} concentration is between 29.74–86.46 mg/l. In general, the mineralization of geothermal waters is characterized by an increase in Mg^{2+} content. High Mg^{2+} concentration signifies the washing of Mg^{2+} from rocks near the surface (Nicholson, 1993). The increase in magnesium mineralization can be due to the magnesium containing olivine mineral. Cl is a parameter suited for the determination of the mixture since the chemistry of the thermal waters is different from that of cold waters. Cold waters yield a chloride concentration that is lower than geothermal waters. It is generally difficult to detect cold fresh water input to a geothermal system at an early period (Kipng'ok and Kanda, 2011). The decrease in chloride concentration and the increase in bicarbonate concentration might indicate water – rock interaction in thermal waters (Giggenbach and Glover 1992). The chloride value of the geothermal waters at the region was measured between 5.93–7.96 mg/l in May 2011 sampling period and between 6.1–8.59 in October 2011. The chloride value of cold waters varies at lower intervals (generally 2.83–3.76 mg/l). The fact that the chloride value (9.23 mg/l) of the geothermal well (well/521) is higher that the chloride value (on average 7.2 mg/l) of mineral

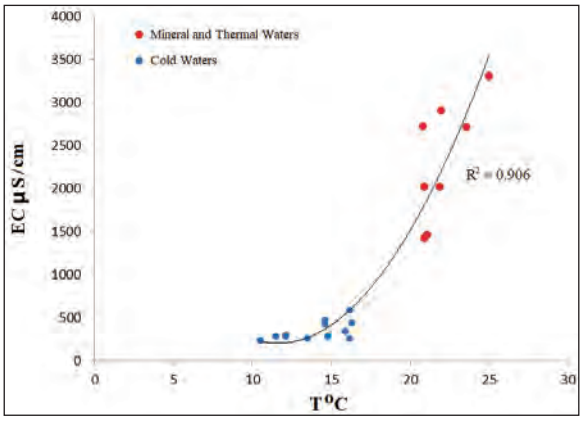

Figure 5- Temperature - EC chart.

and thermal water springs verify the cold water mixing during the rising up of thermal waters to the surface. Sulfate (SO_4^{2-}) concentrations have been measured between 12.7–92.8 mg/l in mineral and thermal waters and between 0.001–3.01 mg/l in cold waters. Prophyry copper-pyrite and/or stokwork type mineralization were observed in the study area according to the studies based on geotectonic environment. The main sulfurous minerals are pyrite (FeS_2) and chalcopyrite ($CuFeS_2$) while sphalerite [(Zn,Cu)S], galenite (PbS), pyrotite (Fe_7S_8), and bornite (Cu_5FeS_4) are less. Marcasite (FeS_2), chalcocite(Cu_2S) and covellite (CuS) are detected as secondary sulfurous minerals (Dumanlılar et al., 1999). The fact that the SO_4^{2-} concentrations of mineral and thermal waters are greater in comparison to cold waters can be explained by the reaction of H_2S with oxygen at different levels and the increase of SO_4^{2-} concentrations as a result of the dissolution of sulfurous minerals (Pasvanoğlu et al., 2005). The fact that Na^+/K^+ ratio is high in thermal waters is seen as an indication of the existence of lateral flow reactions close to the surface and the conductive cooling in geothermal waters (Nicholson, 1993). The solubility of silicon is quite low at normal groundwater temperatures but high in geothermal waters (Truesdell, 1984). The fact that silicon dioxide values are measured differently in geothermal well (well/541;146.9 mg/l) and in the mineral and thermal spring (mineral and thermal spring 1(1992); 78 mg/l) is another verification of cold water mixing.

According to IAH (1979) the classification of waters is given in table 1. Total equivalents of cations and anions were considered as 100% and ions with more than 20% (meq/l) were calculated for the classification. It has been observed that İspendere mineral and thermal waters are in general at the Mg-Ca-HCO_3 and Ca–Mg–HCO_3 mixing interval and that the cold waters are generally at the Ca-Mg-HCO_3 and $CaCO_3$ mixing interval.

Piper diagram is another classification method used in the classification of water samples and enables to define the dominant geochemical process of aqua-chemistry in a more precise manner (Piper, 1944). To define composition class, Back and Hanshaw (1965) suggested subdivisions of the tri-linear diagram (Figure 6). The chemical data of the water samples collected from different locations in the study area have been marked on the Piper diagram and the chemical data have been grouped in the 5th region. From the analysis of the Piper diagram, HCO_3^- is the dominant anion whereas Ca^{2+} and Mg^{2+} are the most dominant cations. According to the Piper diagram, mineral and thermal waters in the study area have been classified as Mg-HCO_3 facies, cold waters have been classified as Ca-HCO_3 facies. From the plot it is observed the water samples exhibit that the alkaline earth metals (Ca^{2+}, Mg^{2+}) significantly exceed the alkalis (Na^+, K) and weak acid (CO_3^{2-}, HCO_3^-) exceed the strong acid (Cl^-, SO_4^{2-}) (Figure 6). The Ca–HCO_3 water type indicates dissolution of calcite, whereas the Mg–HCO_3 water type indicates dissolution of ophiolites and dolomites containing magnesium.

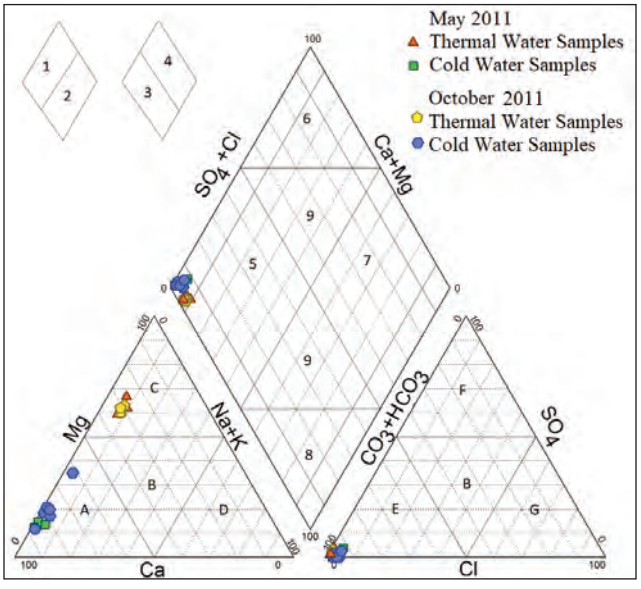

Figure 6- Piper diagram.

Schoeller (1962) diagram has been drawn in order to compare the chemical parameters of water samples taken from different locations and to determine some of the chemical properties (Figure 7). The element distributions of thermal and cold waters have yielded similar reflections on the semi-logarithmic Schoeller diagram. Cations have been ordered in mineral and thermal waters as $rMg^{2+}>rCa^{2+}>rNa^{+}+rK^{+}$ and anions as $rHCO_3^{-}>rSO_4^{2-}>rCl^{-}$ whereas cations in cold water have been ordered as $rCa^{2+}>rMg^{2+}>rNa^{+}+rK^{+}$ and anions as $rHCO_3^{-}>rSO_4^{2-}>rCl^{-}$.

Another diagram used in the classification of geothermal waters is Giggenbach (1991) triangular diagram. In this diagram, the geothermal waters are classified according to the concentration of chloride (Cl^{-}), sulfate (SO_4^{2-}) and bicarbonate (HCO_3^{-}) ions (in mg/kg). Accordingly, it has been observed that all waters are in shallow or mixture waters region (Figure 8).

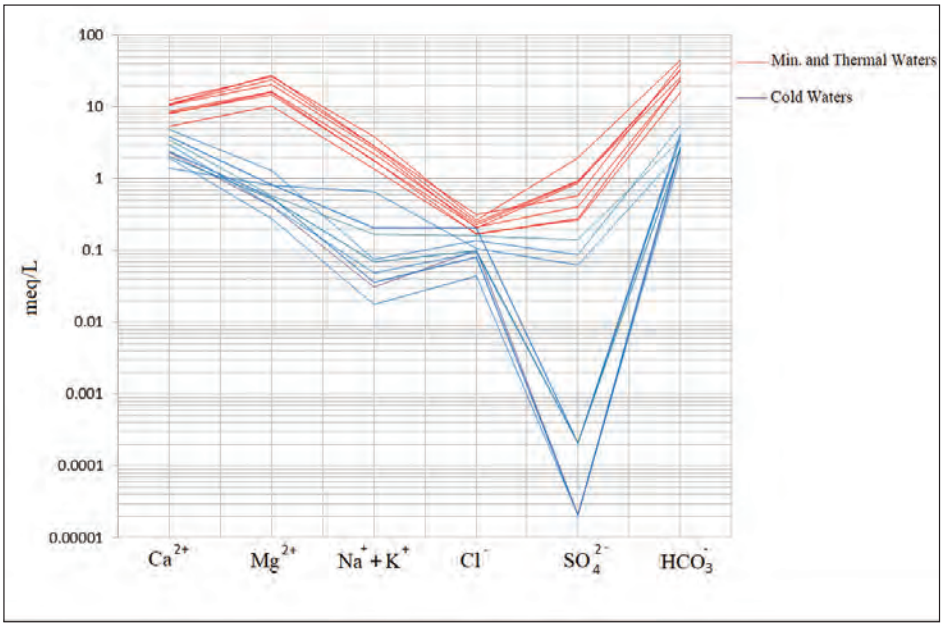

Figure 7- Schoeller diagram.

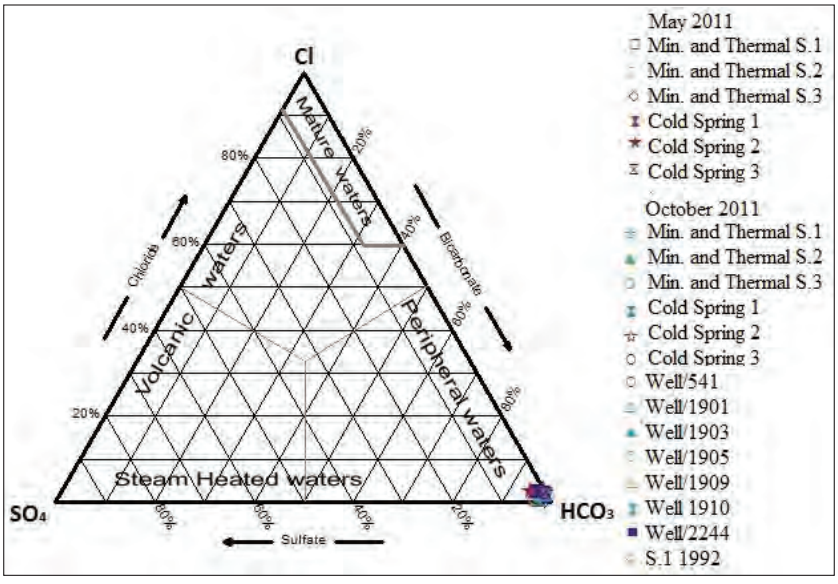

Figure 8- The triangular diagram for waters at study area (Giggenbach, 1991).

In addition, the İspendere thermal and cold waters are included in the immature waters group according to the Giggenbach equilibrium diagram (Figure 9). Hence, cation geothermometers have not be used in estimated aquifer temperature calculations since they will not yield results that are close to the actual values (Giggenbach, 1988). The reservoir rock temperatures calculated by quartz geothermometer are estimated between 95-132° C (Table 2).

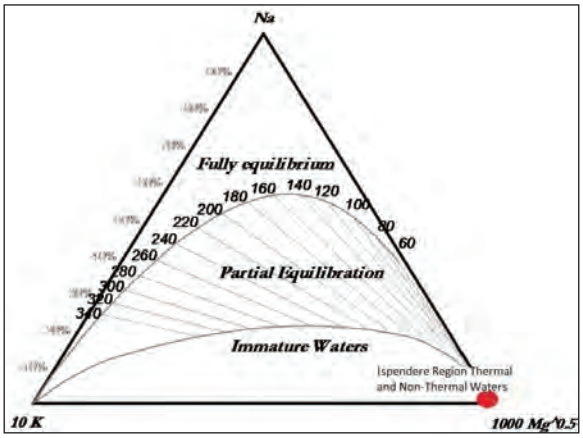

Figure 9- Giggenbach equilibrium diagram.

4.2. Isotope Geochemistry

Negative values that characterize water according to standards in isotope analyses indicate isotope depletion (light in terms of isotopes), whereas positive values indicate isotope enrichment (heavy in terms of isotopes) (IAEA, 1998; Demer, 2008). The oxygen-18 versus deuterium values ($\delta^{18}O - \delta^{2}H$) of the world rainfall stations in the world generally intensify on a linear line defined as the Global Meteoric Water Line. The equation of this line (1) defines the relationship between ^{18}O and ^{2}H in the rain waters collected around the world (Craig, 1961*b*).

$$\delta^{2}H = 8\delta^{18}O + d \text{ (‰ SMOW)} \quad (1)$$

The value of *d* in this equation is known as "deuterium excess" and is defined as the indicator of the evaporation amount of sea water that is the source of rain. The *d* value of the Global Meteoric Water Line is 10 and it is a function of the relative humidity in the atmosphere over the oceans. The value of d reaches more positive values at places where evaporation is higher and varies locally according to the climate conditions that are dominant in geological epochs. This value for the Mediterranean climate that is dominant in our country is +22 ‰ (Gat, 1971; IAEA, 1981; 1983).

In this chapter, the oxygen-18 ($\delta^{18}O$), deuterium ($\delta^{2}H$), and tritium (^{3}H) content of the water samples evaluated to understand the water-rock relationship as well as the thermal water cycle. The oxygen-18 values varied between; –8.09‰ and –9.23‰ (SMOW), deuterium values between –60.5‰ and –64.8‰ (SMOW) in mineral and thermal water springs in May 2011 and between –8.99‰ and –9.20‰ (SMOW) in October 2011, whereas the deuterium values varied between –61.2‰ and –68.3‰ (SMOW). In cold water springs, the oxygen-18 values varied between;–8.73‰ and –10.4‰ (SMOW) in May 2011, deuterium values between –53.2 ‰ and –64.4‰ (SMOW), in October 2011 the variations were between –9.03‰ and –10.8‰ (SMOW) and for deuterium between –53.4‰ and –68.6‰ (SMOW) (Table 2). The oxygen-18-deuterium relationship of the waters between May 2011 and October 2011 was given in figure 10. Several local meteoric water lines have been determined for İspendere region, Malatya. The Local Meteoric Water Line (LMWL) closest to our study sites is given by the water samples collected at the Kırkgöze Sub-basin ($\delta^{2}H = 8\ \delta^{18}O + 14.87$) of Pekkan et al. (2008). According to the oxygen-18 and deuterium isotope data acquired periodically, mineral and thermal water springs are located close to the Global Meteoric Water Line (Craig, 1961*a*), whereas cold water springs are

Table 2- Some geothermometric equations and calculated reservoir temperatures of the thermal waters in İspendere Region, Malatya.

Geothermometer	Equation	Thermal Spring	Thermal Well
T measured (˚C)		19 -22	25
T Qz – no st. Loss (Fournier, 1973)	$=\frac{1309}{5,19-\log S_iO_2}-273,15$	123,7	159,86
T Qz – max. st. loss at 100 ˚C (Fournier, 1973)	$=\frac{1522}{5,75-\log S_iO_2}-273,15$	121,36	151,63
T chalcedony, no steam loss (Fournier, 1977)	$=\frac{1032}{4,69-\log S_iO_2}-273,15$	95,69	135,89
T chalcedony - max. st. loss at 100 ˚C (Fournier, 1977)	$=\frac{1182}{5,09-\log S_iO_2}-273,15$	96,46	131,23
T chalcedony, no steam loss (Arnorsson ve ark., 1983	$=\frac{1112}{4,91-\log S_iO_2}-273,15$	95,31	132,24

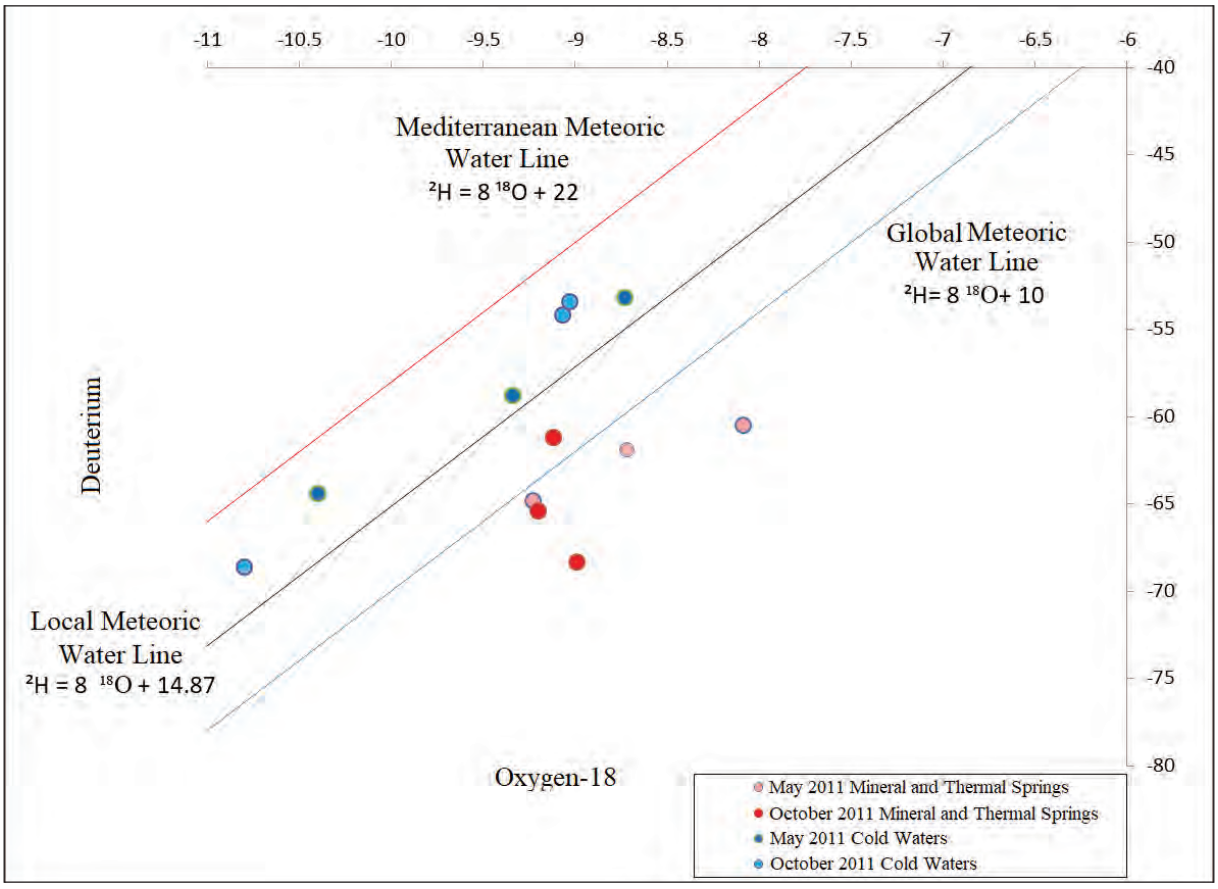

Figure 10- Oxygen-18-deuterium plots of water resources in the study area.

located between the Global Meteoric Water Line and the Mediterranean Meteoric Water Line (Dansgaard, 1964) (Figure 10). Thermal and cold water springs have similarities among themselves and it has been determined that they are of meteoric origin. The $\delta^{18}O$ and $\delta^{2}H$ values of the springs aren't significant observed shift from the GMAIL in both seasons. Only mineral and thermal springs in wet season were light affected by evaporation factors.

The tritium value in mineral and thermal waters was between 0 – 1.1 TU in May 2011 and between 0–0.41 TU in October 2011. These values are close to detection limits in both seasons. The tritium value in the same period was between 4.45–5.95 TU in May 2011 and between 5.11–6.19 TU in October 2011 for cold water springs (Table 1). It is thought as a result of the tritium values of the İspendere mineral and thermal waters, <0,5 [excluding the May 2011 analysis result of thermal spring number 2 (1.1 ± 0.9 TU)] it displayed deep circulation for about 50 years and above (Figure 11). The relationship between tritium-electrical conductivity in the waters was given in figure 12. The decrease in tritium content and the increase in electrical conductivity show a correlation between the long residence time and slow rate of regeneration of the groundwater system. Cold waters have comparatively low electrical conductivity (EC ≤ 435) and high tritium (≥ 4.45 TU) values corresponding to rainfall, indicating fast recharge and short flow path. Mineral and Thermal water samples with no seasonal variation (Table 1) in tritium contents show relatively longer residence time with slow movement and that is also evident by low tritium values (< 1.1 TU). These waters have been in contact with geological units for a longer period and dissolves salts increasing its EC.

5. Conclusion

In this study, geothermal and hydrochemical characteristics of mineral and thermal waters in the İspendere geothermal fields are described. The results and interpretations that have been obtained from this study and the geothermal borehole data (292 m depth, maximum temperature of 25°C) were listed below:

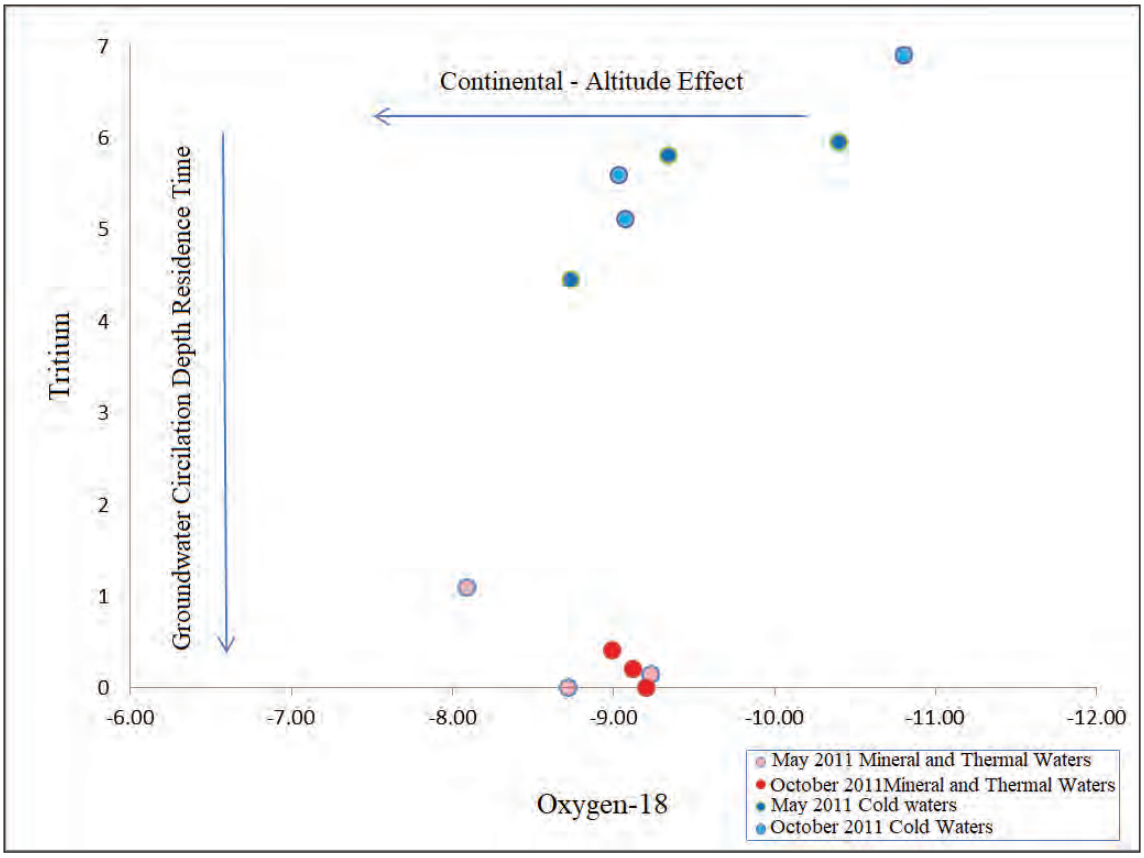

Figure 11- Tritium - Oxygen-18 chart.

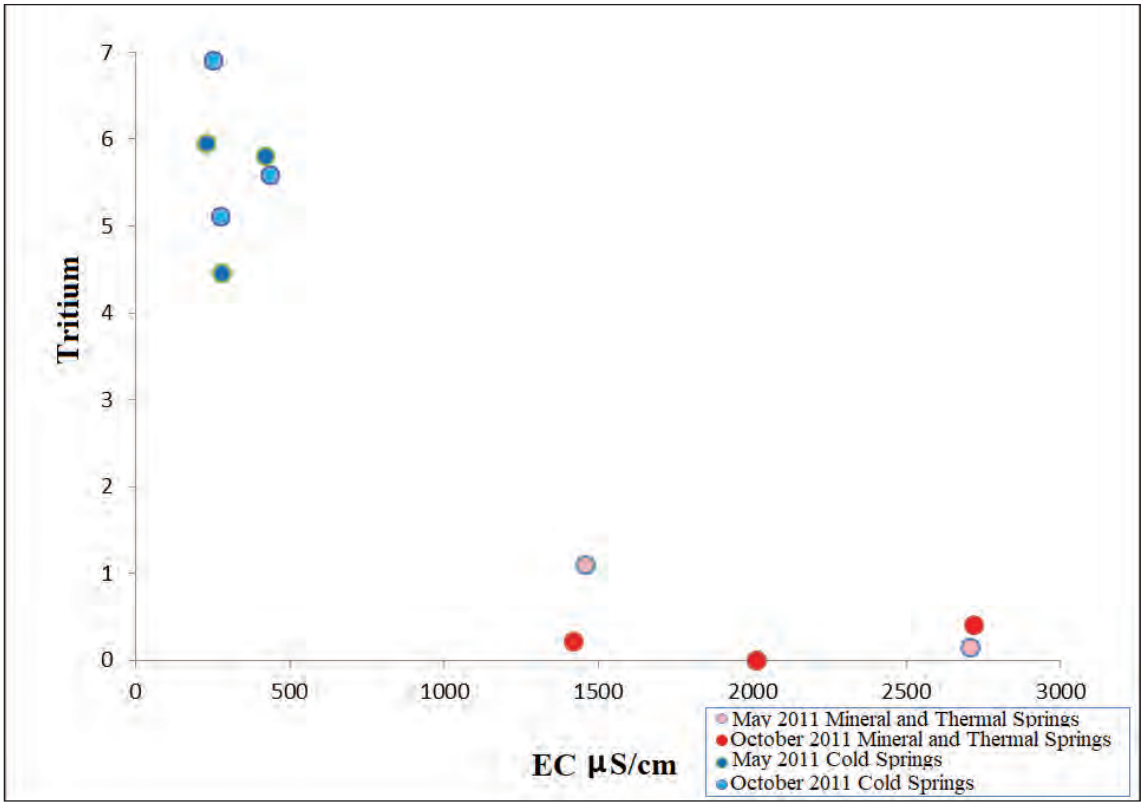

Figure 12- Tritium - EC chart.

1. It has been determined that the İspendere region has low geothermal potential because of intensive cold water mixing. Mineral and thermal waters in the study area have been classified as Mg-HCO_3 water type, cold waters have been classified as Ca-HCO_3 water type.

2. The cations in the mineral and thermal waters have been listed as $rMg^{2+}>rCa^{2+}>rNa^{+}+rK^{+}$ and the anions as $rHCO_3^{-}>rSO_4^{2-}>rCl^{-}$, whereas the cations in the cold waters have been listed as $rCa^{2+}>rMg^{2+}>rNa^{+}+rK^{+}$ and the anions as $rHCO_3^{-}>rSO_4^{2-}>rCl^{-}$. It has been determined that the mineral, thermal waters and cold waters are of meteoric origin and they have been defined as about 50 years and above waters because of their low tritium content.

3. The İspendere thermal and cold waters have been evaluated within the scope of shallow and peripheral flow immature mixture waters according to the Giggenbach diagrams.

4 Based on the quartz geothermometers, reservoir rock temperatures were calculated as 95-132° C for İspendere thermal well and springs.

5. The light $\delta^{18}O$ values of the cold springs from which samples were taken within the scope of this study as well as the high tritium and low chloride and EC values in comparison with the thermal waters indicates that these springs are fed by rains at high altitude and that they surface in a short time. That is why; these cold waters have been classified as young waters with shallow circulation.

Acknowledgement

This research was supported by IUBAP (Inonu University Scientific Projects Unit) under the project number of IUBAP 2011/46. The authors are grateful for Editor and anonymous reviewers for their helpful and constructive comments on an earlier draft of this paper.

References

Afşin, M., Canik, B. 2013. Orta Anadolu'daki bazı jeotermal sularda su kimyası ve izotopik değişimlerin anlamı, Aksaray Üniversitesi Jeoloji Müh. Bölümü Baki Canik Su Medeniyeti Semp. s.24.

APHA. 2005. Standard methods for examination of water and wastewater 21st ed. American Public Health Association, Washington D.C.

Arnórsson, S., D'Amore, F., Gerardo-Abaya, J. 2000. Isotopic and Geochemical Techniques in Geothermal Exploration, Development and Use: Sampling Methods, Data Handling, Interpretation (ed. Arnórsson S), International Atomic Energy Agency Publication, Vienna.

Arnorsson, S., Gunnlaugsson, E., Svavarsson, H. 1983. The chemistry of geothermal waters in Iceland III., chemical geothermometry in geothermal investigations. Geochim Cosmochim Acta. 47, 567–577

Anees, M., Shah, M.M. Qureshi, A.A. 2015. Proc. Earth Planet. Sci. 13, 291–295.

Baba, A., Sanliyuksel D. 2011. Hydrogeochemical and isotopic composition of a low-temperature geothermal source in northwest Turkey: case study of Kirkgecit geothermal area. Environ Earth Sciences. 62, 529–540.

Back, W., Hanshaw, B.B. 1965. Advances in hydroscience. In chemical Geohydrology, Academic Press, New York, Vol. 11, p-49.

Battistel, M., Hurwitz, S., Evans, W., Barbieri, M. 2014. Energy Proc. 59, 359–365.

Beyarslan, M. 1991. Petrographic Properties of the ophiolite of İspendere (Kale-Malatya). Firat University, Institute of Science. M.Sc. Thesis, pp 57.

Beyarslan, M., Bingo,l A.F. 2010. Ultramafics and Mafic Bodies in Cumulates of Ispendere and Kömürhan Ophiolites (SE Anatolian Belt, Turkey). Turkish Journal of Science and Technology. 5(1), 19- 36.

Boyed, C.E. 2000. Water Quality: An Introduction. Kluwer Academic Publisher, New York, 330 p.

Browne, P.R.L. 1991. Mineralogical guides to interpreting the shallow paleohydrology of epithermal mineral depositing environments. Proc 13 th NZ Geothermal work – shop, Auckland. 263-270.

Bojadgieva, K., Dipchikova, S., Benderev, A., Koseva, J. 2002. Thermal Waters and Balneolody in Bulgaria. GHC Bulletin, March, 18-25

Chenaker, H., Houha, B., Valles, V. 2017. Isotope studies and chemical investigations of hot springs from North-Eastern Algeria, J. Mater. Environ. Sci, 8 (12), pp. 4253-4263.

Clark, I.D., Fritz, P. 1997. Environmental Isotopes in Hydrogeology, Lewis Publication. Pp 328. New York.

Craig, H. 1961*a*. Isotopic variations in meteoric waters. Science. 133, 1702–8.

Craig, H. 1961*b*. Standard for reporting concentration of deuterium and oxygen-18 in natural waters. Science. 113, 1833–34.

Çetindağ, B., Afşin, M., Canik, B. 1993. Hydrogeological investigation of mineral and thermal water of İspendere (Malatya). Suat Erk Symposium Ankara, Turkey. 403-410. (In Turkish).

Chandrajith, R., Barth, J.A.C., Subasinghe, N.D., Merten, D., Dissanayake, C.B. 2013. Geochemical and isotope characterization of geothermal spring waters in Sri Lanka: Evidence for steeper than expected geothermal gradients. Journal of Hydrology.476, 360-369.

Dansgaard, W. 1964. STab. isotopes in precipitation. Tellus. 16, 436–438.

Demer, S. 2008. Hydrogeological, hydro-geochemical and isotope geochemical investigations of the groundwater in Isparta and its nearly environs and monitoring of the drink water quality. Suleyman Demirel University, Institute of Science, 182 p. PhD. Thesis, Isparta, Turkey. (In Turkish).

DMI. 2010. General Directorate of State Meteorological Service, in Turkish.

DSİ. 1991. Kapıkaya Dam planning report. the General Directorate of State Hydraulic Works. Ankara, Turkey. (In Turkish).

Dumanlılar, Ö. 1993. Geology and petrography of magmatites of İspendere (Malatya) region: A.U. Institute of Science, M.Sc. Thesis, Ankara, Turkey. pp 62. (In Turkish).

Dumanlılar, H., Aydal, D., Dumanlılar, Ö. 1999. Geology, Mineralogy and Geochemistry of Sulphide mineralization of İspendere (Malatya) Region. Bulletin of Mineral Research and Exploration. 121, 225-250. (In Turkish).

Ersoy, A.F., Sönmez, S.Ç. 2014. Hydrogeochemical and isotopic characteristics of the Ilica geothermal system (Erzurum, Turkey). Environ Earth Sci, 72: 4451-4462.

Fournier, R.O. 1973. Silica in lhermal waters laboratory and field investigations. Proceedings of the International Symposium on Hydrogeochemistry and Biochemistry, Tokyo, Vol 1, Clark Co, Washington DC. 122–139.

Fournier, R.O. 1977. Chemical geothermometers and mixing models for geothermal systems. Geothermics. 5, 41–50.

Gat, J.R. 1971. Comments on the STab. Isotope Method in Regional Groundwater Investigations. Water Resources Research. 7, 980-993.

Giggenbach, W.F. 1988. Geothermal solute equilibrium. Derivation of Na- K- Mg- Ca geoindicators. Geochim Cosmochim Acta. 52, 2749–2765.

Giggenbach, W.F. 1991. Chemical techniques in geothermal exploration. In: D'Amore, F. (coordinator), Applications of geochemistry in geothermal reservoir development. UNITAR/UNDP publication, Rome, 119-142.

Giggenbach, W.F., Glover, R. 1992. Tectonic regime and major processes govering the chemistry of water and gas discharges from the Rotorua geothermal field. Geothermics, 21, 121–140.

Gunnlaugsson, E. 2008. Importance Of Chemıstry In Geothermal Exploratıon And Utılızatıon Presented at the Workshop for Decision Makers on Direct Heating Use of Geothermal Resources in Asia, organized by UNU-GTP, TBLRREM and TBGMED, in Tianjin, China,

Gürocak, Z., Alemdağ, S. 2002. Kinematical Assessments on Rock Slopes at The Kapıkaya (Malatya) Dam Site. Bulletin of Faculty of Engineering of Cumhuriyet University, Serie A-Earth Sciences. 19(2), 151-164.

Harvey, K. 2007. Healing Touch. Sawubona, 75-76.

Hayashi, M. 2004. Temperature-electrical conductivity relation of water for environmental monitoring and geophysical data inversion. Environmental Monitoring and Assessment 96:119–128.

Hellman, M.J. Ramsey, M.S. 2004. Analysis of hot mineral springs and associated deposits in Yellowstone National Park using ASTER and AVIRIS remote sensing. J. Volcanol. Geotherm. Res. 134 (1-2) 195-219.

Hem, J.D. 1985. Study and Interpretation of the Chemical Characteristics of Natural Water. 3rd Edition, US Geological Survey Water-Supply Paper 2254, 246 p.

Hugh, P., Taylor, H. P. Jr. 1974. The application of oxygen and hydrogen isotope studies to problems of hydrothermal alteration and ore deposition. Economic Geology. 69, 843-883.

IAH (International Association of Hydrogeologists). 1979. Map of Mineral and Thermal Water of Europe, Scale 1: 500,000. International Association of Hydrogeologists, London.

IAEA. 1981. Stable. isotope in hydrology, IAEA. Tech., Rep. International Atomic Energy Agency - Ser., No 210, pp 339.

IAEA. 1983. International Atomic Energy Agency, Guidebook on Nuclear Techniques in Hydrology, IAEA. Tech. Rep. Ser., No 91, pp 439.

IAEA. 1998. Analytical quality in the IAEA isotope hydrology laboratory: Some recent improvements. Water and environment news, IAEA, No.3, pp 5-7.

IAEA. 2010. Overview of Laboratory Isotope Analyses Methods for Water Resources Studies. International Atomic Energy Agency, Vienna.

Geothermal Prossesing Report. 2010. İspendere mineral and thermal water processing report, Special Provincial Administration General Secretary (Unpublished, In Turkish). Malatya, Turkey.

Kipng'ok, J., Kanda, I. 2011. Introductıon To Geochemıcal Mappıng Presented at Short Course VI on Exploration for Geothermal Resources, organized by UNU-GTP, GDC and Ken Gen, at Lake Bogoria and Lake Naivasha, Kenya, Oct. 27 – Nov. 18.

Mazor, E. 2004. Chemical And Isotopic Groundwater Hydrology. Marcel Dekker Inc., New York, pp 453.

Nicholson, K. 1993. Geothermal Fluids, Chemistryand Exploration Techniques.Springer-Verlag, Berlin.

Olivier, J., Van Niekerk, H.J., Van der Walt, I.J. 2008. Physical and chemical characteristics of thermal springs in the Waterberg area in Limpopo Province, South Africa. Water SA Vol. 34 No. 2.

Panichi, C., Gonfiantini R. 1978. Environmental isotopes in geothermal studies. Geothermics. 6, 143 – 161.

Parlak, O., Nurlu, N., Rızaoğlu, T., Karaoğlan, F., Bağcı, U., Önal, A., Kürüm, S. 2010. Tectonic Setting and Significance of İspendere (Malatya) Ophiolite within the SE Anatolian Orogenic Belt, IV. National Geochemistry Symposium. 45 – 46. (In Turkish).

Pasvanoğlu, S. 2013. Hydrogeochemistry of mineral and thermalized waters in the Diyadin(Ağri) area, Eastern Turkey, Applied Geochemistry. 38, 70-81.

Pasvanoğlu, S., Canik, B., Arıgün, Z. 2005. Hydrochemical Investigation of Banaz-Hamamboğazı Mineral and thermal Water, II. Isotope Techniques in Hydrology Symposium, İzmir, Turkey. 209-225. (In Turkish).

Pasvanoğlu, S., Chandrasekharam, D. 2011. Hydrogeochemical and isotopic study of mineral and thermalized waters from the NevŞehir (Kozakli) area, Central Turkey. Journal Volcanology and Geothermal Research. 202 (3-4), 241-250.

Pekkan, E., Bayarı, S., Şensoy, A, Şorman, A., Arıkan, A. 2008. Investigation of the precipitation-discharge dynamics of Kırkgoze basin (upper euprates, Erzurum-Turkey) by using sTab. isotopes, III. Isotope Tecniques in Hydrology Symposium, S.205-213. (In Turkish).

Petraccia, L., Liberati, G., Masciullo, S.G. 2005. Water, mineral waters and health. Clin. Nutrit. 25 (3) 377-385.

Piper, A.M. 1944. A graphic procedure in the geochemical interpretation of water analyses. American Geophysical Union, 25, 914-923

Schoeller, H. 1962. Les Eaux Souterraines. Masson and Cie, Paris, 642pp.

Sheppard, S.M.F. 1981. STab. isotope geochemistry of fluids. D. T. Rickard and F.E. Wickman (Eds.), Chemistry and geochemistry of solutions at high temperatures and pressures. Physics and Chemistry of the Earth. 13/14, 419-445.

Sorensen, J.A., Glass, G.E. 1987. Ion and Temperature Dependence of Electrical Conductance for Natural Waters. Analytical Chemistry, 59, 1594-1597.

Truesdell, A.H. 1984. Introduction to chemical calculations. Fluid Mineral Equilibria in Hydrothermal Systems, R. W. Henley et al. (eds.). Revised Economic Geology. 1, 1-8.

Yazgan, E., Gültekin, M.C., Poyraz, N., Sirel, E., Yıldırım, H. 1987. Malatya güneydoğusunun jeolojisi ve Doğu Toroslar'ın jeodinamik evrimi. Maden Tetkik ve Arama Genel Müdürlüğü Rapor No: 2268, Ankara. (In Turkish) (unpublished).

Bull. Min. Res. Exp. (2019) 158: 327-344

Bulletin of the Mineral Research and Exploration

http://bulletin.mta.gov.tr

The use of electromagnetic and vertical electrical sounding methods in groundwater exploration

Hafiz MOHAMMED NAZIFI[a*] and Levent GÜLEN[a]

[a] *Sakarya University, Dept. of Geophysical Engineering, Serdivan, Sakarya, Turkey orcid.org/0000-0002-3762-6563*
[b] *Sakarya University, Dept. of Geophysical Engineering, Serdivan, Sakarya, Turkey orcid.org/0000-0002-3572-8785*

Research Article

Keywords:
2D pseudo resistivity maps, electromagnetic (EM) inversion, vertical electrical sounding (VES), groundwater exploration, Ghana.

ABSTRACT

Electromagnetic (EM) profiling and Vertical Electrical Sounding (VES) studies were carried out for groundwater exploration in the Twifo – Hemang Lower Denkyira Districts of Ghana. These two geophysical methods were used for exploring the groundwater potentials beneath Achiase Community, Mbaa Mpe Hia Community and Moseaso Community. This paper seeks to encourage the use of inversion for interpreting electromagnetic data rather than the usual qualitative interpretation method using line graphs and also the use of apparent resistivity maps as 2D pseudo resistivity maps to support interpretations of the 1D inversion results (in cases where the available budget could not permit 2D and or 3D inversion). These would help in enhancement of obtained results, reduce ambiguity and help decision making. The EM results revealed that; the three communities are underlain by two layers with the first layer having the thickness range between 2 to 10 m and the second layer is a half space. The results from VES studies indicate that; Achiase Community and Mbaa Mpe Hia No. 2 community are underlain by three geoelectrical layers and Moseaso Community is underlain by four geoelectrical layers. On the basis of this study the Moseaso Community is ranked highest in terms of groundwater potential followed by the Achiase community and finally the Mbaa Mpe Hia No.2 Community. Several sites were recommended for drilling boreholes for water supply in these communities.

Received Date: 20.05.2017
Accepted Date: 10.04.2018

1. Introduction

The availability of quality water for both drinking and domestic usage is of primary concern to people living in rural communities. Most rural communities in the Sub – Saharan Africa depend mostly on surface water and water from hand-dug boreholes whose qualities are questionable and some of these sources dry out during long dry seasons.

The exploration for clean groundwater is therefore necessary. There are some fundamental questions concerning groundwater which needs to be answered and some of these questions are; how much groundwater is available, and what is its quality? These are exploration and production questions for which geophysical techniques can help to answer (Fitterman and Stewartj, 1986).

Geophysical techniques have proven to be successful in groundwater explorations. Electromagnetic Methods and Direct Current Resistivity (DRC) Methods have been successfully used for decades in the investigation of groundwater resources. The Electromagnetic equipment, the EM 34-3 equipment (Geonics) is one of the most popular EM field systems used in groundwater prospecting. It is a portable EM device which directly measures conductivity at shallow depths.

The fundamental of Slingram System or HLEM method are described in several applied geophysical papers such as; McNeill 1980; Frischknecht et al. 1991; Spies and Frischknecht 1991; Keller and Frischknecht 1977.

* *Corresponding author: Hafiz MOHAMMED NAZIFI, mohammednazifi@gmail.com*
https://dx.doi.org/10.19111/bulletinofmre.451557.

The EM data obtained from most geophysical investigations and studies such as Carrasquilla et al., 2007; Chegbeleh et al., 2009; Menyeh et al., 2005; Somiah, 2013; Tsikudo Kwasi, 2009; Anechana, 2013, which were conducted using Slingram techniques or HLEM method were interpreted qualitatively although inversion programs such as 1D laterally constrained inversion (Monteiro Santos, 2004) and AEMINV (Pirttijärvi, 2014) are available to public.

The conventional VES used in this work, has also been used in several works to produce good results. The electrical resistivity gives reasonably accurate results among other methods that can be used to understand the subsurface layers and basement configuration in groundwater prospecting (Olakunle Coker, 2012). In this work, dc resistivity data were interpreted by the use of the catalogue of master curve types, by 1D inversion approach and by apparent resistivity map approach as used by Nejad et al. (2011).

This paper emphasizes the importance of the use of EM inversion in the interpretation of EM34-3 data and its integration with the conventional qualitative interpretation of data obtained from EM34-3 for groundwater explorations. It demonstrates the usefulness of apparent resistivity maps in VES data interpretation together with the 1D inversion of VES data, particularly in the case where there is limited data for 2D or 3D inversion and in a project with limited funds.

1.1. Study Area

The study area comprises of three communities namely; Achiase, MbaaMpeHia No 2 and Moseaso (Figure 1) which are located within the Twifo – Hemang Lower Denkyira district of the Central Region of Ghana. The district is located between latitudes 5°50'N and 5°51'N and longitudes 1°50'W and 1°10'W. The district lies in the semi - equatorial climate zone marked by double maxima rainfall. The mean annual rainfall range between 1,750 mm and 2,000 mm with the wettest period in June and October and the driest in March. It has fairly high uniform temperatures ranging between 26° C (in August) and

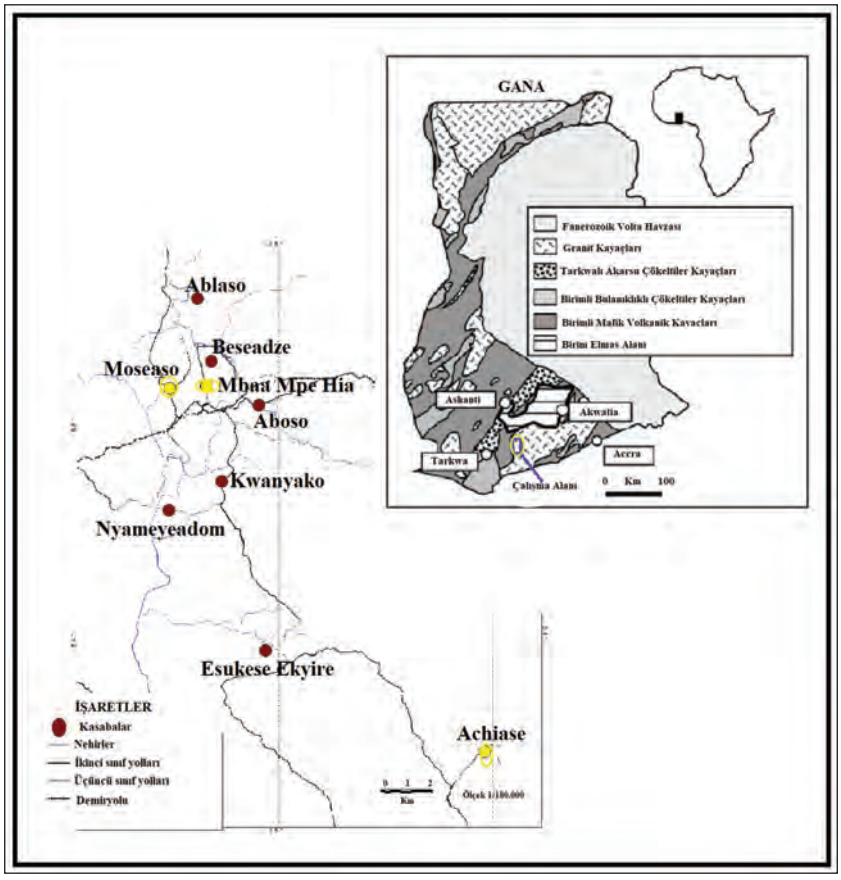

Figure 1- Simplified geological map of Ghana (adapted and modified from Wymana et al.,2008 and Mainoo et al., 2007) showing the study areas in yellow colour.

30°C (in March). The vegetation in the district consists of basically two forest types; the tropical rainforest to the South and the moist semi-deciduous forest to the North. The vegetation has been largely disturbed by human activities through farming and logging among others (Anon, 2012).

Basic granitic intrusives and granites underlie almost all the study area. Major rock types comprise of well - foliated, medium-grained, potash-rich muscovite-biotite granites, granodiorites and pegmatites (Figure 1). Granites found in the study area are Post-Tarkwaian and can be divided into three groups: Bongo Granites, Dixcove Granite Complex and Cape Coast Granite complex.

The Cape Coast granites are often associated with schists and gneisses, and intrude the Lower Birimian meta-sediments. One characteristic of the granite is that it is not inherently permeable, but secondary permeability and porosity have developed as a result of fracturing and weathering (Gyamera and Kuma, 2014).

Intense weathering along fractures and veins had permitted water percolation to form groundwater reservoirs. Aquifers are therefore located where secondary porosity has developed. The two main aquifer types are (i) the weathered zone or 'regolith', which develops on the crystalline basement rocks, and (ii) fracture zones within the bedrock (Mainoo et al., 2007).

2. Methodology

Two geophysical methods namely; DCR and Slingram (HLEM) were used in this work.

2.1. HLEM Survey

Electromagnetic apparent conductivity values were obtained using both horizontal dipole (HD) and vertical dipole (VD) modes at 20-meter spacing.

Graphs of apparent conductivities or the terrain conductivity (in mhos/m) on vertical axes versus station intervals (in meters) on horizontal axes were plotted. Our interest is in the vertical conductors and since VD orientation is relatively sensitive to vertical conductors (Thamke et al., 1998), therefore points where the VD conductivities exceeded the HD conductivities were noted for VES measurements. Other points were also selected for VES point based on experience. Points near waste dumps and toilet facilities or under a roofing of buildings were avoided, although these points may have high conductivities or crossover points.

AEMINV (Pirttijärvi, 2014) computer program was used for inversion and interpretation of the obtained data. The computer program was originally developed for geophysical interpretation of frequency-domain airborne electromagnetic (AEM) data using one-dimensional (1-D) layered earth model, it can also be used to interpret ground EM data as was used here.

According to the user's guide to the program (Pirttijärvi, 2014); the model parameters are the electrical resistivity and thickness of the layers and the resistivity and magnetic susceptibility of the basement layer. The inversion is made independently for each profile point using one-dimensional layered earth model. A resistivity pseudo-section is obtained by plotting the resistivity-thickness values below adjacent data points with coloured rectangles. Starting from an initial model an iterative linearized inversion with adaptive damping is used to update model parameters so that the data error, i.e., the difference between the measured and the computed data is minimized. Laterally constrained inversion is achieved by minimizing the roughness of the model, i.e. the variation of the model parameters between neighbouring points together with the data error. As a result of the constrained (Occam) inversion, a smoothly varying resistivity-thickness model is obtained. The roughness and/or the fix/free status the parameters can be set manually to allow discontinuities and to incorporate a priori data in the model (Pirttijärvi, 2014).

2.2. DCR Survey

The VES measurements were done in selected locations along the EM profiles and they were carried out using an ABEM Terrameter SAS 1000C and the Schlumberger electrode array with a maximum AB/2 spacing of 83.0 m.

The quantitative interpretations were done using RES1D inversion (Loke, 2001). The model parameters of the 1D inversion are the electrical resistivity, the thickness of the layers and the depth of the layers from the Earth surface.

Two qualitative methods of interpretation were used. These methods are the catalogue of master curve

types method and the apparent resistivity map (2D pseudo resistivity maps) method. Corrected apparent resistivity values were used in creating the apparent resistivity maps. The aim of the project which is to locate points of high groundwater potential for hand dug or drilling of groundwater for public water supply. Because of this aim, the apparent resistivity maps were created using a specific colour scale.

Based on available data information on existing boreholes in and around 5 Km radius of the study areas (see table 1) and the estimated 1D earth models based on 1D inversion results the VES, presence of groundwater within aquifers in the study areas were classified as; high amount of groundwater (0 – 200 Ωm); moderate amount of groundwater (200 – 500 Ωm); little amount of groundwater (500 – 800 Ωm); very little amount of groundwater (800 – 1100 Ωm) and lastly zones with no water ground (≥1400 Ωm). With the estimated 1D earth models as the main models and supported by apparent resistivity maps as 2D pseudo resistivity maps, recommendation for drilling a well at a point is given when the point falls within the first three classes or groups. Unless the community has generally low level of groundwater, points within the fourth class never get recommended. The main aim for using this kind of model is to recommend points where well could run throughout the year.

The apparent resistivity maps as used in this work, reflect the lateral variation of apparent resistivity of subsurface over a horizontal plane at a certain depth (Nejad et al., 2011). The concept utilised in creating the apparent resistivity maps is the rule-of-thumb that; the maximum exploration depth or depth of penetration of AMNB method is 1/3 to ¼ of the maximum distance of AB (Frohlich et al., 1996). Safest exploration depths according to ¼ of max AB/2 were used to construct

Table 1- Available data information on existing boreholes in and around 5 Km radius of the study areas.

Available data on existing boreholes in and around			
5 Km radius of Achiase Community			
Community	**BH No.**	**Depth (m)**	**Lithology**
WATRESO	27/I/51-1	26	Gneiss
WATRESO	27/I/51-2		
NYAMEBEKYERE	27/H/68-1	28	Quartz Diorite
NYAMEBEKYERE	27/H/68-2	34	
NYAMEBEKYERE	27/H/68-3	40	
NYAMEBEKYERE	27/H/68-4	37	Granite
NYAMIENI	27/H/59-1	40	
NYAMIENI	27/H/59-2	40	
Available data on existing boreholes in and around			
5 Km radius of Moseaso Community			
Community	**BH No.**	**Depth (m)**	**Lithology**
NYENASI	48/E/79-2	73	
Available data on existing boreholes in and around			
5 Km radius of Mbaa Mpe Hia No. 2 Community			
Community	**BH No.**	**Depth (m)**	**Lithology**
NYENASI	48/E/79-2	73	
TWIFO PRASO	48/F/74-1	27	Schist
TWIFO PRASO	48/F/74-2	28	Schist
TWIFO PRASO	48/F/74-3	31	Schist
TWIFO PRASO	48/F/74-4	28	Schist
TWIFO PRASO	48/F/74-5	37	Schist
TWIFO PRASO	48/F/74-6	28	Schist
TWIFO PRASO	48/F/74-7	25	Schist

the apparent resistivity maps at distances AB/2 = 1.5, 6.3, 27.0, 58.0 and 83.0 m. The drilling decisions were made based on the estimated 1D earth model and the apparent resistivity maps as a support to the estimated 1D earth model.

3. Results and Discussions

The EM 34-3 equipment was used for EM profiling to outline shallow conductive structures which might be associated with local groundwater circulation. EM profiling was conducted along eleven (11) profiles across the three communities.

Three EM traverses were run in the Achiase Community (Figure 2). One of the traverses has a length of 350 m and the other two have the length of 250 m. Generally the curves of traverse A and C display high terrain conductivity for HD than VD which is interpreted to mean general decrease in weathering with depth. Both HD and VD curves of all the traverses are erratic in nature which is interpreted to mean a complex subsurface structures beneath the study area. There are few crossover points on the graphs (see Figure 3) and these points together with a point with high VD conductivity values were recommended for further investigations.

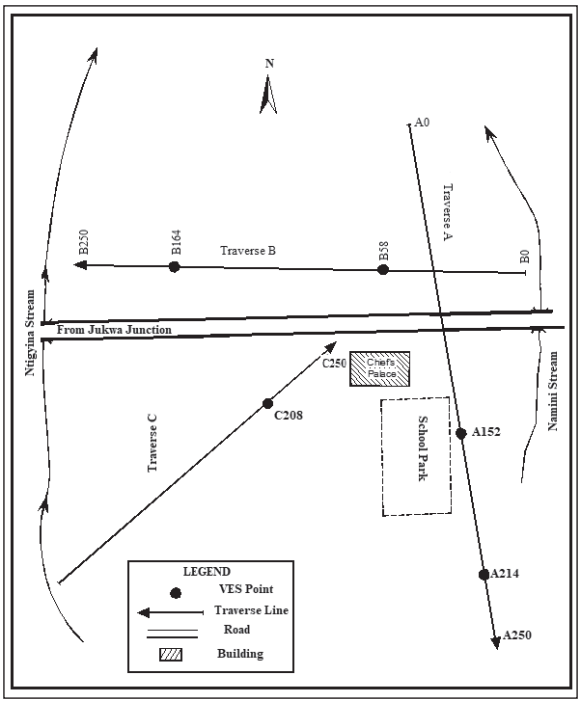

Figure 2- Schematic layout of Achiase Community (not to scale).

The VD inversion results (see Figure 4) revealed two layers beneath the study area with the first layer having a thickness range of 1 – 10 m and the second layer's thickness is half space. The resistivity values is

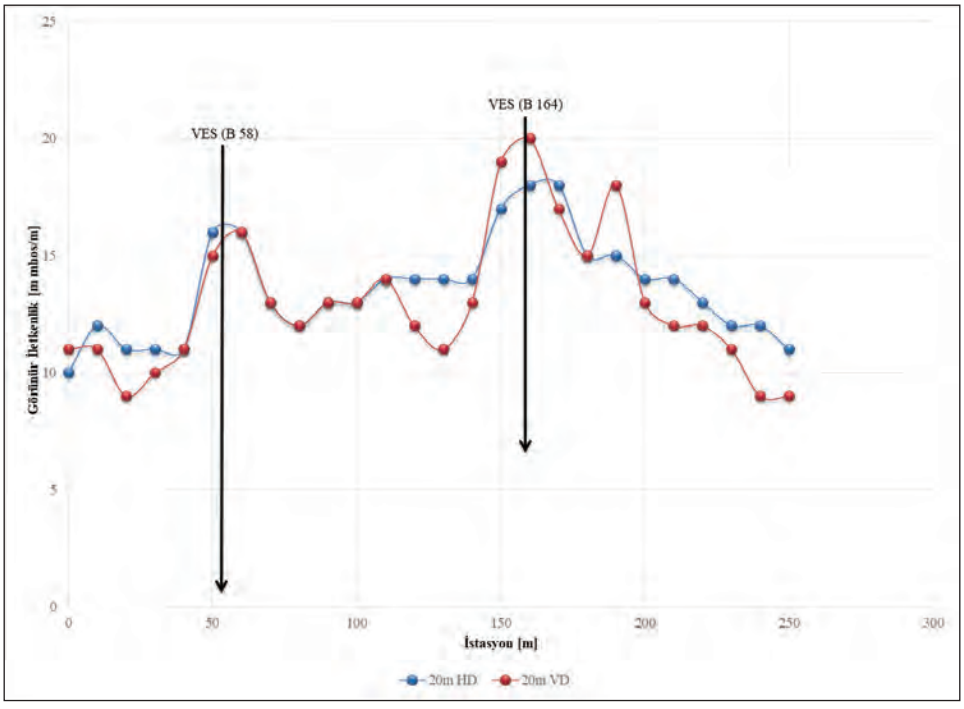

Figure 3- Terrain conductivity curves along traverse B in Achiase Community.

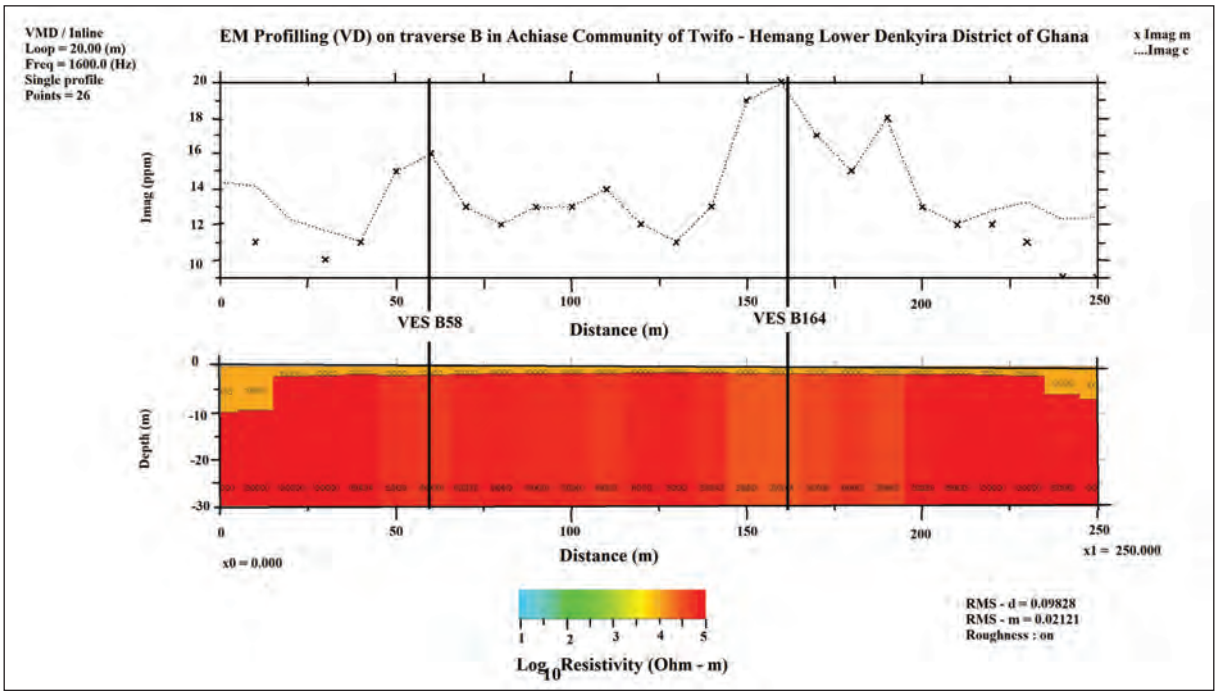

Figure 4- EM inversion result (VD mode) on traverse B in Achiase Community.

in logarithmic scale and the resistivity value of the first layer ranges from 2.5 – 3.5 Ωm. The resistivity value of the second layer is between 3.0 – 5.0 Ωm. There is a good agreement between the inversion results and the terrain conductivity graphs.

In Mbaa Mpe Hia No.2 Community, the EM profiling was conducted along four traverses (Figure 5). The traverse A was run in SSE – NNW direction, traverse B in NNW – SSE direction, traverse C in N – S direction and traverse D in SE – NW direction. The terrain conductivity distribution obtained from this community shows relatively high conductivity ranging between 7 mS/m and 18 mS/m. The profile lengths of all traverses run in this community were 250 m. figure 6 and 7 show the EM terrain conductivity and EM inversion along traverse B respectively.

In the Moseaso Community four traverses were conducted across it (Figure 8). Traverses B and D were conducted in E – W direction, traverse A in W – E direction and traverse C in the S – N direction. The traverse lengths in this community range between 200 m and 250m. The maximum terrain conductivity value is 16 mS/m and the minimum terrain conductivity value is 7 mS/m. The terrain conductivity values in this community are generally low. Figure 9 and 10 below display the EM terrain conductivity and EM inversion along traverse D respectively.

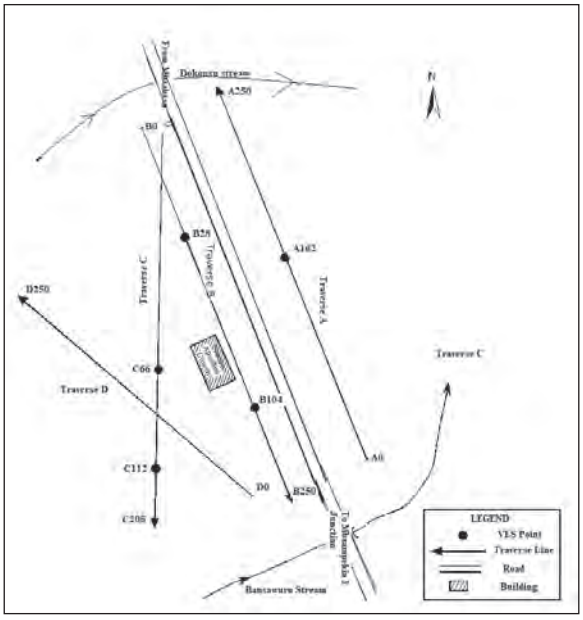

Figure 5- Schematic Layout of Mbaa Mpe Hia No. 2 Community (not to scale).

The EM inversion produced two-layered earth model for all profiles in the study areas. The model resistivity values range from 100 Ωm to 100000 Ωm, logarithm resistivity with an average 0.10% RMS difference between the measured and the calculated values. The study area is located within

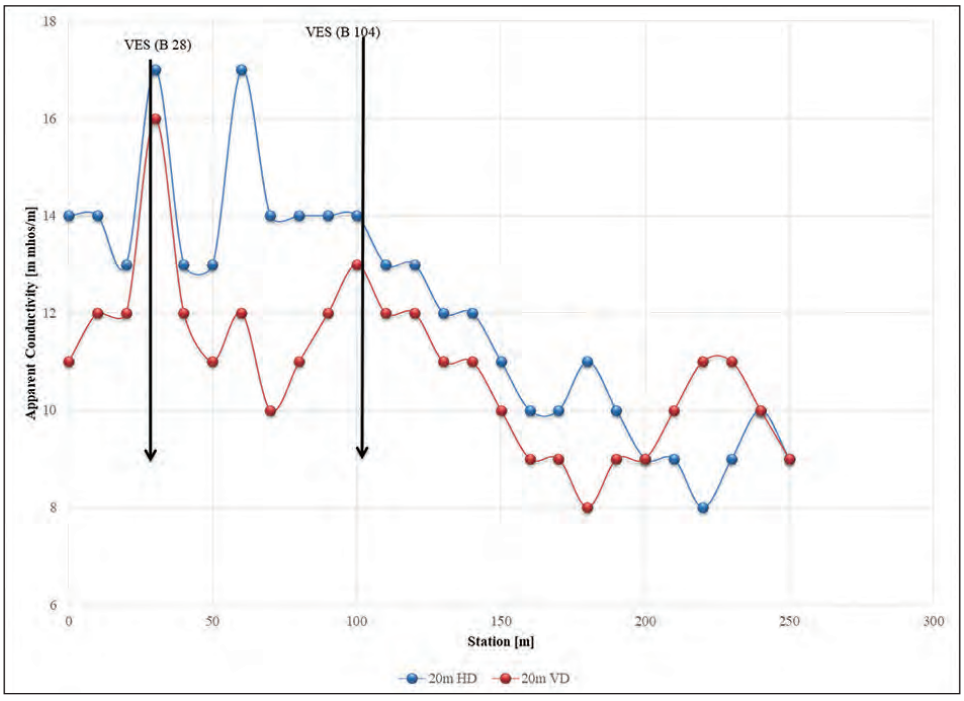

Figure 6- Terrain conductivity curve along traverse B in Mbaa Mpe Hia No.2 Community.

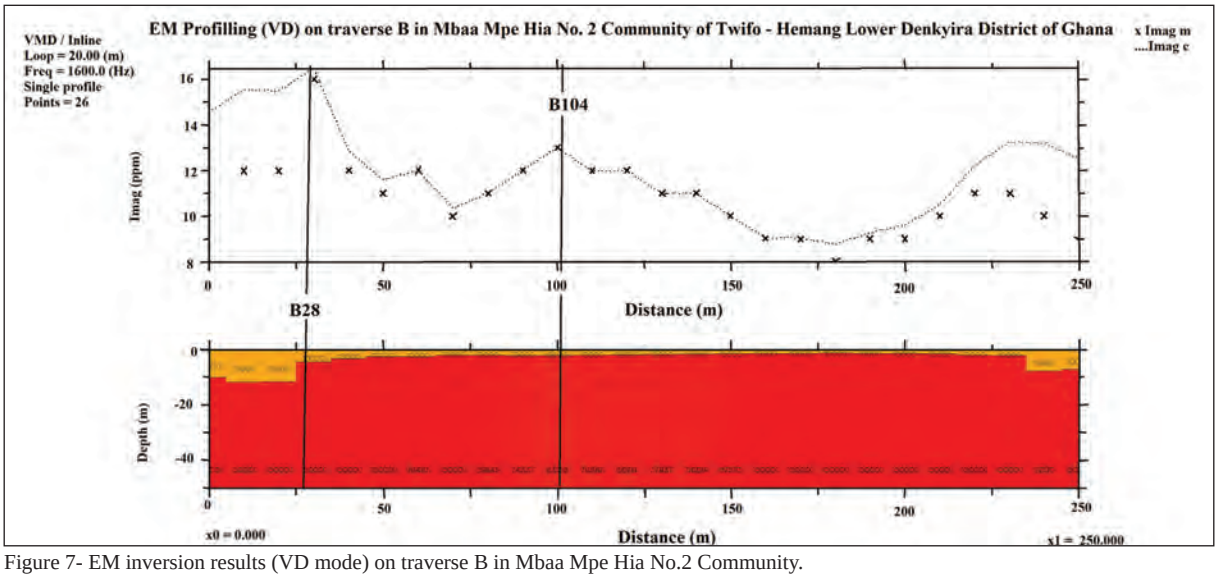

Figure 7- EM inversion results (VD mode) on traverse B in Mbaa Mpe Hia No.2 Community.

granite formation and the nominal resistivity values for granite ranges between $3x10^2$ to $3x10^6$ Ωm. The nominal resistivity values for weathered granite also ranges between $3x10^{-5}$ to $3x10^2$ Ωm (Reynolds, 1997). Increase in the interconnection of pores (permeability) and fractional volume of the rock occupied by water lead to the decrease in resistivity values. In this regard, sections on the EM inversion (Figures 4, 7 and 10) that displayed relatively low resistivity are interpreted to be associated with fractures and or weathering within the subsurface and are of interest in this work. Some points displayed low resistivity values but were not selected for further investigation, because they were located at points which have a high probability of groundwater contamination.

A total of 16 VES stations were recommended for further investigation using the DCR method across

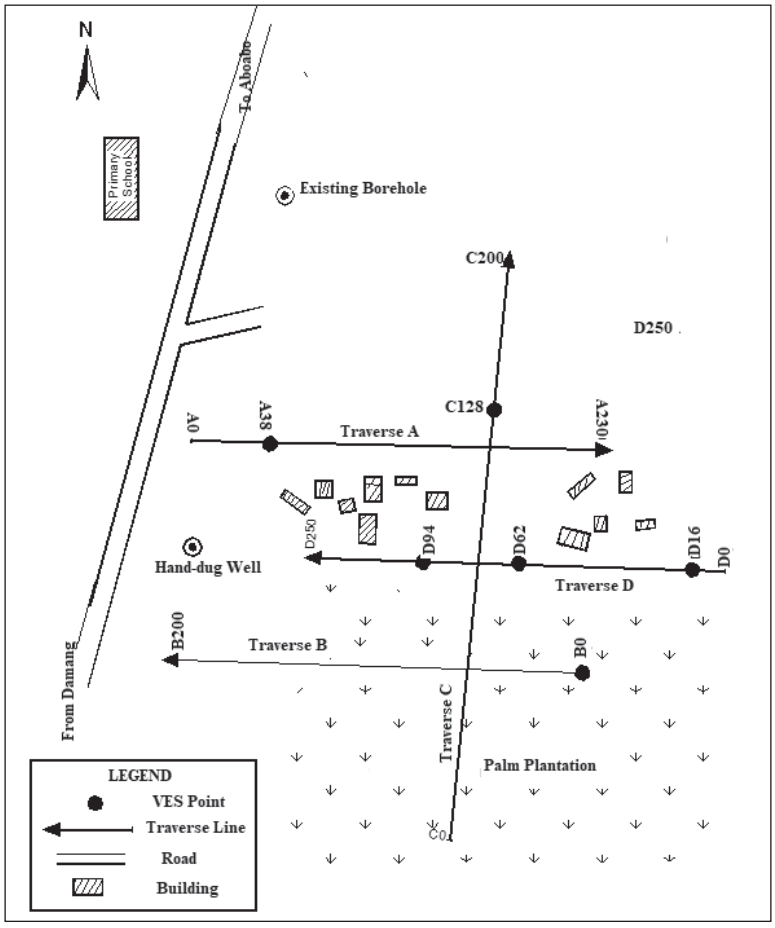

Figure 8- Schematic layout of Moseaso Community (not to scale).

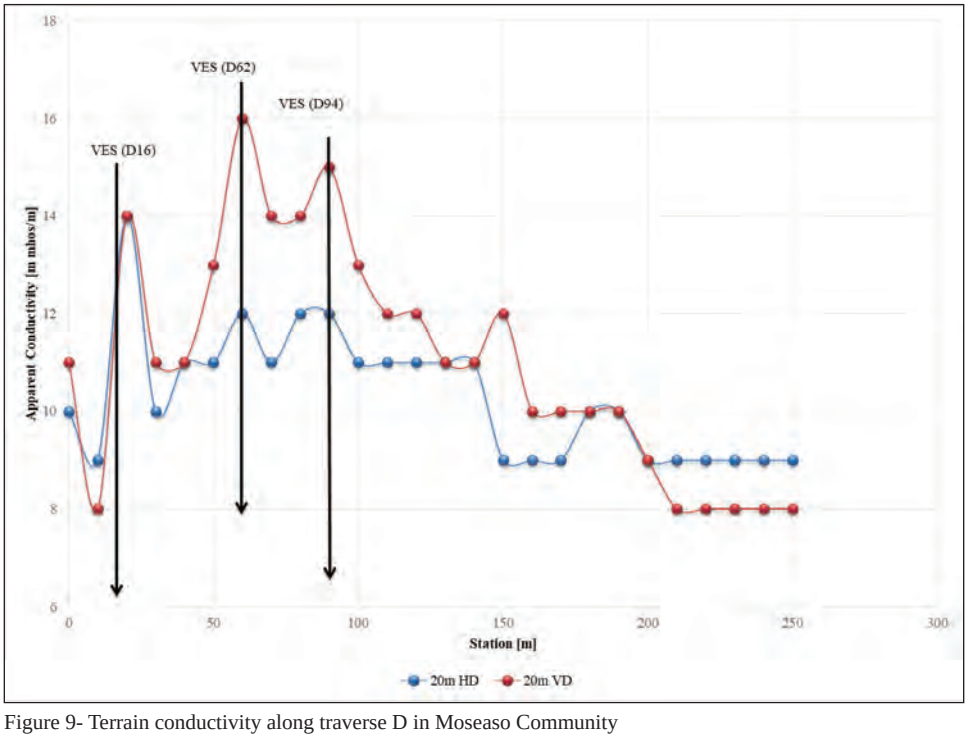

Figure 9- Terrain conductivity along traverse D in Moseaso Community

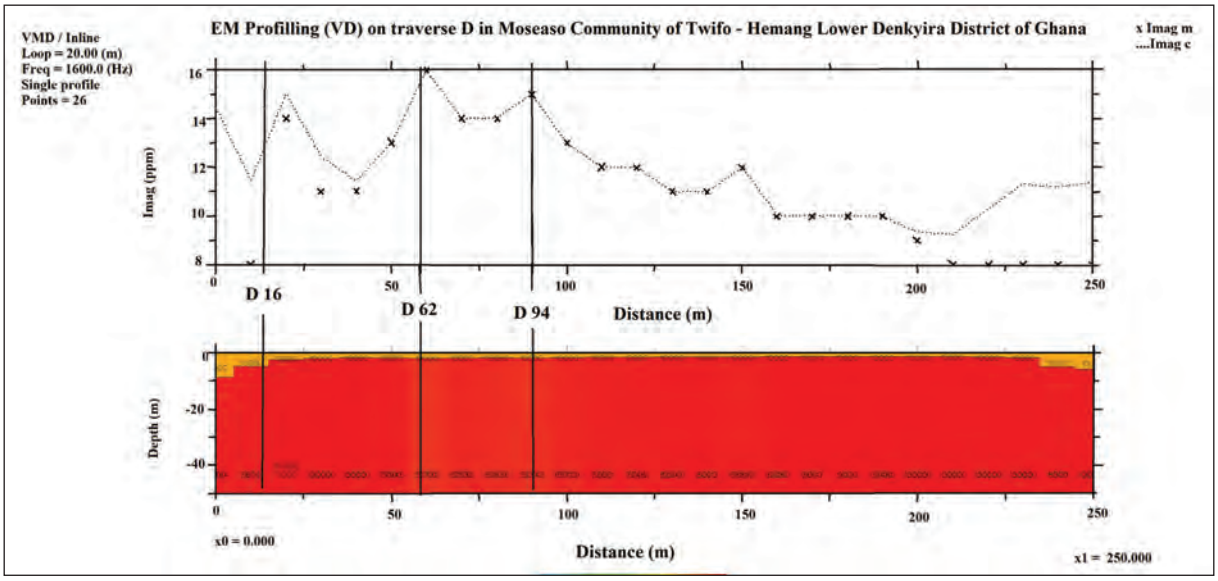

Figure 10- EM inversion result (VD mode) on traverse D in Moseaso Community.

the three communities. See figures 11, 12 and 13 for some of the estimated 1D earth models based on 1D inversion results obtained from these communities. Six VES stations in the Moseaso Community and five VES stations each in Mbaa Mpe Hia No. 2 Community and Achiase Community.

The curve types obtained in the study include H, A, KH and QH. The dominant curve type is the H curve type with 43.75% occurrence, which is followed by the QH type having 25.00% occurrence. The A curve type has 18.75% and the KH types have 12.50% occurrence respectively. The H and KH curve types

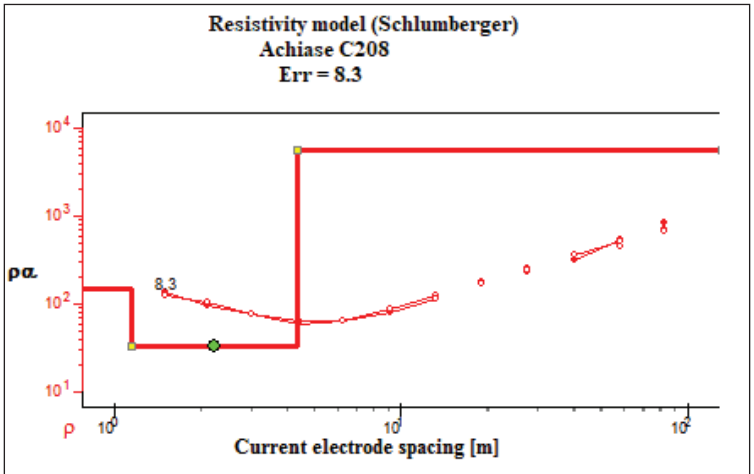

N	ρ	h	z
1	148.91	1.14	0/0
2	33.45	3.22	1.14
3	5721.62		4.36

Figure 11- 1D inversion result at station C208, Achiase Community

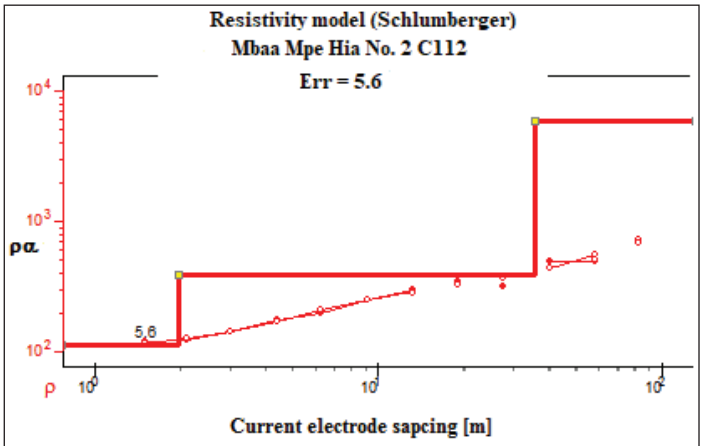

N	ρ	h	z
1	112.20	1.98	0/0
2	388.45	33.57	1.98
3	5962.44		35.55

Figure 12- 1D inversion result at station C112, Mbaa Mpe Hia No.2 Community.

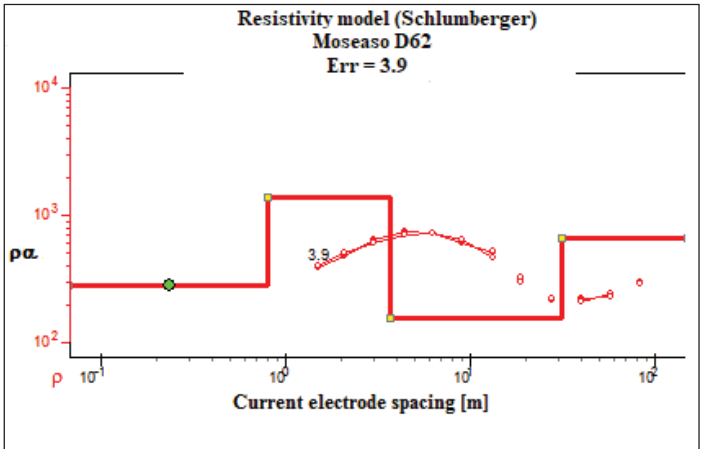

N	ρ	h	z
1	283.27	0.80	0/0
2	1400.88	2.90	0.80
3	154.57	27.50	3.70
4	671.13		31.20

Figure 13- 1D inversion result at station D62, Moseaso Community.

are often associated with groundwater possibilities (Omosuyi, 2010, Okafor and Mamah, 2012).

Analysis of VES curves conducted within the Achiase Community revealed a 3 – layered structure. The first layers have thicknesses ranging from 1.10 – 5.82 m and resistivity values between 59.55 – 1204.4 Ωm. The second layers also have thicknesses ranging between 3.22 – 19.65 m and resistivity values ranging between 33.45 -289.28 Ωm. The bedrock has resistivity values from 2479 – 9815 Ωm. The shape of the sounding curves revealed only one A- type and four H- typed. According to the available data (Table 1) on 8 existing boreholes around the Achiase Community, the borehole depths are within the range of 26.0 – 40.0 m and average of about 35.0m. This depth range are comparable to the depths of aquifers as obtained from the VES inversion results in table 2.

Generally, from the 1D inversion results in table 2, it could be inferred that; the subsurface of the study area in the Achiase community is underlain by a good aquifer. This is because of the geology of the area. In this type of geology generally areas with low resistivity values are associated with aquifers. All VES stations might contain enough groundwater for public water supply beneath them. As it could be seen from figure 11, VES stations such as B164, A152 and C208 that show relatively low resistivity values as summaries in table 2. Also as it could be seen from both table 2 and figure 14 VES C208 might contain groundwater but because of the depth of the first two layers, it was ranked last in groundwater potential. Table 2 provides a summary of the VES results including a rank-list of the selected points for drilling.

The analyses of the VES curves from Mbaa Mpe Hia No.2 Community suggested that; the community is generally underlain by three geoelectrical layers although two VES station revealed four-layered structure. The first layer has resistivity value raging 112.2 – 653.70 Ωm and may be intercepted at a mean depth of 1.51 m. The second layer which is generally expected to be the water-bearing layer has a thickness range of 3.10 – 33.57 m has a mean resistivity value of 256.65 Ωm. The third layer has resistivity value ranging 120.97 – 9347.90 Ωm.

From table 1, the 8 existing boreholes around the Mbaa Mpe Hia No.2 Community have depths ranging from 25.0 – 73.0 m and the average depth of about 34.5 m. Comparing the information in table 1 with the VES results in table 3, only one out of the five VES station have expected aquifer depth within that range. The boreholes reported in table 1 are in and around 5Km from Mbaa Mpe Hia No.2 Community and that there

Table 2- Ranked VES points (summary of 1D inversion results) for borehole drilling at Achiase Community

VES Point	Layer	P(Ω-m)	Depth (m)	Thickness (m)	Rank	Location (GPS)	Curve Type
B 164	1 2 3	59.55 89.84 9815.42	1.1 20.75 -	1.1 19.65 -	1	5.29323 K 1.30728 B	A
B 58	1 2 3	1232.85 240.06 43868.7	0.83 22.29 -	0.83 19.65 -	4	5.29356 K 1.30728 B	H
A 214	1 2 3	756.05 289.28 2479.11	2.91 13.63 -	2.91 10.72 -	3	5.29275 K 1.30651 B	H
A 152	1 2 3	752 180.71 8310.8	5.82 13.33 -	5.82 7.51 -	5	5.29303 K 1.30833 B	H
C 208	1 2 3	148.91 33.45 5721.62	1.14 4.36 -	1.45 3.22 -	2	5.29256 K 1.30833 B	H

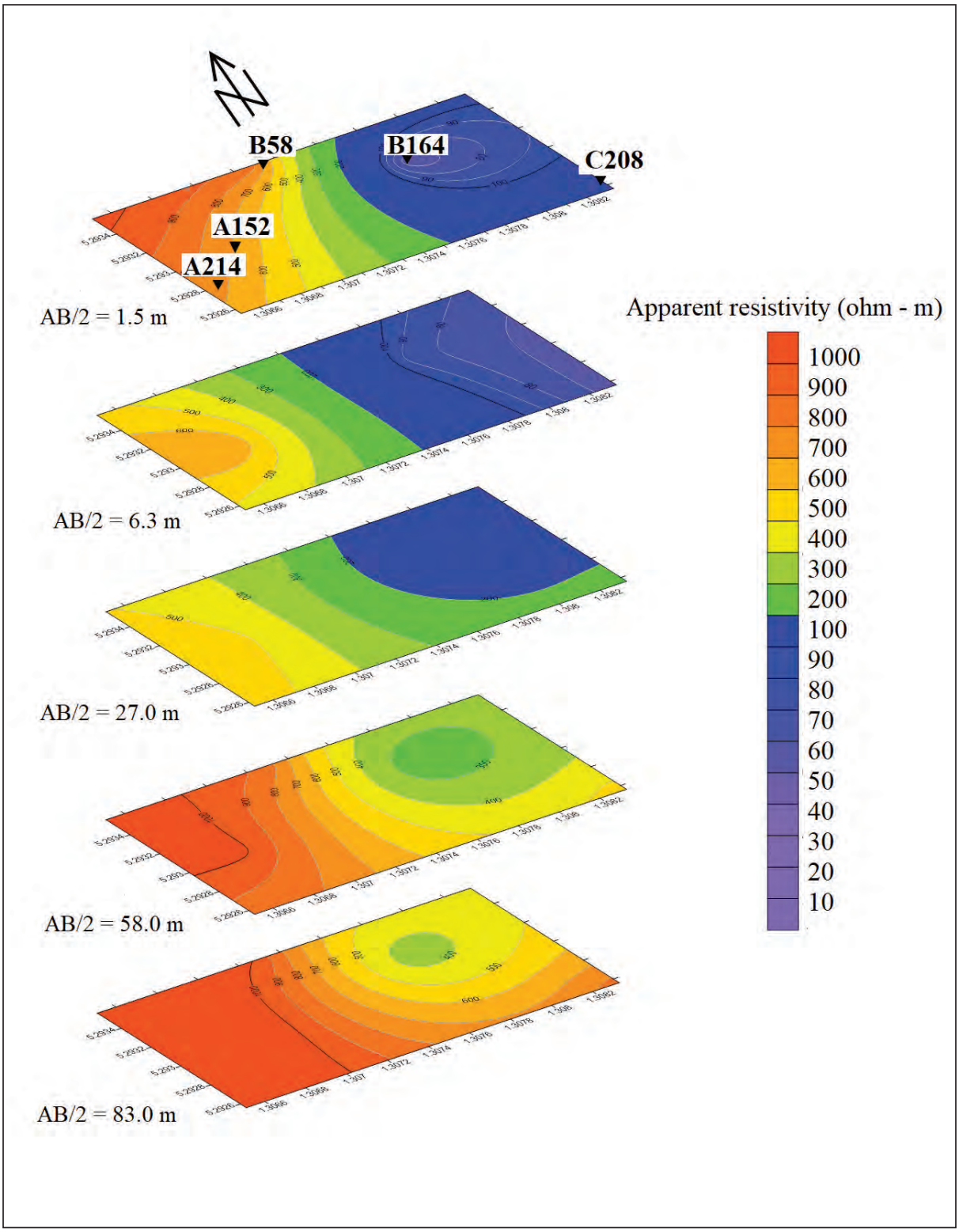

Figure 14- Apparent resistivity maps in Achiase Community.

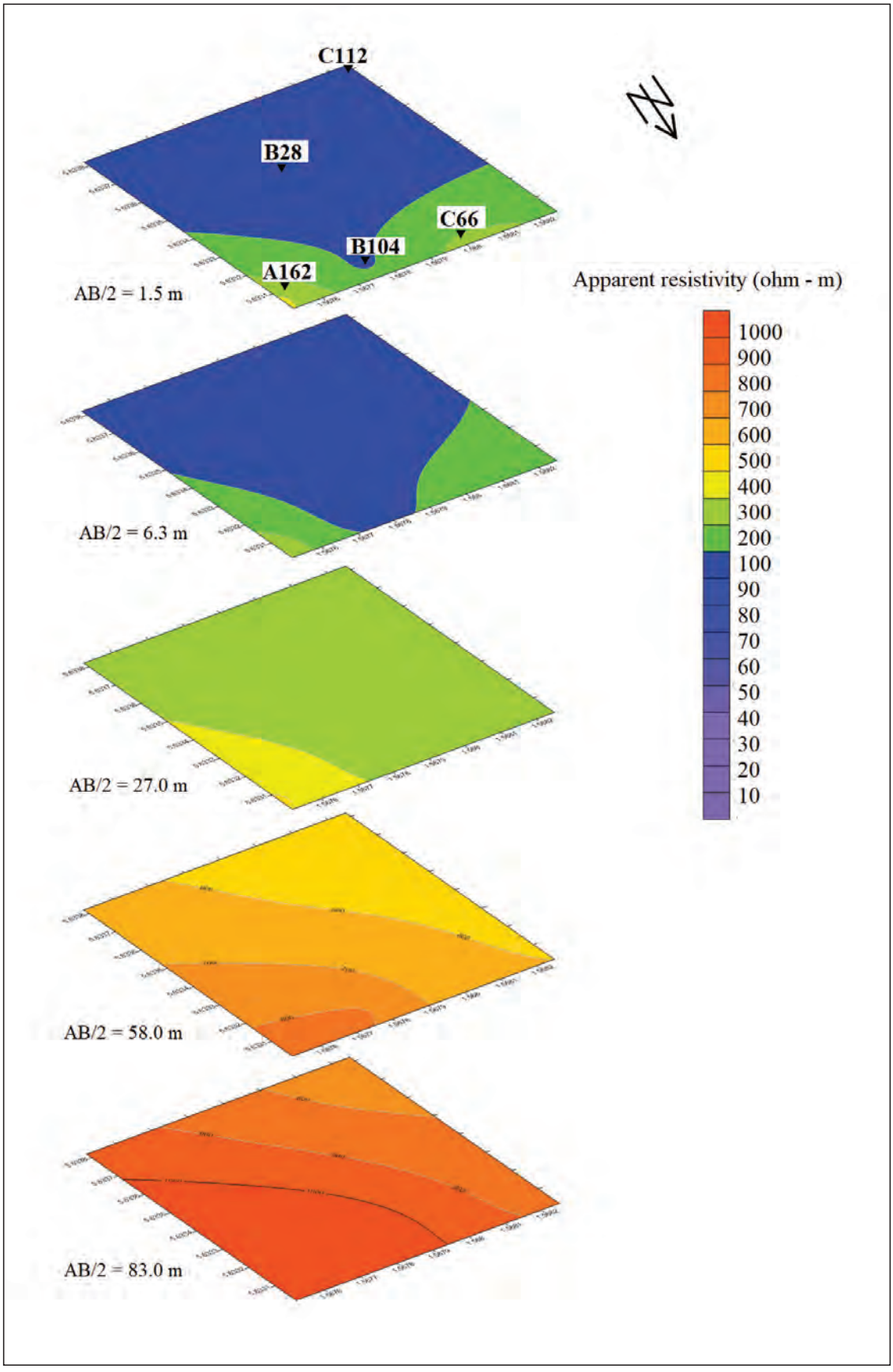

Figure 15- Apparent resistivity maps in Mbaa Mpe Hia No.2 Community.

Table 3- Ranked VES (summary of 1D inversion results) points for borehole drilling at Mbaa Mpe Hia No.2 Community.

VES Point	Location (GPS)	Layer	P(Ω-m)	Thickness (m)	Depth (m)	Rank	Curve Type
C 112	5.63382 K 1.56825 B	1 2 3	112.2 388.45 5962.44	1.98 33.57 -	1.98 35.55 -	1	A
B 28	5.63352 K 1.56786 B	1 2 3	122.32 148.35 3573.44	1.88 9.1 -	1.88 10.98 -	2	A
B 104	5.63308 K 1.56776 B	1 2 3	192.54 121.85 9347.9	1.6 6.77 -	1.6 8.37 -	3	H
A 162	5.63307 K 1.56752 B	1 2 3 4	438.54 391.37 296.56 4061.89	1.5 3.1 11.67 -	1.5 4.6 16.27 -	4	H
C 66	5.63302 K 1.56800 B	1 2 3 4	653.7 233.21 120.97 4241.54	0.6 3.5 6.9 -	0.6 4.1 11 -	5	QH

might be a change in lithology. Generally, in Mbaa Mpe Hia No.2 Community the expected aquifers are shallower than those boreholes reported in table 1.

It can be seen from table 3 that; all the first three layers have relatedly low resistivity values with maximum aquifer depth of 16.27 m. Base on the 1D inversion results as summarized in table 3, it could be inferred that; generally, all the VES points investigated might contain an appreciable amount of groundwater. This could also be seen on the apparent resistivity maps in figure 15. VES C112 is ranked first, followed by VES B28, B104, A162, and C66.

The VES results suggested that Moseaso Community is generally underlain by four geoelectrical layers. Out of the five VES stations investigated, only one station revealed three layered model for the subsurface. Generally, the first layer has resistivity values ranging from 179.63 – 1206.62 Ωm and can be intercepted at a mean depth 2.83 m. The second layer has a thickness range of 2.90 – 12.36 m, and a mean resistivity value of 892.73 Ωm. The third layer which is expected to be water-bearing has a thickness ranging from 12.20 - 28.8 m and a mean resistivity value of 794.21 Ωm. The fourth layer has resistivity values ranging between 671.13 Ωm and 2572.31 Ωm (Figure 16).

In table 1 information of only one borehole around 5 Km from this community is shown and that the depth of the borehole is 73 m. Two wells are shown in the Schematic Layout of Moseaso Community (Figure 8) but information from only one well (Existing borehole) is available. And that the information on the existing borehole which is available is the VES result and it is shown in table 4 below. From the table 4 we can see that the existing borehole (EBH) has a shallow depth compared to results we obtained from this work. 1D inversion results in table 4 and the support of figure 12 show that areas around the existing borehole might contain good aquifer than areas we investigated. In future groundwater exploration project, interest should be given to areas towards the north of this community around the existing borehole as could be seen in figure 8.

By comparing 1D inversion results in tables 2 – 4, it could be inferred that Moseaso Community has the best aquifer among the three communities.

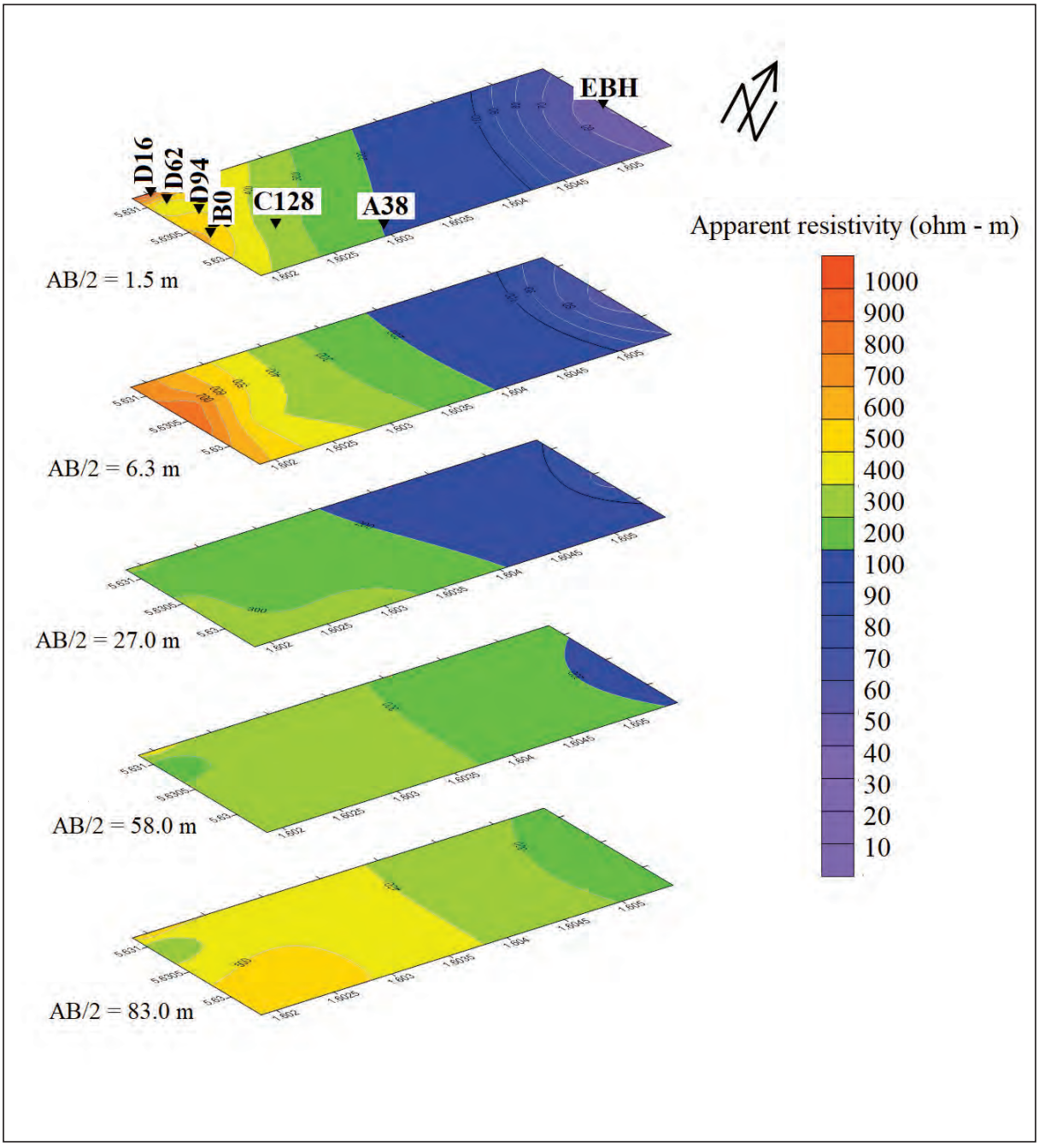

Figure 16- Apparent resistivity maps in Moseaso Community.

Table 4- Ranked VES (summary of 1D inversion results) points for borehole drilling at Moseaso Community.

VES Point	Layer	P(Ω-m)	Depth (m)	Thickness (m)	Rank	Location (GPS)	Curve Type
A 38	1 2 3 4	179.63 940.32 199.98 1287.38	1.66 6.46 27.36 -	1.66 4.8 20.9 -	6	5.62964 K 1.60300 B	KH
D 62	1 2 3 4	283.27 1400.88 154.57 671.13	0.8 3.7 31.2 -	0.8 2.9 27.5 -	1	5.63095 K 1.60199 B	QH
D 94	1 2 3 4	399.13 1422.52 216.74 895.42	0.77 3.84 32.64 -	0.77 3.07 28.8 -	2	5.63069 K 1.60206 B	QH
D 16	1 2 3 4	1206.62 521.33 209.14 1992.83	2.49 9.8 25.6 -	2.49 7.31 15.8 -	5	5.63118 K 1.60200 B	QH
B 0	1 2 3 4	643.81 986.1 83.51 2572.32	0.95 8 12.2 -	0.95 8 12.2 -	3	5.63036 K 1.60187 B	KH
C 128	1 2 3	417.77 115.21 3901.36	10.34 22.7 -	10.34 12.36 -	4	5.63024 K 1.60238 W	H
Mevcut Makine Kazılmış Kuyu (EBH)	1 2 3	61.5 34 1568.7	5.8 12.7 -	5.8 6.9 -		5.63035 K 1.60544 B	

4. Conclusion

The importance of water to us as living things cannot be underestimated, because it is a basic necessity of life. Although we depend on water for both our domestic and industrial activities most people and communities are not ready to pay much for groundwater exploration using geophysical methods as they could pay for other exploration methods, because of some economic factors. Electromagnetic methods especially the EM 34-3 and electrical resistivity methods still remain the cheapest and effective methods for geophysical exploration of groundwater. Data interpretation methods such as the use of inversion for interpreting electromagnetic data rather than the usual qualitative interpretation method using line graphs and use of apparent resistivity maps as 2D pseudo resistivity maps to support the 1D resistivity inversion results (in case the available budget could not permit 2D and or 3D inversion) would help enhance the quality of obtained results, reduce ambiguity and help decision making based on the obtained results.

The quantitative interpretations of EM method were used in the selection of points for the VES

investigation of groundwater in this study. The EM results show that all the three communities were underlain by two geological substrata. The first layer is the topsoil with depth ranging from 2 to 10 m and the second layer is a half space. The decision on selection of the traverse for further investigation is based on the resistivity of the second layer. The resistivity values of the EM inversion results range between 100 Ωm to 100000 Ωm.

16 VES stations were selected across the three communities for further investigations and their results revealed that; Achiase Community and Mbaa Mpe Hia No. 2 community are underlain by three geological substrata and Moseaso Community is underlain by four geological substrata. All VES points investigated show evidence of groundwater availability and hence are recommended for drilling or hand – dug wells. Boreholes or wells are to be drilled or hand-dug based on the rank stated in tables 2-4. From the results of VES investigations, Moseaso Community is ranked highest in terms of groundwater availability followed by Achiase community and finally Mbaa Mpe Hia No.2 Community.

Acknowledgement

The authors are grateful to Mr. Evans Manu of Council of Scientific and Industrial Research – Groundwater Division (CSIR-GWD) of Ghana for providing them with the dataset for this work. They are also grateful to Prof. Kwesi Preko and Dr. David Dotse Wemegah, all of Kwame Nkrumah University of Science and Technology, Kumasi-Ghana, for the various roles they played in obtaining the data used in this work. We thank four anonymous reviewers for their constructive criticisms of the manuscript which improved the paper.

References

Anechana, R. 2013. Groundwater potential assessment of Kintampo North Municipality of Ghana using the electromagnetic method and vertical electrical sounding. Master thesis, Kwame Nkrumah University of Science and Technology, Kumasi (unpublished).

Anon, 2012. Twifo Hemang Lower Denkyira Distric. Twifo Heman Lower Denkyira District Assembly. Available at: http://thld.ghanadistricts.gov.gh/ (Accessed January 31, 2016).

Carrasquilla, A., A. Gonçalves, C., Ulugergerli, E. 2007. Evaluating the performance of difference geophysical methods for groundwater prospecting in Espirito Santo Basin - Southeast Brazil. Tecnociencia, 9(2), pp.89–106.

Chegbeleh, L.P., Akudago, J.A., Nishigaki, M., Edusei, S.N.K. 2009. Electromagnetic Geophysical Survey for Groundwater Exploration in the Voltaian of Northern Ghana. Journal of environmental Hydrology, 17, 1–16.

Fitterman, D.V., Stewartj, M.T. 1986. Transient electromagnetic sounding for groundwater. Geophysics, 51(4), 995–1005.

Frischknecht, F.C., Lasbon, V.F., Spies, B.R., Anderson, W.L. 1991. Profiling methods using small sources. In N. M. Nabighian, ed. Electromagnetic methods in applied geophysics, 105–270.

Gyamera, E.A., Kuma, J.S., Okae-Anti, D. 2014. Hydrogeological studies on soils developed over granitic deposits. International Journal of Advance Agricultural Research,, 2, 29–40.

Keller, G.V., Frischknecht, F.C. 1977. Electrical methods in geophysical prospecting. In International series of monographs in electromagnetic waves. UK, p. 517.

Koroney, A. 2013. Groundwater exploration using shallow geophysical methods Franklin County, Pennsylvania. Masters thesis ,Shippensburg University. p. 26 (unpublished).

Loke, M.H. 2001. RES1D. , p.7. Available at: www.geoelectrical.com.

Mainoo, P.A., Agyekum, W. A., Dapaah-Siakwan, S., Darko, P.K. 2007. Hydrogeological Investigations to Select Borehole Drilling Sites in ten Communities of the Twifo-Hemang Lower Denkyira District of Central Region of Ghana, Accra, Ghana p.324 (unpublished).

McNeill, J. 1980. Electromagnetic Terrain Conductivity measurement at Low induction Number, Geonics Ltd., Technical Note. Ontario, Canada. Available at: http://www.geonics.com/pdfs/technicalnotes/tn6.pdf.

Menyeh, A., Noye, R.M., Danuor, S.K. 2005. Prospecting for Groundwater using the Electromagnetic Method in the Voltaian Sedimentary Basin in the Northern Region of Ghana - A Case Study of the Gushiegu - Karaga District. Journal of Science and Technology, 25(2), 53–65.

Mohammed Nazifi, H. 2015. The use of integrated geophysical methods for groundwater exploration in Ghana. Masters thesis, Sakarya University. p.242 (unpublished).

Monteiro Santos, F.A. 2004. 1-D laterally constrained inversion of EM34 profiling data. Journal of Applied Geophysics, 56(2),123–134.

Nejad H.T., Mumipour M., Kaboli R., Najib O. A. 2011. Vertical electrical sounding (VES) resistivity survey technique to explore groundwater in an arid region, Southeast Iran. Journal of Applied Sciences. 11(23). 3765-3774.

Okafor, P., Mamah, L. 2012. Integration of Geophysical Techniques for Groundwater Potential Investigation in Katsina - Ala, Benue State, Nigeria. The Practical Journal of Science and Technology. 13(2). 463–474.

Olakunle Coker, J. 2012. Vertical electrical sounding (VES) methods to delineate potential groundwater aquifers in Akobo area, Ibadan, South-western, Nigeria. Journal of Geology and Mining Research, 4(2), 35–42.

Omosuyi, G. O. 2010. Geoelectric Assessment of Groundwater Prospect and Vulnerability of Overburden Aquifers at Idanre, Southwestern Nigeria. Ozean Journal of Applied Sciences. 3(1). 19 – 28.

Pirttijärvi, M. 2014. AEMINV, Laterally constrained 1-D inversion of EM profile data, User's guide. Oulu, Finland.

Reynolds, J.M. 1997. An introduction to applied and environmental geophysics, West Sussex, England: John Wiley and Sons Ltd. p. 710

Somiah, J. 2013. Application of Electromagnetic and Electrical Resistivity Methods in Investigating Groundwater Resources of The Sunyani Municipality in The Brong-Ahafo Region of Ghana. Master thesis, Kwame Nkrumah University of Science and technology, Kumasi. p. 150 (unpublished).

Spies, B.R., Frischknecht, F.C. 1991. Electromagnetic Sounding. In N. M. Nabighian, ed. Electromagnetic methods in applied geophysics, 285–425.

Thamke Joanna, N., Craigg Steven, D., Mendes Thomas, M. 1998. Use of terrain electromagnetic geophysical methods to map saline-water contamination, East poplar oil field, Northeastern Montana. Symposium on the Application of Geophysics to Engineering and Environmental Problems. 205-214.

Tsikudo Kwasi, B. 2009. Geophysical investigation for groundwater in the Gushiegu - Karaga and Zabzugu - Tatale District of the Northern Region of Ghana using the electromagnetic method. Kwame Nkrumah Universty of Science and Technology, Kumasi. p. 148 (unpublished).

Wymana, D.A., O'Neillb, C., Ayer, J. 2008. Evidence for Modern-Style Subduction to 3.1 Ga: A Plateau – Adakite – Gold (Diamond) Association. Condie, K.C., Pease, V. (Eds.), (GSA Special Paper 440),129–148.

Bull. Min. Res. Exp. (2019) 158: 345-352

Bulletin of the Mineral Research and Exploration

http://bulletin.mta.gov.tr

An approach to obtain the structural information from the electrical resistivity well logging curves

Doğan Can KARATAŞ[a*], Uğur ZAMAN[b] and Emin U. ULUGERGERLİ[c]

[a] *Çanakkale Onsekiz Mart University, Fac. of Eng.,Terzioğlu Campus 17020 Çanakkale, Turkey orcid.org/0000-0001-7386-7463*
[b] *General Directorate of Mineral Research and Exploration, Ankara, Turkey orcid.org/0000-0002-8440-9254*
[c] *Çanakkale Onsekiz Mart University, Fac. of Eng.,Terzioğlu Campus 17020 Çanakkale, Turkey orcid.org/0000-0001-5639-1109*

Research Article

Keywords:
Resistivity well log, resistivity normal log, resistivity well log modelling, resistivity well log research depth, resistivity well log inversion.

Received Date: 26.07.2017
Accepted Date: 08.04.2018

ABSTRACT

In well logging measurements, the effect of the fluid in the well on the resistivity log curves and the investigation depth/distance for 16 and 64 inches logs were investigated in two-dimensional numerical modeling with the assumption that underground structures are symmetrical. Structural information was obtained via recovering the real resistivity values by using the inversion rather than empirical approaches. Generally, in the case of using the conductive fluid (1 ohm.m<) depending on the ratio of unit thickness (k) with respect to the length of log (l) (i.e. k/l), the insulating formations produce an "M" shaped signs for k/l<1 and appears as the conductive unit that cause fictitious structures in the data. The depth/distance of the research on the other hand causes deviations in the resistivity of structure due to tool length and distance. By the help of the inversion study one of the possible models is obtained. Contribution of this method to such studies is the reveal of compatibility of the resistivity model and data that usually neglected in other approaches.

1. Introduction

In well-logging studies, the physical properties of geological units are obtained. In resistivity logging, the current is applied directly into the geological unit and the real resistivity is obtained by measuring the voltage difference within the same geological unit as long as the unit is sufficiently thick (Figure 1). In practice, this case is very rarely encountered. Since the layer thickness is less than the logging device, the measured value is influenced by the resistivity of the layers on the lower and upper sides of the unit (so-called shoulder effect), as well as the real resistivity of the target unit. In addition, the boreholes itself filling fluid, invasion zones and the lateral transitions in the geological units also affect the measurements (Figure 2). The assessment of the complex data due to shoulder effect, the size of the measuring device and geological conditions has been the subjects of different studies (e.g. Woodhouse, 1978; Anderson, 2001; Nam et al 2010; Rodríguez-Rozas and Pardo, 2016). The

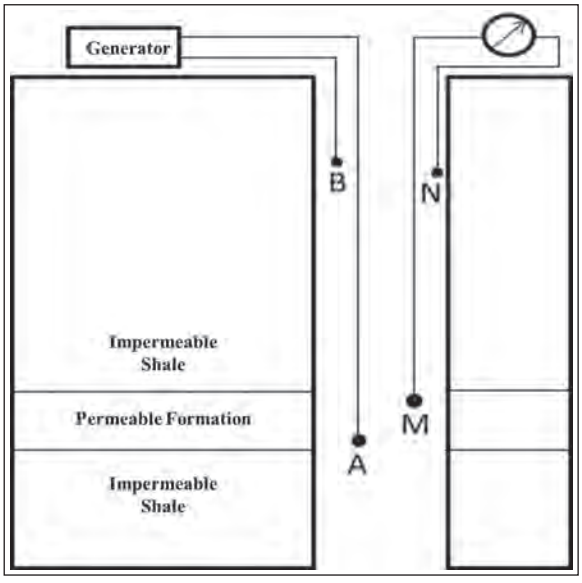

Figure 1- Simple schematic view of the normal electrical resistivity log.

* *Corresponding author: Doğan Can KARATAŞ, karatas.can.dogan@gmail.com*
http://dx.doi.org/10.19111/bulletinofmre.451546.

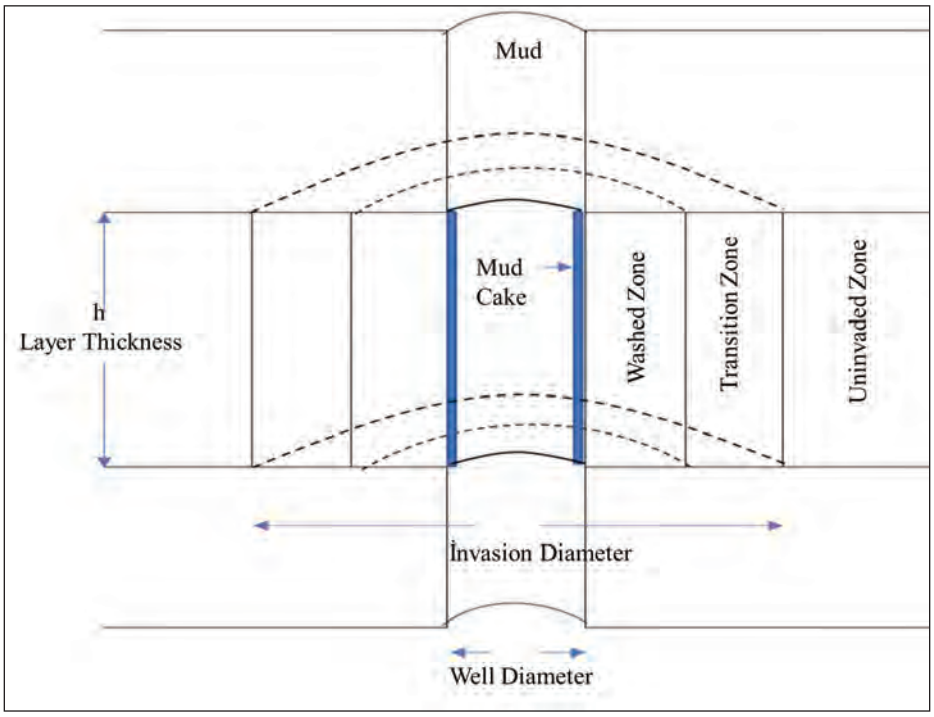

Figure 2- The view of layers that formed in well log study (Layers were shown as symmetrically with respect to well center).

behavior of the curves represents the filtered and simplified images of underground structures. In this sense, the values obtained from logging yield not real but apparent resistivity curves similar to those measured at the surface (e.g. Ulugergerli, 2011). As in many geophysical methods, the electric well logs often encounter with the problem of recovering the large number of parameters from a limited number of data. In practice, in order to obtain the resistivity of invasion zone and the formation either master curves or charts are utilized (e.g. Scott, 1978) or complex underground structures are imaged by multidimensional modeling (e.g. Liu et al., 1994; Yang and Ward, 1984; Pardo et al., 2008) from the apparent resistivity curves acquired in the well.

When charts are utilized, thin layered structures give erroneous results due to the applied corrections and assumptions. Most of the published charts have been produced for vertical drilling wells. As the charts became increasingly invalid, developing new approaches for the interpretation became crucial. Modeling has begun to develop from recognition of the non-functionality of the charts. Due to the development of computer technology, numerical modeling studies replaced the charts. Anderson (2001) outlined the historical development of the use of the modeling in well-logging. With the widespread use of digital modeling, the effect of both logging environment and device on the measurement has also been investigated through the researchers.

As an example, Dutta (1994) studied the calculation of resistivity and depth of invasion zones, formed by the drilling mud, from apparent resistivity curves via an infinitely thick layer. Modeling studies were followed by the inverse solution assessment studies and the inverse solution of both electric and electromagnetic logs has been the subject of various studies. One of the examples of these studies is Liu and Lin (2002). These authors have studied the joint inversion of induction, lateral and normal logs. They have described the joint inversion of induction and galvanic log measurements as an approach that needs to be carefully considered because of the problem of converging to local minima.

In the following years, Pardo et al. (2007), have studied the electrical resistivity log measurements, different electrode configuration and anisotropic effects using three-dimensional modeling of in deviated wells.

Both referred and also other studies in the literature indicated that the insufficient number of data obtained from the well-logs and the excess number of parameters

that are desired to be solved have been main obstacles to numerical modeling studies. This obstacle has also opened the way to attempt to try different approaches in studies carried out in these kind and similar cases (e.g. Ahmadi et al., 2013). It is an undeniable fact that modeling studies are necessary to determine precise relationship between the measured data and wells and surrounding geology. In the following sections, the term modeling includes both the acquisition of observable data (forward solution) and the estimation of the parameters from measured data (inverse solution). The use of three-dimensional models that includes all structural changes in the forward solution studies, and the requirement of searching whole solution space in inverse solution create a heavy computation burden to the user. When the simplified model and the source points are considered, if the number of parameters to be solved per data in the symmetric model is n then it will be n^2 in three-dimensional model. An approach that does not require excessive computational power was chosen in this study. Geological structures in the well and the surrounding area were assumed to be symmetrical. With this approach, it is assumed that geological boundaries lay only horizontally and vertically and the number of parameters decreases. Geological units are defined as concentric cylindrical structures (Figure 2). This approach will provide a sufficient accuracy for the immediate vicinity of the well. This approach will continue to be valid in coal-bearing basins where electrical logs are widely used. On the other hand, it should be kept in mind that this approach will be invalid in fully complicated environments (e.g. conglomerate) or dipping beds.

Direct current (DC) logs have already been studied on the symmetrical environment. Ulugergerli (2011) jointly inverted the short (SN, 16 inches) and long (LN, 64 inches) normal log curves using the conjugate gradient (CG) relaxation and the conventional CG approach and obtained the underground model. The use of a vector-to-matrix multiplication instead of a partial derivatives matrix in CG inverse solutions reduces the memory requirement and provides a fast solution (e.g. Mackie and Madden, 1993; Zhdanov, 2002). Ulugergerli (2011), using the artificial and real well data, compared the advantage of log types on the inverse solution in addition to relative superiorities of the approaches used in the inversion. It was emphasized that, as expected, information about the formation could be obtained from long normal log while short normal log provides information about the invasion zone and around the well. The investigation depth/range of logs was defined as proportional to the device size. In addition to these issues, the effect of mud cakes has been mentioned.

In this article, how the research depths are affected by the mud cake will be investigated in DC resistivity curves. For this purpose, in the following sections, 2D modeling studies and simple but efficient models were used to quantify numerically the effect of mud and depth of investigation.

In the second part of the study, the well-logging data were modeled with the inversion program. Synthetic and real data were used for this purpose.

Although the physical changes occurring in the wells starting from the well itself are investigated, the definition of depth of investigation will be used in the place of the survey range or distance to provide the consensus in terminology with surface geophysical studies in the following sections.

2. Problem Definition

As mentioned in the previous section, during the resistivity logging survey, changes in the well diameter and the zones invaded by mud affect the normal electric resistivity curves. The SN and LN resistivity logs will be considered in this study. Measurements are taken with the help of four ring electrodes placed on the device lowered into the well. In practice, although different scales are used, the order is as B, N, M and A. The electrodes B and N are accepted to be positioned infinitely far from M and A. Although the values may vary depending on the manufacturer, the distance may be given in the following manner. Electrode B is 328 ft above the N electrode. The N electrode is 600 or 960" above the nearest electrode M. The measurement is named according to AM range; AM = 16'' for SN and AM = 64" for LN. The KN interval was used to monitor the invasion areas, while the UN range was produced to determine the true resistivity of the clean section, but, due to the invasion zones, the measured value includes the effect of both the invasion zones and the clean unit (Zamansky, 1980; Gianzero, 1981; Anderson, 2001 and Pekin, 2002).

Theoretically, the investigation depths at which SN and LN curves are affected are given as twice the spacing of current and voltage electrodes located on the device (Pekiner, 2002). The investigation depth is estimated as ~80 cm (2.6 ft) for the SN log, and

as ~320 cm (10.4 ft) for the LN log. It is generally thought that the SN log curve is influenced by layers of invasion originating from the well (Pekiner, 2002).

Since the values recorded with logs are equivalent to the apparent resistivity gathered from surface surveys, they cannot be used for interpretation directly. The true resistivity of the units should be obtained. The real formation resistivity values may not be obtained by modeling the logging data using only one measurement technique. Geological information and auxiliary logs may be needed.

The models to be used in this study include the layers formed due to the fluid in the well. Three models were created, namely the mud, the transition zone in which the fluid flows through the layer and the invasion zone in which the fluid is located. With these models, the effects of the fluid inside the well on the KN curves according to the regions were investigated.

2.1. Numerical Modeling

The Finite Element method was used to obtain the desired log from a symmetric underground model (Ulugergerli, 2011). In order to fully process the shoulder effect, B and N electrodes, which should be theoretically at infinite, are placed at the finite distances and all electrode positions are used in the geometric coefficient calculation. The mesh used in the modeling was initiated by rather fine cells (0.1") then expanded to coarse cells while moving away from the well. To satisfy the boundary conditions, very large cells were added at the end of the mesh.

In the inverse solution phase, the reweighted conjugate derivative was used (e.g. Zhdanov, 2002). The program stops when either a predetermined number of iterations or the selected misfit value is reached or there is no significant improvement between two consecutive misfit values.

3. The Effects of Invaded Layers

The model considered includes fluid-filled wells and invaded zones on the target layer. For simplicity, the invasion zone in the host rock was not included. The addition of this unit will not provide any additional information since all resistivity values will be shifted with the same ratio.

Fluid-related models define cases; (a) when there is only the mud in the well wall, (b) the model in which the mud and the washed zone are present and (c) and all three components exist. The aim in this section is to examine the effect of the specified models on the resistivity log curves measured by the SN (16'') device (Figure 3 and figure 4).

Considering the model in the 16 'curves (Figure 3a), it is seen that the curve (-) shows the presence of the layer (Rt = 5 ohm.m) passing through the mud (0.2 ohm.m), but the value that should be 5 ohm.m is seen as 3.6 ohm.m. When the washed zone is added (Rxo = 0.5 ohm.m, figure 3b) to the model, it is seen that the curve (o) gives low resistivity values (3.2 ohm.m) under the influence of this belt. In the latter model (Figure 3c) it is also seen that the curve (+) gives lower resistivity value (2.85 ohm.m) with the addition of all zones (mud, washed and transition zone). When

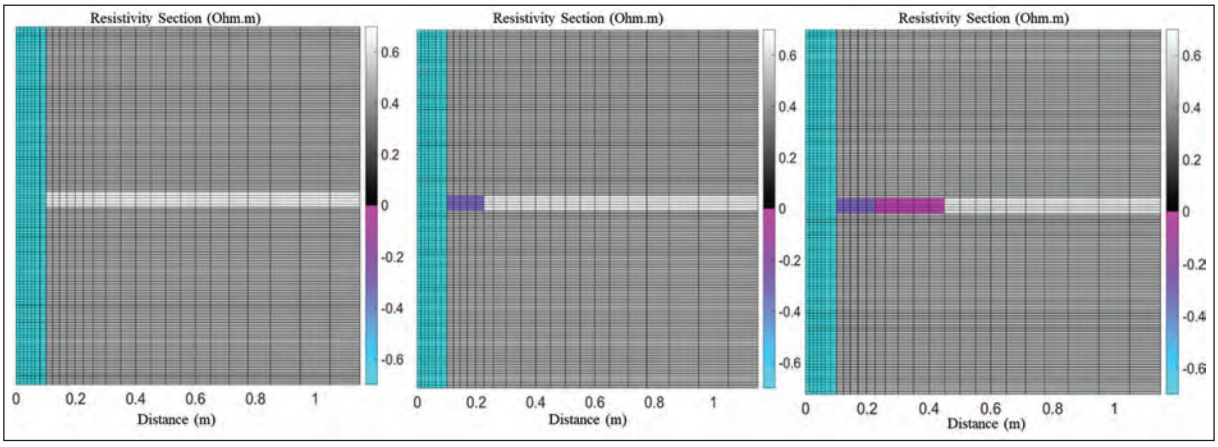

Figure 3- Underground models; a) well model, b) well and the washed zone and c) model consisting of the well, washed zone and transition belt.

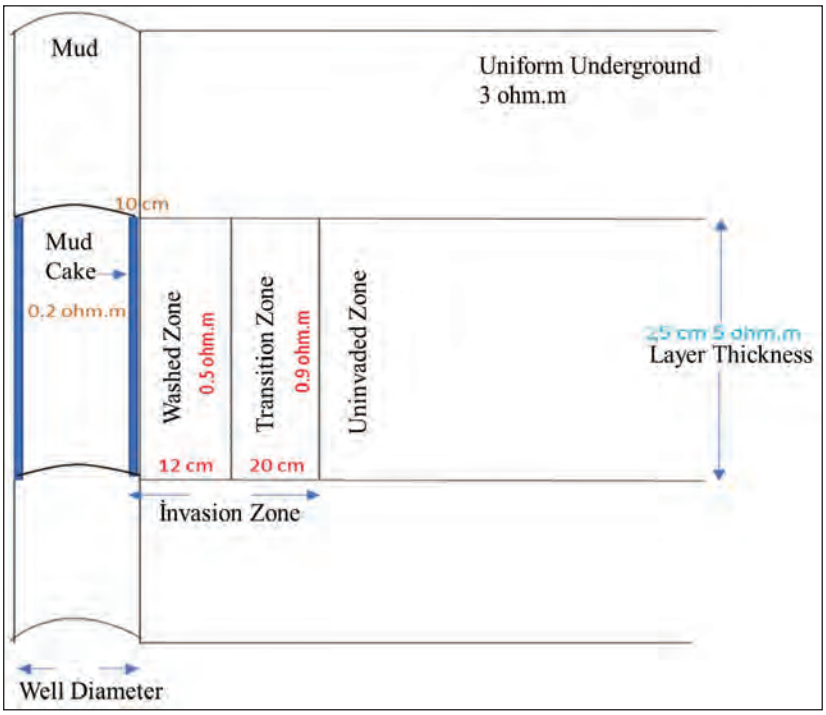

Figure 4- The representative view of the underground utilized in models.

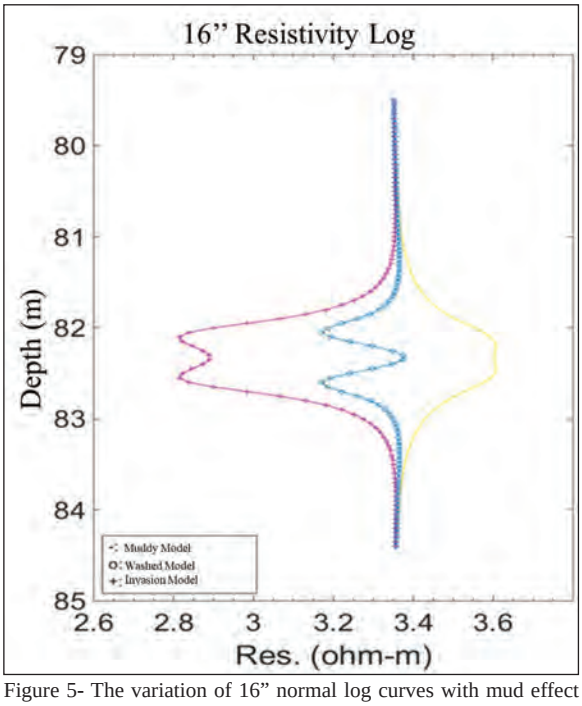

Figure 5- The variation of 16" normal log curves with mud effect and "M" shaped anomaly.

the models were examined, it was observed that, due to the artificial layering caused by the fluid, the SN log curves could not reach the layer resistivity (5 ohm.m) that was expected to be measured but remain at lower values (Figure 5).

Generally; charts are used in order to correct the effect of the fluid induced mud. (see Scott, 1978). The results obtained by these charts and our results were compared in figure 6, and it is not possible to make a prediction for the resistivity of the target layer in the correction using a chart, and it cannot be said that this correction has removed the effect of the mud.

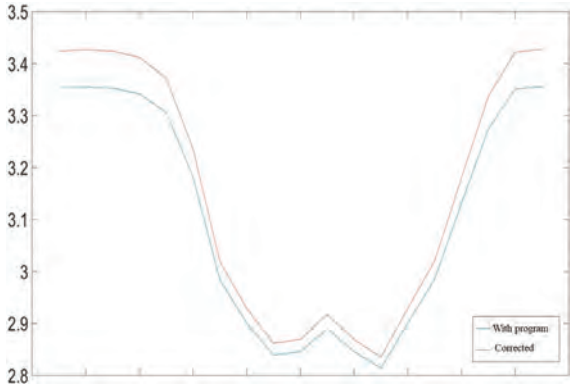

Figure 6- Mud-corrected data (yellow) and the data obtained from this study (blue) are shown. Vertical axis is ohm.m, horizontal axis is the depth.

4. Depth of Investigation

A series of models were used to examine the research depth of SN and LN logging devices. Models were prepared such that a unit with a resistivity of 10 ohm.m and infinite length inside the homogenous host of 1 ohm.m. In order to observe the effect to the research depth, the unit was gradually moved away from the well wall. In the first model created, the layer starts from the well. The theoretical investigation depth of the SN device is 80 cm, which is twice the instrument range. In the first four models, the unit remains in the depth of investigation of the short normal log tool. In subsequent models, the unit moves away from the investigation depth. In the used models, the distance of the unit to the well wall was taken as 0 cm, 20 cm, 40 cm, 78 cm, 155 cm, 325 cm, 550 cm and 750 cm, respectively (Figure 7).

When the models are compared; moving away from the semi-infinite unit of 10 ohm.m from the vertical measurement line inside the 1 ohm.m resistive underground causes proportional decrease in the resistivities of the 16 '' curves. The reading for the first model (0 cm) converges to 10 ohm.m. As SN tool moves away from the boundary of the investigation depth, it deviates from the resistivity value of the target layer. When the theoretical investigation depth is approached, the reading gives the resistivity of the target unit as ~4.5 ohm.m. Very low values (<2.5 ohm.m) are observed after 1.5 m distance.

The theoretical investigation depth of the 64'' tool includes the first six models, but the curves of the 20 cm and 40 cm models have opposite effects, giving more resistivity values than the LN curve produced by the adjacent unit (0 cm). When the theoretical investigation depth of the UN is approached, there is observed a resistivity value (<3.25 ohm.m) three times lower than the unit's required value. When the theoretical investigation depth exceeded, then the values decreased below 1.7 ohm.m.

It is also seen that the curves obtained between the first and last models in both curves give a difference of about 10 ohm.m. In other words, the structure does not affect the data. With exceeding the theoretical investigation depth, the decrease in the SN and LN resistivity curves takes the form of increasing linear change with depth (trend) rather than structural effect.

5. Inversion of Real Data

In this section, two-dimensional models of underground were generated by inversion using short normal real resistivity well log data. Software developed by Ulugergerli (2011) which uses CG.

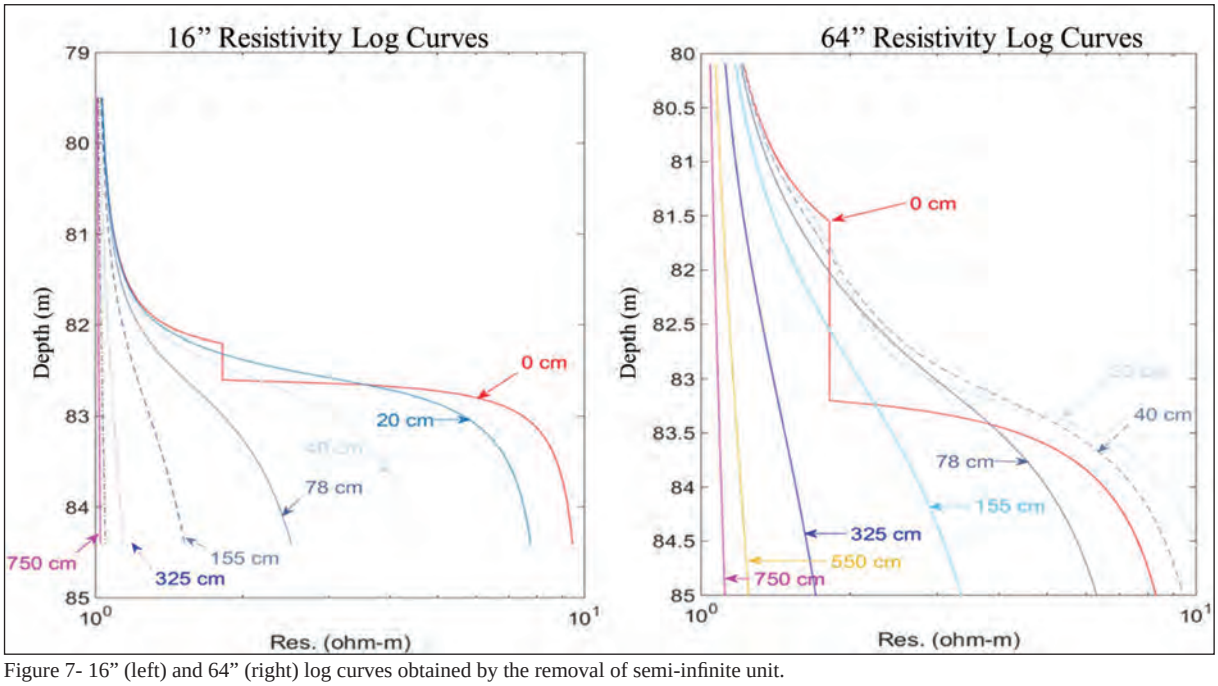

Figure 7- 16" (left) and 64" (right) log curves obtained by the removal of semi-infinite unit.

The section depth is 120 meters and the short normal resistivity values measured at every 0.5 meters were used. The number of data used is 240 and the mud was given as 4 cm thickness.

The resistivity data obtained from the well-logging survey were presented in figure 8. Real SN data (+) and calculated data (continuous line) were shown together for the inverse solution parameters are upgraded and fit between curves is improved at each iteration. The initial model has produced automatically. The inverse solution process made seven iterations and stopped at 0.0056357 misfit value.

The geological structure of the region was reported as volcanic rocks (Basalt, Andesite, Tuff) up to 1500 meters. It is known that the resistivity increase in the range of 230-260 m was interpreted as intact basalt.

When the obtained underground model is examined, it can be said that the resistivity values correspond to the basalt resistivity values (400 ohm.m). A sharp increase in the resistivity at about 233 meters forms a unit (dark blue) in the model which starts about 25 cm after the well wall and extends up to 2 meters.

The inversion study aims to recover the extremely large number of parameters, generally from insufficient and inadequate data. Such problems are encountered especially in surface studies with potential field methods. If comparison of calculated and measured data was assessed alone as the quality of the result the response of different models will provide similar misfit. The problem, defined as a multi-solution, point out that the inverse solution, as a mathematical sequence of operations, finds one of many possible models as a solution. Thus, in addition to the model found in this study, the response of many models will also provide similar misfit.

The validity of the results obtained due to the lack of data should be examined and interpreted in the direction of expectations.

6. Results

In the case of simple underground models, the effects of the mud and the drilling hole can be calculated and removed from the resistivity deviation curves by means of empirical formulas.

By means of modeling studies, the variation of the investigation depth based on the behaviors of normal curves can be revealed. In this study, the negative effect of the mud on the 16 ‘’ resistivity logging curves were investigated with mud formed layers. The

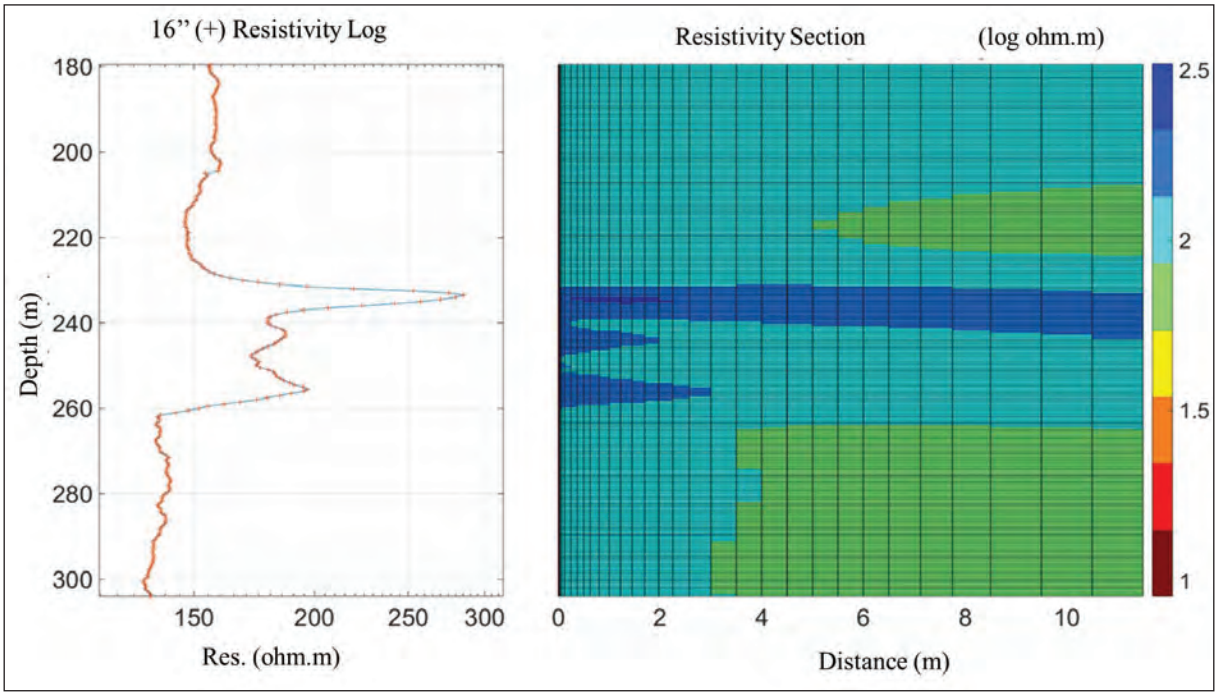

Figure 8- Short normal log data (+) and predicted model curve (straight blue line) on the left and two dimensional model of the underground with respect to the curve on the right.

negative effect of the washed and transition zones on the investigation depth is observed in the models.

The influence of the semi-infinite layer on the depth of investigation is also shown with the help of the models. Beyond the theoretical, the depth of investigation, the formal variation of the data is changed.

A representative model of the underground was produced from the real field data with the inversion program. The program produces a model for the underground in a shorter time than other manual methods do.

Acknowledgements

This study was carried out within the scope of project number 1174 supported by ÇOMÜ BAP. We would like to thank the Mineral Research and Exploration of General Directorate for the use of the well logging data.

References

Ahmadi, A., M., Zendehboudi, S., Lohi, A., Elkamel, A., Chatzis, I. 2013. Reservoir permeability prediction by neural networks combined with hybrid genetic algorithm and particle swarm optimization. Geophysical Prospecting, 61(3), pp.582-598.

Anderson, B. I. 2001. Modeling and Inversion Methods for the Interpretation of Resistivity Logging Tool Response, DUP Science.

Dutta, D.J. 1994. TRANS4: a FORTRAN program for computing apparent resistivity departure curves for an infinitely thick bed with transitional invaded zone in borehole geophysics. Computers and Geosciences 20 (3), pp.293–311.

Gianzero, S. 1981. The mathematics of resistivity and induction logging. The Technical Review. 29(1), pp.4–32.

Liu, Q. H., Anderson, B., Chew, W. C. 1994. Modeling low-frequency electrode-type resistivity tools in invaded thin beds. IEEE Transactions on Geoscience and Remote Sensing, 32(3): pp.494–498.

Liu, Q., Lin, H. 2002. Joint inversion of induction/lateral/normal logs, case studies at Shenli field site, China.

Mackie, R.L., Madden, T.R. 1993. Three-dimensional magnetotelluric inversion using conjugate gradients. Geophysical Journal International, 115(1), pp.215-229.

Nam, M.J., Pardo, D., Torres-Verdín, C. 2010. Assessment of Delaware and Groningen effects on dual-laterolog measurements with a self-adaptive hp finite-element method Geophysics. 75. DOI: 10.1190/1.3496670

Pekiner, Y. 2002. Kuyu Logları Tekniğiyle Yeraltının Keşfi, Seçkin Yayıncılık.

Pardo, D., Torres-Verdín, C., Paszynski, M. 2008. Simulations of 3D DC borehole resistivity measurements with a goal-oriented hp finite-element method. Part II: Through-casing resistivity instruments Computational Geosciences. 12: 83-89. DOI: 10.1007/s10596-007-9061-y

Pardo, D., Paszynski, M., Torres-Verdín, C., Demkowicz, L. 2007. Simulation of 3D DC borehole resistivity measurements with a goal-oriented hp finite-element method, Part I: laterolog and LWD. Journals of the Serbian Society for Computational Mechanics 1, pp.62–73.

Rodríguez-Rozas Á., Pardo, D. A. 2016 priori fourier analysis for 2.5D finite elements simulations of logging-while-drilling (LWD) resistivity measurements Procedia Computer Science. 80: 782-791. DOI: 10.1016/j.procs.2016.05.368

Scott, J. H. 1978. A FORTRAN algorithm for correcting resistivity logs for borehole diameter and mud resistivity.

Ulugergerli, E. U. 2011. Two dimensional combined inversion of short- and long-normal dc resistivity welllog data. Journal of Applied Geophysics, 73 (2011) pp.130–138.

Woodhouse, R. 1978. The Laterolog Groningen Phantom Can Cost You Money. Paper R presented at the 1978 SPWLA Annual Logging Symposium.

Yang, F.W., Ward, S.H. 1984. Inversion of borehole normal resistivity logs. Geophysics 49, pp.1541–1548.

Zamansky, P. 1980. Simulation des laterologs par la m´ethode des ´el´ements finis. Schlumberger Paris Engineering internal report. Project 21-44-00.

Zhdanov, M. S. 2002. Geophysical inverse theory and regularization problems (Vol. 36). Elsevier.

PUBLICATION RULES FOR THE BULLETIN OF THE GENERAL DIRECTORATE OF MINERAL RESEARCH AND EXPLORATION

1. Aims of Publication

- To contribute to the providing of scientific communication on geosciences in Turkey and international community.
- To announce and share researches in all fields of geoscientific studies in Turkey with geoscientists worldwide.
- To announce scientific researches and practices on geoscientific surveys carried out by the General Directorate of Mineral Research and Exploration (MTA) to the public.
- To use the journal as an effective media for international publication exchange by keeping the journal in high quality, scope and format.
- To contribute to the development of Turkish language as a scientific language.

2. Scope

At least one of the following qualifications is required for publishing the papers in the *Bulletin of Mineral Research and Exploration*.

2.1. Research Articles and Review Articles

2.1.1. Original Scientific Researches

- These articles cover and contribute to the main subjects of the earth sciences, the original scientific researches and its results related to all aspects of disciplines in geoscience like exploration and evaluation of the underground sources and environmental problems, and
- The studies, which apply new aspects and methods for the solution of problems about the earth sciences and researches, which apply new aspects and methods for the solution of the problems, in the engineering sciences carried out in MTA.

2.1.2. Review articles

- These papers include comphrehensive scholarly review articles that summarize and critically assess previous geoscientific researches with a new perspective and reveal a new approach.

2.2. Discussion/Reply

- This type of article is intended for the discussion of papers that have already been published in the latest issue of the *Bulletin.* The discussion/reply type articles, which criticize all or a part of a recently published article, are published in the following first issue if it is submitted within six months after the publication of the *Bulletin*.
- The discussions are sent to the corresponding author of the original paper to get their reply before publication. The discussions abut the paper with two or more authors are sent only to the corresponding author.
- If the review article is not published within the prescribed preiod then it is published alone. Later sent replies are not published. Re-criticising of the replies is not allowed.
- The authors should obey the rules of scientific ethics and discussions in their discussion/reply papers. The papers in this category should not exceed four printed pages of the journal including figures and tables etc. The format of the papers should be compatible with the “Spelling Rules” of the *Bulletin.*

2.3. Short Notes

- The short notes part of the *Bulletin* covers short, brief and concisely written research reports for papers including the data obtained from ongoing and/or completed scientific researches and practices related to geoscience and new and/or preliminary factual findings from Turkey and worldwide.
- The short notes will follow a streamlined schedule and will normally be published in the following first or second issue shortly after submission of the paper to the *Bulletin*.
- This type of articles should not exceed four printed pages of the journal including figures, tables and an abstract.

3. Submission and Reviewing of Manuscripts

Manuscript to be submitted for publishing in the Journal must be written clearly and concisely in Turkish and/or English and prepared in the *Bulletin of Mineral Research and Exploration* style guidelines. All submissions should be made online at the **http://.dergi.mta.gov.tr** website.

- The manuscript submitted for reviews must not have been published partially or completely previously in another journal.

- The rejected manuscripts are not returned back to author(s) whereas a letter of statement indicating the reason of rejection is sent to the corresponding author.

- Submitted manuscripts must follow the *Bulletin* style and format guidelines. Otherwise, the manuscript which does not follow the journals' style and format guidelines, is given back to corresponding author without any reviewing.

- Every manuscript which passes initial Editorial treatise is reviewed by at least two independent reviewers selected by the Editors. Reviewers' reports are carefully considered by the Editors and associated editors.

- The manuscript that need to be corrected with the advices of reviewer(s) is sent back to corresponding author(s) to assess and make the required corrections suggested by reviewer(s) and editors. The authors should prepare a letter of well-reasoned statement explaining which corrections are considered or not.

- If there are any suggestions given by editors and referees that are not accepted and corrected by the author, then it should be sent to the Editor's Office with corrected copies of the report explaining the reason for not accepting these suggestions and corrections.

- Figures and tabless should be 1/3 of the main text.

- To be published in the *Bulletin of Mineral Research and Exploration*, the printed lenght of the manuscript should not exceed 30 printed pages of the journal including an abstract, figures and tables. The publication of longer manuscripts will be evaluated by Editorial Board if it can be published or not.

- The authors must do the reviewer's corrections and proposals in 60 days and must upload to the system.

- At the printing stage after the last control, the first print of the manuscript are sent to the author/ authors in pdf version and asked from the author/ authors to make the press control.

4. Publication Language and Periods

- *The Bulletin of Mineral Research and Exploration* is published at least twice a year and each issue is published both in Turkish and English. Thus, the manuscripts are accepted in Turkish or English. The spelling and punctuation guidelines of Turkish Language Institution are preferred for the Turkish issue. However, the technical terms related to geology are used in accordance with the decision of the Editorial Board.

5. Spelling Draft

- Manuscripts should be written in word format in A4 (29.7 x 21 cm) size and double-spaced with font size Times New Roman 10-point, margins of 25 mm at the sides, top and bottom of each page.

- The formulas requiring the use of special characters and symbols must be submitted by the symbols part of the Microsoft Office Word Program on computer.

- Initial letters of the words in sub-titles must be capital. The first degree titles in the manuscript must be numbered and left-aligned, 10 point bold Times New Roman must be used. The second degree titles must be numbered and left-aligned, they must be written with 10 point normal Times New Roman. The third degree titles must be numbered and left-aligned, they must be written with 10 point italic Times New Roman. The fourth degree titles must be left-aligned without having any number; 10 point italic Times New Roman must be used. The text must continue placing a colon after the title without paragraph returns (See: Sample article: http://bulletin.mta.gov.tr).

- One line spacing must be left after paragraphs within text.

- Paragraphs must begin with 0.5 mm indent.

- The manuscript must include the below sections respectively;

  - Title Page
  - The Name and Surname of the author and * sign (Adress, e-mail adres must be given at the bottom of the page)
  - Abstract
  - Key Words

- Introduction
- Body
- Discussion
- Conclusion
- Acknowledgements
- References

5.1. Title of the Article

- The title must be short, specific and informative and written with small letters font size Times New Roman 10-point bold. The title mustn't contain the subjects insufficiently processed in the article.

5.2. The Name of the Author, Address and E-Mail Adress

- The name and surname of the author/authors must be written without affiliations. Name must be written in small letters, the surname must be written in capital letters.
- At the affiliation (work adres) written after the name and the surname of the author/authors only the name of the company must be written, the author's job mustn't be written.
- Information about the adresses must be given at the next line as 10-point and italic.
- At the articles with two or more than two authors, the numbers must be written above the surnames of the authors, the informations about their adresses must be given at the next line by leaving one space line. Also, at this part the corresponding author must be indicated by the (*) symbol and the telephone, FAX and e-mail address of the corresponding author must be given.
- Abbreviations must not be made while writing the name of the uthor and the affiliation adres. Adresses must be given in Turkish in the Turkish version, in English in the English version.
- At the end of the article the name of the corresponding author and contact informations must be added.

5.3. Abstract

- The abstract must be understandable before having a look at the text.
- The abstract should state briefly the overall purpose of the research, the aim of the article, its contributions to the known theories, new data, principle results and major conclusions.
- Tha abstract must contain short and brief sentences.
- Addressing other sections and illustrations of the text or other writings must be avoided.
- The information, which have not been mentioned in the text, must not be in the abstract.
- The article must be written as one paragraph, preferably. Please provide an abstract which doesn't exceed 200 words.
- The abstract must be written with 10-point, normal Times New Roman in single-spaced lines.
- "Abstract" must not be given for the writings that will be located in "Short Notes" section.
- The English abstract must be under the title of "Abstract".

5.4. Key Words

Immediately after the abstract, please provide up to 5 key words and with each words seperated by comma. These key words will be used for indexing purposes.

5.5. Introduction

- The introduction section should state the objectives of the work, research methods, location of the study area and provide an adequate and brief background by avoiding a detailed literature survey.
- Non-standard or uncommon classifications or abbreviations should be avoided. But if essential, then they must be defined at their first mention and used consistently thereafter. Seperate paragraphs could be organized for each of the subjects at the introduction part. If it is necessary, the subtitle can be given for each of them (for example method, material, terminology etc.).
- When pre-information is needed for facilitating the understanding of the text, this section can also be used (for example, statistical data, bringing out the formulas, experiment or application methods, and others).

5.6. Body

- In this chapter, there must be data, findings and opinions that are intended to convey to the reader about the subject. The body section forms the main part of the article.
- The data used in other sections such as "Abstract", "Discussions", and "Results" are caused by this section.
- While processing the subject, the care must be taken not to go beyond the objective highlighted in the "Introduction" section. The knowledge, which do not contribute to the realization of the purpose of the article or are useless for conclusion, must not be included.
- All data used and the opinions put forward in this section must prove the findings obtained from the studies or they must be based on a reference by citation.
- The guidance and methods to be followed in processing subjects vary according to the characteristics of the subjects mentioned. Various topic titles can be used in this section as many as necessary.

5.7. Discussions

- Discussion of the data and findings that are objectively transferred in the Main Text section of the article should be done in this section. This must be written as a seperate section from the results section.

5.8. Conclusions

- The main conclusion of the study provided by data and findings of the research should be stated concisely and concretely in this section.
- **T**he subjects that are not mentioned sufficiently and/or unprocessed in the body section must not be included in this section.
- The conclusions can be given in the form of substances in order to emphasize the results of the research and to make the expression understandable.

5.9. Acknowledgements

In this section, the significant contributions made in the realization of investigation that form the topic of the paper is specified. While specifying contributions, the attitude diverted the original purpose of this section away is not recommended. Acknowledgements must be made according to the following examples.

- This study was carried out within scope of .....project.
- I/we would like to thank to …… for contributing to the development of this article with his/her critiques.
- Academic and/or authoritorial affiliations are written for the contributions made because of requirement of ordinary task.

For example:

- o "Prof. Dr. İ. Enver Altınlı has led the studies".
- o "The opinions and warnings of Dr. Tandoğan Engin are considered in determining the chemistry of chrome minerals."

- The contributions made out of the requirement of ordinary task:

For example:

o "I would like to thank to Professor Dr. Melih Tokay who gives the opportunity to benefit from unpublished field notes"; "I would like to thank to the preliminary-Plan Chief Engineer Ethem Göğer, State Hydraulic Work, 5th Zone". Academic and / or task-occupational titles are indicated for such contributions.

- The contributions, which are made because of requirement of ordinary task but do not necessitate responsibility of the contributor mustn't be specified.

For example:

o Sentences such as "I would like to thank to our General Manager, Head of Department or Mr. / Mrs. President ……who has provided me the opportunity to research" must not be used.

5.10. References

- All references cited in the text should be given in the reference list.
- The authors must be careful about the accuracy of the references. Publication names must be written in full.

- Reference list must be written in Times New Roman, 9-point type face.
- The reference list must be alphabetized by the last names of the first author of each work.
- If an author's more than one work is mentioned, then ranking must be made with respect to the publication year from old to new.
- In the case that an author's more than one work in the same year is cited, the lower-case alphabet letters must be used right after publication year (for example; Saklar, 2011a, b).
- If the same author has a publication with more than one co-author, firstly the ones having single author are ranked in chronological order, then the ones having multiple authors are ranked in chronological order.
- In the following examples, the information related to works cited is regulated in accordance with different document/work types, considering punctuation marks as well.
- If the document is located in a periodical publication (if it is an article), then the information about the document must be given in the following order: surnames of the author/authors, initial letters of author's/authors' first names. Year of publication. Name of the document. Name of the publication where the document is published, volume and/ or the issue number, numbers of the first and last pages of the document.

For example:

  - o Pamir, H.N. 1953. Türkiye'de kurulacak bir hidrojeoloji enstitüsü hakkında rapor. Türkiye Jeoloji Bülteni 4, 1, 63-68.
  - o Barnes, F., Kaya, O. 1963. İstanbul bölgesinde bulunan Karbonifer'in genel stratigrafisi. Maden Tetkik ve Arama Dergisi 61, 1-9.
  - o Robertson, A.H.F. 2002. Overview of the genesis and emplacement of Mesozoic ophiolites in the Eastern Mediterranean Tethyan region. Lithos 65, 1-67.

- If more than one document by the same authors is cited, first the documents having single name must be placed in chronological order, second the documents having two names must be listed in accordance with the chronological order and second author's surname, and finally the docments having multiple names must be listed in accordance with chronological order and third author's surname.
- If the document is a book, then; the surname of the author/authors, initial letters of the author's/ authors' first names. Year of publication. Name of the book (initial letters are capital). Name of the organization, which has published the book, name of the publication where the document is published, volume and/ or the issue number, total pages of the book.

For example

  - o Meric, E. 1983. Foraminiferler. Maden Tetkik ve Arama Genel Müdürlüğü Eğitim Serisi 23, 280 s.
  - o Einsele, G. 1992. Sedimentary Basins. Springer-Verlag, 628 p.

- If the document is published in a book containing the writings of various authors, the usual sequence is followed for the documents in a periodic publication. Then the editor's surname and initial letters of their name/names are written. "Ed.", which is an abbreviation of the editor word, is written in parentheses. Name of the book containing the document (initial letters are capital). Name of the organization which has published the book. Place of publication, volume number (issue number, if any) of the publication where the document is published, numbers of the first and last page of the document.

For example:

  - o Göncüoğlu, M.C., Turhan, N., Şentürk, K., Özcan, A., Uysal, Ş., Yalınız, K. 2000. A geotraverse across northwestern Turkey. Bozkurt, E., Winchester, J.A., Piper, J.D.A. (Ed.). Tectonics and Magmatism in Turkey and the Surrounding Area. Geological Society of London Special Publication 173, 139-162.
  - o Anderson, L. 1967. Latest information from seismic observations. Gaskell, T.F. (Ed.). The Earth's Mantle. Academic Press. London, 335-420.

- If the name of a book, where various authors' writings have been collected, is specified, those must be indicated respectively: book's editor/

editors' surname/surnames and initial letters of their name/names. "Ed.", which is an abbreviation of the editor word, must be written in parentheses. Year of Publication. Name of the book (initial letters are capital). Name of the organization which has published the book, total pages of the book.

For example:

- o Gaskel, T.F. (Ed.) 1967. The Earth's Mantle. Academic Press, 520 p.

- If the document is an abstract published in a Proceedings Book of a scientific activity such as conference/symposium/workshop …etc., the information about the document must be given in the following order: surnames of the author/authors, initial letters of author's/authors' first names. Year of publication. Title of the abstract. Name, date and place of the meeting where the Proceedings Book is published, numbers of the first and last pages of the abstract in the Proceedings Book.

For example:

- o Yılmaz, Y. 2001. Some striking features of the Anatolian geology. 4. International Turkish Geology Symposiums 24-28 September 2001, London, 13-14.

- o Öztunalı, Ö., Yeniyol, M. 1980. Yunak (Konya) yöresi kayaçlarının petrojenezi. Türkiye Jeoloji Kurumu 34. Bilim Teknik Kurultayı, 1980, Ankara, 36

- If the document is one of the unpublished documents as a report, lecture notes, and so on, the information about the document must be given by writing the word "unpublished" in parentheses at the end of information about the document after it is specified in accordance with usual order which is implemented for a document included in a periodic publication.

For example:

- o Özdemir, C. Biçen, C. 1971. Erzincan İli, İliç ilçesi ve civarı demir etütleri raporu. *General Directorate of Mineral Research and Exploration Report No: 4461*, 21 p. Ankara (unpublished).

- o Akyol, E. 1978. Palinoloji ders notları. EÜ Fen Fakültesi Yerbilimleri Bölümü, 45 p., İzmir (unpublished).

- The followings must be specified for the notes of unpublished courses, seminars, and so on: name of the document and course organizer. Place of the meeting, name of the book, corresponding page numbers must be given.

For example:

- o Walker, G. R. Mutti, E. 1973.Turbidite facies and facies associations. Pacific Section Society for Sedimentary Geology Short Course. Annaheim. Turbitides and Deep Water Sedimantation, 119-157.

- If the document is a thesis, the followings are written: surname of the author, initial letter of the author's first name. Year of Publication. Name of the thesis. Thesis type, the university where it is given, the total number of pages, the city and "unpublished" word in parentheses.

For example:

- o Seymen, İ. 1982. Kaman dolayında Kırşehir Masifi'nin jeolojisi. Doçentlik Tezi, İTÜ Maden Fakültesi, 145 s. İstanbul (unpublished).

- Anonymous works must be regulated according to the publishing organization.

For example:

- o MTA. 1964. 1/500.000 ölçekli Türkiye Jeoloji Haritası, İstanbul Paftası. Maden Tetkik ve Arama Genel Müdürlüğü, Ankara.

- The date after the name of the author is not given for on-printing documents; "in press" and / or "on review" words in parenthesis must be written. The name of the article and the source of publication must be specified, volume and page number must not be given.

For example:

- o Ishihara, S. The granitoid and mineralization. Economic Geology 75th Anniversary (in press).

- Organization name, web address, date of access on web address must be indicated for the information downloaded from the internet. Turkish sources must be given directly in Turkish and they must be written in Turkish characters.

For example:

- o ERD (Earthquake Research Department of

Turkey). **http://www.afad.gov.tr**. March 3, 2013.

- While specifying work cited, the original language must be used; translation of the title of the article must not be done.

6. Illustrations

- All drawings, photographs, plates and tables of the article are called as "illustration".
- The illustrations must be used when the use of them is inevitable or when they facilitate the understanding of the subject.
- While selecting and arranging the illustrations' form and dimensions, the page size and layout of the *Bulletin* must be considered. The unnecessary loss of space must be prevented as much as possible.
- The pictures must have high quality, high resolution suitable for printing.
- The number of illustrations must be proportional to the size of the text.
- All illustrations must be sent as in separate files independent from the text.
- While describing illustrations in the text, the abbreviations must be avoided and descriptions must be numbered in the order they are mentioned in the text.
- Photographs and plates must be given as computer files containing EPS, TIFF, or JPEG files in 600 dpi and higher resolutions (1200 dpi is preferable) so that all details can be seen in the stage of examination of writing.

6.1. Figures

- Drawings and photos (except for the plates in the text) will be evaluated together as "Figure" and they must be numbered in the order they are mentioned in the text.
- The figures published in the *Bulletin of Mineral Research and Exploration* must be prepared in computer considering the dimensions of single-column width 7.4 m or double-column width 15.8 cm. Figure area together with the writing at the bottom should not exceed 15.8x21in maximum.
- Unnecessasry details must not be given in figures or care must be taken not to use much space for information transfer.
- Figures must be arranged in such a way to be printed in black/white or colored.
- The figure explanations being justified in two margins must be as follows:

  Figure 1- Sandıklı İlçesinin (Afyon); a) güneybatısının jeolojik haritası, b) İnceleme alanının genel dikme kesiti (Seymen 1981), c) Türkiye'nin önemli neotektonik yapıları (Koçyiğit 1994'den değiştirilerek).

  Figure 1- a) Sandıklı ilçesinin güneybatısının jeolojik haritası, b) İnceleme alanının genel dikme kesiti (Seymen 1981), c) Türkiye'nin önemli neotektonik yapıları (Koçyiğit 1994'den değiştirilerek).

- Drawings must be made by well-known computer programs painstakingly, neatly and cleanly.
- Using fine lines, which can disappear when figures shrinks, must be avoided. Symbols or letters used in all drawings must be in Times New Roman and not less than 2 mm in size when shrink.
- All standardized icons used in the drawings must be explained preferably in the drawing or with figure caption if they are too long.
- Linear scale must be used for all drawings. Author's name, figure description, figure number must not be included into the drawing.
- Photos must be in quality and quantity that will reflect the objectives of the subject.

6.2. Plates

- Plates must be used when needed a combination of more than one photo and the publication on a special quality paper.
- Plate sizes must be equal to the size of available magazine page space.
- Figure numbers and linear scale must be written under each of the shapes located on the Plate.
- The original plates must be added to the final copy, which will be submitted, if the article is accepted.
- Figures and plates must be independently numbered. Figures must be numbered in Latin numerals and plates with Roman numerals (e.g., Figure1, Plate I).

- There must be no description text on Figures.

6.3. Tables

- All tables must be prepared preferably in word format in Times New Roman fonts.
- Tables together with table top writing must not exceed 15x8 cm in size.
- The table explanations being justified in two margins must be as follows:

Table 1- Hydrogeochemical analysis results of geothermal waters in the study area.

7. Nomenclature and Abbreviations

- Non-standard and uncommon nomenclature abbreviations should be avoided in the text. But if essential, then they must be described as below. In cases where unusual nomenclatures and unstandardized abbreviations are considered to be compulsory, the way followed and method must be described.
- Full stop must not be placed between the initials of words for standardized abbreviations (MER, SHW, etc.).
- Geographical directions must be abbreviated in English language as follows: N, S, E, W, NE …etc.
- The first time used abbreviations in the text are presented in parenthesis, the parenthesis is not used for subsequent uses.
- The metric system must be used as units of measurement.
- Figure, plate and table names in the article must not be abbreviated. For example, "as shown in the generalized stratigraphic cross-section of the region (Figure 1……..."

7.1. Stratigraphic Terminology

Stratigraphic classifications and nomenclatures must be appropriate with the rules of International Commision on Stratigraphy and/or Turkish Stratigraphic Committee. The formation names, which have been accepted by International Commision on Stratigraphy and/or Turkey Stratigraphy Committee, should be used in the manuscript.

7.2. Paleontologic Terminology

Fossil names in phrases must be stated according to the following examples:

o For the use of authentic fossil names;

e.g. Limestone with *Nummulites*

o When the authentic fossil name is not used;

o e.g. nummulitic Limestone

o Other examples of use;

e.g. The type and species of Alveolina/ Alveolina type and species

- Taxonomic ranks must be made according to the following examples:

Super family: Alveolinacea Ehrenberg, 1939	*Not reference, Not stated in the Reference section*
Family: Borelidae Schmarda, 1871	
Type genus: *Borelis* de Montfort, 1808	
Type species: *Borelis melenoides de Montfort, 1808*; *Nautilus melo* Fitchel and Moll, 1789	
Borelis vonderschmitti (Schweighauser, 1951) (Plate, Figure, Figure in Body Text)	*Schweighauser, 1951 not reference*
1951 *Neoalveolina vonderschmitti* Schweighauser, page 468, figure 1-4	*Cited Scweighauser (1951), stated in the Reference section.*
1974 *Borelis vonderschmitti* (Schweighauser), Hottinger, page, 67, plate 98, figure 1.7	*Cited Hottinger (1974), stated in the Reference section.*

- The names of the fossils should be stated according to the rules given below:

  - o For the first use of the fossil names, the type, spieces and the author names must be fully indicated;

    Alveolina aragoensis Hottinger

    Alveolina cf. *aragoensis* Hottinger

    Alveolina aff. *aragoensis Hottinger*

  - o When a species is mentioned for the second time in the text;

    A.aragoensis

    *A.*cf.*aragoensis*

    *A.*aff.*aragoensis*

  - o It is accepted as citiation if stated as *Alveolina aragoensis* Hottinger (1966).

- The statement of plates and figures (especially for the articles of paleontology):

  - o for the statement of species mentioned in the body text;

  Borelis vonderschmitti (Schweighauser, 1951).

  (plate, figure, figure in the body text).

  - o When cited for other articles;

  1951 *Neoalveolina vonderschmitti* Schweighauser, page 468, figure 1-4, figure in body text

  1974 *Borelis vonderschmitti* (Schweighauser), Hottinger, page 67, plate 98, figure 1-7

- For the citation in the text

  (Schweighauser, 1951, page, plate, figure, figure in the body text)

  (Hottinger, 1974, page, plate, figure 67, plate 98, figure 1-7, figure in the body text.)

8. Citations

All citations in the body text must be indicated by the last name of the author(s) and the year of publication, respectively. The citations in the text must be given in following formats:

- For publications written by single author;

  - It is known that fold axes of Devonian and Carboniferious aged units around Istanbul is in NS direction (Ketin, 1953, 1956; Altınlı, 1999).

  - Altınlı (1972, 1976) defined the general characteristics of Bilecik sandstone in detail.

- For publications written by two authors;

  - The upper parts of the unit contain Ilerdian fossils (Sirel and Gündüz, 1976; Keskin and Turhan, 1987, 1989).

- For publications written by three or more authors;

  According to Caner et al. (1975) the Alıcı formation reflects the fluvial conditions.

  The unit disappears by wedging out in the East direction (Tokay et al., 1984).

- If reference is not directly obtained but can be found in another reference, the cross-reference should be given as follows:

  - It is known that Lebling has mentioned the existence of Lias around Çakraz (Lebling, 1932: from Charles, 1933).

9. Reprints

The author(s) will receive (2) two hard copies of the related issues.

10. Copyright and Conditions of Publication

- It is necessary that the work submitted for the publication must be original and has not been previously unpublished in whole or partially.

- It is necessarry that the authors who send their publications to the *Bulletin of Mineral Research and Exploration* hereby accept the conditions of publication of the Bulletin in advance.

- All copyrights of the accepted manuscripts belong to MTA. The author or corresponding author on behalf of all authors (for papers with multiple authors) must sign and give the agreement under the terms indicated by the Regulations of Executive Publication Committee. Upon acceptance of an article, MTA can pay royalty to the authors upon their request according to the terms under the "Regulations of Executive Publication Committe" and the "Regulations of Royalty Payment of Public Office and Institutions"

All the information and forms about the *Bulletin of Mineral Research and Explorations* can be obtained from **http://dergi.mta.gov.tr**